5101-238
Flat-Plate
Solar Array Project

DOE/JPL-1012-95
Distribution Categories UC-63b

Proceedings of the Flat-Plate Solar Array Project Research Forum on the High-Speed Growth and Characterization of Crystals for Solar Cells

(July 25, 26 and 27, 1983, at Port St. Lucie, Florida)

(NASA-CR-173746) PROCEEDINGS OF THE FLAT-PLATE SOLAR ARRAY PROJECT RESEARCH FORUM ON THE HIGH-SPEED GROWTH AND CHARACTERIZATION OF CRYSTALS FOR SOLAR CELLS (Jet Propulsion Lab.) 652 p HC A99/MF A01 G3/76
N84-28614
THRU
N84-28648
Unclas
19875

April 15, 1984

Prepared for
U.S. Department of Energy
Through an Agreement with
National Aeronautics and Space Administration
by
Jet Propulsion Laboratory
California Institute of Technology
Pasadena, California

JPL Publication 84-23

5101-238
Flat-Plate
Solar Array Project

DOE/JPL-1012-95
Distribution Categories UC-63b

Proceedings of the Flat-Plate Solar Array Project Research Forum on the High-Speed Growth and Characterization of Crystals for Solar Cells

(July 25, 26 and 27, 1983, at Port St. Lucie, Florida)

April 15, 1984

Prepared for
U.S. Department of Energy
Through an Agreement with
National Aeronautics and Space Administration
by
Jet Propulsion Laboratory
California Institute of Technology
Pasadena, California

JPL Publication 84-23

Prepared by the Jet Propulsion Laboratory, California Institute of Technology, for the U.S. Department of Energy through an agreement with the National Aeronautics and Space Administration.

The JPL Flat-Plate Solar Array Project is sponsored by the U.S. Department of Energy and is part of the Photovoltaic Energy Systems Program to initiate a major effort toward the development of cost-competitive solar arrays.

This publication reports on work done under NASA Task RE-152, Amendment 66, DOE / NASA IAA No. DE-AI01-76ET20356.

ABSTRACT

The High-Speed Growth and Characterization of Crystals for Solar Cells Research Forum was held on July 25-27, 1983, at the Sandpiper Bay Hotel in Port St. Lucie, Florida. The Research Forum was arranged into eight interactive sessions and addressed theoretical and experimental phenomena, applications, and characterization including stress/strain and other problem areas that limit the rate of growth of crystals suitable for processing into efficient, cost-effective solar cells. The Flat-Plate Solar Array Project of the Jet Propulsion Laboratory sponsored the meeting. Thirty-five invited papers were presented. Discussion periods followed each presentation. These Proceedings are a record of the papers and the discussions.

FOREWORD

The Research Forum on High-Speed Growth and Characterization of Crystals for Solar Cells was held at the Sandpiper Bay Hotel in Port St. Lucie, Florida, July 25 through 27, 1983. There were 68 participants, and 35 technical presentations were made. Meeting attendance was broad-based, as evidenced by the source breakdown of papers: 16 from industrial laboratories, 13 from universities, and 6 from government laboratories. The Forum was sponsored by the Flat-Plate Solar Array Project of the Jet Propulsion Laboratory.

The objectives of the Forum were to address theoretical and experimental phenomena, applications, characterization and all problem areas related to high-speed crystal growth, to define future areas of research, and to provide the opportunity for unrestricted technology exchange among those attending. The format used to achieve these objectives involved eight intensive sessions, consisting of four to five papers each, over the three-day period. Time for each paper was equally divided between presentation and discussion periods. This format provided a successful exchange of ideas.

This Proceedings document includes each speaker's manuscript and a transcript of the discussion period following each paper. Each of the manuscripts is printed, without changes, as received from the author. The discussion sections have been edited with the intent of enhancing the clarity and continuity of each discussion.

It is hoped that this Proceedings document will serve as a reference for the broad field of high-speed crystal growth.

Katherine A. Dumas
Proceedings Editor

RESEARCH FORUM ORGANIZING COMMITTEE

Katherine A Dumas	Co-Chairman
James K. Liu	Co-Chairman
Taher Daud	
Andrew Morrison	
Mary Phillips	Forum Coordinator

CONTENTS

SESSION I: OVERVIEW

K. Koliwad, Chairman

N84 28615

HIGH-SPEED GROWTH OF SILICON CRYSTALS: FLAT-PLATE SOLAR ARRAY PERSPECTIVE

K. M. Koliwad and A. R. Mokashi
Jet Propulsion Laboratory, California Institute of Technology
Pasadena, California

ABSTRACT

Silicon crystal growth continues to be an area of considerable technological and programmatic interest to the Flat-Plate Solar Array Project (FSA). Developing a low-cost crystal growth technology is critical to achieving the U.S. Department of Energy program goal of $0.70 per peak watt photovoltaic (PV) module technology. Silicon sheet is the centerpiece of the PV module. The shape and quality of the sheet as well as the growth process impose considerable requirements on the polysilicon material and on solar-cell and module fabrication. The cost of materials dominates the cost of PV modules; hence, the PV technology has to be based on unique material-conserving sheet-growth processes. The technology strategy of the Project is aimed primarily at developing that base. The direction of the development of sheet technologies pursued by the Project has been toward minimizing material use while achieving maximum throughput and higher sheet quality within the bounds of low-cost requirements. The objective of this paper is to put into perspective the significance of growth speed in meeting FSA goals. FSA technical goals are described and an analysis of the growth process parameters that influence the add-on price of the silicon sheet is presented.

INTRODUCTION

The cost of silicon sheet is a major barrier to achieving the goal of $0.70 per peak watt of energy from crystalline silicon photovoltaic (PV) modules, set by the National Photovoltaic Program of the U.S. Department of Energy (DOE). The Flat-Plate Solar Array Project (FSA), sponsored by DOE, has been supporting research in low-cost silicon sheet growth processes. The direction of that effort has been toward the development of material-conserving processes that are capable of achieving maximum throughput and higher sheet quality within the bounds of low-cost requirements. Silicon-ribbon growth processes have been the primary technologies assessed that have potential to meet DOE's goal of $0.70 per peak watt.

DOE's specific research objectives in this area have been to resolve generic impediments to the improvement of ribbon growth speed and quality (Reference 1.) These two aspects (ribbon growth speed and quality) are expected to play a major role in the achievement of the technology for $\$90/m^2$, 15% efficient crystalline silicon flat-plate modules. The objective of this paper is to put into perspective the significance of growth speed in meeting the cost goals, with specific reference to silicon ribbon technologies.

PRICE AND TECHNICAL GOALS

The overall price goal of $0.70 per peak watt for a flat-plate PV module is broken into add-on price goals for the various component elements that make up the module. Table 1 lists the various add-on price goals that FSA is striving to achieve (Reference 2.) The relative differences in add-on prices reflect the difficulties in achieving the technology required of those components. Given these price targets, analyses of the technologies have been carried out to arrive at technical goals. Table 2 lists the various technical goals that have to be met, for example, by the dendritic web (web) and Edge-Defined Film-Fed Growth (EFG) silicon-ribbon processes (Reference 2.) Web and EFG are cited as examples because of their maturity and their high potential for success. It should be noted that the technical goals are process-specific; for example, a lower growth rate for web takes into account its potential for higher solar-cell conversion efficiency.

SENSITIVITY ANALYSIS

Analytical studies (References 3 and 4) show that the add-on prices of ribbons are very sensitive to the key technical goal of throughput (area of ribbon produced per minute) that relates to the ribbon growth rate. Figure 1 shows the dependence of the add-on price of web on the growth rate. Other cost factors, such as duty cycle and labor, are parameterized. The data used for the base case referred to in Figure 1 are shown in Table 3. Figure 2 shows the effect on the add-on price of variations in cost parameters from the base case. Figures 3 and 4 depict similar analysis for EFG.

These results point strongly toward the growth rate in ribbon processes as a key technical barrier to achieving the cost goals; hence, research on growth-rate enhancement is of highest priority in the large-area silicon sheet development effort of FSA. The quality of the ribbon must be adequate for attainment of 15% efficient modules.

KEY TECHNICAL ISSUES

The technical issues in achieving high silicon-ribbon growth rates are nontrivial. This conference is expected to explore these issues in depth. The following are the general technical issues associated with throughput and quality.

Throughput:

High crystalline rate,
Thermal stresses,
Flatness

Quality:

Equilibrium crystal structure,
Impact of chemistry of growth environment,
Structural defects and purity,
Defect behavior control

ORIGINAL PAGE IS
OF POOR QUALITY

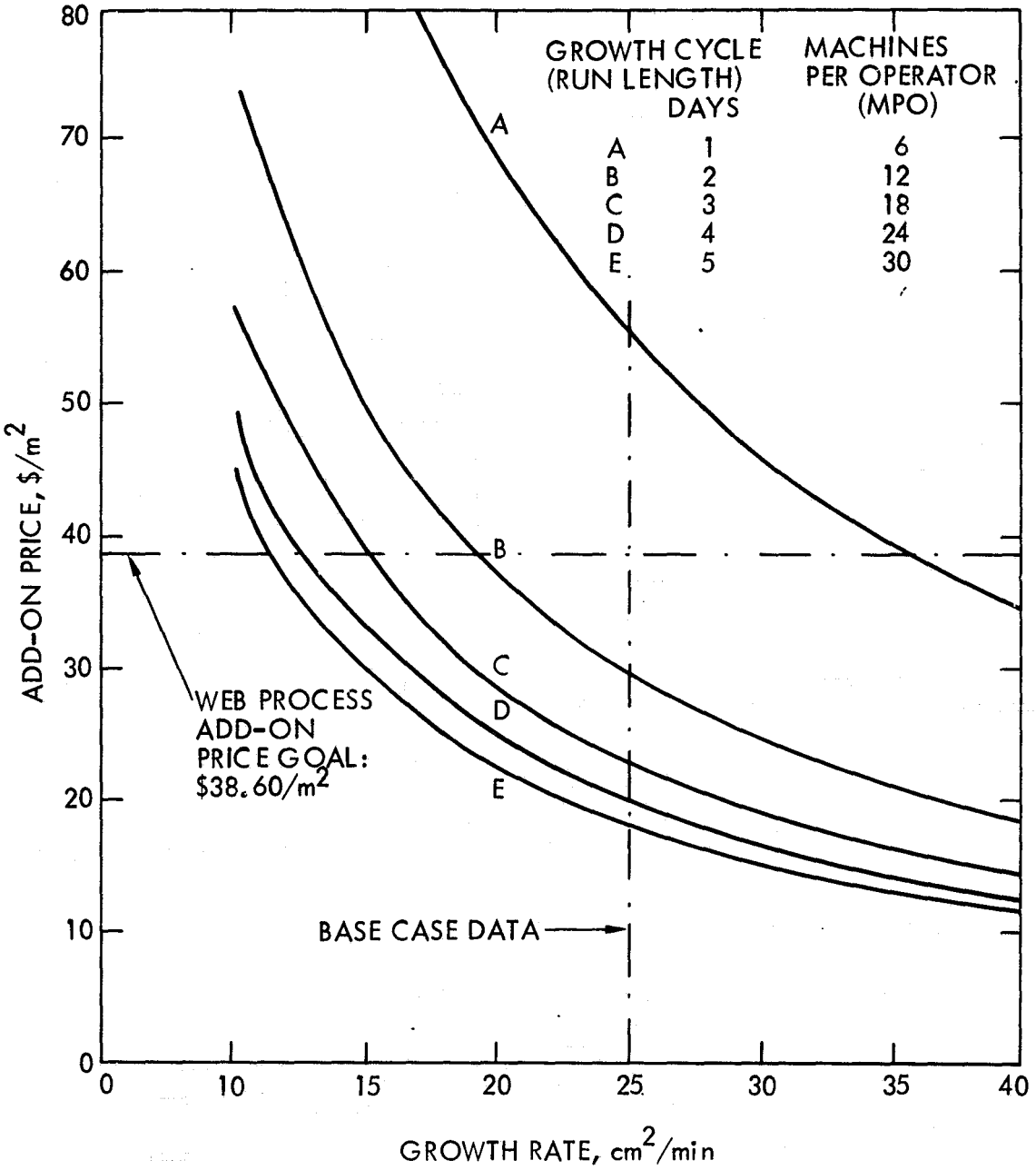

NOTE: BASE-CASE DATA REFER TO A PRODUCTION UNIT CONSISTING OF ONE FURNACE, GROWING ONE 5-cm-WIDE RIBBON AT A RATE OF 5 cm/min. IT IS ASSUMED THAT 18 SUCH FURNACES ARE OPERATED BY ONE PERSON

Figure 1. Add-on Price Sensitivity to Growth Rate of the Web Ribbon Growth Process

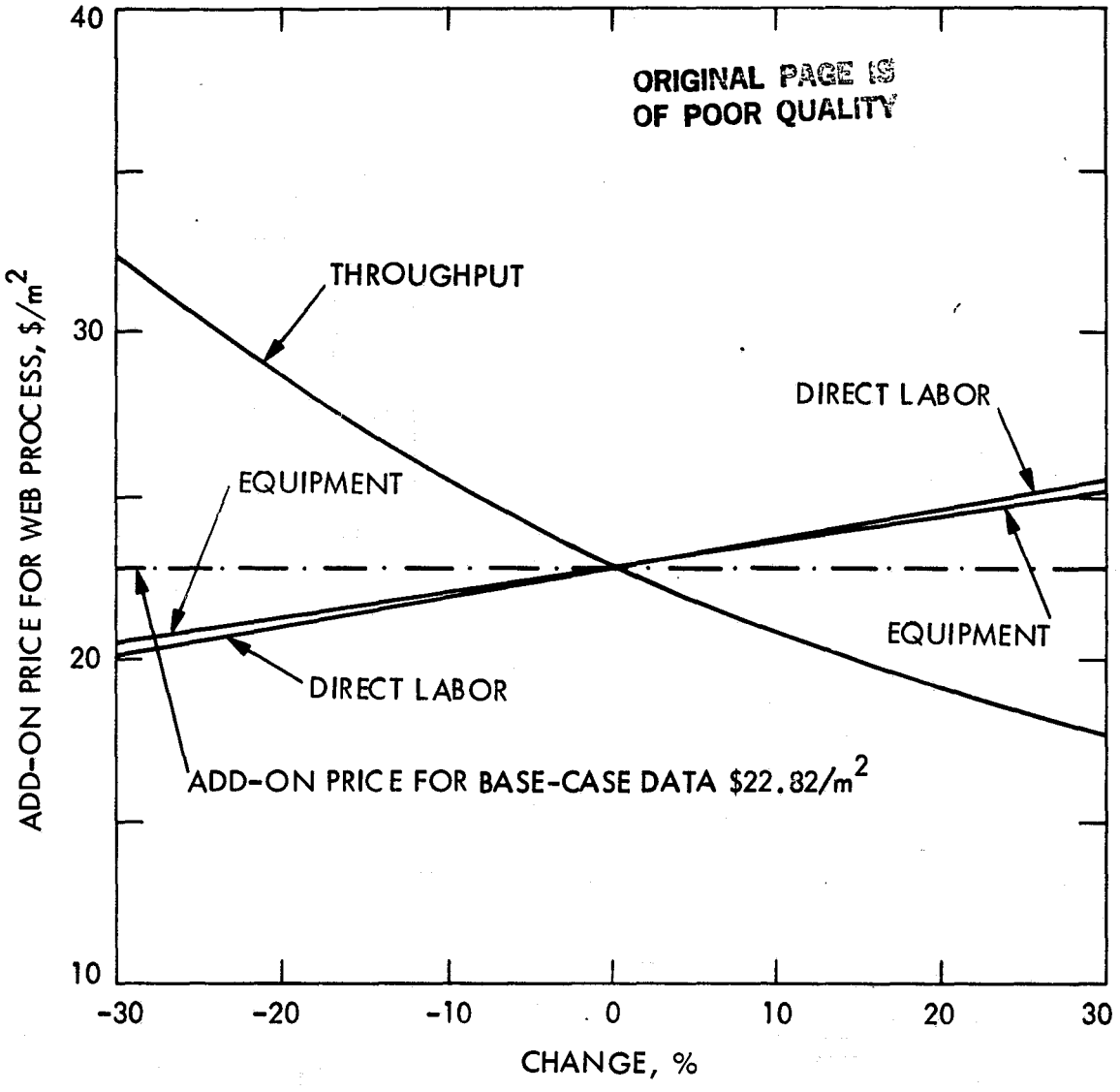

NOTE: BASE-CASE DATA REFER TO A PRODUCTION UNIT CONSISTING OF ONE FURNACE GROWING ONE 5-cm-WIDE RIBBON AT A RATE OF 5 cm/min. IT IS ASSUMED THAT 18 SUCH FURNACES ARE OPERATED BY ONE PERSON

Figure 2. Add-on Price Sensitivity to Throughput and Some Cost Parameters of the Web Ribbon Growth Process

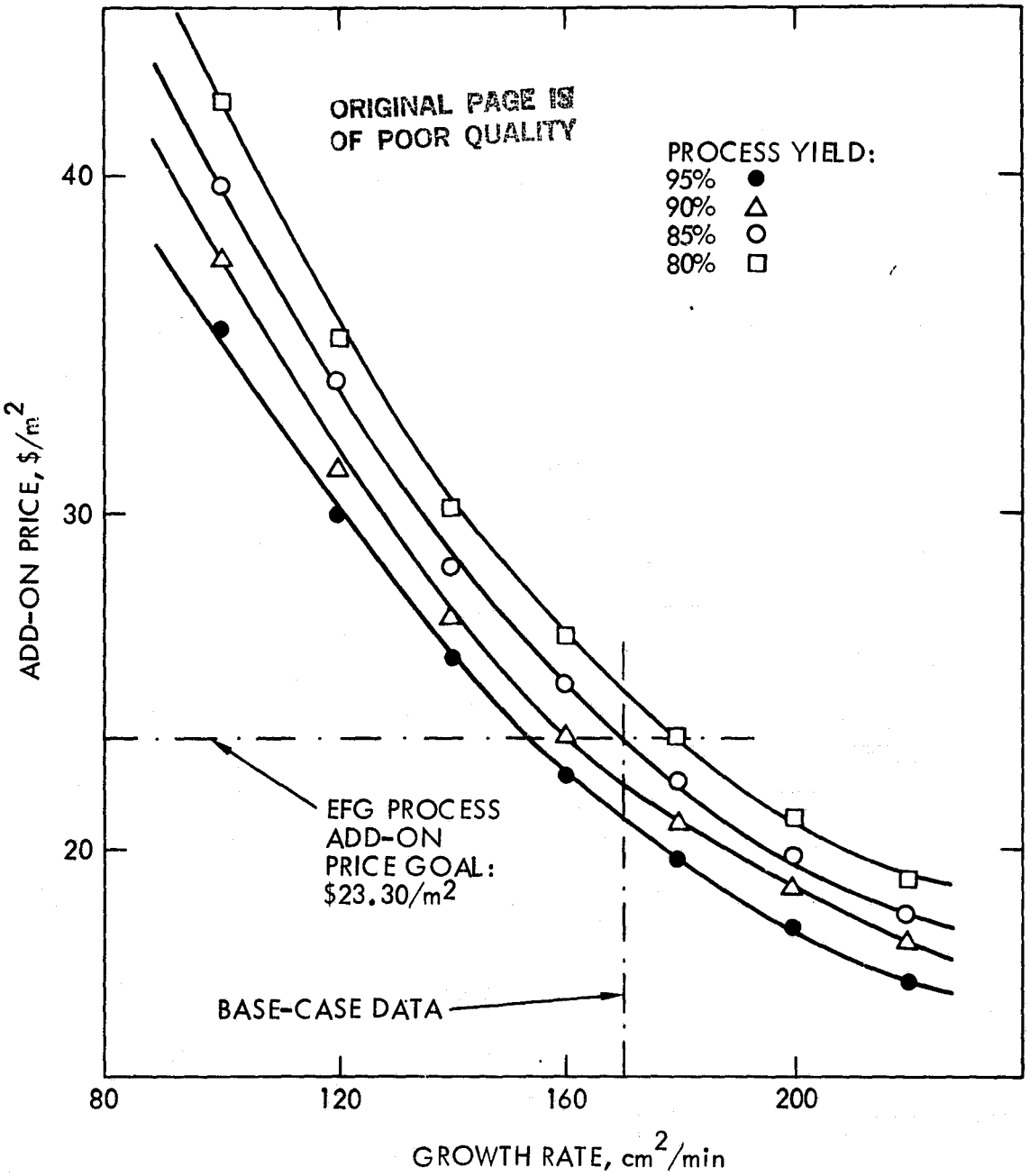

NOTE: BASE-CASE DATA REFER TO A PRODUCTION UNIT CONSISTING OF ONE FURNACE GROWING FOUR 10-cm-WIDE RIBBONS SIMULTANEOUSLY AT A RATE OF 4.25 cm/min. IT IS ASSUMED THAT THREE SUCH FURNACES ARE OPERATED BY ONE PERSON

Figure 3. Add-on Price Sensitivity to Growth Rate of the EFG Ribbon Growth Process

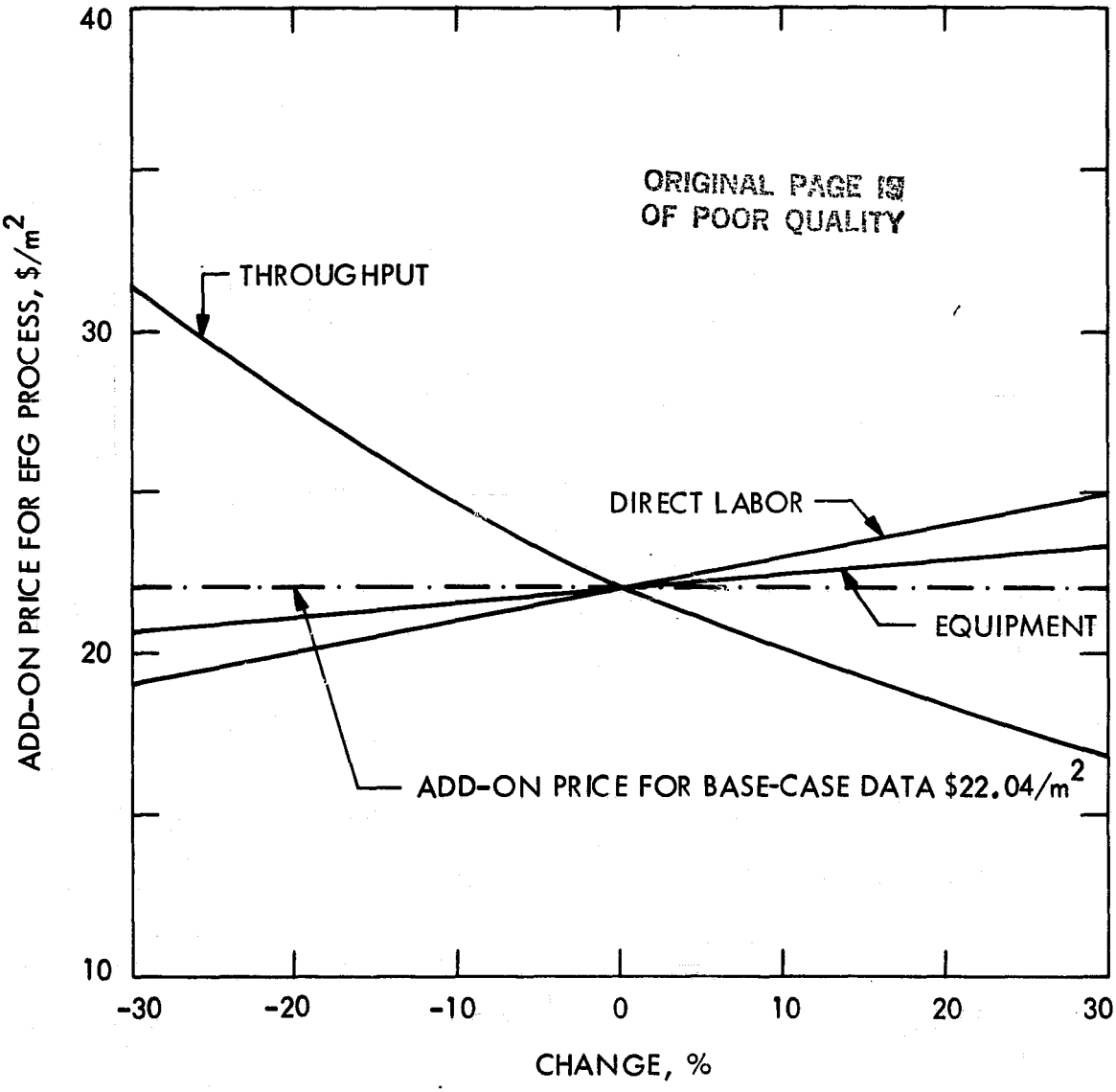

NOTE: BASE-CASE DATA REFER TO A PRODUCTION UNIT CONSISTING OF ONE FURNACE GROWING FOUR 10 CM WIDE RIBBONS SIMULTANEOUSLY AT A RATE OF 4.25 cm/min. IT IS ASSUMED THAT THREE SUCH FURNACES ARE OPERATED BY ONE PERSON

Figure 4. Add-on Price Sensitivity to Throughput and Some Cost Parameters of the EFG Ribbon Growth Process

Table 1. FSA Add-On Price Allocation Guidelines for Various Components of PV Modules Using Sheet Produced by EFG or Web Processes

Module Component	Guidelines
Silicon (polycrystalline)	$14/kg
Sheet Alternatives:	
EFG	$23.3/m^2 of wafer
Dendritic Web	$38.6/m^2 of wafer
Cell Fabrication	$21/m^2 of cells
Encapsulation Materials	$14/m^2 of module
Module Assembly	$14/m^2 of module

Table 2. Technical Goals to be Achieved by EFG and Web Processes

Parameter	Sheet Alternatives	
	EFG	Web
Encapsulated Cell Efficiency, %	12	14
Packing Efficiency, %	95	95
Module Efficiency, %	11.4	13.3
Sheet Thickness, mils	8	6
Silicon Mass Yield --Sheet Processing, %	80	80
Cell Yield, %	95	95
Module Yield, %	99.5	99.5

Table 3. Base-Case Data for Throughput Used for Sensitivity Analysis

Production Parameters	Sheet Alternatives EFG	Web
Number of Furnaces per Production Unit	1	1
Number of Ribbons per Furnace	4	1
Ribbon Width, cm	10	5
Growth Rate, cm/min	4.25	5
Run Length, h	160	72
Duty Cycle, %	90	90
Process Yield, %	90	100

NOTE: Remaining relevant base-case data for estimating add-on prices are given in References 3 and 4 for web and EFG processes respectively.

REFERENCES

1. National Photovoltaics Program Five Year Research Plan 1984-1988, U.S. Department of Energy, May 1983.

2. Aster, R. W., Price Allocation Guidelines, January 1980, JPL Publication 80-51, JPL Document No. 5101-68, Rev. A, Jet Propulsion Laboratory, Pasadena, California, January 15, 1980.

3. Mokashi, Anant R., Sensitivity Analysis of the Add-On Price Estimate for the Silicon Web Growth Process, JPL Publication 81-112, JPL Document No. 5101-175, Jet Propulsion Laboratory, Pasadena, California, December 15, 1981.

4. Mokashi, Anant R., and Kachare, A. H., Sensitivity Analysis of the Add-On Price Estimate for the Edge-Defined Film-Fed Growth Process, JPL Publication 81-37, JPL Document No. 5101-171, Jet Propulsion Laboratory, Pasadena, California, March 15, 1981.

DISCUSSION

RAVI: You mentioned a deadline, in your talk, for the currently supported technologies to mature and be commercially competitive by 1986. Why is there a fixed time limit? Why not 18 years?

KOLIWAD: Looking from a programmatic point of view, we have been supporting these programs for the last eight years and we see that the resolution of the problems and issues has to happen before what we, at that time, called achievement of these goals by 1986. We still want to maintain the rationale that was put forward at that time for achieving low-cost photovoltaics by 1986. We have reduced the thrust of the program towards very critical items. I am sure that most of the people are familiar with the original goals and why they were set to be in 1986. This is consistent still with that schedule. Of course now there is an urgency felt which was not present in 1974 when the goals were set. This is because there is a considerable amount of activity both from outside the United States and from the thin-films area. So we have to decide whether this technology is going to make it or break it, at least from a program point of view.

SUREK: One word that was not put up as a critical problem is yield. In both quality and rate it is very important that these rates be achieved, and that throughput and quality be achieved at rates exceeding 99% or so. Otherwise you really will not have a process, if you just demonstrate short periods of growth or one 20% cell.

KOLIWAD: The sensitivity of the yield is just as high as throughput. As a matter of fact, the curves were falling on each other, so I took one out. But the point is extremely important because one factor, given that everything else is perfect, will determine the cost of power. That, of course, is yield. All of this has to be more than just a laboratory 'one-time' feasibility study. We should be able to repeat it time and again.

SEIDENSTICKER: [Regarding a low-temperature EBIC viewgraph showing dislocations in web.] We have grown a lot of web that is very low-stress but I would be pretending if I did not comment that not all of the web we grow is very low-stress. The material does not look like what I have normally seen for a low-stress web. It has moderate stress that is quite adequate for device purposes but definitely not zero.

KOLIWAD: Yes. The point I was trying to make was that we should be aware of how we relieve the stresses because this may result in a significant amount of dislocation generation, and so on.

D2

IS THERE A SPEED LIMIT?

N84 28616

Bruce Chalmers

Harvard University
Cambridge, Massachusetts 02138

1. INTRODUCTION

My assignment is to discuss "fundamental barriers limiting the rate of growth of crystals suitable for processing into cost efficient effective solar cells". I will first review the physical conditions that permit the growth of sheet directly from the melt in order to identify the factors which control the speed of growth; I will then discuss the application of these criteria to various possible growth configurations, with specific reference to the effects that increase of speed has on those aspects of the resulting material that bear on the quality of the solar cells made from it. Finally, I will make some comments on what I see as the most useful directions for future research in this area.

2. PHYSICAL CONDITIONS GOVERNING GROWTH OF SHEET FROM THE MELT

Steady-state growth of sheet from the melt is possible only if three conditions are met. a) Thermal balance must be maintained. b) The meniscus that controls the crystal geometry must be in static equilibrium. c) The crystal geometry must be stable against operational fluctuations in temperature and pull speed.

a. Thermal Balance

The transformation of melt into crystal is accompanied by the release of the latent heat of fusion which, for silicon, is 4138 joule/cm^3. The rate at which the crystal grows is governed only by the rate at which the latent heat is removed from the solid-liquid interface. There are four ways in which heat can leave the interface: i) conduction, ii) radiation, iii) Peltier cooling, and iv) transport in the moving crystal.

i) Conduction. In principle, heat can be conducted away from the interface into the crystal and into the liquid. The heat flux is equal to the product of the temperature gradient and the thermal conductivity. For conduction to take place into the liquid, it is necessary for the liquid near the interface to be supercooled, a condition that is not conducive to the maintenance of a smooth, uniformly advancing interface, although a stable smooth interface may be attainable if the temperature gradient in the crystal is sufficiently large.

PRECEDING PAGE BLANK NOT FILMED

ii) Radiation. Solid silicon is transparent to that portion of the spectrum that lies below the band gap, which at the melting point is 0.6 eV. This corresponds to a wavelength of 2 μm. About two-thirds of the energy of the black body spectrum at 1685°K has wavelengths above 2 μm. It is estimated that, under ideal conditions, "light piping" could remove enough heat from the interface into the crystal to provide for growth at about 3 cm/min. However, the actual contribution of light piping is probably considerably less because of absorption and scattering in the imperfect and impure crystals we are concerned with. The liquid is not transparent at any wavelength.

iii) Peltier effect. When an electric current passes through the junction between two dissimilar conductors, heat is either absorbed or evolved, according to the characteristics of the materials and the direction of the current. In this sense, liquid and crystalline silicon are two dissimilar materials; latent heat can therefore be removed from the solid-liquid interface by means of a current. However, the current also causes joule heating of both the crystal and the liquid through which it must pass. Thus, the joule heating negates the effect of the Peltier cooling.

iv) Transport in the moving crystal. While some heat is carried away from the interface by the crystal as it moves, it is thought that this makes only a minor contribution to the overall removal of latent heat.

These four mechanisms remove latent heat from the interface where growth takes place and they therefore determine the growth rate (Fig. 1); however, for growth to continue at a uniform rate, the heat extracted from the interface must be continuously dissipated from the crystal and, when the liquid is supercooled, from the liquid (Fig. 2). Heat loss by the crystal occurs mainly by radiation, although conduction into a moving gas is also effective. In both cases, the heat must reach the surface by conduction from the interface. The amount of latent heat to be dissipated is proportional to the speed of growth and to the thickness, while the rate of loss from the surface at a given temperature is independent of the thickness. It follows that, for a given set of cooling conditions, a thinner ribbon will grow faster than a thicker one. To a first approximation, for a given radiative environment, the maximum possible rate of growth is inversely proportional to the square root of the thickness. It should be added that the actual rate of growth is, in some systems, less than the theoretical maximum because heat which is conducted through the liquid to the interface to stabilize the position of the interface must also be dissipated.

b. Capillary Equilibrium

Steady-state growth requires that the thickness remain constant so long as thermal balance is maintained. What happens when thermal balance is upset is discussed below under the heading of "stability". It has been established experimentally for the general case of silicon

growing from its melt that for the thickness to remain constant during growth, it is necessary for the liquid surface to make an angle of 169° to the surface of the crystal. This angle depends on two conditions: the restraint imposed on the meniscus at the end remote from the growing crystal, and the curvature of the meniscus surface that is required to balance any difference in pressure between that of the liquid and the ambient gas outside. The curvature is governed by the equation $\Delta P = \gamma(1/R_1 + 1/R_2)$ where ΔP is the pressure difference, γ is the surface tension and R_1 and R_2 are the principal radii of curvature of the surface. R_1 is the radius of curvature in the vertical plane, and R_2 is the radius in the orthogonal direction. R_2 is infinite for the sides of a flat ribbon; for the edges R_2 is related to the radius of the edge (Fig. 3). The way in which these criteria are met in the various sheet growth configurations is discussed later.

c. Stability

The question of stability revolves around what happens if steady-state growth conditions (i.e., speed or temperature) are temporarily perturbed. Does growth revert to its previous steady-state condition, or is growth terminated? This is in fact a quantitative question; how much temporary departure (in terms of extent and of time) can be tolerated? The answer to this question tells us how close the control must be, and, therefore, whether a proposed set of conditions is conducive to routine growth. A second, closely associated, question is how much variation of growth conditions is permissible if the thickness and the width of the sheet are to remain within specified limits. In the context of the present discussion, an important issue is how the stability is affected by increasing the speed of growth. While it can be said here that most of the configurations to be considered have inherent stability, the effect of speed must be discussed in relation to each specific case; in this sense, "inherent stability" means that steady-state growth is possible over a useful range of conditions around those selected as optimum. "Steady state" implies that the rate of advance of the interface (growth rate) is equal to the "pull rate". If the pull rate is changed, the growth rate is, for the time being, still governed by the pre-existing thermal conditions, and is therefore unchanged. The two speeds no longer match and the interface moves to a new position. For example, if the "pull speed" is suddenly decreased, the interface moves towards the liquid, and vice versa. Exactly similar effects result from a change in the temperature of the liquid. If the temperature of the liquid is lowered, less heat is conducted to the interface (or more from it) in the liquid. More latent heat is required to maintain the heat balance and the growth rate therefore increases. In a stable system, this imbalance is self-correcting, and steady-state resumes with a different sheet thickness. These considerations apply to the faces of the sheet and, therefore, to its thickness. The edges are subject to somewhat different constraints; if they are defined by a meniscus, the constraints are much more restrictive, but there are alternatives; either to have no edges or to use solid edges.

3. CHARACTERISTICS OF SHEET MATERIAL

I have so far discussed the conditions under which sheet can be grown. It is abundantly evident that no one, so far, has been able to grow sheet silicon that even remotely approaches the ideal stress free, defect free single crystal that is flat, smooth, of uniform thickness and pure except for a uniform concentration of a dopant. However, effective solar cells can be made from material that departs substantially from these criteria. But the extent of these departures must be kept within limits, either in order that cells can be made, or in order that they will have cost effective properties.

I advance the hypothesis, for discussion, that any strategy that is adopted to increase the linear speed of growth will invoke a penalty in relation to one or more of these properties. The maximum useful growth speed will, therefore, be a trade-off between the reduced cost associated with higher speed and the resulting degraded properties.

We must next, therefore, examine the causes for these departures from the ideal, and determine how they are affected by the speed of growth. These problems fall into four categories: A) effects associated with thermal stress, B) imperfections, C) impurity effects, and D) geometrical problems.

A. Thermal Stress

I address this question first because its solution determines whether cells can be made at all, rather than the properties of the cell if it can be made. Stress arises during the cooling of an object if the rates of cooling are unequal in different parts of the material. In the case of a sheet growing from the melt, the temperature gradient in the solid at the interface must be sufficient to remove the latent heat of fusion, and it is zero in that part of the material that has reached room temperature. When these stresses exist at very high temperatures, they may be relieved by relaxation (creep) processes; these are essentially time dependent. It follows that less stress relief will occur at high growth rates than at low growth rates if other conditions are constant. If insufficient stress relief occurs, the sheet may buckle, or it may contain residual stresses, or both. As might be expected, it is found that if buckling occurs under a given set of growth conditions, it can be prevented by a reduction in speed; it is also true that buckling and residual stress problems can be mitigated by adjusting the temperature profile through which the sheet cools to allow relaxation to take precedence over buckling, and to allow the stress to "anneal out" during cooling. However, it should be recognized that stress relaxation takes place by the generation and movement of point defects and dislocations, and that the level of imperfection of the crystal increases with the amount of relaxation and therefore of the amount of stress that has been relieved by relaxation. It follows that the level of imperfection increases with the stress that would have been present if no relaxation

had occurred. It is relatively easy to calculate the thermal stresses in the purely elastic (i.e., no relaxation) case.

B. Imperfections

All the imperfections found in sheet silicon can be divided into two categories: those that originate at the solid-liquid interface as disturbances to the orderly growth of the crystal by the process of each atom from the liquid attaching itself to a site in which it becomes part of the crystal, and those that originate later as a result of stress, precipitation or diffusion. It may be reasonable to assume that those imperfections that arise at the interface or as a result of stress will be aggravated by increasing the speed, while those that depend on diffusion processes may be reduced. I will not attempt to categorize all the many types of imperfections, or to predict in any detail what the effect of growth speed should be; but it is evident that increased speed is likely to be detrimental to the perfection of the material, and therefore to its properties.

C. Impurities

It must be assumed that the liquid from which the sheet is grown is impure; it will contain those residual impurities that are present in the silicon that is used, any impurities that arise from crucible, die and ambient atmosphere, and (from a chemical but not an electrical point of view) the dopant. It has been customary to assume that one of the differences between die-grown sheet and Czochralski (CZ) material is that the effective distribution coefficient for impurities is unity for sheet and, for most impurities, much smaller for CZ; that is to say, die-grown sheet has the same impurity content as the liquid, while CZ is much purer. This is true only in a very limited sense, for the following reasons.

The redistribution of impurities during solidification depends on the well-established fact that a new crystal grows with each solute having a concentration that bears a specific ratio to the concentration of that solute in the liquid immediately adjacent to the growth interface. This ratio is to a very good approximation the equilibrium distribution coefficient k_o. For most solutes in silicon, this ratio is less than unity, ranging from 0.8 for boron to 10^{-5} or less for metallic impurities; this means that the new crystal that is growing at any instant contains less solute than the liquid in contact with the growth interface. Solute is therefore rejected into the liquid, where it is redistributed by diffusion and, in some cases, by convective motion of the liquid. The simplest case is that in which the rejected solute moves into the liquid by diffusion alone. In this situation, the crystal starts to grow with a solute concentration that is lower than that in the liquid by a factor of k_o. As growth proceeds, rejected solute gradually "piles up" just ahead of the advancing interface, and the solute concentration in the growing crystal increases (Fig. 4). This continues until the steady state is reached in which the concentration in the crystal is equal to that in the undisturbed liquid (Fig. 5). This is what is assumed to happen in a

crystal growing from a meniscus of limited depth. However, one important feature of this sequence of events has been largely ignored; this is that steady state is not immediately achieved and in some cases is approached so slowly that in practice it is never reached. The important characteristic of this initial transient is how much crystal can be grown before steady state is effectively reached; this is the extent d of the transient (Fig. 6), given by the formula $d = D/k_o R$ where D is the diffusion coefficient of the relevant solute in the liquid, k_o is as defined above and R is the rate of growth of the crystal. Assuming the reasonable value of $D = 5 \times 10^{-4}$ cm^2 sec^{-1}, we find the values of d shown in Table I.

This means that for elements with low values of k_o, such as titanium and iron, and, especially at low speeds, a very substantial amount of material can be grown before the steady-state condition is even approached;the crystal is substantially purer, in terms of the most detrimental impurities, than the liquid. These numbers must be used with caution, because the formula is based on the assumption that the interface is planar and normal to the growth direction; curvature or inclination of the interface will modify the result in some, if not all, configurations. The assumption of redistribution of solute by diffusion alone is not always valid, because convective motion of the liquid may be superimposed on the diffusion process. This occurs only if the hydrodynamically stagnant boundary layer is thinner than the diffusion layer. The thickness of the diffusion boundary layer (δ) is given by $\delta = D/R$. Values of δ as a function of R are shown in Table II for a diffusion coefficient D of 5×10^{-4} cm^2 sec^{-1}. For low speeds of growth, the thickness of the hydrodynamic boundary layer is likely to be less than that of the diffusion layer; this increases the rate at which solutes are removed from the vicinity of the interface, and increases the purity of the resulting crystal. An extreme case is that of Czochralski growth, in which convection is greatly enhanced by rotation and growth is, in the current context, very slow. However, the values for the thickness δ of the diffusion layer are valid only when steady state has been reached; as noted above, the most significant impurities approach steady state very gradually, and the thickness of the boundary layer approaches its steady-state value equally gradually. It follows that while solutes with values of k_o close to unity, such as boron and carbon, will quickly reach their steady state distribution, which is governed by the relative thicknesses of the diffusion and the convectional boundary layers, the solutes with very low distribution coefficients will, for very long periods of growth, have very thin diffusion zones, with very low concentrations at the interface, so that steady state inferences are completely invalid.

If the initial transient is an important factor in achieving higher purity than would be expected from the k = 1 concept, it may be found that continuous growth at steady state is not the optimum strategy for high electrical quality. It is apparent, also, that if the initial transient is useful as a purification tactic, there is a penalty for increasing the growth speed, as the length of the transient is inversely proportional to

the growth speed.

All the foregoing comments on the distribution of solute are based on the assumption that the interface is planar and perpendicular to the pull direction. This assumption is seldom, if ever, completely valid. In most, if not all cases, the interface as a whole is curved in the "through the thickness" direction. It is usually concave to the liquid, and either accidentally or deliberately inclined, and in some cases there is dendritic growth, in which the departures from flatness of the interface are extreme and localized. In such cases the solute distribution will be very far from uniform and far from ideal. Under these circumstances, the simple "planar, perpendicular" analysis must be modified, but, again, transient effects may be much more significant than the steady state.

There is one further assumption built into the foregoing discussion of solute segregation; this is that there is no formation of solid phases other than silicon. This is not necessarily true, because the liquid adjacent to the interface would, at steady state, contain C_o/k_o of each solute that is present. In a typical case (for EFG) the amounts of various solutes and the corresponding values of k_o and C_o/k_o are given in the Table III. It is clearly impossible that the liquid at the interface should contain less than 50 percent of silicon; it follows that particles of foreign phases must form in the liquid long before steady state is reached, at least in those conditions in which the diffusion layer is too thin to be appreciably disturbed by convection; i.e., at high speeds of growth.

I have discussed imperfections and solutes as two unrelated problems; but they may interact in the sense that impurity segregation may aggravate the defects. If the interface is concave to the liquid, as is necessarily the case for some configurations, the solutes tend to be concentrated towards the center plane of the sheet, or to one side or the other if the interface is tilted. The resulting increased concentration causes depression of the liquidus temperature which in turn increases the local curvature of the interface; this can lead to the formation of grains in the interior of the ribbon, an effect which has been found to be detrimental to the electrical characteristics of the material. The heat flow equations dictate that if increased speed is achieved by increasing the heat extraction from the sheet, increased curvature of the interface must result; thus again, conditions that are conducive to higher speed may be detrimental to cell quality. If, however, higher speed is achieved by decreasing the thickness of the sheet, this consideration does not apply, and in any case, thinner sheet is less subject than thicker sheet to the "center grain" problem.

D. Geometrical Problems

To be useful, sheet must be of reasonably uniform thickness, of uniform width and it must be smooth enough to be suitable for cell making by a simple, inexpensive process. Different growth configurations have their own specific problems in these areas; it is convenient to discuss

them in relation to the details of the method used for controlling the shape.

4. APPLICATION OF THE PRINCIPLES TO SPECIFIC SHEET GROWTH CONFIGURATIONS

Any growth configuration that simultaneously satisfies the thermal balance, capillary equilibrium and stability conditions can be used for the growth of sheet material; the various techniques can be classified according to the ways in which the criteria are met.

There are three basic ways in which thermal balance can be achieved; the latent heat can be removed from the interface, where it is generated, by conduction parallel to the axis of the crystal; this subdivides into the case in which conduction is away from the interface into the crystal only and that in which part of the latent heat is conducted into the liquid. In both these cases, the interface is essentially perpendicular to the axis of the ribbon. The other category is that in which the latent heat is removed from the interface by conduction in a direction that is substantially inclined to the axis of the ribbon. These three configurations are shown diagramatically in Fig. 7, a, b, and c. Capillary equilibrium must be maintained along the faces and at the edges. Along the faces, the position of the meniscus may be defined by a die, or the meniscus may merge into the free surface of the liquid. At the edges, there are three possibilities; a) the meniscus may be defined by a die, b) the edges may be integral with solid components that move with the crystal;the solid components can be dendrites that grow in advance of the ribbon interface or they can be fibers of some other material which is wetted by liquid silicon and to which the edge of the ribbon adheres, or c) a closed shape can be used, in which case there are no edges (Fig. 8).

The crystal growth configurations to be considered are A) EFG, B) free meniscus, Bi) web, Bii) edge supported growth, C) inclined interface growth. The various configurations are classified in Table IV according to the ways in which the two criteria are met.

A. Edge Defined Film Fed Growth (EFG)

In EFG, the lower extremity of the meniscus is everywhere defined by the edge of the die. Capillary equilibrium requires that the angle between the meniscus and the die top exceeds 30°, and steady-state growth requires that the meniscus makes an angle of 169° to the ribbon surface. The maximum meniscus height for an edge is much less than for a flat surface, and three options are therefore available; either the ribbon is grown with sufficiently precise control to maintain the meniscus height at the edges within the permissible limits, or the ribbon is grown with its edges substantially thicker than the remainder, or edgeless or closed shape growth is used.

All of these configurations can be used for growth of sheet material. The ribbon options have the advantage that continuous growth is possible,

but they have the disadvantage that the meniscus cannot be maintained at the desirable uniform high level across the whole of the width. Closed shape growth is inherently intermittent because a tube does not share the property of a ribbon of being flexible and coilable, but the much less stringent meniscus height condition allows the control technique to be much simpler for closed shapes than for ribbon. The thickness of the sheet can be controlled by observing the meniscus height and maintaining it at the desired value by adjusting either the temperature or the growth speed.

In EFG, the heat balance is established by equating the latent heat plus heat conducted to the interface by the liquid with heat leaving the interface by conduction, radiation and convective transport; the sum of these must equal the heat dissipated by the ribbon into its surroundings. If heat loss from the ribbon surface is entirely by radiation, the maximum possible speed is found to be related to thickness as shown in Fig. 9. These speeds could be reached only if a) the total radiation environment of the ribbon were $0^{o}K$ and b) no heat reached the interface by conduction in the liquid. In regard to the former condition, it makes little difference if the radiation environment is at $300^{o}K$ (room temperature) instead of $0^{o}K$; but the stresses developed if free radiation is allowed are so high that, except for extremely narrow ribbon, fracture would occur. The second problem is that the position of the interface would be completely unstable if there were zero temperature gradient in the liquid. Therefore, two major modifications are needed: the temperature profile must be modified to eliminate buckling and to reduce the residual stress to an acceptable level, and a positive temperature gradient must be maintained in the liquid; this decreases the amount of latent heat that can be removed. Both of these requirements reduce the maximum speed of growth.

Completely stress free growth would be possible only if the initial temperature gradient (corrected for change in expansion coefficient) could be maintained down to a temperature at which no creep or plastic relaxation occurs, and then approaching and reaching room temperature by decreasing the gradient gradually enough to avoid catastrophically high stresses. At useful speeds of growth (for example 2.5 cm/min) and with a 200°/cm gradient in the liquid, the initial gradient in the crystal would be about 1300°/cm (at 5 cm/min, it would be 2100°/cm). It is not possible to maintain a gradient of 1300°/cm from $1410^{o}C$ to $600^{o}C$ (i.e., for 6 mm) and then to "level off" to room temperature depending only by radiation. The rate of change of gradient, further, would be so high that the material could not possibly emerge intact. It is therefore necessary to reduce the rate of change of temperature gradient by means of an afterheater; a strategy that has been successful is to decrease the gradient rapidly in the temperature range in which creep and recovery can keep pace with the stress building action of the change of gradient, then to maintain a constant temperature gradient until the temperature has reached the non-plastic regime. This is the "linear afterheater" strategy (Fig. 10a).

The maximum speed that can be reached may be limited either by thermal or by stress considerations. If the gradient at the interface is reduced sufficiently for the ribbon to enter the linear regime at the required temperature, the rate of growth is limited by the rate of extraction of latent heat; it is necessary also for there to be sufficient time for the stresses to relax while the temperature is still high enough for relaxation to take place. If the limitation is thermal, the ribbon simply will not grow at a higher speed; if it is stress, the strip is buckled if it is grown too fast. The highest speed attainable in this way is about 3 cm/min (0.05 cm/sec) for a 0.03 cm ribbon. An alternative procedure is to cool the ribbon very rapidly by means of a "cold shoe" with or without forced gas cooling and then to re-heat it so that the stress can relax before it enters the linear regime (Fig. 10b). In this way, speeds of up to 0.085 cm/sec (5 cm/min) have been reached.

While thermal conditions allow thinner ribbons to be grown at higher speeds than thicker ones, the reverse may be true for stress, because the critical stress for buckling is proportional to the square of the thickness.

Some increase in speed can be achieved by decreasing the amount of heat reaching the interface by conduction in the liquid; the same thermal conditions exist above the interface if the latent heat is increased (by increasing the speed) to compensate for the decreased flux from the liquid. The disadvantage is that stability is decreased as the temperature gradient in the liquid is reduced; the interface position fluctuates more for a given change in speed or temperature. This can be critical at the edges (when there are any), because the meniscus is necessarily low there. There are two penalties that detract from the quality of the material as the speed is increased. In the first place, the increased initial gradient means that the rate of change of gradient around the point D in Fig. 10 must be greater than for the slower growth case. This leads to increased crystal imperfection because more relaxation is required. A second, and perhaps more serious problem, is that the increased rate of heat extraction causes an increase in the curvature of the interface, resulting in degradation of the structure of the material in the center of the ribbon.

It therefore appears likely that no really drastic increase in the linear speed of growth in EFG will be attainable without unacceptable penalties; a modest increase might be achieved by a combination of thinner ribbon, reduced gradient in the liquid and the use of transverse temperature gradients. But I do not expect useful material to be grown by EFG at linear speeds in excess of 5 cm/minute. This limitation exists because an essential feature of EFG is that the initial longitudinal (i.e., vertical) temperature gradient is inextricably coupled with the growth speed.

B. Free Meniscus Growth

In principle it is not necessary for the lower edge of the meniscus to be controlled except at the edges of a ribbon or the corners of a closed shape; web growth and edge supported growth are examples in which only the edges are restrained. The thermal and stress conditions are, in principle, no different in free meniscus growth from those discussed above for EFG. The speed limitations are, therefore, quite similar. In these cases, the meniscus merges into the free surface of the liquid. For steady-state growth, the interface must be at about 7 mm above the liquid level, since that is the level at which the meniscus surface makes the required 169° angle with the ribbon surface. It is therefore not possible to use the meniscus height as a measure of the thickness when the meniscus is free.

In web growth the liquid in the vicinity of the edges must be supercooled to maintain growth of the edge dendrites; the liquid from which the web itself grows can be supercooled at most to a very limited extent, because otherwise dendritic growth would occur in preference to web growth. I think that it is most unlikely that the temperature gradient into the liquid exceeds 20°/cm, which would contribute about 0.2 cm per minute to the growth rate, or could be used to reduce the gradient required in the ribbon for a fixed growth rate by about 60°/cm. It follows that web growth may have a minor, but will not have a major, speed advantage over EFG. In edge supported growth, a moving fiber supports the edge of the ribbon. In this case the melt is maintained throughout above the melting point, so that some heat is conducted to the interface by the liquid.

A major difference between EFG (and other techniques in which a die is used), and both the web and the edge supported techniques is that in the latter, the meniscus is not separated from the bulk liquid, as it is by a die. The solute rejected into the liquid at the interface can, therefore, mix with the bulk liquid and it might be expected that more effective purification of the crystal (by rejection of solute during solidification) would be obtained. It is true that the value of k_{EFF} calculated for this configuration is far lower than the $k_{EFF} = 1$ assumed for EFG. However, the calculation applies to k_{EFF} when steady state has been reached. It is open to question whether these calculations are any more valid than the assumption that $k_{EFF} = 1$ for EFG, in view of the very long initial transients for the low k_o impurities and therefore the very gradual increase in thickness of the diffusion layer for these solutes.

C. Inclined Interface Growth

The remaining option is to depart from the condition that the interface is essentially perpendicular to the growth direction. This is exemplified in horizontal growth or low angle growth. In this configuration (Fig. 11), the heat of fusion and the heat conducted from the liquid are dissipated largely from the upper surface. The actual rate of growth (perpendicular to the interface) is small compared with the pull

rate. The ratio of the speeds is equal to sin θ. θ can be quite small. It is possible to grow ribbon at very high rates, such as 80 cm/min, by using this configuration; this may not be the limit, as in principle it is possible to make the angle θ as small as desired. Thermal stress is no longer a problem of the same magnitude as with theoretical growth configurations, because the temperature gradient from A to B can be made small and uniform until the elastic range is reached. Some stress may exist around A because of a change of longitudinal gradient, but this occurs only at a temperature very close to the melting point. In principle, it would be possible to eliminate stress entirely by adjusting the longitudinal gradient in AB to the same value as the longitudinal gradient in AC.

A second potential advantage of this configuration is impurity segregation away from the upper surface towards the lower surface. Part of this segregation may be negated by diffusion during cooling (especially if this is very slow), but the upper surface and the material closest to it should be substantially purer than the material close to the lower surface.

The above remarks depend on the assumption that the "leading edge" A advances uniformly with respect to the liquid. However, it must be noted that while the interface CD advances relatively slowly, the crystal at C grows to the left at a rate equal to the rate of growth of the ribbon; i.e., up to 80 cm/min. In order to achieve such speeds of growth, it is necessary for the liquid adjacent to the tip to be supercooled. The major part of the latent heat must be extracted into the liquid; in order to extract it through the solid, a temperature gradient in the crystal at the interface would have to be of the order of 25,000 degrees per centimeter. The tip must be a cylinder of small radius that loses heat primarily by conduction outwards into the liquid. The configuration at the tip is shown in Fig. 11; the radius of the tip depends on the speed; for high speeds it is probably less than a micron. While it has been demonstrated that it is possible to supercool the liquid sufficiently to propagate the tip at more than 1 cm/second, supercooling of the liquid by two or three degrees would be required. This produces instability of the cylindrical leading edge, which causes the edge to advance as a series of dendritic spikes, with the interdendritic spaces "filling in" subsequently (Fig. 12). As a result, the upper surface will have a series of ridges and the solute segregation will be towards the interdendritic region rather than towards the lower surface. Thus, the material grown at very high speed may not be as suitable for cell making as ribbon grown in the other configurations, even though there is no stress in it. There may be a maximum speed at which inclined interface growth can be achieved without the leading edge becoming dendritic; this should be amenable to theoretical as well as experimental study.

The solute distribution resulting from inclined interface growth should be very favorable if dendritic growth is avoided. The total "growth distance" is approximately the ribbon thickness. The "diffusion layer", therefore, will have only about 0.025 cm of growth in which to

establish itself; all the solute that is excluded from the crystal must either remain in the crystal near D (Fig. 11) or be swept away by the relative motion of the interface and the liquid. The diffusion layer, however, will be quite thin for the more critical solutes. If a slope of 1 to 50 ($\theta = 1^{o}$) is assumed, the thickness of the diffusion layer will have reached the following values for solutes of interest;

Boron	Carbon	Aluminum	Titanium	Iron
0.02 cm	0.002 cm	$5x10^{-5}$ cm	$2.5x10^{-4}$ cm	$2x10^{-4}$ cm

These values are independent of growth speed. This indicates that, with the exception of boron, the solute distribution will be unaffected by relative motion of the growing crystal and the liquid. It also means that the segregated solute will be largely concentrated in an extremely thin layer at the lower surface. The concentration at the upper surface ($k_o C_o$) would be (for a liquid whose composition is typical of EFG material);

	Boron	Carbon	Aluminum	Titanium	Iron
C_o (ppm)	0.02	1.5	2.2	0.3	1.1
$k_o C_o$ (ppm)	0.02	0.12	$4.4x10^{-3}$	$3x10^{-6}$	$9x10^{-6}$

It has been estimated that the effect of diffusion during cooling will be small for those elements with diffusion coefficients in solid silicon of 10^{-5} or less in the $1300^{o}K$ to $1600^{o}K$ range. This includes Al, Cr, C, Fe among others. However, for copper, for which D is about 10^{-4} cm^2 sec^{-1} at $1400^{o}K$, the segregation produced during solidification will largely disappear during cooling.

These estimates, it must be emphasized, are valid only if the interface is essentially flat; i.e., is not dendritic in nature. If it is dendritic, as noted above, the segregation pattern will be largely transverse and should not be conducive to good cell performance.

The control of thickness in inclined interface growth also presents problems. The thickness depends on four parameters; pull speed, temperature of liquid, extent of cooling and distance between the leading and the trailing edge. There is no readily observed indication (such as meniscus height in EFG) of thickness, and the problem of developing a feedback loop for automatic thickness control is therefore not trivial.

5. CONCLUSIONS

To summarize these considerations, it is apparent that any increase of speed leads to some degradation of quality; if growth is vertical (interface perpendicular to the ribbon length), higher speed leads to either buckling or increased residual stress or more defective crystallinity and to a less favorable distribution of solutes; if growth

is horizontal (interface inclined to growth direction), high speed leads to degraded surface topography and to undesirable transverse segregation of solutes. The problem therefore is to select the configuration that gives the highest speed that is compatible with acceptable quality.

In addressing the problem of optimizing the growth conditions, it is necessary to examine what is meant by "speed of growth". In the foregoing remarks, I have taken "speed" to mean linear speed (cm/sec); but it could be argued that this is irrelevant and that we should really define speed as either a) area per machine hour or b) area per operator hour. Some combination of these two parameters with the actual duty cycle achievable and the cost of consumables leads to a third, c) area per dollar. And this must be combined with cell making costs and the resulting efficiency to give the "bottom line", d) peak watts per dollar. It may well be found that it is better to increase the width of a ribbon or the total width of ribbon growing from a machine than the speed; multiple ribbons and closed shapes are examples of increased width; and it may be found that a group of very simple "slow" single ribbon machines have economic advantages over very complicated, faster multiple ribbon machines; and discontinuous growth may have advantages over continuous growth because of transient effects.

It is clear that there are a number of areas in which more information is needed. We need a better understanding of the stress problem; in particular, we do not have adequate quantitative data on the deformation and stress relaxation of silicon at very high temperatures to be able to make proper use of the computer model that has been developed to predict buckling and residual stresses under specified temperature profiles. With this information, we should be able to specify the temperature profile (vertical and horizontal) that combines absence of buckling, acceptable residual stress level, acceptable level of imperfections and maximum speed. Once we know what temperature profile we would like to produce in the ribbon, we will need more information on how to produce it in a growing ribbon. Third, we need to know more about the actual interface shape and the resulting solute distributions that are produced by growth in specified temperature profiles; fourth, we need to study in detail the transient effects related to the rejection of solutes at the solid-liquid interface; fifth, we need to understand the conditions governing the advance of the "leading edge" of an inclined interface; and, sixth, we need more information on the effect of speed and thermal profiles on crystal defects, as well as the effects of these defects and their interaction with impurities on cell performance. The extent to which defects are detrimental to photovoltaic performance, and their dependence on speed of growth, is a major area of ignorance; are the imperfections a direct function of speed, or are they in fact caused by the stress which is, in some configurations, an unavoidable consequence of the thermal profiles required for fast growth?

I hope that I will learn during this meeting that my own state of ignorance on these questions greatly exceeds our collective ignorance; if not, much research remains to be done before we can be confident that the best possible way of growing sheet for solar cells has been found.

FIGURE CAPTIONS

1. Heat balance at interface for ribbon growth.

2. Heat balance for ribbon growth.

3. Condition for capillary equilibrium

$$\frac{1}{R_1} + \frac{1}{R_2} = \Delta P$$

4. Solute concentration ahead of the interface during growth with planar front.

5. Concentration of a solute in the crystal and in the liquid.

6. The initial transient.

7. Thermal configurations for a) EFG, b) web, and c) inclined interface growth.

8. Meniscus shape and constraints for a) EFG; side of ribbon, b) web and edge supported growth; side of ribbon, c) EFG; edge of ribbon, d) web; edge of ribbon, e) edge supported growth; edge of ribbon, f) EFG; closed shape.

9. Maximum theoretical growth speed for EFG as a function of thickness.

10. Vertical thermal profiles to produce stress-free ribbon.

11. Horizontal growth.

12. Schematic representation of dendritic growth into a supercooled liquid.

TABLE HEADINGS

Table I. Length of Initial Transient for Various Solutes and Speeds of Growth.

Table II. Thickness of Diffusion for Boundary Layer.

Table III. Calculated Concentrations of Solutes in the Liquid at the Interface for EFG at Steady State for Single Phase Solidification.

Table IV. Sheet Growth Techniques Classified According to Thermal and Capillary Conditions.

Fig. 1

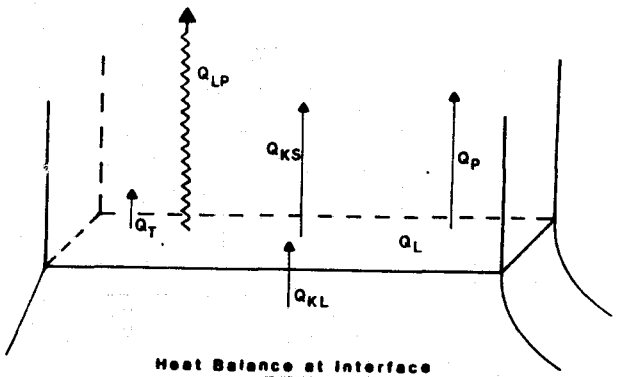

Heat Balance at Interface

$$Q_L = Q_{KS} - Q_{KL} + Q_{LP} + Q_P + Q_T$$

Q_L = Latent Heat = LV Joule/cm^2

Q_{KS} = Heat Conducted Into Crystal = $K_C G_C$

Q_{KL} = Heat Conducted From Liquid = $K_L G_L$

Q_{LP} = Heat Removed From Interface by Light Piping

Q_P = Heat Absorbed at Interface by Peltier Effect

Q_T = Heat Transported From Interface by Moving Crystal

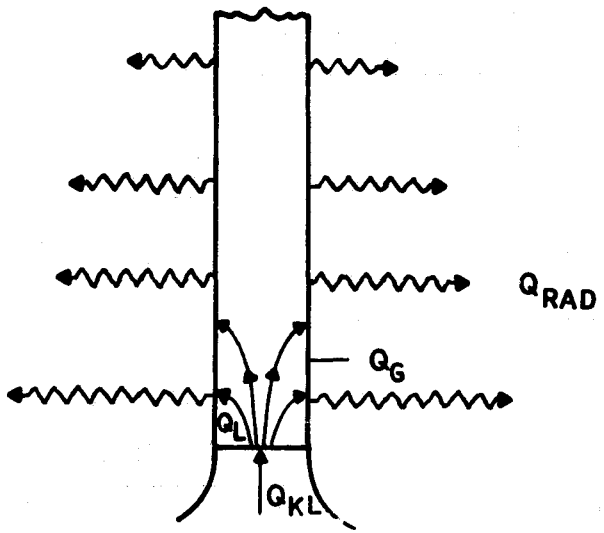

HEAT BALANCE

$$Q_L + Q_{KL} = Q_{RAD} + Q_G$$

Fig. 2

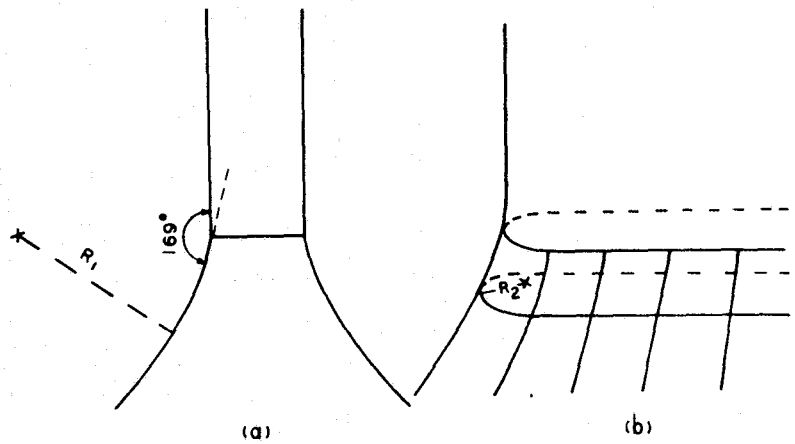

Fig. 3

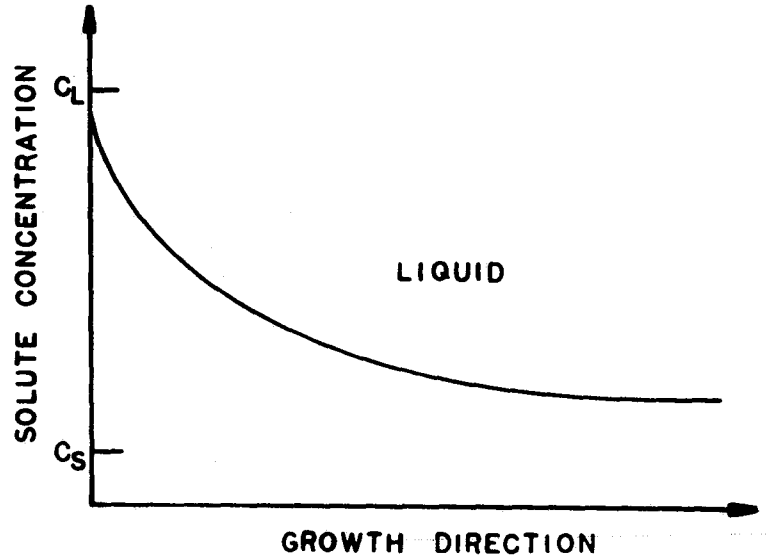

Fig. 4

Fig. 5

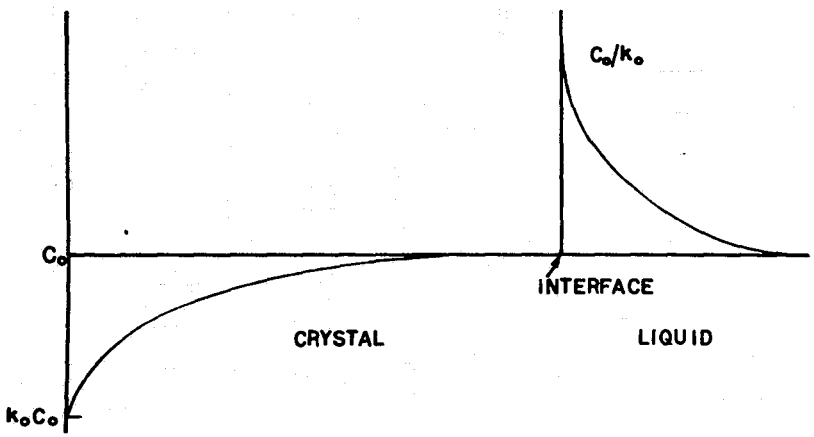

Fig. 6

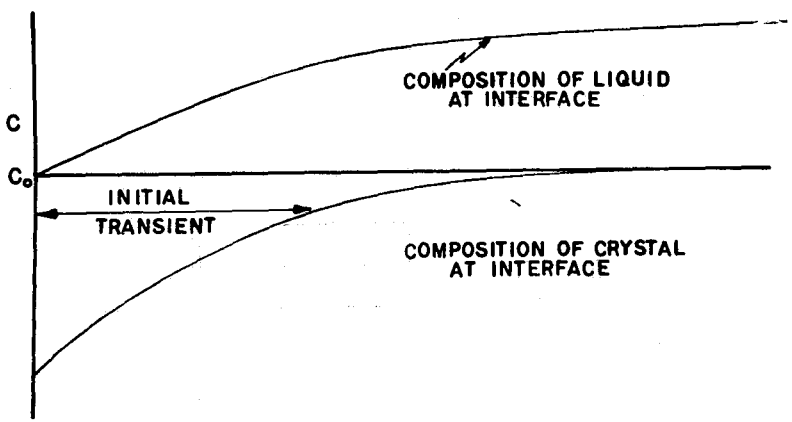

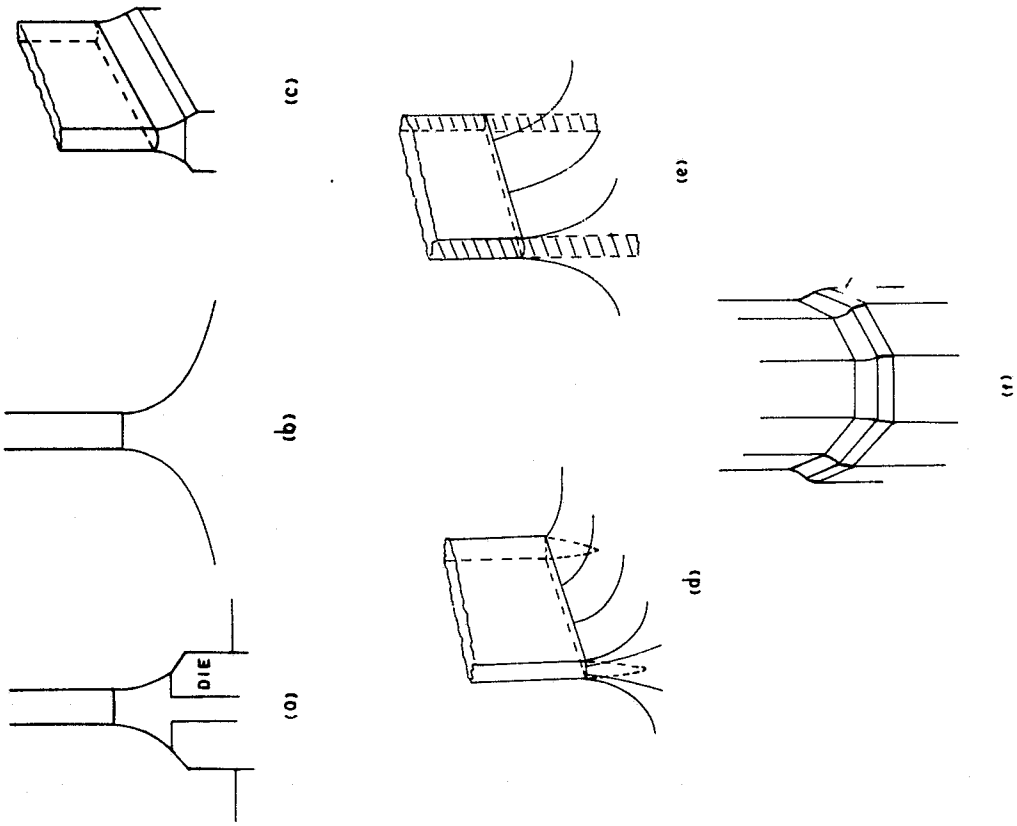

Fig. 8

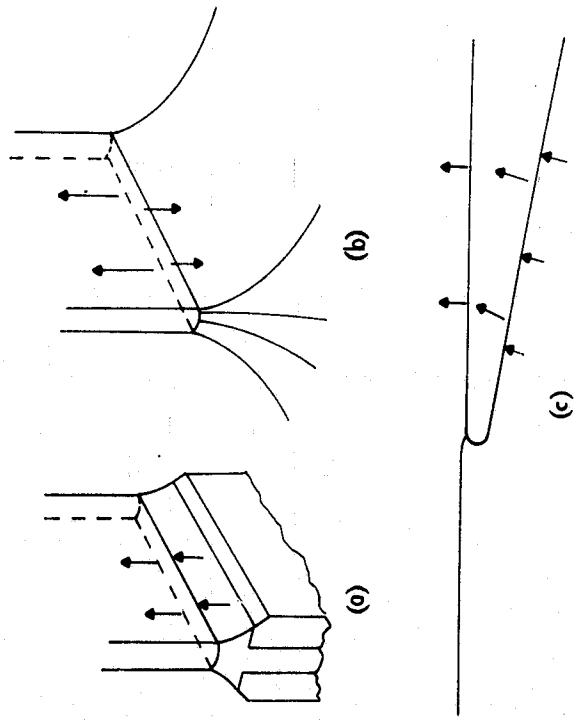

Fig. 7

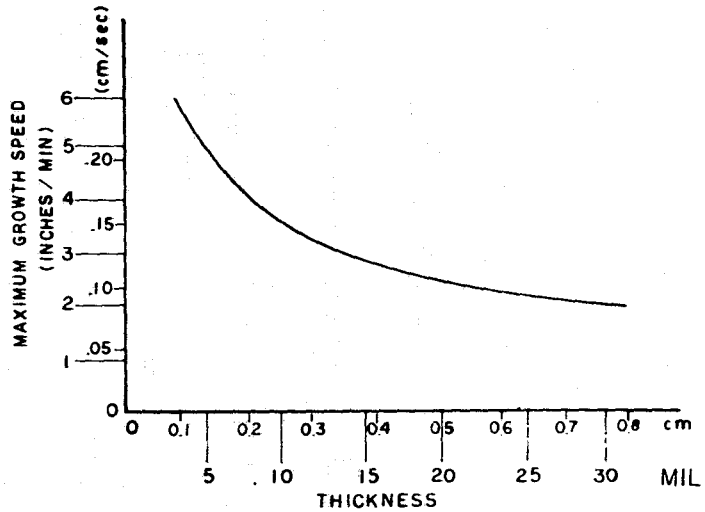

Fig. 9

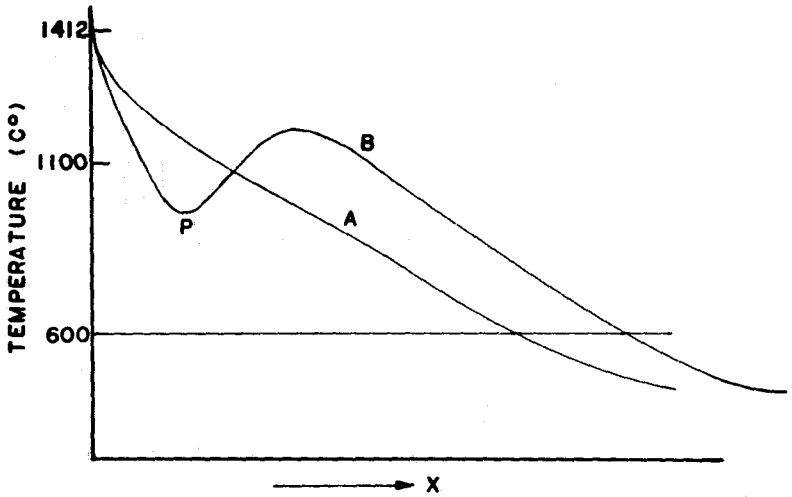

Fig. 10

Fig. 11

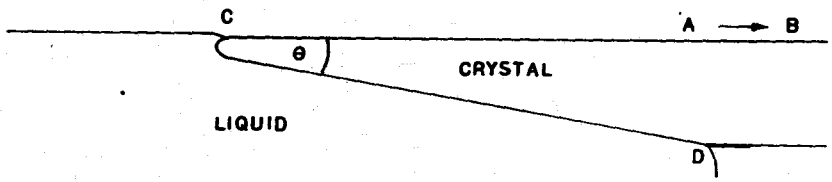

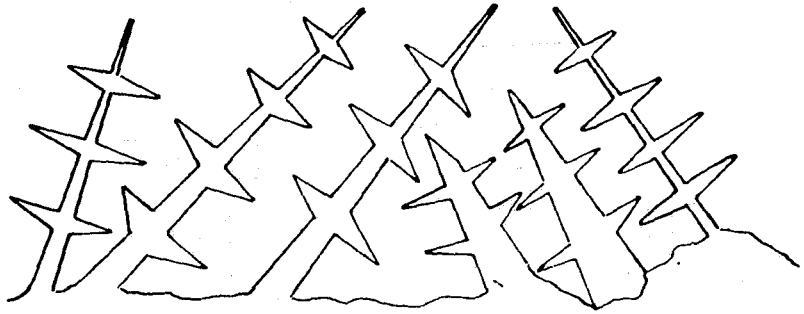

Fig. 12

Table I. Initial Transient d.

Element	Boron	Carbon	Aluminum	Titanium	Iron
Speed of Growth k_o	0.8	0.08	$2x10^{-3}$	10^{-5}	$8x10^{-6}$
0.1 cm/min	0.4 cm	4 cm	150 cm	$2x10^{5}$ cm	$4x10^{5}$ cm
2.5 cm/min	0.015	0.15	5.9	1190	1488
10.0 cm/min	0.004	0.04	1.5	299	374
20.0 cm/min	0.002	0.02	0.75	150	187
60.0 cm/min	$3x10^{-4}$	0.01	0.25	50	62

Table II. Thickness of Diffusion Boundary Layer.

R cm/min	0.1	2.5	5	10	20	60
δ cm	0.3	0.01	0.006	0.003	0.002	$5x10^{-4}$

Table III. Calculated Concentration of Solutes at Interface for Steady State.

	Concentration (ppm)	k_o	C_o/k_o (ppm)
B	0.02	0.8	0.03
C	1.4	0.08	17
Al	1.5	$2x10^{-3}$	750
Ti	0.54	10^{-5}	54,000
Cr	0.56	10^{-5}	56,000
Fe	1.6	$8x10^{-6}$	200,000
Ni	1.1	$8x10^{-6}$	134,000
Cu	0.8	$4x10^{-4}$	2,450
			450,514

Table IV. Thermal Configuration.

Capillary Configuration	Heat Extraction Parallel to Pull Direction		Heat Extraction Inclined to Axis
	Heat Flow into Crystal and from Liquid	Heat Flow into Crystal and into Liquid	
Outer edges of side meniscus constrained	EFG (Ribbon)		
1. Edges constrained by die.	Stepanov		EFG with Displaced Die
2. Edgeless.	EFG (Closed Shape)		
Outer edges of side meniscus free			
1. Edges constrained by dendrite.		Web	
2. Edges constrained by moving fiber.	Edge Supported Growth		
One side free, the other constrained.			Horizontal Growth

DISCUSSION

SUREK: I was surprised by some of your initial transient numbers, and I hope some people would go back and recalculate for their systems. It seems that virtually nothing has been grown under steady-state conditions, if you quote something like 15 meters for EFG at a relatively low speed.

CHALMERS: That is exactly what I am saying.

SUREK: Basically, none of these ribbon growths have ever occurred under truly steady-state conditions, including EFG.

CHALMERS: I invite you to recalculate the numbers. Will you tell us what results you get when you have done it? If they are wrong, so much the better, but I think they are right.

AST: You get tremendously long transient lengths of 13 meters, for material that has very small k_c like iron or copper. That material also has very high diffusion coefficients in the solid phase. Did you include the diffusion coefficient in the solid phase, and does it make a difference?

CHALMERS: I don't think it makes any difference at that stage. It does make a difference in another context. If you depend on segregation during solidification to give you part of the crystal of higher purity than the rest, then diffusion of copper during cooldown is going to very much reduce the effect, at the very least, and it may eliminate it all together.

AST: Yes, typical diffusion coefficients in a liquid are something like 10^{-5}, 10^{-6} and in the solid state may be as high as 10^{-8}. If you get two orders of magnitude difference in the time scale--

CHALMERS: This is perfectly correct, but I don't think this affects what happens at the moment of solidification. It does affect where the solutes go in the solid after this has happened, but I don't think it affects the actual growth interface problem.

GLICKSMAN: If you have a very long initial transient, isn't that usually suggestive of the fact that very slight convective motions of the liquid will then tend to cause a significant mixing and therefore begin to become the dominant part of the transport mechanism?

CHALMERS: I think not, because part of the initial transient effect is that the diffusion layer itself builds up slowly. It does not immediately reach its steady-state thickness, and when it is very thin, as it is in the beginning, the convective transport is going to be ineffective, so I think this adds to the effect. The initial transient is very effective in suppressing the convective transport of the solute.

GLICKSMAN: Right, but someplace between the very thin layer and these rather long lengths that you calculate on the order of many centimeters--it would seem that the hydrodynamic boundary layer thickness would become thinner than the ultimate buildup.

CHALMERS: Yes, it will, but I think it might take a long time, and the faster you go the thinner the diffusion layer is going to be, because there is less time for diffusion of the solute away from the interface; therefore, the diffusion layer is thinner if you grow faster. Here is one of the various tradeoffs that you will have to worry about.

GLICKSMAN: In horizontal ribbon growth, you thought that the region near the tip of the growing ribbon, in order to compensate for the high pull speed, would have to be severely supercooled. It would seem that one could arrange by thermal configuration to simply have the liquid nominally at the melting point to prevent any heat flow back into the liquid, and then arrange a strategy whereby the latent heat (including the tip) must flow back through the solid and then radiate through the horizontal surface. Do you see that as a problem?

CHALMERS: I have a number here. Incidentally, I was hoping you might be able to throw some more light on this particular problem. It seems to me that in order to grow at really high speeds, such as 60 centimeters a minute, you would need to have an enormous temperature gradient in the leading edge--in the crystal itself, if all the heat were to be extracted in that direction, and I don't think that is feasible. This is many thousands of degrees per centimeter, and I don't think you can pull out the latent heat from the solid in the vicinity of that leading edge at that rate, whatever you do. I think the latent heat has to go substantially into the liquid. But if there is a way of doing it, so much the better.

GLICKSMAN: I think it does work, and again I think we reached a similar conclusion to what you have mentioned, that when you calculate either through a radiation boundary condition or some sort of a heat clamp model, then the numbers seem to indicate that there is adequate opportunity to dissipate the latent heat. Of course, what seems to save the day is that the tip radius of curvature, if it is sufficiently small, winds up cutting down the path for the heat flow from the tip out. The gradients are probably fairly severe right within the first few radii near the exit of the horizontal ribbon, but again it seems that there is adequate opportunity to remove latent heat by a solid-state conduction process.

GRABMAIER: You mentioned that the stresses in the ribbons are a serious problem. Do you think it is possible to reduce the stresses in the ribbon while growing the ribbon?

CHALMERS: If you grow the ribbon slowly enough, I believe that you can.

GRABMAIER: If you have a high-speed growth, do you have to anneal your ribbons afterwards in a long-time annealing process?

CHALMERS: Yes. Let me show you one more viewgraph that I didn't show before. Two strategies have evolved for doing this at Mobil. The first is shown by curve A, in which the length of the crystal from the interface

upwards is the X axis. It starts at 1412°C, which is the melting point, and A is the so-called linear after-heater strategy in which you bring the temperature profile to a linear condition before the temperature falls below about 1100°C. This allows enough annealing at low speeds that you get into a linear regime, A, and you can then finish up with zero speed. In the other strategy for higher speed, shown by curve B, it has a steeper temperature gradient at the interface to get down to a lower temperature, then it is reheated up to point B, and then again you enter a linear cooling regime at about 1100°. In this manner again you can achieve stress-free material, in principle at least, at a somewhat higher speed.

N84 28617

OVERVIEW OF BULK SILICON CRYSTAL GROWTH

Jerry W. Moody

Monsanto Electronic Materials Company

St. Peters, Missouri

Introduction

The modern electronics industry requires homogeneous, dislocation-free silicon with prescribed and tightly controlled electrical properties. Two techniques are used to grow silicon crystals to meet these specifications: Czochralski and float-zone crystal growth. Growth rates have not been of prime concern in the commercial evolution of these techniques. Rather, the prime thrust has been directed toward increasing the size and improving the homogeneity of the crystals. In about twenty years the diameter of commercially available silicon wafers have increased from 25 mm or less to 150 mm or larger. Starting charge sizes have increased from a few hundred grams to 40-60 kilograms. Equipment being introduced today is scaled for even larger charges and crystals.

Although growth rates are not of prime concern, it does behoove the crystal grower to grow crystals as fast as is compatible with crystal quality and homogeneity. This paper reviews the Czochralski and float-zone techniques and examines the consequences of high growth rates in the growth of electronic grade silicon.

The Czochralski and Float-Zone Crystal Growth Systems

Figure 1 is a schematic illustration of a modern Czochralski silicon crystal growth system. Here, the silicon melt is contained in a fused silica crucible which, in turn, is held in a graphite holder. Heat is supplied by a graphite heater and the entire hot zone is surrounded by graphite insulation. The whole is contained in a stainless steel, water-cooled chamber. Provisions are made to lift and rotate both the crucible and crystal. Nowadays Czochralski silicon crystals are most often grown in an argon purge under reduced pressure (10-50 torr). The purge rate and flow pattern are adjusted to keep the melt clear of silicon and carbon monoxide gases which are generated in the hot zone.

The heat generated at the solid liquid interface is conducted up the crystal and is radiated to the cooler parts of the apparatus as suggested by the arrows in Figure 1. (Convection losses contribute only a small part to the cooling of the crystal.) However, the growing crystal is also exposed to radiation from the hotter melt surface and crucible wall. These radiations, in effect, reduce the temperature gradient in the crystal and affect the growth rate.

Thermal conditions are much different in float-zone crystal growth which is illustrated in Figure 2. Here a polycrystalline feed rod is melted by an R-F coil. Illustrated is the one-turn, needle-eye coil which is in general use today. This coil has an inner diameter smaller than the feed rod and permits the growth of large diameter single crystals. The shape of the melting and freezing interfaces are suggested by the dashed lines in Figure 2. A relatively thin layer of melt clings to the convex (to the melt) conical interface of the melting feed rod. The freezing interface in the single crystal is concave to the melt, forming a sort of cup to hold the melt. Thus a short, stable, liquid zone is maintained between the large feed rod and the single crystal. In practice, the feed rod is "pushed" through the needle-eye coil and the single crystal is lowered from the coil. The relative rates of movement are adjusted to maintain the desired diameter of the single crystal.

Again, the heat flows are suggested by the arrows in the figure. Heat flows away from the liquid zone - up the feed rod and down the single crystal and is radiated to the cooler parts of the apparatus. Because of the absence of a large radiating heat source thermal gradients in the single crystal are higher than in Czochralski growth, permitting, as will be seen, higher growth rates.

Growth Rates

Although interface kinetics and constraints on crystalline perfection are important, crystal growth rate in both the Czochralski and float-zone systems are determined ultimately by the heat fluxes at the solid/liquid interface. Under steady state conditions (constant crystal diameter, solid/liquid interface at a fixed position) the heat conducted away from the interface through the crystal must equal the heat conducted to the interface from the hotter regions of the melt plus the latent heat of fusion liberated by the freezing melt.

Billig[1] and Cizek [2] have examined this heat balance and have derived the now familiar equation (Figure 3) relating maximum crystallization rate to radius. In deriving the equation, it was assumed:

(1) no convection and negligible temperature gradients in the melt

(2) heat loss from the crystal is by radiation to a cold environment

(3) solid/liquid interface is planar

(4) thermal conductivity of the crystal varies inversely with temperature

(5) emissivity is temperature independent.

Although none of these assumptions are, in fact, valid, the equation does serve as a measure of ultimate crystallization rates and suggests conditions by which growth rates may be enhanced. An important point to note is that the maximum growth rate varies inversely with the square root of the crystal

radius.

The function is plotted in Figure 4 using values of the constants appropriate for silicon (curve labeled "Billig - Cizek"). Also shown in the Figure are the range of growth rates which are, or have been, used in the electronic material industry. The theoretical curve indicates that 100 mm diameter crystals could be grown at over 15 inches/hour. However, the practical rate realized for the Czochralski growth of electronic grade silicon is less than about 4 inches/hour. Note, however, that the data for Czochralski grown crystals roughly parallel the theoretical curve; that is, the growth rate varies inversely with the square root of the crystal radius.

Although float-zone growth rates and the one point for a pedestal puller (shown in Figure 4) are not as high as theoretical, they are considerably higher than that for Czochralski growth. The reason for the difference is the higher thermal gradients realized in the float-zone systems. Billig and Cizek ignored possible thermal radiation interactions between the crystal, melt surface, crucible wall, and heater in their analysis. In fact, as mentioned previously, the Czochralski crystal "sees" a hot melt surface and crucible wall as it grows, rather than the cold environment assumed by Billig and Cizek. Rea [3] has considered the effects of these interactions and derived the function illustrated by the curve labeled "Rea" in Figure 4. Rea's analysis predicts much lower growth rates than Billig-Cizek. However, even the Rea model leads to much higher growth rates than are presently realized in Czochralski growth. (The agreement between the Rea curve and float-zone growth rates must be considered fortuitous.)

Neither Rea not Cizek-Billig considered heat convection from the melt to the interface. This sensible heat has been calculated [4] to be greater than the latent heat in one particular Czochralski geometry. At least a small temperature gradient must exist in the melt for crystal growth to be possible at all. How changing the temperature gradients in the melt affects crystal growth will be discussed later.

Most of the Czochralski crystal growth machines in use today are designed for 100 mm diameter crystal. They can accommodate crucibles of from 10 to 14 inch diameter holding 12 to 40 kilograms of charge. The machines can economically produce 75 mm and 125 mm diameter as well as 100 mm diameter electronic grade silicon. The new machines, currently being introduced, are designed for 150 mm crystal and will be useful for diameters from 100 mm to 200 mm. It should be realized that, although the linear growth rate varies inversely with the square root of the diameter, the cross sectional area grown in unit time increases with the 3/2 power of the diameter.

The diameter of float-zone crystals has lagged behind that of Czochralski crystals. However, 100 mm float-zone crystal is now available commercially and a 125 mm crystal was exhibited at a recent trade show.

Effects of Enhanced Growth Rates

The shape of the solid/liquid interface is a sensitive function of the growth rate in both Czochralski and float-zone systems. In both cases the freezing interface is concave toward the melt at growth rates commonly employed and become more concave with increasing growth rate. Figure 5 is a photograph of a typical interface in a Czochralski grown, 100 mm diameter crystal. The growth interface was made visible by precipitating oxygen (which is incorporated into the crystal in striae which correspond to the interface) in a sample cut parallel to the growth direction. After the precipitation heat-treatment, the sample was etched to reveal the striae. It will be noted that the interface is roughly spherical in shape. A measure of the shape of the interface is the height of the interface above the melt surface as measured at the center of the sample. This measurement is plotted in Figure 6 as a function of growth rate for a 100 mm diameter crystal. The interface shape also depends on melt depth and rotation rates. In general, the interface becomes less concave as the crystal is pulled and the melt is diminished. The dependence on rotation rates is more complex. The data in Figure 6 were taken on samples from near the seed end of crystals grown with the crystal rotating faster than the crucible (in opposite directions) as is common practice.

At the stage of growth illustrated in Figure 6 the concavity of the interface increases linearly with growth rate. At higher growth rates it is possible that the meniscus would become unstable and separate from the crystal. However, before this happens in the growth of dislocation free single crystals other effects become manifest. To increase growth rates in conventional Czochralski systems, the common practice is to reduce the power to the heater. This, in effect, reduces the thermal gradients in the melt. Now, the low index faces of silicon grow at different rates under equilibrium conditons. The fastest growing faces are (1-1-0) and the slowest growing faces are (1-1-1). When melt thermal gradients are reduced to enhance growth rates, equilibrium conditions are approached and the growth rate dependence on orientation becomes apparent. The fast growing directions begin to dominate and the crystal shape is likely to change. Round crystals being grown in the (1-0-0) direction tend to become squarish while (1-1-1) crystals become triangular or hexagonal. If the conditions persist long enough, gross deformation of crystal shape may occur. Figure 7 is a photo of a cross-sectional sample taken from a dislocation-free (1-0-0) crystal grown under low thermal gradients in the early stages of deformation. The squarish cross-section is obvious . Figure 8 is a photo of another cross-sectional sample taken from the same crystal in a later stage, showing extreme deformation of shape. Now the crystal has assumed a three-lobed shape. At this point the crystal was still dislocation-free. Shortly after this point the crystal lost perfect structure and the boule became polycrystalline and became round again. A round polycrystalline rod can be grown under much lower thermal gradients (and at higher growth rates) than is possible for a dislocation-free, single crystal.

Crystals such as illustrated in Figure 7 and 8 are obviously not suited for electronic device application. The growth rate selected by the silicon grower is the highest rate which permits a nearly round high quality crystal to be grown at an acceptable yield and throughput. These are the growth

rates illustrated previously in Figure 4.

Unusually high growth rates cause other problems in float-zone growth. As growth rates are increased in this case, it becomes more difficult to melt the interior of the polycrystalline feed rod. The conical melting interface (Figure 2) extends deeper and deeper into the molten-zone as growth rate is increased. Ultimately, a central core of unmelted rod obtains. Dislocation-free single crystals cannot, of course, be grown under such conditions. If power to the coil is increased to insure complete melting of the feed rod, the molten zone becomes so large that surface tension forces can no longer support it and the zone is split. Again, the highest rate is selected that permits the growth of round, dislocation-free crystals at acceptable yields. As shown in Figure 4, practical float-zone growth rates are about twice as high as those for Czochralski growth.

Impurity Segregation

The impurity profiles in float-zone and Czochralski grown crystals are illustrated in Figure 9. The profiles differ significantly. The difference, of course, is due to the fact that in one case a small molten zone is moved through a polycrystalline rod which is assumed to be uniformly doped at C_o. In the Czochralski case, the crystal is "pulled" from a large melt containing the impurity at C_o. The segregation behavior in the two cases has been treated extensively by Pfann[5] and the expressions describing the segregation are given in the Figure. Here: g is the fraction frozen, x is the zone length, and l is the crystal length. The symbol k_e is the effective segregation coefficient.

Segregation coefficients are defined in Figure 10. The equilibrium segregation, k_o, is the ratio of the solubility of the impurity in the solid phase to its solubility in the liquid. It may be obtained from the temperature-composition equilibrium phase diagram of the system. Crystals are not usually grown under strictly equilibrium conditions and practical segregation depends on experimental conditions. The well-known Burton, Prim and Slighter[6] expression for the effective segregation coefficient is also given in Figure 10. It is noted that the effective segregation coefficient tends from k_o to 1 as the growth rate is increased. Also listed in Figure 10 are the equilibrium segregation coefficients for some common impurities or dopants in silicon. There is some doubt about the value for oxygen. However, at present it is generally accepted as being greater than 1.

Because of segregation effects and the build-up, or depletion, of impurity at the solid/liquid interface, constitutional supercooling and interface breakdown can occur under certain conditions of silicon crystal growth. Growth conditons which lead to constitutional supercooling and cellular growth are given in Figure 11[7]. High growth rates and impurity concentrations, and low temperature-radients and segregation coefficients lead to the onset of constitutional supercooling.

The most common dopants used in electronic grade silicon are boron, phosphorus and antimony. Dopant concentrations of boron and phosphorus are usually so low that constitutional supercooling is not encountered in the

growth of silicon doped with these impurities. However, it is common to dope antimony containing crystals to rather high concentrations and cellular growth is frequently encountered before the entire crystal is grown. Figure 12 is an example of cellular growth resulting from constitutional supercooling during the growth of an antimony doped crystal. In this case, the cell boundaries contain an antimony-rich phase.

Electronic grade silicon is grown from starting charges of the highest purity. If a less pure starting charge is used, as has been proposed for "solar-grade" silicon, constitutional supercooling may become more of a problem. Metallurgical or "solar-grade" silicon is apt to be contaminated with a variety of heavy metals having very low segregation coefficients. Hopkins, et. al.[8] have examined the possibility of constitutional supercooling in such cases. Although they conclude that solar-cell performance rather than constitutional supercooling would probably determine the permissable impurity concentrations, they point out the possibility of interface breakdown at high crystal growth rates.

Conclusions

Modern silicon crystal growth systems have been built with crystal size in mind. However, to be most cost effective even large crystals should be grown at the highest possible growth rate. The practical growth rates in use in modern systems are well below theoretical growth rates. An examination of the Billig-Cizek assumptions and equations for maximum growth rate leads to suggestions for modifying present day equipment to permit higher growth rates. The approach is to minimize temperature gradients in the melt and to increase gradients in the solid.

First, the sensible heat conducted through the melt is a major factor in limiting Czochralski growth rates. It was pointed out previously that at least a small temperature gradient was necessary to grow a ground single crystal and to prevent spurious nucleation and crystallization. Perhaps a system of baffles to control fluid and heat flow might lead to the minimum necessary temperature gradient.

On the other hand, it may be easier to increase the temperature gradient in the Czochralski crystal than to decrease gradients in the melt. Rea[3] showed how radiations from the hot crucible and melt surface reduce thermal gradients in the crystal to limit growth rates. It should be a relatively simple matter to devise a shield to protect the growing crystal from radiations from hotter parts of the system. In addition it should be possible to increase the rate of heat loss from the crystal by increasing convection losses. Czochralski systems operate under an argon purge at 10-50 torr. Convection heat transfer is insignificant compared to radiation transfer under such conditions. Convective losses could be increased by operation under higher pressures and purge rates.

Float-zone systems are better suited for high crystal growth rates. In this case the major problem is supporting a molten zone wide enough to be assured of complete meltthrough. An R-F coil designed to optimize levitational forces may be the solution to this problem.

Extensive calculations and experimentation would be required to determine how much these approaches, or others, would enhance bulk silicon crystal growth rates. It is doubtful that the impetus for such research will derive from the electronic materials industry. Large crystal diameters and homogeneity remain the prime concern of these suppliers. Rather, it is expected that the necessary work will be done by those to which low cost is a, if not the, major factor - the solar cell industry.

References

(1) E. Billig, Proc. Royal Soc., 229, 346, (1955)

(2) T. F. Cizek, J. Appl. Phys., 47, 440, (1976)

(3) S. N. Rea and P. S. Gleim, Final Report, J.P.L. Contract No. 954475, April 1977.

(4) D. E. Steinmeyer, private communication.

(5) W. G. Pfann, "Zone Melting", John Wiley and Sons, (1958)

(6) J. A. Burton, R. C. Prim, and W. P. Slichter, J. Chem. Phys., 21, 1987, (1953)

(7) W. A. Tiller, K. A. Jackson, J. W. Rutter and B. Chalmers, Acta. Metallurgical, 1 428, (1953)

(8) R. H. Hopkins, R. G. Seidensticker, J. R. Davis, P. Rai-Choudhury, P. D. Blais and J. R. McCormick, J. Crystal Growth, 42, 493, (1977)

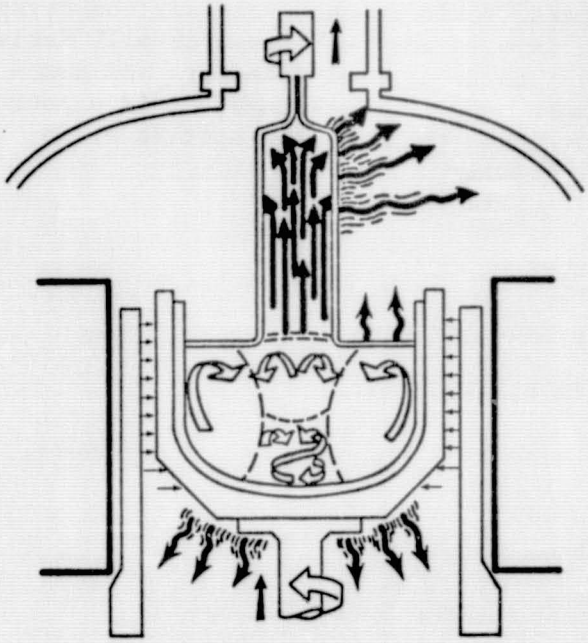

Fig. 1 Czochralski Crystal Puller Schematic

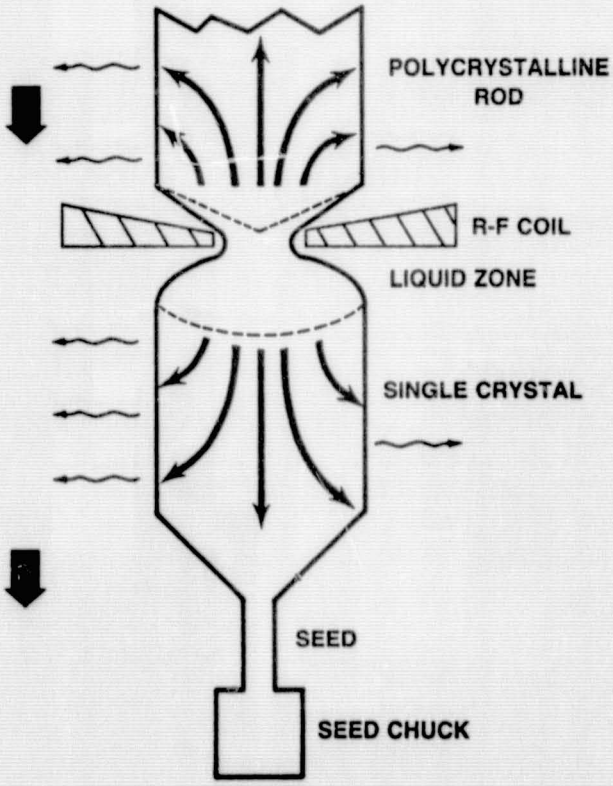

Fig. 2 Float Zone Crystal Growth of Large Diameter Silicon

ORIGINAL PAGE IS
OF POOR QUALITY

Fig. 3 Billig-Cizek Expression for Maximum Crystallization Rate

$$R_{max} = \left(\frac{1}{L\rho}\right)\left(\frac{\sigma\varepsilon\kappa T^5}{\Omega}\right)^{1/2}$$

where:

R_{max}	=	maximum crystallization rate
L	=	latent heat of fusion
ρ	=	density of crystal at melting temperature
σ	=	Stefan-Boltzmann constant
ε	=	emissivity of the crystal
κ	=	thermal conductivity of the crystal
T	=	melting temperature of the crystal
Ω	=	crystal radius

Fig. 4 Growth Rate as a Function of Crystal Diameter

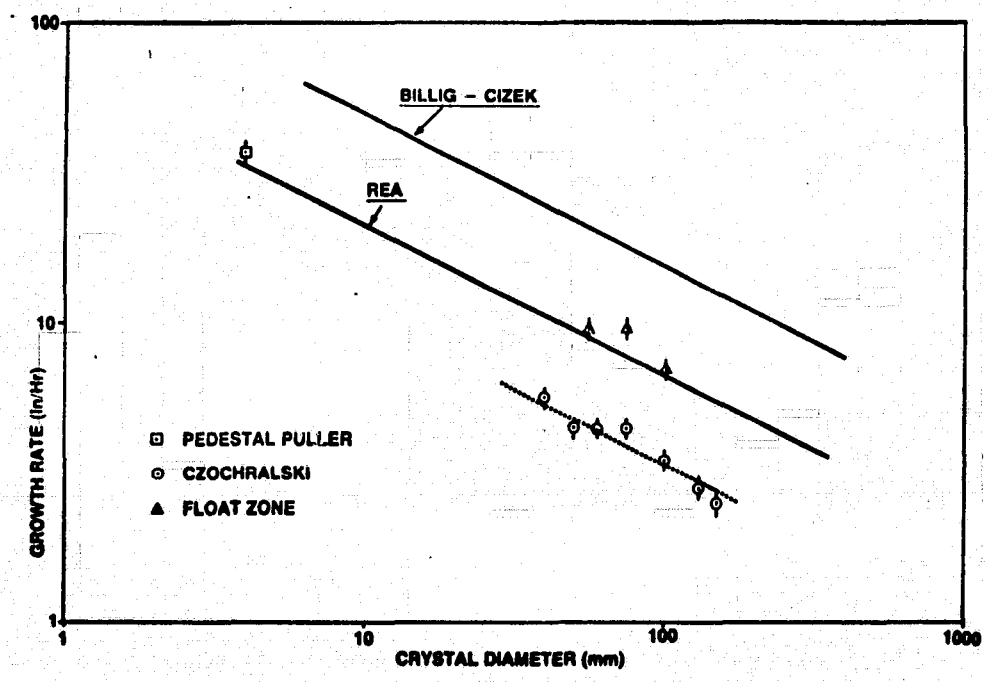

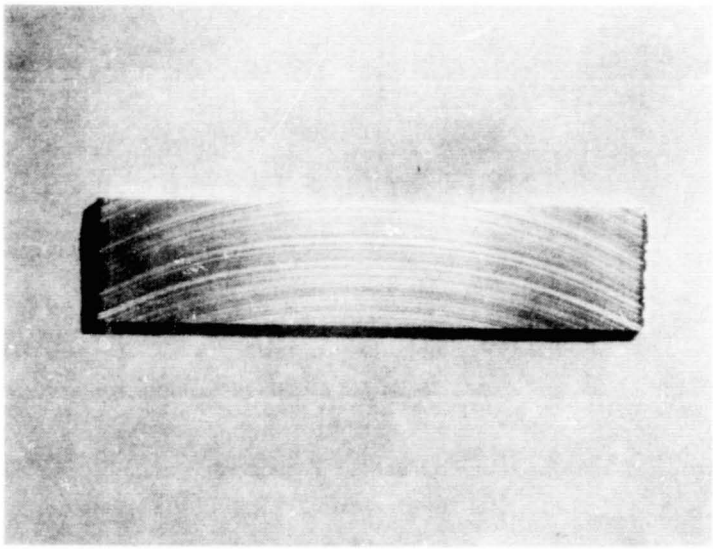

Fig. 5 Growth Interface in 100 mm Diameter Czochralski Crystal

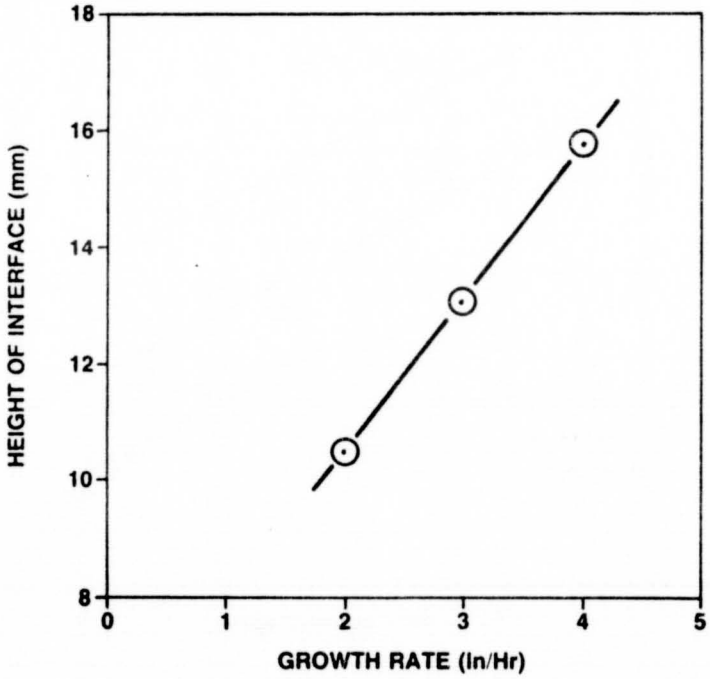

Fig. 6 Effect of Growth Rate on Interface Concavity

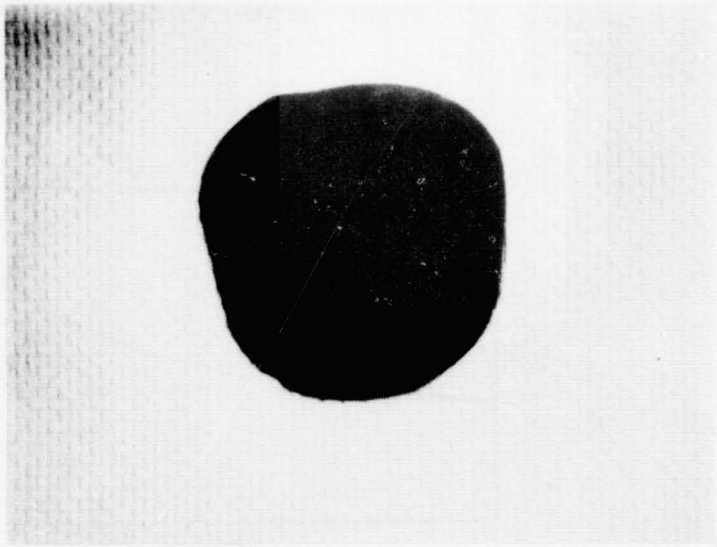

Fig. 7 Effect of Low Thermal Growth Gradients on Crystal Shape - Early Stage of Deformation

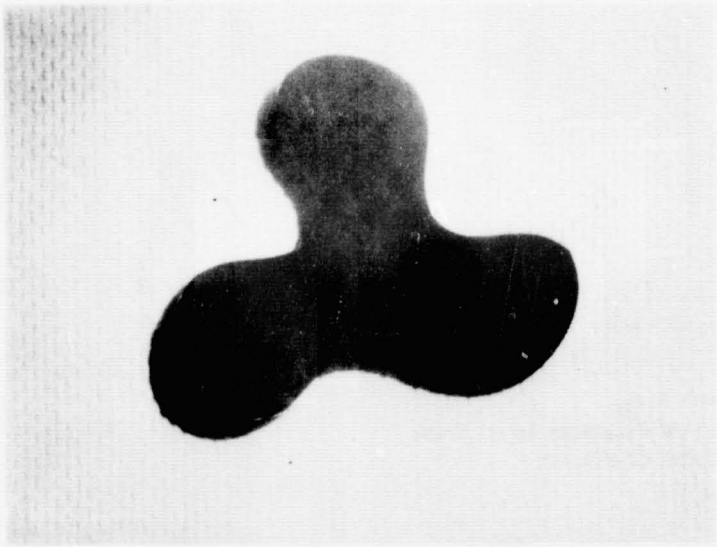

Fig. 8 Effect of Low Thermal Gradients on Crystal Shape - Extreme Deformation

Fig. 9 Impurity Segregation

CZOCHRALSKI: $C = keCo\,(1 - g)^{ke-1}$

FLOAT – ZONE: $C = Co - Co\,(1 - ke)e^{-kex/l}$

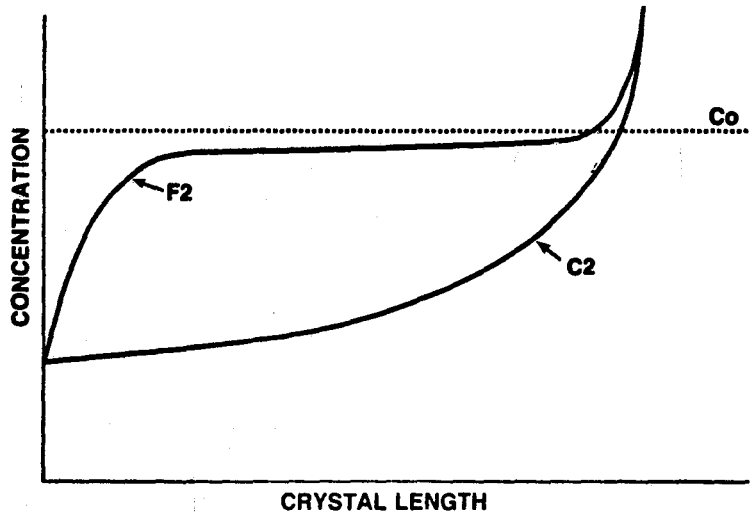

ke = Effective Segregation Coefficient
Co = Initial Concentration
g = Fraction of Melt Frozen
x = Length of Float-Zone
l = Total Length of Float-Zone Crystal

EQUILIBRIUM

$$ko = \frac{Cs}{Cl}$$

Cs = Sol. in Solid
Cl = Sol. in Liquid

EFFECTIVE

$$ke = \frac{ko}{ko - (1 - ko)e^{-\left(\frac{f\delta}{D}\right)}}$$

f = Growth Rate
s = Diffusion Boundary Layer Thick
D = Diffusion Coefficient

ELEMENT	ko
B	0.8
P	0.35
Sb	0.023
Ga	0.008
Al	0.002
O	1.25 (?)

Fig 10 Segregation Coefficients

Fig. 11 Conditions for Constitutional Supercooling

$$\frac{G}{f} \leq \frac{mCo\,(1-k)}{D\,k}$$

G = Temperature Gradient In Solid
f = Growth Rate
m = Slope of Liquidus Curve
Co = Impurity Concentration
k = Segregation Coefficient
D = Diffusion Coefficient

Fig. 12 Cellular Growth in Sb-doped (1-0-0) Silicon

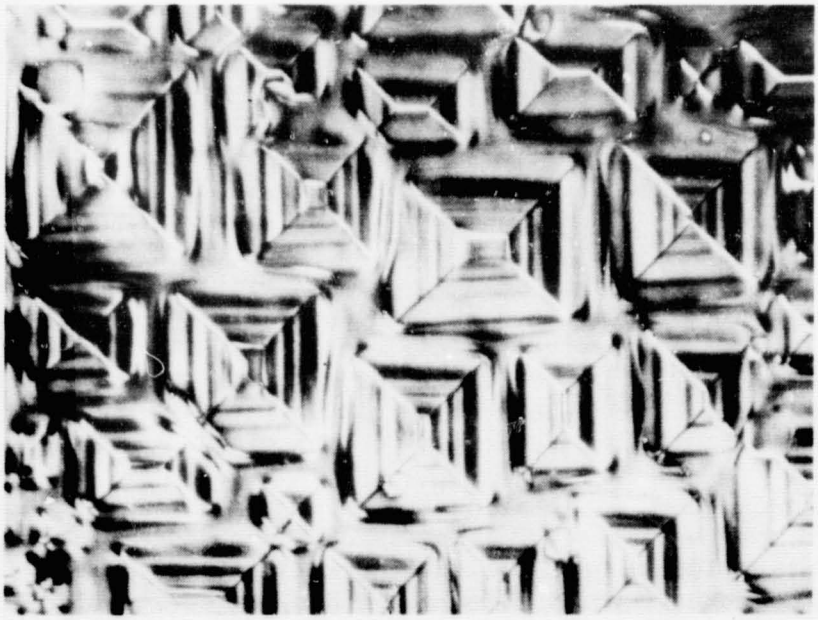

DISCUSSION

KALEJS: You talked on one hand of growth of defect-free Czochralski, and on the other hand about increasing growth rates up to the limit allowed by heat transfer, and ultimately growth of material that has defects. Could you give us an idea, roughly, of at what speeds this may occur and how this may be a function of diameter--in other words, can you get to higher speeds at lower-diameter Czochralski before you get these defects? Also, what do you think is the contributing factor that basically destroys the initially dislocation-free material as speed is increased?

MOODY: I have no evidence that, in the growth of dislocation-free crystals, even the strains introduced because of the growth rates realized in Czochralski and in float-zone growth are a cause of loss of structure. Even the crystal with tremendous deformation grown in the three-lobe manner was dislocation-free to that point. Then it lost structure, perhaps not because of the strain that was in it, but because of extreme variation in the temperature gradients around it. The modern crystals are free of line dislocations. The Czochralski crystals in particular contain a lot of oxygen and, as the crystal cools, oxygen can precipitate and introduce point defects or small dislocation loops. These are not grown in, per se, but occur as the crystal is cooled.

KALEJS: You basically don't think they are impurity-limited at this stage?

MOODY: Not in the electronic-grade material. They just don't contain enough impurities. Only in the case of antimony, where we do end up with concentrations high enough toward the tail end of a crystal, is the concentration high enough to cause interface breakdown.

SCHWUTTKE: I would like to address the problem of perfection of Czochralski crystals. I think that too much emphasis is placed on characterizing Czochralski crystals by saying they are perfect, they are defect-free, because they show zero dislocations. This is totally insufficient. Today's Czochralski crystals are composite in structure. You have indicated that this is primarily due to the high content of oxygen and other impurities.

Regarding the problem of homogeneity of impurities--Czochralski crystals are anything but perfect. Concerning electronic-grade material today, used for VLSI, we are facing one major problem. The main problem is a lack of homogeneity of minority carrier lifetime in Czochralski crystals. Czochralski crystals of 4-inch or 5-inch, or larger, diameter deteriorate completely due to local fluctuations of the minority carrier lifetime.

MOODY: When I talk about dislocation-free high-quality Czochralski crystals, I mentioned they were free of line dislocations, not free of precipitates and dislocation loops. A float-zone crystal is much freer than that, but even there we do have point defects. I did try to stress in my paper that the thrust in development and research, particularly now in the electronic

materials industry, is toward improving the homogeneity of the crystals. We aren't very concerned with high growth rates, particularly for the VLSI applications. We have to improve the homogeneity of these crystals.

SCHWUTTKE: I want to point out that if you go to larger-diameter ingots, to continue to tail off is a waste of time and material.

MOODY: I agree with you. It took at least two hours to tail off on this particular crystal. Some means of gently separating the crystal from the melt must be done, because generally the slip goes back about one diameter. This crystal is about 20 inches long, and if we lost seven inches because of slip by suddenly jerking it out of the melt, that cuts our productivity tremendously.

C. K. CHEN: Could you comment on the uncertainty in the segregation coefficients for oxygen (you stated about 1.25) and what is the range that different people report for this number?

MOODY: The range is from about 0.7, which was one of the earlier estimates of the segregation coefficients, to 1.25.

LIN: The segregation coefficient was reported earlier by Bell in 1964 or 1965 to be in the 0.5 to 0.6 range. In 1973 a Japanese group published a paper claiming that by doing the float-zone experiment, by purging oxygen in ambient and quenching it and studying the solubility at three points, the result was 1.25. This 1.25 was derived from the slope of the liquidus. It came to my attention several years ago from analyzing the interface properties of oxygen that it actually shows the same behavior as the commonly used dopants such as phosphorus and arsenic. Consequently, I did a crystal-pulling experiment (published in the February issue of the Journal of Applied Physics) in which I varied the pull speed from 1 to 10 and then compared it with the Burton-Prim-Slichter (BPS) equation and found the oxygen has a faster incorporation rate, at higher speeds, which is in agreement with the BPS. I used boron as a reference in the same experiment and calculated it to be 0.25, which is smaller than arsenic (0.3). This evidence has been supported by a second experiment and the accurate value should be somewhere between 0.25 and 0.3.

ROSEMEIER: By what techniques does the crystal-growing industry characterize zero-dislocation materials: etching, topography, TEM or EBIC, or what?

MOODY: All of them. Generally, though, it is by etching techniques. We are looking for line dislocations, not dislocation loops.

N84 28618 D4

CRYSTALLIZATION OF SILICON RIBBONS

Status Report

by Martin H. Leipold
Deputy Area Manager
PV Components Research Area
Flat-Plate Solar Array Project

INTRODUCTION

The use of silicon crystallized in ribbon form offers substantial advantages for low-cost photovoltaic modules. The flat ribbon form makes use of the starting silicon highly efficient, resulting in substantial cost reductions in the final module when compared with the wafering of cast materials. In addition, the rectangular form offers high packing density for more efficient modules. The negative aspects relate primarily either to polycrystalline form or to limited rates of crystallization. It is the purpose of this research forum to address the latter point, to establish more precisely the approach to improvements in this technical area; this paper attempts to generalize common features of silicon ribbon growth and, conversely, to identify aspects that cannot be generalized.

DISCUSSION

There is a wide variety of detailed approaches to the growth of silicon ribbons, but one general requirement is a means of stabilizing the fluid silicon in a flat shape. The various technological approaches to silicon-ribbon growth have been summarized extensively and are listed in Table 1 (Reference 1). The means of stabilization may be mechanical, such as filaments in edge-supported pulling (ESP) growth, or capillary forces, as in the edge-defined film-fed growth (EFG) approach. Thermal stabilization of the edges is important in low-angle sheet growth and dendritic-web growth, although in reality, dendrites are thermally induced, and the web itself is mechanically stabilized by the dendrites. The detailed nature of the stabilization mechanism is important in that it places varying thermal constraints on the crystallization environment. For example, in the case of dendritic web, slight supercooling in the liquid is necessary for the dendrites to grow. The range of temperature available is limited by the actual melting point of silicon on the high side and by spontaneous crystallization on the low side. This range is generally of the order of 4°C (Reference 2). In contrast, the use of mechanical filaments, as in ESP, stabilizing the edge reduces the thermal constraints greatly. Again, the lower limit is that of spontaneous crystallization, and the upper limit is that temperature at which the meniscus collapses before sufficient heat of fusion is removed for a solid ribbon to be attained. This range is generally 10°C to 20°C.

A second consideration in the general aspects of ribbon growth is the mechanism by which the latent heat of fusion is removed from the crystal-liquid interface. Silicon has the highest molar heat of fusion of any element: more than 430 calories per gram. At temperatures near the melting point, silicon is

Table 1. Technological Approaches to Flat Ribbon Growth

Means of Edge Stabilization	Common Names
Mechanical	
Filaments	Edge-supported pull (ESP)
Incoming Crystal	Ribbon-to-ribbon (RTR)
Dendrites	Dendritic web (see web below)
Capillary Die	Edge-Defined Film-Fed Geowth (EFG) Capillary-Aided Shaping Technique (CAST)
Die	Inverted Stepanov (IS)
Substrate	Silicon on Ceramic (SOC) Ribbon against Drop (RAD)
Thermal	Low-angle sheet LASS Dendrites for dendritic web

largely optically opaque to radiation, and all of the heat of fusion must be transported away from the growth interface by conduction. Some results suggest a limited degree of transparency, but this should be common to all ribbons.

This fundamental mechanism for heat removal is common to all of the ribbon-growth methods, but there are two special exceptions. The first relates to methods such as dendritic-web, which uses a supercooled liquid, permitting removal of some of the latent heat by conduction into the liquid (generally accepted to be about 20%). The second variation in the details of heat conduction relates to the physical orientation of the growth interface to the direction of ribbon growth. Figure 1 compares the details. With ribbon in which the crystallization front is perpendicular to the ribbon motion (Figure 1a), Surek (Reference 3) has shown that to maximize the rate of removal of the latent heat of fusion, and thus the growth rate, it is necessary to impose a very steep temperature gradient in the solid. Depending upon the exact heat-removal configuration chosen, results suggest maximum gradients of several thousand degrees Celsius per centimeter, and crystallization rates of 10 to 15 cm/min are potentially achievable at practical thicknesses. In contrast, if the crystallization front is at a significant angle to the ribbon growth direction, the heat generation and its subsequent removal can be distributed over substantial length, offering tremendous increases in ribbon

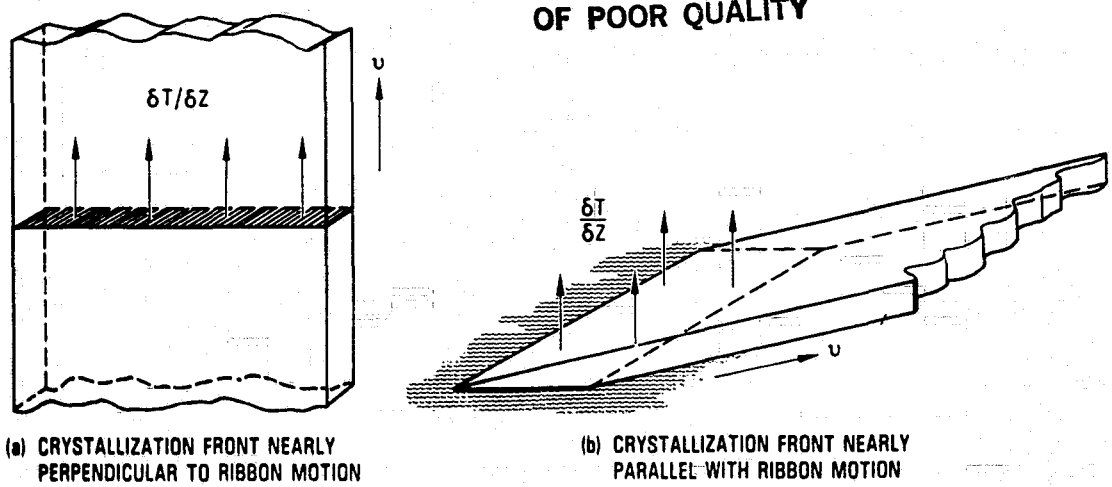

Figure 1. Relative Position and Size of Crystallization Front, Ribbon Motion (ν), and Thermal Gradient δT/δZ (Perpendicular to Crystallization Front)

throughput. This approach is best typified by low-angle sheet growth (Figure 1b).

Another aspect of ribbon growth in which some generalizations are apparent is that of the crystal structure. With the exception of dendritic web, all silicon ribbon growth eventually obtains an equilibrium crystalline structure in which the surface of the ribbon is close to {110}, the growth direction is [211], and significant numbers of twin planes lie parallel to the growth direction and perpendicular to the surface. This is shown in Figure 2a. The fundamental reason for the stability of this structure is not known, although two possible explanations have been proposed but not proven (Reference 4). The structure is commonly observed in all supported and unsupported silicon ribbon growth except dendritic-web. It has also been observed in germanium and gallium arsenide. Dendritic-web ribbon growth, in contrast, is absolutely dependent upon the existence of the specific growth orientation shown in Figure 2b for growth of dendrites (Reference 5). Web growth has been observed with the loss of twin planes through the central region of the ribbon, but loss of the dendrite growth direction results in complete breakdown of the process.

A feature common to both processes is the potential for {111} planes (the slowest growth plane) in silicon to exist stably nearly perpendicular to the growth direction. This arrangement also provides reentrant angles at the twin planes to provide nucleation sites for new planes. Desirable thermal configurations and appropriate location of nucleation sites are thus satisfied by both of these configurations. The fact that these are the only crystal arrangements observed suggests that they may be the only stable ones.

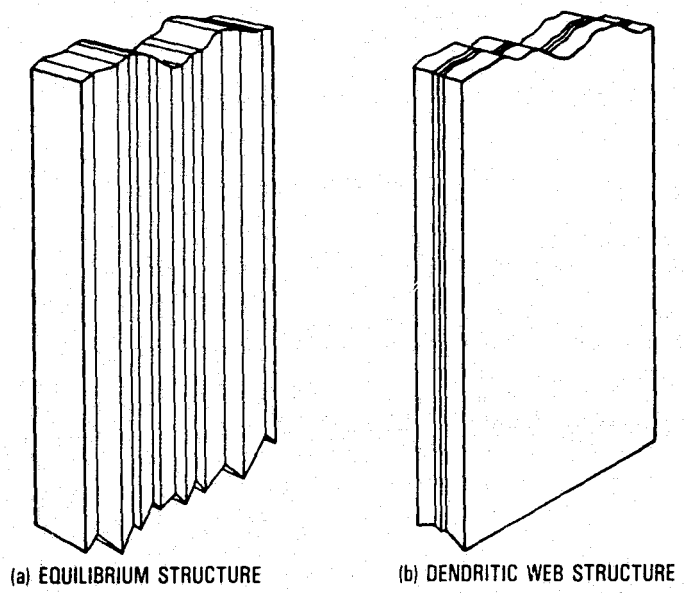

Figure 2. Crystallographic Orientations in Ribbon Growth and Probable Crystallization-Front Shapes

While the emphasis at this meeting is on the nature of the crystallization process, some consideration of stress development and stress states is required. This results from the direct interrelationship of crystallization behavior, thermal configuration and development of stress. Figure 3 is a generalized view of crystallizing silicon ribbon. There are six regions of behavior: liquid, crystallization, plastic with thermal gradients,* plastic without thermal gradients, elastic with thermal gradients and elastic without thermal gradients. All crystallizing ribbons pass through these states. Table 2 shows suggested relative significances of the various regions to the growth process. By comparing the relative importances in this table, it is possible to estimate the level of understanding and the properties, particularly the mechanical properties, that control. For example, the vertical-growth methods that must accommodate high thermal gradients and therefore are difficult to control in a plastic zone present difficulties in ribbon deformation. Conversely, low-angle methods, in which all of the heat is removed in the crystallization zone, do not have such gradients in the plastic zone and therefore do not present deformation problems.

*The term "thermal gradients" is used to describe any random gradient. In reality, certain selected gradients are benign: e.g., those in which the second derivative with length is zero.

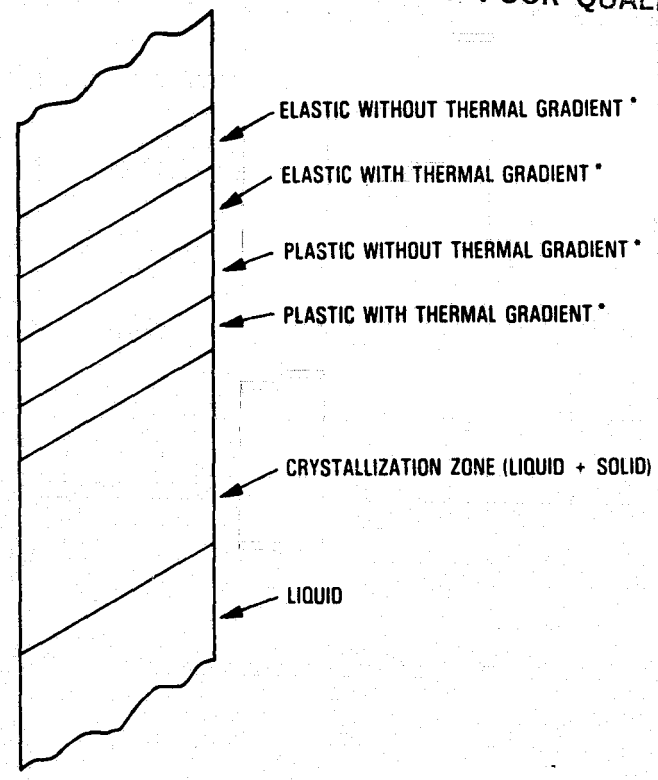

*"THERMAL GRADIENT" DESCRIBES ANY RANDOM GRADIENT

Figure 3. Thermal Zones in Ribbon Crystallization

Although the fundamental limitations of a group of growth processes as shown in Table 2 may be quite similar, there still may be significant practical differences in the ease with which the required fundamental conditions may be achieved. Thus, the ribbon-to-ribbon growth process, which has only a very limited mass of material in the liquid state, lends itself more easily to rapid rates of heat extraction than do methods in which a large crucible of molten silicon is used as the source. These practical considerations are not discussed in detail here.

The crystallization behavior of any material is affected by its impurity content. Constitutional supercooling and related phenomena can be important. With silicon-ribbon growth, as practiced for use in low-cost terrestrial photovoltaics, the impurity problem is greatly reduced. Purity requirements on the ribbon, for it to produce acceptable efficiencies, are stringent; impurity content must be kept quite low. Conversely, however, the solubilities of many contaminant species in silicon are also very low. Ribbon crystal structures that are related to compositional effects have been observed in ribbons grown under unusual conditions, including capillary-aided growth with unconventional dies. The general view is that metallic impurities, whose presence must be less than 10^{16} atoms/c^3 or so, are not likely to be influential. The most

Table 2. Relative Importance of Thermal Zones in Various Ribbon-Growth Techniques

	Liquid	Crystal-lization	Plastic	Elastic w/thermal	Elastic w/o thermal
ESP	med	low	high	med high	med
RTR	very low	low	high	med high	med high
Web	med high	low	high	med	med high
EFG/CAST	med	low	high	med high	med
SOC	med	med low	*	*	*
RAD	med	med low	*	*	*
LAS	med	high	very low	very low	very low

*Substrate-controlled.

likely remaining impurity candidates that may have significant influence on crystallization behavior are carbon and oxygen. Their role in the crystallized ribbon, although not well understood, is not highly detrimental. Under the worst conditions, carbon does appear as silicon carbide precipitates in which dislocation structures surrounding the precipitates produce traps (Reference 6). The generic {112} [110] crystallization configuration does not appear to be related to the presence or absence of any specific impurities, and the web dendrite structure is likewise not impurity-dependent. Thus it is likely that the detailed shape of the crystallization front is not influenced by impurities at present crystallization rates. Increased crystallization rates could enter a new regime, but since most growth methods experience short-term growth at high rates, no problem is likely to be encountered.

Compositional variations in silicon ribbon as grown for photovoltaics may be controlled to some extent by creating a flow in the liquid adjacent to the crystallization front (Reference 7). This may be used to redistribute to some advantage the impurities in the solid ribbon. There does not appear to be evidence that such redistribution influences the crystallization process.

CONCLUSIONS

From this review it appears that several general conclusion may be drawn:

(1) Purity constraints for reasonable solar-cell efficiency require that silicon-ribbon growth for photovoltaics occur in a regime in which constitutional supercooling or other compositional effects on the crystallization front are not important.

(2) A major consideration in the fundamentals of crystallization is the removal of the latent heat of fusion. The direction of removal, compared with the growth direction, has a major influence on the crystallization rate and the development of localized stresses.

(3) The detailed shape of the crystallization front appears to have two forms: that required for dendritic-web growth, and that occurring in all others.

(4) After the removal of the latent heat of fusion, the thermal-mechanical behavior of all ribbons appears similar within the constraints of the exothermal gradient.

(5) The technological constraints in achieving the required thermal and mechanical conditions vary widely among the growth processes.

REFERENCES

1. Morrison, A.D., "Sheet Silicon Cell/Module Technology," Semiconductor Materials, in press.

2. Seidensticker, R.G., and Hopkins, R.H., "Silicon Ribbon Growth by the Dendritic Web Process," J. Crystal Growth 39, 6, 1971.

3. Swartz, J.C., and Chalmers, B., "EFG Process Applied to the Growth of Silicon Ribbons," J. Electron. Mater. Vol 4(2), pp. 255-279, 1975.

4. Leipold, M.H., and DeAngelis, R.J., "Structure Development in Silicon Sheet by Shaped Crystallization," Proceedings of the International Photovoltaic Energy Conference, Luxembourg, p. 782, September 27-30, 1977.

5. Hamilton, D.R., and Seidensticker, R.G., "Propagation Mechanism of Germanium Dendrites," J. Appl. Phys. 31, 1165, 1960.

6. Hari Rao, C.V., Bates, H.E., and Ravi, K.V., "Electrical Effects of SiC Inclusions in EFG Silicon Ribbon Solar Cells," J. Appl. Phys. 47 6, p. 2614, June 1976.

7. Kalejs, J., "Impurity Redistribution in EFG," J. Crystal Growth, p. 329, Oct. 1978.

DISCUSSION

GLICKSMAN: I think we do want to be careful in distinguishing the terms equilibrium growth and steady state, because when we begin to talk about faceting and supercooling, we are talking about departures from equilibrium--whereas we may have very non-equilibrium crystal growth, but occurring at steady state.

LEIPOLD: Good point.

MILSTEIN: You mentioned equilibrium structures as being of two types, and I would mention some results that Simon Tsuo, Rick Matson and Jeff Hurd have obtained on ESP ribbons grown at SERI. They observed that for rather thick ribbons you obtain a random structure (this is using electron channeling), whereas for thinner (100-150 μm) ribbons you obtain the equilibrium structure that you described. The thought in my mind is whether, when you go to thinner ribbons, there is an effect due to surface free energy that only becomes apparent when the surface-area-to-volume ratio becomes large.

N84 28619

OVERVIEW OF CHARACTERIZATION TECHNIQUES FOR HIGH SPEED CRYSTAL GROWTH

K.V. Ravi

Mobil Solar Energy Corporation
16 Hickory Drive, Waltham, Massachusetts 02254, U.S.A.

ABSTRACT

Features of characterization requirements for crystals, devices and completed products are discussed. Key parameters of interest in semiconductor processing are presented and characterization as it applies to process control, diagnostics and research needs is discussed with appropriate examples.

INTRODUCTION

A wide variety of approaches to characterizing silicon crystals and devices have been developed over the years. The techniques and the sophistication achieved have evolved as characterization needs have increased or changed in response to technological innovation. With the advent of new technology development geared towards achieving cost effective photovoltaic power generation, a new dimension has been introduced into the science and technology of materials characterization. In general, materials characteristics and characterization techniques employed for characterizing crystals intended for photovoltaic applications are not significantly different from those employed for characterizing crystals grown for conventional semiconductor devices.

In this paper an overview of characterization approaches will be presented. Since the subject matter of semiconductor characterization is very large with many specialized and general purpose techniques available for characterization, this paper will selectively discuss a few pertinent approaches and no attempt will be made to be comprehensive.

Prior to discussing characterization approaches a brief discussion of properties of crystals and devices of interest to photovoltaics will be presented.

MATERIALS PROPERTIES

The general objectives in developing a technology for high speed crystal growth for photovoltaic applications are self evident. The achievement of low costs requires high productivity in conjunction with

low materials costs. In the pursuit of productivity increases, an essential requirement is that the material properties of interest be maintained at the desired level. Characterization approaches will have to include characterization of crystals, devices and functional products represented by photovoltaic modules, since interactive effects among various processes play a very important role in determining the performance and yield of the product.

The interactive nature of photovoltaic product manufacturing can be represented as shown in Figure 1. The interactions which modify properties occur at every stage of the process from the growth of crystals to the operation of photovoltaic modules in the field. Some selected considerations include the following:

(i) Interactions between the raw material and the properties of the resulting crystal play an important role in crystal growth from the melt. Key factors include defect introduction processes, impurity incorporation phenomena, segregation effects and homogeneity of dopants, impurities and point defects in the crystal. Important concerns of the future include the influence of silicon of less than semiconductor grade purity levels on the above phenomena. Critical issues include the effects of growth rates, crystal dimensions and thermal environment during solidification and subsequent cooling to room temperature.

(ii) Interactions between the crystal and the various thermal, chemical and mechanical operations involved in device fabrication are important in determining the properties of the device which relate to the conversion efficiency of solar cells. Critical issues include the influence of junction formation conditions (time, temperature, surface reactions, ambients) on the properties of the p-n junction and the bulk of the crystal, interactions between the silicon and metals used as electrical contacts (intermetallic formation, ohmic contacts, resistivity, etc.) and the response of the crystal to various thermal and mechanical stresses integral to the fabrication process.

(iii) Interconnection and packaging effects on solar cell properties are of concern to assure maximum performance and reliability of the product. Important properties include the integrity of the bond between the interconnect material and the metallization on the device, the influence of packaging related stresses on the integrity of the device and interconnection related electrical losses due to factors such as electrical mismatch, cracked cells, etc.

(iv) Interactions between photovoltaic modules and the environment are important in determining module reliability and lifetime. Issues of interest include interconnect fatigue due to thermal cycling, possible impurity migration effects over time, localized hot spots due to broken cells and corrosion of contacts due to packaging related failures.

Key materials characteristics which can have a significant impact on the cost, the yield, the conversion efficiency and reliability of

photovoltaic products can be broadly classified into electrical, structural and chemical properties as follows:

ELECTRICAL PROPERTIES

Electrical properties of importance include the resistivity, conductivity type and the minority carrier lifetime (or diffusion length). The absolute magnitude of these parameters as well as their distribution through the thickness and across the surface of the crystal are important. In devices, electrical characteristics of interest include minority carrier lifetimes in various regions of the solar cell such as the front junction region and the bulk of the crystal or wafer. In addition, the terminal characteristics such as the open circuit voltage, the short circuit current and the fill factor, of course, determine the conversion efficiency of the solar cell. The spectral response of the device is a good indicator of relative quality of various regions of the device.

STRUCTURAL-MECHANICAL PROPERTIES

Structural characteristics which can have a strong impact on the electronic and mechanical properties of crystals and devices include deviation from single crystallinity, defects such as grain boundaries, dislocations, stacking faults, precipitates and point defect/impurity complexes. Both the type and the distribution of imperfections play a key role in determining characteristics of importance.

Variables of a mechanical nature include flatness of the crystals with special reference to shaped crystals grown directly from the melt, surface quality from the point of view of surface topography and roughness and the edge quality of the crystal. Since very high process yields are a requirement in low cost photovoltaic manufacture, mechanical properties such as short and long range residual stresses, hardness, notch sensitivity and flexure strength are important in order that the crystals can withstand thermal and mechanical forces encountered during device processing and packaging.

CHEMICAL PROPERTIES

Chemical or compositional properties of importance include impurity concentration, distribution and lattice location. Key impurities are the dopant impurities, transition metals, oxygen and carbon. In addition, the influence of point defects and point defect associates may be important in solar cells.

Chemical characteristics of devices involve p-n junction profiles, junction depths and any thermal processing induced changes in the lattice location and configuration of impurities. Chemical effects also become important in solar cell processing involving wet or dry chemical

approaches such as etching, deposition of dielectric films for anti-reflection coatings, metallization, interconnection and packaging.

In characterizing materials and devices one can divide the various characterization techniques and approaches into a hierarchy ranging from characterization for process control through diagnostics to research requirements.

HIERARCHY OF CHARACTERIZATION APPROACHES

In an overview of characterization techniques, it is found that the particular techniques adopted are determined by the needs. The amount and type of information derived, the sophistication of the techniques utilized and the time required for characterization all have an impact on the approaches utilized. Typical characterization is done in response to three general requirements, viz. (a) process control (b) diagnostics and (c) research.

PROCESS CONTROL

Characterization for process control is important in ongoing technology development, pilot production and manufacturing operations. The needs are for rapid, accurate and statistically significant data of relevance which provide an indication of the state and reproducibility of a given process. The key attributes of characterization techniques for process control are listed in Figure 2 and discussed below in greater detail.

(a) Process control requires on line characterization and measurement. Examples of online measurements include measurement of crystal dimensions such as width, thickness, flatness and the uniformity and reproducibility of these parameters. An obvious online measurement technique is device characterization to determine terminal characteristics of solar cells and modules.

(b) Measurement techniques for process control should be non-destructive and preferably non-contact. Examples include mercury probe techniques for resistivity measurements, and infrared techniques for thickness measurement.

(c) Online measurement techniques should be rapid in order to provide quick feedback to permit corrective action to be taken on a given process if measurements indicate deviation from standard operating conditions.

(d) Process control techniques need to be flexible and adaptable to changing conditions as the technology evolves. Such techniques, in analogy with flexible automation, may be termed flexible characterization techniques.

(e) Process control measurement techniques are frequently integrated into equipment utilized to practice the process. This is done to provide online, real time feedback of information for maintaining the process in the required condition.

(f) Measurement of key parameters in a manufacturing environment may require interfacing with computers and be integrated into a total manufacturing information system. Information such as process yields, materials consumption rates and throughput of machines needs to be monitored, collected and analyzed on a real time basis.

An example of a process control measurement technique is the automatic monitoring and control of the width of silicon ribbons grown by the Edge-defined Film-fed Growth (EFG) process. Whereas the thickness dimension of the ribbon is inherently stable during solidification as a consequence of the presence of the shape defining die, the edges of the ribbon are only partially stable since the meniscus acquires a second radius of curvature at the ribbon edges.[1] As a result, minute temperature changes at the ribbon edges can cause changes in ribbon width. To cope with this problem, automatic edge position control devices have been developed. This system involves observation of the ribbon ends at the solid liquid interface by means of a TV camera equipped with anamorphic optics which preferentially magnify the vertical dimension of the image over the horizontal dimension (Figure 3). The image so obtained is electronically analyzed and information fed back to either movable radiation shields or miniature resistance heaters on either side of the die. Automatic temperature adjustments are made in response to changes in ribbon width, or position of the ribbon ends to thermally stabilize the ribbon ends, thus maintaining constant ribbon width.[2]

This system embodies most of the key requirements of characterization or measurement for process control. The edge position of the ribbon is determined on a real time, contact-less basis. The information so derived is used for feedback control to continuously adjust for deviations from standard operating conditions.

This system is also a good example of obsolescence of a technique in the face of changing technology. A variation of the EFG process involves the production of sheet silicon by growing tubular crystals of silicon shaped in the form of a hollow polygon. Such crystals, called "nonagons" since they are composed of polygons with nine flat sides each ~5 cm in width, have no edges, unlike ribbons, and hence do not require edge position control devices.[3]

The long range aim of all process control techniques is to be eliminated as a result of achieving a high degree of reproducibility in the process. As increasingly lower manufacturing costs are sought, the necessity for characterization for process control should be eliminated. An example where this has already occurred is in the manufacture of small signal (low power) transistors and diodes. The reproducibility of the terminal characteristics of these devices is such that electrical

characterization of individual devices is no longer done and the product is sold to the customer with a guaranteed minimum acceptable performance with no testing at the factory. A similar objective is an important one for photovoltaics.

DIAGNOSTICS

Material and device diagnostics form the most widely employed approaches in semiconductor process and technology development. Diagnostics, as the word implies, has its origin in failure analysis whereby a non-functioning device is characterized to unearth the causes for failure. Today, diagnostics applies in a broader context whereby cause and effect relationships are examined in an iterative process to develop particular processes towards a desired end goal. In general, diagnostic approaches involve detailed studies of interactions between material characteristics such as defect structure and distribution, impurity content and distribution and relevant electrical parameters such as minority carrier lifetime, p-n junction characteristics, etc..

Diagnostic approaches can be practiced in two different ways. One approach is to rely on statistics whereby large amounts of data, such as solar cell terminal characteristics, are gathered and compared with another parameter of interest such as, for example, the minority carrier diffusion length in the crystal. Information so derived can be used to make appropriate changes in the process and any new correlations tested, again, by the use of statistics. Such approaches are useful in obtaining broad based information.

A second, and more fundamental approach to diagnostics is the iterative process whereby individual crystals or devices are subjected to appropriate chemical, mechanical, thermal and electrical forces followed by observation by suitable means. Such techniques are generally time consuming, require detailed analysis and interpretation and are aimed towards providing key information for process development leading to increased yields, enhanced performance and reduced costs. Some examples of diagnostic approaches in semiconductor technology development are presented below:

(a) An assessment of the influence of dislocations in the crystal on the reverse I-V characteristics of p-n junctions built in the crystal is of interest since a large majority of crystal growth techniques currently being developed for low cost photovoltaics result in crystals with relatively high densities of dislocations. Figure 4 shows dark reverse I-V characteristics of diodes with different densities of dislocations.[4] Dislocation density measurements were made by simple preferential etching and optical microscopy techniques. A doubling of the dislocation density is observed to result in an increase of the reverse leakage current by an order of magnitude at a reverse voltage of 30V.

A more detailed examination of individual dislocations can be achieved by using an SEM operated in the electron beam induced current (EBIC) mode. Figure 5 shows two sets of dislocations observed in the EBIC mode at different values of reverse bias on the p-n junction. At the zero bias or low reverse bias conditions, the dislocations function as recombination centers. At higher values of reverse bias, individual current enhancement regions are observed as discrete sites along the dislocations, indicating local impurity decoration of the dislocations. Information of this type can now be utilized to examine the crystal growth and device processing operations to determine if dislocation and impurity introduction processes occur at crystal growth or during processing.

(b) The influence of crystal growth rates on defect density and distribution through the thickness of silicon ribbons grown by the EFG technique has been examined by Rao et al.[5] Figure 6 shows cross sectional optical micrographs of silicon ribbons grown at rates ranging from 2 cm/minute to 5.6 cm/minute. When the growth rate exceeds ~2.5 cm/minute, a subsurface structure is observed to develop. This subsurface structure is composed of small grains with random grain boundaries whereas ribbons grown at growth rates below ~2.5 cm/minute exhibit an ordered structure largely composed of twins and linear arrays of dislocations. To further extend the diagnostic approach, the influence of the subsurface grain structure on the properties of solar cells fabricated in such crystals has to be assessed and the particular conditions during high speed crystal growth that contribute to the generation of the subsurface structure must be determined.

Issues of interest include interface shape effects on the generation of the subsurface structure, possible constitutional super cooling effects, the influence of impurities and the tendency for dendritic crystallization at high growth rates. Device related phenomena that might be affected by the subsurface structure include its effects on minority carrier lifetime, lifetime and dopant gradients, the effect on the back surface field in n+p p+ structures, etc. A complete analysis of the phenomena necessitates characterization and measurement at all stages of the process commencing with crystal growth and its precursor, the raw material, through device fabrication and measurements.

(c) A third example of diagnostics is a more fundamental approach that blends into the category of research into fundamental phenomena. The influence of heat treatments on the relative concentrations of vacancies and interstitials in silicon is examined by observation of the growth and shrinkage of faulted and prismatic dislocation loops in oxidized silicon.[6]

Figure 5. Electron beam induced current (EBIC) images of two sets of dislocations imaged under different conditions of reverse bias on the diode. At high reverse voltages, discrete current generation centers are observed along the dislocations, indicating local impurity decoration.

Figure 7 shows a series of transmission electron micrographs of an oxidation induced stacking fault in Czochralski silicon. Figures 7(a)-(c) show the fault imaged under three different diffracting conditions. In 7(b) and (c) only the partial dislocation bounding the fault is in contrast ((c) is a weak beam image). At the leading edge of the fault are seen numerous dislocation loops which lie on (111) planes parallel to the main fault. Figure 7(d) and (e) show the fault following annealing in a non-oxidizing ambient for 5 minutes each at 1100°C. Annealing results in the shrinkage and annihilation of the small dislocation loops as well as the acquisition of straight line segments by the partial dislocation bounding the fault, indicating a shift in the relative concentrations of interstitials and vacancies. Since the fault and the prismatic loops are extrinsic in nature, their shrinkage upon annealing in a non-oxidizing ambient indicates an increase in the local vacancy concentration and a concomitant reduction in the local interstitial concentration.

(d) An important subject of interest in crystals grown at high rates is the influence of defects, which appear to be an inevitable consequence of high rate growth, on electrical characteristics of the material. In particular, grain boundary effects on device characteristics have come under increasingly detailed scrutiny in recent years. A particularly interesting phenomena is that of hydrogen passivation of defects in silicon crystals. Hanoka et al.[7] have shown that hydrogen ion implantation has the effect of electrically passivating grain boundaries in EFG silicon ribbons. The phenomena has been monitored by the use of the EBIC technique. Figure 8 shows EBIC micrographs of a region of an EFG ribbon solar cell before and after hydrogen passivation. Prior to passivation, a larger number of grain boundaries in the form of recombination centers are observed as dark lines. Following passivation, none of the defects are observed to function as recombination regions. Hydrogen passivation is also observed to enhance the efficiency of solar cells, as expected from the EBIC data.

Clearly, further analysis and study is required to determine the specific effects of hydrogen in defective crystals and devices. Questions such as the nature of interactions between hydrogen and defects such as dislocations and with lifetime reducing impurities such as the transition metals need to be answered.

RESEARCH

Materials and device characterization in research is a very broad ranging field of activity and it is generally difficult to describe any

---

Figure 7. Transmission electron micrographs of an oxidation-induced stacking fault subjected to heat treatment. (a) and (d) are imaged with ($\bar{1}11$) reflection. (b) and (e) are imaged with a ($\bar{1}13$) reflection, and (c) is a ($\bar{1}13$) weak beam image. See text for discussion.

---

specific features of such activity. Characterization assists in investigation of fundamental phenomena of interest. The objectives are to obtain basic information about materials, devices and processes without any particular constraints being applied to the investigatory process. Two examples of characterization for unearthing basic phenomena in semiconductor processing are discussed below:

(a) The formation of microdefects in silicon crystals grown from the melt is a well known phenomena.[4] Continuing controversy as to the nature of microdefects is now beginning to yield to new measurement techniques and to new theoretical treatments. The generally accepted mechanism of microdefect formation in Czochralski and float zoned crystals is that of association between silicon interstitials and impurities such as carbon at the solid liquid interface. The association between interstitials and impurities has been postulated to result in the formation of droplets of liquid silicon in the solidifying crystal just ahead of the solid liquid interface.[8] The inhomogeneous incorporation of carbon and transition metal impurities in the solidifying crystal is postulated to result in locally increased absorption of infrared radiation from the furnace ambient with the result that droplets of liquid silicon are retained just ahead of the solid liquid interface. The droplets will be distributed in a non random fashion conforming to the distribution of impurities. Using transmission X-ray topography techniques Chikawa and Shirai[8] have obtained some evidence for this mechanism. Figure 9 shows a series of transmission X-ray topographs of a thin silicon crystal during the course of melting. Before complete melting of the crystal, small black dots appear which are postulated to be local droplets of liquid silicon forming in the crystal at temperatures below the absolute melting point of the crystal as a whole. During crystal growth from the melt, an inverse of this effect can result in the retention of local droplets of silicon in the solidified crystal at temperatures just below the melting temperature of the crystal. When these droplets subsequently solidify, a local increase in the concentration of silicon atoms (interstitials) results due to the higher density (by about 10%) of liquid silicon as compared to solid silicon. These excess interstitials can condense to form localized microdefects in the form of prismatic dislocation loops or stacking faults. An analogous mechanism for the generation of crystallographic defects in EFG silicon ribbons has been proposed by Rao et al.[5]

(b) In the investigation of fundamental phenomena, it is often difficult to work with practical crystals and devices produced as part of a manufacturing or commercial enterprise. Many analytical techniques do not lend themselves to the study of real devices due to difficulties associated with the geometry of devices, physical access to p-n junctions etc. In such cases, crystals can be processed to simulate process conditions (time, temperature, ambients, etc.) encountered in the production of practical products and the structures so derived studied by the use of suitable techniques.

An example of this is the investigation of the phenomena known as electrical "piping" in high speed transistors typical of those used in logic circuits and high frequency devices. Electrical pipes are localized high conductivity regions which cause unwanted conduction between the emitter base and the collector base junctions of transistors. This problem is found to be particularly acute in structures made with very shallow junctions (< 0.5 μm) which are typical of high speed logic circuits and microwave transistors. Shallow junctions, of course, are also a feature of solar cells.

Although the electrical pipe manifests itself in the completed device, it has been found that the physical origins of this electrical defect can be traced all the way back to the crystal growth step.[4] Figure 10 shows EBIC micrographs of a transistor at two stages of its fabrication process.[9] The top two micrographs show the device after the formation of the collector base junction. A large density of local recombination centers are observed as discrete spots. The device is then removed from the SEM and subjected to phosphorus diffusion to form the emitter base junction following which the device is re-examined in the SEM. Discrete recombination centers are also observed in the completed transistor which are the electrical pipes. An immediate conclusion is that every emitter pipe emanates from a base defect present prior to emitter diffusion and emitter diffusion itself does not create new recombination centers or pipes. Additionally, not all the base defects convert into emitter pipes. Further detailed transmission electron microscopy has established that the emitter pipes are composed of localized micropits in the surface of the emitter surrounded by a network of dislocations (Figure 11). The base defect is generally composed of oxidation induced stacking faults often decorated by impurities. The origin of oxidation induced stacking faults is the conversion of microdefects in the crystal to stacking faults during thermal oxidation performed to allow selective diffusion for device fabrication.[10]

CONCLUSIONS

Although a vast array of characterization techniques have been developed and deployed in analyzing crystals and devices, the search for newer and better techniques continues. An idealized characterization scheme for in situ characterization of crystals during growth is depicted in Figure 12. The challenge facing characterization technology is to develop a universal probe or set of probes which suitably interact with the growing crystal, the interface, the liquid meniscus and the ambient to generate information on a real time basis. The desired information ranges from process variables such as temperature and temperature distribution to chemical information such as the composition and distribution of impurities and structural and electrical information. A universal characterization scheme of this type is the "holy grail" of the characterization scientist, the search for which continues.

REFERENCES

1. T. Surek, J. Appl. Phys., 47, 4384 (1976).

2. F.V. Wald, Annual Progress Report, DOE/JPL 954355 (1981).

3. A.S. Taylor, R.W. Stormont, C.C. Chao, and E.J. Henderson, 15th IEEE Photovoltaic Specialists Conference, (New York: IEEE; 1981), p. 589.

4. K.V. Ravi, Imperfections and Impurities in Semiconductor Silicon, John Wiley & Sons, 1981.

5. C.V.H.N. Rao, M.C. Cretella, F.V. Wald, and K.V. Ravi, J. Cryst. Growth, 50, 311 (1980).

6. K.V. Ravi, Philos. Magazine, 30, 1081 (1974).

7. J.I. Hanoka and C.H. Seager, D.J. Sharp and K.J.G. Panitz, Appl. Phys. Lett., 42, 618 (1983).

8. J. Chikawa and S. Shirai, J. Cryst. Growth, 39, 328 (1977).

9. C.J. Varker and K.V. Ravi, in: Semiconductor Silicon, ed. H.R. Huff and E. Sirtl, p. 785 (1977).

10. K.V. Ravi and C.J. Varker, J. Appl. Phys., 45, 263 (1976).

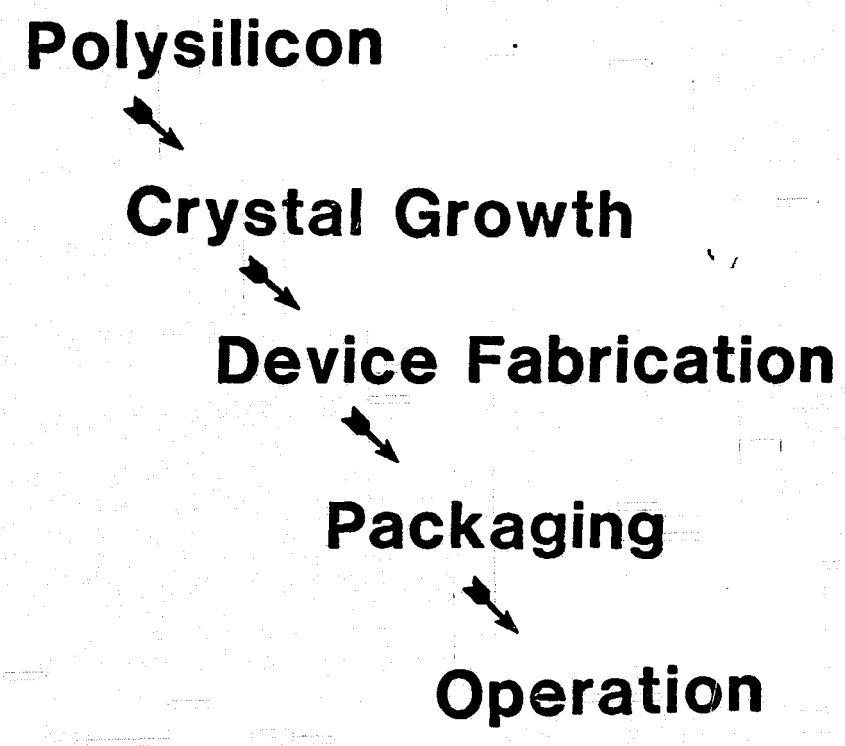

FIGURE 1: INTERACTIVE NATURE OF PHOTOVOLTAIC PRODUCT MANUFACTURE

Process Control

- On Line Characterization
- Nondestructive, Contactless
- Rapid
- Flexible
- Integrated Into Manufacturing
- Automated Measurements
- Obsolescence

FIGURE 2: TYPICAL FEATURES OF CHARACTERIZATION FOR PROCESS CONTROL

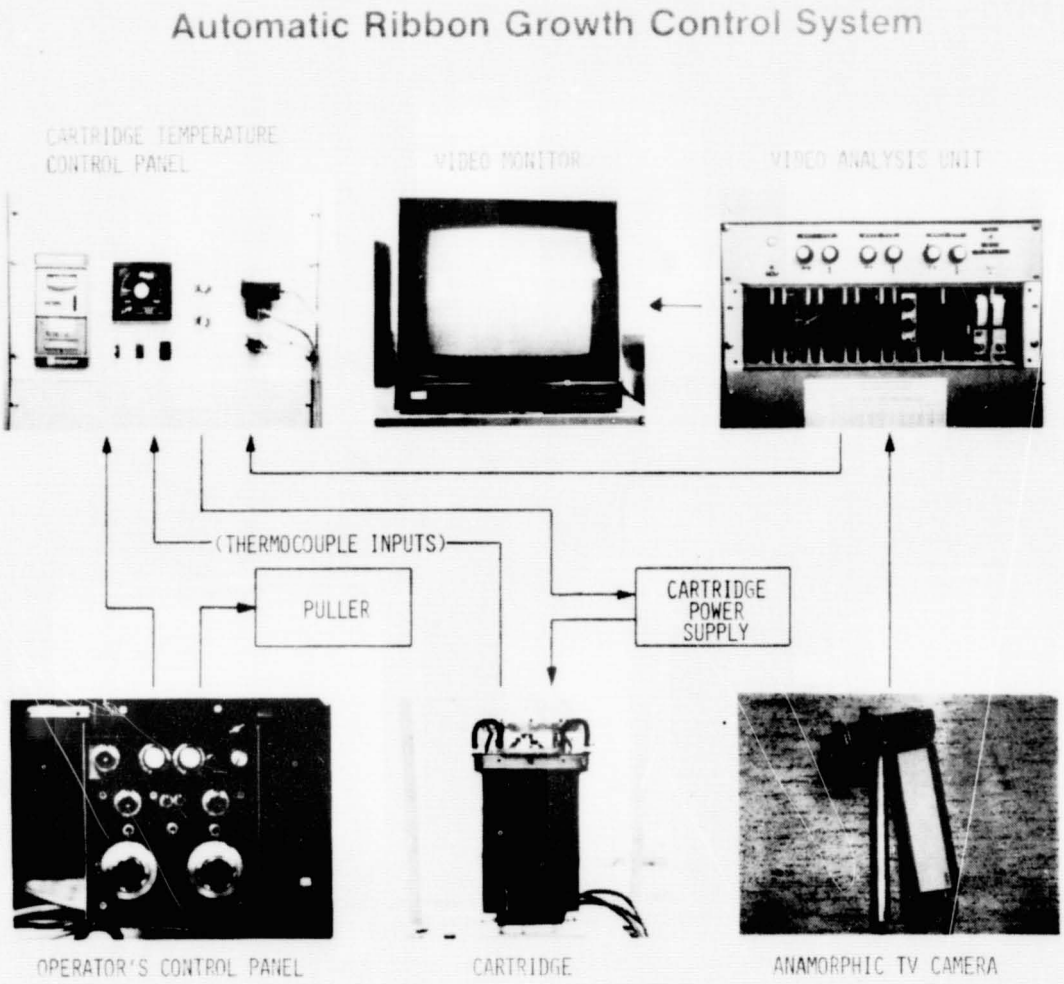

FIGURE 3: KEY ELEMENTS OF AUTOMATIC RIBBON WIDTH CONTROL SYSTEMS [2].

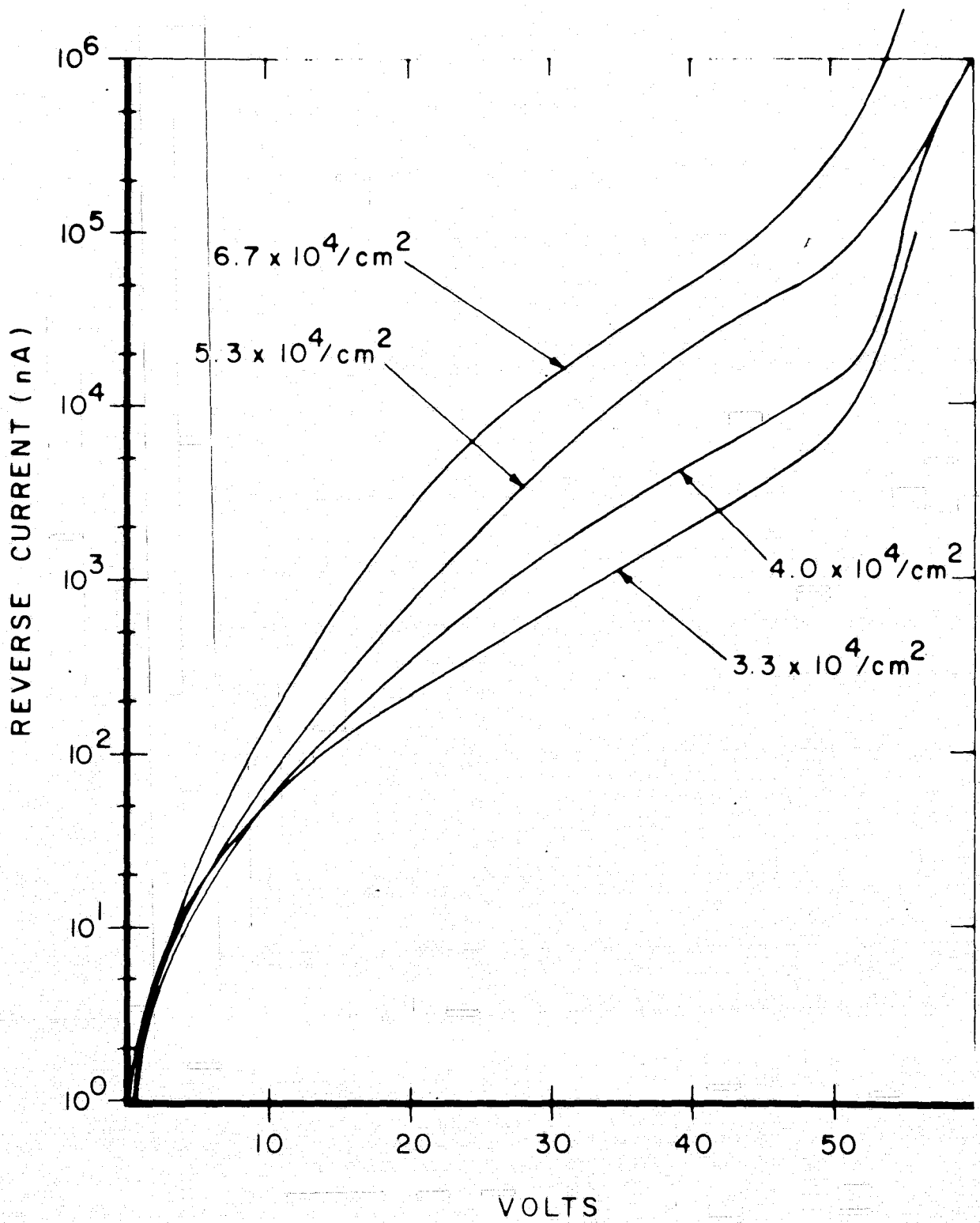

FIGURE 4: DARK REVERSE I-V CHARACTERISTICS OF SHALLOW p-n JUNCTIONS ($X_j \approx 0.5$ μm) AS A FUNCTION OF DISLOCATION DENSITY.

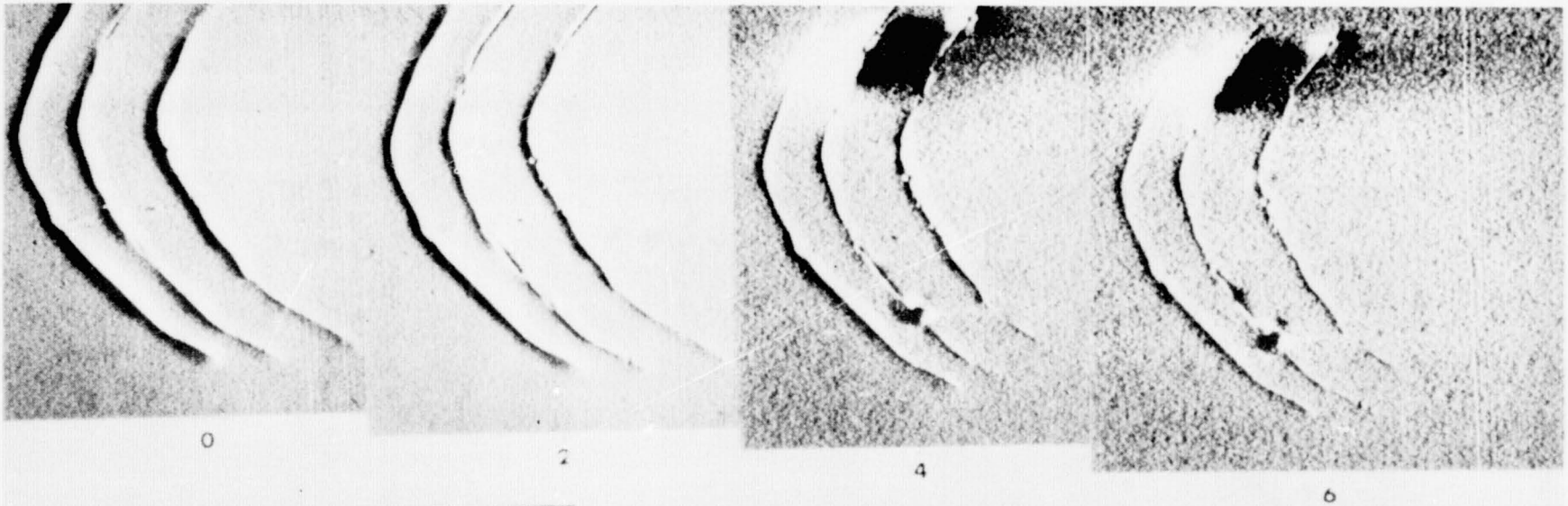

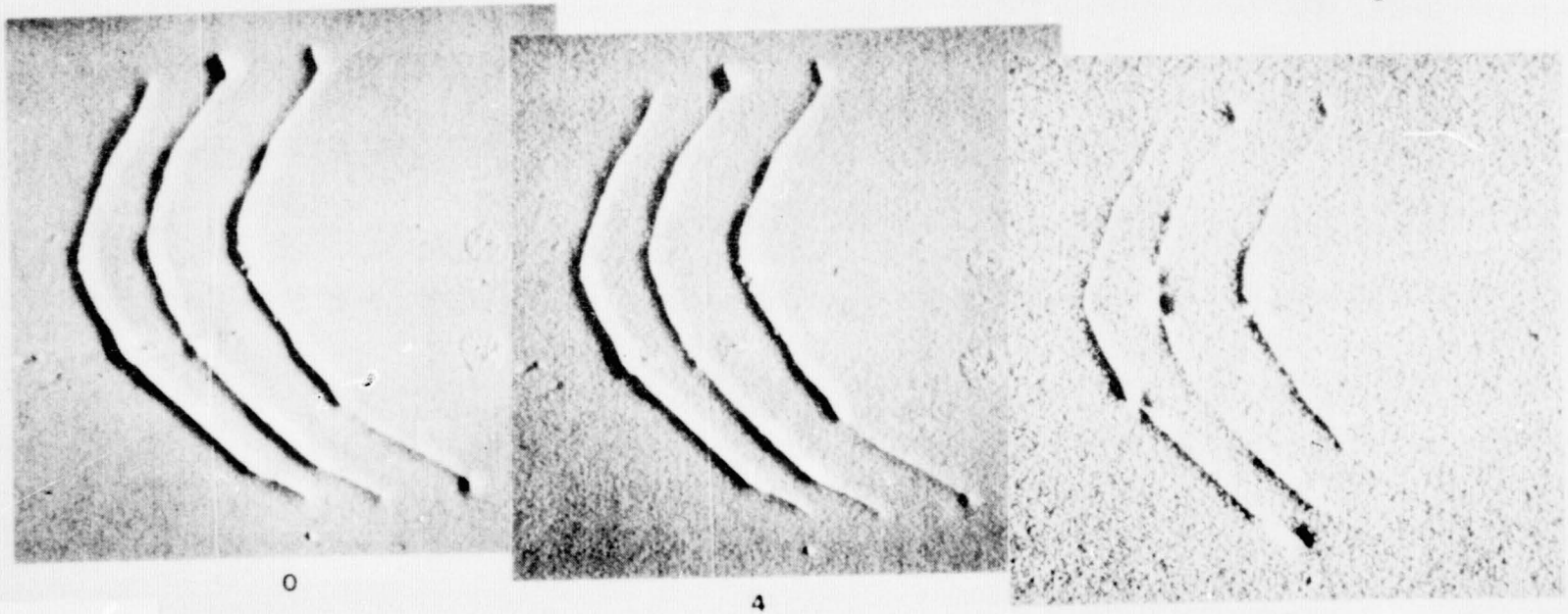

FIGURE 5: 20 μm

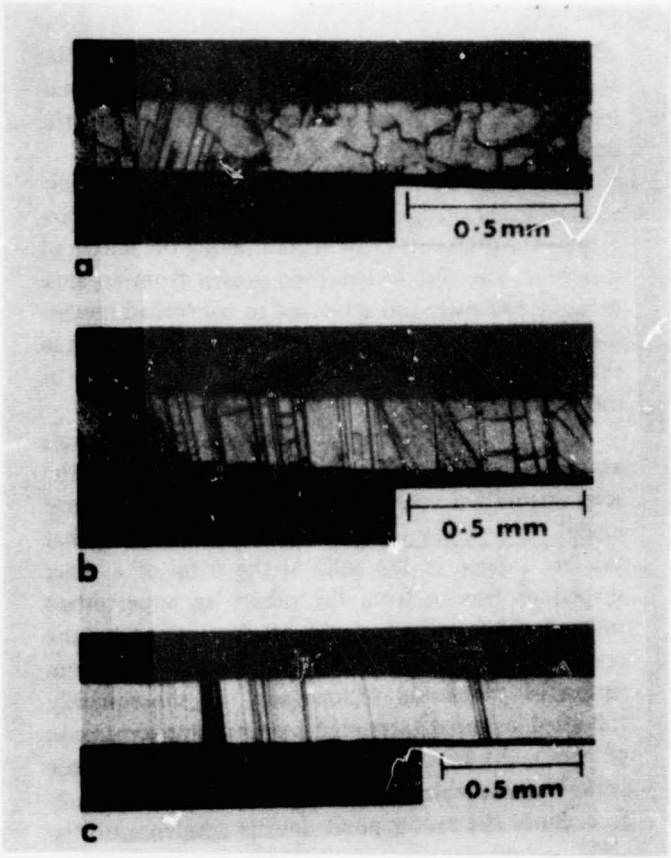

FIGURE 6: CROSS SECTIONAL VIEWS, PERPENDICULAR TO THE GROWTH DIRECTION OF RIBBONS GROWN AT VARIOUS SPEEDS (a) AND (b) SHOW SUBSURFACE GRAIN STRUCTURE IN RIBBONS GROWN AT 4.5 AND 5.6 cm/minute, RESPECTIVELY. NOTICE THE LACK OF SUBSURFACE GRAIN STRUCTURE IN RIBBONS GROWN AT 2.0 cm/minute SHOWN IN (c)[5].

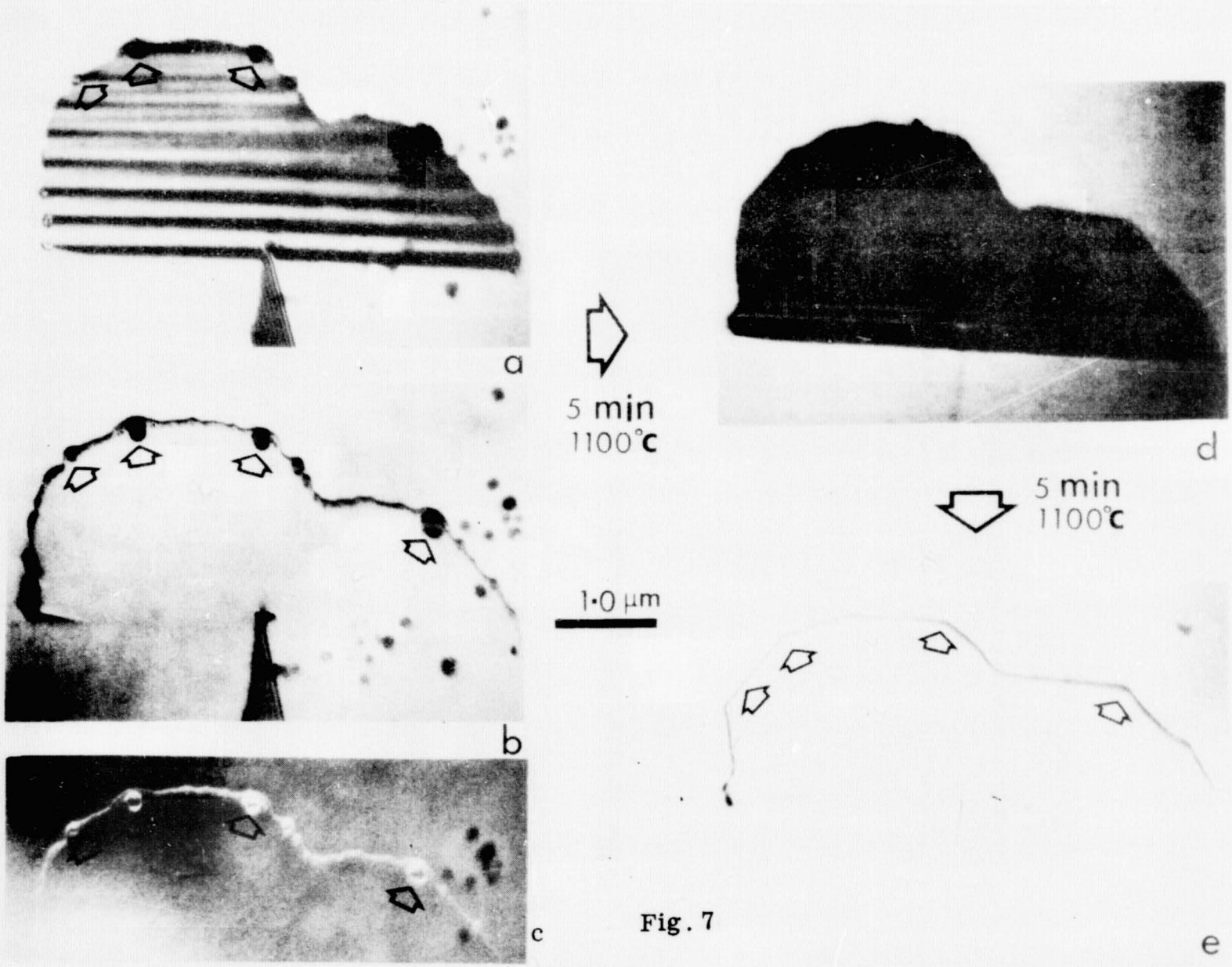

Fig. 7

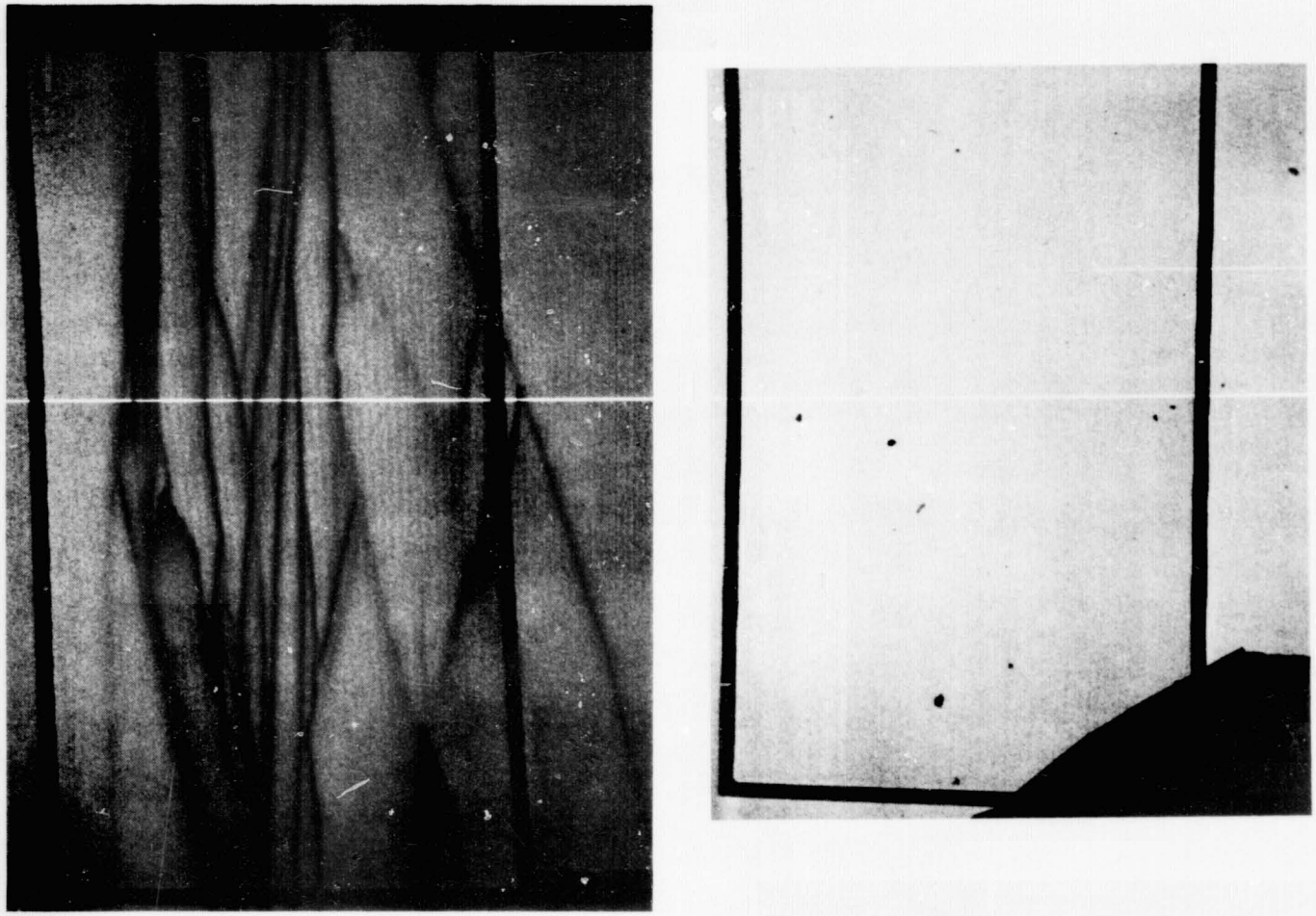

FIGURE 8: EBIC IMAGES OF A PORTION OF A EFG RIBBON SOLAR CELL BEFORE (LEFT) AND AFTER (RIGHT) HYDROGEN PASSIVATION. (FROM HANOKA et al. [7]).

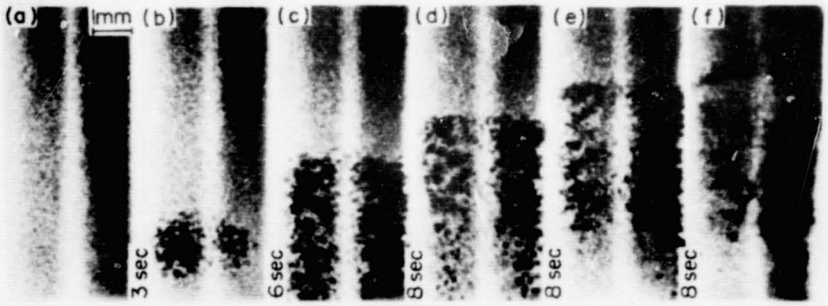

FIGURE 9: TRANSMISSION X-RAY TOPOGRAPHS SHOWING A SEQUENCE OF IMAGES OF A DISLOCATION FREE CRYSTAL MELTED RAPIDLY. MELTING OCCURS AFTER ABOUT 8 SECONDS. PRIOR TO COMPLETE MELTING, BLACK SPOTS APPEAR IN THE TOPOGRAPHS (b-c) WHICH ARE ATTRIBUTED TO LOCAL DROPLETS OF LIQUID SILICON IN A SOLID MATRIX (FROM CHIKAWA AND SHIRAI[8).

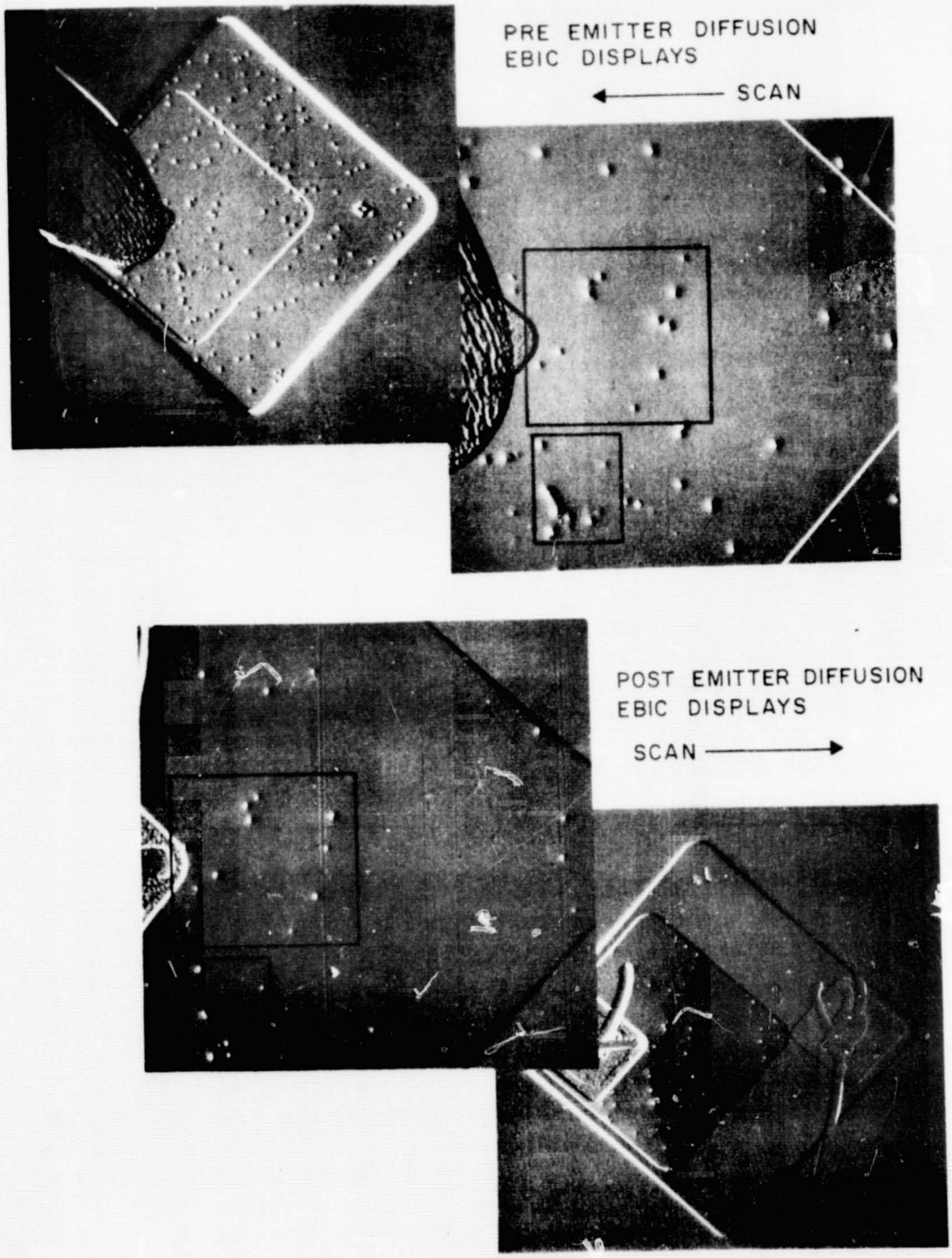

FIGURE 10: EBIC MICROGRAPHS OF A TRANSISTOR IN TWO STAGES OF ITS FABRICATION. THE TOP MICROGRAPHS SHOW THE DEVICE PRIOR TO EMITTER DIFFUSION AND FOLLOWING BASE DIFFUSION. THE BOTTOM MICROGRAPHS SHOW THE DEVICE FOLLOWING EMITTER DIFFUSION. A DIRECT POSITIONAL CORRESPONDENCE BETWEEN BASE RECOMBINATION SITES FORMED PRIOR TO EMITTER DIFFUSION AND ELECTRICAL PIPES FORMED AFTER EMITTER DIFFUSION IS INDICATED (VARKER AND RAVI[9]).

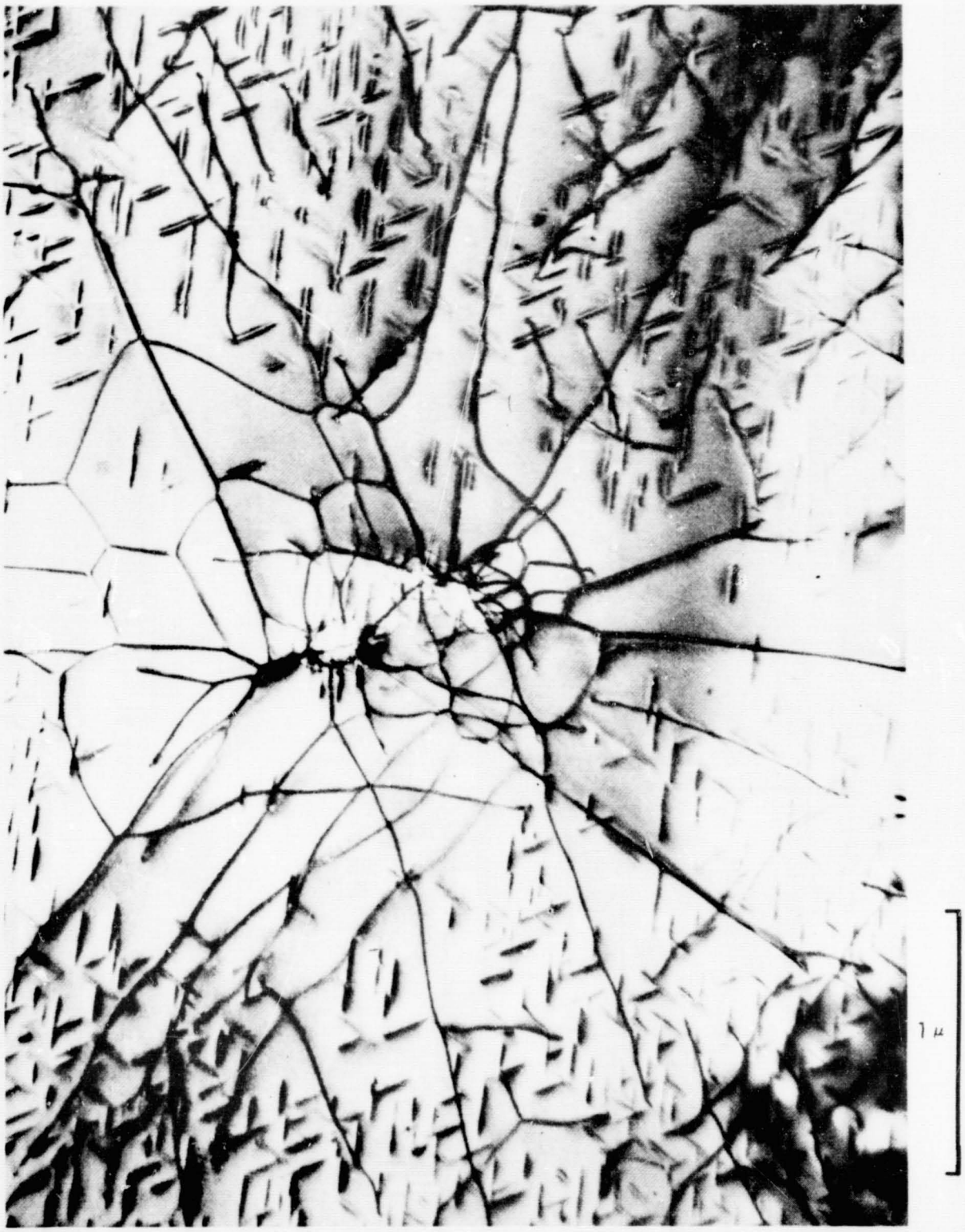

FIGURE 11: TRANSMISSION ELECTRON MICROGRAPH OF A TYPICAL ELECTRICAL PIPE SHOWING THE CENTRAL CORE COMPOSED OF SUBMICRON-SIZED PITS SURROUNDED BY A NETWORK OF DISLOCATIONS. THE NEEDLE-SHAPED FEATURES ARE SiP PRECIPITATES FORMED DUE TO PHOSPHORUS SUPERSATURATION AT THE SURFACE DURING EMITTER DIFFUSION.

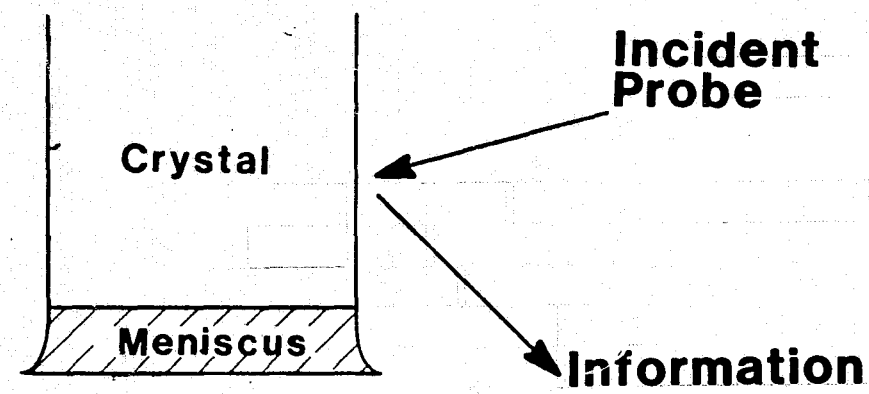

- Temperature
- Temperature Distribution
- Minority Carrier Lifetime
- Thickness

- Chemical Properties - -C, O, Metals, Dopants, Point Defects
- Structure
- Crystal Shape
- Stress

FIGURE 12: SCHEMATIC OF AN IDEALIZED CHARACTERIZATION SCHEME FOR IN-SITU CHARACTERIZATION DURING CRYSTAL GROWTH.

C-2

DISCUSSION

AST: When the dislocation density was increased by a factor of 2, the reverse leakage current went up by a factor of 10. Then you said that it is actually the microplasmas that form on these decorated dislocations that cause the increase in the leakage current. That says there is a 1:1 correlation between the dislocation density and the impurity decorations. In other words, your samples that have a factor of 2 or higher dislocation density have more precipitates in them than the ones that have less, and that is very puzzling. Usually, you would think that if the dislocation density goes up, the impurity decoration per dislocation goes down. Could you make any comment on this?

RAVI: I think it depends on whether the impurity comes from a source-limited diffusion source, or an infinite source. One speculation is that you have a lot of impurities and if you didn't have dislocations they would be more homogeneously distributed, or distributed in such a fashion that they are not electrically significant. But if you have dislocations, you have no local nucleation sites or precipitant formation, and this infinite source of impurity continues to precipitate as more and more dislocations are available.

AST: The point is that there is a correlation between the dislocation density and the impurity agglomerates. You must assume that when the dislocation density is a factor of 2 higher, you get more precipitates per square area, which generates the microdefects, than when dislocation densities are lower. When you have a nucleation mechanism on dislocations you would think that these guys go to this dislocation. In the higher case, there is less decoration per dislocation, given the same amount of impurity.

RAVI: I think it depends on the impurity content available.

MILSTEIN: Dieter [Ast] is assuming that a single dislocation is electrically active, and if you have twice as many you should have twice as much leakage current. The point may be that it takes more than one dislocation to introduce this leakage current and therefore, by raising the density and having agglomerates of dislocations in some sense, the probability of finding the correct agglomerate goes up proportionately and you see this result. It may not necessarily be due solely to impurities.

RAVI: Certainly. This is the perennial question. Is it impurities or is it defects, and I don't think the evidence is out yet.

GRABMAIER: In one picture, I could see that you were very successful in passivating your ribbon material. What have you done?

RAVI: It is basically ionizing hydrogen using a source known as a Kauffman ion source. Then you implant the hydrogen ions into the surface of the crystal.

GRABMAIER: But that is a very expensive process.

RAVI: It is not an expensive process. You can continuously implant hydrogen into moving crystals on a belt at rates of a thousand an hour. So it is not expensive. We don't know how stable these devices are under operating conditions and how reproducibly you can get efficiencies starting at different qualities of levels.

MILSTEIN: As far as hydrogen passivation goes, the cell that was shown here was passivated in a plasma source at 275° substrate temperature over a period of four minutes. Carl Seager has observed, as well as other people, that in very short periods of time it is possible to eliminate the electrically active defects over depths, in polycrystalline materials, of hundreds of µm using a plasma source for hydrogen. This is an area of great excitement and interest.

SUREK: I would like you to project a little. What sort of process control do you see needed?

RAVI: We need on-line rapid interactive process-control techniques. But they cannot become a crutch. You have to be able to eliminate them. I will give you an interesting example: in the semiconductor industry, they make what I call small signal devices, little transistors and diodes, low-power devices. For the last eight to ten years, these have been made and sold to customers without ever testing them. They have the process down to such a degree of precision that they don't have to test anything. They guarantee a minimum performance to the customer and sell them by bag lots.

That is the way solar cells have to be. We can't afford to test solar cells to get the cost down in the future. Testing of a device or a module is a process-control tool. It is characterization for process control. Now, starting from that end, you go all the way through the operation to something like measuring the height of the meniscus and having a feedback control system to make sure it stays where it is. And each one of these process control techniques, I think, has a different life span. As the technology improves, you have to reach this Utopian ideal when you have no process control. It is a perfect process. But they won't have them for a long time, so I think the answer is, we need these kind of process-control tools and techniques for on-line characterization measurement and control. And a lot of them, resistivity, thickness, all of these things have to be measured.

SESSION II: THEORY OF CRYSTAL GROWTH

W. Wilcox, Chairman

N84 28620

THE EFFECT OF SOLIDIFICATION RATE ON MORPHOLOGICAL STABILITY*

Robert F. Sekerka
Carnegie-Mellon University
Pittsburgh, Pennsylvania

ABSTRACT

The onset of morphological instability is the precursor of the cellular or dendritic mode of growth that determines the microstructure of a solidified material. At low solidification rates, the criterion for the onset of morphological instability parallels closely the criterion of constitutional supercooling; in particular, the propensity for instability increases with solidification velocity. At somewhat larger rates of solidification, however, the results of the perturbation theory of morphological instability differ significantly from the predictions of constitutional supercooling. This arises because the critical wave length for instability decreases as solidification rate increases and thus the effects of capillarity (solid-liquid surface tension) play a strong stabilizing role. This gives rise to the concept of absolute stability, according to which the system will always be stable for a sufficiently large rate of solidification. This enhanced stabilization by capillarity is, however, only present so long as local equilibrium is maintained at the solid-liquid interface. If local equilibrium is not maintained, such that the interfacial temperature drops below its equilibrium value by an amount dependent on growth rate, oscillatory morphological instabilities can occur. The differences among these various stability criteria will be illustrated by means of some simple two-dimensional diagrams that should supplant the conventional plots of (temperature gradient)/(growth rate) vs. alloy concentration.

Introduction

The onset of morphological instabilities is the precursor of the cellular or dendritic mode of growth that determines the microstructure of a solidified material. Early thermodynamically based studies concluded that such instabilities take place at the onset of constitutional supercooling.[1] Later analysis[2] of this problem by means of perturbation theory gave rise to a dynamical theory of instability. At low rates of solidification, constitutional supercooling and stability theory give similar results but at high rates of solidification, they differ.

* Also published in the proceedings of the U.S.-Japan Cooperative Science Program Seminar on "Solidification Processing" held on June 26-29, 1983, in Dedham, Massachusetts.

It is our purpose in this paper to show how the differences between constitutional supercooling and stability theory can be represented by means of some simple two-dimensional diagrams. Furthermore, at even higher rates of solidification, the assumption of local equilibrium at the solid-liquid interface breaks down and the dynamical theory of stability must be modified accordingly.[3-5] These modifications, that account for such things as non-equilibrium incorporation of solute, will be discussed briefly in terms of the same simple two-dimensional diagrams.

Constitutional Supercooling versus Stability Theory

For unidirectional solidification of a dilute binary alloy with liquidus slope m, one has constitutional supercooling[1] and expects instability whenever

$$G_L/(mG_C) < 1 \tag{1}$$

where G_L and G_C are, respectively, temperature and solute gradients in the liquid at the solid-liquid interface. Conservation of solute at the solid-liquid interface yields

$$G_C = V\, C_\infty(k-1)/(Dk) \tag{2}$$

where V is the growth velocity, C_∞ is the concentration of solute in the bulk liquid, k is the distribution coefficient, and D is the diffusivity. Accordingly, Eq(1) may be written in its usual form

$$G_L/V < (1-k)(-mC_\infty)/(Dk) \tag{3}$$

which is viewed as a critical ratio of temperature gradient to growth velocity.

The dynamical criterion for instability[2] differs from constitutional supercooling in two important respects: (1) The temperature gradient G_L in Eq(1) is replaced by the weighted average

$$G^* = (k_S G_S + k_L G_L)/(k_S + k_L) \tag{4}$$

of the temperature gradients G_S and G_L in solid and liquid, respectively; here, k_S and k_L are thermal conductivities of solid and liquid, respectively; (2) The right hand side of Eq(1) is replaced by a stability function S, the value of which lies between 0 and 1 and the role of which leads to enhanced stabilization. Thus, the dynamical instability criterion is[6]

$$G^*/mG_C < S(A,k) \tag{5}$$

where we have indicated that depends on the distribution coefficient k and the parameter

$$A = [k^2/(1-k)](\Gamma V/D)[T_M/(-mC_\infty)] \tag{6}$$

where T_M is the absolute melting temperature of the pure solvent and Γ is a capillarity length, equal to Υ/L where Υ is the solid-liquid surface tension and L is the latent heat of fusion per unit volume. The function $\mathcal{S}$ as a function of A for various k is shown in Fig. 1. We note that $\mathcal{S}$ decreases from 1 to 0 as A increases from 0 to 1; furthermore, since A is proportional to Γ, we see that the enhanced stabilization made possible through the function $\mathcal{S}$ is due to capillarity, i.e., the tendency of the system to minimize its solid-liquid surface energy by maintaining a planar interface.

Except for high growth velocities, A is usually small so $\mathcal{S} \sim 1$ and Eq(5) becomes approximately

$$G^*/mG_C < 1 \tag{7}$$

which we call the modified constitutional supercooling criterion because it closely resembles Eq(1) except for the replacement of G_L by G^*. Since conservation of heat at the unperturbed solid-liquid interface demands that

$$LV = k_S G_S - k_L G_L, \tag{8}$$

we have

$$G^* = [2k_L/(k_S+k_L)]\, G_L + LV/(k_S+k_L). \tag{9}$$

The modified constitutional supercooling criterion, Eq(7), can, therefore, be written in the form

$$G_L/V = -L/(2k_L) + [(k_S+k_L)/(2k_L)](1-k)(-mC_\infty)/(Dk). \tag{10}$$

A plot of G_L/V versus C_∞, as in Fig. 2, shows strong similarity between Eq(10) and Eq(3), the differences being only a change in slope by a factor of $[(k_S + k_L)/(2k_L)]$ and a finite intercept, $-L/(2k_L)$. The finite intercept is negligible at small growth velocities but the difference in slope can be significant at all growth velocities. Often, however, this difference in slope is not obvious because of uncertainties in the value of D which also appears as a factor in the slope.

At rapid rates of solidification, the parameter A can become large (see Eq(6)) because the diffusion length D/V becomes small. Thus, the onset of instability occurs at shorter wavelengths that are more comparable to the capillary length Γ. Because, however, A depends on V and C_∞, it is no longer possible to represent the stability criterion on the axes of Fig. 2 by a single curve. One could, for instance, fix V, note that A would then depend only on C_∞, and plot a family of curves of G_L/V versus C_∞ for various values of V. Alternatively, one could plot a family of curves for various values of G_L. Such representations are effectively three-dimensional. Of course, A also depends explicitly on k, but k is fixed for a given material.

Simple two-dimensional diagrams may be obtained as follows: We substitute Eq(2) into Eq(5) and rearrange to obtain

$$G^*/V = [(1-k)(-mC_\infty)/(Dk)]\, \mathcal{S}(A,k). \tag{11}$$

We then note that division of Eq(11) by V creates the variable C_∞/V on the right hand side and that this variable is proportional to A^{-1}. Thus, Eq(11) may be rewritten in the form

$$(G^*/V^2)[D^2/(kT_M\Gamma)]\ A^{-1}\mathcal{S}(A,k). \tag{12}$$

Since A^{-1} is proportional to C_∞/V, it follows that a plot of G^*/V^2 versus C_∞/V will result in a single curve for each material. Furthermore, since $\mathcal{S}\to 1$ as $V\to 0$, the low velocity limit of this plot (large G_L/V^2 and C_∞/V) would be expected to yield G^*/V^2 proportional to C_∞/V, a factor of $1/V$ could be divided from each of these variables, and one would obtain G^*/V proportional to C_∞ which is effectively the modified constitutional supercooling criterion.

In fact, the limiting behavior of $\mathcal{S}(A,k)$ as $A\to 0$ must be accounted for carefully and it turns out that a log-log plot is necessary to obtain a simple asymptotic behavior in the $V\to 0$ ($A\to 0$) limit. Such a plot is shown in Fig. 3 from which the asymptotic behavior at small V is clear and the enhanced stabilization at large V results in a curve that tends toward the vertical in the limit of absolute stability, $A\to 1$.

An alternative two-dimensional diagram may be obtained in terms of somewhat different variables. Indeed, if Eq(12) is multiplied by A^2, then inverted, and then its square root is taken, one obtains

$$(1-k)(-mC_\infty/T_M)(k^3\Gamma G^*/T_M)^{-1/2} = (A\mathcal{S})^{-1/2}. \tag{13}$$

The left hand side of Eq(13) depends on the ratio $C_\infty/(G^*)^{1/2}$. Taken together, Eqs(12) and (13) provide a parametric representation of G^*/V^2 versus $C_\infty/(G^*)^{1/2}$ with A as the parameter. The result is shown in Fig. 4 which has a slope of +2 for $A\to 0$ (the low V limit) and a slope of −2 for $A\to 1$, the limit of absolute stability. Since $\mathcal{S}=A$ at the crossings where log $\{(G^*/V^2)[D^2/(k\Gamma_M\Gamma)]\} = 0$, it follows that these crossings occur at the same values of the abscissa in Figs. 3 and 4.

We emphasize that while both Figs. 3 and 4 are general, Fig. 3 is convenient to view as a function of G^* versus C_∞ at fixed V and Fig. 4 is convenient to view as a function of V versus C_∞ at fixed G^*.

Influence on Stability of Departure from Local Equilibrium

As stated in the introduction, even the dynamical theory of stability must be modified at very rapid rates of solidification to account for departures from local equilibrium at the solid-liquid interface.[3-5] This may be done by adopting boundary conditions at the solid-liquid interface of the form

$$v = f\,(T_e-T_I,\ C_I,\ T_I), \tag{14a}$$

$$C_{SI} = C_I\,k\,(v,\ C_I,\ T_I) \tag{14b}$$

where T_e is the equilibrium temperature at the solid-liquid interface (with due respect for composition and curvature), T_I is the interface temperature, C_I is the concentration of solute in the liquid at the interface, and C_{SI} is the concentration of

solute in the solid at the interface. Eq(14a) allows the interface temperature to depart from its equilibrium value in order to give rise to a finite growth velocity while Eq(14b) implies that the distribution coefficient k is a function of growth velocity V and other interfacial conditions.

A stability analysis can be carried out by expanding Eqs(14) about the values V, C_{IO}, and T_{IO} that are presumed to correspond to growth with a planar interface. The result is

$$v = V + \mu_T [(T_e - T_{eo}) - (T_I - T_{IO})] + \mu_c (C_I - C_{IO}) + \mu_A (T_I - T_{IO}) \tag{15a}$$

$$k = k_o + k_v (v - V) + k_c (C_I - C_{IO}) + k_A (T_I - T_{IO}) \tag{15b}$$

where

$\mu_T = \partial f / \partial (t_e - T_I)$,
$\mu_c = \partial f / \partial C_I$,
$\mu_A = \partial f / \partial T_I$,
$k_v = \partial k / \partial V$,
$k_c = \partial k / \partial C_I$
and $\mu_A = \partial k / \partial T_I$. The quantity

$$k_o = k(V, C_{IO}, T_{IO}) \tag{16}$$

is the distribution coefficient that corresponds to unperturbed conditions; it might differ substantially from the equilibrium distribution coefficient

$$k_E = k(0, C_{IO}, T_{IO}) \tag{17}$$

where C_{IO} is no longer independent of T_{IO} but is related as depicted by the liquidus line of the appropriate phase diagram.

A stability analysis has been carried out[3,4] for the general case of Eqs(15); however, the functions in Eqs(14) are not well known, so the parameters μ_T, μ_c, μ_A, k_v, k_c and k_A cannot be specified reliably. We shall, therefore, suppress the explicit dependence of Eqs(14) on C_I and T_I and discuss only some effects of the kinetic coefficients μ_T and k_v.

Analysis shows that the stability criterion depends explicitly on k_o, μ_T, and k_v. Most theories and measurements[5] show that k_o lies between k_E and unity and approaches unity at high V. This alone would have a tendency to enhance stability because for $k_o \to 1$, an alloy would tend toward the solidification behavior of a pure substance. Nevertheless, a finite value of k_v leads to new destabilizing effects as follows: Suppose that the perturbed interface position is given by

$$z = Vt + \delta_o e^{\sigma t + i\omega x} \tag{18}$$

where δ_o is the small amplitude of a perturbation, σ and ω are temporal and spatial parameters of that perturbation, and the actual shape is the real part of the given complex expression. Then the corresponding interface velocity (in the z direction, which

is all that matters for a linear analysis) is

$$v = V + \sigma\delta_0 e^{\sigma t + i\omega x}. \tag{19}$$

With k_c and k_A suppressed, as stated above, Eq(15b) yields

$$k = k_0 + k_V \sigma\delta_0 e^{\sigma t + i\omega x}. \tag{20}$$

Thus, the partition coefficient varies along a perturbed interface and can give rise to local solute redistribution without the need for lateral diffusion, a process which is very ineffective at high velocities.

We refer to the redistribution of solute via Eq(20) as the "solute pump" mechanism. Detailed analysis shows that it can lead to instabilities for conditions between those for modified constitutional supercooling and the predictions of an analysis with k_V and μ_T set formally equal to zero but with the distribution coefficient equal to k_0. Furthermore, these instabilities are oscillatory in time, a fact related to the phase shift in interface velocity (and k) relative to interface position when the real part of σ is zero (marginal stability) and the imaginary part of σ is nonzero.

Thus, the regions between the curves of Figs. 3 and 4 and the lines for modified constitutional supercooling may be regions where oscillatory instabilities occur. This is illustrated in Fig. 5 for $G_L = 0$, for $k_0 = 1/2$, and for $Vk_V/(1-k_0) = 1$, which might[5] be an upper limit for k_V. The dashed curves are boundaries for the onset of oscillatory instabilities and are labeled by values of the parameter $D/(T_M \Gamma \mu_T)$, large values of which suppress oscillatory instabilities. The curve labeled >1.3 is indistinguishable from the curve for $k = 1/2$ in Fig. 3.

Conclusions

The effect of solidification rate on morphological instability can be understood in a straightforward way so long as local equilibrium at the solid-liquid interface is a good approximation. In this case, either of Figs. 3 or 4 provides a simple two-dimensional diagram of the stability criterion. For rates so rapid that non-equilibrium effects are important, the stability criterion is modified in a complicated way that depends on the non-equilibrium value, k_0, of the distribution coefficient and also explicitly on differential kinetic coefficients (such as μ_T and k_V) that relate changes in local growth conditions to changes in growth velocity and solute concentration in the solid. Depending on the values of these kinetic coefficients, oscillatory instabilities can occur for conditions intermediate between those predicted by the modified constitutional supercooling criterion and the results of stability theory in which k_0 is used but μ_T and k_V are neglected.

Acknowledgments

The author is grateful to the National Science Foundation, Division of Materials Research, Grant Number DMR 78-22462 for financial support, to Hassan M. El Zayyat for writing the computer programs from which Figs. 3 and 4 were constructed, and to S. R. Coriell for a critical reading of the manuscript.

References

1. W. A. Tiller, K. A. Jackson, J. W. Rutter and B. Chalmers, Acta Met. 1, 428 (1953).

2. W. W. Mullins and R. F. Sekerka, J. Appl. Phys. 35, 444 (1964).

3. S. R. Coriell and R. F. Sekerka, in: Rapid Solidification Processing Principles and Technologies, II, Eds: R. Mehrabian, B. H. Kear, and M. Cohen (Claitor), Baton Rouge, LA (1980), p. 35.

4. S. R. Coriell and R. F. Sekerka, J. Crystal Growth 61, 499 (1983).

5. W. J. Boettinger, S. R. Coriell and R. F. Sekerka, in: Proceedings of Rapid Solidification Processing: Principles and Technologies III, Ed: R. Mehrabian, NBS Internal Report (1983). Accepted for publication in a special issue (edited by H. Jones and W. Kurz) on Solidification Microstructure in Materials Science and Engineering.

6. R. F. Sekerka, J. Appl. Phys. 36, 264 (1965).

Figure 1

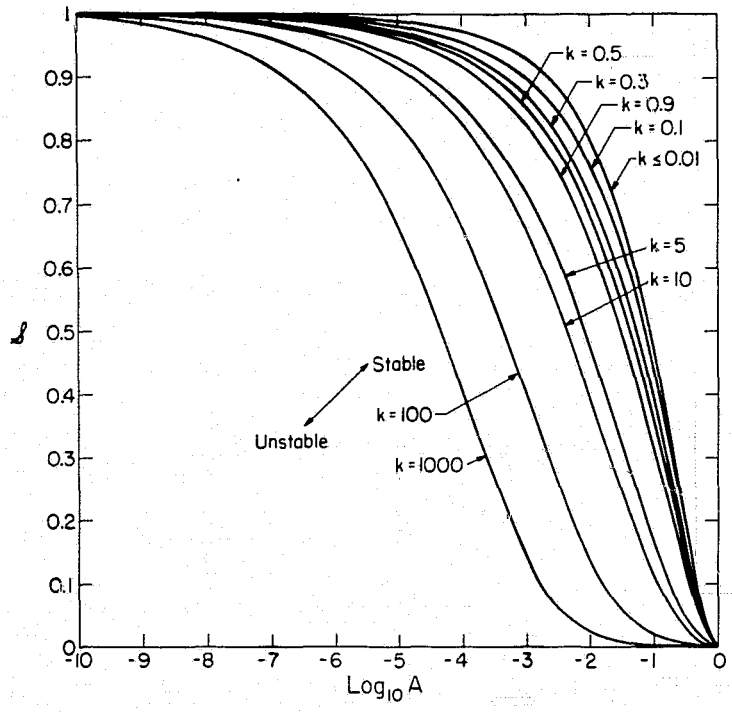

The stability function $\mathcal{S}$ versus $\mathrm{Log}_{10}A$ for various values of the distribution coefficient k

Figure 2

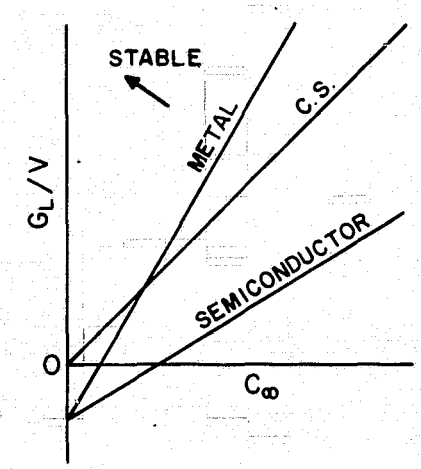

Comparison (arbitrary units) of the constitutional supercooling (C.S.) criterion with the modified constitutional supercooling criterion for a metal with $k_S = 2k_L$ and a semiconductor with $k_S = k_L/4$

Figure 3

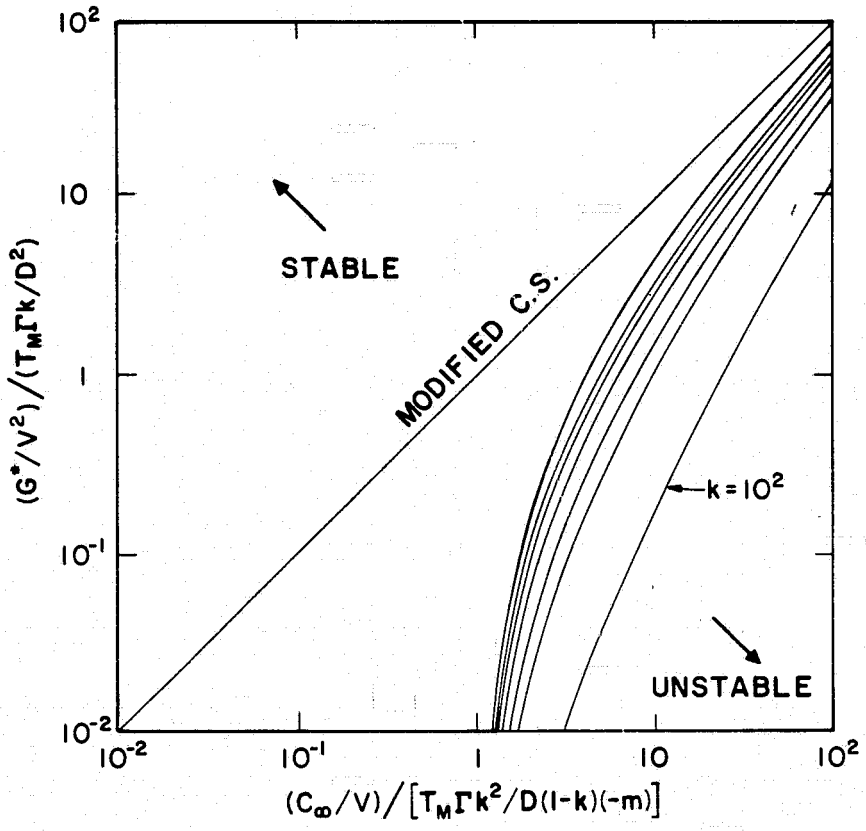

Stability diagram corresponding to Eq (12). From right to left, the curves correspond to values of the distribution coefficient $k = 10^2$, 10, 5, 2, 0.5, 10^{-1}, $\leq 10^{-2}$

Figure 4

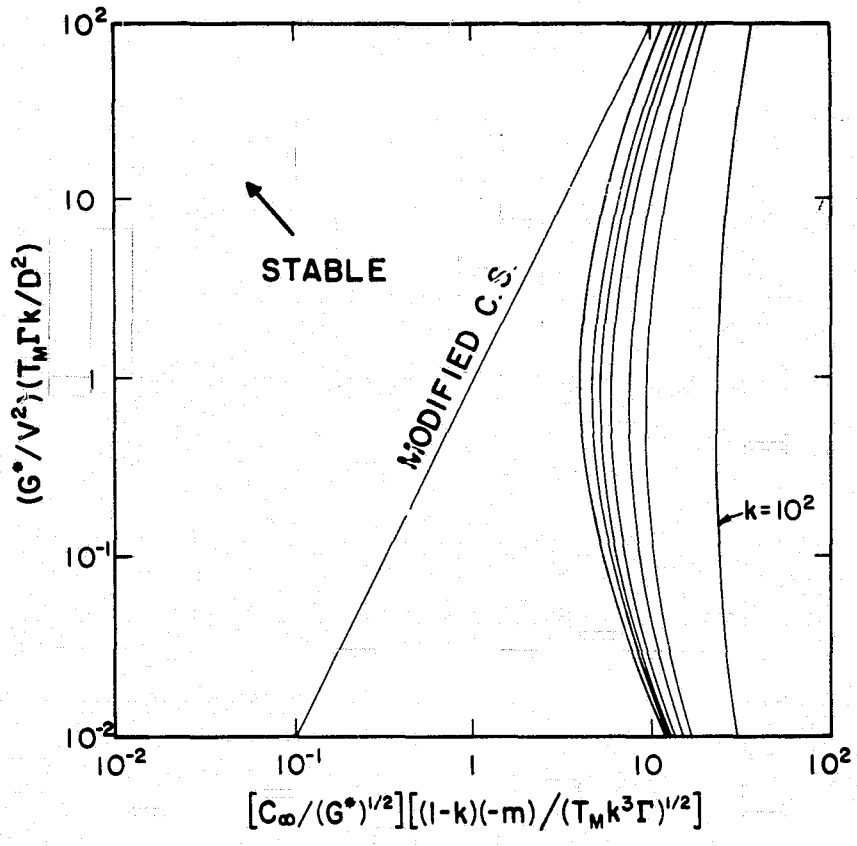

Stability diagram corresponding to the simultaneous solution to Eqs (12) and (13). From right to left, the curves correspond to values of the distribution coefficient k - 10^2, 10, 5, 2, 0.5, 10^{-1}, $\leq 10^{-2}$

Figure 5

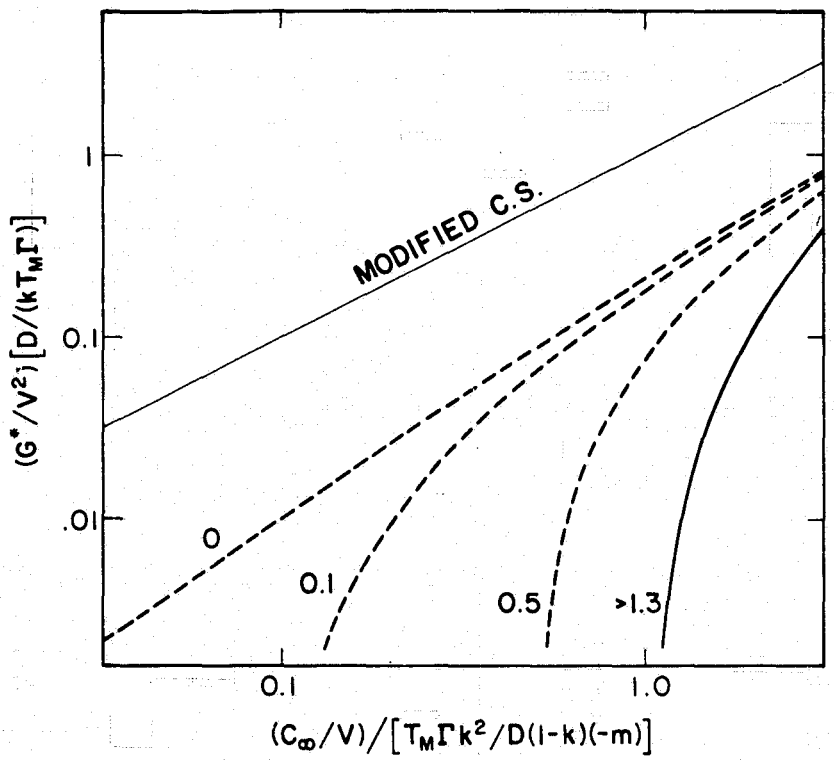

Stability diagram under conditions of departure from local equilibrium at the solid-liquid interface. Dashed lines, labeled by values of $D/(T_M\Gamma\mu_T)$, mark the onset of oscillatory instabilities for $G_L = 0$, $k_0 = ½$ and $Vk_V/(1-k_0) = 1$. The line labeled > 1.3 is indistinguishable from the line labeled k = ½ in Fig 3

DISCUSSION

MORRISON: Have you calculated what the sizes of the regions in that oscillatory distribution might be for actual crystal-growth conditions?

SEKERKA: Yes, we have. Everything is scaling like $(DV)^{1/2}$. So it depends on exactly what velocity you are talking about. In terms of practical numbers, you are looking in the sub-μm range, where you need an electron microscope to see the segregation. Bill Boettinger has solidified a number of alloys where he thinks he has seen this type of nonequilibrium segregation pattern. It is very tricky, depending on which way the thing was growing and exactly how one does the sectioning. I don't think he is willing yet to say 'yes, I have found it.' But I think we are pretty close.

GILMER: I think you have to be a Maxwell's demon to actually do much better than the existing kinetic laws, or to come up with a relationship that is much better than the existing kinetic laws. The problem is that the potential energy variation through the interface is absolutely critical in determining the quantity of material that is trapped.

SEKERKA: It is extraordinarily sensitive to that. So I think that any sort of pseudomacroscopic model, although it can predict trapping, is kind of empiricizing the trapping rather than really calculating it.

GILMER: In fact, one of the things we have been investigating recently is the potential energy variation through the interface. I think probably more important than this low-potential-energy region in the interface itself is the rate at which the potential energy of the impurity approaches the bulk potential energy as that impurity is buried deeper into the crystal. In other words, if there is stress associated with the presence of the impurity, then this is going to increase gradually, and so the impurity can get immobilized before it reaches its bulk potential energy. This leads to extremely high trapping rates.

SEKERKA: The Baker model even has a discontinuity in the slope of the energy at that point and, depending on where that discontinuity occurs, you can shift those k values all over the map.

GILMER: What is your objection to a linear dependence on the velocity and the distribution?

SEKERKA: I was a little surprised by it. I had thought k versus V ought to be sigmoidal, and ought to start out flat and come up. I felt that we were not seeing any slight slopes of k at low velocities. Now maybe it is just too slight to see. Of course, if you plot it on a log-log plot it will make a sigmoid out of anything.

GILMER: I think that initial slope is small, but I think it is there.

SEKERKA: It might be.

WHITE: Regarding your prediction of an oscillatory instability, I think we have seen something that very closely resembles that. It's for one or two of the group of four impurities in silicon when you solidify at about four or five meters per second. The microstructure is definitely different from that present in what you call your normal instability.

SEKERKA: That is what should happen, and I was absolutely flabbergasted when we calculated this thing. I thought the calculations were spurious, until we checked the mechanism.

TRANSPORT PROCESSES IN DENDRITIC CRYSTALLIZATION

M. E. GLICKSMAN
Materials Engineering Department
Rensselaer Polytechnic Institute
Troy, New York 12181

ABSTRACT

Free dendritic growth refers to the unconstrained development of crystals within a supercooled melt, which is the classical "dendrite problem". Great strides have been taken in recent years in both the theoretical understanding of dendritic growth and its experimental status. The development of this field will be sketched, showing that transport theory and interfacial thermodynamics (capillarity theory) were insufficient ingredients to develop a truly predictive model of dendrite formation. The convenient, but incorrect, notion of "maximum velocity" was used for many years to estimate the behaviour of dendritic transformations until supplanted by modern dynamical stability theory. The proper combinations of transport theory and morphological stability seem to be able to predict the salient aspects of dendritic growth, especially in the neighborhood of the tip. The overall development of cast microstructures, such as equiaxed zone formation, rapidly solidified microstructures, etc., also seems to contain additional non-deterministic features which lie outside the current theories discussed here.

Introduction and Background

Despite the fact that dendrite formation seems to involve both steady-state attributes (near the tip) and time dependent features (side branches), the earliest models employed steady-state descriptions of needle-like, branchless dendrites growing in a shape preserving manner.[1-3] The dendrite was assumed to grow at a constant axial rate, V, into a melt of uniform supercooling, ΔT, such that the surrounding thermal field would appear to be stationary in a coordinate frame traveling with the dendrite tip. The steady-state shape was chosen, ab initio, such that the prescribed solid-liquid interface remained at its bulk thermodynamic melting temperature, T_m. Imposition of an isothermal boundary condition retained linearity of the heat flow solution and led to a large class of steady-state "dendrite" solutions which depended on the arbitrarily chosen shape. Ivantsov's solution for the paraboloid of revolution is typical of these linear shape-preserving solutions, namely

$$\Delta\Theta = Pe^{P}E_1(P), \tag{1}$$

where $\Delta\Theta = \Delta T\ C/L$, is the non-dimensional supercooling (also termed the Stefan number), $\Delta T = T_m - T_\infty$, where T_∞ is the temperature far from the dendrite, C and L are the molar specific heat of the melt and the molar latent heat of fusion, respectively, and E_1 is the exponential integral, a tabulated function. Equation 1 relates $\Delta\Theta$ to the Péclet number, $P = VR/2\alpha$, where R is the radius of curvature of the dendrite tip, and α is the thermal diffusivity of the melt. The inverse of Eq. 1, although not expressible in terms of known functions, does establish that $VR = f(\Delta\Theta)$, which provides an infinite range of hyperbolic solutions, i.e., unbounded

values for V and R for a given value of $\Delta\Theta$. Clearly, the transport solutions for the steady-state dendrite lack uniqueness when the only physical length scale introduced into the problem is the characteristic, but unknown, diffusion distance, α/V, or, alternatively, the equally unknown dendrite tip radius of curvature, R. This limitation was recognized over twenty years ago by Bolling and Tiller[4], who then introduced a non-linear boundary condition into the problem which effectively places an upper bound on V and a lower bound on R. Bolling and Tiller suggested that local thermodynamic equilibrium along the dendrite surface requires that the melting temperature, T_e, is a function of the mean interfacial curvature, κ, namely, $T_e = T_m - \Gamma\kappa$, which is the well known Gibbs-Thomson equation. Here $\Gamma = \gamma\Omega/\Delta S$; γ is the solid-liquid surface energy; Ω is the molar volume of the solid; and ΔS is the molar entropy of fusion. The Gibbs-Thomson equation requires, therefore, that the dendrite grows with a <u>non-isothermal</u> interface.

Introduction of the non-isothermal temperature boundary condition raised a severe difficulty, inasmuch as the steady-state shapes which were treated as a class of shape preserving solutions by Horvay and Cahn[2] no longer simultaneously satisfied both energy conservation and the non-isothermal equilibrium temperature boundary condition. Several approximate theories were developed in which the interface shape was chosen to satisfy either energy conservation[5-7] or the non-isothermal condition[8,9], and a decade ago, a self-consistent theory was finally developed[10] which determined the dendrite shape as part of the solution and satisfied both physical requirements. All of these non-isothermal theories shared the common result that the values of V and R, which constitute possible operating

states lie along curves with a maximum in the value of V. Figure 1, shows two typical V versus R relationships at a fixed value of the supercooling. The value of V at the maximum was selected as the probable operating state over the manifold of possible operating states. Space considerations do not permit a full review of the reasons used to incorporate within these theories the hypothesis that the maximum velocity is the unique velocity characterizing axial dendritic growth. A few remarks are in order, however, concerning the value of the tip radius corresponding to the condition of maximum velocity. As shown in Figure 1 the states of maximum velocity for non-isothermal models have tip radii such that the Péclet number at $V = V_{max}$ is one-half that of the isothermal Ivantsov model. The tip radius for the Modified Ivantsov model is just twice the critical radius R^*, where R^* is that radius which depresses the dendrite tip temperature by an amount equal to the supercooling. Without a temperature difference between the interface and the supercooled melt, latent heat cannot be transferred and $V = 0$. R^* is easily estimated from the Gibbs-Thomson relationship by finding the value of $\kappa^* = 2/R^*$ which reduces the tip temperature, T_e, to T_∞. Figure 1 corresponds to a dimensionless supercooling $\Delta\Theta = 0.05$, which is relatively small, yet as seen in this figure $R^* \approx 10^{-5}$cm. Even Temkin's analysis predicts a tip radius of only 10^{-4}cm, which is much smaller than the observed scale of dendrites at such small supercoolings. Of course, estimates from theory for the size scale R depend sensitively on the parameters chosen for the critical radius, namely

$$R^* = \frac{2\Gamma C}{\Delta\Theta L}, \qquad (2)$$

among which Γ is least well known, insofar as it contains the solid-liquid

interfacial energy, γ. Thus, even qualitative observations of dendritic structures led some investigators to suspect that the hypothesis of maximum velocity was incorrect, long before quantitative kinetic data were available to challenge its validity directly.

The lack of reliable interfacial energy data actually precluded a definitive test of the maximum velocity hypothesis until 1976, when R. J. Schaefer, J. D. Ayers, and the writer developed a method for initiating free dendritic growth within a large (30 cc) volume of a well-characterized substance.[11] The method, called the capillary injection technique, permits unimpeded growth of a dendritic mass, eliminating interactions of the solidification front with container walls. Kinetic data were acquired over almost three decades in dendrite velocity with an accuracy of about 3% for succinonitrile (SCN), a transparent, BCC, plastic crystalline material, with freezing characteristics similar to many cubic metals. SCN also has the desirable properties of a convenient melting temperature (58.08 C), ease of purification via zone refining, ability to sustain moderate levels of supercooling (up to 10 K), and well studied thermophysical parameters, including especially its solid-liquid interfacial energy.[12] The kinetic data obtained for SCN were correlated by a power law expression, namely

$$V = \beta \mathcal{L} \Delta\Theta^{b} , \qquad (3)$$

where β and b are numerical coefficient and exponent, respectively, and $\mathcal{L} = 2\alpha\Omega\Delta SL/\gamma C$ is a lumped parameter representing the characteristic velocity of the material. The value of b was determined to be about 2.5, in excellent agreement with the non-isothermal theories of Temkin[8], Trevedi[9] and Nash and Glicksman[10], but the value of β was found to be in serious dis-

agreement with all of these theories. Shortly after the demonstration that all theories of dendritic growth that are based either on the hypotheses of maximum growth velocity[8,13] or on minimum rate of entropy production[14] fail in the case of SCN, it was then shown that kinetic observations of dendrite growth in ice/water also fail to agree with such theories.[15] The maximum velocity predictions of β for both ice/water and SCN were higher by factors of about three and seven, respectively, than were the measurements of β. Again, as in the case for SCN, accurate values of the thermophysical parameters for ice/water were essential in comparing theory with observation, including especially the value for γ.[16]

Morphological Stability and Time Dependence

As outlined in the previous section, purely steady-state theories of shape preserving dendritic growth all failed, the level of their sophistication notwithstanding. Indeed, even solving the steady-state growth problem with non-linear boundary conditions in an exact self-consistent form[10] served to show mainly that the maximum steady-state velocity was a relatively poor upper bound to the true operating state. Two disparate viewpoints arose on this issue: 1) that the steady-state optimized dendrite was correct to first order, but needed inclusion of nonsteady-state features such as side branching[17,18], and 2) that dendritic growth was intrinsically time-dependent and unstable.[19,20,21] Analyses based on the first point of view showed that the steady-state needle dendrites were unstable when tested for morphological stability using linear perturbation methods fashioned after those first used by Mullins and Sekerka[22] and by Voronkov.[23] An unfortunate aspect of these

approaches was that the steady-state dendrite shapes themselves were only approximations, and therefore were intrinsically unstable <u>without</u> perturbation. Consequently, viewpoint (1) only served to emphasize the deficiency of steady-state approaches, and did not lead to new insights into the problem. The second viewpoint was originally proposed a decade ago by Oldfield[19] who was the first investigator to stress that the size of a dendrite tip might be selected through a balance of destabilizing forces arising from diffusion by stabilizing forces arising from capillarity. He found by simple logic and some numerical analysis that

$$VR^2 \simeq 100\alpha\Gamma\frac{C}{L}\,, \tag{4}$$

which, as we shall show, is remarkably close to the results obtained later by linear perturbation analysis. Oldfield also demonstrated through computer generated cinematography that such a dendrite was actually a fully time-dependent object, with branches emanating as waves from a <u>nearly</u> steady-state tip. The numerical character of Oldfield's work, unfortunately, prevented its wide acceptance at that time.

The proper estimation of size scales for morphologically unstable systems begins with Mullins and Sekerka's ideas that any Fourier component of a perturbed planar interface represented as $\delta = \delta_o \exp(i\omega x)$ is subject initially to a time dependence described by $\delta(t) = \delta\exp(\sigma t)$, where σ, in general, is a complex eigenvalue of the linearized dynamical equations of the interface motion.[21] The quantity ω is the Fourier component's wave number, t is time, and δ_o denotes the initial (small) amplitude of this component at t = o. If the real part of σ is negative, then the perturbation decays to zero amplitude, whereas if the real part of σ is positive then

δ grows exponentially. If σ is purely imaginary, then on average the amplitude of δ remains equal to δ_o and the interface is deemed to be marginally stable. The condition of marginal stability for a pure material growing from its supercooled melt may be shown to be[21]

$$Re(\sigma) = 0 = -\Gamma\omega^{*2} - \bar{G} , \tag{5}$$

where $\bar{G}$ is the average thermal gradient (weighted by the thermal conductivities of each phase) and ω^* is the wave number of the marginal perturbation. We now adopt the remarkable suggestion originally made by Langer and Müller-Krumbhaar[22] that the wavelength, $\lambda^* = 2\pi\omega^{*-1}$, of the marginal perturbation sets the scale of the dendrite tip radius, R. Moreover, the average temperature gradient acting on the tip may be found from the transport solution of the <u>unperturbed</u>, steady-state, shape preserving dendrite. For example, the paraboloid of revolution, as described by Ivantsov's solution[2], is an isothermal shape with a zero gradient within the solid phase and with a dimensionless temperature gradient in the melt phase ahead of the tip $G_\ell = -2P$. Again, P, the Péclet number, can be related to the supercooling through Eq. 1. and thus the average dimensionless gradient $\tilde{G} = -P$. The gradient $\tilde{G}$ can be dimensionalized to $\bar{G}$ by rescaling by the characteristic temperature L/C divided by the dendrite tip radius, R. Thus, the average temperature gradient at the dendrite tip is

$$\bar{G} = \frac{-P}{R}\frac{L}{C} = \frac{-VL}{2\alpha C} . \tag{6}$$

If Eq. 6 is substituted into Eq. 5 we find that the marginally stable state $Re(\sigma) = 0$ occurs when $R = \lambda^*$, which after some rearrangement yields the

condition for growth

$$VR^2 = 8\pi^2 \frac{\alpha C\Gamma}{L} , \tag{7}$$

which, except for a slight difference in the numerical coefficient, agrees with Oldfield's expression, Eq. 4.

Equation 7 is the central result obtained from dynamical analysis of dendrite tip motion. If we recall the definition $P = VR/2\alpha$, then Eq. 7 may be recast in an especially convenient form, namely

$$P = \frac{4\pi^2}{R} \frac{C\Gamma}{L} . \tag{8}$$

Now, Ivantsov's transport solution, Eq. 1, may be written in a non-linear operator form as $\Delta\Theta = Iv[P]$, where $Iv[\ ]$ represents the series of operations carried out on the right-hand side of Eq. 1. We can <u>formally</u> invert Eq. 1 to stress that P is some function of $\Delta\Theta$, viz.,

$$P = Iv^{-1}[\Delta\Theta] , \tag{9}$$

although the inversion operator $Iv^{-1}[\ ]$ cannot be represented exactly by any known series of algebraic or transcendental operations. Nonetheless, the inversion operator $Iv^{-1}[\ ]$ exists, if only as a graph or an asymptotic expansion. Equations 8 and 9 can now be combined, eliminating explicit dependences on P, to yield the operating state of the dendrite under marginally stable dynamical conditions. Specifically, we find that

$$R = \frac{4\pi^2}{L} \frac{C\Gamma}{Iv^{-1}[\Delta\Theta]} , \tag{10}$$

and

$$V = \frac{\mathcal{L}}{4\pi^2} \{Iv^{-1}[\Delta\Theta]\}^2 , \tag{11}$$

where $\mathcal{X}$ is the same group of material parameters defined earlier as the characteristic velocity. The correspondence between the power law approximation, Eq. 3, and the kinetic expression, Eq. 11, now becomes obvious.

If Eq. 2 is inserted into the right-hand side of Eq. 8 we see that

$$P = 2\pi^2 \frac{R^*}{R} \Delta\Theta , \tag{12}$$

which shows that a second length scale, namely $R^*\Delta\Theta/2$, has been introduced into the dendrite problem, however, not through the boundary conditions (as in the non-isothermal steady-state theories) but rather through the dynamical stability criteria, Eqs. 5-7, as applied to an isothermal model. The length scale $R^*\Delta\Theta/2 = \Gamma C/L$ is often referred to as the capillary length, and is purely a property of the solidifying phases. The dendritic operating state as defined by R (Eq. 10) and V (Eq. 11) represents a unique "decomposition" of the transport solution, Eq. 9. The decomposition of the Péclet number is specified by the numerical factor, $1/4\pi^2$, which appears in Eq. 11, and its reciprocal in Eq. 10. This "separation" parameter, usually termed σ^* in the stability literature[22,24], depends somewhat on the details of the stability analysis. For example, Table I contains a summary of some of the published values of σ^*. Despite major differences in the various stability models cited in Table I, the values cluster tightly around the mean $\langle\sigma^*\rangle = 0.022 \pm 13\%$. Models as disparate in geometry as the planar front, discussed above, and the spherical tip[20,24-27] predict σ^* values only about 30% different.

Scaling Laws and Experimental Observations

An interesting scaling relationship for dendrites can be obtained from the stability analysis by inserting Eq. 2 into Eq. 10 and then solving for the ratio of the tip radius to the nucleation or critical radius, R/R^*. We find that

$$\frac{R}{R^*} = \frac{2\pi^2 \Delta\Theta}{Iv^{-1}[\Delta\Theta]} , \tag{13}$$

which by virtue of Eqs. 1 and 9 and the definition of σ^* may be rewritten in the forms

$$\frac{R}{R^*} = \frac{1}{2\sigma^*} \frac{Iv[P]}{P} = \frac{e^P E_1[P]}{2\sigma^*} . \tag{14}$$

In the range of small supercoolings ($\Delta\Theta \ll 1$), specifically where the value of P is sufficiently small that $E_1(P) \rightarrow -\ln P$, Eq. 14 becomes

$$\frac{R}{R^*} (\Delta\Theta \ll 1) \rightarrow \frac{-\ln P}{2\sigma^*} . \tag{15}$$

The value of R/R^* predicted from Eqs. 13-15 over the typical range of experimentally useful "small supercoolings" ($10^{-3} < \Delta\Theta < 0.1$) is of the order of 100, clearly indicating that marginally stable dendrites ought to grow with their tip radii much larger than R^*, which is a morphological scaling law at variance with the steady-state theories that predict small multiples of R^*. Figure 2 shows measurements of SCN dendrite tip radii, obtained by Huang and the author[24], scaled to the critical radii, R^*. These data show that the value of R/R^* is well approximated by Eqs. 13-15. The precise fit of the data in Fig. 2 to the scaling law is limited at very small supercoolings by the presence of convection. Convection effects, relative to transport by diffusion, become negligible in SCN above a super-

cooling of about 1K[29], and, as shown in Fig. 2, a rather close correspondence occurs near and above $\Delta T = 1K$. It is unfortunate that obtaining reliable morphological data above a supercooling of 2K is, at present, not technically feasible with SCN. This is due simply to the difficulty in obtaining adequate photographic resolution of the dendrite tip structure as the tip radius decreases to 1μm and its speed exceeds 1mm/sec. Figure 3 shows a series of SCN dendrite tips growing at increasing levels of supercooling, and emphasizes that the micrographs decline in optical quality as the supercooling increases, which requires higher magnification to resolve the morphology. Lappe[30] has confirmed many of the morphological and kinetic measurements originally reported by Huang[31], and has further demonstrated that at a supercooling of 2K, or beyond, a growing SCN dendrite can not be resolved optically to permit an accurate measurement of the tip radius. Figure 3 also shows another effect which might be explained by the scaling law shown in Fig. 2 and described in Eqs. 13 and 14, namely, that the dendrites are not self-similar, except for the tip itself. Inspection of the micrographs in Fig. 3 show that the side branches intrude on the tip as the supercooling increases, due primarily to the faster amplification rate of the marginal eigenmode, ω^*. It would be of extreme interest to follow this trend into the regime of large supercoolings and rapid solidification where a great deal of current research interest is focussed. For the present, we can accept that the ratio R/R^* should decrease at large supercooling, with the dendrite becoming commensurately less stable. Eventually, the interfacial molecular attachment rate will become rate limiting, causing the interface to depart radically from local equilibrium and from the scaling laws based on local

equilibrium. This remains as an interesting topic of research.

Finally, the fundamental assertion of Langer and Müller-Krumbhaar is proved by the data in Fig. 4, where the scaling law $\lambda^* \simeq R$ is shown to hold for SCN over two decades of supercooling. Specifically, $R = 1.2\lambda^*$ in Fig. 4, which is equivalent to an error in Eq. 10 of 20% in the value of $\sigma^* = 1/4\pi^2$. As shown in Table I, the analysis of tip stability based on spherical harmonics almost provides the σ^* value needed, viz., $\sigma^* = 0.021$. Although the differences among the σ^* values appearing in Table I seem modest, the detailed physical assumptions employed in each stability analysis are markedly different. For example, the planar front model bears little geometrical similarity to a dendrite tip and cannot include factors such as crystal symmetry or anisotropy. The spherical harmonic model, by comparison, only approximates the total tip geometry of a dendrite, yet by judicious selection of the harmonic index (ℓ=6) this model can reflect the cubic nature of SCN as well as the fact that instabilities amplify and propagate along the four {100} planes which contain the <100> growth axis. Figure 5 shows the actual details of the tip configuration for SCN at low supercooling and provides convincing evidence for the growth shape anisotropy and wave development of the marginal eigenmode.

Recently, Singh has obtained accurate thermophysical, kinetic, and morphological data on pivalic acid (PVA) dendrites growing freely from the supercooled state.[28] PVA has an FCC crystal structure, a low entropy of fusion, and a ten-fold higher anisotropy in its solid-liquid surface energy as compared to SCN. If the stability condition, Eq. 7, is plotted as a log-log plot of $V(\Delta\Theta)$ versus $R(\Delta\Theta)$, then we would expect a straight line with a slope equal to -2, and an ordinate position which depends on the

value of σ^*. Figure 6 shows such a log-log plot of Singh's data for PVA dendrites. These data are in accord with the predictions of Eq. 7, and yield a σ^* value in excellent agreement with stability theory. (See Table I.) To date, two materials, a BCC anisotropy system (SCN) and an FCC high anisotropy system (PVA) have been shown to display kinetics and tip morphologies which are in quantitative agreement with the dynamical theory of dendritic growth at low to moderate levels of supercooling. Much work remains to establish such correspondences over broader classes of materials such as metals, semiconductors, and ceramic crystals.

Free Dendrites in Alloys

The growth of dendrites in pure materials is limited to "thermal" dendrites, of the type described in the previous section. Thermal dendrites merely segregate the system's enthalpy during the two-phase coexistence of solid and liquid. After total solidification occurs all vestiges of the prior dendritic structure vanishes. In alloys, on the other hand, dendrites also segregate solute additions and impurities, causing a wide range of effects that collectively produce dendritic cast structures. In both continuous and shaped castings, much of the dendritic structure forms by directed solidification, wherein the latent heat is extracted through the solidifying mass to the external environment. This process often results in the formation of columnar dendritic grains, which lie outside the scope of this paper. In certain alloys, and commonly in the latter stages of the freezing of a casting, freely growing alloy dendrites can occur, which are commonly referred to as equiaxed grains, because of their isometric development within the casting. The formation of equiaxed grains is a technically important but poorly understood subject[34-36], and controlling the transition

from columnar dendritic to equiaxed grains is of great interest in both continuous and shaped casting of alloys.

A quantitative description of free dendritic growth in alloys requires simultaneous solution of the thermal and solutal transport equations as well as modification of the marginal stability criterion. Trivedi and Tiller[37] have given careful consideration to the problem of steady-state alloy dendrites, but their results depended on the use of the hypothesis of maximum velocity, limiting the usefulness of their predictions. Langer[38] has shown that inclusion of solute diffusion introduces yet another length scale related to the diffusion distance D/V, where D is the diffusivity of the solute in the melt phase. The operating state of an alloy dendrite depends on both temperature and concentration fields adjacent to the solid-liquid interface. These fields are related through the phase diagram for growth velocities, supercoolings, or supersaturations which are not too large. The total driving force must include the free energy to permit diffusion, as well as heat flow and capillarity. Any adequate description of alloy dendrites must provide an explanation for the fact that small alloy additions first <u>increase</u> the speed of dendrites, at fixed supercoolings with respect to the liquidus temperature, and after passing through a maximum growth speed, then <u>decrease</u> their speed. Early observations in $KC\ell-H_2O$ by Lindenmeyer[39] showing this speed maximum with varying solute concentration have been confirmed in systems other than ice-water solutions.[40] In fact, the speed increase in SCN-argon alloys is now known to be associated with a decreasing tip radius, which may be qualitatively described as due to the diminished stability associated with the constitutional gradient surrounding

an alloy dendrite. Suffice it to say that small alloy additions increase the value of σ^* and cause the intersection of the marginal stability curve (VR^2 = const.) with the transport solution (VR = const.) to occur at larger values of V and smaller values of R. Further increases of solute concentration merely depress the interface temperature toward the melt temperature and consequently restrict the growth rate by limiting the transport of latent heat. Of course, it is just as correct to say that at higher alloy concentrations, solute diffusion becomes the dominant transport process, which is limited by the lower chemical (versus thermal) diffusivity. A new quantitative theory of alloy dendritic growth by Kurz, Lipton, and the author[41] shows that the operating state of an alloy dendrite depends on the unique interfacial temperature and solute concentrations which simultaneously satisfies heat flow, solute diffusion, and marginal stability. Figure 7 shows a comparison of free dendritic growth rates measured by Chopra[42] in SCN-acetone alloys with this theory. Inasmuch as the diffusion coefficient for acetone molecules in molten SCN was independently measured by Chopra[42], there are no free parameters in the theory. An adequate theory of alloy dendrite growth will permit identification of those features of the alloy system and the solidification process which contribute to equiaxed grain formation. Such a theory would be of inestimable help in designing cast microstructures from first principles, and thereby optimizing the solidification process toward achieving proper crystallite distributions and better properties.

Summary and Conclusions

- The experimental status and theoretical understanding of dendritic crystal growth have evolved over the past three decades from shape preserving linear solutions of the equations of heat flow, which admit to a non-predictive multiplicity of operating states, to linear perturbation methods leading to unique dynamic growth states in agreement with precision measurements. This progress has not been uniform, but required a sequence of major developments from both experiment and theory, as well as overturning plausible, but incorrect concepts.

- The fundamental concepts of constitutional supercooling and interfacial breakdown ultimately were refined into dynamical morphological stability theory. Stability methods combined with thermal and solutal transport theory now clearly show that dendritic growth is inherently a dynamically unstable process. This dynamical viewpoint removes much of the confusion surrounding the relationship between time-dependent features such as side branches and steady-state aspects of dendrites in the neighborhood of the tip.

- The review of various stability models for dendritic growth reveals that in the case of pure materials the separation or stability parameter, σ^*, varies only moderately with radically different stability geometries. To date, the most accurate stability model appears to be that which approximates the dendrite tip as a portion of a sphere with cubical distortions reflecting the triaxial crystalline anisotropy of the solid phase.

- Quantitative assessment of theory through kinetic and morphological measurements requires accurate determination of the solid-

liquid interfacial energy. Unfortunately, such data are available for only a few systems, thereby limiting the scope of such assessments.

- The theory of free dendritic growth appears to be extendable to dilute binary alloys by allowing for the combined destabilizing influences of the thermal and solutal diffusion fields. This is in contrast to directed dendritic growth, such as in the columnar zone of castings, in which the thermal distribution results in a positive temperature gradient that is stabilizing. Recent measurements on alloy dendrites suggest that this approach yields quantitatively correct predictions which may provide an explanation for the formation of equiaxed grains in the central regions of castings.

- The extension of the dynamical theory of dendritic growth to large supercoolings or supersaturations and high growth rates remains uncertain. For example, morphological scaling laws are restricted to situations where departures from local interfacial equilibrium are relatively small. This remains an important area for study with potential significant impact on rapid solidification processes and other high-rate crystal growth technologies.

Acknowledgement

The author is grateful for the support provided to him by the National Science Foundation, under grant DMR-8308052, and by the National Aeronautics and Space Administration, under grant NAG3-333. Thanks are also due to my collaborators who kindly provided access to work in progress, including Drs. N. B. Singh and M. Chopra, Rensselaer Polytechnic Institute, Dr. J. Lipton, Concast Standard AG, Zurich, Switzerland, and Professor W. Kurz, Materials Dept., EPFL, Lausanne, Switzerland.

TABLE I

Values of the "separation" parameter σ^* for freely growing dendrites

σ^*	Stability Model	Ref.
0.02	Oldfield's "force balance"	19
0.0253	Planar front	21, 24
0.025	Parabolic eigenstate	22, 32, 33
0.0192	Spherical harmonic (ℓ=6)	24-27, 20

σ^* exp.	System	Ref.
0.0195	SCN	24
0.022	PVA	28

References

1. J. C. Fisher, as referenced by Bruce Chalmers, Principles of Solidification, p. 105, John Wiley & Sons, Inc., New York (1964).

2. G. P. Ivantsov, Dokl. Akad. Nauk, SSR, 58, 567 (1947).

3. G. Horvay and J. W. Cahn, Acta Met., 9, 695 (1961).

4. G. F. Bolling and W. A. Tiller, J. Appl. Phys., 32, 2587 (1961).

5. R. F. Sekerka, R. G. Seidensticker, D. R. Hamilton and J. D. Harrison, Investigation of Desalination by Freezing, Westinghouse Res. Lab. Rep., Ch. 3 (1967).

6. M. E. Glicksman and R. J. Schaefer, J. Cryst. Growth, 1, 297 (1967).

7. M. E. Glicksman and R. J. Schaefer, J. Cryst. Growth, 2, 239 (1968).

8. D. E. Temkin, Dokl. Akad. Nauk, SSR, 132, 1307 (1960).

9. R. Trevedi, Acta Met., 18, 287 (1970).

10. G. E. Nash and M. E. Glicksman, Acta Met., 22, 1283 (1974).

11. M. E. Glicksman, R. J. Schaefer and J. D. Ayers, Met. Trans., A7, 1747 (1976).

12. R. J. Schaefer, M. E. Glicksman and J. D. Ayers, Phil. Mag., 32, 725 (1975).

13. C. Zener, Trans. AIME, 167, 550 (1964).

14. I. Jin and G. R. Purdy, J. Cryst. Growth, 23, 25 (1974).

15. T. Fujioka, Ph.D. Thesis, Carnegie-Mellon U. (1978).

16. S. C. Hardy, Phil. Mag., 35, 471 (1977).

17. G. R. Kotler and W. A. Tiller, J. Cryst. Growth, 2, 287 (1968).

18. R. Trivedi and W. A. Tiller, Acta Met., 26, 67 (1979).

19. W. Oldfield, Mat. Sci. Engr., 11, 211 (1973).

20. R. D. Doherty, B. Cantor and S. Fairs, Met. Trans., A9, 621 (1978).

21. W. W. Mullins and R. F. Sekerka, J. Appl. Phys., 34, 323 (1963).

22. J. S. Langer and H. Müller-Krumbhaar, Acta Met., 26, 1681; 1689; 1697 (1978).

23. V. V. Voronkov, Sov. Phys. Solid State, 6, 2378 (1964).

24. S. C. Huang and M. E. Glicksman, Acta Met., 29, 701 (1981).

25. S. R. Coriell and R. L. Parker, J. Appl. Phys., 36, 632 (1965).

26. S. R. Coriell and R. L. Parker, Proc. ICCG, Boston, Mass. 1966, Suppl. to J. Phys. Chem. Solids, H. Steffen Peiser, Ed., J-3, 703 (1967).

27. R. Trivedi, H. Franke and R. Lacmann, J. Cryst. Growth, 47, 389 (1979).

28. Narsingh Bahadur Singh private communication.

29. M. E. Glicksman and S. C. Huang, Adv. Space Res., 1, 25 (1981).

30. U. Lappe, KFA Report, Kernforschungsanlage Jülich, FRG, (1980).

31. S. C. Huang, Ph.D. Thesis, Rensselaer Polytechnic Institute (1979).

32. J. S. Langer and H. Müller-Krumbhaar, J. Cryst. Growth, 42, 11 (1977).

33. J. S. Langer, Rev. Mod. Phys., 52, No. 1, 1 (1980).

34. M. H. Burden and J. D. Hunt, J. Cryst. Growth, 22, 99 (1974).

35. S. Witzke, J. P. Riquet and F. Durand, Acta Met., 29, 365 (1981).

36. Hasse Fredriksson, in Materials Processing in the Reduced Gravity Environment, Guy E. Rindone, Ed., Elsevier Science Publishing Co., Inc., 619 (1982).

37. R. Trivedi and W. A. Tiller, Acta Met., 26, 679 (1978).

38. J. S. Langer, Physico Chemical Hydrodynamics, 1, 41 (1980).

39. C. Lindenmeyer, Ph.D. Thesis, Harvard U. (1959).

40. M. E. Glicksman, Narsingh Behadur Singh and M. Chopra, in Materials Processing in The Reduced Gravity Environment of Space, Guy E. Rindone, Ed., 461, Elsevier Science Publ. Co., Inc. (1982).

41. W. Kurz, J. Lipton and M. E. Glicksman, unpublished work (1983).

42. M. Chopra, Ph.D. Thesis, Rensselaer Polytechnic Institute (1983).

Figure 1

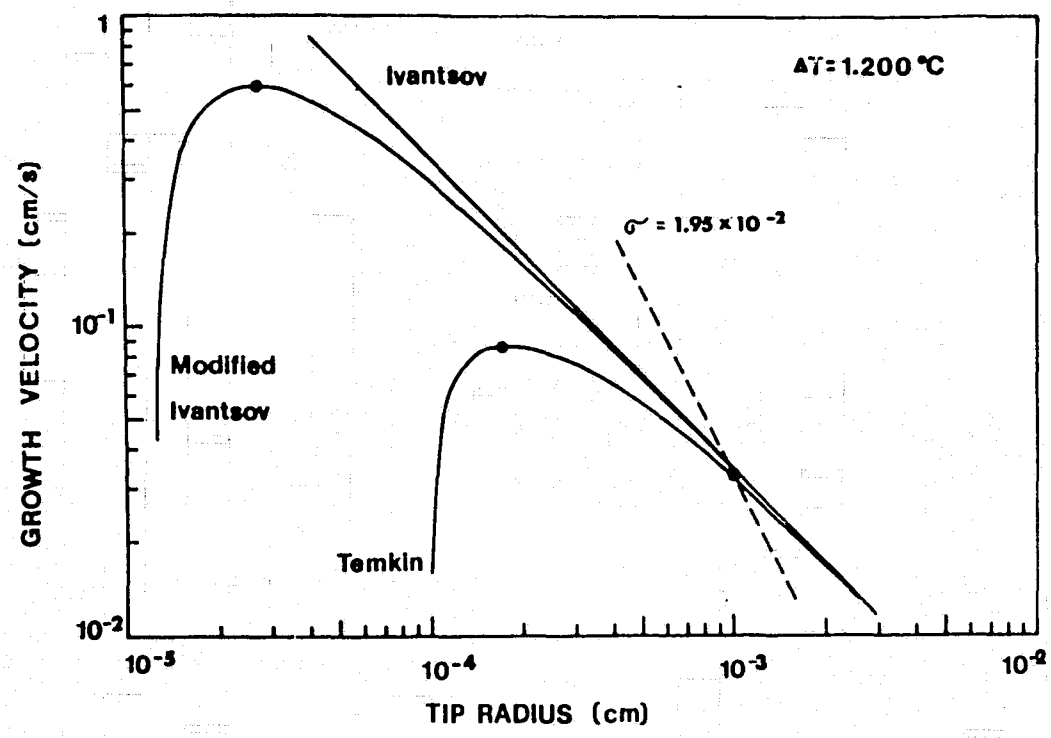

Velocity (log scale) vs. dendrite tip radius (log scale) at fixed supercooling. The isothermal (Ivantsov) solution is characterized by VR = const., whereas the non-isothermal solutions (Temkin and Modified Ivantsov) show progressive departures from the line VR = const. as the tip radius decreases. The broken curve, VR^2 = const., represents the condition of marginal morphological stability with a separation constant $\sigma^* = 1.95 \times 10^{-2}$, close to those discussed in the text.

Figure 2

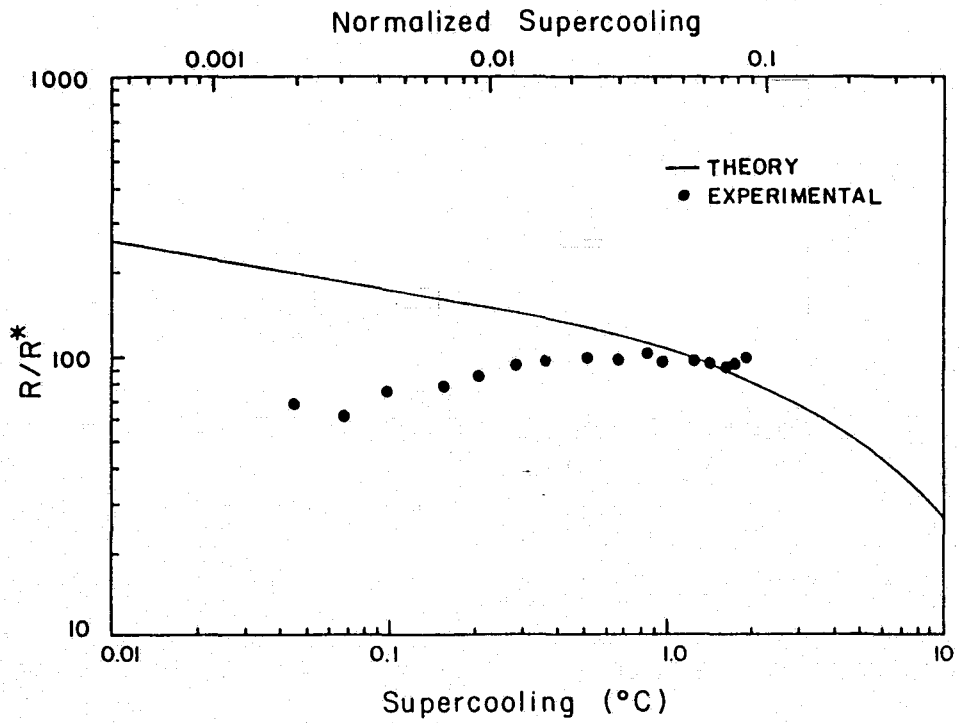

Dendrite tip radius, R, scaled to the critical radius, R^*, (log scale) vs. supercooling (log scale). Data, based on measurements performed on SCN, show that the operating states of dendrites occur at large multiples of R^*, in agreement with predictions from linear stability theory (solid curve). The disparity noted at small supercoolings between the theoretical scaling law and the experimental data is due to convection in the melt.

Figure 3

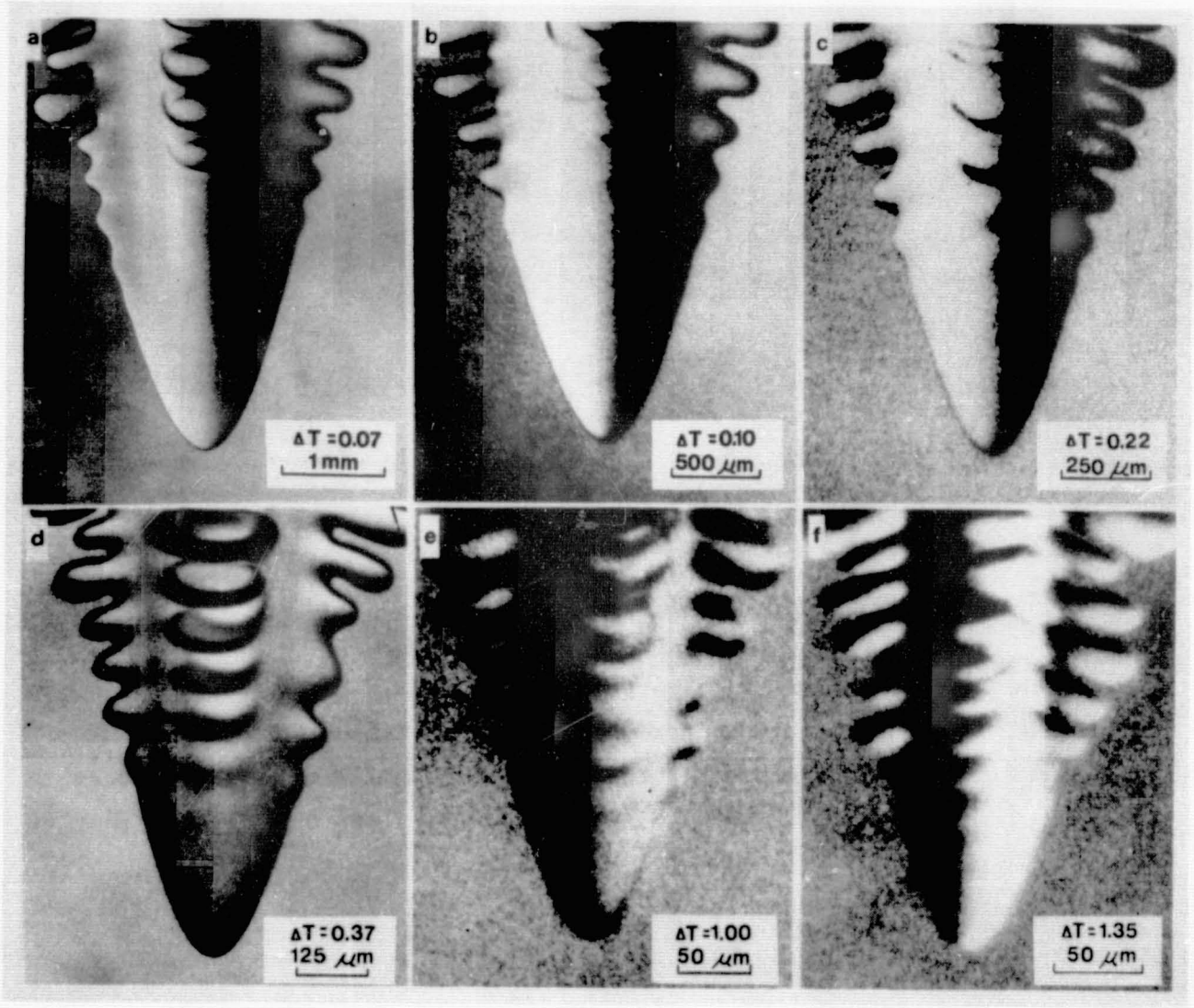

Tip morphologies of SCN dendrites growing at various supercooling. Photographic magnifications have been adjusted to produce constant apparent tip radii. Note that at increasing supercoolings the side branches amplify more rapidly and encroach upon the steady-state region near the tip.

Figure 4

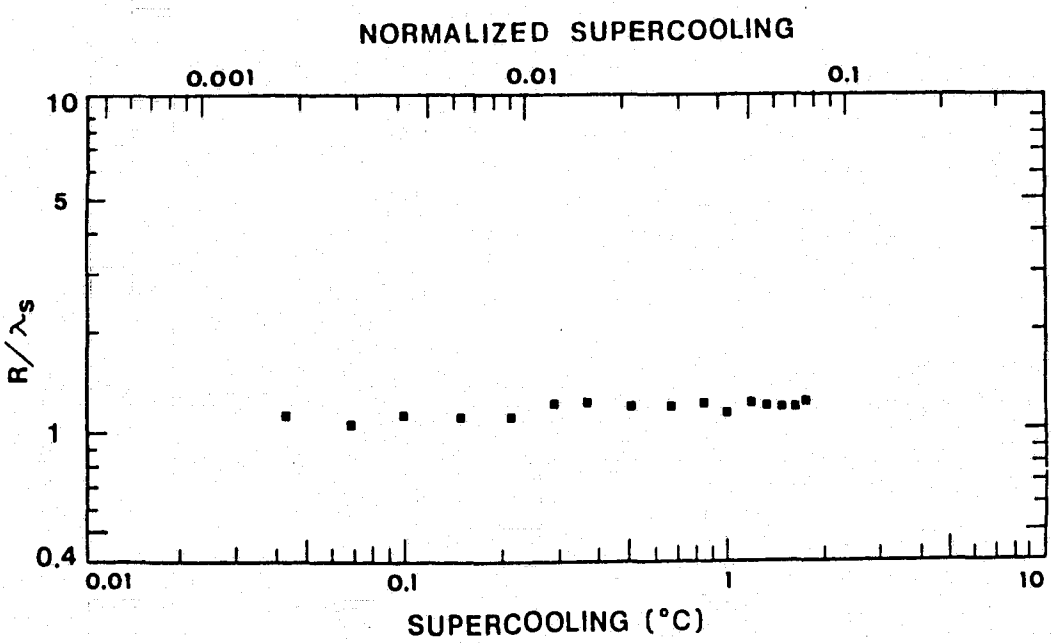

Dendrite tip radius, R, scaled to the wavelength of the marginal eigenmode λ^* (log scale) vs. supercooling (log scale). The scaling law demonstrated here remains valid over at least two decades in supercooling, viz., $R/\lambda^* = 1.2$. The fixed ratio of R to λ^* clearly demonstrates the close connection between the steady-state features, such as the tip radius, and the dynamical behavior related to the kinetic eigenstate.

Figure 5

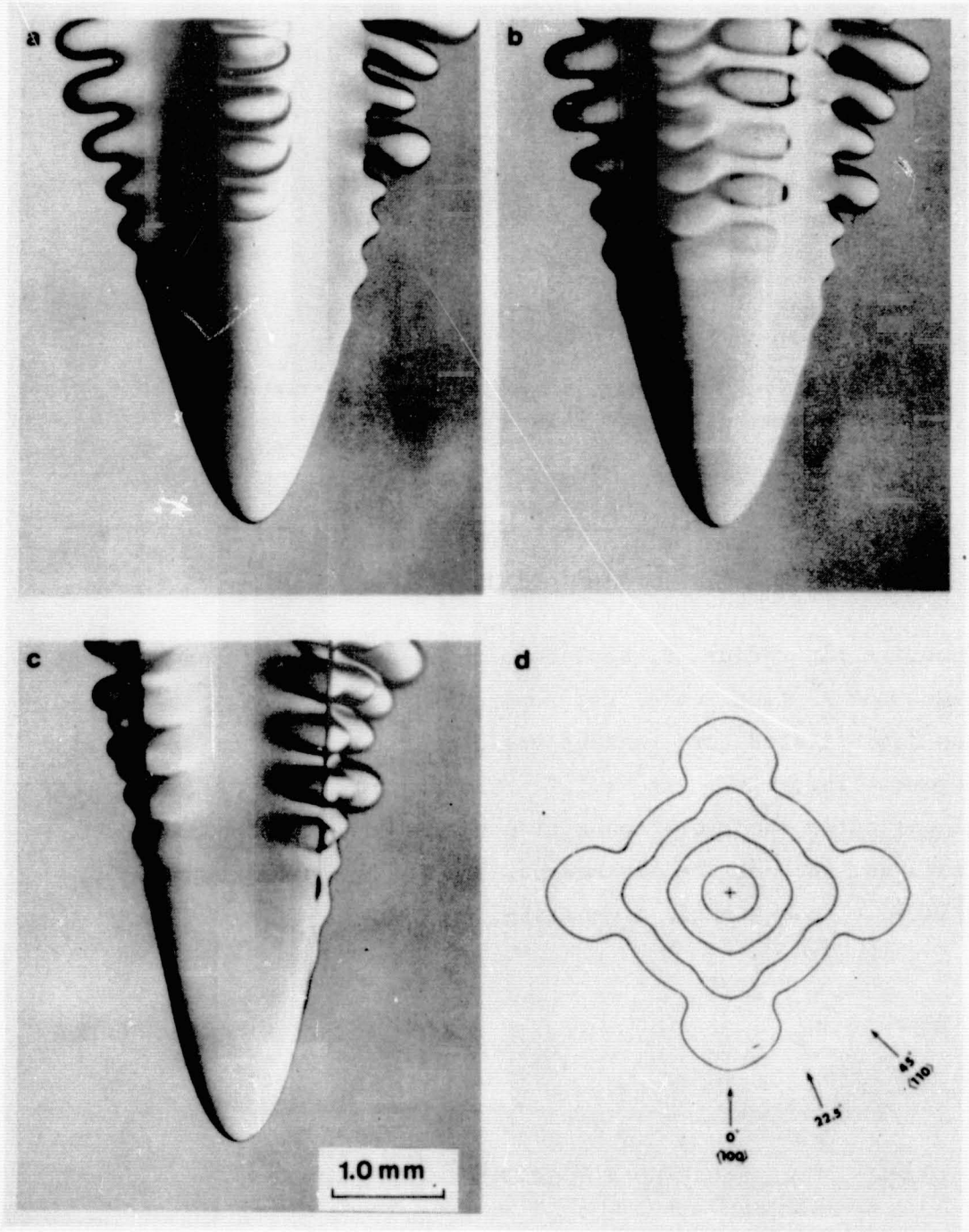

Anisotropic aspects of dendritic tip structures in SCN. The three views a, b, and c correspond to the viewing angles 0°, 22.5°, and 45° shown schematically in d. The side branches extend in the four <100> directions, however, near the tip the dendrite becomes a body of revolution.

Figure 6

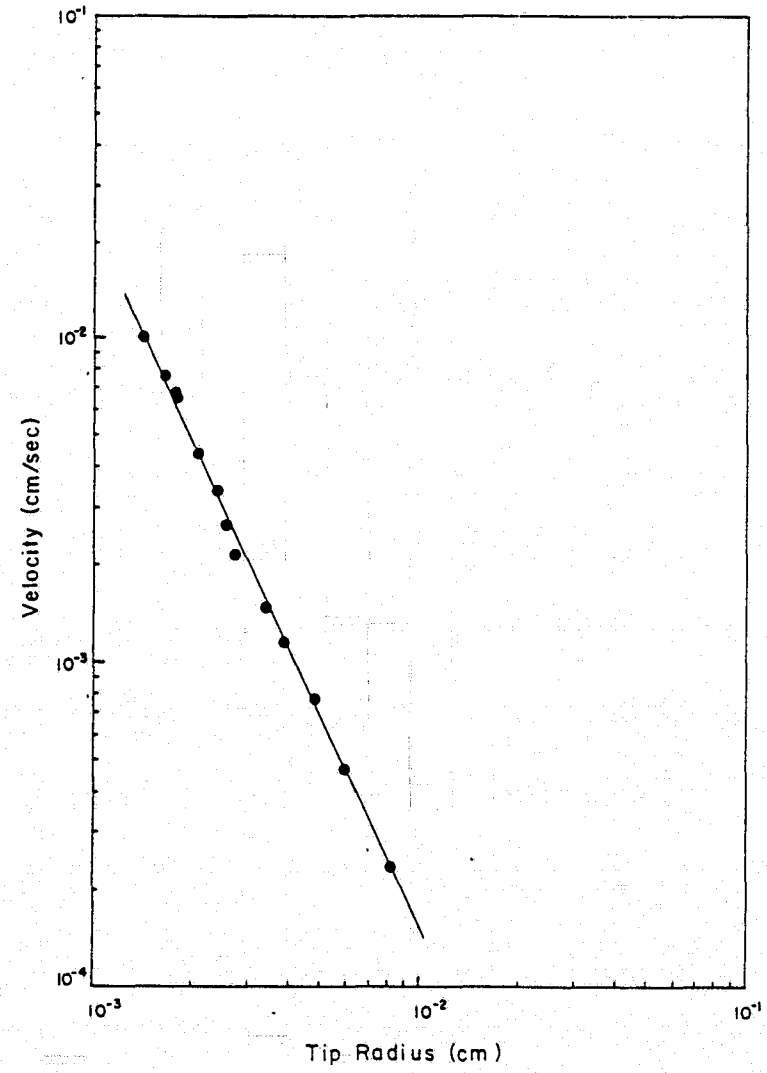

Velocity (log scale) vs. dendrite tip radius (log scale) at various supercoolings for PVA. The slope of these data is -2, in agreement with the requirement of marginal stability theory that VR^2 = const. The separation constant σ^* = 0.022 derived from these data is in excellent agreement with models discussed in the text.

Figure 7

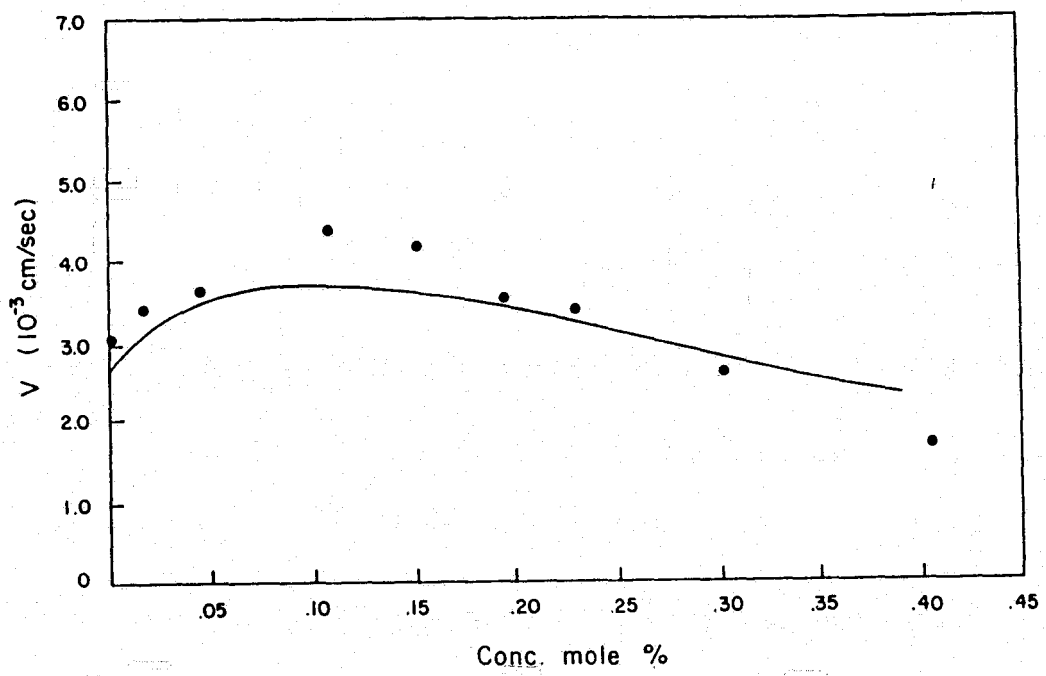

Dendrite growth velocity vs. composition for SCN-acetone alloys at a fixed supercooling with respect to the liquidus temperature. Theoretical curve derived from marginal stability analysis for equiaxed crystal growth. Comparison of theory and experiment is based on a "zero parameter" basis, because the diffusion coefficient for acetone in molten SCN has been measured independently.[42]

DISCUSSION

CISZEK: I am trying to see what conclusions we can draw about applying the information from the succinonitrile system to silicon, and the two things that come to mind are, first, that these are with much larger anisotropy and surface free energy in silicon compared with the succinonitrile system, and the other one seems to be the fact that dendrites and silicon are often associated with a (111) twin plane on the spine whereas we don't see that in your three-dimensional ones. Could you comment on those points?

GLICKSMAN: First of all, ask "Do we really know the surface energy anisotropy between solid and liquid silicon?" I am not referring to the kinetic faceting mechanism that we are all aware of. Do we really know gamma as a function of theta? I posit "No, we don't." There are highly anisotropic faceting systems that, when one looks at the equilibrium energies, turn out to be rather modest in their anisotropy. I am not convinced that the faceting aspects of silicon necessarily imply extremely high anisotropy. The second aspect that you mentioned is the twin-plane mechanism--there is no question about it, silicon finds a way of having the attachment kinetics become speedy enough to keep up with the transport mechanism. Apparently, with the tendency to form kinetic {111} facets, silicon does indeed form the twin plane mechanisms and, from the dendrite studies by Hamilton and Seidensticker, we know that these twin planes are there and that they are important. We also know that the gross morphology of the dendrite tip is not that dissimilar to what I have shown you with this rough interface system. So the study of transport mechanisms and the fundamental physics, and how morphological stability comes in, is somewhat independent of the fact that a silicon crystal does in fact have multiple twin planes in it, so that the interface doesn't depart too far from equilibrium. I tend to look at that as a special circumstance for silicon, but if you look at its effect on the overall dendritic morphology, it does not change it that dramatically. There are certainly detailed differences, but I am trying to say that if you want to learn something about the overall transport fields and their relationship, don't study silicon. But let's try to apply it to silicon.

CISZEK: You don't seem to see the same kind of branching phenomenon when you look at these {111} twin planes.

GLICKSMAN: In silicon you will form what we call a faceted dendritic structure, where the side branches indeed show kinetic faceting tendencies. The structure of a silicon dendrite is definitely trying to branch, but instead of getting these smooth waves, since you have this (111) hang-up in terms of the facet plane, the structure evolves in detail somewhat differently. I believe the fundamental physics near the tip is not too dissimilar to the model systems that I have reported on, and I think the challenge now is to take that understanding and transfer it properly to understanding silicon crystal growth.

SEKERKA: You remarked that you were surprised that a system with less than 1% anisotropy of surface tension could give rise to such a variation in the morphology around the dendrite tip. That is amazing, if it is indeed surface energy, but I wonder if in that system there might not be a hundredfold difference in anisotropy of kinetics with direction, and if that may not be the thing that is setting the differences in morphology. Have you any way separating those out in your mind?

GLICKSMAN: You pose a difficult question, and I suppose all I can say is: inasmuch as the tip region covers not 90°, but perhaps 50° of the selected growth axis, we have now shown that that fully fulfills the parabolic shape; that is, it falls off in such a way that the normal growth velocity is related to the cosine of that angle. There is no strong evidence that succinonitrile is in fact departing from local equilibrium over a wide range of driving forces. Now, you are saying the attachment mechanism is very, very fast, but there is still some sort of an anisotropy operating within the rough interface context. We have recently done some measurements on a system that has a 5% anisotropy. We have measured the surface energy independently, and it has about 10 times the anisotropy that succinonitrile has. We see by comparing these two kinds of dendrites what, on a comparative basis, is for sure the change in the surface energy anisotropy. Admittedly the attachment mechanism may be dragged along, but if we at least look at what we know, in terms of the measured energy dependence on orientation, the surface-energy anisotropy seems to impose itself in a very understandable way. On the tip shape, the tendency is to form these branching sheets, and in fact the suppression of the side-branching wave and the way the wave develops. These are unpublished data on a new system. I think we are gathering information that shows that even very small anisotropy seems to pick out the growth direction. We have no evidence that the big departures from local equilibrium occur as you go off the preferred direction.

SEKERKA: I don't know if big departures are necessary. You know the perturbation theory that Sam and I did had both effects in it, and they are sort of mathematically inseparable except for some traveling waves in the case of the anisotropy. A little bit of either gets you going, and I guess you are looking for the one that has the biggest kick.

GLICKSMAN: That is correct.

SEIDENSTICKER: When we did some work in the early '60s on germanium, we found that the presence of at least two twin planes was absolutely essential to relieve the attachment kinetic limitations in the growth of the germanium dendrites. In that case, we found that there was a very direct relationship between the spacing of the twin planes and the tip curvature. About four years ago Dick Hopkins and I started out to do some similar work with silicon, and we found that that the same effect apparently did not exist.

N84 28622 D8

USE OF THE BURTON-PRIM-SLICHTER EQUATION AT HIGH GROWTH RATES

William R. Wilcox
Department of Chemical Engineering
Clarkson College of Technology
Potsdam, New York 13676

ABSTRACT

The following must be assumed in order to derive the classic Burton-Prim-Slichter equation for segregation during crystal growth: isobaric, isothermal, isopotential or uncharged species, binary, planar interface, steady state, constant diffusion coefficient in fluid, no diffusion in crystal, no lateral convection within fluid film at interface with complete mixing beyond (stagnant film model), and either density, total concentration or partial molar volumes constant in the fluid phase. In addition, the effective distribution coefficient and the interfacial distribution coefficient must be defined properly. The velocity in the equation is the growth rate times a factor correcting for the difference in volumetric properties between crystal and fluid. The stagnant film thickness is found to be a function of freezing rate, with the precise functionality depending on the type of stirring occurring in the growth fluid.

INTRODUCTION

For many years the Burton-Prim-Slichter equation has provided the basis for interpreting experimental segregation data and for predicting the influence of stirring and finite freezing rate on the effective distribution coefficient k_{eff} (1). However, many assumptions were made implicitly in its derivation. In order to make these assumptions clear, we rederive here the BPS equation from the most general assumption-free mass transfer equations.

In using the BPS equation it has generally been assumed that the stagnant film thickness δ is independent of freezing rate v_c. In the second part of this paper we use results from the hydrodynamic literature to show that δ can be a strong function of v_c at even moderate freezing rates.

DERIVATION OF BPS EQUATION

The starting point is the general multicomponent diffusion equations of Reference (2). The notation is the same as in Reference (2), and is also given here at the end. The subscripts denote first the component (i for multicomponent, A and B for binary), and second the phase (c for crystal and f for fluid; either liquid or gas). The superscript r denotes that a standard reference system is used, mole centered (m), mass centered (') or volume centered (v). These represent the choices of average fluid velocity that may be used. This is necessary because each component moves at a different velocity v_i in a fluid with mass transfer taking place. The

diffusion equations are written in terms of the general parameters Z_i^r, α_{ij}^r and Y_i^r, which can take the values shown in Table 1.

In the absence of chemical reactions, the multicomponent mass transfer equation is given by (2):

$$\nabla \cdot J_{if}^r + \nabla \cdot C_{if} v_f^r = -\partial C_{if}/\partial t \tag{1}$$

The most common phenomenological expression used for the diffusion flux J_{if}^r in an isobaric, isothermal, isopotential (or non-electrolyte) system is:

$$J_i^r = -\sum_{j=1}^{n-1} \alpha_{ij}^r D_{ij}^r \nabla Y_j^r \tag{2}$$

Note that the flux of component i depends not only on its own concentration gradient ∇Y_i but on the gradients of the other constituents as well.

TABLE 1

Diffusion Parameters in Different Reference Systems

Reference System	Z_i^r	α_{ij}^r	Y_i^r	Average Velocity	$\Sigma Z_i^r C_i$
Mass centered	M_i	ρ	W_i/M_i		
	M_i	$C^2 M_i M_j/\rho$	X_i/M_i	$v' = \Sigma W_i v_i$	ρ
(const. ρ)	M_i	1	$C_i = \rho_i/M_i$		
Mole centered	1	C	X_i		
	1	ρ^2/CM_iM_j	W_i	$v^m = \Sigma X_i v_i$	C
(const. C)	1	1	$C_i = CX_i$		
Volume centered	$\overline{V}_i$	1	C_i		
(const. $\overline{V}_i$)	$\overline{V}_i$	$C^2\overline{V}_j\overline{V}_i$	$X_i/\overline{V}_i$	$v^v = \Sigma F_i v_i$	1
(const. $\overline{V}_i$)	$\overline{V}_i$	$\rho^2\overline{V}_i\overline{V}_j/M_iM_j$	$W_i/\overline{V}_i$		

Equation (1) must be greatly simplified, via the following:

(a) Binary, with $J_A^r = -\alpha_{AB}^r D_{AB} \nabla Y_A^r$. Note that D_{AB} is independent of reference system, whereas D_{ij}^r was not.

(b) One dimensional problem, so $\nabla = \partial/\partial y$. This is true only if the interface is planar and if there is no convection parallel to the interface (no stirring).

(c) D_{AB} is constant, enabling us to move D_{AB} out of the differential.

(d) Steady state, so $\partial C_{Af}/\partial t = 0$.

(e) $\Sigma Z^r_{if} C_{if}$ and Z^r_{if} are constant. This causes $\nabla \cdot v^r_f = 0$, thereby eliminating the $C_{Af} \nabla \cdot v^r_f$ term.

Note that the conditions in (e) correspond to constant density ρ_f for the mass centered system, constant total concentration $\underline{C_f}$ for the mole centered system, and constant partial molar volumes $\overline{V}_{Af}$ and $\overline{V}_{Bf}$ for the volume centered system. A constant density is approximated by some organic mixtures and by very dilute systems ($C_{Af} << C_f$). Constant C_f is found for ideal gas mixtures, while constant $\overline{V}_{Af}$ is fairly good for most liquid and gas mixtures. Thus the volume-centered system is the one of most general applicability. However, as pointed out later the average velocity appearing in the hydrodynamic equations is the mass-average velocity v'.

With assumptions (a) through (e), Equation 1 becomes:

$$D_{AB} \frac{\partial^2 C_{Af}}{\partial y^2} - v^r_f \frac{\partial C_{Af}}{\partial y} = 0 \tag{3}$$

At this point we don't yet know what is the fluid velocity v^r_f. The condition $\nabla \cdot v^r_f = 0$ and absence of lateral convection insure that it is constant. (If $\Sigma Z^r_{if} C_i$ and Z^r_{if} are <u>not</u> both constant, v^r_f is likewise not constant.) We feel that v^r_f must be related to the crystal growth rate v_c. The relationship is found by a material balance at the freezing interface, taking the interface to be fixed at y = 0 and assuming no diffusion in the solid (2,3):

$$v^r_f = v^r_f(0) = -v_{cf} = -v_c \frac{Z^r_{Af} C_{AC} + Z^r_{Bf} C_{BC}}{Z^r_{Af} C_{Af} + Z^r_{Bf} C_{Bf}} \tag{4}$$

The negative sign comes from the fact that v^r_f is directed out of the interface into the fluid (positive y), while v_{cf} and v_c are traditionally taken to be in the opposite direction. Equation (4) gives for the parameter $(v_{cf}/v_c) = \rho_c/\rho_f$ for the mass-centered system, C_c/C_f for the mole centered system, and $\overline{V}_{Af} C_{AC} + \overline{V}_{Bf} C_{BC}$ for the volume centered system. For $C_{Af} << C_f$, all are equivalent.

To solve Equation (3) with $v^r_f = -v^r_{cf}$ we need the boundary conditions:

$$\left.\begin{array}{ll} \text{at } y = 0 \text{ (interface):} & C_{Af} = C_{A0} \\ \text{at } y = \delta^r: & C_{Af} = C_{A\infty} \end{array}\right\} \tag{5}$$

Note that this is equivalent to assuming the stagnant film model, in which it is imagined that there is no lateral convection within a layer of thickness δ at the freezing interface, with complete mixing beyond this giving a uniform concentration $C_{A\infty}$. Note that the value of δ depends on the reference

system. The solution to Equations (3) and (5) is

$$\frac{C_{Af}-C_{A0}}{C_{A\infty}-C_{A0}} = \frac{1-\exp(-yv^r_{cf}/D_{AB})}{1-\exp(-\delta^r v^r_{cf}/D_{AB})} \tag{6}$$

To obtain the BPS equation we need a material balance for the impurity A across the interface. Assuming no diffusion in the solid this is, at $y = 0$:

$$v_c C_{AC} = D_{AB} \frac{\partial C_{Af}}{\partial y} + C_{A0} v^r_{cf} \tag{7}$$

If we differentiate Equation (6) and substitute into Equation (7) we get the BPS equation only if we define the distribution coefficients as follows:

$$k^r_0 = \frac{C_{AC}}{C_{A0}(v^r_{cf}/v_c)} \quad ; \quad k^r_{eff} = \frac{C_{AC}}{C_{A\infty}(v^r_{cf}/v_c)} \tag{8}$$

The correct form of BPS is thereby:

$$k^r_{eff} = \frac{k^r_0}{k^r_0 + (1-k^r_0)\exp[-\delta^r v_c (v^r_{cf}/v_c)/D_{AB}]} \tag{9}$$

Note that k^r_0 is <u>not</u> the equilibrium distribution coefficient, but is the interfacial distribution coefficient. At low freezing rates they may be identical, but as shown in other papers in this volume and elsewhere, they certainly are not equal at high freezing rates. It is also worth noting that Eqs. (8) actually correspond to common usage, because concentrations have been based on analyses of solids rather than on concentrations in the liquid at the melting point. Since the liquid has a density different from that of the solid, when one melts a solid the impurity concentration (in atoms/volume) changes.

VARIATION OF STAGNANT FILM THICKNESS

There is no such thing as a stagnant film in convective mass transfer, even if it is erroneously called by the sophisticated sounding name "boundary layer." In actuality the lateral velocity parallel to a solid surface (such as a freezing interface) only <u>approaches</u> zero as one approaches the surface. In mass transfer problems, the fictitious film thickness δ is <u>defined</u> as that giving the correct answer. In that sense, within the validity of the other assumptions made, the BPS equation is correct because δ is defined as having that value required to make it correct. In practice, therefore, δ must be obtained from experiments, from solutions of the <u>real</u> boundary-layer equations, or solutions of the exact hydrodynamic and mass transfer equations. It turns out that δ is a function of D_{AB}, the kinematic viscosity ν, and the freezing rate v_c.

In correlating segregation data, a convenient technique is to rearrange BPS into the form:

$$\left(\frac{1}{k^r_{eff}} - 1\right) = \left(\frac{1}{k^r_0} - 1\right) \exp\left(-\frac{\delta^r v_c (v^r_{cf}/v_c)}{D_{AB}}\right) \tag{10}$$

such that one plots experimental values of $\ln(1/k^r_{eff} - 1)$ vs. growth rate v_c. However, this is useful only if δ^r is not a function of v_c. Similarly in predicting segregation from theory, values of δ are by far most available for $v_c = 0$. (We denote these as δ^*. The available solutions are nearly all for constant ρ_f because the mass-centered velocity appears in the usual hydrodynamic equations.) But does $\delta = \delta^* =$ constant? We can answer this for only some mass transfer situations, using experimental data and theoretical results in the existing literature. Most of the results were actually for heat transfer, requiring substitution of Sherwood number Sh for Nusselt number Nu, concentration gradient for temperature gradient, and Schmidt number Sc for Prandtl number Pr.

The methods used to convert the literature results to a form useful and familiar to us were outlined in Reference (4) and are based on Equations (6) and (7). The equations used are:

$$\frac{\delta^r}{\delta^*} = \frac{\ln(1 + \varepsilon^r_v)}{\varepsilon^r_v (Sh/Sh^*)} \tag{11}$$

$$\frac{\delta^* v^r_{cf}}{D_{AB}} = -\varepsilon_v \frac{Sh}{Sh^*} \tag{12}$$

where the interfacial velocity parameter ε^r_v is defined as:

$$\varepsilon^r_v = \frac{C_{A\infty} - C_{A0}}{C_{AC}/(v^r_{cf}/v_c) - C_{A0}} \tag{13}$$

and $$\delta^r v^r_{cf}/D_{AB} = -\ln(1 + \varepsilon^r_v) \tag{14}$$

Note that for constant ρ_f in the mass-centered system, $\varepsilon'_v = (W_{A\infty} - W_{A0})/W_{AC} - W_{A0})$ while for constant C_f, $\varepsilon^m_v = (X_{A\infty} - X_{A0})/(X_{AC} - X_{A0})$. All of the results to be discussed were obtained using the mass-centered system.

Figure 1 shows results for laminar flow caused by an infinite rotating disk. The theoretical curves are the same as those presented in 1969 (4). It is interesting to note that for liquids (high Sc), the "exact" results of Burton, Prim and Slichter (1), the results of the hydrodynamicists (5,6), and the recent results of Wilson (7) all agree. The others considered an infinite body of liquid, while Wilson used an infinite non-rotating plane parallel to the rotating disk. Consequently Wilson's δ^* values were about 15% larger than the others obtained. That is, the non-rotating parallel surface reduced the mass transfer. In addition, Wilson summarized her

results in a simple equation, which becomes in the present notation:

$$\frac{\delta'}{\delta^*} = \frac{1}{1 + 0.0699\ \delta' v'_{cf}/D_{AB}} \tag{15}$$

Also shown on Figure 1 are data for segregation of Sb in Czochralski growth of Ge, published as a companion article (8) to the BPS theoretical paper. The scatter is considerable. A statistical treatment of the data revealed the predicted dependence of δ' on rotation rate and no dependence of δ'/δ^* on freezing rate. That is, within experimental accuracy the data agree with the theory.

On the other hand, the data on dissolution of KBr and sucrose in water (9) do not agree with theory. This was attributed to variable properties. In such concentrated solutions, viscosity, density and diffusion coefficient are all functions of composition, while the simple theory assumes that all of these properties are constant.

It is of interest to determine the error caused by neglecting the freezing rate dependence of δ' in the BPS equation. From Equation (9),

$$\%\ \text{error} = 100\% \left[\frac{k'_0 + (1-k'_0)\exp(-\delta' v'_{cf}/D_{AB})}{k'_0 + (1-k'_0)\exp(-\delta^* v'_{cf}/D_{AB})} - 1 \right] \tag{16}$$

Figure 2 shows that for typical Czochralski growth rates ($\delta^* v'_{cf}/D_{AB} \sim 1$), the error never exceeds 10%. Similarly for $0.2 \lesssim k'_0$ the error is 10% or less at all freezing rates. However for $k'_0 \leq 0.1$ and moderate freezing rates the error becomes sizeable, and increasingly so as k'_0 decreases. At very large freezing rates the error again decreases. As v_{cf} increases the mass transfer becomes increasingly determined by diffusion and by the crystallization flow, and less and less by convective mixing; $k_{eff} \rightarrow 1$, corresponding to steady state in the absence of mixing.

Many excellent theoretical results are available for laminar forced convection over a flat plate, for many different Sc and angles of impingement. For liquids, δ' is smaller than δ^* by about 30% at $\delta^* v_{cf}/D_{AB} \sim 5$. Several theories for turbulent forced convection on a flat plate have been proposed for gases. They do not agree well with one another, but none predicts that δ' deviates from δ^* by more than 30%. The experimental data show considerable scatter about $\delta'/\delta^* = 1$. Such convective situations do not appear to be important for rapid solidification and so are not presented in detail here.

There are many theoretical results for buoyancy-driven free convection, but few are relevant to our present interests. Most are for convection on a vertical flat plate caused solely by concentration differences. Furthermore, the theories do not agree with one another. In solidification it is usual to find the convection controlled by temperature differences, especially for small impurity contents. The only relevant study I found for such a situation is that of Cardner and Hellums (10,11). Representative results are shown in Figure 3. The Grashof number Gr_{heat} represents the driving force for natural convection caused by temperature differences ΔT, whereas Gr_{mass}

is that for concentration differences ΔC_{Af}. The values Pr = 0.2 and Sc = 5 approximate the properties for a liquid metal. Note that as the variation of density due to ΔT increases in importance, the deviation of δ from δ^* increases significantly. Thus one would not expect segregation data for thermally-driven free convection to fit BPS even at moderate freezing rates.

The hydrodynamicists have performed many studies on the influence of finite interfacial flow (v_{cf}) on mass transfer. However, few of these are of direct interest in solidification. There are no such studies, for example, for thermally-driven free convection in a horizontal boat or in a vertical Bridgman ampoule. Such geometries would require numerical approaches; and hopefully careful experiments performed out to large $\delta v_{cf}/D$.

CONCLUSION

The classic BPS equation is expected to work well for Czochralski growth at all freezing rates, unless the equilibrium distribution coefficient is small or severe non-equilibrium interfacial processes occur. Solidification in unstirred systems with buoyancy forces present is another matter. BPS probably breaks down even at moderate growth rates. Plots of $\ln(1/k_{eff}-1)$ vs. growth rate would be expected to show deviations from linearity even at $\delta v/D \sim 1$. Numerical solutions giving δ/δ^* vs. $\delta v/D$ for typical geometries would provide considerable insight, but are unlikely to be general enough to allow confident predictions of segregation for all situations and systems.

Acknowledgement

This work was supported by NASA via Contract NAS8-34891. I am grateful to Professors Taylor and Subramanian for their encouragement. Clarkson's library was of immense assistance in gathering the immense literature on the effect of transpiration on heat and mass transfer.

REFERENCES

1. J. A. Burton, R. C. Prim and W. P. Slichter, J. Chem. Phys. 21, 1987 (1953).
2. W. R. Wilcox, Ch. 3 in Preparation and Properties of Solid State Materials, Vol. 2, Dekker, NY (1976).
3. W. R. Wilcox, J. Crystal Growth 12, 93 (1972).
4. W. R. Wilcox, Mat. Res. Bull. 4, 265 (1969).
5. D. W. Zeh and W. N. Gill, AIChE Journal 14, 715 (1968).
6. D. R. Olander, J. Heat Transfer, Trans. ASME C84, 185 (1962).
7. L. O. Wilson, J. Crystal Growth 44, 371 (1978).
8. J. A. Burton, E. D. Kolb, W. P. Slichter and J. D. Struthers, J. Chem. Phys. 21, 1991 (1953).
9. A. S. Emanuel and D. R. Olander, Int. J. Heat Mass Transfer 7, 539 (1964).
10. D. V. Cardner, Ph.D. Thesis, Rice University (1963). University Microfilm 63-7155.
11. D. V. Cardner and J. D. Hellums, I/EC Fund. 6, 376 (1967).

NOMENCLATURE

C	Total molar concentration ($=\Sigma C_i$) (mol/m^3).
C_i	Molar concentration of component i (mol/m^3).
D^r_{ij}	Multicomponent diffusion coefficient in reference system r (m^2/s).
D_{AB}	Binary diffusion coefficient (m^2/s).
F_i	Volume fraction of i ($= C_i V_i$).
J^r_i	Diffusion flux relative to r-average velocity v^r ($= C_i(v_i - v^r)$) ($mol/m^2 \cdot s$).
K	Mass transfer coefficient ($= DSh/L$) (m/s).
k	Distribution coefficient (See Eq. 8).
L	Characteristic dimension or length (m).
M_i	Molecular weight of i (g/mol).
Pr	Prandtl number (ν/κ).
Sc	Schmidt number (ν/D_{AB}).
Sh	Sherwood number ($(\partial(W_A - W_{A\infty})/(W_{A0} - W_{A\infty}))/\partial(y/L)$).
$\overline{V}_i$	Partial molar volume of i (m^3/mol).
v^r	Average velocity in y direction in r reference system (m/s).
v_c	Crystal growth velocity (m/s).
v_i	Velocity in y direction of component i (m/s).
v^r_{cf}	Crystallization flow velocity in negative y direction taking interface as fixed at y=0 (m/s). Same as V in figures.
W_i	Weight fraction of i in mixture.
X_i	Mole fraction of i.
Y^r_i	Composition variable (See Table 1).
y	Distance from interface into fluid.
Z^r_i	Weighting factor (See Table 1).
α^r_{ij}	Weighting factor (See Table 1).
δ^r	Fictitious stagnant film thickness (m).
ε^r_v	Interfacial velocity parameter (See Eq. 13)
κ	Thermal diffusivity (m^2/s).

μ	Viscosity (g/m·s)
ν	Kinematic viscosity (= μ/ρ)(m^2/s).
ρ	Total density (g/m^3).

Subscripts

A	Solute in binary mixture.
B	Solvent in binary.
c	Crystal.
eff	Effective value.
f	Fluid (liquid or gas).
i	Component i in multicomponent mixture
j	Component j.
0	Value at interface.
∞	Value in bulk fluid.

Superscripts

m	Mole centered (based on mole-average velocity).
v	Volume centered (based on volume-average velocity).
'	Mass centered (based on mass-centered velocity).
*	Value for zero interfacial velocity ($v^r_{cf} = 0$, $v_c = 0$, $\varepsilon_v = 0$).

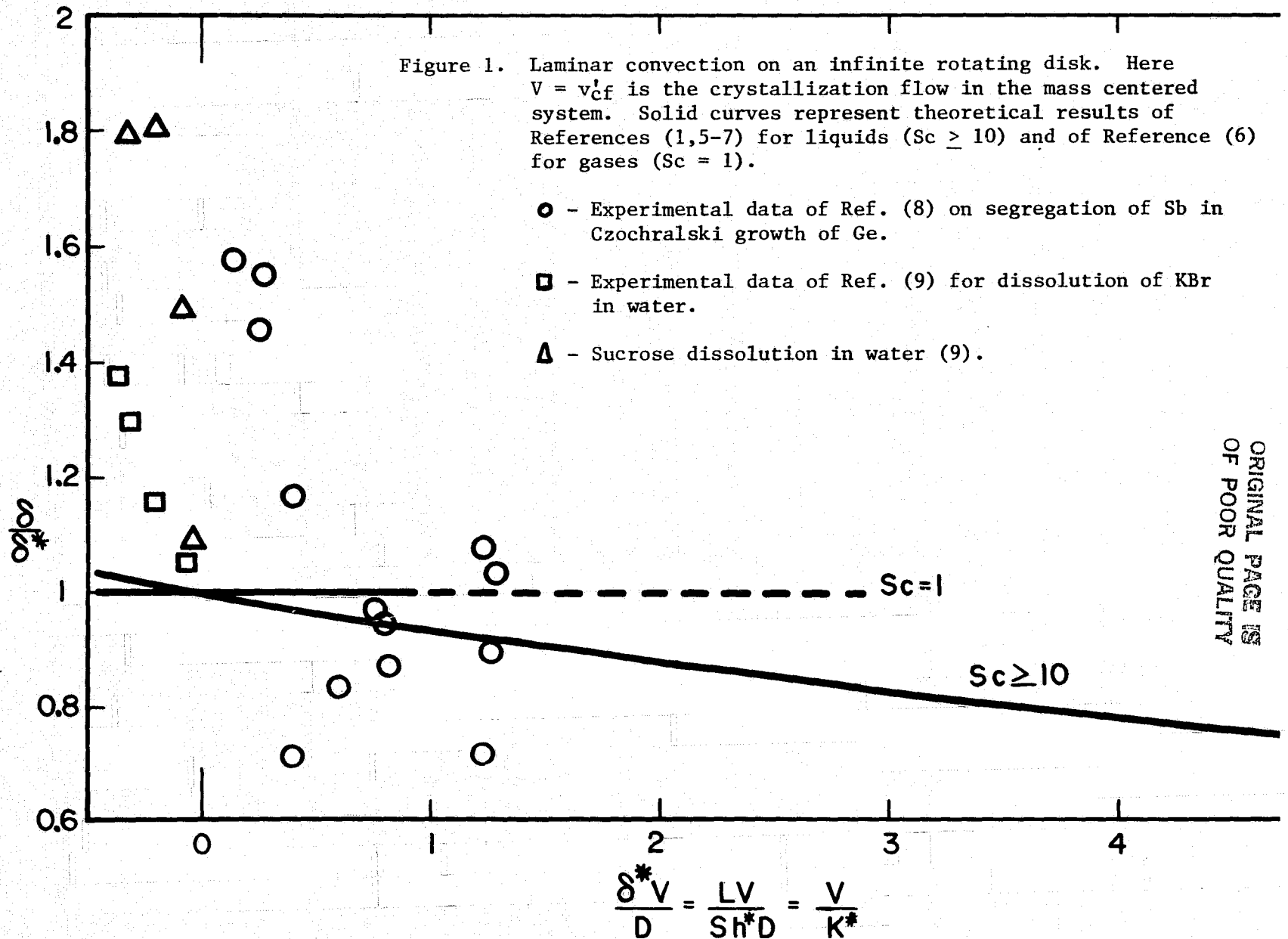

Figure 1. Laminar convection on an infinite rotating disk. Here $V = v'_{cf}$ is the crystallization flow in the mass centered system. Solid curves represent theoretical results of References (1,5-7) for liquids ($Sc \geq 10$) and of Reference (6) for gases ($Sc = 1$).

○ - Experimental data of Ref. (8) on segregation of Sb in Czochralski growth of Ge.

□ - Experimental data of Ref. (9) for dissolution of KBr in water.

△ - Sucrose dissolution in water (9).

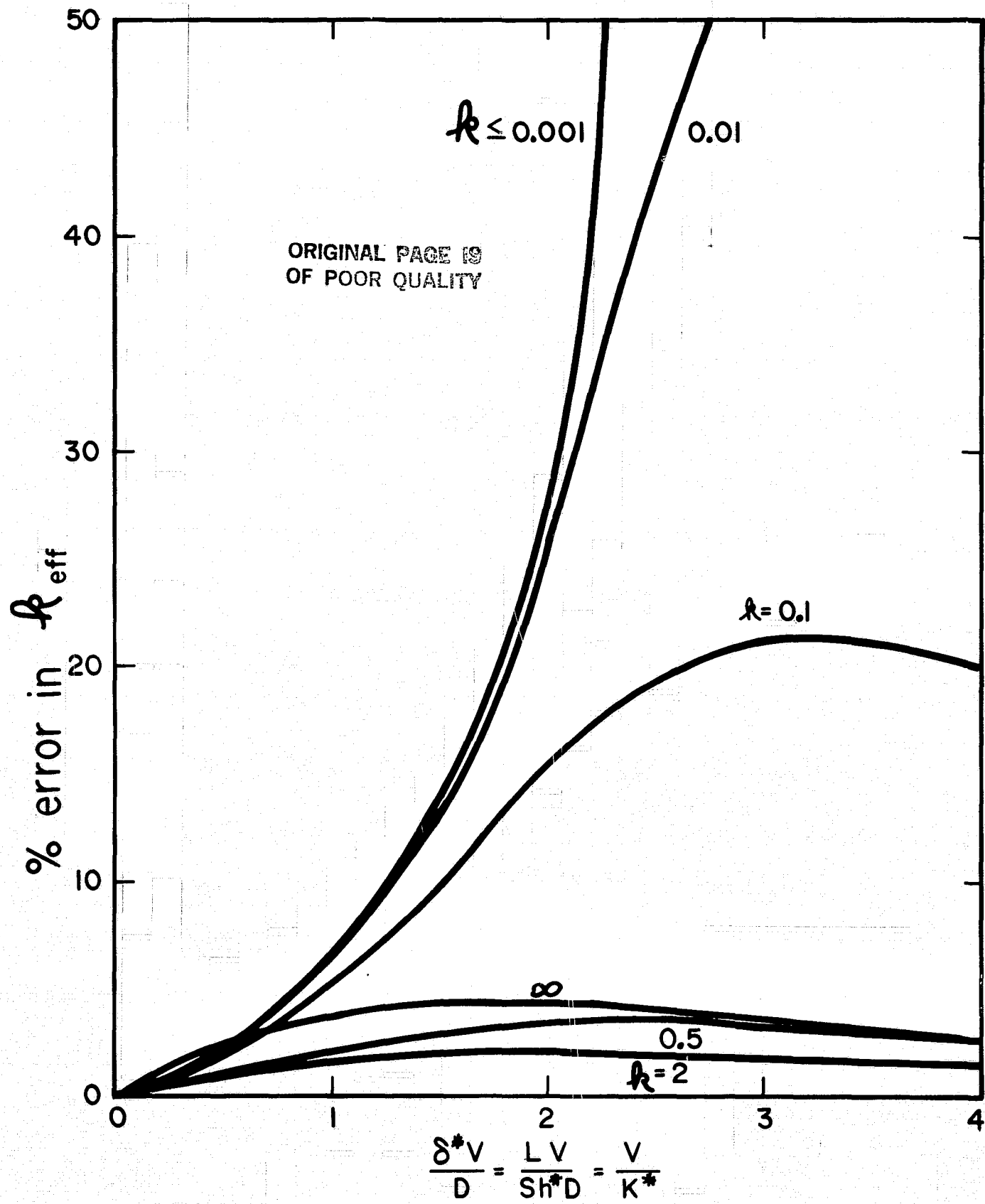

Figure 2. Error in calculating effective distribution coefficient by assuming $\delta' = \delta^*$ for liquid on rotating disk. From Eq. (16) and curve for Sc $\geq$ 10 in Figure 1.

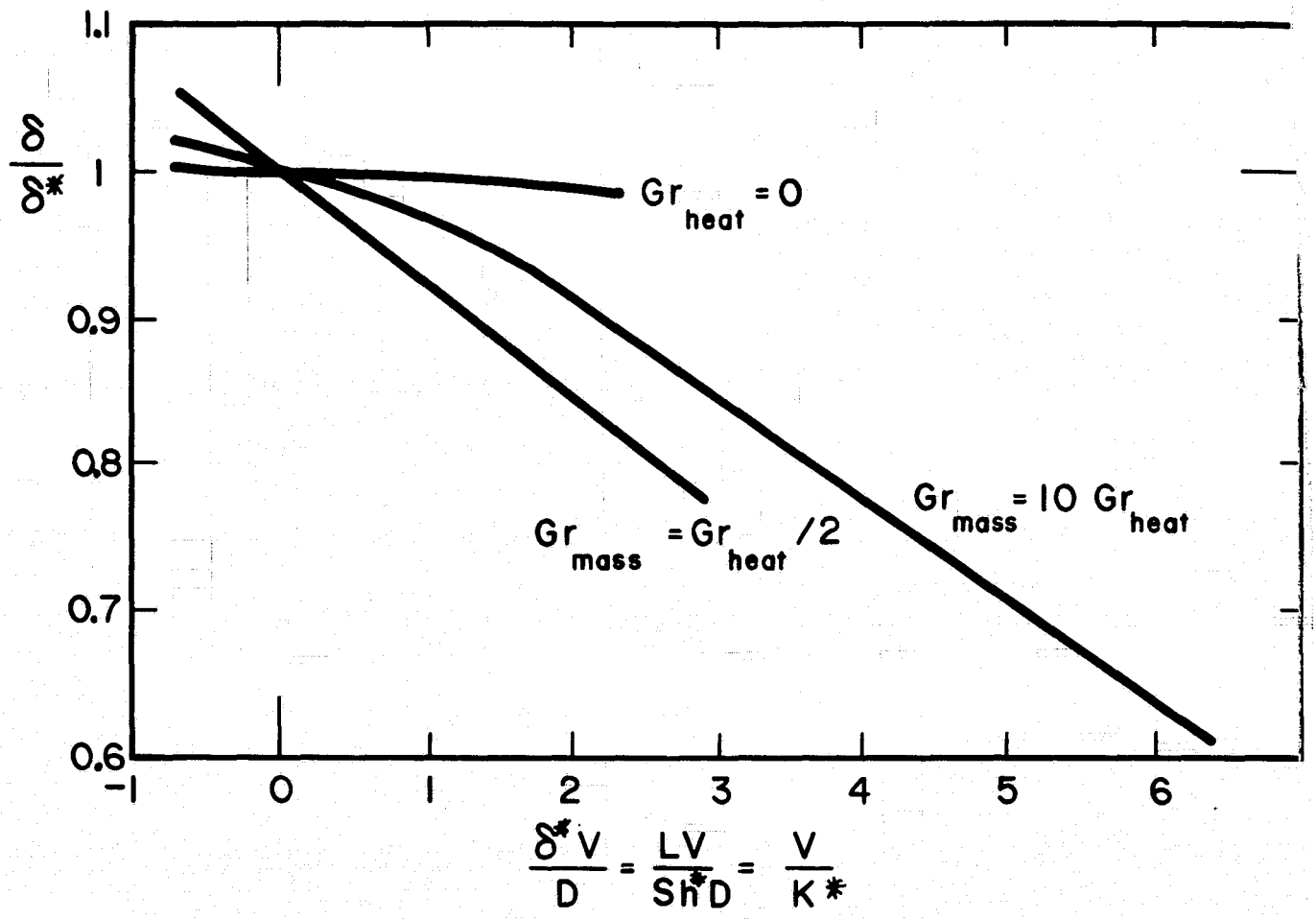

Figure 3. Buoyancy-driven free convection on a vertical flat plate caused by both temperature differences and concentration differences (10,11). Gr_{mass} is proportional to the density difference caused by ΔC_{Af} and Gr_{heat} to that caused by ΔT.

DISCUSSION

MORRISON: Based on your analysis of the Burton-Prim-Schlichter equation, do you have a comment on Bruce's [Chalmers] calculations of very high impurity concentrations at the growth interface in real growth systems?

WILCOX: I'm not sure I see the relation. If you are forming particles in the liquid, they may be swept away or be second-phase particles. It is well known that if the carbon concentration gets high you get silicon carbide particles in silicon.

N84 28623

MODELS OF RAPID SOLIDIFICATION

George H. Gilmer

Jeremy Q. Broughton

AT&T Bell Laboratories

Murray Hill, New Jersey 07974

ABSTRACT

Laser annealing studies have provided much information on various consequences of rapid solidification, including the trapping of impurities in the crystal, the generation of vacancies and twins, and on the fundamental limits to the speed of the crystal-melt interface. In this paper we review some of the results obtained by molecular dynamics methods of the solidification of a Lennard-Jones liquid. An indication of the relationship of interface speed to undercooling for certain materials can be derived from this model. Ising model simulations of impurity trapping in silicon are compared with some of the laser annealing results. The consequences of interface segregation and atomic strain are discussed.

MODELS OF RAPID SOLIDIFICATION

George H. Gilmer

Jeremy Q. Broughton

AT&T Bell Laboratories

Murray Hill, New Jersey 07974

I. Introduction

The trapping of impurities and other effects of rapid solidification have been intensively studied by pulsed laser melting and resolidification of semiconductors[1]. Laser annealing techniques of this sort can produce crystals with impurity concentrations that exceed by several orders of magnitude those which are obtained by conventional crystal growth. In addition to the effects on the impurity diffusion in the fluid, the process of incorporating the impurity at the interface is modified. Crystal-melt interface velocities up to 18 m/s have been achieved for silicon[2]. A laser pulse with sufficient energy to melt a crystal to a depth of several microns is applied, and the steep temperature gradients that result also provide rapid cooling after the pulse terminates. Recrystallization starts when the interface cools below the melting point, and the latent heat released is readily transferred to the interior of the crystal. In this case, heat conduction is not the only factor that controls the interface velocity, and the finite rate of atomic rearrangement also causes observable effects. The large amount of data that has become available recently should provide answers to fundamental questions concerning the mechanism of crystal growth and intrinsic limits on the solidification rate.

Rapid solidification also can induce changes in the crystal structure and composition. Material in the region of the interface is, of course, in transition from the

fluid to the crystalline state. The interface region is limited in thickness to a few atomic diameters, as discussed below. Therefore, the rearrangement of the atoms in this region must occur in a time of $\approx 10^{-10}$ sec for velocities of 10 m/s. Some of the properties characteristic of the disordered liquid may be trapped in the solid, unless the mobility of the atoms in the interface is extremely large.

Laser annealing has produced crystalline material with large concentrations of certain impurities. In some cases, the maximum equilibrium solubility can be exceeded by several orders of magnitude. These new materials may have useful properties. Rapid growth can also lead to a degeneration of the crystal structure. In the case of silicon grown behind a (111) interface, speeds of ≈ 5 m/s produce some lattice defects, but at higher speeds the crystalline symmetry is lost completely, and amorphous material is formed[2]. Apparently there is not enough time for the atoms to reach the ordered crystal structure.

Progress in understanding these phenomena can be made by comparisons of the new data with atomic-scale models of solidification. Direct observations of the crystal-melt interface are not possible in most cases; the experiments yield only information on the rates of solidification and the structures before and after laser processing. Computer simulation models can represent the interface structure in detail. In principle, the parameters of the model can be adjusted to match the experiment, and the resulting growth mechanisms and structures can be studied. The fast growth regime is a convenient one to model, because a large sample of material can be crystallized in a relatively small amount of computer time.

Two different models of crystal growth will be discussed in this parer. First, a system of particles interacting by means of a Lennard-Jones (LJ) potential is treated[3]. This potential is most appropriate for noble gas systems, but similar properties are expected for other atomic systems such as the simple metals which also have hard-core repulsions. The molecular dynamics technique is used to calcu-

late the detailed trajectories of ≈1000 particles. The growth rates obtained from this model provide information on the time scales involved in the restructuring of the material in the interface. Also, the generation of lattice defects can be observed, since no constraints are placed on the atomic motion other than those resulting from the boundary conditions. Some conclusions on the crystallization of silicon can be derived from these results.

Impurity trapping has been simulated using Monte Carlo techniques and the kinetic Ising model[4,5]. A perfect lattice structure is assumed *a priori*, and lattice sites are permitted to occupy one of three states: a mean-field liquid, crystal type A (the host species), and crystal type B (the impurity). Transitions from liquid to the crystalline state and the reverse occur at rates that are consistent with the relative energies and entropies of the two states according to the principle of microscopic reversibility. This relatively simple model can be studied under a range of conditions and reliable data on impurity trapping can be obtained. The model exhibits most of the known mechanisms of crystal growth. The long-wavelength perturbations of the interface structure that lead to the roughening transition are included, and their effects on the rate of crystal growth have been considered[6].

Molecular Dynamics Models of Crystal-Melt Systems.

The structure of the crystal-melt interface in a system of LJ particles has been examined in depth[7-10]. We will return to this subject later in our discussion of impurity trapping. Because of the fast crystallization kinetics, it is also possible to measure crystal growth rates. Landman et. al.[11] have simulated the motion of atoms in a slab initially in the supercooled liquid state, but which was placed in contact with a crystal surface. Ordering of the atoms into layers was observed first, and then the localization of the atoms at lattice sites within the layers. An interface speed of ≈100 m/s was estimated during the early stages of ordering, if the parameters of the model appropriate for argon were inserted. The melting and

resolidification of a two-component system has also been simulated, with the energy for melting deposited in a manner similar to that of a laser source[12]. Some segregation of the impurity to the free surface was observed.

Steady-state crystallization rates were measured for a range of temperatures below the melting point (T_m) by Broughton et. al.[3] A system with a FCC (100) crystal-melt interface was equilibrated in a box elongated in the direction normal to the interface, as illustrated in Fig. 1. Periodic boundary conditions were applied in the parallel directions. Particles at the two ends of the box were coupled to a "heat bath" at a selected temperature T_0 by means of random and dissipative forces[13]. Crystal growth was observed when T_0 was reduced below T_m; the interface advanced into the supercooled liquid. New particles with coordinates appropriate for a liquid were supplied at the lower end of the box at a rate that was adjusted to keep the interface roughly in the center of the box. Crystalline material extruded from the top was removed.

The measured growth rates are illustrated by the circles in Fig. 2. The interface velocity is plotted *vs.* the temperature T in the center. T is always higher than T_0 because of the latent heat released during crystallization. Dimensionless units for temperature and velocity are given[14]. The maximum velocity corresponds to ≈ 80 m/s for argon. The most surprising aspect of these data is the rapid crystallization at low temperatures. Most materials for which reliable data is available exhibit sharply reduced rates at low temperatures, as expected for an activated process[15]. That is, they can be described as the product of an Arrhenius factor $F(T)$ and a term that accounts for the net production of crystalline material resulting from microscopic crystallization and melting events,

$$R = F(T)[1-\exp(-\Delta\mu/kT)]. \qquad (1)$$

Here $F(T)$ has the dimensions of velocity and represents the rate at which the interface would move if all transitions from liquid to crystal were permanent. The

reverse transition from crystal to liquid is represented by the term $\exp(-\Delta\mu/kT)$, where $\Delta\mu$ is the difference in chemical potential between the liquid and the crystal. Near T_m it can be approximated by the expression

$$\Delta\mu = \Delta S(T_m - T), \tag{2}$$

where ΔS is the entropy of fusion. The Arrhenius factor is often represented by an expression of the type[16]

$$F(T) = Daf_0/\Lambda^2, \tag{3}$$

where D is the diffusion coefficient in the liquid and Λ is the mean free path. It is assumed that atoms in the adjacent liquid of thickness a impinge on the crystal surface at a rate proportional to D/Λ^2. A site factor $f_0 < 1$ is included to account for the fact that some of these collisions do not contribute to crystal growth, either because they are not sufficiently close to a lattice site or because the region neighboring the site is relatively disordered. The low entropy of fusion $\Delta S = 1.62$[17] insures that the surface is above the roughening transition temperature[6] and therefore the growth sites are not limited by a lateral growth mechanism such as two-dimensional nucleation or spiral growth. The diffusion coefficient in the liquid usually has an Arrhenius form $D = D^0\exp(-Q/kT)$, where D^0 and Q are independent of temperature. This equation describes the supercooled LJ liquid over the range from T_m down to $0.4T_m$ where the high viscosity prevents accurate measurements[17]. The driving force $\Delta\mu$ can be calculated accurately even at large undercoolings (unlike eq. (2)) using thermodynamic data from the bulk crystal and the supercooled liquid[17].

The solid curve in Fig. 2 is a plot of eqs. (1) and (3) with the appropriate values of $\Delta\mu$ and D. The supercooled LJ liquid becomes highly viscous at low temperatures; the glass transition occurs at $T \approx 0.25$[17,18], whereas the measured interface velocities in this region are quite large. Crystallization is apparently not limited by an activated process. Even a very small activation barrier would reduce the

growth rate significantly at low temperatures. Turnbull and Bagley[19] had argued earlier that crystallization of simple melts should not be limited by the liquid diffusion rate, since movement across the interface is less impeded by "backscattering".

The large atomic mobility in the interface is apparently the result of a density deficit in this region. Interface densities intermediate between the two bulk phases are observed at the melting point[7-10]. There is no indication of voids, and the diffusivity of the interfacial atoms is approximately equal to that of the bulk liquid. However, as the temperature of the interface is reduced below T_m, the density of the interface region drops, and at T =0.15 it is 5% lower than that of the fluid phase[3]. Thus, the amount of free volume available for atomic motion increases at low temperatures. This extra free volume could be caused by the large viscosity of the liquid phase. At the large growth rates observed, there is little time for the liquid to relax, and hence the misfit between the liquid and the crystal is increased. En hanced diffusion of atoms at the interface between two solid phases is commonly observed in experiments on grain boundary diffusion[20].

In the absence of a potential energy barrier the rate at which liquid atoms in the interface could move to lattice sites is determined by the average thermal velocity, $(3kT/m)^{1/2}$. If they travel a distance λ, the interface velocity is

$$R = (a/\lambda)(3kT/m)^{1/2} f_0[1-\exp(-\Delta\mu/kT)]. \qquad (4)$$

The dashed curve in Fig. 2 has been plotted with λ=0.4a, the average distance from the center of points uniformly distributed in a sphere, and f_0=0.27. This expression is in good agreement with the data over the full range of T, and has no activation energy whatsoever. Apparently the atoms in the liquid can rearrange into a crystal lattice along a path in configuration space that involves a monotonic reduction in potential energy.

This unexpected conclusion applies only to simple atoms and molecules. The crystallization of ordered alloys would involve the diffusion of atoms to the correct

sublattice sites, and may involve an activated process. Similarly, the crystallization of most molecular crystals requires a reorientation of the molecules, and would also be inhibited at low temperatures. Often measurements of crystallization rates at large undercoolings are consistent with eqs. (1) and (3), although the apparent activation energy for growth may be somewhat smaller than that for diffusion in the bulk liquid[21]. This seems to indicate that the interface contains extra free volume, although not enough to avoid some activated rearrangements of the liquid material.

If eq. (4) is applicable to other materials, approximate values of the maximum growth rates can be obtained by scaling with $(T_m/m)^{1/2}$. Accordingly, we estimate maximum rates of 400 m/s for nickel and 430 m/s for silicon. Interface velocities of 50 m/s have been measured for Ni dendrites growing into a supercooled melt at $0.9T_m$[22]. The complex heat transport is not easily analyzed, but the velocity data of Fig. 2 imply an interface temperature of $0.96T_m$. This is a 70^oC undercooling at the interface, a surprisingly large value for such a simple system. The maximum velocity measured for the crystallization of silicon is only 18 m/s as mentioned earlier, and this indicates that the mobility of interfaces in covalent materials is much smaller.

An increase in the number of lattice defects was noted during the growth of the LJ crystal at low temperatures. The crystalline material formed at $T=0.05$ contained 0.5% vacancies, whereas the equilibrium concentration of vacancies at this temperature is less than 10^{-30}. Twinning was also observed. In every instance this process began as a defect involving a single row of atoms in a partially ordered (100) layer. The atoms were displaced by a distance $a/2$ in a direction parallel to the row. The next layer to crystallize usually contained two adjacent rows displaced, and so on until the entire layer was in the new position and was again in a perfect (100) configuration. Examination of this geometry shows that two (111)

twin planes are formed. Significant reduction of the growth rate was observed while the defective material was in the interface. This contrasts with the usual assumption that defects enhance the rate of growth by providing sources of steps and other growth sites. In this case the intrinsically rough interface is probably not much affected by additional steps or disorder. The strain and reduced bonding in the crystal reduce the difference in free energy between the crystal and the melt, and fewer of the impinging atoms are trapped in the ordered state. More important, perhaps, is the fact that the presence of the twinned material provides alternative sets of sites where the atoms of the liquid can crystallize. Competition between the different sites retards crystallization. Unpublished data for growth on the (111) interface demonstrates this effect. The close packed layers may stack in the FCC abcabca... sequence, or as ababab... to form HCP material. The energy difference between these two lattices is extremely small, and near T_m the crystalline material does not have a regular stacking sequence. The growth rate on this face is only 50% of (100) rate. The initial crystallization of a layer produces domains on the two sets of sites and misfit boundaries between domains. The necessity to eliminate the high-energy misfit boundaries delays the crystallization process.

Ising Model of Impurity Trapping

The regrowth velocities achieved by laser annealing are five or six orders of magnitude larger than those of conventional growth methods. During Czochralski growth the distribution of impurity in a crystal is usually calculated by the Burton, Prim and Slichter theory[22]. The concentration at the interface is obtained from the rate of transport in the fluid, and the corresponding crystal concentration is often determined from the phase diagram.

At high velocities there is much less time for equilibration between the crystal and the melt through the exchange of atoms at the interface. The distribution

coefficient K may deviate from the equilibrium value; K is the ratio of the impurity concentration in the crystal to that in the liquid *at the interface*. Impurities with low equilibrium solubilities in the crystal lattice provide the most dramatic examples of trapping. Bismuth and indium in silicon have equilibrium distribution coefficients $K^e \approx 5\times10^{-4}$; whereas $K \approx 0.3$ at velocities of $5\ m/s$[24]. The high concentrations of these elements are particularly surprising since the energies of the impurity atoms actually increase during crystallization. Simple rate-theory ideas imply that the fraction of these impurities crystallizing would *decrease* as the interface is undercooled, since the probability of a transition to the state with the higher energy becomes smaller at a lower temperature. Instead, K increases by several orders of magnitude.

There are several possible explanations of this result. A diffuse transition region between the crystal and the melt, perhaps hundreds or thousands of Angstroms thick, would certainly enhance the trapping process. As the interface advances, the impurity becomes enmeshed in a viscous medium before its energy rises to the value in the bulk crystal. When the medium starts to become rigid, the impurity is immobilized, and can escape only if a backwards fluctuation in the position of the interface occurs with sufficient amplitude to reach the impurity. The crystallization of the impurity and the creation of the state of high energy occur gradually. The single impurity crystallization event of small probability in the basic rate-theory model is replaced by a series of partial crystallization events with probabilities that are slightly smaller that those of the host atoms. Therefore, at high undercoolings when crystallization is much more likely than melting, the impurities and host atoms condense at nearly the same rate, and impurities should be incorporated at approximately the liquid concentration.

Trapping would also be enhanced by the preferential segregation of impurities in the region of the interface between the crystal and the melt. The high concen-

tration of impurities in the region where solidification occurs would increase their probability of crystallization. It should be noted, however, that the impurity concentration at the interface will saturate as the number of impurities in the liquid is increased, and this may occur at relatively low concentrations in the liquid phase.

Finally, local strain in the crystal resulting from atomic size mismatch or from electronic effects could affect trapping. Bismuth has an atomic diameter that is larger than that of silicon. Compressive stress would increase gradually as the impurity becomes buried deeper in the crystal where outward relaxation is not possible. As in the case of the diffuse interface, the atom is immobilized *before* the full energy of the bulk state is approached. Again, the increase in energy is distributed over many crystallization events, and this could be expected to increase the rate of trapping.

Atomic scale models provide an excellent means for testing these different hypotheses. The possibility of a diffuse interfacial region can only be tested with models that permit atomic positions and displacements of a very general nature such as the molecular dynamics systems discussed earlier[7-10]. Trajectories of atoms in layers belonging to the interfacial region indicate an abrupt transition from the crystalline state to that of the fluid. On the crystalline side of the interface, the atoms execute vibrational motion in the immediate neighborhood of lattice sites, whereas on the fluid side the motion is diffusive in nature with little evidence of a preference for lattice positions. In the case of FCC interfaces with LJ potentials, the transition from bulk fluid to bulk crystal appears to occur within a distance of about three atomic diameters. Trajectories of atoms in the (111) layers are shown in Fig. 3[10]. In layer 5, on the crystal side of the interface, the atoms spend most of their time vibrating around lattice sites. Only one diffusion event is recorded during this period. In the next layer, the vibrational amplitude is much larger, but the layer is still highly ordered. Layer 7 appears to have crystalline and

fluid regions coexisting, and layer 8 has little indication of crystalline order. This suggests that the transition of an atom from liquid to crystal is quite sudden and most could be assigned to one state or the other. Further evidence of the sharp change in structure at the interface is given in Fig. 4. Layer-resolved radial distribution functions are shown, where r is the projection onto the plane of the interface of the distance between two particles in the layer. Layer 5 shows a split second peak characteristic of the crystal, whereas this feature is totally absent in layer 7. Measurements of local diffusion coefficients also indicate that the interfacial region is of a similar thickness. On the other hand, interface density profiles exhibit oscillations in density that persist for a large distance into the liquid for the FCC (111) and (100) orientations, and suggest rather diffuse interfaces for these two cases, but not in the case of the (110) face. The data illustrated in Fig. 5 clearly shows that the density oscillations on the liquid side are not accompanied by significant variations in the potential energy, and therefore should have little effect on the properties of the liquid in this region. The FCC (111) and (100) layer spacings correspond closely to the peak in the liquid structure factor, and the magnitude of this peak indicates a large susceptibility to potential oscillations of this wavelength. Figs. 5 and 6 show both the density profile and the average potential energy of atoms in the (111) and (110) interfaces, respectively. We can conclude that the effective interface is quite sharp for most processes that are dependent on atomic mobility. The LJ potential is most appropriate for the noble gases, although similar results are expected for simple metals and other systems whose structures are are determined primarily by the packing of spheres. This potential is not appropriate for silicon, but the entropy of fusion is 50% lower than that of silicon and this should produce, if anything, a more diffuse interface in the LJ system. We can essentially exclude the diffuse interface idea for explaining the trapping of impurities.

A plot of the Ising model data for the distribution coefficient of bismuth is shown in Fig. 7[5]. Here $\Delta\mu$ is given by eq. (2), and ΔS =3.24 for the host species. The lower curve is the result of the simple Ising model, with no preferred bonding of the impurity at the interface and no delay in the potential energy rise corresponding to strain. In this case, a small increase is observed with $\Delta\mu$, and this is an improvement over the simple rate theory, but does not match the large increase observed in the experiments.

The upper curve was obtained with the effects of segregation and strain included. The large change in K occurs at a small undercooling; it increases by two orders of magnitude over a small $\Delta\mu$ region, and then appears to saturate (note the logarithmic scale for K). This is consistent with the experiments. Variations in K with crystallographic orientation have been observed, with the largest K values on the (111) interface[24]. This result is also obtained from the Ising model calculations, and is a consequence of the slower (111) kinetics during crystal growth. The primary rate limiting factor during regrowth of the molten layer is the conduction of latent heat away from the growing interface. This means that the velocity is determined primarily by the thermal conditions, and that the (111) face must fall back to a cooler region with a correspondingly larger $\Delta\mu$ in order to maintain this velocity. As clearly seen in Fig. 7, the larger $\Delta\mu$ will always produce a larger value of K.

Conclusions

Molecular dynamics calculations of solidification have shown that simple atomic systems can crystallize at very high rates which are limited only by the thermal motion of the atoms. The interface between the crystal and the glass can move at extremely low temperatures, and the glassy state is unstable when placed in contact with the crystal. Rapid growth at low temperatures produces a high concentration of vacancies an an occasional twin plane when growth occurs on the

(100) face. Growth on the (111) is significantly slower, and does not produce a consistent lattice structure because of the extremely high probability for twinning. ,PP The two factors that have the greatest influence on the trapping of impurities with low equilibrium distribution coefficients are interface segregation and atomic strain. With these factors included in the Ising model of the diamond cubic lattice, the calculations are in good agreement with laser annealing experiments on silicon.

References

(1) *Laser-Solid Interactions and Transient Thermal Processing of Materials*, J. Narayan, W. L. Brown and R. A. Lemons, Eds. (North-Holland, Amsterdam, 1983)

(2) A. G. Cullis, *ibid*, p. 75.

(3) J. Q. Broughton, G. H. Gilmer and K. A. Jackson, Phys. Rev. Lett. **49**, 1496, (1982).

(4) G. H. Gilmer and K. A. Jackson, in: "Crystal Growth and Materials", E. Kaldis and H. J. Scheel, eds. (North-Holland, Amsterdam, 1977), p. 79.

(5) G. H. Gilmer, Ref. 1, p. 249.

(6) Reviews of crystal growth kinetics and surface structures based on the Ising model: J. P. van der Eerden, P. Bennema, and T. A. Cherepanova, in: "Progress in Crystal Growth and Characterization", B. R. Pamplin, ed. (Pergamon, Oxford, 1979) vol. 3, p. 219; J. D. Weeks and G. H. Gilmer, Adv. Chem. Phys. **40**, 157 (1979).

(7) Y. Hiwatari, E. Stoll and T. Schneider, J. Chem. Phys. **68**, 3401 (1978).

(8) J. N. Cape and L. V. Woodcock, J. Chem Phys. **73**, 2420 (1980).

(9) J. Q. Broughton, A. Bonissent and F. F. Abraham, J. Chem. Phys. **74**, 4029 (1981).

(10) J. Q. Broughton and G. H. Gilmer, submitted to J. Chem. Phys.

(11) U. Landman, C. L. Cleveland and C. S. Brown, Phys. Rev. Lett. **45**, 2032 (1980).

(12) C. L. Cleveland, U. Landman and R. N. Barnett, Phys. Rev. Lett. **49**, 790 (1982).

(13) J. C. Tully, G. H. Gilmer and M. Shugard, J. Chem. Phys. **71**, 1630 (1979).

(14) All units are related to the well depth ϵ and length σ in the LJ potential ϕ,

$$\phi = 4\epsilon[(\sigma/r)^{12} - (\sigma/r)^{6}],$$

where r is the distance between particles.

(15) P. J. Vergano and D. R. Uhlmann, in: "Reactivity of Solids", J. W. Mitchell, ed. (Wiley, New York, 1969).

(16) J. Frenkel, Phys. Z. Sowjetunion **1**, 498 (1932).

(17) J. Q. Broughton and G. H. Gilmer, J. Chem. Phys. **79**, 5095 (1983).

(18) W. D. Kristensen, J. Non-Cryst. Solids **21**, 303 (1976).

(19) D. Turnbull and B. G. Bagley, in: "Treatise on Solid State Chemistry", N. B. Hannay, ed. (Plenum, New York, 1975), vol. 5, p. 526.

(20) F. J. A. den Broeder, Acta. Metall. **20**, 319 (1972).

(21) J. H. Magill and H.-M. Li, J. Crystal Growth **20**, 135 (1973). J. H. Magill and D. J. Plazek, J. Chem. Phys. **46**, 3757 (1967).

(22) G. A. Colligan and B. J. Bayles, Acta. Metall. **10**, 895 (1962).

(23) J. A. Burton, R. C. Prim and W. P. Slichter, J. Chem. Phys. **21**, 1987 (1953)

(24) P. Baeri, G. Foti, J. M. Poate, S. U. Campisano and A. G. Cullis, Appl. Phys. Lett. **38**, 800 (1981).

Figure Captions

Fig. 1. Schematic diagram of a cross-section of the three-dimensional crystallization system employed in the simulations.

Fig. 2. Molecular dynamics data (open circles) for the velocity of the crystal-melt interface *vs.* interface temperature. The solid curve corresponds to eqs. (1) and (3), and the dashed curve to eq. (4).

Fig. 3. Trajectories of atoms in successive layers in the LJ crystal-melt interface, as projected onto a plane parallel to the interface.

Fig. 4. Two-dimensional radial distribution functions $g_L(r)$ in layers of the (111) interface.

Fig. 5. Density profile and potential energy per particle for the (111) interface. Vertical lines indicate the bulk crystal layer positions.

Fig. 6. Density profile and potential energy per particle for the (110) interface.

Fig. 7. Distribution coefficient *vs.* $\Delta\mu/kT$ as obtained from an Ising model of the diamond cubic lattice. The hexagons indicate the results for the simple Ising model, whereas the squares and triangles represent the (100) and (111) faces, respectively, with interface potential energy functions corresponding to segregation and stress

Figure 1

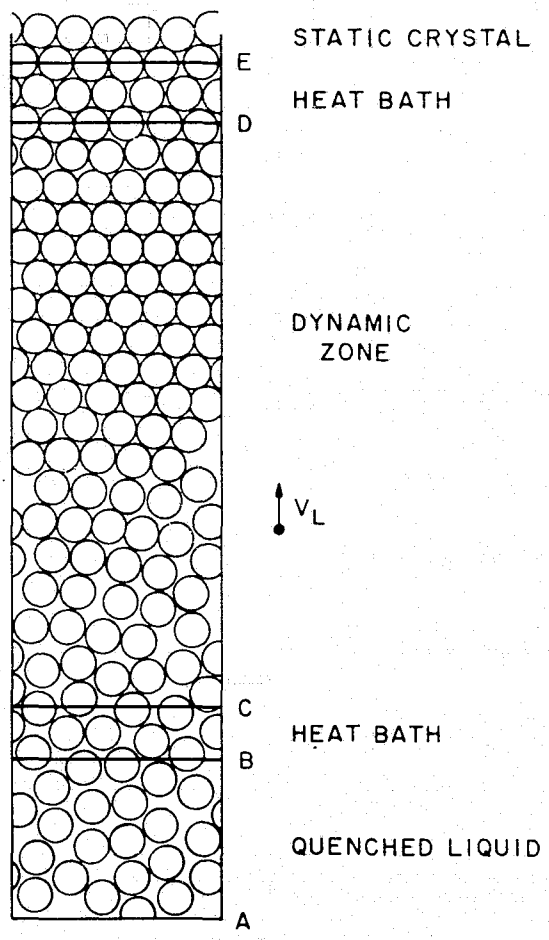

Figure 2

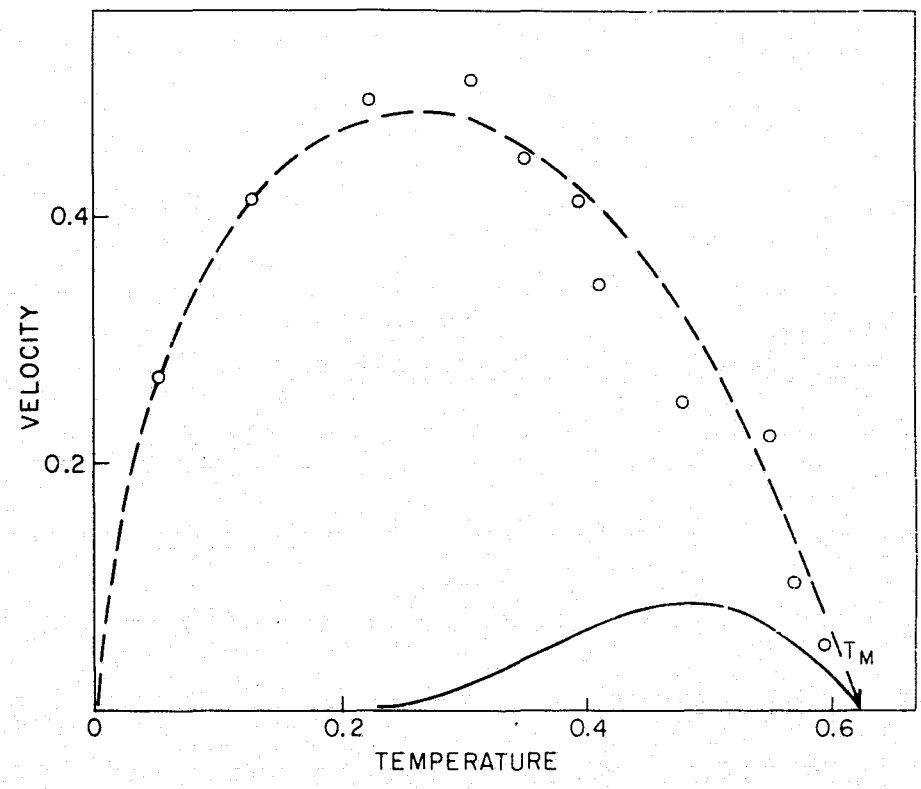

Figure 3

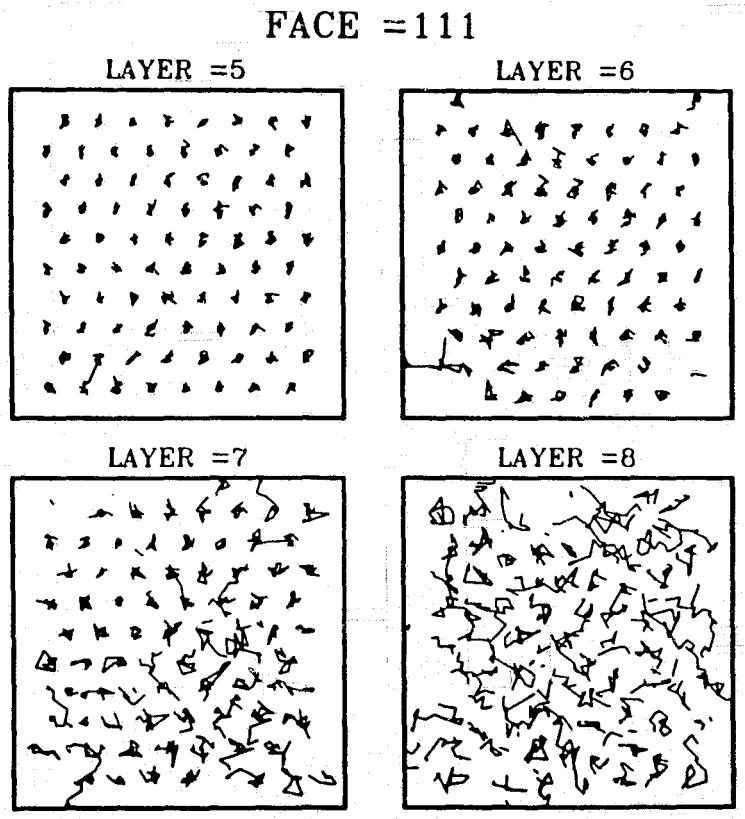

Figure 4

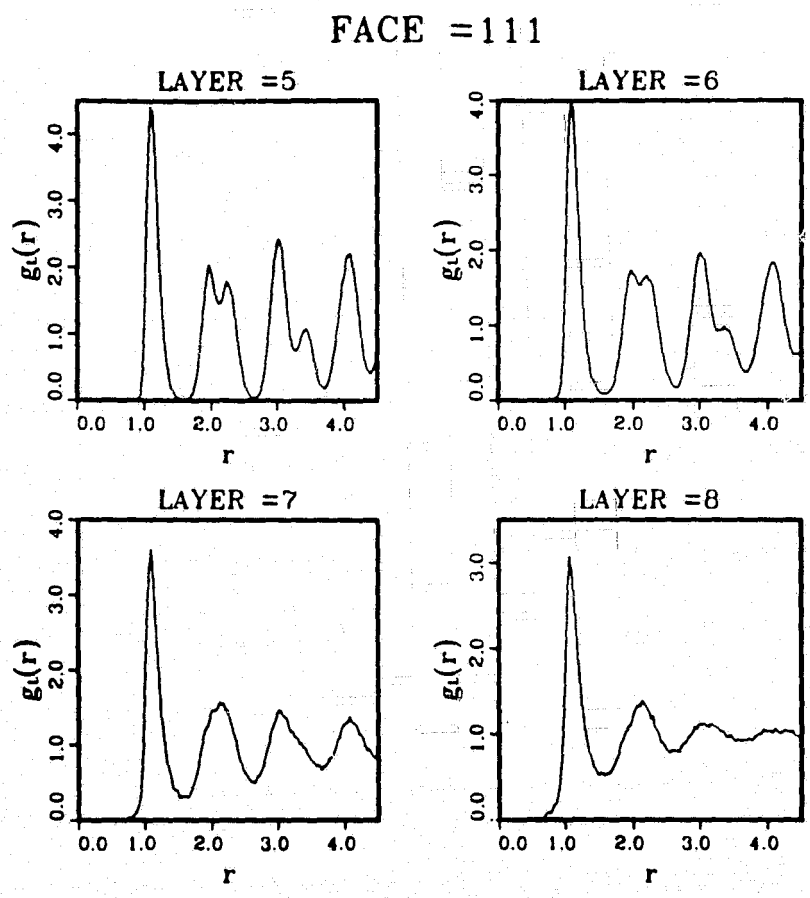

Figure 5

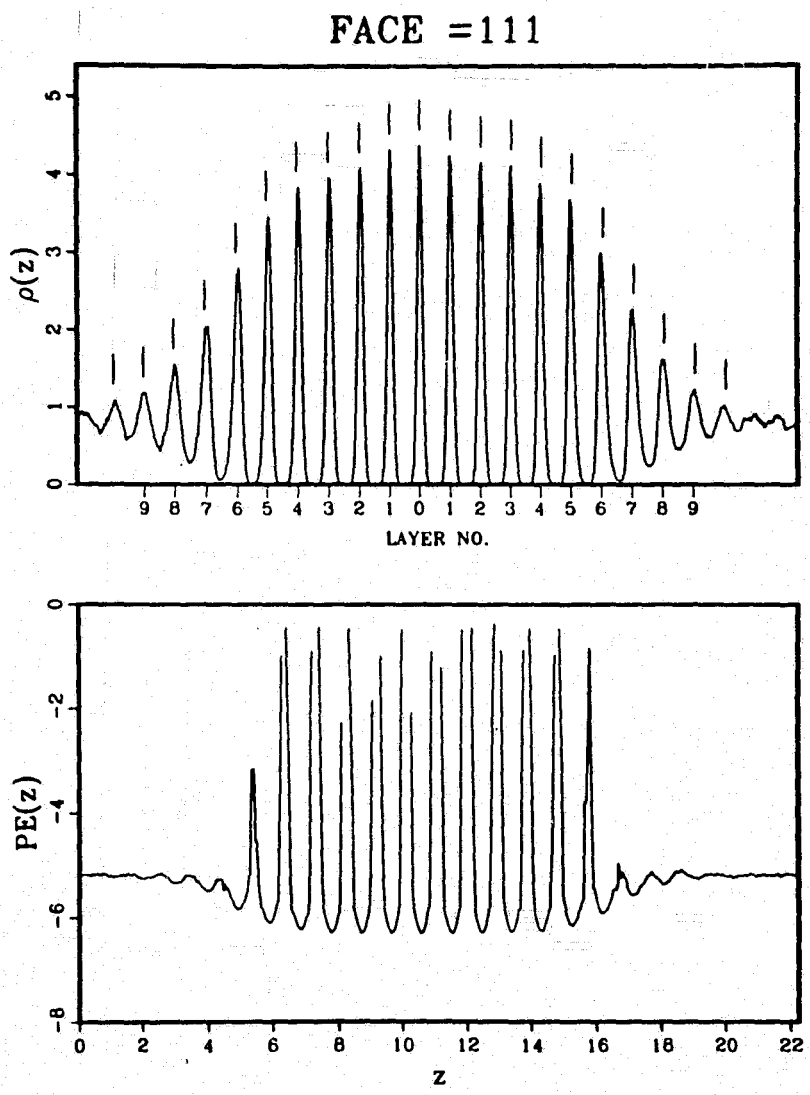

Figure 6

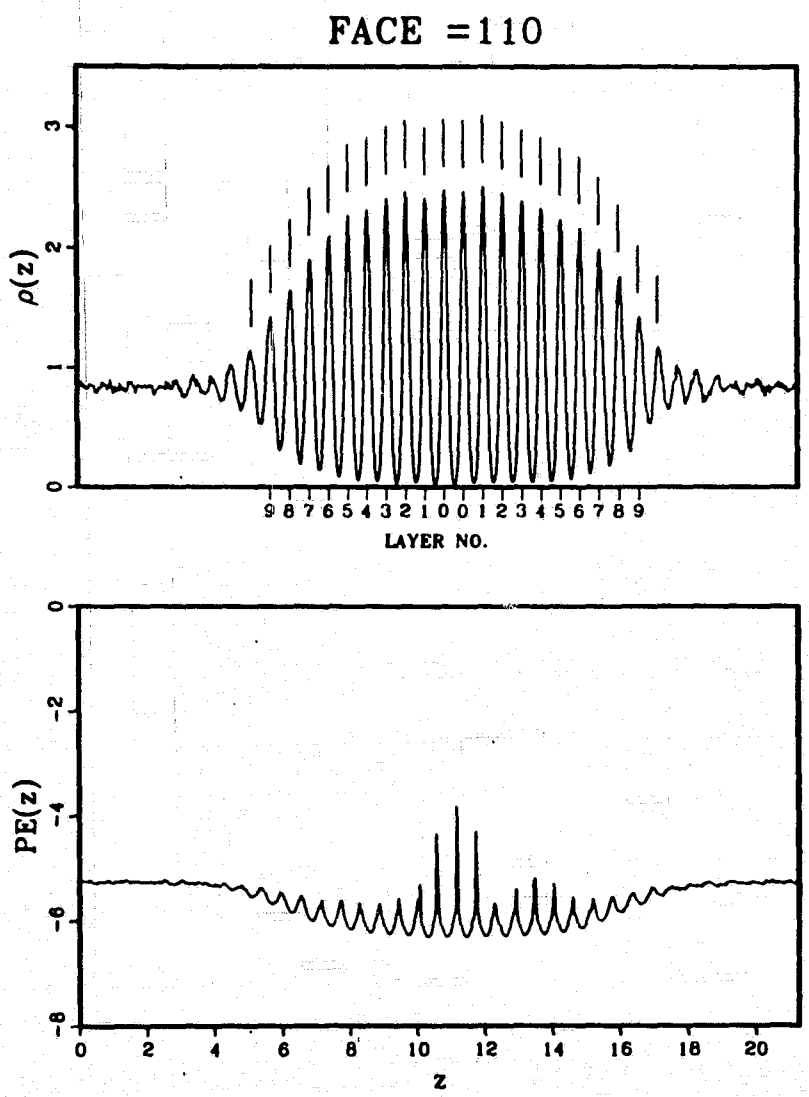

Figure 7

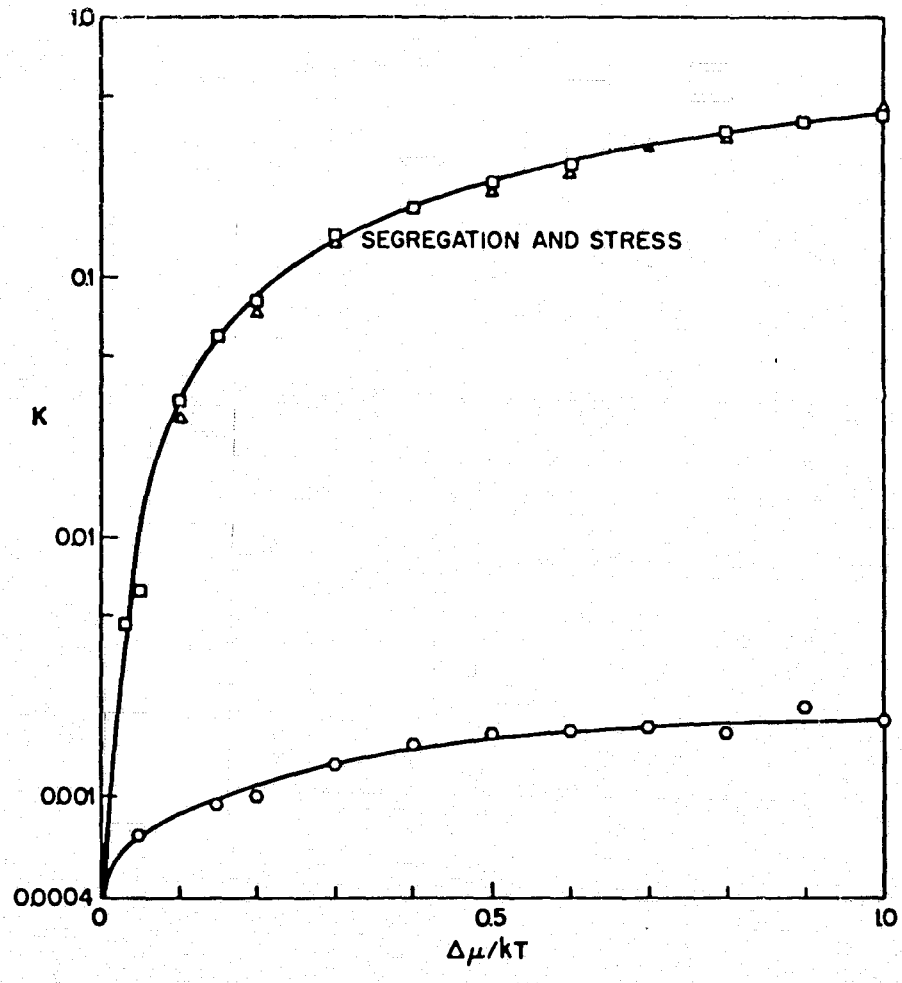

DISCUSSION

GLICKSMAN: You mentioned some comparative work between material like silicon and some of the Leonard-Joner material. I wondered whether one has to correct for the fact that there is a considerable electronic component in the latent heat of these diamond cubic materials like silicon. Perhaps a good deal of that latent heat is superfluous, since it is just carried by the band structures of the electrons responding to the surrounding structure.

GILMER: Yes. I think what that is going to do is make the potential energy variation through the interface more gradual, and I don't know any way of getting quantitative numbers on what that variation is. I do think that the structural change through the interface is quite sharp. I don't think that is going to be determined by this band structure calculation. This is more of a long-range effect and the structure is determined more by the covalent bonding than by the local ordering.

GLICKSMAN: Part of the latent heat in the case of the diamond cubic materials has been ascribed to a profound electronic change, with the silicon essentially being a metal and the other being a semiconductor. For isostructural types with similar bonding, they find that you can almost consider that to be a kind of electronic component. Should that be included or should that be subtracted out in terms of the way you assign the bonding energies which are in fact proportional to a latent heat?

GILMER: I think that should be subtracted out. In other words, the effective latent heat in determining interfacial roughness should be the short-range interactions.

MILSTEIN: You mentioned that you had done an analysis that suggested that even at 0.2 relative temperature, you were seeing glass going to crystalline solid. What material did that refer to?

GILMER: The closest material to the Leonard-Jones system is the noble gases. Probably quite applicable also are the metallic systems and any system that has more or less a spherically symmetrical potential and a hard core.

MILSTEIN: If that is the circumstance, I think Marty's [Glicksman] comment might apply equally well if you are dealing with a normal system where the solid is more dense than the liquid. If you look at the interface, the atoms ought to be farther apart in the supercooled liquid than they are in the solid, and therefore there is room for them to rattle around. Whereas, when you talk about a material like silicon that goes the other way in density, that's going to be a very tough thing to have happen.

GILMER: That is not a problem in this model because the two ends of the boxes in the model were adjusted to maintain constant pressure throughout the system. Therefore, if there is a density change upon crystallization, the top layer of the crystal actually moves down and fills in that excess

volume that is created as you go to the more dense phase. What we were trying to do was model something that was open to the atmosphere, that would not have any strain developing because of the volume change. But there does appear to be some extra free volume in that interfacial region. I actually do a measurement in which I have measured the number of atoms in the layers of the crystal and going down into the liquid, and the one that was closest to the transition region of the interface actually had about a 5% lower volume than either the bulk liquid or the crystal. So there does seem to be a density deficit in that region. You don't see a density deficit at the melting point, but this is at low temperatures and I think what is happening is that you have this huge growth rate, and you have this rigid glassy material coming up against the crystal, and it just does not have time to fill in all the holes and intimately wet the crystal surface. So it is partly the high growth rate that prevents it from filling in, I think. It looks like the {111} is actually going to slow down at low temperatures.

SEKERKA: Could you tell me more about what happens in heat-bath regions in your simulation?

GILMER: The particles in this region are subjected to external forces that are random and dissipative in nature. It is a Langevin-type system. The ratio of the random to dissipative force determines the temperature. Since they are fairly strongly coupled in those two regions, we can clamp the temperature fairly close to the number that we set. What we wanted to do is to get the motion of the interface to be able to take care of the latent heat. In such a small system, only about 10 atomic layers away from the interface, we have this heat bath where we can do that very effectively and get these high velocities. In an experimental system, of course, all that is going to happen is that when this thing starts growing, it is going to heat up very high, close to the melting point, and continue to propagate. In this system we wanted to include the low-temperature behavior also, and that was the reason for clamps. They are in effect coupled to an external heat bath.

SEKERKA: You showed temperature versus height, and I don't know what those units are, and where is 10, and why is the temperature maximum there?

GILMER: Ten is where the interface is releasing its latent heat.

SEKERKA: Aren't you making the layer B-C hot and D-E cold?

GILMER: No. This is a different type of temperature profile. In fact, it is unstable. If the interface starts to move out of the box we can always push in more liquid in order to keep it at the center.

SEKERKA: You are growing a supercooled liquid?

GILMER: That is right.

ABBASCHIAN: Your models imply that you really don't have a sharp transition from faceted growth to a continuous growth. Is that correct?

GILMER: That is correct. There is no sharp kinetic transition predicted between a faceted growth and a continuous growth. The transition occurs as a function of temperature. In none of the models that we have studied do we see this faceted-to-continuous transition as a function of kinetics. That is a continuous transition. As you increase the undercooling, you get more clusters, but that goes up in a continuous fashion. You don't see any break in the growth-rate curve or anything of this type.

ABBASCHIAN: Do you consider clusters in the supercooled liquid?

GILMER: This is a very basic model in the sense that the only thing I am assuming is an interaction; I solved Newton's equations, and whatever happens, happens. If there is clustering going on in the liquid, then it is in my model.

WILCOX: You mentioned that for a typical Czochralski growth of silicon you have a supercooling of 2°C from your model. Do you know of any experimental confirmation of that?

GILMER: No. There have been some heat-conduction calculations of the supercooling of the (111) face during Czochralski growth, but I have based that purely on calculations, not on any measurements.

N84 28624 D10

THE EFFECT OF GROWTH RATE ON INTERFACE MORPHOLOGY

R. Trivedi and K. Somboonsuk
Ames Laboratory, USDOE and Department of
Materials Science and Engineering
Iowa State University, Ames, IA 50011

Abstract

Since significantly different solidification structures of a given alloy can be obtained by varying experimental growth rates, it is desirable to understand the basic factors which control the formation and stability of these microstructures as growth conditions are altered. Directional solidification experiments are described in this paper and the results obtained in metallic and transparent organic systems are presented. Emphasis will be placed on the characteristics of dendritic structures obtained under different solidification conditions. Specifically, the effect of the growth rate on the primary dendrite spacing, the secondary dendrite spacing and the dendrite tip radius is discussed. It is shown that significant changes in the primary spacing is observed when a dendrite to cellular transition takes place at lower velocities. It is found that the primary cellular spacing is much smaller than the primary dendrite spacing so that a maximum in the primary spacing occurs as a function of velocity at the dendrite-cellular transition. A theoretical model is also described which quantitatively explains various microstructural features of dendritic and cellular structures.

1. Introduction

Crystal growth studies are generally carried out under controlled solidification conditions, and the characteristics of crystals grown under such conditions are governed by the alloy or impurity composition (C_∞), the growth velocity (V) and the temperature gradient at the interface (G). In order to separate the effect of each of these variables, controlled solidification studies have been carried out on alloys of different compositions, and these studies have enabled us to obtain a greater insight into the characteristics of crystals. Through such studies, it has become possible to understand the conditions under which a planar interface becomes unstable and under which planar to cellular to dendritic structural transitions occur [1]. Most of these controlled solidification studies have been carried out for metallic systems or for organic systems with low entropies of fusion. We shall describe these results so as to obtain a broader perspective of our

current understanding of the solidification phenomena. Specific attention will be directed toward understanding the microstructural characteristics of cellular and dendritic interfaces.

2. Directional solidification studies

In directional solidification experiments, both the growth rate and the temperature gradient in liquid may be independently controlled so that one can study the crystal growth characteristics as a function of either the temperature gradient (at constant growth rate) or the velocity (at constant temperature gradient). The experimental set-up consists of a heating furnace and a water-cooled chamber which are separated by an insulating material. The temperature gradient is controlled by controlling the temperature of the furnace. The alloy, which is placed in a tube, is then allowed to solidify at a constant rate by moving the thermal assembly at a constant rate. After the steady-state growth is established, the alloy is solidified for a short time and quenched [2, 3]. The interface characteristics and solute redistribution are then studied. A similar, although a much simpler, system can be designed to study in situ the directional solidification of transparent materials [4]. A schematic diagram of such a system is illustrated in Fig. 1.

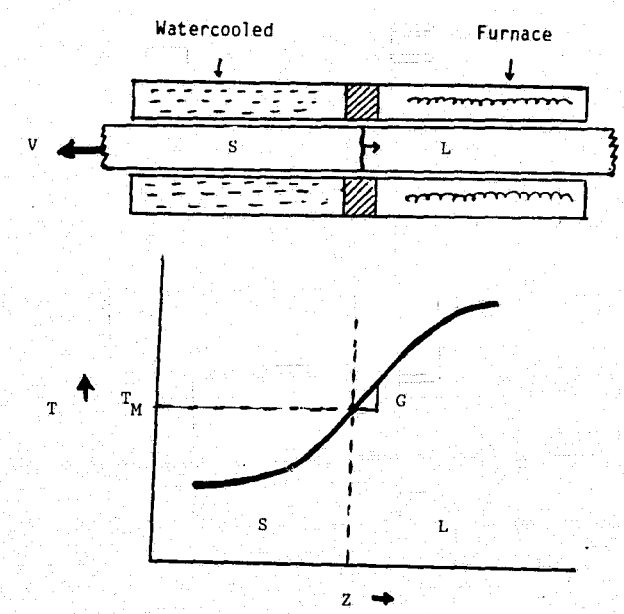

Fig. 1. A schematic illustration of the directional solidification system.

Let us first examine some of the major concepts provided by the directional solidification studies. Initially, the nature of the solid-liquid interface for a given alloy composition and for a fixed temperature gradient is examined. Figure 2 shows that effect of the increasing growth rate on the shape of the solid-liquid interface for succinonitrile- 4 wt% acetone solution [5]. At very low velocities, a planar interface is observed. However, as the growth rate is increased, the interface becomes unstable and perturbations in the shape begin to appear. If any defects, such as grain boundaries are present, instabilities originate at these defect sites. These instabilities grow with time and readjust themselves until a steady-state interface shape is obtained. Figs. 2a and 2b shows the steady-state cellular interface shapes. If the growth rate is increased further, steady-state dendritic structures are observed, as illustrated in Fig. 3. If the crystal is grown at higher velocities, then the dendrites become finer in size and the spacings between the dendrites become smaller. However, at a sufficiently high speed, the dendritic structure may again become unstable, giving rise to a planar interface.

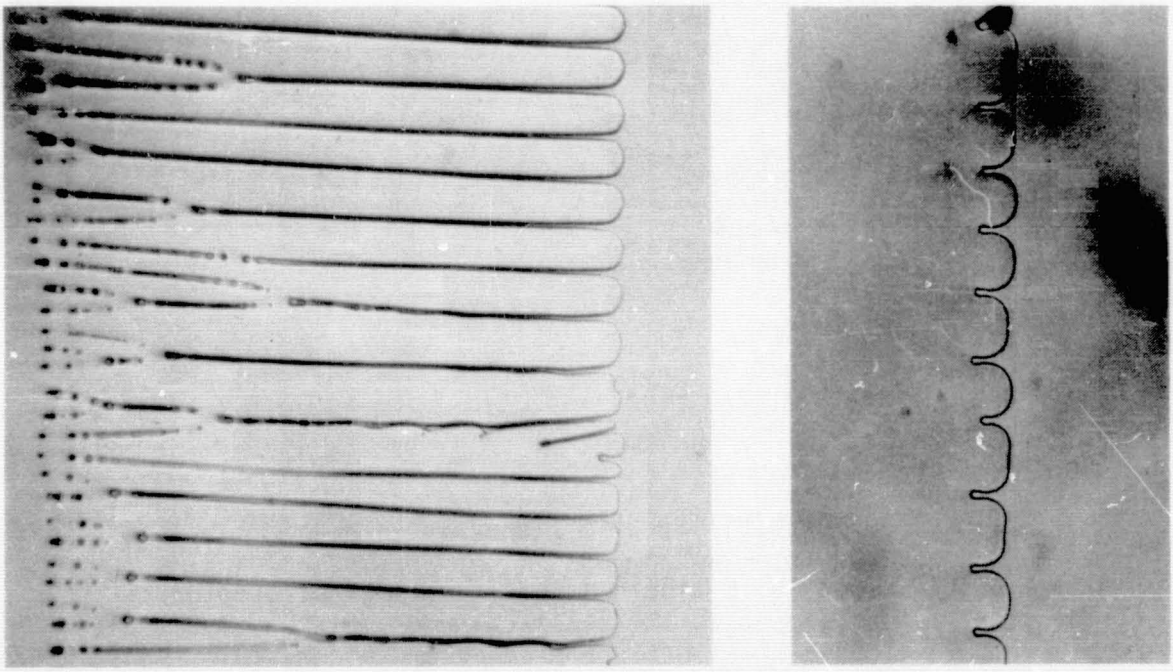

(a) (b)

Fig. 2. Steady-state interface structures in the succinonitrile-4 wt% acetone system obtained under the directional solidification conditions of G=67 K/cm and (a) V=0.40 μm/sec (b) V=0.68 μm/sec. From reference (5).

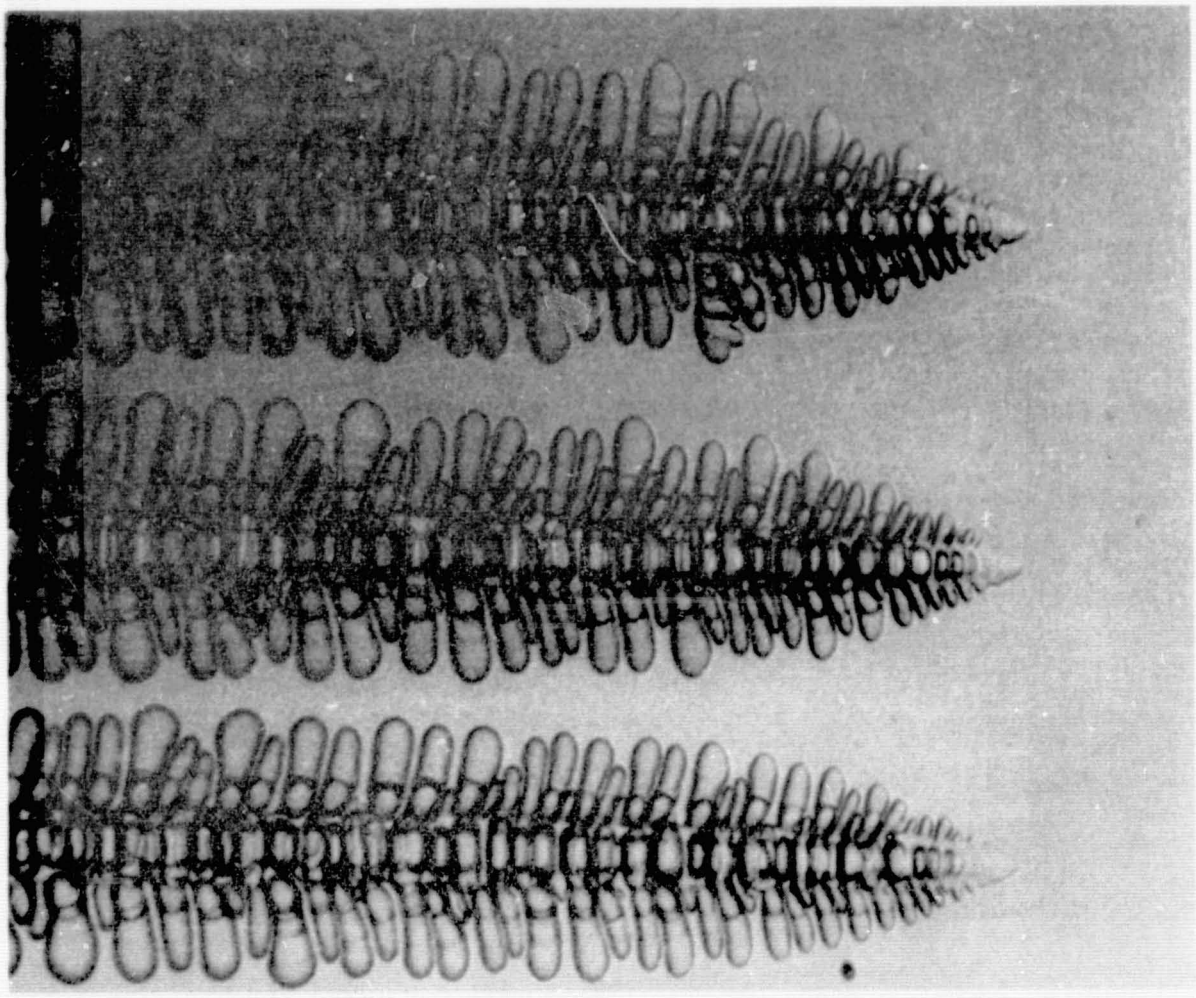

Fig. 3. Steady-state dendritic interface structure in the succinonitrile-4 wt% acetone system. Directional solidification conditions were G=67 K/cm and V=6.7 μm/sec.

3. Stability of a planar interface

The stability of solid-liquid interface was first studied by Tiller et al. [6]. They used the simple argument that a planar interface, if it develops a small protuberence, would be unstable and the protrusion would grow faster than the planar elements of the interface if the liquid region ahead of the interface had a greater degree of supercooling than the liquid region at the interface. Thus, a crystal surface in a pure undercooled melt would always be unstable, whereas an interface moving at a constant velocity in an alloy system with a positive temperature gradient in the liquid would be unstable only when

$$V > G_L D / \Delta T_0 \qquad (1)$$

where G_L is the temperature gradient in liquid at the interface, D the solute diffusion coefficient in liquid and ΔT_0 the equilibrium freezing range of the alloy. Tiller [7] subsequently pointed out that

the stability of the interface should also depend upon the temperature gradient in the solid. He modified equation (1) to the form

$$V > GD/\Delta T_0 \qquad (2)$$

where G is the average temperature gradient in liquid whose value was suggested as $G = (K_L G_L + K_S G_S)/(K_L + K_S)$, where K_L and K_S are thermal conductivities of liquid and solid, respectively.

The major shortcomings of the above treatments are that they do not include the effects of solid-liquid interface energy and interface attachment kinetics. Both these effects would tend to stabilize a planar interface to a greater growth rate value. A more rigorous interface stability analysis which included the effect of an isotropic interface energy was developed by Mullins and Sekerka [8]. They carried out the stability analysis by perturbing a planar interface with a sinusoidal profile and then determining the condition under which the amplitude of perturbation would grow with time. When solute effects are significant, they found that the contribution from the interface free energy was small, and the interface would be unstable when

$$V > GD/\Delta T_0 S \qquad (3)$$

where S is a stability parameter whose values are typically between 0.7 to 0.9 under normal solidification conditions [1]. This result shows that the surface energy tended to stabilize the interface to slightly higher growth rates than those predicted by the modified constitutional supercooling criteria, given by equation (2).

The results of the stability analysis developed by Mullins and Sekerka also show that surface energy effects will be very important for two cases, one in which the growth rates are very high, and the other in which the solute content is very small. They found that a planar interface would always be stable at very high growth rates, i.e., when

$$V > (D\,\Delta T_0\,\Delta S/k\,\gamma) \qquad (4a)$$

or

$$(\gamma/\Delta S\,\Delta T_0) > (D/Vk) \qquad (4b)$$

where γ is the interfacial energy, k the equilibrium solute partitioning function and ΔS the entropy of fusion per unit volume. Equation (4b) shows that a planar interface would be stable when the effective capillarity distance is greater than the effective diffusion length, so that the capillarity effect completely dominates the solute effect.

Another important result can be obtained from the analysis of Mullins and Sekerka when the solute content is quite small. In such a case, a stabilizing force due to a solute build-up will be small and the stability of an interface will be controlled by surface energy effects. The effect of the surface energy will be significant when the wavelength of perturbation is small. However, for larger wavelengths, the surface energy effect would be small and interface would become unstable. Thus, a critical wavelength exists where the interface just

becomes unstable. The value of this critical wavelength, λ^*, can be expressed as [9, 10]

$$V\lambda^{*2} = \text{constant} \tag{5}$$

where the value of the constant depends on the system parameters only. Thus, as the growth rate is increased, smaller wavelength perturbations begin to become unstable.

4. Cellular and dendritic growth

When the growth rate of the interface is increased above the critical velocity for the planar interface breakdown, the interface assumes a periodic profile of small wavelengths. However, this periodic profile coarsens with time, such that the spacing between the perturbations increases until a steady-state spacing is established, Fig. 4. After the initial transient, the interface assumes a cellular or dendritic shape which does not alter with time. These steady-state structures are generally characterized by the primary spacing, λ_1, and the radius of curvature, ρ, of the advancing front. In case of dendritic structures, an instability at the side of the dendrite occurs whose periodicity is characterized by the initial secondary dendrite arm spacing, λ_2.

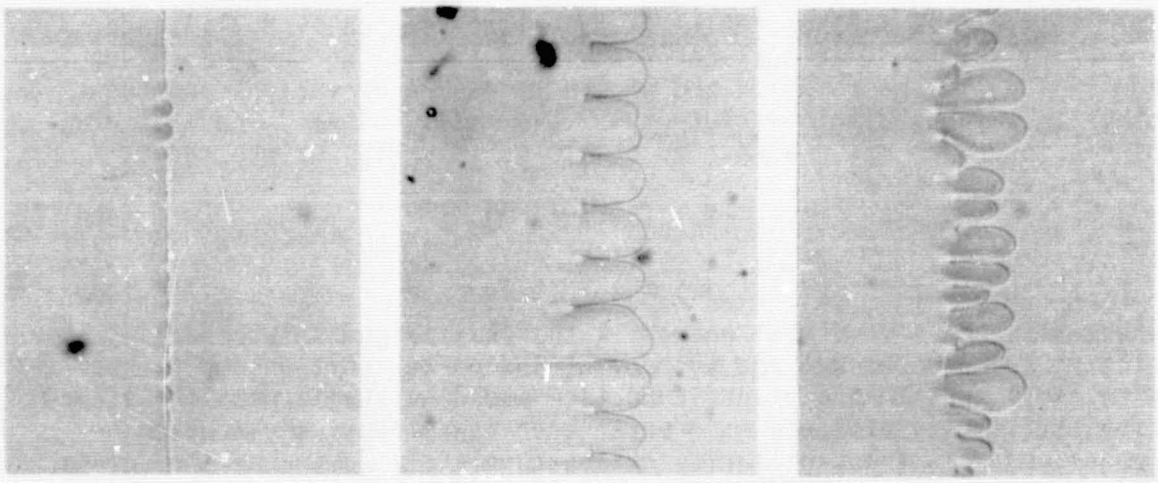

(a) (b) (c)

Fig. 4. The breakdown of a planar interface and the establishment of the steady-state profile in directionally solidified succinonitrile-4 wt% acetone. G=67 K/cm, V=0.50 μm/sec. (a) t=36 min, (b) t=40 min, (c) t=148 min.

A detailed experimental study of λ_1, λ_2 and ρ have been carried out in succinonitile-4 wt% acetone solution by Somboonsuk, Mason and Trivedi [4], and their results are shown in Fig. 5. A number of interesting features are observed. (1) The primary spacing goes through a maximum as the growth rate is increased. (2) The maximum in the primary spacing is correlated with the cellular to dendritic transition velocity. (3) The decrease in λ_1 at low velocity is related to the sharp increase in the tip radius. (4) The secondary dendrite spacing near the tip region is proportional to the radius of dendrite tip. In fact, λ_2/ρ is found to be a constant equal to 2.2 ± 0.3, as shown in Fig. 6. Such a scaling law is found to be true even when the temperature gradient and the composition are altered. The existence of such a scaling law was first hypothesized by Sharp and Hellawell [11] who reported $\lambda_2/\rho \simeq 2$ for aluminum dendrite growth in the Cu-Al system. The first detailed experimental study on λ_2/ρ was reported by Huang and Glicksman [12] who found $\lambda_2/\rho = 3.0$ for dendrite growth in undercooled pure succinonitrile liquid. The study by Somboonsuk, Mason and Trivedi [4] shows that the scaling law between λ_2 and ρ also exists in dendritic structures formed during the directional solidification of alloys. Although λ_2 and ρ are closely related in a simple manner, no simple correlation is found between λ_1 and ρ. Fig. 7 shows that λ_1/ρ increases sharply with velocity in the cellular region and the ratio increases only slowly with velocity in the dendritic region.

In order to understand these experimental results it is important to realize that in a controlled solidification experiment, the shape and location of the interface is uniquely established for given experimental conditions. For a pure material the interface should be located at the melting point of the material if interface kinetic effects are neglected. Thus, a planar interface will exist whose location coincides with the melting point isotherm. However, for alloys, the location of the interface is not easy to predict since the interface can exist at any temperature between the solidus and the liquidus temperatures. If growth conditions are such that a planar interface exists, then it is located at the solidus temperature. However, under the growth conditions of a non-planar interface there exists a degree of freedom in the temperature at which the advancing front can locate. Consequently, multiple solutions are possible. We shall now examine the reasons for these multiple solutions and then discuss how the system chooses a specific solution to uniquely characterize the interface under given experimental conditions.

There are two important microstructural parameters, ρ and λ_1, which we would like to predict. These parameters have a dimension of length, so that we may first define appropriate dimensionless parameters that are important in characterizing the microstructure. Since the kinetics of the growth are controlled by solute diffusion, thermal diffusion and interfacial free energy, we may define the characteristic lengths of these processes as follows:

C-3

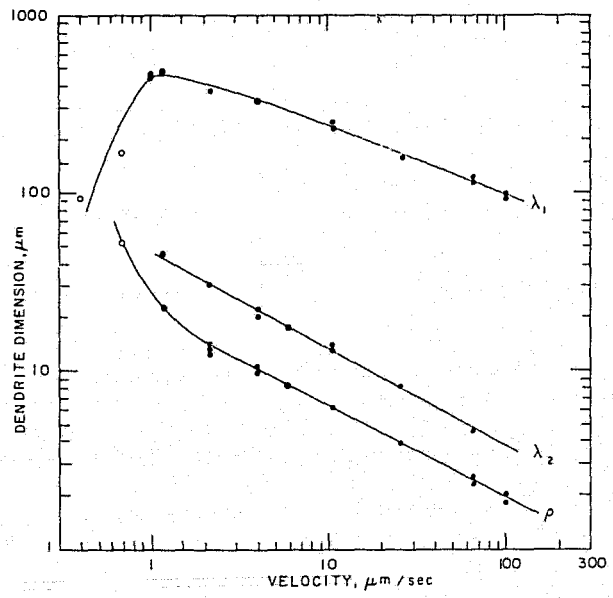

Fig. 5. Variation of λ_1, λ_2 and ρ with growth rate, V, in succinonitrile-4 wt% acetone system. G=67 k/cm. o cells, ● dendrites. From reference (4).

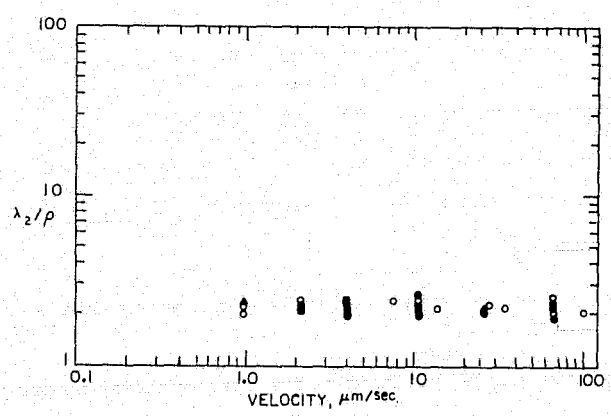

Fig. 6. The variation of λ_2/ρ as a function of velocity. From reference (4)

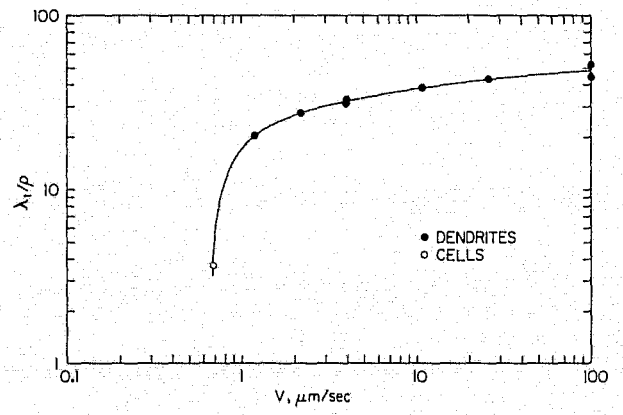

Fig. 7. The variation of λ_1/ρ as a function of velocity. From reference (5)

$$\text{thermal length, } \ell_t = k\,\Delta T_0/G \tag{5a}$$

$$\text{diffusion length, } \ell_s = 2D/V \tag{5b}$$

$$\text{capillary length, } \ell_c = \gamma/\Delta S k\,\Delta T_0 \tag{5c}$$

where G is the weighted average temperature gradient at the interface. Since the characteristics of the interface are determined by the relative effects of these processes, we may define the two dimensionless parameters as:

$$\mathcal{A} = \ell_c/\ell_s = \gamma V/2\,\Delta S\,\Delta k\,\Delta T_0 \tag{6a}$$

$$\mathcal{Y} = \ell_s/\ell_t = 2GD/Vk\,\Delta T_0 \tag{6b}$$

These dimensionless parameters, $\mathcal{A}$ and $\mathcal{Y}$, describe the experimental conditions imposed upon the system. Note that $\mathcal{A}$ is directly proportional to V, whereas $\mathcal{Y}$ is inversely proportional to V. Consequently, the parameter $\mathcal{A}$ will predominate at large V and the parameter $\mathcal{Y}$ will predominate at low velocities.

Our aim is to predict the microstructural features, ρ and λ_1 for given experimental conditions. We may thus define the following two dimensionless parameters to characterize these variables.

$$p = \rho/\ell_s = V\rho/2D \tag{7}$$

and

$$\Lambda = (\lambda_1/\rho)(\lambda_1/\ell_t) = \lambda_1^2 G/\gamma k\,\Delta T_0 \tag{8}$$

Our aim is now to obtain a relationship between p or Λ with the experimental parameters $\mathcal{A}$ and $\mathcal{Y}$.

Recently, Trivedi [5] has shown that the interaction between the neighboring dendrites is weak so that the dendrite tip characteristics can be determined from the model which neglects the interaction between the neighboring dendrites. Once the dendrite tip characteristics are known, the weak interactions between the dendrites will next be considered to obtain the primary dendrite spacing. From the simultaneous solution of solute and thermal diffusion equations, Trivedi [13] has derived the following relationship for the dendrite tip undercooling

$$\Delta T/\Delta T_0 = [\phi k/1-\phi(1-k)]\,[1+\tfrac{1}{2}\mathcal{Y} N_g(p) + (2\mathcal{A}/p^2)f(p)] \tag{9}$$

where $\Delta T = T_M + mc_\infty - T_t$, in which T_M is the melting point of pure solvent, m the slope of the liquidus, c_∞ the initial composition and T_t the tip temperature. ϕ is the Ivantsov function equal to $p\cdot\exp(p)E_1(p)$ and $N_g(p)$ and f(p) are functions of p which are defined in reference (13). Note that the above relationship does not give a unique solution but predicts ρ (or p) as a function of the tip temperature. This result is shown schematically in Fig. 8, which illustrates that tip temperature can vary between the solidus and the liquidus temperature and the tip radius value will depend on the tip temperature assumed by the dendrite. Since the unique tip characteristics are

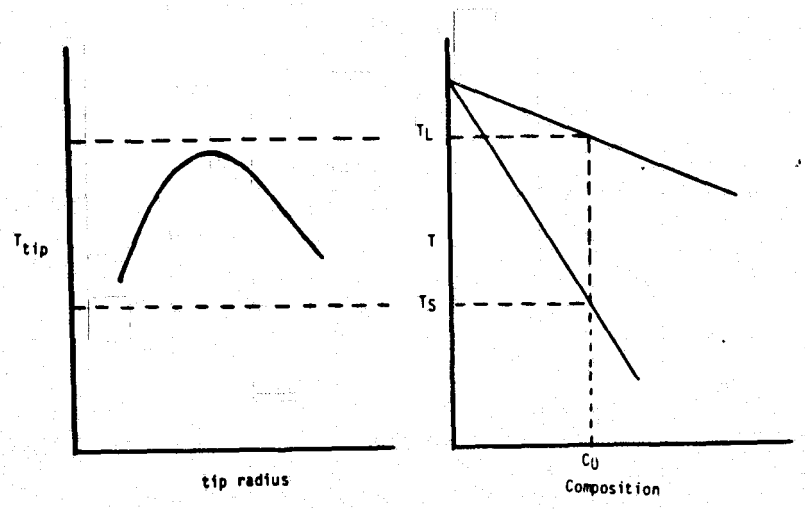

Fig. 8. A schematic illustration of the multitudes of theoretical tip radii which are possible for given growth conditions.

observed experimentally for given values of $\mathcal{A}$ and $\mathcal{G}$, it is necessary to find a specific tip temperature which the interface chooses under given experimental conditions. It is now well established in literature [4, 9, 10] that the specific temperature selected by the system is determined by the stability of the dendrite tip. Trivedi [13, 14] has derived a general stability criterion applicable to the dendrite growth under directional solidification conditions. This stability criterion is given by the following relationship [13, 14]

$$C_t/C_\infty \xi_c = (1/2)\mathcal{G} + \mathcal{A}L/p^2 \qquad (10)$$

where C_t is the tip composition, L the stability constant, and ξ_c is a function of solute peclet number, p. The function ξ_c is unity for small p values but approaches zero as p becomes infinity. This additional relationship allows one to uniquely determine ρ as a function of the experimental variables $\mathcal{A}$ and $\mathcal{G}$. Fig. 9 compares the result of this analysis with the experimental data in succinonitrile-4 wt% acetone system, and the agreement is found to be quite good. Consequently, we may conclude that marginal stability criteria appears to be valid for dendrite growth under directional solidification conditions and the dendrite tip characteristics are not strongly influenced by the presence of neighboring dendrites.

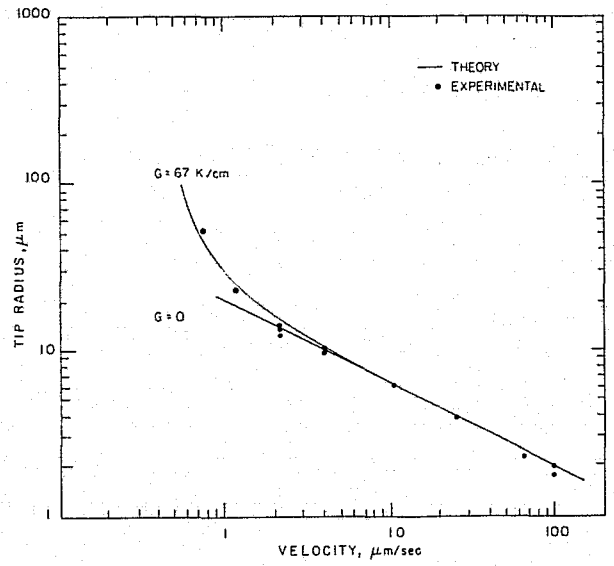

Fig. 9. Variation of dendrite or cell tip radius with velocity. From reference (4).

Fig. 10. Theoretical plot of V vs. ρ.

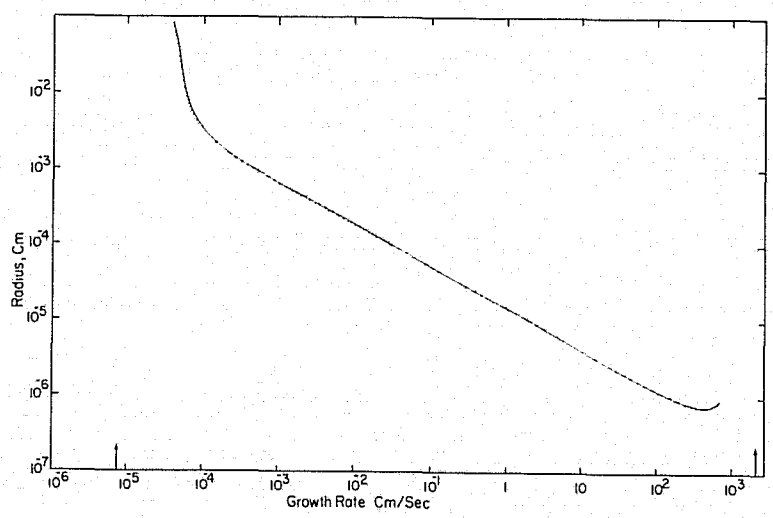

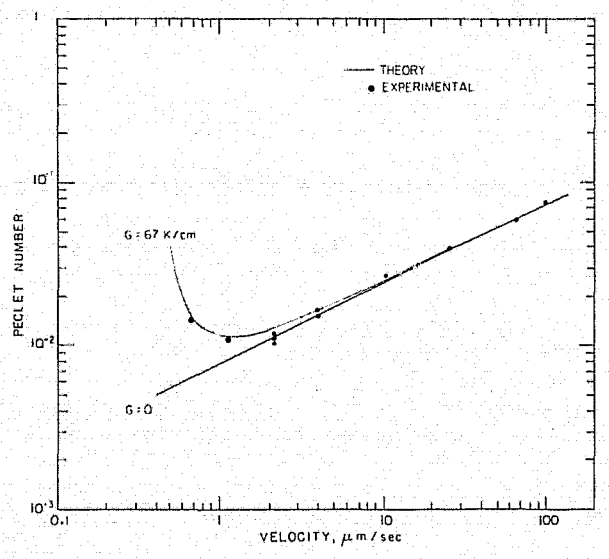

Fig. 11. The variation of solute peclet number with velocity. From reference (4).

Fig. 10 shows the variation of ρ with V over a wide range of velocities. Note that when V approaches the planar interface condition, ρ tends to go to infinity. The value of the tip radius increases sharply at both the velocities which correspond to the planar interface stability. Fig. 11 shows the variation in p vs. V. Again, a good agreement is found. Note that for a given value of p, two solutions for velocity are obtained. One solution represents the dendritic structure whereas the other represents the cellular structure. For the experimental conditions described in this paper, the minimum in p is associated with the maximum in λ_1 and also with the dendrite to cellular transition.

From the consideration of the interactions between neighboring dendrites, Hunt [15] has derived an expression which relates the primary spacing with the dendrite tip characteristics. Trivedi [16] has modifed Hunt's treatment to predict the primary spacing, and the result is given by

$$\Lambda = 4\sqrt{2}\ \mathscr{A} L/p^2 \qquad (11)$$

Fig. 12 compares the experimental data on the primary spacing variation with the result given by the above expression. The agreement between the theory and experimental data is found to be quite good. The theory precisely predicts the velocity at which maximum in λ_1 occurs.

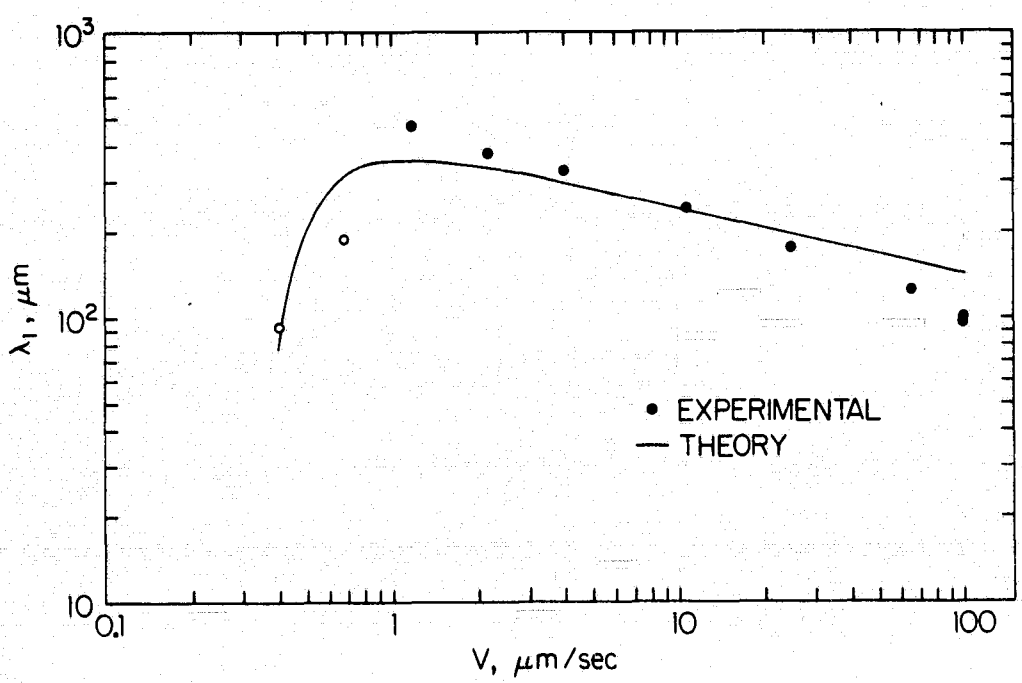

Fig. 12. A comparison of theory and experimental data for the primary dendrite (or cellular) spacing obtained in a directionally solidified succinonitrile-4 wt% acetone mixture. From reference (5)

The extrapolation of the theory in the high velocity regime shows that the primary dendrite spacing decreases with the growth rate and finally approaches zero as the velocity approaches the value given by the absolute stability of a planar interface. Note that in these calculations we have ignored the variation of k with velocity. This variation in k with velocity will alter the behavior of ρ and λ_1 at high velocities so that a proper theoretical analysis needs to take this variation into consideration.

5. Conclusions

The changes in interface shape as a function of growth rate are described for the solidification of binary alloys under directional solidification conditions. Experimental results and theoretical models have been presented to characterize the tip radius, primary spacing and secondary dendrite arm spacings. It is shown that the marginal stability criteria explains the experimental results quantitatively. A maximum in primary spacing as a function of velocity is observed and this maximum corresponds to the minimum in the peclet number. Also, for the experimental conditions presented in this paper, the maximum in λ_1 corresponds to the velocity at which cellular to dendrite transition takes place.

6. References

1. M. C. Flemings, Solidification Processing (McGraw-Hill, New York, 1974).
2. C. M. Klaren, J. D. Verhoeven and R. Trivedi, Met. Trans. 11A (1980) 1853.
3. J. T. Mason, J. D. Verhoeven and R. Trivedi, J. Cryst. Growth 59 (1982) 516.
4. K. Somboonsuk, J. T. Mason and R. Trivedi, Met. Trans. (submitted)
5. R. Trivedi, Met. Trans. (submitted)
6. W. A. Tiller, K. A. Jackson, J. W. Rutter and B. Chalmers, Acta Met. 1 (1953) 428.
7. W. A. Tiller, in The Art and Science of Growing Crystals, ed. J. J. Gilman (John Wiley and Sons, Inc., New Yor, 1963).
8. W. W. Mullins and R. F. Sekerka, J. Appl. Phys. 35 (1964) 444.
9. J. S. Langer and H. Müller-Krumbhaar, Acta Met. 26 (1978) 1691.
10. S. C. Huang and M. E. Glicksman, Acta Met. 29 (1981) 701.
11. R. M. Sharp and A. Hellawell, J. Cryst. Growth 11 (1971) 77.
12. S. C. Huang and M. E. Glicksman, Acta Met. 29 (1981) 717.
13. R. Trivedi, J. Cryst. Growth 49 (1980) 219.
14. R. Trivedi, Acta Met. (submitted)
15. J. D. Hunt, in Solidification and Casting of Metals (The Metals Society, Book 192, Longon, 1979).

DISCUSSION

ABBASCHIAN: Have you plotted your primary and secondary arm spacing versus the cooling rate?

TRIVEDI: No. You may recall, from the radius data, the secondary arm spacing is proportional to the radius and the radius is independent of the temperature gradient at large velocities. The primary spacing data are quite different. They are distinctly dependent on gradient. The cooling rate will not properly describe the primary spacing, but it will the secondary spacing.

ABBASCHIAN: When you change the velocity, does the temperature gradient change also, or are you keeping that constant?

TRIVEDI: No. In the succinonitrile system, the thermal conductivity of the solid and liquid are about the same across the whole sample.

FERBER: Regarding the use of the spherical harmonics to analyze what is going on at the tips of the dendrites, is that based on some theoretical reasoning or is it just something that happened to fit what is experimentally observed?

TRIVEDI: There is a strong theoretical basis for that. Based on the paper by Mullins and Sekerka, one finds that the stability conditions depend upon the local temperature gradient and the local composition gradient. If you go to a number of different shapes, you find that the shape does not change the condition very much. We have done some work on cylinders, spheres, uniplanar interfaces, and you get the same basic relationship between local conditions of temperature and concentration gradients. Consequently, if you use a simple model of spherical harmonics on the tip, and you look at the stability conditions in terms of temperature gradient, and composition gradient, and then use that precise value of temperature and composition for a parabolic cylinder, you get a fairly good agreement. Professor Glicksman has studied the undercooled case and our work shows that this is really true.

SEKERKA: Cells don't have parabolic tips. What does that mean? Does that mean that if I try to describe the shape it leads off like the fourth derivative instead of the second, or does it mean that it only follows the second derivative for a shorter time?

TRIVEDI: If you measure the dendrite tip, you can almost always fit a parabola. As soon as you go cellular, your parabola will fit a very small region but then it will deviate. This deviation from a parabolic shape is associated, with cells, to dendrite transition.

SEKERKA: So it deviates more quickly rather than starting off like the fourth derivative.

TRIVEDI: That is right.

SESSION III: MELT SPINNING

D. Ast, Chairman

N84 28625

RAPIDLY SOLIDIFIED ALLOYS MADE BY CHILL BLOCK MELT-SPINNING PROCESSES

H. H. Liebermann

Metglas Products - An Allied Company
6 Eastmans Rd.
Parsippany, New Jersey 07054

Chill block melt-spinning (CBMS) processes are used to make rapidly solidified microcrystalline and amorphous alloy ribbon, flakes, etc. Fundamentals of CBMS processes are discussed in light of recent advances. Special regard is given to ribbon geometric defects (edge serrations, surface asperities, etc). Photomicrographs of CBMS ribbon solidification microstructures are used to compare local solidification rates, especially in the vicinity of ribbon defects.

INTRODUCTION

The solidification of molten metals and alloys into continuous filament or ribbon has been practiced for nearly a century using various methods [1]. Early work on the casting of metallic filaments satisfied the need to economically prepare these materials in filamentary form. Materials aspects of rapid solidification technology such as solid solution extension, microstructural refinement, and the occurrence of metastable phases were not recognized until some twenty years ago [2]. Present day processing and materials research have lead to the development of rapidly solidified materials with novel microstructures, compositions and properties.

A process which is widely practiced to manufacture continuous rapidly solidified ribbon is chill block melt-spinning (CBMS), in which a stream of molten alloy is brought into contact with a rapidly moving substrate surface. A molten alloy puddle forms on the moving substrate, resulting from continued melt impingement; this puddle serves as a local reservoir from which ribbon is continuously formed and chilled. The most common substrate surfaces described in the literature are the inside of drums [3] or wheels [4,5], the outside of wheels [6-11], and belts [9]. Because of its practicality, the most commonly used substrate is a rapidly rotating wheel. Two common CBMS techniques are free jet melt-spinning (FJMS) [6-8] and planar flow casting (PFC) [9, 10]. Figure 1 shows a schematic diagram of both processes. In the free jet process, molten alloy is ejected under gas pressure from a nozzle to form a free melt jet which impinges on the substrate surface. In the planar flow method, the melt ejection crucible is held very close to the moving substrate surface, which causes the melt to be simultaneously in contact with the nozzle and the moving substrate. This entrained melt flow damps perturbations of the melt stream and thereby improves ribbon geometric uniformity. The initial quench rate and final ribbon geometry in FJMS depend on the nature of the melt puddle. For example, a puddle which is smooth and unchanging during the course of FJMS typically results in ribbons with well-defined edges and surfaces. Such geometric uniformity is desirable because it results in a uniform local quench rate through the ribbon thickness.

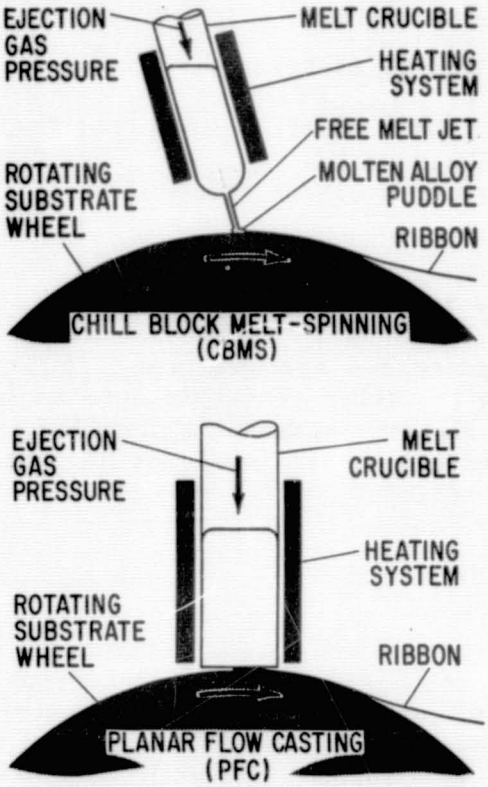

Fig. 1 Schematic representations of the Free Jet Melt-Spinning (FJMS) and Planar Flow Casting (PFC) processes.

MELT STREAM INSTABILITIES AND RIBBON IMPERFECTIONS

The control of ribbon thickness in CBMS has been described in terms of the propagation of a thermal boundary layer through the molten alloy puddle [7, 12, 13]. A schematic representation of the melt puddle given by Kavesh [7] is shown in Figure 2. In this model, a solid boundary layer forms at the chill surface and propagates into the melt puddle to form a ribbon. Alternatively, solidification models based on momentum boundary layer predominance [14, 15] and a combination of thermal and momentum boundary layers [16] have also been proposed. A precise description of CBMS ribbon formation is made difficult by the simultaneous occurrence of heat transfer and mass transfer. Experimental evidence and the comparison of theoretical models with experiment suggest that both of these factors may determine ribbon thickness.

Imperfections in CBMS ribbon geometry stem from a variety of sources which include the nature of the molten alloy stream, the substrate, and the atmosphere in which melt-spinning is conducted. Variations in the molten alloy stream during CBMS will cause corresponding non-uniformities in the ribbon product. For example, the relatively easy destabilization of free

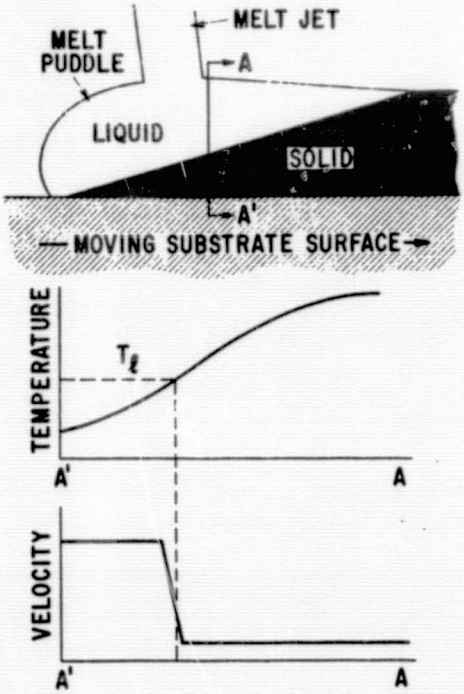

Fig. 2 Schematic diagram showing the propagation of a boundary layer through an FJMS melt puddle [7].

cylindrical and planar jets of molten metals and alloys [17-19] has been shown to result from a metallic liquid having high surface tension and low viscosity. Therefore, factors such as melt ejection nozzle geometric imperfections and vibrations imposed upon a free liquid jet [20] can cause premature disruption of the jet into droplets. The finite roughness of any real substrate surface in CBMS can cause peturbation of the molten alloy puddle when melt-spinning at high speeds. Effects of geometric roughness elements on the flow of fluid over an otherwise flat surface have already been investigated [21, 22]. Melt puddle disruption caused by substrate surface roughness elements can result in molten alloy droplet spraying and in irregularities in ribbon width and thickness. In addition, the presence of foreign contaminant films on the substrate surface during FJMS can result in complete non-wetting of the melt on the substrate[23]. Finally, the perturbation of the molten alloy puddle during FJMS has also been found to depend on whether or not the gas boundary layer established on the rapidly moving substrate surface in a gaseous medium has a hypercritical Reynolds number [24], as shown schematically in Figure 3. Figure 4 shows the effect of melt-spinning amorphous alloy ribbons in various gaseous atmospheres [25]. In addition to the ribbon edge serrations, melt-spinning in a gaseous environment may cause increased ribbon surface roughness [26] and penetration of gas beneath the melt puddle to form small pockets in the underside of the ribbon [27, 28] as shown in Figure 5 [29]. Such small non-contact areas result in a local loss of intimate alloy-substrate contact which reduces local heat transfer and thereby results in a locally modified solidification microstructure in the ribbon.

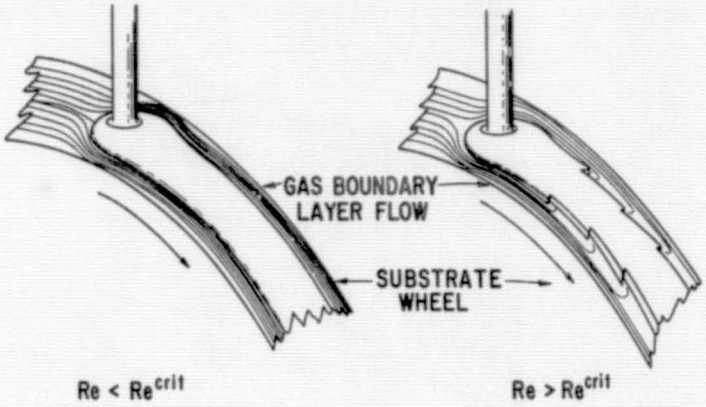

Fig. 3 Schematic diagram showing the influence of gas boundary layer Reynolds number on FJMS ribbon edge definition.

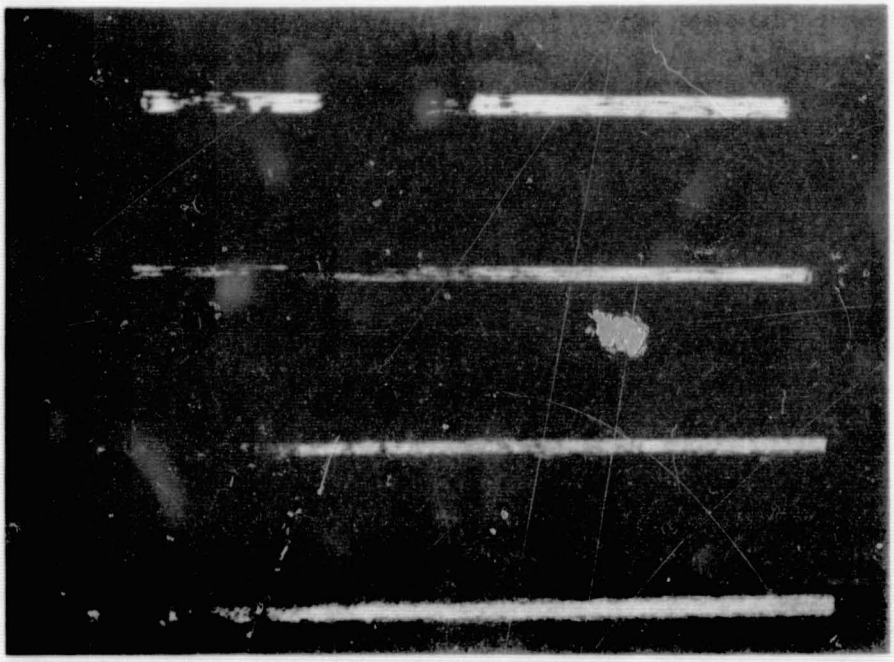

Fig. 4 Photograph of approximately millimeter wide amorphous alloy FJMS in various atmospheres.

Many of the instabilities cited may alternately be attenuated by making the proximity between the melt ejection crucible and jet very close. In this way, the flowing melt is entrained and made resilient against perturbation. However, this so-called planar flow casting (PFC) approach requires accurate control of the crucible-substrate gap. In any real melt-spinning system, the substrate expands during processing and makes the gap smaller, which can constrict melt flow entirely. On the other hand, free jet CBMS has a substantial advantage in that the crucible may be situated sufficiently far from the substrate that no alteration or disruption of melt flow occurs.

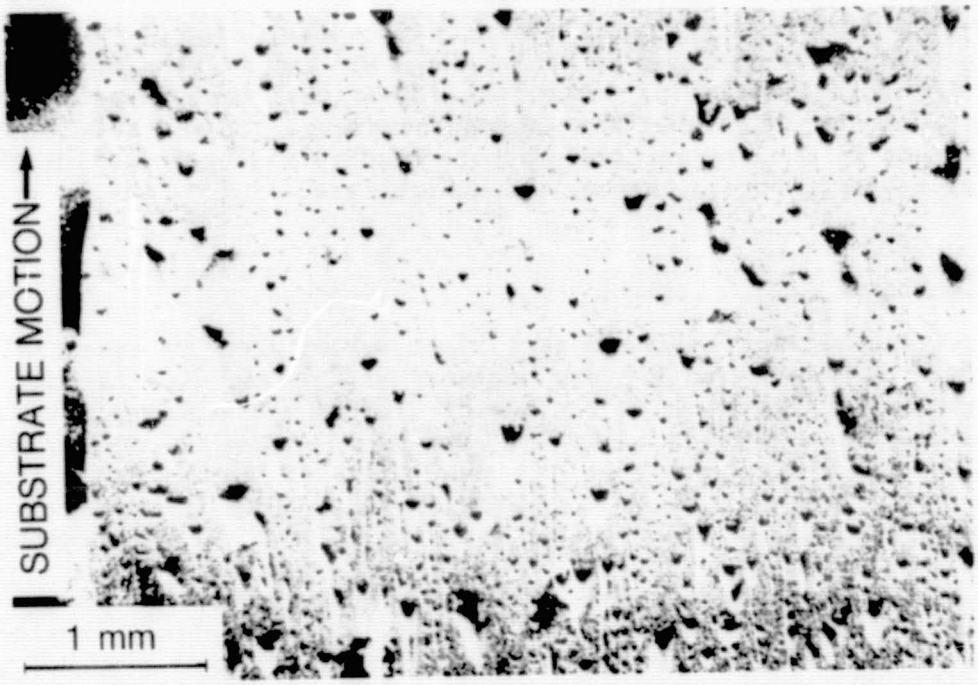

Fig. 5 Micrograph showing small depressions in the substrate contact surface of melt-spun amorphous alloy ribbon.

MELT-SUBSTRATE WETTING AND RIBBON SOLIDIFICATION

The melt-substrate interface is of critical importance in determining the extent to which the molten alloy will wet and spread on the substrate surface. Melt wetting of the substrate surface is influenced by surface films and by the chemical composition similarity between the melt and the substrate materials. The work of Bailey and Watkins [30] suggests that a tendency for mutual solubility between melt and substrate materials would greatly enhance wetting in a static, isothermal situation. Since average ribbon quench rate increases approximately as the inverse square of ribbon thickness for ideal cooling [31], ribbon geometry control and uniformity is of great importance in the fabrication of a product having uniform surface roughness. The distance over which the ribbon remains in contact with the substrate is also an important process variable which affects the average ribbon quench rate.

The interfacial heat transfer characteristics between product and substrate have been mathematically modeled [31-38] and have been found to be at least partially contingent upon the nature of the fluid flow in the area of the melt puddle. Since the average CBMS quench rate is limited by the thickness of the ribbon, there is expected to be a maximum thickness for which a given solidification velocity can be achieved. An excessively thick ribbon will exhibit a continuous change in microstructure through its thickness. This is a result of the change in solidification rate through the thickness. The effects of experimental variables (heat transfer coefficient

between product and substrate, product thickness, etc) on rapidly-quenched samples have been discussed by Jones [36, 37] and by Mehrabian [38]. Their results show that for thin ribbon, the interfacial heat transfer coefficient becomes dominant in establishing the quench rate. Proper selection of wheel material and design are critical factors in determining the value of the heat transfer coefficient and, hence, the quench rate.

SOLIDIFICATION MICROSTRUCTURES

Substrate wetting by the molten alloy during CBMS is essential in order to produce ribbon having uniform geometry and to maximize thermal transport during solidification. As an example of limited melt-substrate wetting, Fig. 6 shows the cross-section of a high purity FJMS silicon ribbon cast in air [38]. The depressions in the ribbon underside are the result of air boundary layer disruption of the melt puddle during CBMS, as has already been discussed. An example of a deviation in the solidification microstructure by limited melt-substrate contact during CBMS is given in Fig. 7 [39]. The chill crystals in the underside of the superalloy ribbon shown are elongated (lateral heat flow) in a local area at which there was limited melt-substrate heat transfer (contact) during CBMS. Similarly, Fig. 8 shows a greater extent of branched dendrites in the vicinity of a non-contact area in the cross-section of superalloy ribbon. Microstructural coarsening can also result from reduced average quench caused by excessive ribbon thickness. Fig. 9 shows a scanning electron micrograph of the solidification microstructure at a tear in the upper surface of thin CBMS superalloy ribbon. Note the highly striated structure which is apparently free of branched dendrites. Fig. 10 shows a similar tear in an excessively thick CBMS superalloy ribbon. The variation in local cooling rate through the thickness of a superalloy ribbon is illustrated by the optical micrograph of Fig. 11. Note that the microstructure changes from equiaxed chill crystal to highly

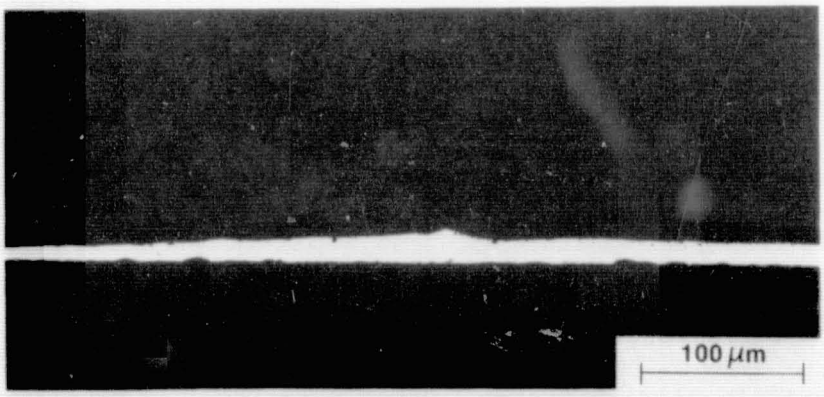

Fig. 6 Transverse section of high purity silicon FJMS on a steel wheel in air [38].

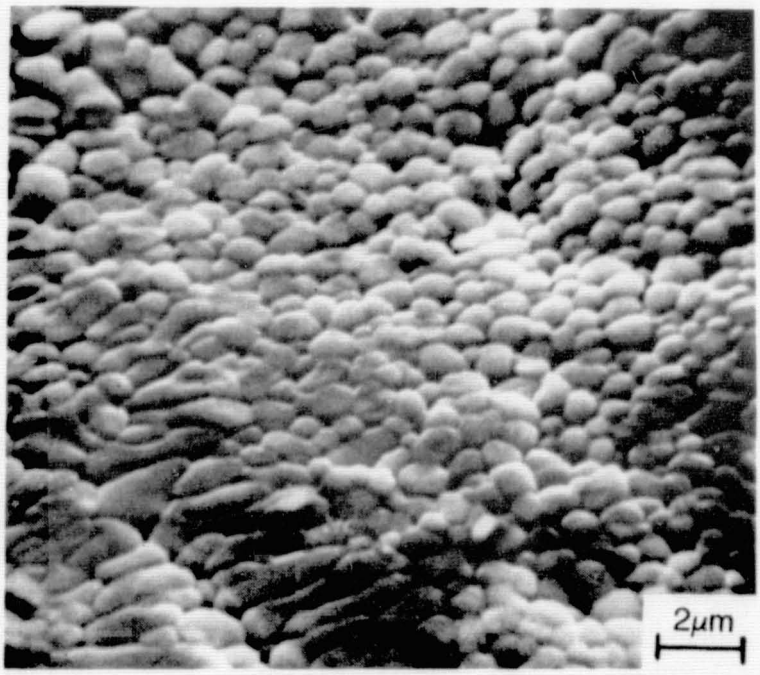

Fig. 7 Scanning electron micrograph of the bottom surface of nickel base superalloy ribbon cast on a copper substrate [39].

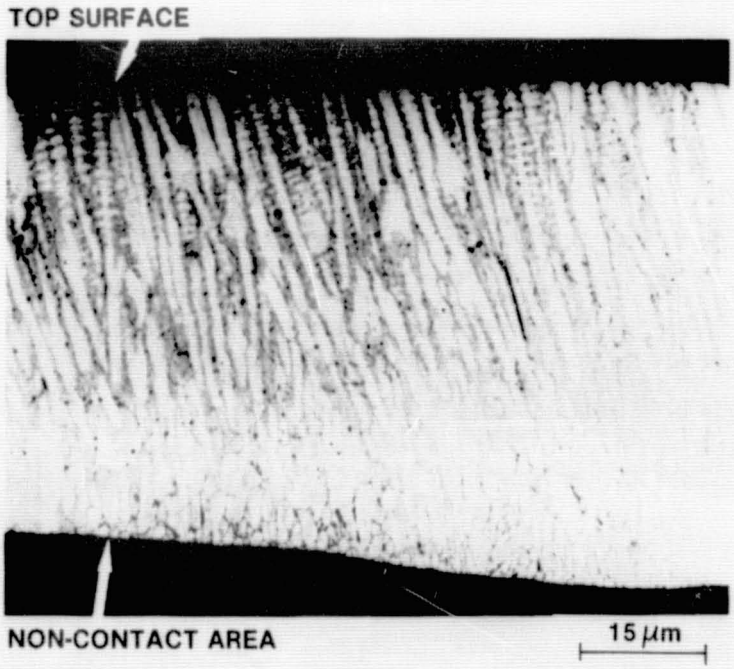

Fig. 8 Optical micrograph of nickel-base superalloy ribbon FJMS on a copper substrate wheel. Enhanced transition to branced dendrite structure occurs above the substrate non-contact part of the sample [39].

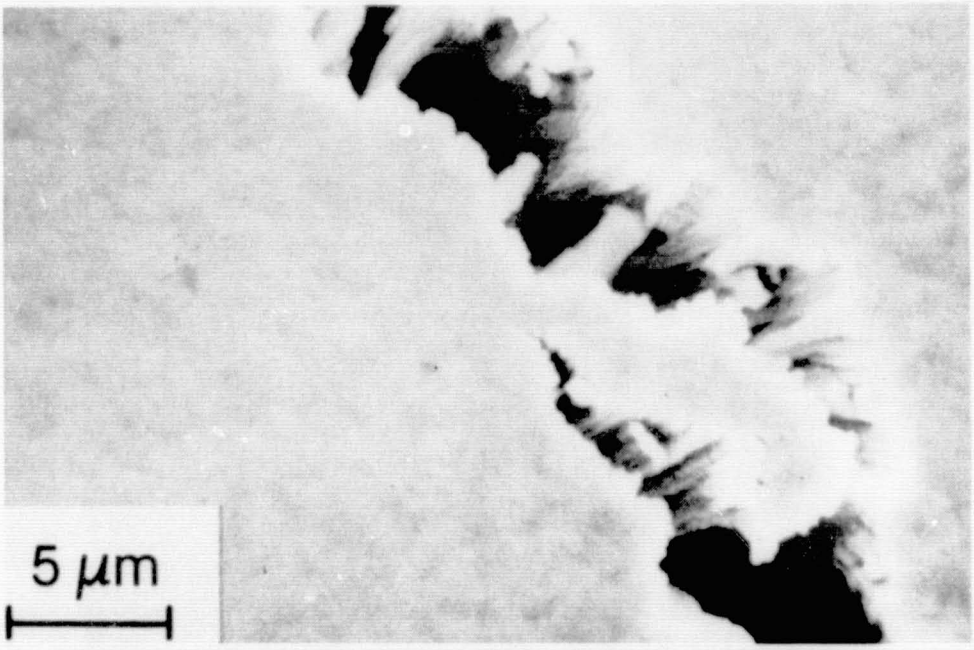

Fig. 9 Columnar solidification microstructure at a tear in the upper surface of thin FJMS nickel-base superalloy ribbon [39].

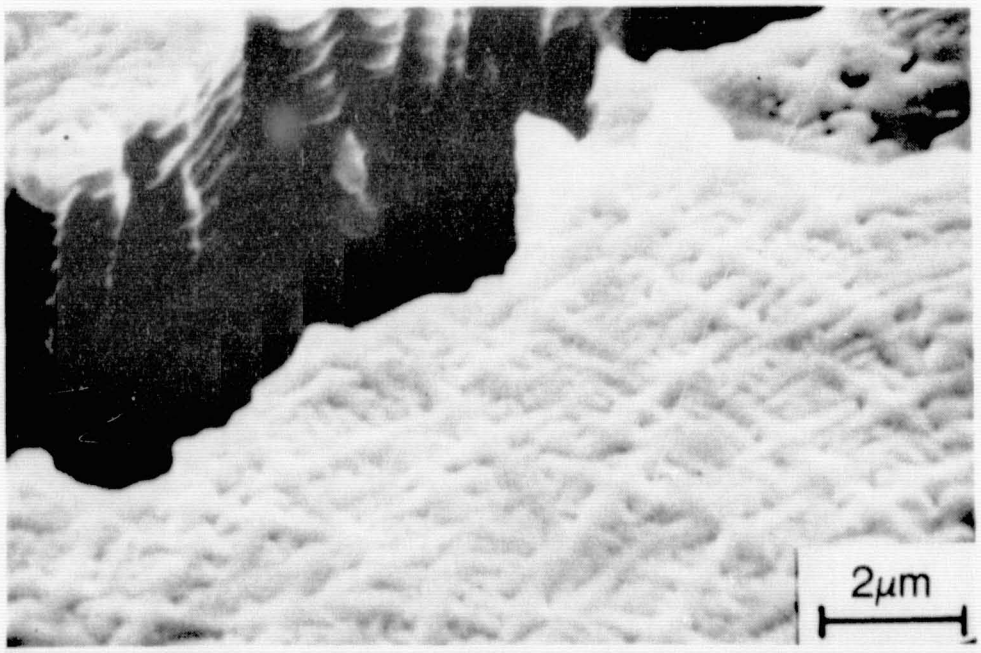

Fig. 10 Well-developed branched dendrite structure at a tear in excessively thick FJMS nickel-base superalloy ribbon [39].

columnar to branched dendrite solidification with distance from the substrate contact side of the ribbon. Similar variations in CBMS superalloy ribbon microstructure have been already reported [39-41]. Fig. 12 shows a schematic diagram of the four solidification microstructure zones which can occur in the CBMS of some crystalline materials. The region nearest the sample-substrate interface is the chill zone and is comprised of fine equiaxed grains of random orientation. A region of columnar crystals grow out of the chill zone and ultimately become dendritic. The presence or absence of each zone illustrated will largely depend on local cooling rate, this being related to the local velocity of the solid-liquid interface during CBMS. Alloy composition also influences the solidification microstructure which forms.

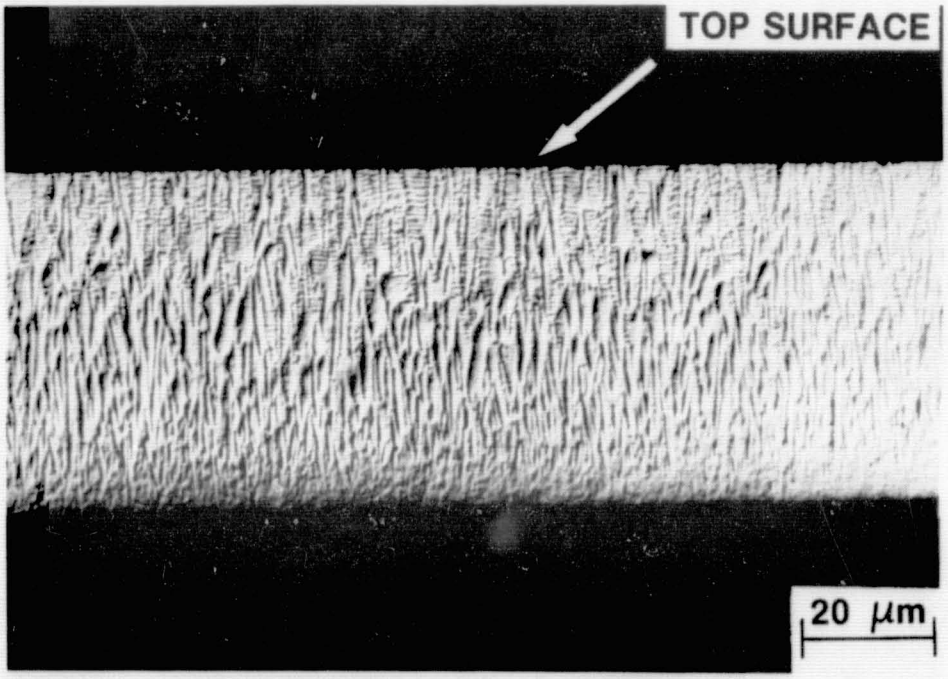

Fig. 11 Optical micrograph showing the cross-section of thick nickel-base superalloy ribbon. The transition from cellular to branched dendrite structure is clearly seen [39].

CONCLUDING REMARKS

The microstructures of materials can be significantly altered by the conditions under which they are solidified. These microstructures range from very coarse dendritic structures with large amounts of segregation, as observed in very large ingots, to the totally non-crystalline microstructures of rapidly solidified melt-spun amorphous alloys [42]. The solidification microstructure depends on two key parameters: the amount of non-equilibrium undercooling in the liquid prior to its solidification and the velocity of

the liquid-solid interface. These parameters are controlled by the nature of the solidification system, which can alter the number of heterogeneous nucleation sites, and by the rate of heat extraction which, in essence, controls the velocity of the liquid-solid interface. While solidification rates are frequently reported in terms of liquid cooling rates, a more meaningful description would be the interface velocity [43]; however, it is experimentally difficult to measure high values of interface velocity in most alloy systems.

At very low interface velocities, no geometrical instabilities occur in liquid-solid interfaces because there is time to dissipate thermal gradients generated by the latent heat of fusion liberated during solidification. An example of this type of solidification is observed in directionally solidified eutectic alloys. Liquid undercooling increases with decreasing temperature gradient in the liquid ahead of the interface. Under these conditions, a small geometric perturbation in the interface will cause the formation of cells and, finally, of dendritic columnar grains. The regions between these primary dendrites contain liquid. Just as the original liquid-solid interface can form primary dendrites, secondary dendrites can form from the primary dendrites. Similarly, tertiary dendrites can form the secondary dendrites, and so on. Dendrite arm spacing has been correlated with the overall solidification rate [44,45] with more rapid solidification rates resulting in finer dendrite arm spacings. Attempts to calculate solidification rates from such empirical relationships have been made difficult because of secondary dendrite arm coarsening [43].

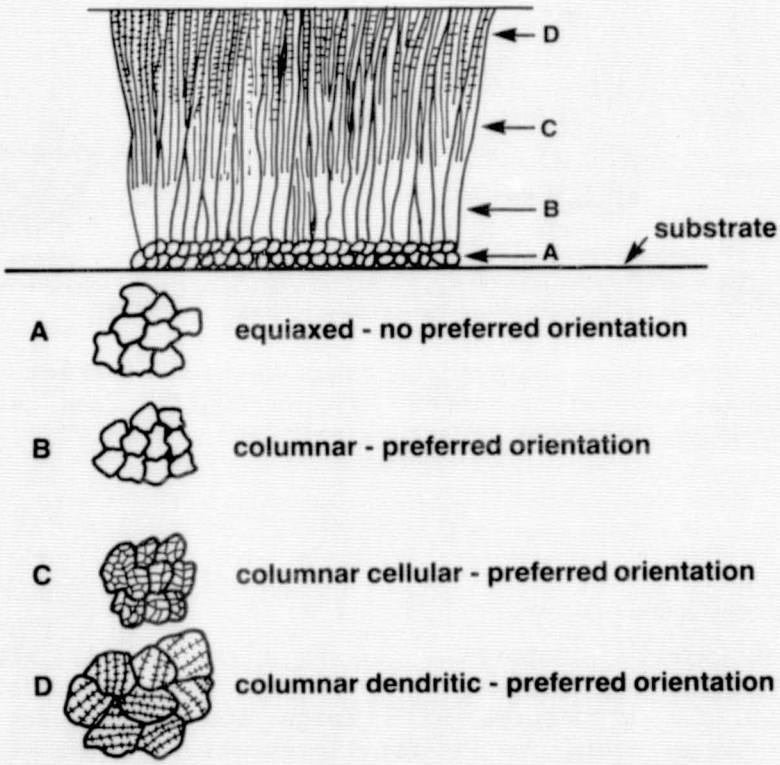

Fig. 12 Schematic representation of solidification microstructures which may be found in CBMS ribbons.

The microstructure of melt-spun ribbons may consist of a variety of these microstructures. Study of microstructure as a function of ribbon thickness can reveal the history of the local solidification processes. At the liquid alloy-substrate interface there is a high degree of undercooling and an extremely high density of heterogeneous nucleation sites. This region of the ribbon may contain fine equiaxed crystals of random orientation.

As the alloy in contact with the moving substrate solidifies, there is no longer the large number of nucleation sites and the temperature gradient will have diminished. Only those equiaxed grains in the chill zone having a preferred crystallographic growth direction aligned with the thermal gradient will grow into the remaining liquid. During growth of these columnar crystals, their number decreases and the cross-section of the remaining crystals increases. This selective crystal growth process results in a preferred orientation. Crystals most favorably oriented will grow most rapidly and survive. In nickel-base superalloys, for example, the favored growth direction is (100). Thus, one would expect (100) type texture in CBMS ribbons. As these columnar dendrities grow, the temperature gradient is reduced and the velocity of the liquid-solid interface is also decreased. If this temperature gradient and velocity are sufficiently diminished, the columnar dendrites will start for form secondary dendrite arms.

REFERENCES

1. Daniels, F. H., U.S. Patent 359,348 (1887); Cole, A. L., U.S. Patent 745,786 (1903); Staples, W. G., U.S. Patent 1,063,895 (1913); Pond, Sr., R. B., U.S. Patent 2, 825,108.

2. Klement, Jr., W., Willens, R. H. and Duwez, P. Nature 187, 809 (1960); Jones, H. and Suryanarayana, C., J. Mat. Sci. 8, 705 (1973); Jones, H., Rep. Prog. Phys. 36, 1425 (1973).

3. Pond, R., Jr. and Maddin, R., Trans. TMS-AIME 245, 2475 (1969).

4. Chen, H. S. and Miller, C. E., Mat. Res. Bull. 11, 49 (1976).

5. Polk, D. E., et al., U.S. Patent 3,881,542 (1975).

6. Strange and Pim, U.S. Patent 905,758 (1908).

7. Kavesh, S. in Metallic Glasses, ASM, Metals Park, OH (1978).

8. Liebermann, H. H., Mat. Sci. Eng. 43, 203 (1980).

9. Narasimhan, M. C., U.S. Patent 4,142,571 (1979).

10. Takayama, S. and Oi, T., J. Appl. Phys. 50, 4962 (1979).

11. Liebermann, H. H., Mat. Sci. Eng. 49, 185 (1981).

12. Kuiken, H. K., Int. J. Heat Mass Transfer 20, 309 (1977).

13. den Decker, P. and Drevers, A. in Metallic Glasses: Science and Technology, vol. I, eds. Hargitai, C., Bakonyi, I., and Kemeny, T., Central Research Institute for Physics, Budapest, Hungary (1981).

14. Vincent, J. H. and Davies, H. A. in Solidification Processing in the Foundry and Casthouse, Warwick, England (1980).

15. Vincent, J. H. Davies, H. A., and Herbertson, J. G. in Proc. Symp. on Continuous Casting of Small Sections, AIME, Warrendale, PA (1981).

16. Katgerman, L., III, Scripta Met. 14, 861 (1980).

17. Grant, R. P. and Middleman, S. AIChE J. 12, 669 (1966).

18. Lienhard, J. H. and Day, J. B., J. Basic Eng. Series D 92, 515 (1970).

19. Liebermann, H. H., J. Appl. Phys. 50, 6773 (1979).

20. Cline, H. E. and Anthony, T. R., J. Appl. Phys. 49, 3203 (1978).

21. Wieghardt, K., Forschungshefte fur Schifftechnik 1, 65 (1953).

22. Leslie, D. C., Rep. Prog. Phys., 36, 1365 (1973).

23. Liebermann, H. H., IEEE Trans. Magn. Mag-13, 1393 (1979).

24. Liebermann, H. H. in Rapidly Quenched Metals III, vol. I, ed., B. Cantor, The Metals Society, London, England (1978).

25. Liebermann, H. H., unpublished research, G. E. Corporate Research and Development, Schenectady, NY (1977).

26. Matsurra, M., Kikuchi, M. Yagi, M., and Suzuki, K., Jpn. J. Appl. Phys. 19, 1781 (1980).

27. Mobley, C. E., Maringer, R. E., and Dillinger, L. in Rapid Solidification Processing Principles and Technologies, eds. Mehrabian, R., Kear, B. H., and Cohen, M., Claitor's Publishing Division, Baton Rouge, LA (1978).

28. Huang, S. C. and Fiedler, H. C., Met. Trans. A 12A, 1107 (1981).

29. Liebermann, H. H., Ph.D. thesis, University of Pennsylvania, Philadelphia, PA (1977).

30. Bailey, G. L. J. and Watkins, H. C., J. Inst. Metals 80, 57 (1952).

31. Ruhl, R. C., Mat. Sci. Eng. 1, 313 (1967).

32. Nakoryakov, V. E., Polasaev, B. G., and Troyan, E. N., Int. J. Heat Mass Transfer 21, 1175 (1978).

33. Anthony, T. R. and Cline, H. E., J. Appl. Phys. 50, 239 (1979).

34. Cline, H. E. and Anthony, T. R., Ibid. p. 245.

35. Pond, R. B., Sr. and Winter, J. M., 69th Annual AIChE Conf., Chicago, IL (1976).

36. Jones, H. in Ref. 27.

37. Mehrabian, R. in Ref. 27.

38. Liebermann, H. H., unpublished research, G. E. Corporate Research and Development, Schenectady, NY (1981).

39. Liebermann, H. H., Maxwell, R. E., Smashey, R. W., and Walter, J. L., Met. Trans. (to be published September, 1983).

40. Davies, H. A., Shohoji, N., and Warrington, D. H. in Rapid Solidification Processing Principles and Technologies II, eds. Mehrabian, R., Kear, B. H., and Cohen, M., Claitor's Publishing Division, Baton Rouge, LA (1980).

41. Belov, A. F., Musiyenko, J. T., Yu. G. Gol'der, and Belotserkovets, U.K., Russian Metallurgy 1, 71 (1980).

42. Polk, D. E. and Giessen, B. C. in Ref. 7.

43. Huang, S. C. and Glicksman, M. E., Acta Met. 29, 701 (1981).

44. Joly, P. A. and Mehrabian, R., J. Mat. Sci. 9, 1446 (1974).

45. Grant, N. J.; Holiday, P.R., Cox, A. R., and Patterson II, R. J.; Glickstein, M. R., Patterson II, R. J., and Shockey, N. E.; Miles, T. E. and Rhodes, J. F. - all in Ref. 27.

DISCUSSION

WARGO: What do you use as the spinning substrate for silicon?

LIEBERMANN: For the sample I showed you, I used copper.

WARGO: Did you find any problem with it sticking to the substrate material?

LIEBERMANN: It did stick somewhat, perhaps one-half inch or an inch with the 3-to-5 gram load I was shooting. Typically, when one runs long, large loads, the adhesion increases with time.

WARGO: What would you guess would be an optimum [substrate] material for silicon?

LIEBERMANN: Silicon. Materials are greedy and they like themselves.

WARGO: When the film goes down [on the wheel] will it adhere, or separate?

LIEBERMANN: I have cast copper on copper and superalloy on superalloy and they do separate for a while before wrapping.

WARGO: What temperature do you keep the spinning wheel?

LIEBERMANN: The wheel is at room temperature until you cast on it, at which point its temperature increases with time. We don't use cooling for the small runs I have shown you here. Of course, at Metglas Products we always use cooling to make a good uniform product.

WARGO: What is the longest run you have made with the superalloy or silicon?

LIEBERMANN: We have not made extensive amounts. We have cast a couple of pounds at one-half-inch widths.

ROSEMEIER: What type of crucible materials did you use for the metglasses as opposed to the silicon material?

LIEBERMANN: For the silicon I used quartz because it is easy to fabricate into any form you desire. If one heats it quickly, quartz is suitable. Metglas is typically melted at a lower temperature. You cast metglas-type material, iron-based materials, at 1000° to 1400°C, which is just fine for quartz.

ROSEMEIER: How important was the orifice diameter in all your techniques for producing a uniform film?

LIEBERMANN: The orifice diameter is quite important because that meters the flow of liquid going to the wheel. The more flow going down, the greater the momentum impact; therefore, the ribbon gets wider. For example, if you increase the orifice diameter or if you increase the ejection pressure you get much more impact and the ribbon width increases. That is not

necessarily the case for the close-up casting. There are different approaches to making a similar product.

GRABMAIER: Do you have any difficulties with the silicon sticking to the quartz?

LIEBERMANN: Slight, for silicon. With silicon I have two experiences. Both were very quick. I melted it very quickly. I don't hold the silicon in quartz. Quartz is forgiving, depending on the thickness of the quartz you use, on the tube diameter, and process conditions. If you do it right, you can use it.

RAVI: I wonder if you can have a narrow machined slot in your spinning wheel so it can shape the ribbon, as you spit the liquid into a narrow slot. Can you machine it into your cylinder so that it doesn't spread sideways?

LIEBERMANN: You could but conversely you could simply take the crucible and put it close to the substrate and I think you would notice that there is not much spreading at all. The ribbon width is very nearly the slot width in this close-up casting. It might be a simpler way to go about it rather than machining your substrate.

GLICKSMAN: If you attempted to quench something like liquid silicon on a silicon wheel--let's take it one step further--take one of those nice seven-inch silicon ingots we heard about this morning and cut it crosswise and grind it into a nice wheel, so it in itself would be a single crystal, do you still think you would get a microcrystalline deposit, or is there any evidence to indicate that could be modified to some extent with silicon?

LIEBERMANN: The multiple casting showed that you may have an epitaxial effect. I don't know to what extent that would happen on a wheel of that type. If anybody is volunteering to send me a disk, I would be happy to try the experiment.

AST: The silicon would almost surely have a silicon oxide layer on it and that makes it difficult.

FAN: You say you have spun silicon on a copper wheel. What is the grain size of the silicon sheet you are spinning off?

LIEBERMANN: I showed one slide in which there was jet cast silicon and the grain size was maybe 200 μm.

AST: That would be very high. This is a slide of the cross section of melt cast silicon ribbon. You can see the grain size is on the order of 20 μm. Most of the grain boundaries are twin-related and are not very detrimental, so from that point it looks reasonable.

GLICKSMAN: [Directed to Ast] What is the substrate?

AST: The substrate was copper. We wanted to see if the grain boundary structure was different if you cast at very high speeds and, interestingly

enough, it turned out that the grain boundary structure was like every other kind of cast silicon. They were basically twin-related boundaries and we had a very hard time finding any high-angle or 'interesting' boundaries.

RAVISHANKAR: I understand that when Wacker started working on silicon (for photovoltaics), the first thing they did was to look at polysilicon to see if they could make solar cells, and they found the grain size was just too small to give any decent efficiencies. Amal Gosh at Exxon has shown from his theoretical modeling that he had to grow at least one millimeter grain size before he could get a decent performance. I am wondering if it is even worth looking at grain sizes of this magnitude if you are really interested in high efficiency?

LIEBERMANN: My interest was more academic than solar-cell-oriented at the time. I was aware of silicon work going on in Japan and I was just curious to see what it was like. I was not directing the processing toward an application such as solar cells.

AST: Can I make another comment? First of all, the recombination velocity of grain boundaries varies at least two orders of magnitude, depending on the kind of grain boundary you have. Second, Dr. Ravi showed this morning that in EFG you can very effectively passivate grain boundaries with a Kaufmann ion source. Somebody should do a little more work on the silicon spun ribbons and see how far they can go with passivation of grain boundaries.

GIESSEN: Concerning your piggy-back picture, where you showed the multiple layers. There were two pictures: one where you had the two jets and then another where you had the resulting four layers. Was that in the same process or was one the piggy-back and the other four times around?

LIEBERMANN: The four ribbons were made with four jets.

GIESSEN: Then probably the lower one was still a little liquid or at least very hot by the time the next one hit it. Do you think so?

LIEBERMANN: Yes. The individual jets were on the order of 1/8 to 1/4 inch apart.

AST: This multiple jet business is very important because it is difficult to make a single ribbon with a thickness of about 60 µm or so. For solar cells you need roughly 200 µm. If you are serious about it, this multiple-jet approach, which Dr. Liebermann did achieve, is very important to get ribbon of sufficient thickness.

LIEBERMANN: If you attempt to make very thick ribbons with existing methods, the melt puddle area just destabilizes completely. The fluid properties do not allow the accumulation of large amounts of metal; therefore, you have to go to an incremental process such as that.

MILSTEIN: About a year ago, Rosa Young took some poly and then ion-implanted it, and using glow discharge, followed it up by a laser anneal. She

produced 2.2% efficient solar cells. Carl Seager then passivated them and they improved to about 4.6%.

NARASIMHAN: On the jet casting of silicon, do you see the central portion of the silicon ribbon vastly thicker than the ends? That is what I have seen in the past.

LIEBERMANN: I haven't checked that. That was a longitudinal section, I showed you, along the ribbon length. I did not look at the cross section to see if the metal was thicker than the edges. In jet casting of amorphous metals you can make ribbons with a mounded center or you can make ribbon with mounded edges, depending on the jet speed.

NARASIMHAN: You are correct. In the case of silicon it has a larger surface tension and peculiarities in wetting behavior. On the superalloys, did you have hafnium added to them?

LIEBERMANN: I don't think so.

ROSEMEIER: You keep producing all this material. By what technique do you take it out?

LIEBERMANN: For small amounts in the laboratory you can wind it and pick it up by hand. For production, as at Metglas Products, you have a winding devices that can wind in line. As you cast it, it just shoots into a winding spool directly at 60 miles an hour.

POLYCRYSTALLINE SILICON SHEETS FOR SOLAR CELLS BY THE IMPROVED SPINNING METHOD

N84 28626

Y. Maeda, T. Yokoyama and I. Hide
Hoxan Research Laboratories, Hoxan Corporation
5-2 Kikusui, Shiroishi-ku, Sapporo 003 Japan

Introduction

The first objective of the photovoltaic program is to reduce the costs of materials since silicon accounts for 65 to 75 percent of the material costs of photovoltaic modules. The current process of producing silicon sheets is based entirely on the conventional Czochralski ingot growth and wafering used in the semiconductor industry. It is clear that this current technology cannot meet the cost reduction demands for producing low-cost silicon sheets. Therefore, alternative sheet production processes such as unconventional crystallization are needed. The production of polycrystalline silicon sheets by unconventional ingot technology is the "casting" technique.[1] Though large-grain (more than 100mm) sheets have been obtained by employing this technique,[2] major problems remain, such as slicing and subsequent material losses. Silicon ribbon growth overcomes deficiencies of the casting process by obtaining the sheet directly from the melt.[3] Thus the need to solve difficulties of several relevant parameter controls, mainly growth stability and impurity effects, are seriously being examined.

New polycrystalline silicon sheets have recently been produced by the spinning process which has been developed by the authors.[4,5] This method has an attractive high-growth rate of a few seconds per sheet as fast as the rapid roller quenching method.[6] Sheets with diameters of 4 - 6 inches or 100mm x 100mm and 0.3 - 0.5mm thick have been obtained by this method. The average grain size was approximately 100μm. The free surface of the sheet has a large number of small projections which rise to approximately 0.1 to 0.3mm due to volume expansion at the moment of solidification. However, for solar cell fabrication and performance, small grain size and surface projections are disadvantageous in terms of energy conversion efficiency and cell surface treatment.

In this paper, we will describe the direct formation process of polycrystalline silicon sheets having large grain size, smooth surface, and sharp edges from the melt with a high growth rate which will surely yield low cost silicon sheets for solar cells. Furthermore, we will describe the photovoltaic characteristics associated with this type of sheet to include an EBIC study of the grain boundaries.

Principles of the Improved Spinning Method

A schematic view of the main part of the setup used for direct production of polycrystalline silicon sheets is shown in Figure 1. Basically, the setup consists of a silicon melting part, a funnel and a spinning mold module. High-purity, semiconductor-grade polysilicon is melted in a quartz

crucible supported by a graphite mold. By inclining the crucible, the silicon melt is poured through a graphite-supported quartz funnel and down onto a graphite or quartz mold module which is mounted on a spinning wheel and maintained at the proper temperature.

In this study, the mold module for forming silicon sheets has been improved; it is associated with the plate which has been used for sheet formation in the initial spinning method. The mold module consists of a bottom mold and top cover plate which form four rectangular cavities. Each cavity is shaved off and contains a guide channel for the silicon to diffuse the moment it is dropped onto the center of the module after passing through a hole located in the center of the top cover. The size of the cavities is determined by the desired shape of the wafer. The mold is made of carbon graphite or quartz. For repeated use in mass production, a graphite mold is superior. When employing a grahpite mold, it is necessary to apply surface coatings of Si_3N_4, SiC film or their compound films to the side which comes in contact with the silicon melt. The coatings between the graphite and silicon melt or solidified silicon serve to suppress the transfer of carbon and prevent contamination of the silicon sheet.

As a practical procedure for producing four p-type silicon sheets from one drop of silicon melt, raw material, with highly boron-doped silicon lumps of $10^{19}/cm^3$ carrier concentration, is loaded into the crucible and melted at 1450 °C. A grahpite mold module having four cavities, each 5.0cm x 5.0cm and 0.5mm thick, is placed on the wheel. The module temperature is adjusted to 1400 °C; the surrounding temperature on and around the module must also be the same. After the spinning speed of the wheel is fixed at 400 rpm, the correct amount of molten silicon is dropped onto the module. At that moment, molten silicon diffuses in each cavity of the module; 15 seconds later, four silicon sheets which are the same size as the cavities are formed. By opening the top plate of the module, the silicon sheets can be removed from the furnace without being required to cool completely.

Characteristics of the Sheet

Figure 2 shows a 5cm x 5cm silicon sheet formed in this study. No small projections resulting from solidification can be seen at the surface, in contrast to the initial spinning method or the roller quenching method. Average surface roughness was a few tens of micrometers. Edges of the sheet shown are as-formed in which three edges are formed with cavity edges in the module and the balance is a free edge, which has the supply point for molten silicon. The ideal amount of raw material, just equal to the weight of four sheets may be maintained in order to obtain these clear edges of each sheet. However, an excess of molten silicon results in an irregular sheet with excess area at the free edge.

The typical grain structure of the sheet is shown in Figure 3. Normal grains and dendrites are observed. Average grain size is approximately 3.0mm, and a few dendrites run in a surface direction and have a length of 20mm to 50mm. The reason that dendrites run seems to be that, in spite of constant temperature of the grahpite module, the temperature gradient rises between the center and the circumference of the module when molten silicon drops onto it.

Characteristics of the sheet are shown in Table 1. Up to now, production rate of the sheet is 4 sheets per 15 seconds. With respect to the growth rate or the sheet area per production time, the present method will have an extremely high production efficiency if used with an appropriate mechanical operation handling and with multiple sheet formation modules. The rectangular sizes can be easily extended from 50mm to 100mm or more by varying cavity size in the mold module. Sheet thickness can be adjusted in a range of 0.1 to 1.0mm by varying the gap thickness of the cavities in the module. In case of present sheet, a range of 0.2 to 0.5mm is optimum for making solar cell. The resistivity of the sheet was around 1 Ω-cm which is nearly equal to the calculated value obtained from the doped carrier concentration. The carrier lifetime was measured by an instrument using a non-contact method by a laser source.

Photovoltaic Properties

P-n junction solar cells using the newly produced silicon sheets were made experimentally. Cells were conventionally fabricated by forming a phosphorus-diffused junction with a 0.3μm n^+ layer on the p-type sheets, metalizing them with an evaporated Ti-Ag grid and contacts, and then applying an Si_3N_4 antireflective coating. The photovoltaic properties of these experimental cells are shown in Table 2. A 10% efficiency cell has I-V characteristic as shown in Figure 4. Almost everyone of these cells has an efficiency rating of more than 9%. In Figures 5 and 6, SEM and EBIC pictures of grain boundaries are shown. As described earlier, the polycrystalline sheet contains both normal grain and dendrite. The pictures display the boundaries between grain and dendrite. It has also been observed that the boundaries between normal grains are much more photoelectrically active than boundaries found between grain and dendrite. These interesting behaviors should be investigated, as well as crystal growth in which both normal grain and dendrite have directional qualities respectively.

Summary

In the practical use of silicon materials, including Cz single crystal wafers for solar cells, casting polycrystalline silicon slices rather than ribbon sheets have been impractical due to the considerable cost factors. From the results of this study, it is evident that the spinning method developed by the authors has a greater potential to meet the goal of a low cost solar cell than even the most recent unconventioanl silicon sheet technologies because of the possibilities of compensating for and surpassing some of the disadvantages of other methods such as growth rate, slicing, material loss and batch producibility.

In particular, with respect to the sheet area production time, the present method will have an exremely high efficiency of production if coupled with an appropriate mechanical operation which has a high-speed sheet handling capability. A moderately calculated production rate of more than $10m^2$ per hour, which is a magnitudinous rise when compared with other unconventional sheet fabrication methods, can be achieved.

References

1. HUBER, D., WAHLICH, R., and HELMREICH, D. : 'Typical properties of multicrystalline silicon material'. Proceedings of 14th IEEE Photovoltaic Specialists Conference, 1980, pp. 316-321

2. HOELSCHER, J. F. : 'The Solarex block IV module'. Proceedings of the 15th IEEE Photovoltaic Specialists Conference. 1981, pp. 745-749

3. WALD, F. V. : 'Crystal 5; Silicon' (Springer-Verlag 1981)

4. MAEDA, Y. and YOKOYAMA, T. : 'Large area silicon sheet for solar cells'. Appl. Phys. Lett., 1982, 41, pp. 242-244

5. MAEDA, Y., YOKOYAMA, T., AND HIDE, I. : 'Large area silicon sheet produced by the spinning method'. Proceedings of the 16th IEEE Photovoltaic Specialists Conference, San Diego, 1982

6. ARAI, K., TSUYA, N., and TAKEUCHI,T. : 'Ultra high speed growth of silicon ribbon for solar cells'. Proceedings of the 14th IEEE Photovoltaic Specialists Conference, 1980, pp. 31-38

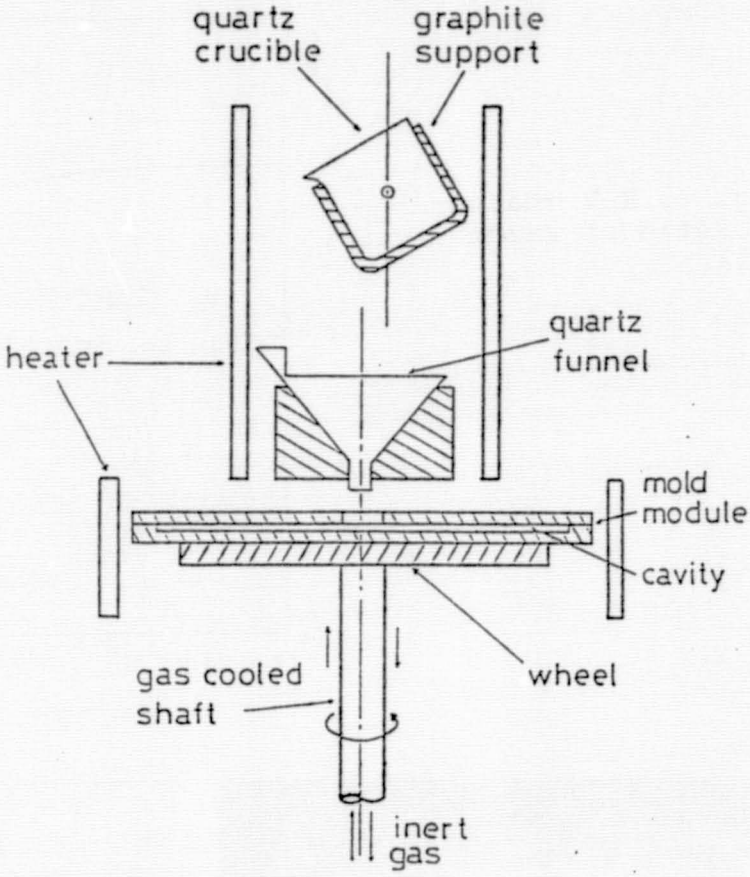

Fig. 1.
Schematic view of the main part of the setup for producing sheet by the improved spinning method.

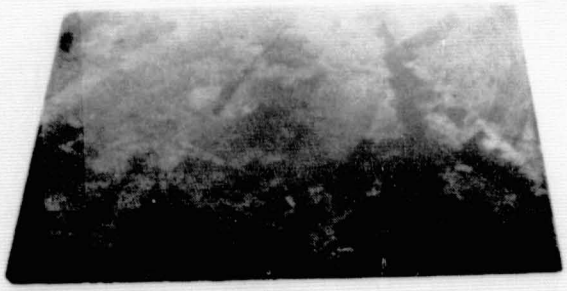

Fig. 2. 5cmX5cm as-formed rectangular Si sheet.

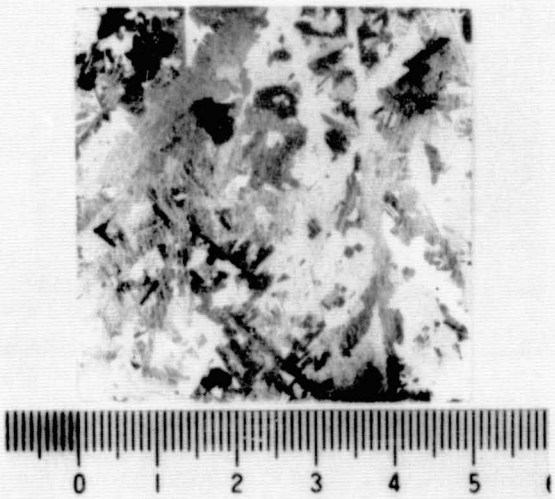

Fig. 3. The typical grain structure at the polished surface of the sheet.

Fig. 4. I-V characteristic of 2x2cm cell.

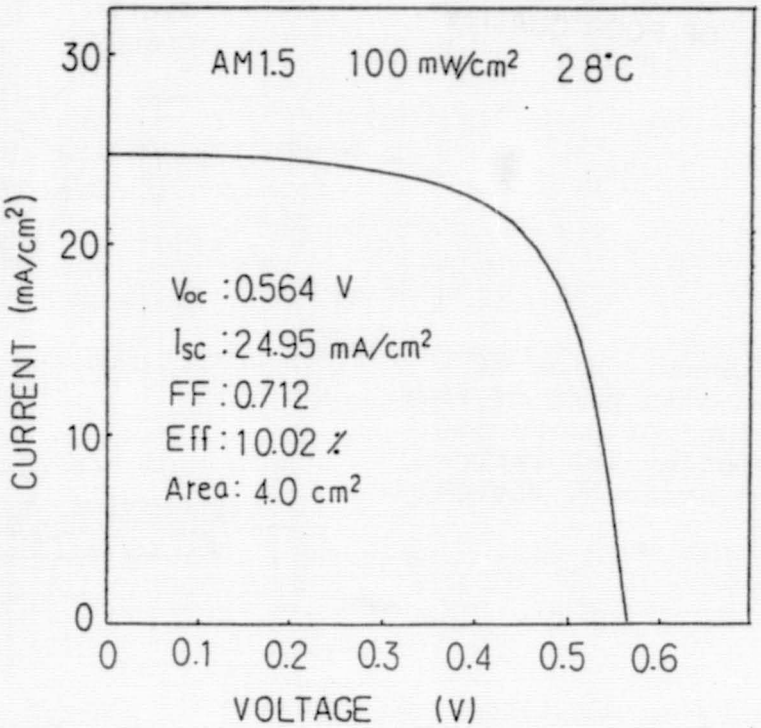

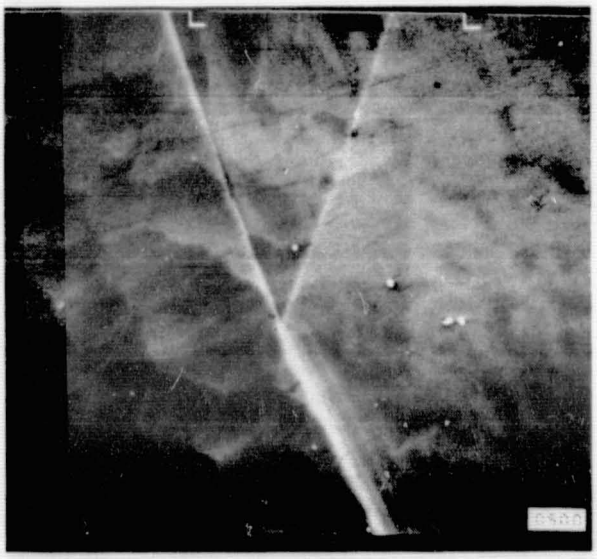

Fig. 5. SEM picture of grain boundaries. Left side is a dendritic grain. Right and upper grains are nomal.

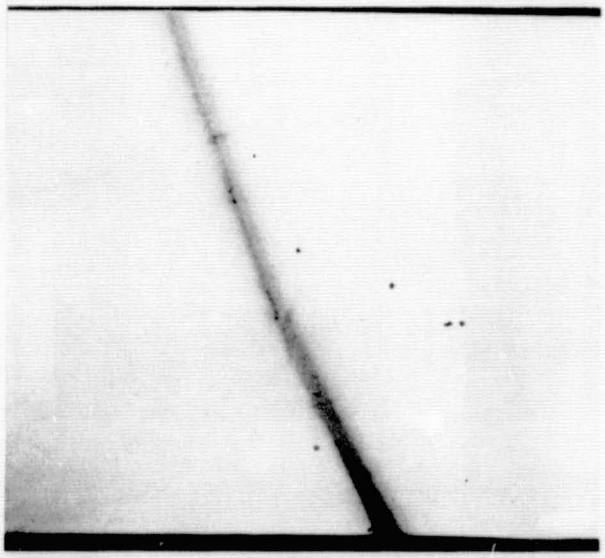

Fig. 6. EBIC picture of grain boundaries showed in Fig.5.

Table 1. Characteristics of silicon sheets

Growth rate	:	4 sheets per 15 seconds.
Size	:	50mm x 50mm.
Minimum thickness	:	0.1 mm.
Crystal structure	:	Polycrystalline and dendritic.
Grain size	:	1 - 10 mm.
Resistivity	:	0.7 - 1.2 Ωcm.
Carrier lifetime	:	1.0 - 1.3 μsec.

Table 2. Photovoltaic properties under AM1.5 100mW/cm^2 28°C.

Area	Open-circuit voltage (V)	Short-circuit current (mA/cm^2)	FF	Efficiency (%)
2x2 cm	0.564	24.95	0.712	10.02
5x5	0.562	25.20	0.670	9.50
5x5	0.560	24.20	0.690	9.35
5x5	0.564	25.00	0.652	9.18

DISCUSSION

FERBER: After pouring the sheet, how much time does it take to cool it down to where you can handle it or take it out of the machine?

MAEDA: After spinning, the cast is moved away and you can then open and pick it up.

GIESSEN: You called the process an advanced spinning process. Metallurgists use a very similar process, a centrifugal casting. What is the difference between what we know as centrifugal casting and this process?

MAEDA: I think it is the same.

NARASIMHAN: How do you accommodate the solidification expansion of silicon in your process?

MAEDA: I showed one edge is free, so expansion is to that edge.

GRABMAIER: Did you simultaneously make four plates in 15 seconds?

MAEDA: Yes, at the same time.

GRABMAIER: What is your mold material?

MAEDA: The mold material is graphite.

GRABMAIER: How often can you use one mold?

MAEDA: I don't know exactly. I have used it for a few tens of times.

GRABMAIER: You claim you can produce around 10 square meters per hour and after 10 plates you have to change your mold. I think you cannot produce that many square meters in one hour.

HELMREICH: Do you have to protect your mold from contamination?

MAEDA: We use a coating of silicon nitride or silicon carbide and their compounds.

RAVI: Can you estimate the cost per square centimeter?

MAEDA: For one 10 x 10 cm sheet, I estimate 55 Japanese yen, which is around 20 or 25 cents, U.S.

FERBER: Have you tried hydrogen passivation to see if it improves the performance of the cells? The Kauffman ion engine passivation that has been reported earlier by Ravi has been very successful on EFG, for example.

MAEDA: No, I have not tried it yet.

DISCUSSION

NOTE: (W. Giessen's presentation was not received for publication.)

NARASIMHAN: Have you ever quenched a peritectic reaction by rapid solidification?

GIESSEN: I think there are a number of metastable crystalline alloy phases that form in peritectic systems, but I don't have an answer off the bat.

WARGO: I just would like to elaborate on what you said about Professor Witt's patent, and that is that it provides, with a couple of bells and Belgian whistles, the possibility of producing solar cells directly in a single step. If you can imagine a thin layer of indium on the chill, then put the semiconductor down first, then the metallization second, you can have a p-type, doped, very, very thin, layer; the semiconductor substrate material, and then finally a back-side metallization, all in a single step.

GIESSEN: Would this require that the intermediate layer be very thin, because melt spinning does not go below 10 μm?

WARGO: That is something that we have not investigated yet.

SUREK: Could you say a few words about what kind of residual stresses you expect in silicon melt-spun material?

GIESSEN: People now have been using substrates without really making a major project of relieving stress in the process. This must be a formidable issue, for which I have no numbers. Whether that is in part due to, or whether the low efficiencies are all due to small grain size, or maybe that is an additional factor, I don't know.

RIBBON GROWTH

Chairman: M. Leipold (Jet Propulsion Laboratory)

N84 28627

ORIENTATION AND MORPHOLOGY EFFECTS IN RAPID SILICON SHEET SOLIDIFICATION

T.F. Ciszek
Solar Energy Research Institute
Golden, CO USA 80401

ABSTRACT

Radial growth anisotropies and equilibrium forms of point-nucleated, dislocation-free silicon sheets spreading horizontally on the free surface of a silicon melt have been measured for (100), (110), (111), and (112) sheet planes. Sixteen mm movie photography was used to record the growth process. Qualitative Wulff surface free energy polar plots were deduced from the equilibrium shapes for each sheet plane. Analysis of the sheet edges has lead to predicted geometries for the tip shape of unidirectional, dislocation-free, horizontally grown sheets growing in various directions within the above-mentioned planes. Similar techniques were used to study polycrystalline sheets and dendrite propagation. For dendrites, growth rates on the order of 2.5 m/min and growth rate anisotropies on the order of 25 were measured.

INTRODUCTION

This work investigates the equilibrium forms or shapes of silicon sheet crystals nucleated at a small diameter and allowed to spread radially outward in all directions on a supercooled horizontal silicon melt surface. Such forms are governed by the variation of surface free energy with crystal orientation as described by the classic work of Wulff (1). Further amplification of Wulff's concepts was provided by Herring (2). In these treatments, a polar plot of specific surface free energy vs. crystal orientation (called a Wulff plot) is constructed. The distance from the origin in a particular direction is proportional to the surface free energy for the crystal orientation corresponding to that direction. In general, the plot is a three-dimensional closed surface with a number of minima and maxima. If planes perpendicular to the radius vector are imagined at each point on the closed surface, then the volume that can be reached from the origin without crossing any planes defines the equilibrium shape or form of the crystal. Since sharp minima or cusps in the polar plot have the shortest radius vectors, planes normal to the radius at these cusp positions will dominate the equilibrium shape.

Sheet crystals are approximately two-dimensional and hence a planar section through the Wulff plot coincident with the sheet surface plane is useful in describing the equilibrium shape. Detailed data for the variation of surface free energy with orientation is not available for silicon. However, it is generally acknowledged that the (111) planes have the lowest surface free energy and vestiges of these planes are responsible for the observable "growth lines" on crystals constrained to grow in a

cylindrical ingot form. The value of the surface free energy for a particular crystal plane is a function of the free bond density. This is lowest for (111) planes.

Observations of (100), (110), (111), (112) and polycrystalline sheets propagating radially from small diameter sources on a free melt surface were made by 16 mm photography. Dendrite propagation was also recorded in this manner. From the films and post-growth examination of the crystals, it was possible to deduce the idealized equilibrium polygonal shapes of the sheets and to construct qualitative Wulf plots which locate the cusp minima in the various sheet planes. In addition, information about growth rate anisotropies in the sheet planes has been obtained. From the geometry of the sheet edges, it is possible to determine the criteria which govern the tip-shape of single-crystal silicon sheets growing horizontally from a melt surface.

EXPERIMENTAL

Silicon was melted in a quartz crucible 60 mm in diameter and 25 mm high. Induction heating with a graphite susceptor was used. The susceptor was insulated by a cylindrical opaque quartz tube with 6 mm wall thickness. An inert atmosphere of argon was maintained in the 400 mm diameter by 1500 mm high growth chamber. The top of the chamber was fitted with a gate valve which allowed reseeding from a second chamber above the first. Thus, all sheet propagation studies could be done from the same melt. Sheet growth was initiated by dipping a cylindrical seed crystal of the desired orientation into the melt and growing a thin neck from the seed at 15 rpm rotation rate in order to produce a dislocation-free, small (0.5 to 1.5 mm dia.) cylindrical crystal. A sheet was then allowed to propagate radially in all directions on the melt surface by setting the vertical pulling speed to zero, dropping the RF generator power level to 94.7% of the value at which the neck was grown, and lowering the rotation rate to 1 rpm. A slow rate was used to avoid imposing a round shape on the spreading sheet. However, a non-zero rate was needed for the purpose of allowing measurements of all crystal faces on movie films of the growth. For each seed orientation, a second sheet was grown from a larger diameter (3.8 to 6.2 mm), dislocation-free, round cylindrical starting condition. Since the transformation from round to equilibrium shape occurs in a distance which is a function of initial round diameter, this allowed viewing the transformation on two different size scales.

The sheets did not grow perfectly flat and tended to have a slightly convex bottom since some growth occurred downward into the melt while the sheets were spreading radially. The radial growth rate of the sheets as they approached their equilibrium shapes was typically in the range 7 to 15 mm/min. for the 5.3% power reductions used in these studies. At some point in the growth, icing from the crucible walls moved radially inward to close proximity with the spreading sheets. The sheets were removed from the melt at this time by quickly pulling the seed upward. The observations of dendrite propagation were made by nucleating dendrites at the crucible walls as large reductions (30-40%) were made in the RF generator power.

Records of the sheet and dendrite growth experiments were made with 16 mm movie photography. The camera was located outside a window of the growth chamber and a polished silicon mirror was used to direct light rays from the growth area to the camera as shown in Fig. 1. A filming speed of 10 frames/sec. was used in the sheet growth studies. The typical growth duration was 140 sec. and since a rotation rate of 1 rpm was used, the crystal revolved just over two times during the filming. This allowed any particular diameter of the growing sheet to be measured 5 times. Measurements were made of the distance between parallel flat faces and of the diameters of the faster growing diagonally opposed regions located angularly between two successive flat faces. Figure 2 is the view the camera sees. In this case, a (110) sheet growing at its equilibrium shape is shown. The measurements were made off the film by passing it under a low-power (8-40X) microscope with a reticle placed over the film. A 50 frames/sec. filming rate was used for the dendrite studies, since the growth rate was much faster than for sheets.

RESULTS AND DISCUSSION

Equilibrium Sheet Shapes

The equilibrium shape of a (100) dislocation-free silicon sheet is a square. Fig. 3a shows this form for a sheet grown from a 1.2 mm dia. round starting shape. The transformation to the square shape occurs in about 3-4 seed diameters and thus the sheet is square at a small size. The idealized square shape is shown in Fig. 3b. The edges are in the four $\langle 011 \rangle$ directions, and the corners lie along the four $\langle 001 \rangle$ directions. The Wulff plot in the (100) plane is expected to have minima at the four (011) planes normal to the sheet surface and larger values in other directions. This is qualitatively shown by the curved, 4-lobed figure surrounding the equilibrium shape.

Sheets nucleated in the (111) plane transform from a round shape to hexagonal with equal 120 degree angles (Fig. 4a). The sides of the hexagonal shape are in $\langle \bar{1}\bar{1}2 \rangle$ radial directions, while the corners are in $\langle \bar{1}10 \rangle$ directions. The Wulff plot is drawn with 6 cusps on the $(\bar{1}\bar{1}2)$ planes bounding the idealized sheet shape in Fig. 4b.

At first glance, the equilibrium shape of (110) sheets also appears to be a regular hexagon (Fig. 5a). However, closer examination shows that there is less symmetry in the (110) shape. Four of the six polygonal sides lie in $\langle \bar{1}11 \rangle$ directions and the angle between two such adjacent sides is only 109.471 degrees as shown in figure 5b. The corners between two such sides lie in $[\bar{1}10]$ and $[1\bar{1}0]$ directions. Two sides of the polygonal shape are opposite each other and in the [001] and $[00\bar{1}]$ directions. These sides make an angle of 125.264 degrees with the $(\bar{1}11)$ type sides. Minima occur both on (001) type planes and on $(\bar{1}11)$ type planes in the qualitative Wulff plot.

The (112) plane sheets are observed to also have six sides in the equilibrium shape as can be seen in the sheet crystal of Fig. 6a. However,

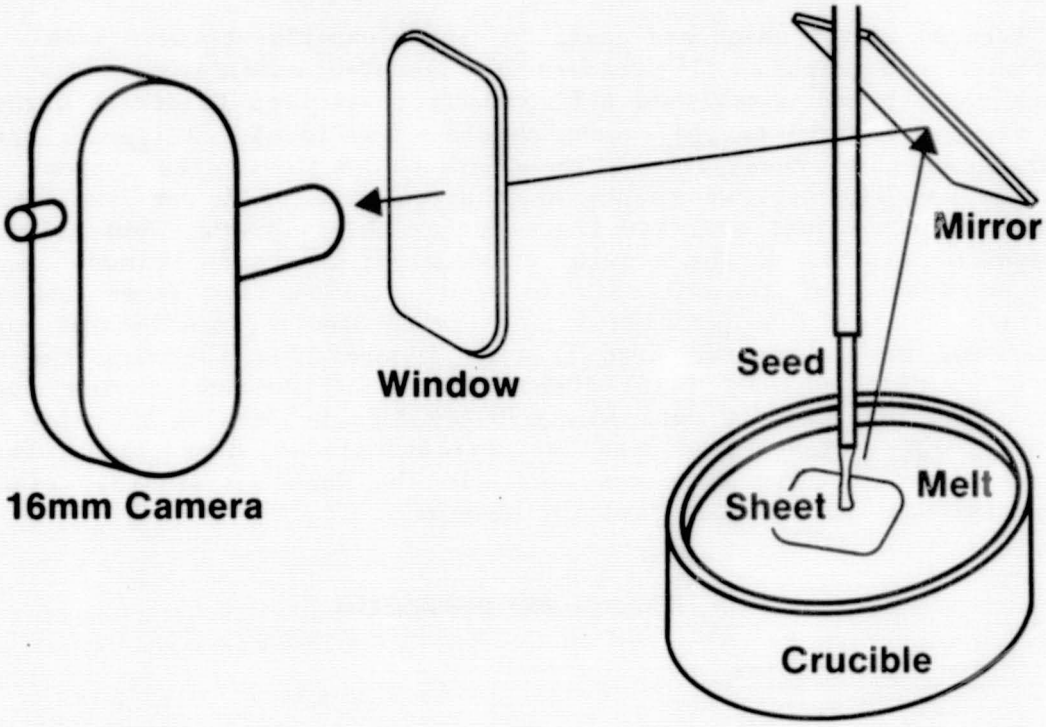

1. Schematic of arrangement used to film radially growing sheets.

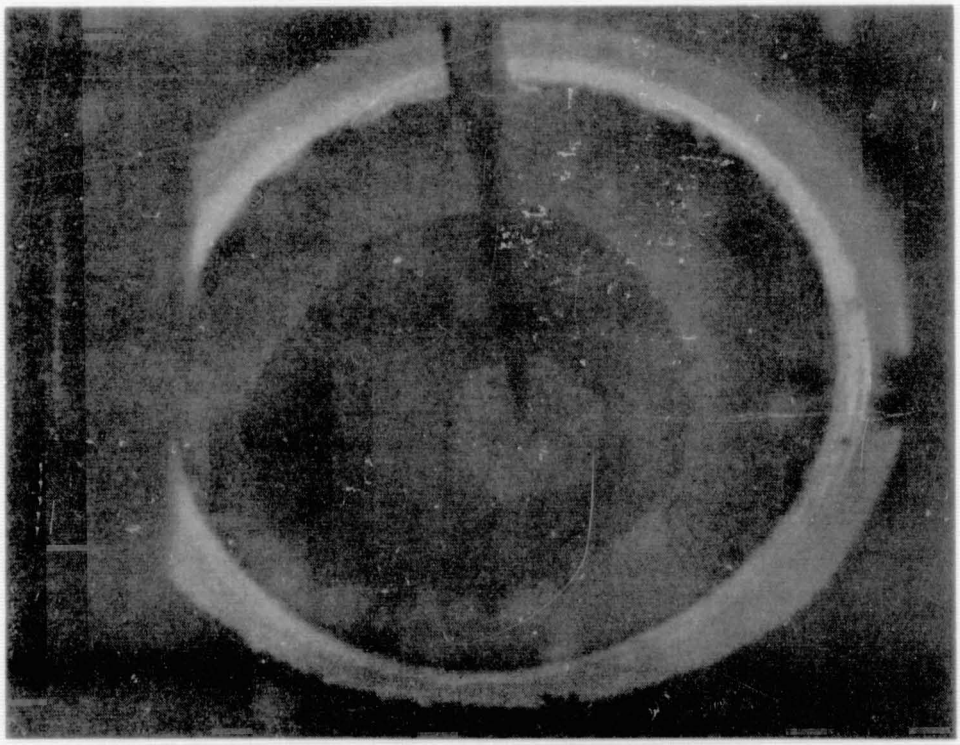

2. One 16 mm frame from a film showing the equilibrium shape of a (110) sheet.

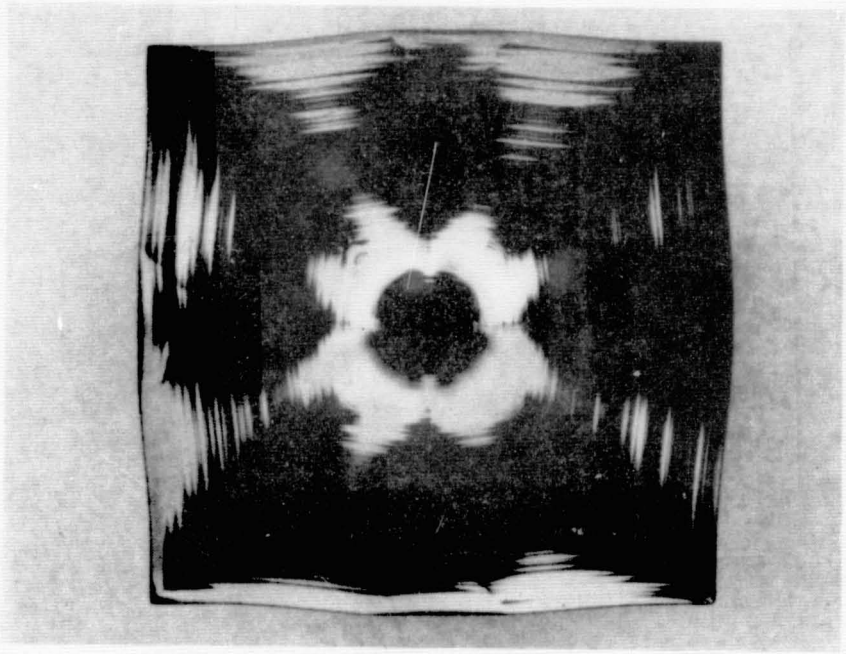

3.a) Final shape of a (100) sheet.

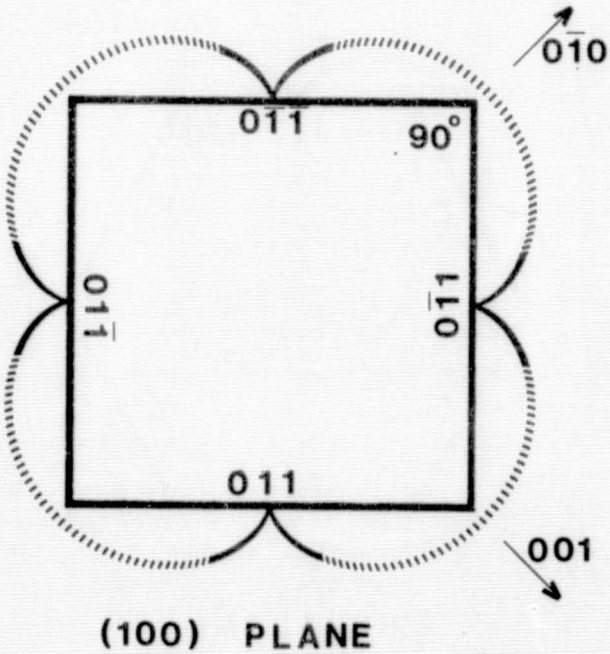

3.b) Idealized equilibrium form and qualitative Wulff plot for a (100) sheet.

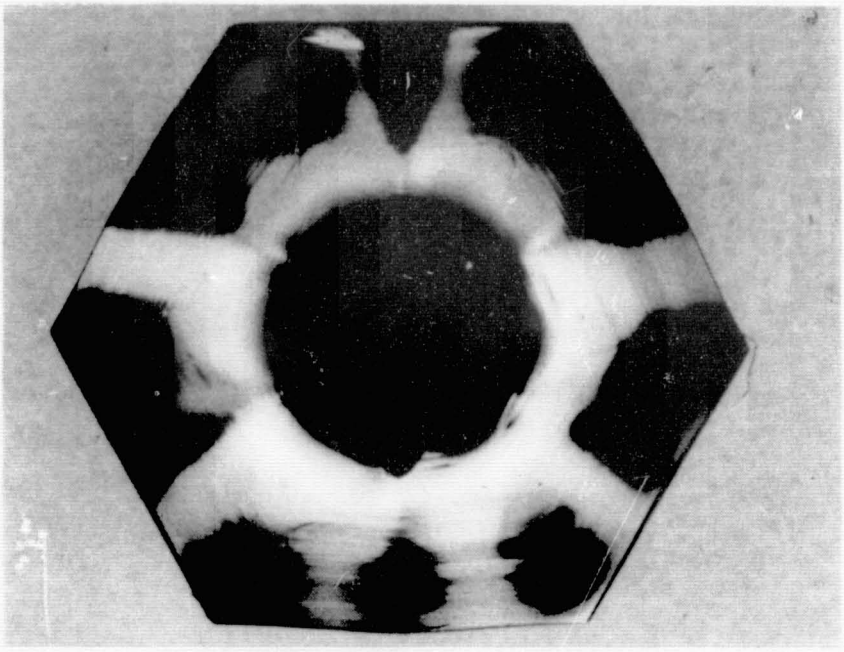

4.a) Final shape of a (111) sheet

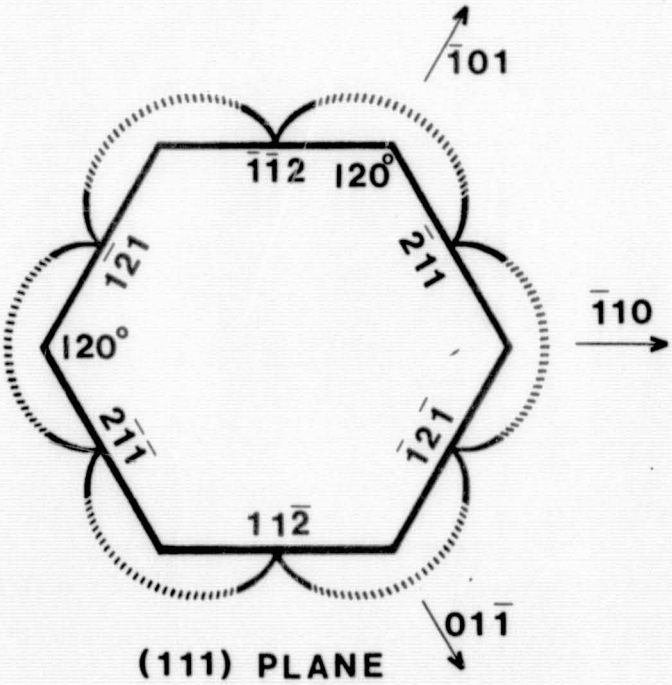

4.b) Idealized equilibrium form and qualitative Wulff plot for a (111) sheet

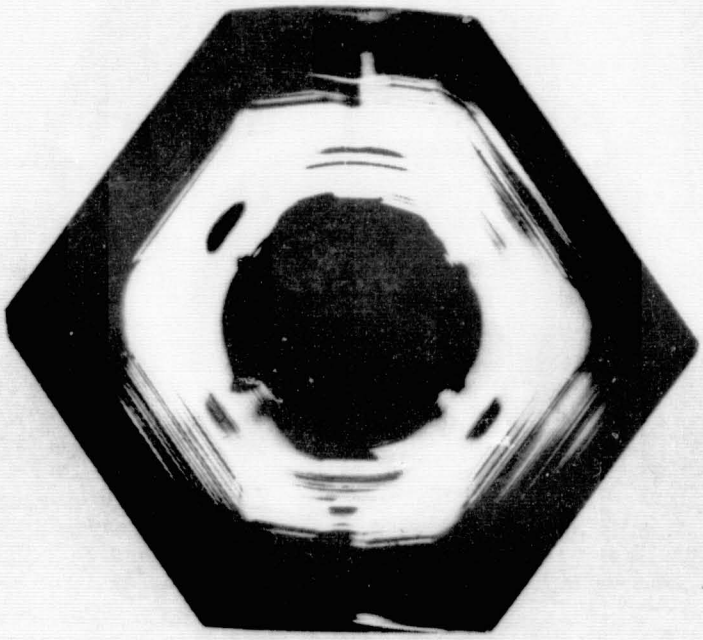

5.a) Final shape of a (110) sheet

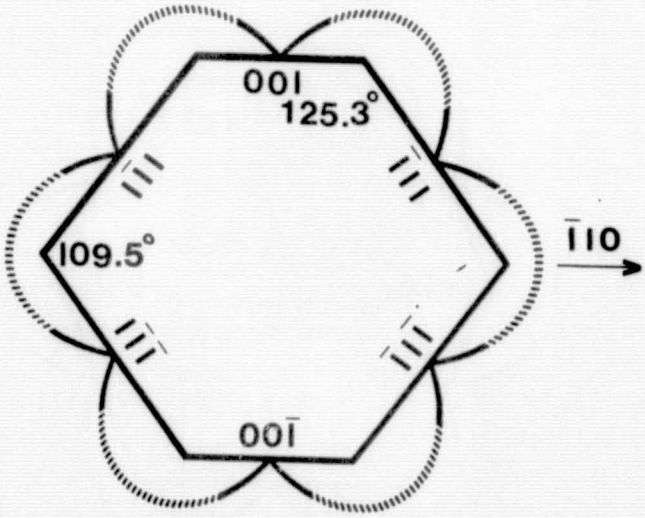

(110) PLANE

5.b) Idealized equilibrium form and qualitative Wulff plot for a (110) sheet

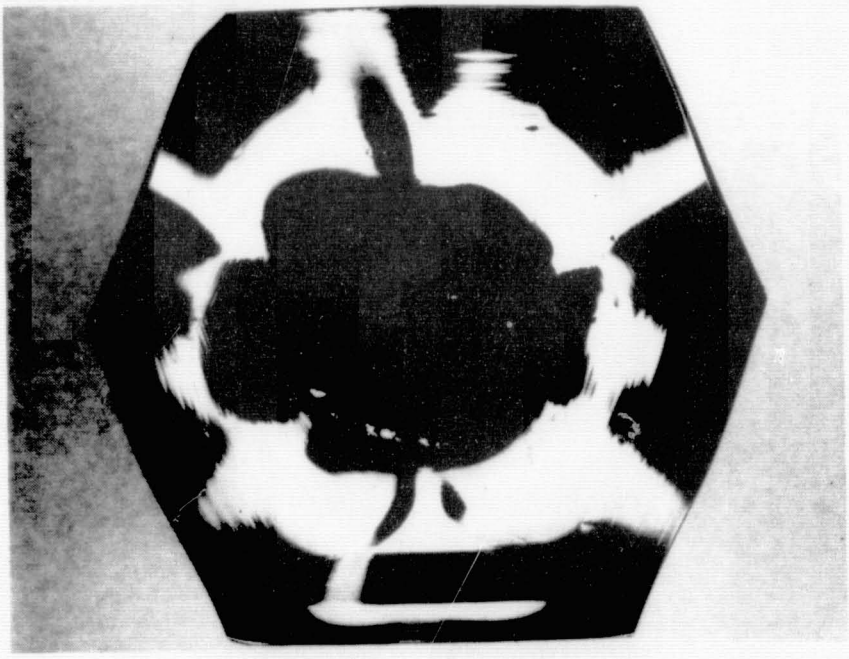

6.a) Final shape of a (112) sheet

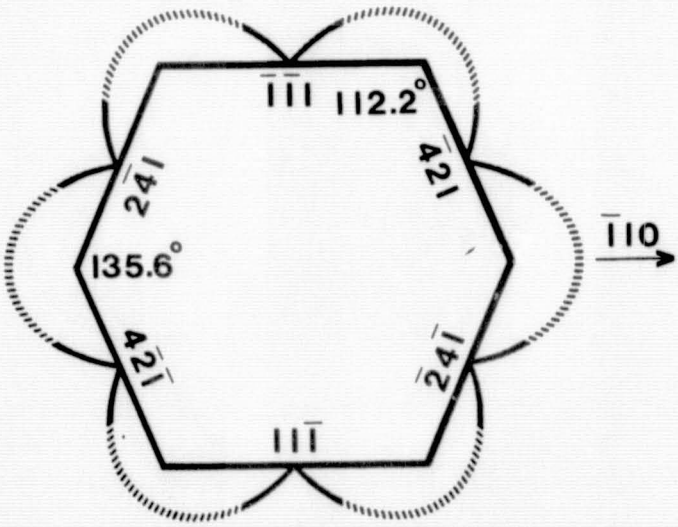

(112) PLANE

6.b) Idealized equilibrium form and qualitative Wulff plot for a (112) sheet

the bounding faces and included angles are different from both the (111) and (110) sheet cases. Two opposite sides are in $\langle\bar{1}\bar{1}1\rangle$ directions. The other four sides correspond to Wulff plot cusps on $(2\bar{4}1)$ type planes. Two adjacent sides of this type make an angle of 135.585 degrees with each other. The corners between these sides are in $[\bar{1}10]$ and $[1\bar{1}0]$ directions. The angle between $(2\bar{4}1)$ and $(\bar{1}\bar{1}1)$ type sides is 112.208 degrees. The deduced Wulff plot shows minima on both $(\bar{1}\bar{1}1)$ and $(2\bar{4}1)$ type planes (Fig. 6b).

The Wulff plots in figures 3-6 are only qualitative. It is reasonably certain that minima occur where they are shown. Whether the minima are sharp cusps or only shallow valleys is not known. There is more uncertainty about the non-minima portions of the plots. Thus, they are shown as dotted lines in the figures. Angles observed on the sheet crystals agree very well with the angles on the idealized equilibrium shapes in the figures. Since no special effort was made to reduce thermal asymmetry in the hot zone, the sheet crystal forms were sometimes asymmetrical. That is, the distance from the seed to two equivalent flat edges was not always equal.

Sheet Edge Geometries

A strong (111) faceting effect was observed on the edge regions of the sheets due largely to the fact that dislocation-free growth was employed for the sheet experiments. In the absence of dislocations, nucleation of new growth is more difficult and larger levels of supercooling arise at the leading edges of the growth front. Faceting accompanies this situation. One (100) sheet was grown from a dislocated starting configuration. Two effects were noted with this sheet. The edge faceting was much less pronounced and in fact was nearly absent. Also, the equilibrium square shape did not completely form, at least not in the growth times available in our experimental set-up. The corners of the sheet remained well rounded.

The edge faceting in dislocation-free sheets always appeared on (111) planes. An example is depicted in the photograph of Figure 7 which shows a (111) sheet mounted in wax to allow viewing of the edge. The central edge facet in the photograph makes a 70.5 degree acute angle with the top of the sheet. It is located in a $\langle 2\bar{1}\bar{1}\rangle$ type direction from the seed. To the left and right of this facet are other edge facets which make a 109.5 degree obtuse angle with the sheet's top surface. These are in $\langle\bar{2}11\rangle$ directions from the seed. All-told, there are three obtuse facets and three acute facets alternating around the sheet edge. Careful scrutiny of Fig. 7 also shows a (111) facet on the sheet top adjacent to the central edge facet. There are 6 of these, one adjacent to each edge facet.

These observations have implications for high-perfection sheet growth solid/liquid interfaces, both in vertical and horizontal modes. It is possible to predict, for example, the sheet tip geometries for a large number of growth orientations from the observations on radially spreading sheets. I've done this for the horizontal, large-area solid/liquid interface growth geometry. Figure 8 shows the expected tip geometries for (111) dislocation-free sheets growing in the $\langle 2\bar{1}\bar{1}\rangle$ and $\langle\bar{2}11\rangle$ type directions,

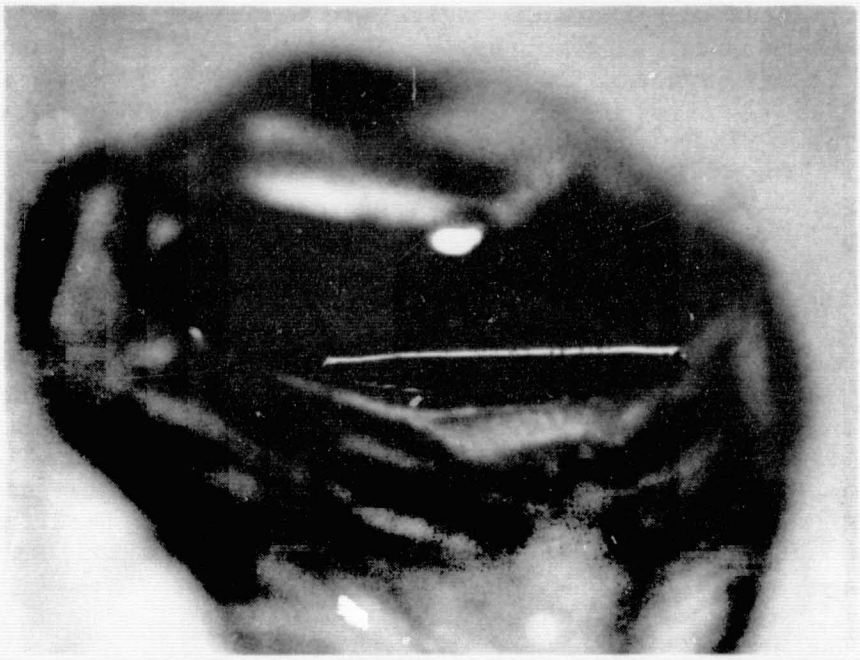

7. Edge facets on a (111) dislocation-free sheet mounted in wax.

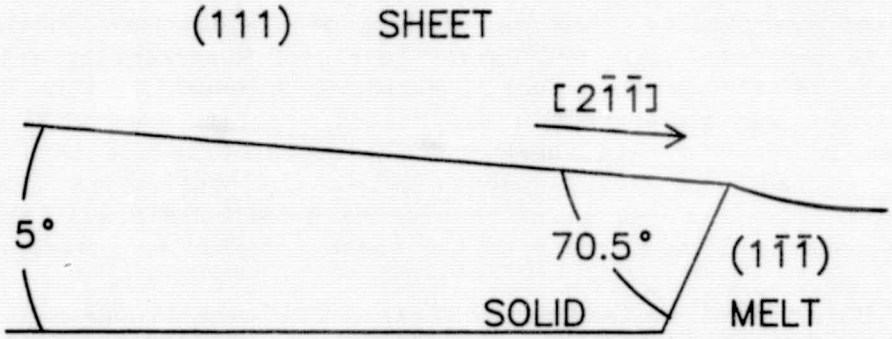

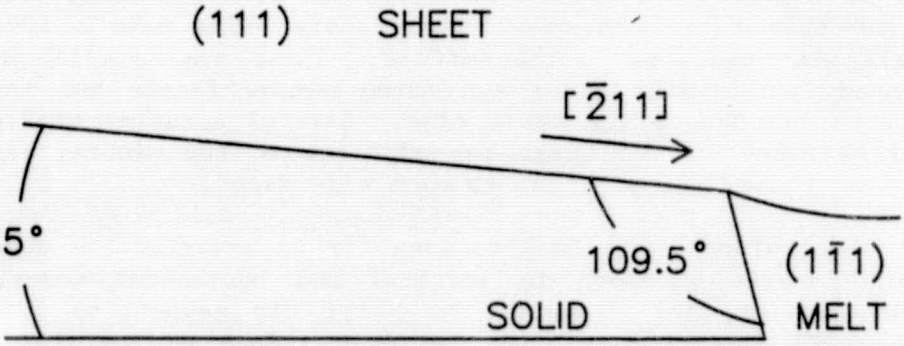

8. Predicted tip geometries for horizontally grown (111) sheets pulled in the $\langle\bar{2}11\rangle$ and $\langle 2\bar{1}\bar{1}\rangle$ directions.

with a 5 degree pulling angle. Note the retrograde tip angle for $\langle\bar{2}11\rangle$ growth.

For (100) sheets, four (111) edge facets appear in $\langle 011\rangle$ directions from the seed. All make 54.7 degree acute angles with the top of the sheet. The expected tip geometry for dislocation-free (100) silicon sheets growing in one of these four directions is given in Figure 9.

The edges of (110) sheets displayed two types of (111) facets. In the four $\langle 1\bar{1}\bar{1}\rangle$ type directions, a 90 degree facet with respect to the sheet plane was found. In the two $\langle 001\rangle$ directions, the facet made a 35.3 degree acute angle with the sheet top. The 144.7 degree obtuse (111) facets were not observed. Predicted sheet tip geometries for horizontal growth are drawn in Fig. 10.

The greatest variety of edge facets was seen in (112) sheets. Figure 11 shows these in the way they would define the tip geometries of horizontal sheets. In the $[11\bar{1}]$ direction, a facet at 90 degrees to the sheet plane was seen, while in the $[\bar{1}\bar{1}1]$ direction two facets appeared. One was at 90 degrees to the sheet plane and a second was at 19.5 degrees. Fig. 12 is a photograph of a portion of the underside of a (112) sheet showing the large-area 19.5 degree facet. The $(\bar{1}\bar{1}1)$ edge of the sheet is at the top in the photograph, and the facet at this edge is also discernable in the photograph. These two facets meet at an included angle of 109.5 degrees. In the $\langle 4\bar{2}\bar{1}\rangle$ directions, acute angle facets of 61.9 degrees were seen, while in the $\langle\bar{4}21\rangle$ directions, the angles were retrograde with a 118.1 degree value.

Growth Rate Anisotropies

As the radially spreading sheets described in this study evolve from the round initial geometry to the polygonal equilibrium shape, it is evident that the growth rates in the directions toward the polygon corners must be greater than the growth rates in directions toward the flat polygon sides. Neither of the rates are constant with time. Initially, the growth rate is slow, since the melt temperature does not respond immediately to the drop in RF generator power. The rate increases slowly at first, and then more rapidly, as the expanding top surface of the solid, with its higher emissivity, becomes an increasingly more effective heat radiator. The slope of a size vs time plot for a particular direction from the seed, at any given time, is the growth rate in that direction at that time. The ratio between rates in different directions is the ratio of slopes of the two size vs time curves at the same instant of time.

Fig. 13 shows the size of (100) sheets along the $\langle 011\rangle$ and $\langle 001\rangle$ directions as a function of time for two different dislocation-free starting diameters, 1.2 mm and 6.2 mm. In both cases, all $\langle 011\rangle$ directions were considered to be equivalent and all $\langle 001\rangle$ directions were considered to be equivalent. Thus, four measurements for each set of directions was made for each revolution of the crystal. A second order polynomial fit was made to the data read from the film in all cases. The small (100) sheet quickly became square and the ratio of slopes in the $\langle 011\rangle$ and $\langle 001\rangle$ directions,

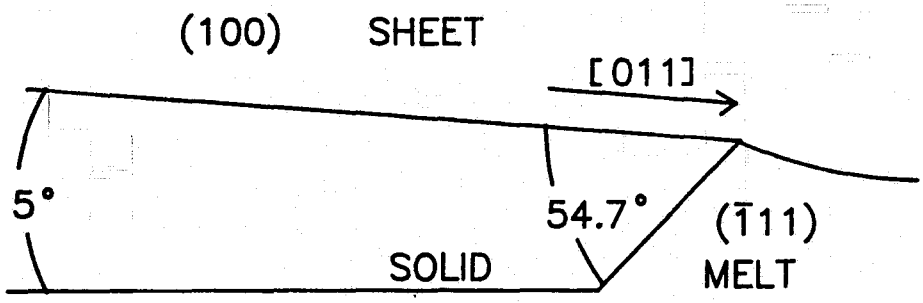

9. Predicted tip geometry for horizontal (100) sheets growing in the <011> directions.

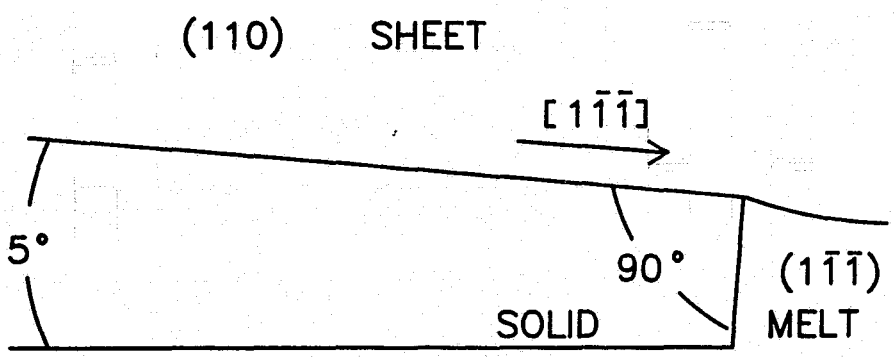

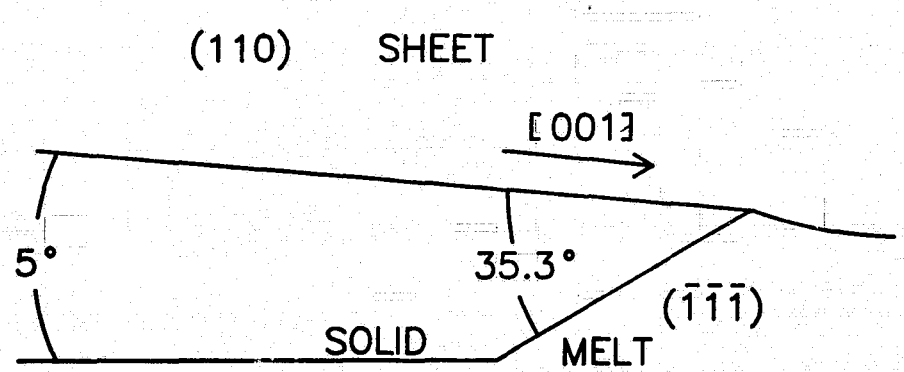

10. Predicted tip geometries for horizontal (110) sheets growing in the <1$\bar{1}\bar{1}$> and <001> directions.

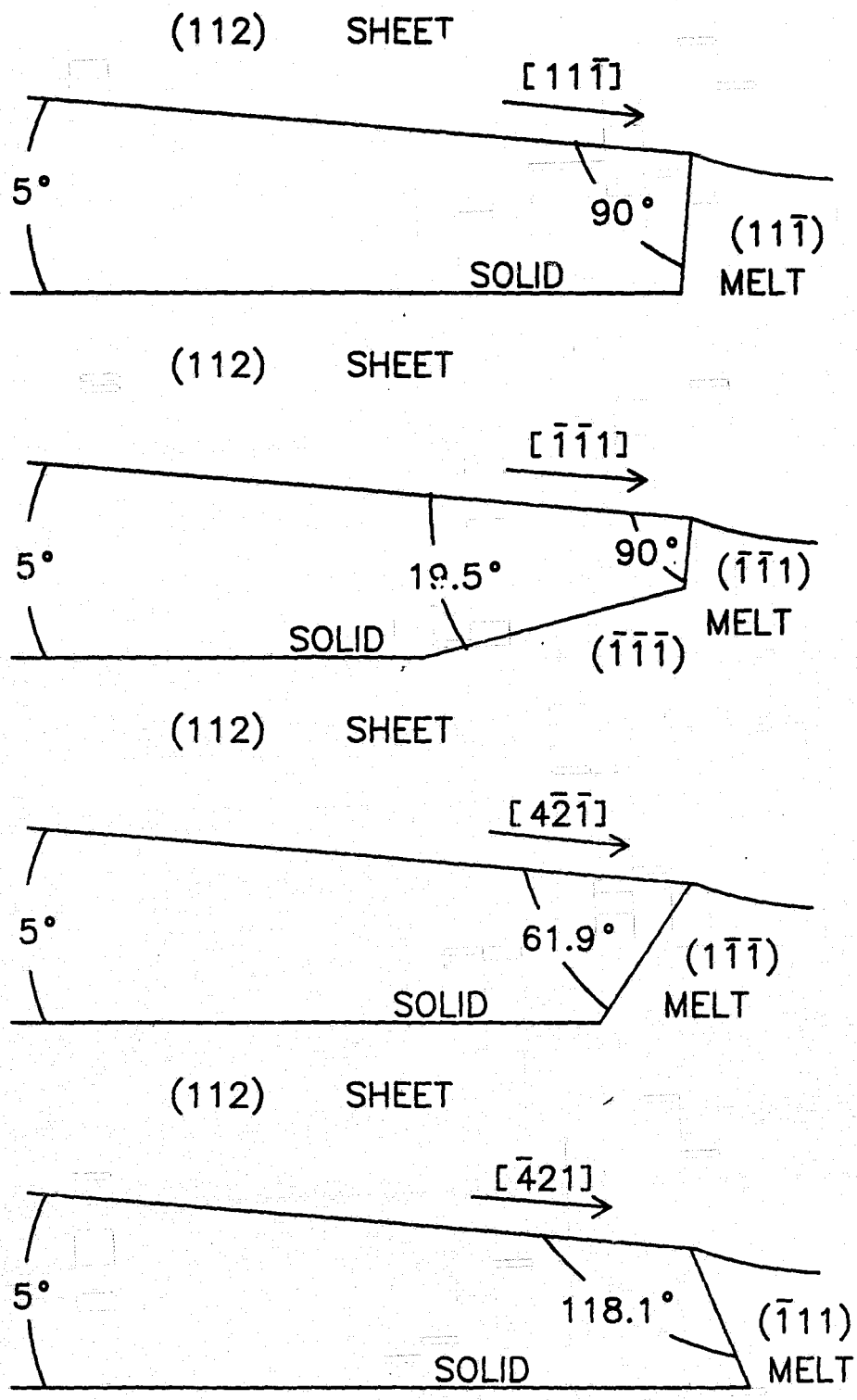

11. Predicted tip geometries for (112) sheets growing in the [11$\bar{1}$], [$\bar{1}\bar{1}$1], <4$\bar{2}\bar{1}$>, and <$\bar{4}$21> directions.

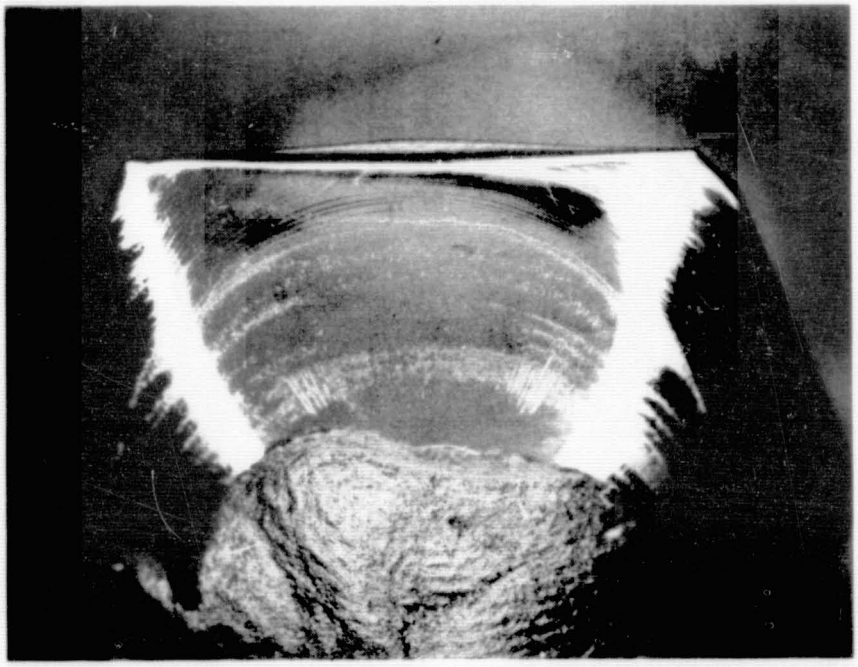

12. Wax mounted (112) sheet showing a large-area ($\bar{1}\bar{1}\bar{1}$) facet on the underside meeting a ($\bar{1}\bar{1}1$) 90° edge facet.

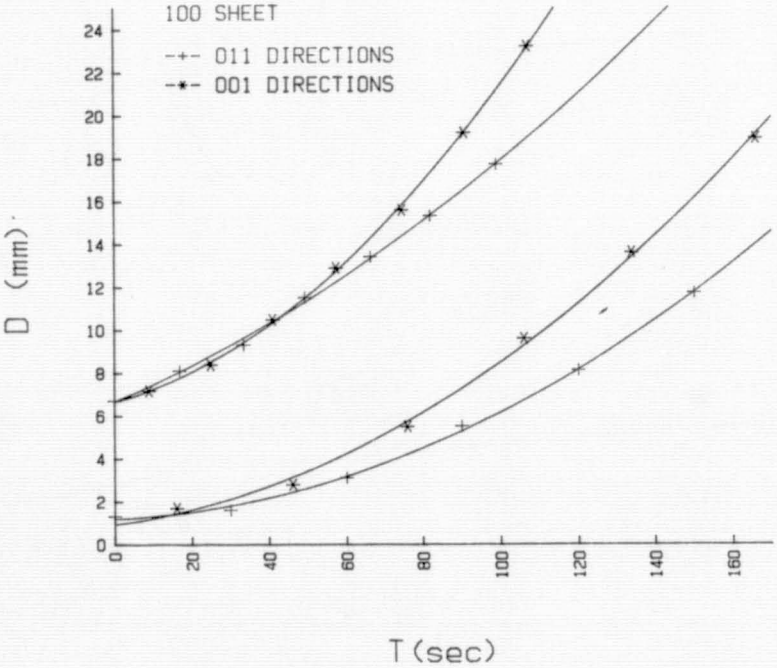

13. Size vs. time for (100) sheets of two different starting diameters.

for large times, is expected to be the geometrically limited value 0.707. The measured growth rate ratios, from the two lower curves, is 0.72. For the larger starting diameter, the sheet had not yet become square by the end of the experiment. Therefore, the rate ratio from the upper two curves is not geometrically limited, and is representative of the true growth rate anisotropy between the <011> and <001> directions. The measured ratio from the upper two curves is 0.62. A growth model for growth rate in the <011> directions being 0.6 times the growth rate in any other directions is shown in Fig. 14. The transformation from round to square is seen to happen in about 3 seed diameters.

Similar behavior, but generally with less anisotropy, was seen for the other sheet planes. In all cases the growth rate in directions toward the cusps in the Wulff plots was lower than the rate in directions toward the lobes. Another example is given in figure 15 where the size of a (110) sheet in the <001> and <1$\bar{1}$0> directions is shown as a function of time. The <001> growth rate is 0.83 as large as the <1$\bar{1}$0> growth rate. For (111) sheets, the <$\bar{1}\bar{1}$2> growth rate was 0.77 as large as the <1$\bar{1}$0> growth rate. Ratios in the vicinity of 0.8 were also seen for (112) sheets.

Polycrystalline and Dendritic Growth

Under the same conditions used in the dislocation-free sheet studies, some polycrystalline seeds were used to initiate sheet growth. The seeds were cut along the diameter of semiconductor-grade, chemical-vapor deposited poly rods. At small sheet diameters, the growth was fairly uniform in all radial directions (see left side of Fig. 16). However, at larger sizes, the effects of orientation-dependent growth rates became very pronounced. This can be observed in the sheets shown in the middle and right sections of Fig. 16. Especially fast growing protrusions were dendritic in nature, like the one at the bottom right in Fig. 16.

An enlarged view of a dendritic protrusion is given in the photomicrograph of Fig. 17. The dendrite is single crystalline on either side of the horizontal spine. The surface features thus are not crystallographic in nature but are probably growth instabilities of constitutional supercooling origin. The dendrite does undergo a change in surface orientation at the spine region. The region above the spine has a surface plane within 2 degrees of (111) as shown by the electron channeling pattern of Fig. 18a. The region below the spine has a surface plane near (115) as shown in Fig. 18b. This indicates that the spine region represents the emergence of an oblique (111) type twin plane making an angle of about 20 degrees with the dendrite surface plane.

Dendrite propagation is extremely rapid in silicon. Sixteen mm films of deliberately nucleated dendrites were measured for growth rate analysis. Different dendrites propagated at different rates due to varying local conditions in the melt (proximity to other dendrites, for example). Figure 19 depicts a representative case for the increase in dendrite length and width with time. Length increases very fast at first, at rates around 2.5 m/min., and then slows as other dendrites crowd the melt and liberate

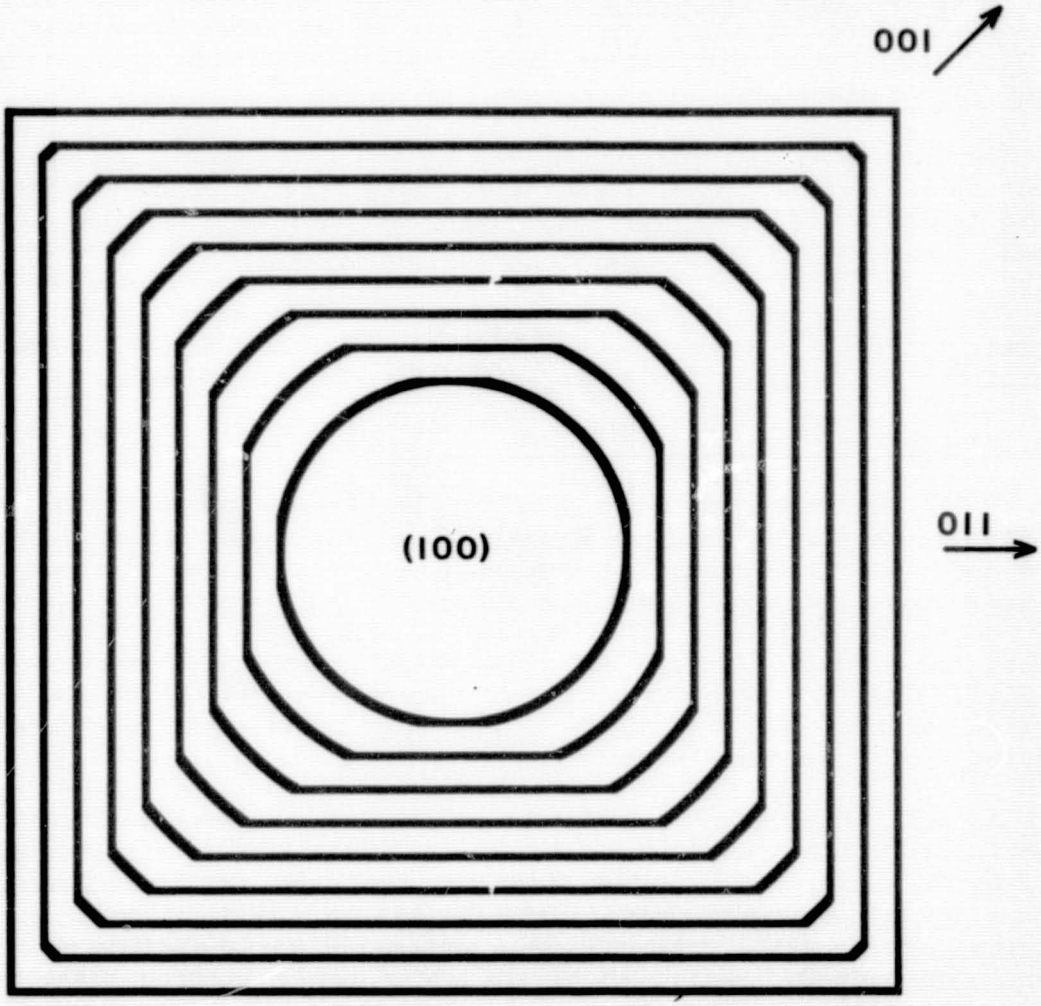

14. (100) sheet growth model for growth rate in <110> directions equal to 0.6 times the rate in all other directions.

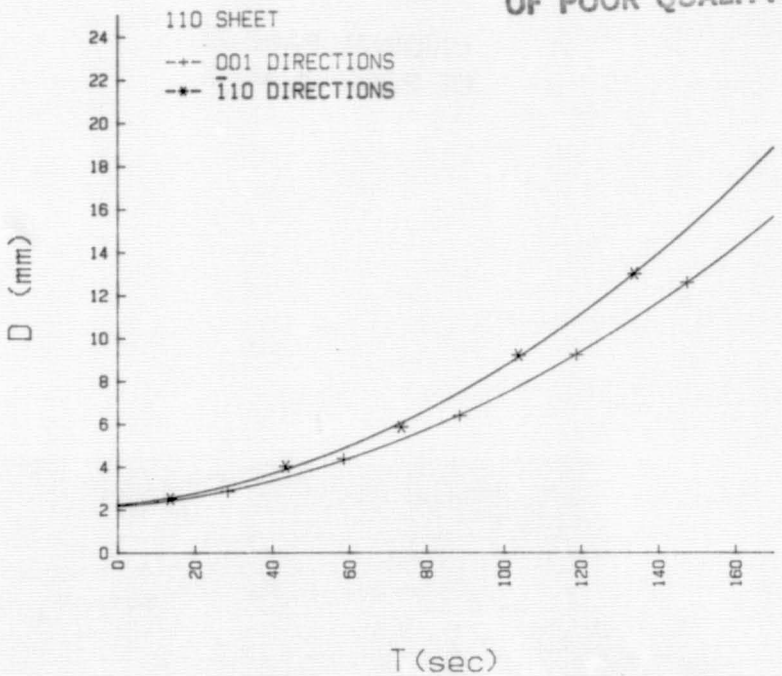

15. Size vs. time for two different growth directions in the (110) sheet plane.

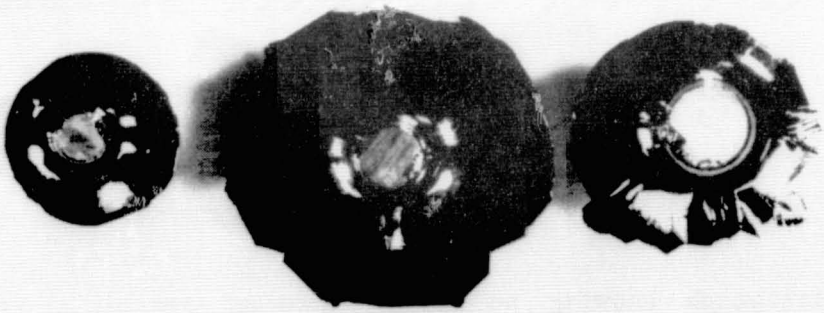

16. Three silicon sheets nucleated from a polycrystalline seed.

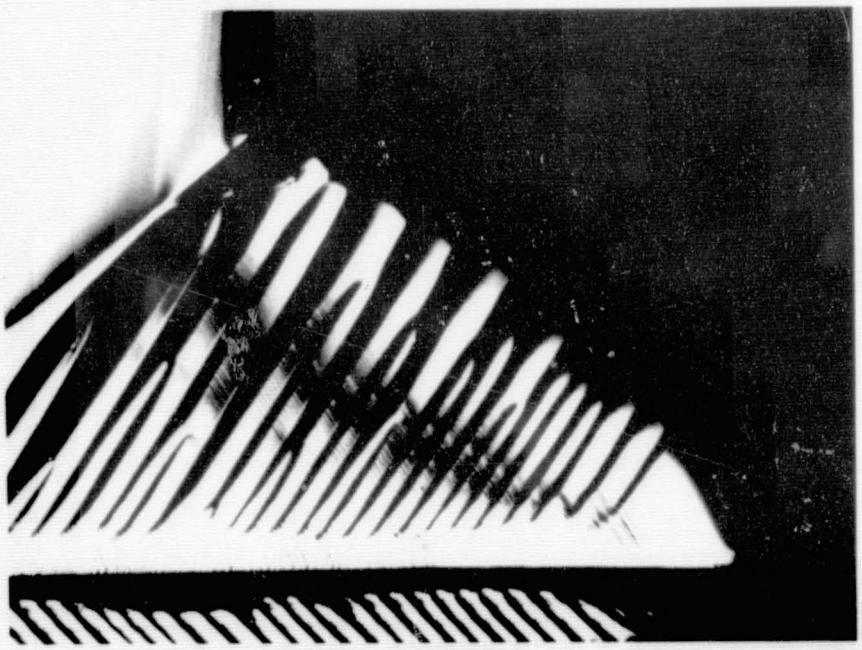

17. Photomicrograph showing an early stage of dendritic growth from a radially expanding polycrystalline sheet. The dendrite protrudes 1.9 mm beyond the adjacent sheet.

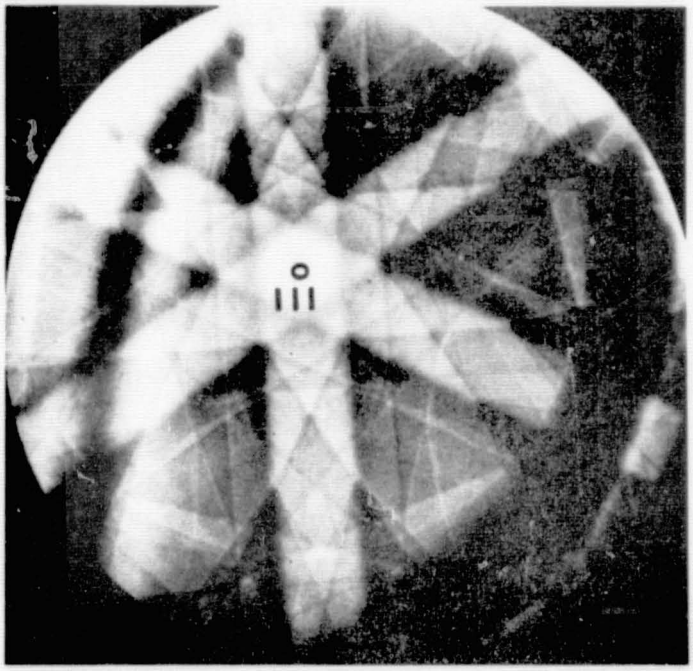

18.a) Electron channeling pattern of region above dendrite spine in Fig. 17.

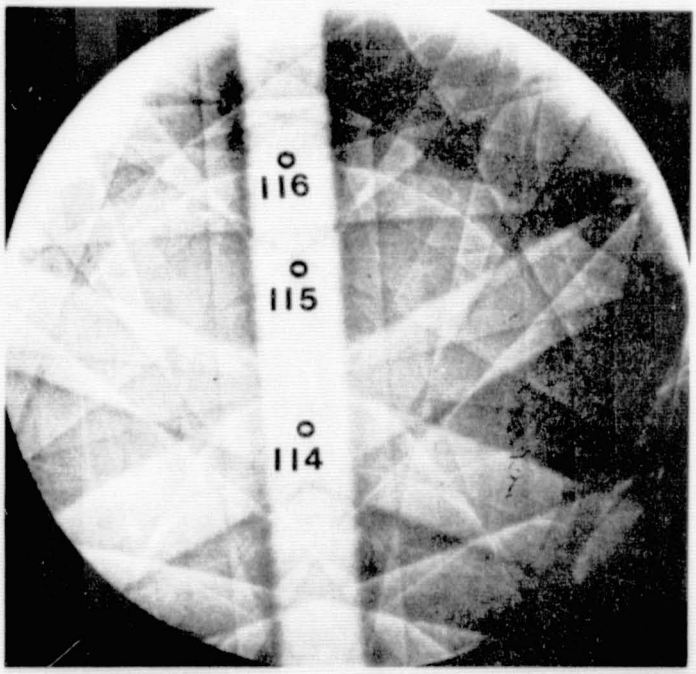

18.b) Electron channeling pattern of region below dendrite spine in Fig. 17.

ORIGINAL PAGE IS
OF POOR QUALITY

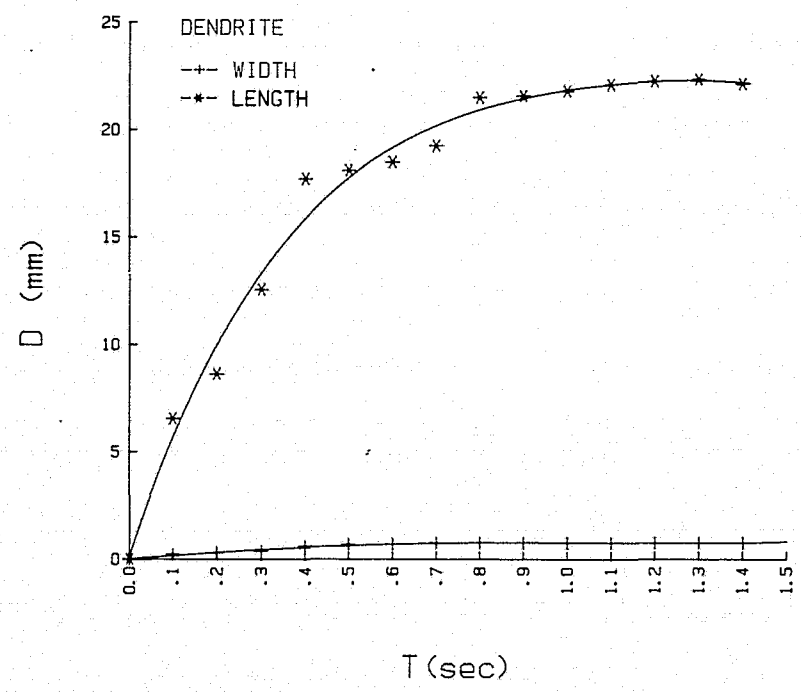

19. An example of the increase in length and width of one dendrite as a function of time.

heat of fusion. The width, on the other hand, increases at a rate which is about 25 times slower.

SUMMARY AND CONCLUSIONS

The technique of studying rapid silicon sheet growth via free spreading of point-nucleated sheets on a supercooled horizontal melt surface has yielded a large amount of information about equilibrium forms, solid/liquid interface sheet tip morphologies, qualitative Wulff surface free energy polar plots, and growth rate anisotropies. The method is versatile in that both very high perfection (dislocation-free) effects and less structured (polycrystalline and dendritic) effects can be studied.

The low surface free energy (111) planes dominate the sheet tip geometry at the solid/liquid interface, determine the equilibrium shape of radially growing sheet crystals (through their intersection with the sheet plane), and contribute to growth rate anisotropies due to the relative difficulty of new growth nucleation on the low free bond density (111) surface. They also play a determining role in fast dendritic growth by virtue of the high free bond density associated with re-entrant edges at a (111) twin boundary. Earlier work on edge-supported pulling of silicon sheets (3) showed that (111) twin plans can block the spreading of spurious random grains. A similar mechanism has recently been found to be important in stabilizing the crystal structure of horizontally grown sheets. In dendritic web growth, (111) twin planes are key elements of the growth process and the (111) web surface is of very high quality. The equilibrium structure of long multicrystalline silicon sheets is dominated by longitudinal grains with (111) boundaries and near <110> surface normals. In summary, the properties of the (111) surface in silicon are of major importance for sheet crystal growth.

ACKNOWLEDGMENTS

Technical assistance by a number of individuals is deeply appreciated. M. Schietzelt helped in the crystal growth experiments, the 16 mm film analysis, and the preparation of figures for the manuscript. J. Hurd also assisted in the film measurements. R. Matson contributed the electron channeling measurements. Support for this work was provided by the U.S. Dept. of Energy partially through SERI and partially through JPL.

REFERENCES

1. Wulff, G., Z. Krist. 34, 449 (1901).

2. Herring, C., Phys. Rev. 82, 87 (1951).

3. Ciszek, T.F., and Hurd, J.L., Proc. of Symp. Electronic and Optical Properties of Polycrystalline or Impure Semiconductors and Novel Silicon Growth Methods, K.V. Ravi and B. O'Mara (eds.), The Electrochemical Society, Inc., Pennington, 213 (1980).

DISCUSSION

SEKERKA: Those are some interesting shapes and experiments, but I have to take strong issue with the use of equilibrium forms or Wulff shapes associated with those. I think these are growth forms and haven't much to do with equilibrium forms except by accident. The equilibrium forms would be dictated by a minimization of free energy at constant volume and would only be obtainable, generally, for very small particles held carefully at equilibrium. I certainly admit that you get faceted sorts of shapes but I think those are definitely growth facets and what you are measuring has to do with an anisotropy of growth rate and very little except by accident with an anisotropy of surface tension or a Gibbs-Wulff construction.

CISZEK: What do we know about the variation of surface free energy in silicon as a function of orientation?

SEKERKA: I don't know whether there has been much in terms of studies there or not, but you would not study it in a growth configuration like that. I think you would have to study it in a steady state, and probably in an equilibrium configuration with small particles.

CISZEK: I am just taking the Wulff theorem definition verbatim.

SEKERKA: I just want to remind you, the Wulff definition pertains to equilibrium and to surface energy minimization, and this system is not doing that by any stretch of the imagination.

CISZEK: For what reasons would you say it is not doing that? Because it is too macroscopic?

SEKERKA: It is too large, too macroscopic, it is growing very rapidly, it has all kinds of secondary structure and interference.

GLICKSMAN: I have done some equilibrium droplet shape measurements on a few systems where, in fact, you can obtain surface-energy anisotropy on droplets equilibrated with a crystal, which is just the inverse experiment to what you thought you were doing here, obtaining equilibrium shape of crystal in contact with the melt. It turns out the equilibration time is generally related to the rearrangement of this object. It is at a constant volume by trapping a droplet inside of a single crystal, as you felt you were trapping a single crystal inside of a liquid. The equilibration time is related to the chemical potential differences that are established when the body is out of equilibrium to the mass rearrangement excited by that chemical potential difference. The chemical potential difference generally is quite small, on the order of a few percent of the mean surface energy, and if the maximum distance is on the order of a millimeter at most, your equilibration times would become essentially infinite insofar as an observation time goes, even with droplets in the submillimeter range. The equilibration times are often on the order of an hour. So you can imagine, for anything of the size of the crystal forming those shapes as quickly as your crystals did, there would

be no opportunity for the different parts of the crystal to communicate with itself through those very small chemical potential differences, which are reflecting the out-of-equilibrium form. So, in fact, I believe what you are observing is a kinetic shape due to the particular growth anisotropy and shape. There is very little relationship to the so-called equilibrium shape.

RAVISHANKAR: Can you comment on what the melt depth was and how the growth rate in the direction of the depth of the melt compared with the spreading growth rate?

CISZEK: The melt depth was about 22 millimeters. The melt diameter was about 60 millimeters, and sheets typically would be about 3 millimeters thick in the middle if they were 1 millimeter thick at the edges.

RAVISHANKAR: What effect would the rotation rate have on the growth rate?

CISZEK: What little we tried with rotation rate was that rotation rate, if it were very fast, would tend to round the hexagonal structure, or the pointed structure, but we saw that rates on the order of one to one-half rpm did not seem to interfere with reaching that equilibrium form.

RAVISHANKAR: Was the crucible rotating?

CISZEK: The crucible was not rotating, just the crystal.

WILCOX: About 15 years ago, the French did a study on kinetic versus equilibrium shapes in alkali halides in water, where they trapped tiny drops of supersaturated solution in Canada balsam and made a very nice time-lapse movie. There, very often, you got the growth forms that slowly transformed to equilibrium shapes, and you could see very clearly that the one had nothing to do with the other, and the time was on the order of hours and even days. This is just to back up what they [Sekerka and Glicksman] were saying.

CISZEK: I would still be interested to know what the variation of surface free energy is in the silicon system. I know it would take a different experiment, but I think it would be minimum where I am saying it is minimum.

FAN: In your experiments, wasn't the (110) the slowest-growing facet? Or was it (111)?

CISZEK: In the growth planes I studied, the anisotropy manifested itself most in the (100) plane but the slow growth was due to an oblique (111) facet in the <110> direction. It's the (111) faceting that is dominating all of this.

LEIPOLD: Is there any way you can bracket the magnitude of the temperature gradient?

CISZEK: No, I didn't really make any attempt to measure the temperature gradient, and as you can see, the growth rates are not constant as a

function of time. It was all done the same. In other words, the temperature drop for all the things I am showing was the same in the melt, but we didn't measure it at this stage. We plan to do that in the future. The growth rate as a function of time is at first a very slow growth as the melt temperature is responding to the drop in our generator power, and then as the area of the sheet increases, and more radiation occurs from the sheet surface, the growth rate is accelerated. It would be a hard experiment to keep constant.

N84 28628

SILICON FOILS GROWN BY INTERFACE-CONTROLLED CRYSTALLISATION

D. Helmreich
Heliotronic GmbH
D-8263 Burghausen
West-Germany

During interface-controlled crystallization (ICC) the chance to accelerate the removal of crystallization heat is the basis for high pulling rates of about 100 mm/min. The forced heat flow from the extended crystallization front to a cooling ramp is controlled by a lubricating melt film which also influences the crystallization behaviour by suppressing nucleation centers.

The basic principles of this foil casting technique are presented and the influences of process parameters on the morphology of prepared silicon foils are demonstrated. Three different types of crystalline structure have been found in silicon foils grown by ICC technique: dendritic, coarse granular and monocrystalline with (111) <211> orientation. The criteria for their appearance are discussed in the light of process variables.

INTRODUCTION

Two basic requirements for fast sheet growth are 1) extension of solid/liquid interface and 2) intensification of crystallization heat removal by aid of heat conduction instead of radiation from the free surface. About 50 W/cm^2 are radiated from a crystallizing silicon melt at a temperature difference of about 1400 ^oC; a temperature difference of only about 10 ^oC is necessary to remove the same amount of heat through ideal heat conduction. Crystallization of a 10 cm wide, 400 μm thick ribbon at a pulling speed of 0,2 cm/s produces about 330 W. This amount of crystallization heat cannot be removed simultaneously through the cross section of the ribbon (10.0,04 = = 0,4 cm^2), even if ideal heat conduction is assumed.

In interface-controlled crystallization (ICC) technology the heat of crystallization is removed through both the already crystallized silicon film and the cooled graphite ramp. The ramp causes an inclination of the crystallization front towards the surface of the foil resulting in an extension of the solid/liquid interface. Pulling velocities of up to 20 cm/min are obtainable with this procedure.

BASIC ASPECTS OF INTERFACE-CONTROLLED CRYSTALLIZATION (ICC)

The principle of ICC is shown in Fig. 1. The silicon melt is contained in a graphite crucible; one side of the crucible is cooled, so that a silicon film can crystallize there.

As graphite is wetted by silicon melt the crystallizing silicon film

would stick to the graphite wall. Direct contact between silicon and graphite has to be prevented by introducing a slag layer between the two materials. If the composition of the slag has a melting point below that of silicon the slag film acts as a lubricant too. The slag layer is of further advantage as it lowers the surface tension of the silicon melt. It thus prevents conglomeration or balling up of the silicon melt and confines the molten and crystallized silicon (liquid encapsulation). Due to the amorphous nature of the slag film nucleation centers are suppressed and, therefore, heterogeneous nucleation is prevented.

In the course of these studies a three component slag system has been used mostly: $CaO \cdot SiO_2 \cdot CaF_2$, with CaF_2 lowering the viscosity as well as the melting point of the slag system. In some experiments SiO_2 has been replaced by Al_2O_3.

Pulling is not restricted to the vertical direction; all angles between 90° and nearly 180° are possible. A modified version where the foil is pulled off nearly horizontally is given in Fig. 2.

GROWTH FEATURES

The silicon melt is prepared with a main and a ramp heater at a well-defined setting (Fig. 3). Lowering of the ramp temperature necessary to crystallize the silicon foil at the ramp is realized with the help of the separate ramp heater. According to the setting a definite temperature gradient can be adjusted. An example of a vertical temperature profile in front of and behind the ramp is given in Fig. 4. In addition, the temperature gradient across the ramp strongly depends on the grade of thermal decoupling of the ramp from the surrounding temperature field. A decoupling of the ramp from the remaining crucible can be obtained through adequate crucible design in order to minimize heat flow from the crucible walls to the ramp. Radiation shields are also helpful to reduce the influences of parasitic radiation.

Fig. 5 shows the situation near the meniscus in a close-up view. The meniscus height is typically 7-8 mm. Stationary crystallization experiments (v=0) have shown that crystallization perpendicular to the ramp surface takes place only in the region of the meniscus, i.e., only part of the ramp is utilized for crystallization. Nevertheless, the solid/liquid interface is about 20 x the cross section of the foil. Balancing of the heat flow showed that at the pulling rates and temperature gradients under consideration crystallization heat removal can be accomplished through the ramp area in the region of the meniscus.

From temperature measurements the temperature gradient G_S in solid silicon foil has been estimated to about 2000 K/cm. The temperature gradient G_L in the melt near solid/liquid interface amounts only to about 10 K/cm. Hence, G_L is by far less stable than G_S.

The analytical correlation between pulling rate v and foil thickness t is given in Fig. 6. As there exists a t^2 v-dependence it has to be concluded that heat removal through silicon foil, slag layer and ramp takes place according to the Newtonian law of cooling. The heat transfer coefficient is calculated from the fitted curve in analogy to the procedure given in /3/. With

$t^2v = 2,5 \cdot 10^{-4}$ cm.s a heat transfer coefficient $h \approx 7.10^{-3} W/cm^2.K$ is found. (Ideal cooling results in a linear dependence t.v = const. and h >> 1).

At v = 0,2 cm/s a foil thickness of about 350 µm is obtained. As the t/v-curve levels out with increasing v reduction of foil thickness only through increase of v seems to be rather ineffective. Improvement of heat removal by lowering of ramp temperature T_R and/or enhancement of heat transfer is to be preferred.

Lowering of ramp temperature T_R

Due to thermal coupling between ramp and silicon melt, lowering of the ramp temperature T_R influences the temperature distribution within the silicon melt. Temperatures as low as to allow constitutional supercooling have to be avoided, because constitutional supercooling provokes dendritic growth. It has been found by experiment, that with increasing v (as a consequence of decreasing T_R) the dendritic network becomes less dense.

There is an additional effect at higher velocities:

As a result of increased heat production and insufficient heat removal an accumulation of heat in front of the ramp is found which leads to an inversion of the temperature gradient G_L and thereby to destabilized growth conditions.

Enhancement of heat transfer

Heat removal is controlled by the slag film. The thermal conductivities of the usable slag systems are about two orders of magnitude lower than those of solid silicon and graphite. Hence, an enhancement of heat removal can only take place via reduction of the thickness of slag film. However, this requires a thin-bodied slag system with low-melting components. Such a system, in turn, exhibits reduced stability because of intensified evaporation or reaction with silicon and/or graphite.

CHARACTERISTICS OF ICC-FOILS

The ICC-foils have been tested with respect to their morphology and photoelectric properties.

Morphology of ICC-foils

Three different appearances of crystalline structure have been found with ICC-foils:

1. dendritic structure with an irregular arrangement of dendrites;
2. specular monocrystalline areas of preferredly (111) <211> orientation, occasionally (111)<110> orientation (rheotaxy, see e.g. /4/);
3. coarse-grained crystalline structure which seems to be an intermediate structure with considerable heterogeneous nucleation and not fully developed dendrites.

The three types of crystalline structure are demonstrated in a sample

given in fig. 7a; a sample with mostly specular morphology is represented in fig. 7b.

Dendritic and lamellar growth are both stable forms of growth. Temperature gradient G_L, growth velocity v, and concentration of the impurity in question C_0 are decisive for the appearance of the respective morphology. The three experimental parameters are connected through the equation /5/

$$C_0 = \frac{k_{eff} \cdot D}{m \cdot (1-k_{eff})} \cdot G_L/v$$

where k_{eff} = segregation coefficient, D = d'ffusion coefficient of the solute in the liquid and m = phase diagram liquidus slope.

Morphology and crystalline structure have been revealed with the help of etching techniques, X-ray topography and X-ray diffraction (Laue).

Dendritic growth

As can be concluded based on the diagram given in Fig. 8, dendritic growth is provoked at high growth velocities. Experiments showed that with increasing pulling rates a multitude of smaller dendrites is formed. With increasing velocity dendrites nucleate at an increasing rate but the network of dendrites becomes less dense because the dendrites have no longer a chance to fully develop.

Likewise, quality and quantity of impurities play a dominant role. The main component of the slag used is calcium silicate; therefore, the main impurity in the system will be Ca with a saturation concentration at the melting point of c_S $(T_m) \approx 10$ ppma. Corresponding to the process parameters a Ca concentration of only about 10 ppba would be sufficient to initiate dendritic growth (see Fig. 8).

Reduction of slag-film thickness reduces the supply of impurities and enhances heat removal through the ramp, thus increasing the temperature gradient G_L. Foils grown from thin resp. thick slag films show quite distinctive characteristics. If a thick film is used, a dendritic structure with a wrinkled surface of the foil developes. Dendritic growth can be suppressed when a thin slag film is used; the surface of the foil is very smooth showing only the feature of the ramp surface.

Coarse-grained structure

Coarse-grained structure starts with the nucleation of dendrites; with this dendritic net a melt film is entrained which crystallizes into a coarse-grained structure. The X-ray topogram of a foil with such a coarse-grained structure shows neither a uniform nor a preferential orientation of the individual grains (see Fig. 9a).

Specular planes

As can be seen in the topogram given in Fig. 9b the transition from the

coarse-grained structure to preferential monocrystalline areas (mirror planes) is abrupt. In most of the cases etching with an alkaline etch revealed a (111) <211> orientation. Repeatedly (111) <110> has been found, too. Etch pit densities are in the range of 5.10^4 - $5.10^5/cm^2$.

The flattened morphology of such specular planes can be interpreted as due to preferential growth at the re-entrant corners of twin junctions /6/. Examination of their cross sections did not reveal with certainty a confirmation of twin planes parallel to the foil surfaces. Occasionally, twin planes near the ramp face of the foil have been found. Seeding experiments with the purpose to enforce the twin growth have not been successful. A pile of silicon wafers with (111) <110> orientation has been tried as well as (111) wafers with twin planes in <211> orientation. In all the seeding experiments a stable growth which was compatible with the given growth parameters set in after a few millimeters, irrespective of the seed used. However, the growth of mirror planes can be initiated by increasing the ramp temperature and thus decreasing the growth velocity. Disturbances through dendritic growth, in either case, have been observed.

Photoelectrical Data

Photoelectrical characterization has been carried out with EBIC and by evaluation of test solar cells. The preparation of 15 x 15 mm^2 test cells had not been optimized. Prior to test cell preparation the samples have only slightly been etched with an alkaline etchant. No mechanical treatment like grinding or lapping had been applied.

The photovoltaic efficiencies of samples with coarse-grained structure and mirror planes are quite similar. Striking differences have not been found. The efficiencies are in the range of 7,5-9,5 AM 1,5. The yet unsufficient values are partly due to low V_{OC} (high specific resistivity of test samples), partly due to low I_{SC} (level of impurities which act as lifetime killers).

EBIC pictures taken from an area with coarse-grained crystalline structure show an electrical activity of grain boundaries (Fig. 10a). Negligible electrical activity is found in areas with mirror planes (Fig. 10b).

CONCLUSIONS

The results of this study may be summarized as follows:

A film of silicon melt is pulled across a carbon ramp under special temperature profile conditions to solidify as a multi- to monocrystalline foil of uncritical width. A slag film of special composition which is still liquid under the crystallization conditions of silicon separates the silicon film from the ramp. This film serves several purposes: a) It enables the separation of the solidified silicon foil from the ramp system (lubrication effect). b) It lowers the surface tension of the silicon melt (liquid encapsulation phenomenon). c) It prevents unwanted nucleation initiated by the ramp surface structure.

The special case of lamellar growth in form of larger monocrystalline areas appears to be of "rheotaxial" nature in connection with certain dendri-

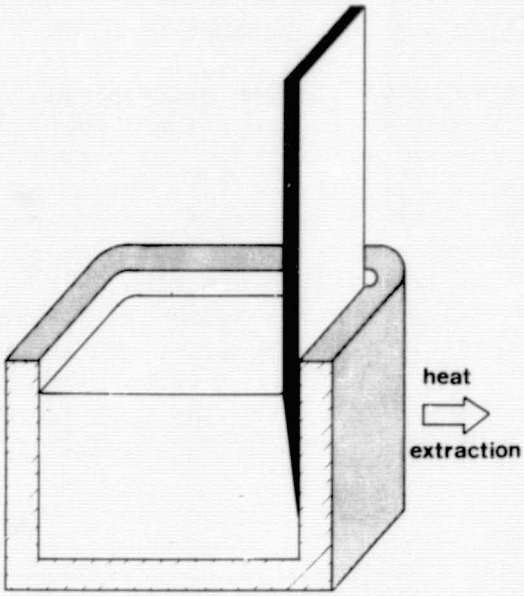

Figure 1 Schematic of interface-controlled crystallization (ICC) method in the vertical arrangement (from /1/)

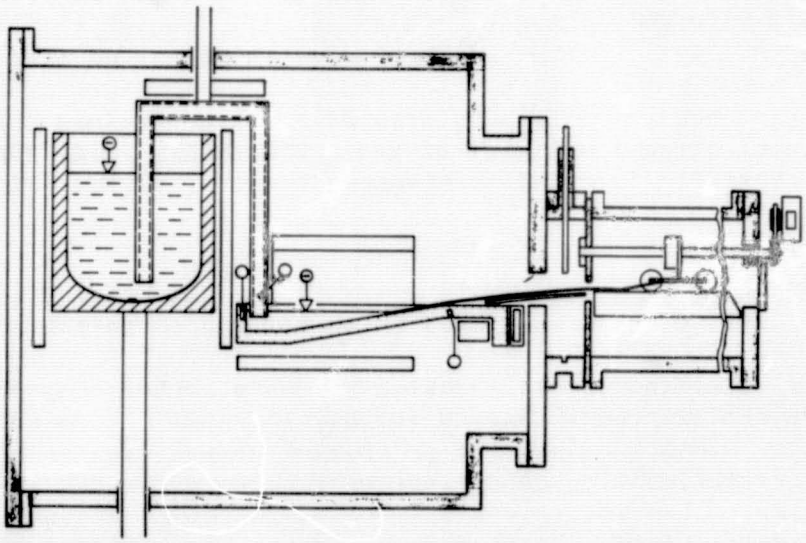

Figure 2 Schematic of a set-up for continuous production of silicon foil by modified ICC method in quasi horizontal arrangement (from /2/)

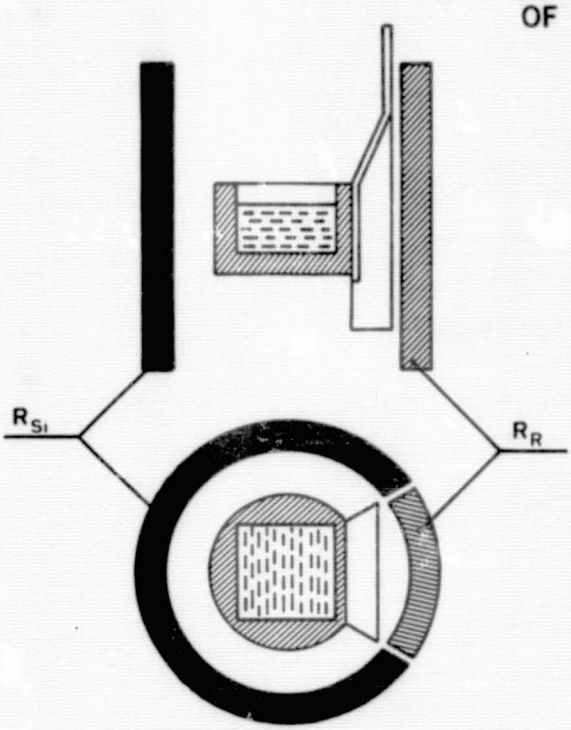

Figure 3 Arrangement of main heater (R_{Si}) and ramp heater (R_R)

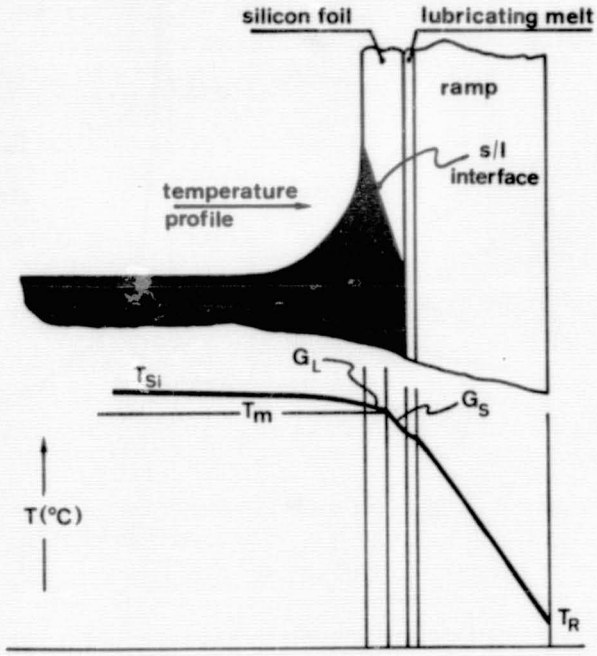

Figure 5 Schematic of meniscus with solid/liquid interface; temperature profile across the meniscus

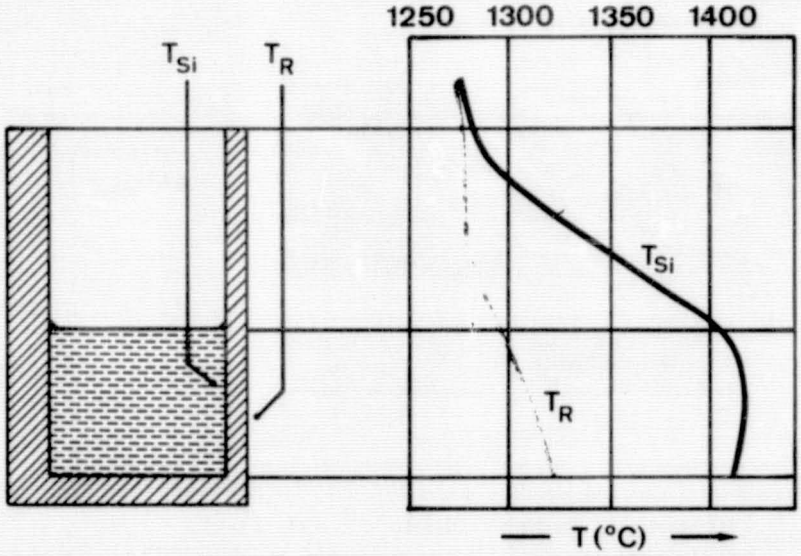

Figure 4 Vertical temperature profile in front of and behind the ramp

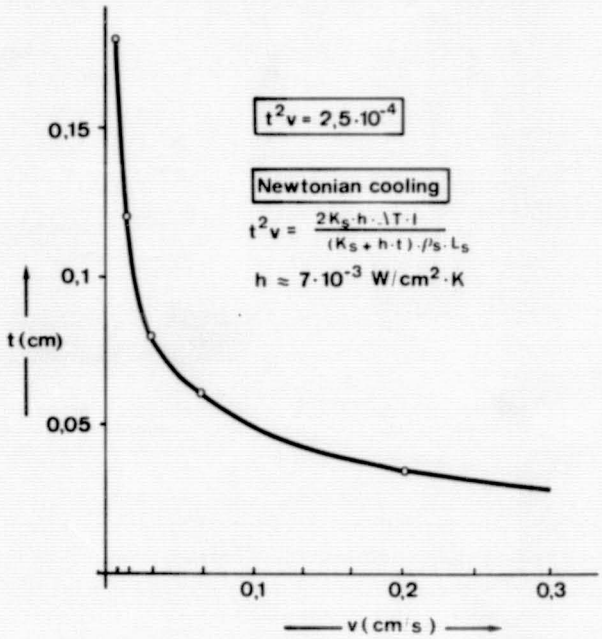

Figure 6 Silicon foil thickness t/vs. pulling rate v

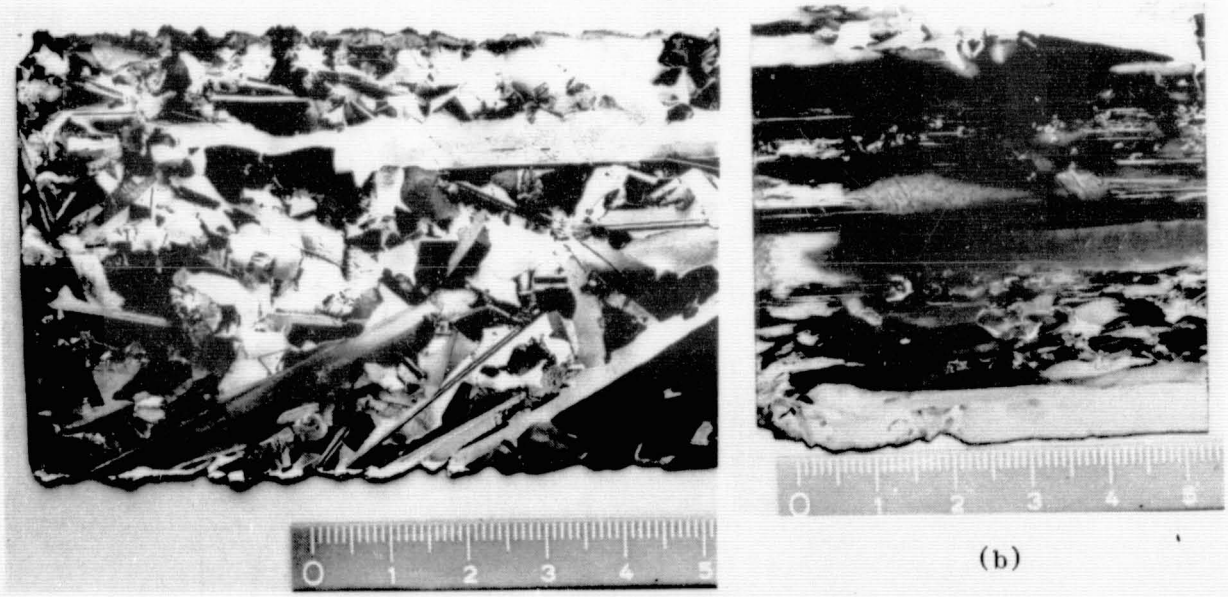

(a) (b)

Figure 7 Different morphologies of ICC-foil:
(a) simultaneous appearance of dendritic, coarse-grained, specular structure;
(b) sample with mostly specular morphology

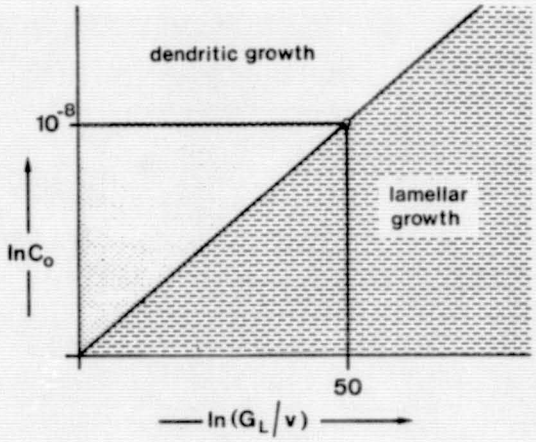

$$C_o = \frac{k_{eff} \cdot D}{m \cdot (1 - k_{eff})} \cdot G_L / v$$

$G_L = 10\,K/cm$ $\quad m = 15\%/200K$

$v = 0{,}2\,cm/s$ $\quad k_{eff}(T_m) = 1{,}6 \cdot 10^{-3}$

$D(T_m) \approx 10^{-10} cm^2/s$

$$C_o = \frac{1{,}6 \cdot 10^{-3} \cdot 10^{-10} \cdot 50}{0{,}75 \cdot 10^{-3}}$$

$C_o \approx 10\,ppba$

$C_S(T_m) \approx 10\,ppma$

Figure 8 Dependence of solidification morphology on temperature gradient G_L, growth velocity v, and impurity content C_o

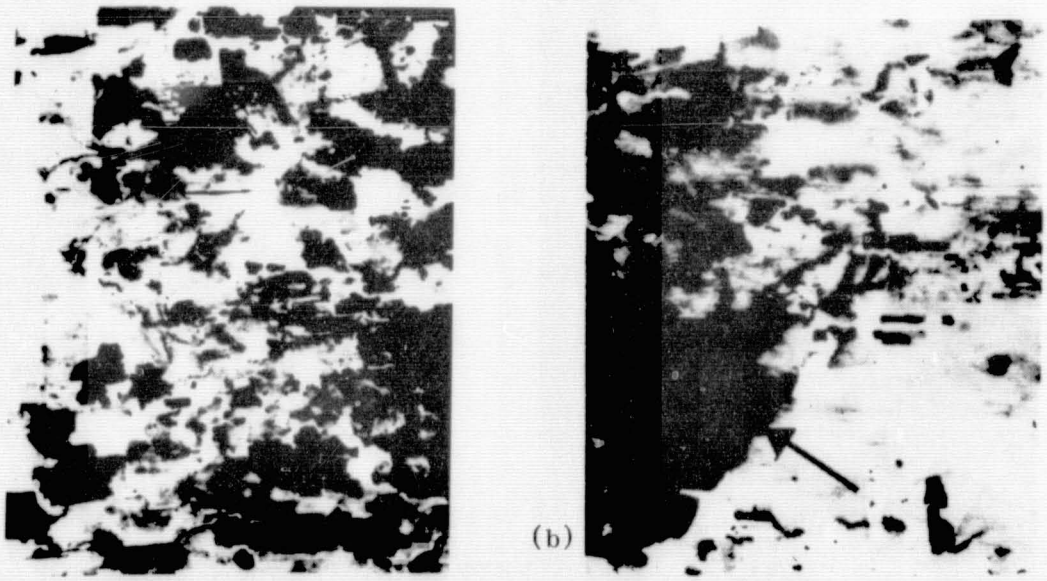

Figure 9 X-ray transmission topogram ($MoK\alpha_1$, $2\bar{2}0$-reflection) of a sample with
(a) coarse-grained crystalline structure;
(b) partly coarse-grained crystalline structure - partly mirror planes (the transition is marked with an arrow)

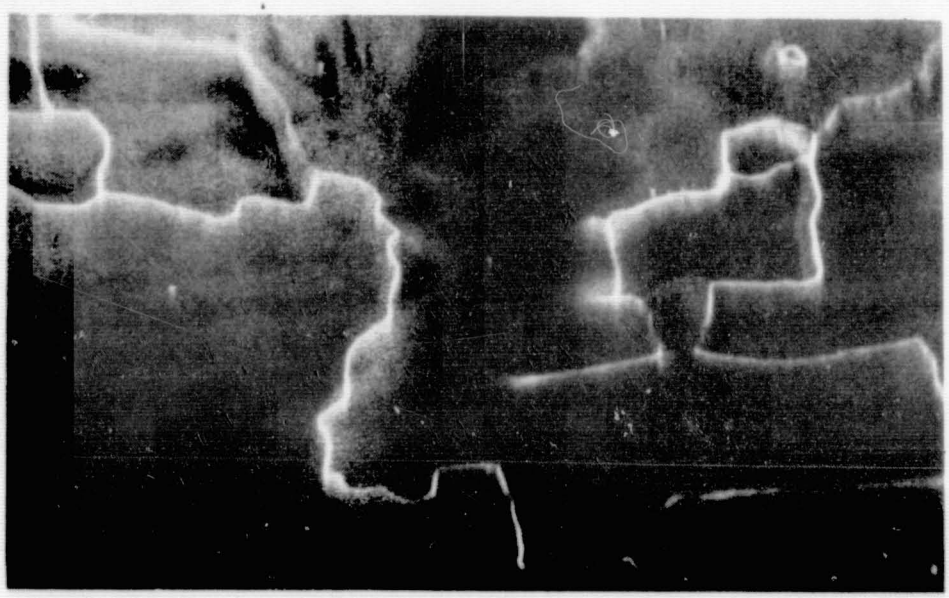

(a)

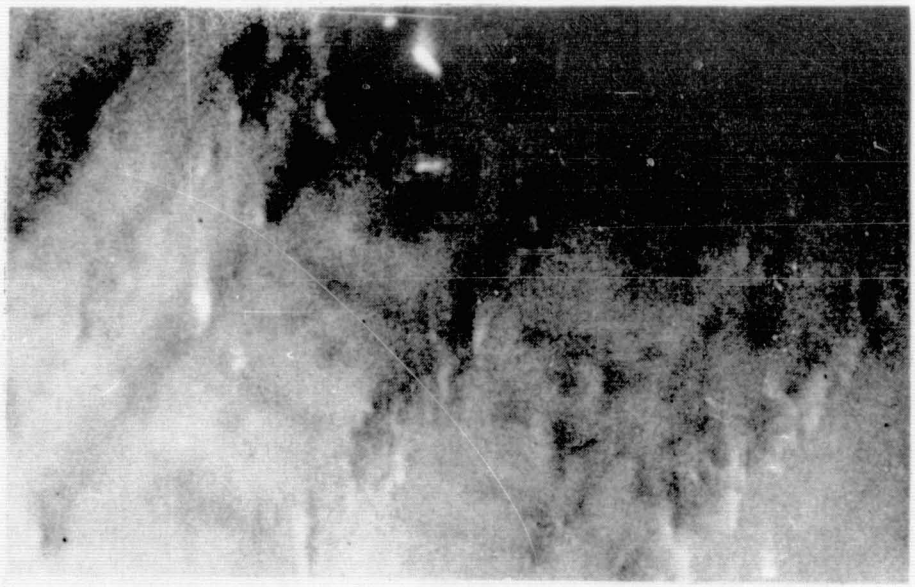

(b)

Figure 10 EBIC pictures of a sample with
(a) coarse-grained crystalline structure,
(b) mirror planes. Magn. 20 x

tic components.

ACKNOWLEDGMENT

The author wishes to thank Prof. E. Sirtl for helpful discussions. This work has been supported by the Bundesministerium für Forschung und Technologie under contract nr. NT 0845/0846.

REFERENCES

/1/ J. Dietl, D. Helmreich, and E. Sirtl in "Crystals: Growth, Properties and Applications", Vol. 5, J. Grabmaier (ed.), Springer Verlag, Berlin (1981), 43

/2/ German Patent (DOS) No. 2903061

/3/ J.A. Zoutendyk, J. Cryst. Growth 50, 83 (1980)

/4/ E. Rasmanis, Proc. Nat. Electron. Conf., Vol.20, 212 (1964)

/5/ W.A. Tiller, in "Art and Science of Crystal Growing" (Wiley & Sons, New York, 1963), pp. 119-150

/6/ R.S. Wagner, Acta Met. 8, 57 (1960)

DISCUSSION

RAVISHANKAR: Can you comment on the purity requirements for the slag, in terms of its effects on solar cell performance?

HELMREICH: When we began our experiments, we used a slag system that we got from technical components, and it turned out that it is not sufficient. Single crystals of calcium fluoride are reaction products with the system, and they come through the oxygen-related compounds of the system.

RAVISHANKAR: If you have to use a very high-purity slag layer, how would it influence the cost of the solar cells that you are making?

HELMREICH: It would be more expensive. Not only because you have to use single-crystal and purified material, but also you will have to find a system that is stable enough to last a long time.

RAVISHANKAR: If you used a high-cost, high-purity slag layer, do you use enough of that slag to have a bearing on the cost of the solar cell?

HELMREICH: I don't know.

MILSTEIN: In liquid encapsulated growth, typically you lose some of the liquid encapsulant with the material you are growing. Does this happen in your system?

HELMREICH: Yes.

WARGO: I really like the idea of using the slag to isolate the liquid and solid silicon from the graphite crucible. It also seems like that is your largest problem in heat transfer. What do you consider to be the major advantage of this particular crystal growth system compared with, for example, low-angle sheet pulling?

HELMREICH: You are correct. We lose some advantage in the heat transfer, but in my opinion the advantage of this system is that you have a glassy-like layer where you have a chance to grow a single-crystalline layer and not have nucleation centers from the layered cell.

RAVISHANKAR: What is the largest grain size you have observed with this kind of growth?

HELMREICH: The grain size of the coarse grain structure of the medium plane size was a few millimeters.

WARGO: Is the liquid encapsulant transparent to the infrared? Because if that is pulled horizontally, and you maintain that liquid encapsulating layer on the surface, and it is transparent to the infrared, there is a very efficient heat-transfer mechanism.

HELMREICH: The slag layer is etched away.

ABBASCHIAN: I noticed you used a diffusion coefficient of 10^{-10}. Isn't that very low, about 5 orders of magnitude low?

HELMREICH: These values have been found by Sigmond of the Fraunhofer-Institut in Munich. He looked for the calcium-silicon system. I questioned this low-diffusion coefficient, but I only have an extension of his curve to the melting point, so probably it could be higher.

RAO: Have you used the slag with impure silicon or metallurgical-grade silicon, and in cases like that do you get classical slagging-type action, where you leach out impurities from the melt, like you find in the steel industry?

HELMREICH: We have dealt only with semiconductor-grade silicon.

LEIPOLD: Was there any temperature gradient on the ramp parallel to the growth direction, or was the ramp designed to have a constant temperature along its length?

HELMREICH: It has a vertical temperature gradient. We intentionally kept the crystallization front fixed near the meniscus.

N84 28629 D15

THE S-WEB TECHNIQUE FOR HIGH-SPEED GROWTH OF Si SHEETS

J.G. Grabmaier and H. Föll
Research Laboratories of Siemens AG, D-8000 Muenchen 83, FRG

ABSTRACT

The supported-web (S-Web) technique was conceived as a method to grow Si-ribbons at large areal growth rates. Its central idea is to pull a net made, e.g., from carbon-fibers, through liquid Si. Webs of liquid Si are drawn out within the meshes of the net and kept stable by the high surface tension of liquid Si. The liquid webs crystallize individually some time after their formation and this allows to obtain a ribbon-shaped body of Si at high speed. First experiments with graphite-grids were encouraging and opened the way for more involved experiments with carbon-fiber nets woven on a suitable loom. Ribbons suitable for the fabrication of solar-cells were obtained at low pulling speeds, but problems were encountered at high pulling speeds. The results of the net-pulling experiments are presented and discussed.

INTRODUCTION

The large-scale manufacture of cheap, but efficient solar cells demands not only cheap starting materials and processes, but also high through-put rates at every step in the production chain. With crystalline Si as basic solar-cell material, any production sequence will contain the controlled crystallization of liquid Si; preferably directly in the form of large-grained sheets or ribbons. Most crystal growth techniques utilized so far (for a review see /1,2/) are limited to areal growth rates $\approx 0{,}05\ m^2/min$; a value far below the demands of large-scale production.

The volume of Si crystallizing per time unit is generally given by the product of the area of the solid-liquid interface and the velocity with which this interface moves perpendicular to itself. Attempts to increase areal growth rates therefore aim at increasing the interface velocity (i.e. the "pulling speed" for most processes), the interface area, or both. The first approach requires very large temperature gradients in order to remove the heat of crystallization and invariably leads to problems with the structural perfection of crystals thus obtained (example: roller-quenching /3/). The experimental evidence collected so far indicates that interface velocities

in excess of ≈5 cm/min will not lead to satisfactory crystals. Increasing the area of the solid-liquid interface thus seems to be more attractive and has shown some promise as demonstrated by "horizontal ribbon growth" (HRG) /4/; "low-angle Si sheet growth" (LASS) /5/ and "interface controlled crystallization" (ICC) /6/. However, stability and morphology problems appear to be associated with these approaches.

The "supported-web" (S-Web) technique /7,8/ is a newcomer to this field. The unique and unconventional idea in this technique is to use a net as a kind of supporting substrate for Si ribbons. In the original concept of the S-Web-technique, the net, made from carbon-, graphite-, or carbon-coated quartz-fibres, is to be pulled through a crucible containing liquid Si at comparatively high velocities. Films or webs of liquid Si are spread out within the meshes of the net where they remain stable for some time due to the high surface tension of liquid Si. Each web then crystallizes individually in a "crystallization zone". The shaping of the Si-ribbon and its crystallization thus would be decoupled and the removal of the heat of crystallization would no longer be speed-limiting. High areal growth rates should be possible because the solid-liquid interface area present at any given time is very large compared to the cross-sectional area of the ribbon, but in contrast to HRG, LASS and ICC the total interface area is now partitioned into many independent interfaces.

This paper gives an overview of the experiments performed so far and discusses the potential and the problems of the S-Web-technique.

EXPERIMENTAL STUDIES

Dip-coating of graphite grids

For a first evaluation of the S-Web-technique, dip-coating experiments were performed with graphite-grids instead of the then unavailable net. The grids were laser-cut from high-density high-purity graphite sheets (typically 60 x 40 x 0,5 mm^3) with mesh-sizes between 1 x 1 mm^2 - 4 x 4 mm^2. These grids were dipped into liquid Si kept at a temperature slightly above the melting point and, after a soaking period of 30 sec - 60 sec, withdrawn with velocities between ≈ 2 cm/min and 200 cm/min. The following results merit mentioning:

i) At pulling speeds ≲ 4 cm/min the graphite was uniformly coated on both sides (Fig. 1a).
ii) If the pulling direction was not perpendicular to the melt surface but inclined by ~ 10°-15°, the graphite grid was coated at one side only for pulling speeds ≲ 4 cm/min (Fig. 1b).
iii) At pulling speeds between ≈10 cm/min - 200 cm/min the meshes of the grid were still filled with Si which exhibited

a peculiar morphology that did not depend on the pulling angle (Fig. 1c). The surface of the graphite grid, however, was not coated.

The first two items are easily understood. At low pulling speeds the solid-liquid interface moves downwards with the same velocity with which the grid is withdrawn; i.e. it is stationary. The crystallization thus occurs continuously and the process as a whole is quite similar to the SOC /9/, RAD /10/ or "contiguous capillary coating" /11/ techniques.

The morphology and defect structure of the specimens obtained at high pulling speeds is typical of "mesh crystallization"; i.e. the individual crystallization of a web of liquid Si contained within a mesh of the grid. Detailed investigations by chemical etching, scanning- and transmission electron microscopy, and in-situ photography of the crystallization process lead to an understandig of the mesh-crystallization process as illustrated in Fig. 2 and Fig. 3. In short, a liquid web is indeed drawn out and persists for some time within a mesh of the grid. Its crystallization starts from the outside of the mesh and proceeds towards the interior; several solid-liquid interfaces or crystallization fronts exist at the same time. Whereever two crystallization fronts meet, a highly defected region containing high-angle grain boundaries, dislocations and SiC-precipitates in high densities is formed. The peculiar shape of the crystallized web is a consequence of the non-zero contact angle of solid Si with its own melt as is outlined in /12/.

The experiments with the graphite grids thus demonstrated that the basic idea of the S-Web-technique is valid in principle, but that at the very minimum the crystallization of the liquid Si-webs has to be controlled in order to progress towards a useful morphology of the coated grid or net.

Introducing the net

Up to now, nets were woven from commercially available carbon rovings (Sigrafil^{R} NF 1) on a standard loom which was slightly modified for this purpose and which could also be used for quartz rovings. The carbon rovings contain 1000 single filaments with diameters of ≈ 8 µm /13/. The minimum mesh-size of the net is 2,5 x 2,5 mm^2; larger sizes are possible. As woven, the net is 1 m in width and of arbitrary length (typically 50 m). Smaller nets are obtained by cutting it to size with scissors. The price of the net is about \$ 15/m^2 (for 2,5 x 2,5 mm^2 mesh size) but is expected to decrease if massproduction would be established.

The carbon rovings are covered with a thin layer of a plastic coating for protection. Before using the net, this coating has to be removed; which is simply done by burning it off. The carbon fibers used contain up to 2 % impurities, mainly Ca, Zn,

Mg, Si. In order to evaluate their influence on the S-Web quality, a portion of the net was cleaned by baking it at ≈2700 °C in a halogen atmosphere. These cleaned nets then contained less than 10 ppm impurities.

Feeding the net into the molten Si principally can be conceived in two ways: i) from below the crucible through a slot in the crucible bottom (similar to the RAD-technique /10/) and ii) from above, turning it around a bar of suitable material that is immersed in the liquid Si. The second possibility, however, is untenable because the net embrittles immediately in contact with liquid Si. Therefore the first option was implemented. The problem, of course, is to avoid leakage of liquid Si through the feed-slot. Whereas this is not impossible (cf. /14, 15/), a leakage-proof system employing a slotted die (Fig. 4) was used for first experiments with continuous net-pulling. The contact-area of liquid Si and the net lies higher than the Si-melt level and leakage thus cannot occur. The uphill flow of liquid Si to the net is achieved, as in the EFG-process /16,17/, by capillary action. The slotted die, besides allowing a leakage-free transport of the net, serves also to shape the meniscus and thereby to influence the coating geometry of the net.

Two apparatus have been set up for experiments: S-Web-puller I and II. No. I is a simple but versatile laboratory-model with RF-heating of the crucible and the possibility of chosing any pulling direction desired; the maximum net width is limited to ≈ 4 cm. No. II is a modified Czochralski crystalpuller with resistance-heated crucible, vertical pulling only, and a maximum net width of 10 cm.

Results of experiments with continuous net-pulling

After some inital trouble with the net getting stuck in the slotted die, fracture of the coated net, temperature inhomogeneities along the exit surface of the slotted die and the like, a standard slotted-die design for the S-Web-puller II emerged as shown in Fig. 4. The large openings on both sides of the slotted die allow a certain portion of the net to remain uncoated and thus to retain its high mechanical strength, a measure that ensures that pulling can continue even if the coated part of the net fractures. The asymmetric shape of the slotted die results in a onesided coating of the net, as it is preferèd for various reasons.

In contrast to the dip-coating experiments, the meshes of the net are not filled with Si at high pulling rates (≳5 cm/min). This is a direct effect of the geometry of slotted die and net and will be discussed later.

At low pulling speeds, exploiting the continuous crystallization mode, one-sided and (with symmetrical slotted dies) double-sided coating of the net is easily achieved; Fig. 5 shows

typical cross-sections. Grain sizes generally are in the 1-2 mm range. If long and wide ($\gtrsim$5 cm) ribbons are grown, a tendency for fracture along the middle is observed. This is quite natural for ribbons (cf. /18/) and not necessarily connected with the net. The problem can be overcome by periodically raising the pulling speed for a short time period and thus to interrupt the coating process. Coating commences automatically as soon as the pulling speed is lowered again. Rectangular sheets, easily separated by breaking, are obtained in this way; Fig. 6 gives an example.

An uncleaned net with mesh sizes of 2,5 x 2,5 mm^2 or 5 x 5 mm^2 was used for most experiments so far. Contamination of melt and S-Web therefore was unavoidable and manifested itself in an unavoidable conversion of the S-Web to n-type (probably caused by Mg) although p-type Si was used as feed-stock. A detailed evaluation of these n-type samples has not been attempted; but it was found that the minority-carrier diffusion length averaged about 20 μm. This is an unexpectedly high value in view of the contamination that must have taken place.

With clean nets, the original doping of the melt is retained in the S-Web ribbons. First measurements with the Si-electrolyte-contact method /19/ and with test solar-cells based on a MIS-junction technology, gave short-circuit currents I_{sc} under AM1 illumination of $\approx$18 mA/cm^2; i.e. about 60 % of the current obtained with reference single crystals. Because no attempts have been made so far to clean the crucible and the slotted die (both are made from high-density high-purity graphite), this I_{sc}-value is considered to be quite encouraging.

The carbon-fibers of the net react with the liquid Si to SiC. Isolated filaments usually are quantitatively converted to SiC, but the SiC formed initially around the tightly packed filaments in a fiber-bundle "screens" the interior which therefore often contains filaments that are only partially reacted to SiC. Reacted filaments are no longer coherent, but rather strings of small SiC-crystals (Fig. 7). It is thought that this reaction, by breaking up the fibers, relieves some of the stress which is introduced by the incompatibility of the thermal expansion coefficients of Si and the carbon rovings.

The density of dislocations and grain-boundaries is sometimes higher in the immediate vicinity of the net, but frequently the net does not introduce major structural disturbances. Single filaments have often been found to be embedded in the Si (as SiC-crystals) without causing any lattice disturbance.

The net, after incorporation into the Si-ribbon, provides an ohmic contact to the Si-ribbon. This was ascertained by I-U-measurements between the frontside of a sample and unreacted carbon-rovings from the uncoated part of the net at the left- and right-hand-side of the coated region. The net thus may be

used as an integral part of the back-side contact necessary for solar-cells.

Using the smaller S-Web-puller I, experiments were conducted with horizontal instead of vertical pulling of the net. For reasons which will be discussed later, horizontal pulling was thought to promote stable liquid Si-webs within the meshes of the net at high pulling speeds. Whereas this assumption was generally true, the morphology and crystallization of specimens obtained at higher pulling speeds was similar to that of the dip-coating experiments and thus too irregular for further processing. At low pulling speeds (around $\approx$(2-3) cm/min) long ribbons ($\approx$30 x 4 cm^2) with fairly large grains could be obtained; an example is shown in Fig. 8.

DISCUSSION

The geometry of coating the net

Of particular interest for the S-Web-technique is the relationship between mesh-size, geometry of the slotted die, and the amount of liquid Si that can be spread out as a liquid web within a mesh. The basic quantities and processes governing this relationship are illustrated in Fig. 9 for both pulling the net through a free surface and through a slotted die possessing a meniscus-defining edge. It is clear from Fig. 9 that after a meniscus was attached to a horizontal bar of the net that emerges from the liquid Si, the next bar has to come up before the two menisci overlap and thereby rupture the Si-web. The most important quantity is the meniscus shape, defined by its radius of curvature R as a function of the meniscus height h. In the simple one-dimensional case shown in Fig. 9, R(h) is given by

$$R(h) = \frac{\gamma}{\rho \cdot g(h_o + h)}$$

with γ = surface tension of liquid Si (720 mJ/m^2), ρ = density of liquid Si (2.53 g/cm^3), g = 9.81 m/sec^2, and h_o = "effective" height of the die-top with respect to the Si-melt level (cf. /16/). An evaluation of this equation, taking into account various boundary conditions for the meniscus as determined by the precise shape of the slotted die, leads to a relation between the maximum mesh-size and the effective die-top height h_o as shown in Fig. 10. The curves given represent only general trends since the precise relation depends on the exact geometry of die-top and net. It is, however, safe to say that vertical pulling always requires mesh sizes $\lesssim$ 4 mm. This is true even for very small h_o-values because the radius of curvature of the meniscus rapidly decreases when it is pulled upwards. In the case of horizontal pulling, the radius of curvature can be kept large at small h_o-values and larger mesh sizes should be possible. This was the incentive for the hori-

zontal pulling experiments and the standard 2,5 x 2,5 mm^2 meshes were indeed filled with liquid Si in this case. Compared to the dipcoating experiments, however, the filling of the meshes occured more haphazardly and the webs often collapsed before crystallization started. The reason for this is that neither the cross-section nor the wetting-angle of a carbon-fiber is a well-defined quantity (as assumed in Figs. 9 and 10).

Outlook

From the experimental and theoretical results described before, it follows that the original concept of the S-Web-technique as outlined in the introduction, is not easily turned into reality. Whereas ribbon growth at low pulling speeds is possible and even may offer some conceptual advantages in comparison to more established methods, it cannot be considered a decisive breakthrough. The goal, clearly, still must be to utilize the intrinsically high areal growth rates of the net-specific mesh-crystallization without sacrificing quality.

One possible way to achieve this goal is illustrated in Fig. 11. The crucial point is the introduction of a temperature gradient perpendicular to the growth direction. The crystallization front thus will be inclined to the growth direction; its total area is large as compared to the ribbon cross-section, and the general geometry is reminescent of HRG, LASS, or ICC /4-6/. Phrased differently, the thin layer of Si covering the net on one side grows in the continuous crystallization mode, whereas the bulk of the ribbon grows in the (transversal) mesh-crystallization mode. Experiments exploring this possibility are in progress.

ACKNOWLEDGEMENT

The contribution of Ms. L. Bernewitz, Dr. R. Falckenberg, Messrs. B. Freienstein, K. Geim and G. Hoyler, who grew and characterized the S-Web-ribbons, is gratefully acknowledged.

This work has been supported under the Technological Program of the Federal Department of Research and Technology of the FRG. The authors alone are responsible for the contents.

REFERENCES

/1/ T. Surek; Proc. Symp. Electronic and Optical Prop. of Polycrystalline or Impure Semiconductors and Novel Si: Growth Methods, eds.: K.V. Ravi and B. O'Hara (Electrochem. Soc.), Pennington (1980) p. 173

/2/ T.F. Ciszek; Proc. 3rd Symp. on Mat. and New Processing Techniques for Photovoltaics (eds.: J.P. Dismukes et al.) The Electrochem. Soc., Vol. 82-8, 1982, p. 70

/3/ N. Tsuya, K.I. Arai, T. Takeuchi, T. Ojima and A. Kuriowa; Jap. J. Appl. Phys., 15, Suppl. 19-2 (1980) 13
/4/ B. Kudo; J. Cryst. Growth, 50 (1980) 247
/5/ H.E. Bates and D.N. Jewett; Proc. 15th IEEE Photovoltaic Spec. Conf. (1981) p. 255
/6/ J. Dietl, D. Helmreich and E. Sirtl in: Crystals-Growth, Properties and Applications "Silicon", Vol. 5; ed.: J.G. Grabmaier (Springer-Verlag) 1981 p. 43
/7/ J.G. Grabmaier, H. Föll, H.A. Aulich and B. Freienstein; Proc. 3rd Symp. on Mat. and New Proc. Techn. for Photovoltaics (ECS Proc. Vol. 82-8) 1982 p. 391
/8/ J.G. Grabmaier, H. Föll, B. Freienstein and K. Geim; Proc. 4th E.C. Photovoltaic Solar Energy Conf.; eds.: W.H. Bloss and G. Grassi (D. Reichel Publ. Cie) 1982, p. 976
/9/ J.D. Zook, B.G. Koepke, B.L. Grung and M.H. Leipold; J. Cryst. Growth 50 (1980) 260
/10/ C. Belouet; J. Cryst. Growth 50 (1980) 279
/11/ T.F. Ciszek and J.L. Hurd; Proc. 14th IEEE Photovoltaic Specialists Conf. (1980) 397
/12/ T. Surek and B. Chalmers; J. Cryst. Growth 29 (1975) 1
/13/ H. Bödes, D. Gölden, Ph. Rose, and H. Würmseher; Z. Werkstofftechnik 11 (1980) 275
/14/ C. Belouet, C. Texier-Herro, H. Mautref, C. Belin, J. Paulin and J. Schneider; J. Cryst. Growth 61 (1983) 615
/15/ J.L. Hurd and T.F. Ciszek; J. Cryst. Growth 59 (1982) 499
/16/ F.V. Wald; as ref. /6/; p. 147
/17/ T.F. Ciszek; as ref. /6/; p. 109
/18/ R.W. Gurtler; J. Cryst. Growth 50 (1980) 69
/19/ V. Lehmann, H. Föll, L. Bernewitz and J.G. Grabmaier; these Proc.

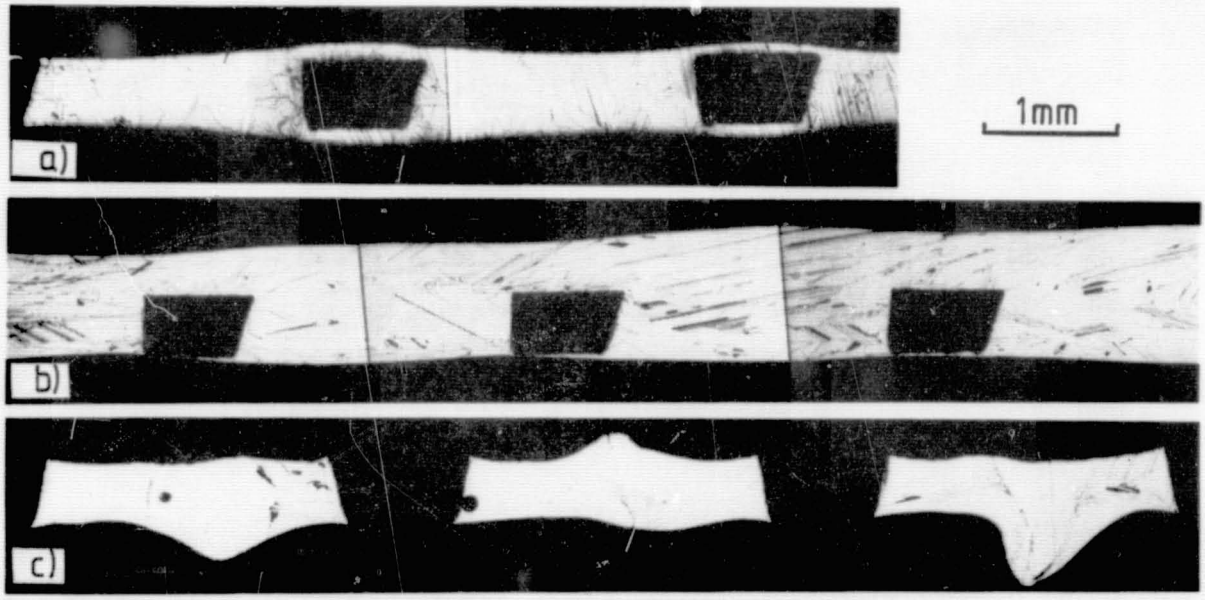

Fig. 1
Coating geometry of graphite grids for a) vertical pulling; b) inclined pulling at low speed; c) pulling at high speed.

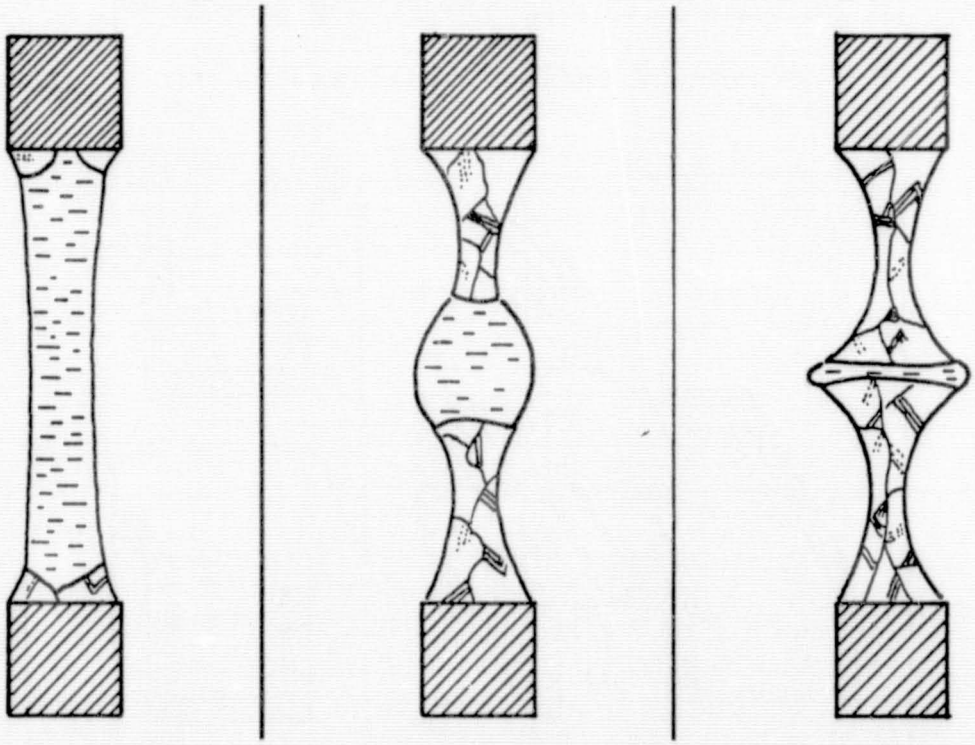

Fig. 2
Subsequent stages of mesh crystallization. For details see text.

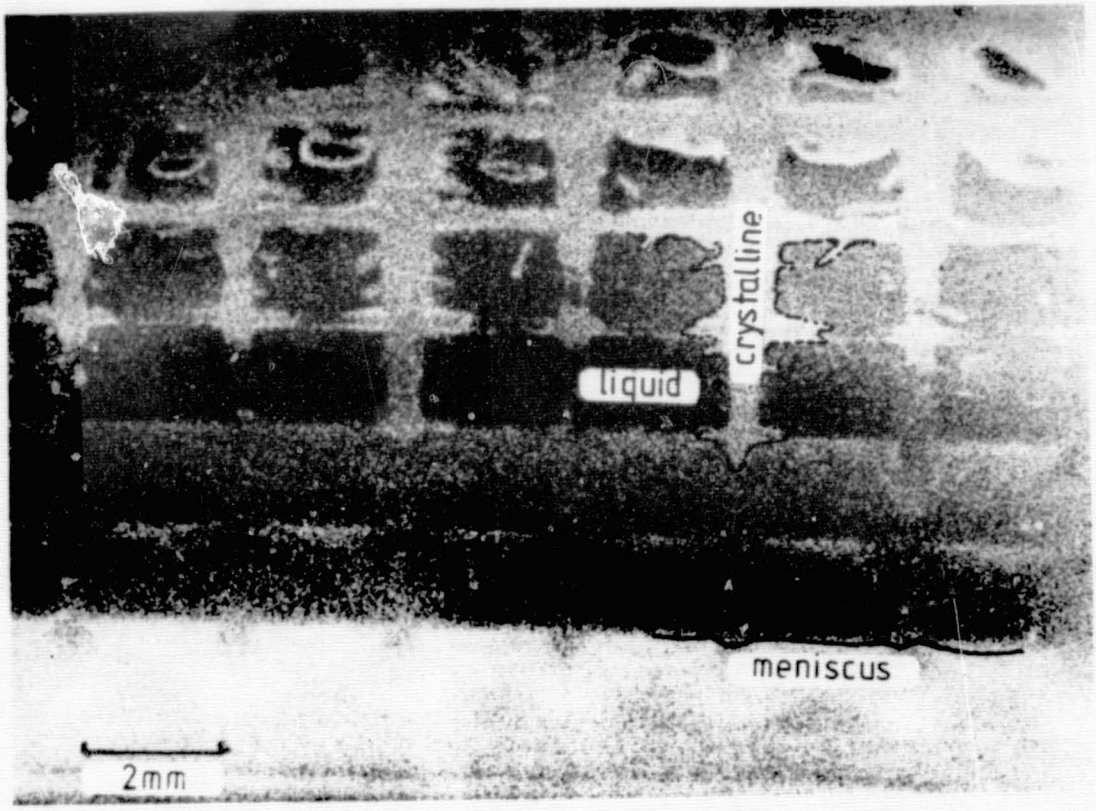

Fig. 3
In-situ photography of mesh-crystallization during withdrawal of a graphite grid.

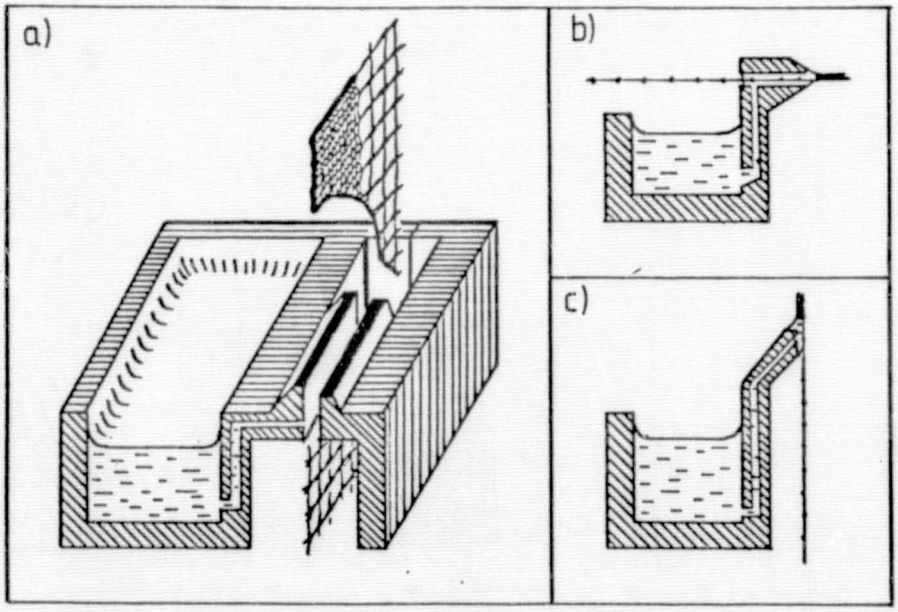

Fig. 4
Examples for slotted dies. a) shows the slotted die used in the S-Web-puller II; b)c) show two examples of slotted dies for horizontal pulling or for one-sided coating.

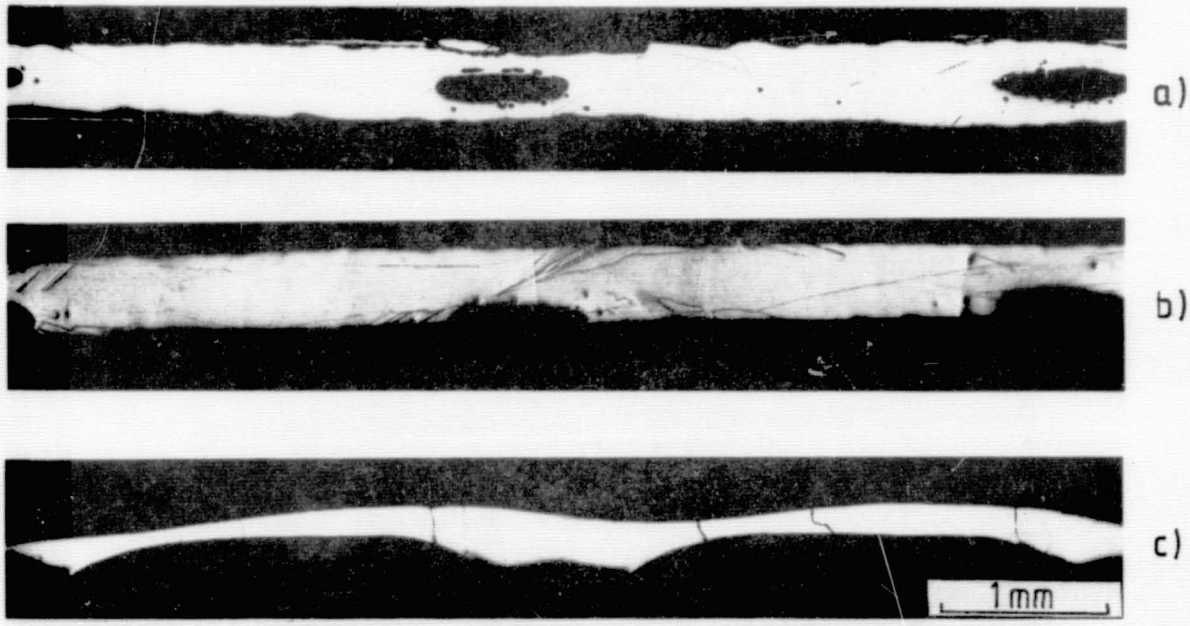

Fig. 5
Typical cross-sections of S-Web specimens obtained with a) a symmetrical slotted die; b) an asymmetrical slotted die as in Fig. 4a; and c) a one-sided die as in Fig. 4c.

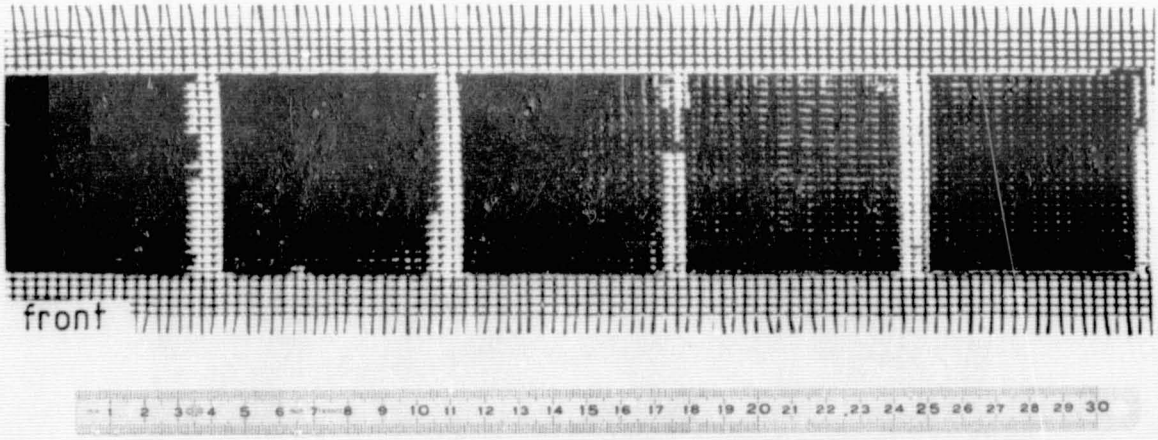

Fig. 6
Front- and back-side of part of a net coated on one side with Si.

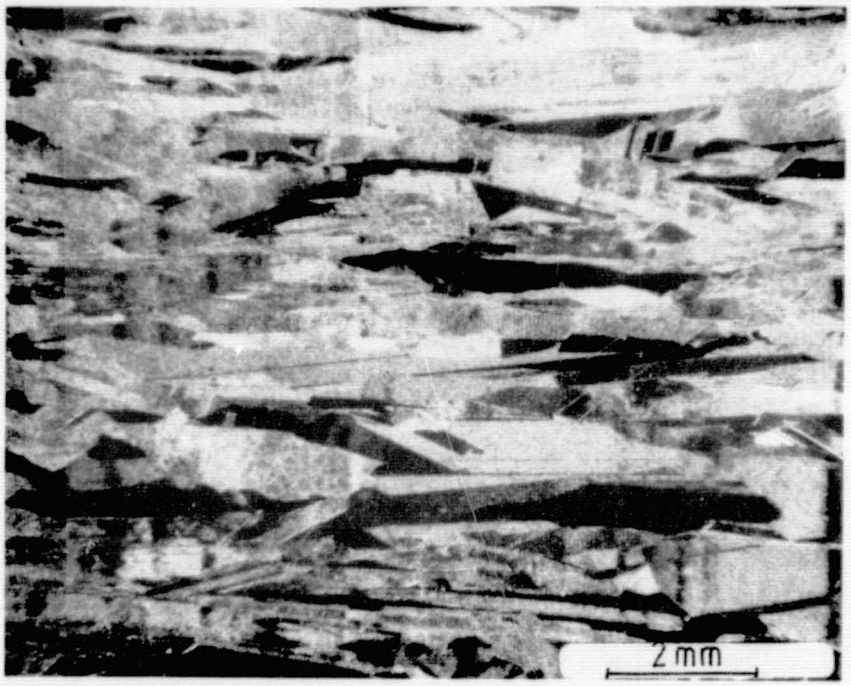

Fig. 7
Examples of carbon-filaments partially converted to SiC.

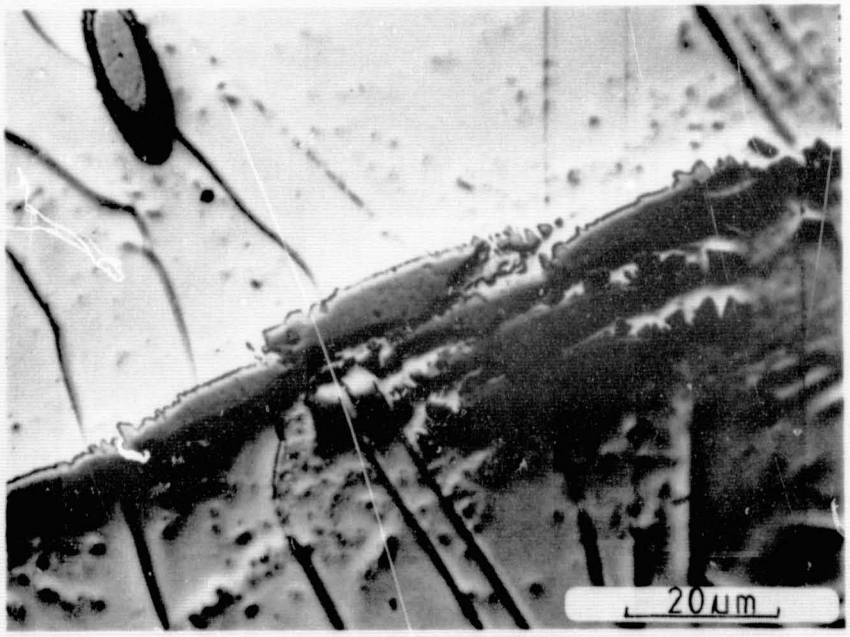

Fig. 8
As-grown surface (KOH-etched) of a horizontally pulled S-Web.

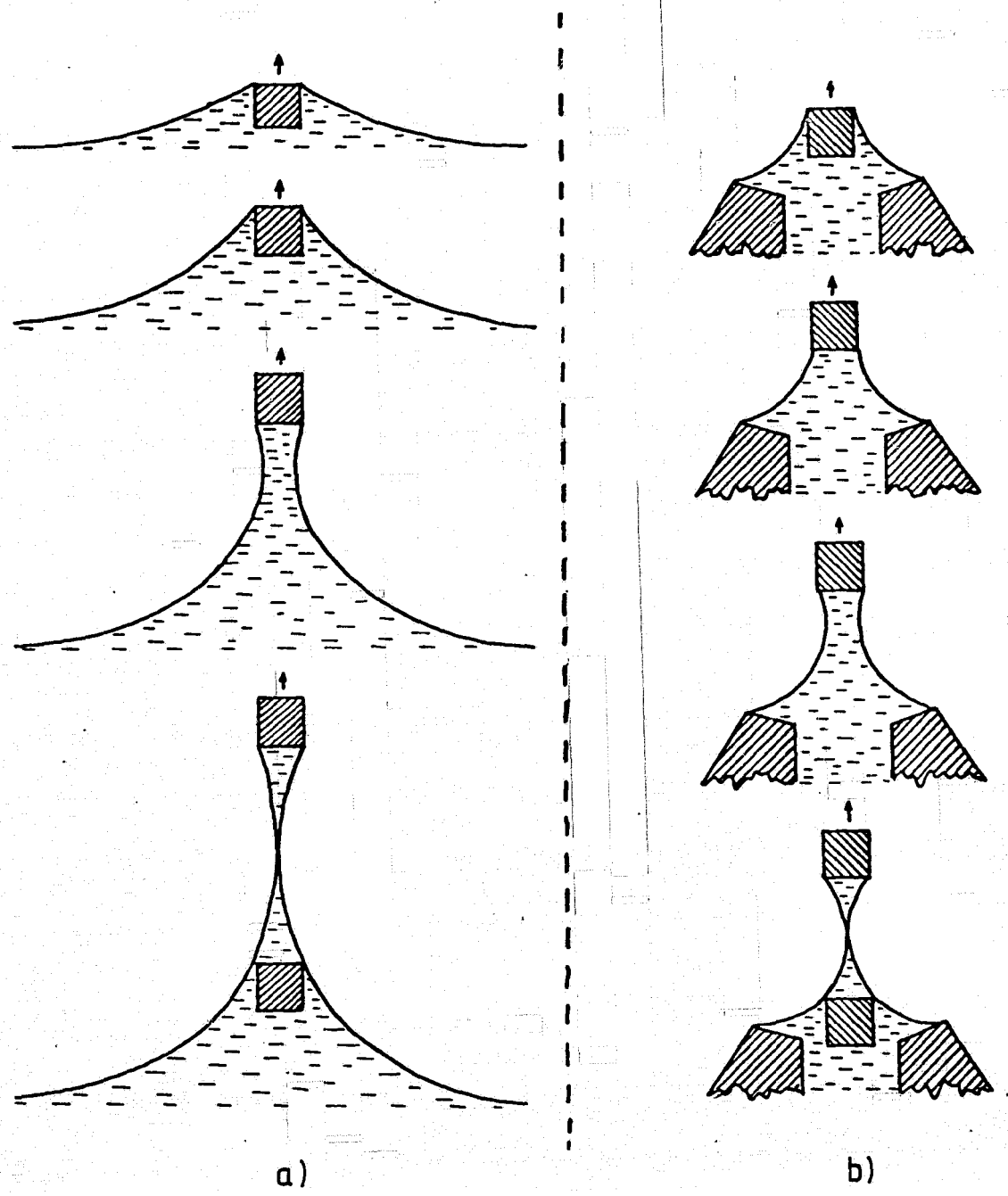

Fig. 9
Successive stages of filling the meshes of an idealized net (rectangular cross-section) with liquid Si for the case of pulling the net through a free surface (9a) or through a slotted die (9b).

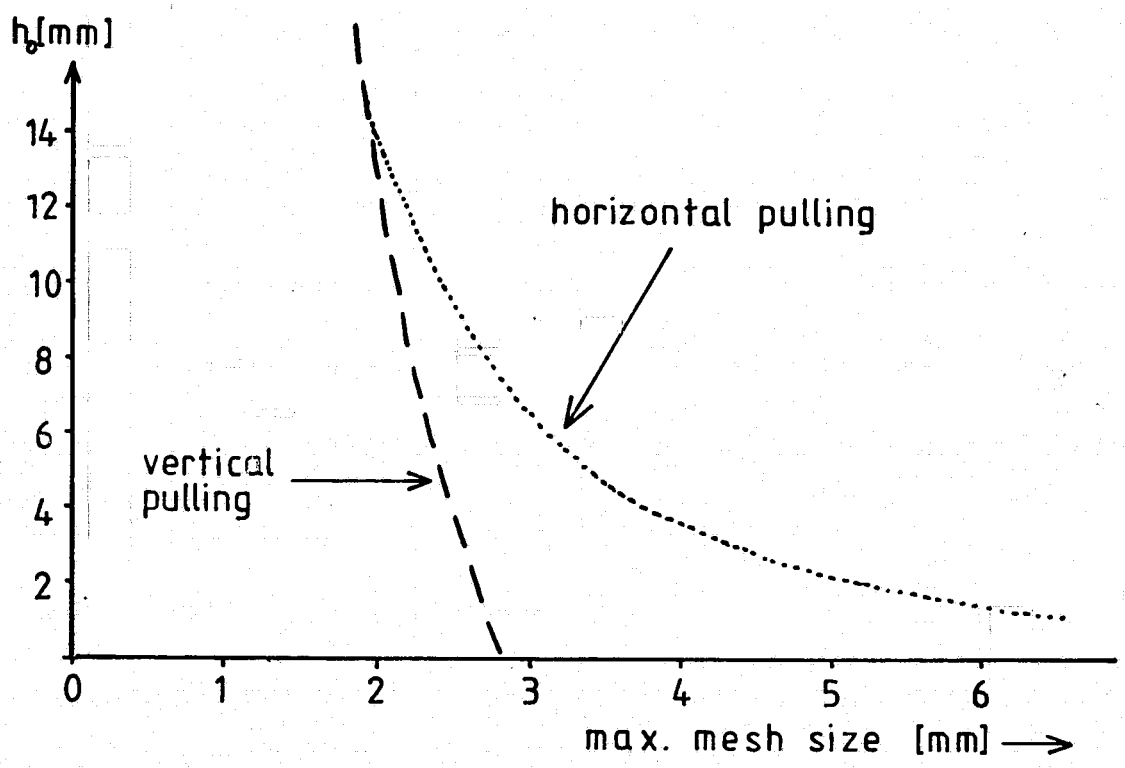

Fig. 10
Maximum mesh sizes for vertical and horizontal pulling for an idealized net with a "thickness" of 0.5 mm.

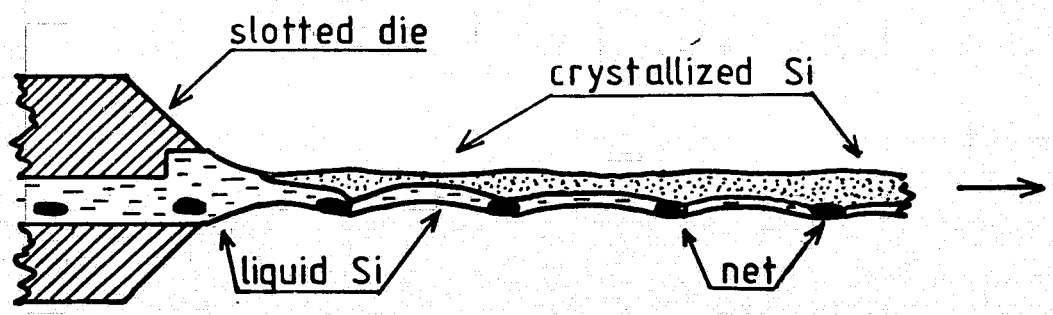

Fig. 11
Proposed geometry for high pulling speed.

DISCUSSION

KALEJS: Where are the advantages in your technique over the better-known vertical-pull techniques of the silicon-on-ceramic (SOC) that was done at Honeywell and the ribbon-against-drop (RAD) process that is being done in France?

GRABMAIER: The processing and the growth are very easy. At the moment we make plates up to 10 centimeters. When we grow vertically at high speeds, we have difficulties coating the mesh.

SCHWUTTKE: The major disadvantage, if you work with silicon-on-ceramic, is how you make a contact on the back. In this particular case you have no problem in making your contact on the back.

KALEJS: I think we should ask Dr. Belouet why he doesn't grow one meter per minute.

BELOUET: I don't really think we can pull at one meter per minute in our process as it is now. In the vertical system that we have, the pulling rate is close to 15 centimeters per minute with a practical thickness.

KALEJS: [Directed to Belouet] So you believe that one meter per minute in your technique is not possible?

BELOUET: As it is now, no. If they (the S-web) want to make a smooth growth, they are in our situation and will have the same pulling rate.

KALEJS: That is the question I was asking--in order to go to one meter per minute in whatever vertical method, you have roughly the same problems with coating the substrate.

BELOUET: Yes.

KALEJS: In the horizontal mode, what do you see different in the crystal morphology at high speeds when the S-web is there? Do you see any differences in morphology from the vertical mode as you increase the speed and keep the net covered?

GRABMAIER: No, but I think it is much easier to grow horizontally than vertically. We can use larger meshes and therefore we need less carbon material. Carbon fiber material is expensive. One square meter costs around $10.

KALEJS: Have you actually grown at 20 centimeters per minute horizontally?

GRABMAIER: No. We are developing that now.

C. K. CHEN: What is the minimum diameter of the carbon fibers that you can use?

GRABMAIER: One filament has a thickness around 7 to 8 μm.

JEWETT: Are you going to be limited in your device quality by the mesh that you use?

GRABMAIER: Maybe. The problem develops when the fibers break, and hook to the surface.

SCHWUTTKE: How good are the cells? What is the average efficiency?

GRABMAIER: This cell has a 7% efficiency with the grid. If you remove the grid, you get a higher efficiency.

BELOUET: Are your silicon carbide contacts ohmic?

GRABMAIER: Yes.

BELOUET: We always found the contrary.

GRABMAIER: Our idea was to incorporate the carbon fiber net in the back contact and we succeeded.

BELOUET: Regarding your concept of the combination of the LASS technique and the S-web, if you pull very fast, I don't see how the crystallinity will not be affected by the mesh and second, the active surface will be quite decreased at those high speeds.

GRABMAIER: I think the combination of LASS with a net is much better than the LASS is now because you will have fewer problems with the temperature, with thickness, with width and a better potential for the production line.

CISZEK: In the work that Jeff Hurd and I reported at the 14th Photovoltaic Specialists Conference in 1980 on a similar technique that we called Contiguous Capillary Coating, we observed a dendritic structure in the meshes as we tried to grow fast. Do you see also a dendritic morphology inside the meshes at your high growth speeds?

GRABMAIER: Sometimes, yes.

SUREK: This is more in the way of a comment and it may answer Dr. Kalejs's and Dr. Belouet's concern. You are decoupling the growth problem from the liquid attachment problem to the web, so the potential advantage of the technique is that you are really dragging the liquid away from the main melt source and crystallizing in a completely different environment, which you can control separately, unlike in LASS or RAD or SOC. So in principle there is decoupling of the wetting of the web and the crystallization that gives you flexibility, and even at higher growth rates you don't have to have dendritic growth, necessarily, because you can control your freezing over a much larger area. You can have a 4-meter-long cooling furnace to control the crystallization of the liquid over the web?

WARGO: I would like to reinforce what Tom Surek just said. That is absolutely true, and I see that as a major advantage of the technique. But if you are growing at faster speeds and you don't get complete filling of the mesh, it seems to me you also showed a technique where you can do

single-sided addition of silicon. Have you thought of a two-step process where in the first run you fill the web and in the second run you do a single sided addition of silicon on top of that filled web?

GRABMAIER: We tried it but we still have more development work left to do.

N84 28630 D16

EDGE STABILIZED RIBBON (ESR); STRESS, DISLOCATION DENSITY AND ELECTRONIC PERFORMANCE

Emanuel M. Sachs
Arthur D. Little, Inc.
Cambridge, MA 02140

ABSTRACT

ESR silicon ribbon has been grown in widths of 1, 2.2 and 4.0 inches at speeds ranging from .6 to 7 in/min, with resulting ribbon thicknesses of 5 - 400 microns. One of the primary problems remaining in ESR growth is that of thermally induced mechanical stresses. This problem is manifested as ribbon with a high degree of residual stress or as ribbon with buckled ribbon. Additionally, thermal stresses result in a high dislocation density in the grown material, resulting in compromised electronic performance.

Improvements in ribbon flatness (reduced buckling) have been accomplished by modification of the ribbon cooling profile. These and other experimental observations based on a wide range of experience with different widths and thicknesses of ESR ribbon are discussed.

The conversion efficiency, electronic performance of ESR material has been limited by poor short circuit current performance. Detailed laser scanner measurements have shown a good correlation between diffusion length and dislocation density, indicating that the high dislocation densities are the primary cause of the poor current performance of ESR materials.

Progress has been made in reducing dislocation densities and improved electronic performance has resulted. Laser scanner data on new and old material will be presented.

Introduction

A schematic illustration of the ESR growth process is presented in Figure 1. In this process, the ribbon is grown directly from the surface of the melt and the edges of the ribbon are stabilized by strings which pass up through the melt and are frozen directly into the growing ribbon. The edge positions of the ribbon are controlled exclusively by capillary action as the meniscus is bounded on the bottom by the melt itself, on the top by the growth interface, and at the two edges by capillary attachment to the wetted strings. As thermal effects no longer play any role in determining the edge position of the ribbon, the temperature control requirements are significantly relaxed as compared with other ribbon growth processes which rely solely or in part on thermal edge position stabilization. Loosening of the temperature control requirements to approximately ±10°C results in excellent growth stability and allows for the growth of thin ribbon with extremely good thickness control. Finally, growth from the melt surface allows for rejection of segregated impurities into the bulk of the melt, thereby taking advantage of the purification due to the directional solidification.

ESR silicon ribbon has been grown in widths of 1, 2.2 and 4.0 inches. Ribbon has been grown over a speed range of .6 - 7 in/min with the ribbon thickness (t) related to speed (V) roughly by the relation $Vt^{1/2}$ = constant. Typically, a pull speed of 1.5 in/min results in ribbon 125 microns thick. Pulling is accomplished using either a stroke puller with a 30 inch travel or a continuous roller puller. 1 inch and 2.2 inch wide ribbon have been grown with the roller puller, while 4.0 inch ribbon has been grown only with the stroke puller. Ribbons 20 - 22" long are produced with the stroke puller, while the roller puller allows for continuous growth. Figure 2 shows some typical 2.2 and 4.0" wide ribbon.

The stability and reproducibility of ESR growth is excellent, owing primarily to the large latitude in temperature control permissible. The primary problems remaining to be solved concern the issue of thermal stress which manifests itself as ribbon which cracks readily, buckled ribbon and compromised diffusion length and electronic performance.

As currently practiced, a minimum of thermal modifiers are used for ESR growth. The growth proceeds directly from the melt surface with the ribbon in radiative communication with the melt surface, the crucible walls, the insulation packs, and the radiation shields which are positioned to reflect heat from the melt surface back to the ribbon. No active after-heating or annealing is imposed, and therefore, the control of ribbon cooling profiles is limited.

While motion through the temperature fields required for growth is the primary factor determining ribbon stress levels, the interaction of the string materials and the silicon must also be considered. Ribbon has been grown with string materials which are higher in expansion than silicon and with materials which are lower in expansion than silicon. The primary differences observed concern stress in the ribbon regions immediately adjacent to the strings, which can profoundly influence the integrity of the entire ribbon, especially during cutting operations. However, it is

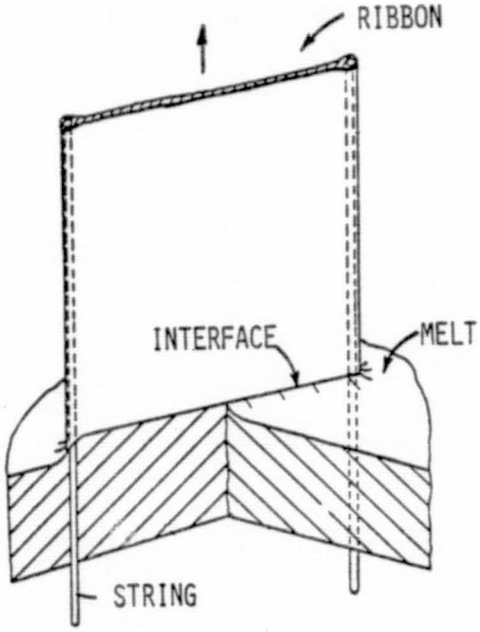

Figure 1 Schematic of Edge Stabilized Ribbon (ESR) Growth Process

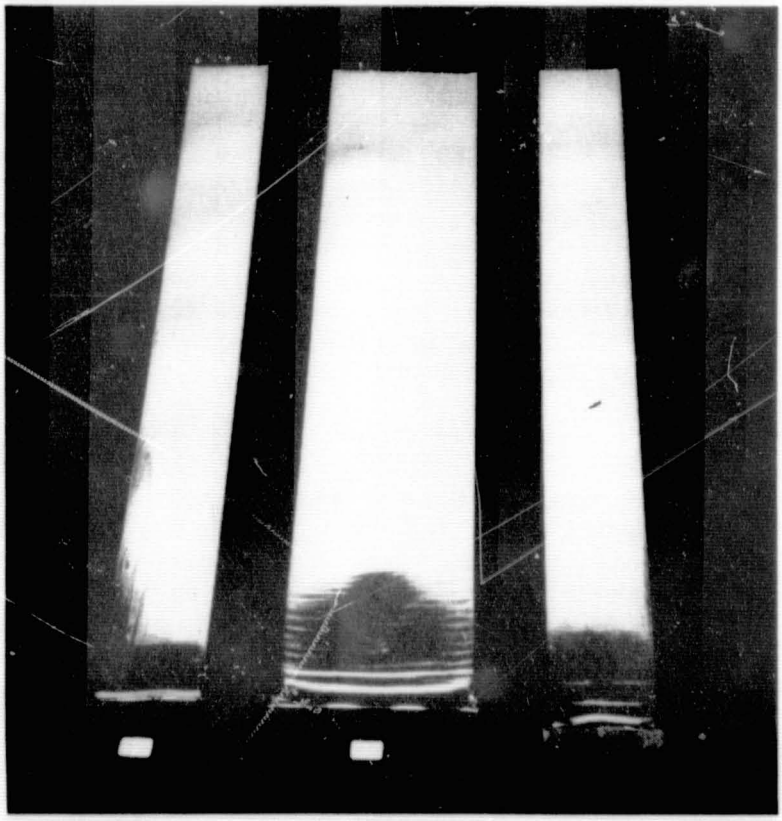

Figure 2 2.2 and 4.0 inch wide ESR ribbon

felt that the fundamental stress problems arise from the bulk of the ribbon, and the string/ribbon interaction will not be extensively discussed in this paper.

Buckling, Residual Stress and Material Handling

The methods used to diagnose the physical manifestations of thermal stress, buckling, residual stress and material handling are, unfortunately, imprecise and qualitative in nature. No direct measurements of residual stress levels are made, as the low strains involved make such measurements extremely difficult. The commonly used method where a ribbon is scribed and split along the length and the divergence of the halves measured is difficult to apply to ESR ribbon because of the influence of the edge string material. Ribbon handling is evaluated primarily by the ease with which the material may be cut into blanks and by the yield during the cutting process.

The overall ribbon flatness and degree of buckling can be readily observed on the grown ribbon. However, it is important to remember that the central portion of the ESR ribbon is unconfined and may move back and forth over the melt surface, resulting in the growth of trough-shaped ribbon. Thus, it is possible to grow in a "buckle" which is not caused by thermal stress in the direct sense, but may be the result of the propagation, or even amplification, of a previous buckle. Thus, detailed observations of the meniscus must be made during growth to try to separate these effects. Use of the stroke puller also helps to isolate the cause of problems as the roller puller is more likely to initiate and propagate problems extraneous to the thermal effects under investigation.

Thus, while thermal stress is a profound problem, its manifestations are difficult to quantify. Nonetheless, some progress has been made and, by force of experience, some conclusions can be drawn.

As with other vertical growth technologies, ESR ribbon displays a very sensitive dependance of buckling on increasing width and decreasing in thickness. For example, 4 mil thick ribbon has been grown flat in 1 inch widths, but is extremely buckled when grown 4 inches wide. This difference is best seen by reference to Figures 3 and 4.

Figure 3 shows four 4" wide ribbons grown from the same melt, all at a thickness of approximately 120 microns. Between ribbons, changes were made to the radiation shielding which redirects the heat from the melt to the ribbon. These changes influence the shape of the cooling profile along the ribbon length and across the ribbon width. The differences in ribbon shape are evident in the photo. The ribbons toward the front have short wavelength, large amplitude buckles, while toward the back, they are flatter in a local sense, but have longer wavelength, larger amplitude deviations from flatness, and, in one case display some buckling across the width. Thus, while the crude temperature profile modifications implimented to date have had dramatic effects, the resulting ribbon is not yet flat.

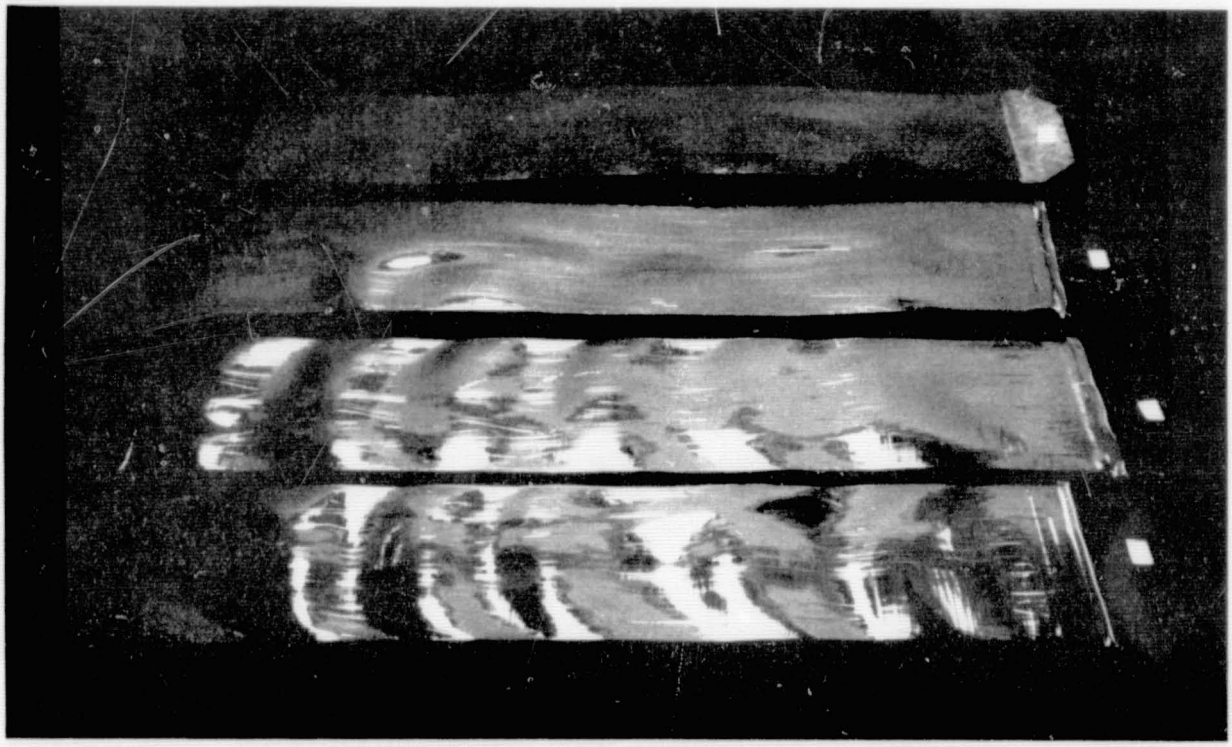

Figure 3. 4.0" wide ESR ribbon, 120 microns thick, showing buckling patterns and amplitudes.

By contrast Figure 4 shows a 1" wide, 90 micron thick ribbon grown with a similar thermal environment. As may be seen in this multiple exposure photograph, this material is flat and flexible.

Observations during growth have clearly revealed that all the "buckling" observed in ESR ribbon is at least in part grown in. The mechanism is as follows. A small deviation from flatness is induced by thermal effects. This results in the pulling direction shifting to slightly off vertical. As has been shown by theory and confirmed by experiments where the pulling axis is shifted off vertical, such pulling results in the movement of the meniscus across the melt surface, and trough-shaped growth results. This motion continues for a time and then reverses (by a mechanism not clearly understood) and the "buckle" passes through the plane defined by the strings and extends to the other side of the ribbon. Thus, the growth mechanism clearly accentuates the effect of thermal buckling.

The effect of melt height has been observed to be profound. A change of 2mm can result in dramatically different buckling, stress, and handling characteristics, ostensibly due to the shift of the interface position with respect to the cooling profiles. Batch replenishment is performed between ribbons to attempt to minimize the influence of melt height changes. Also of importance is the uniformity of thickness across the ribbon width. While our ribbon thickness uniformity is fairly good (for example, typically 200 ± 50 microns across the width), it has been observed that more uniform thickness material is "better behaved" than the poorer material.

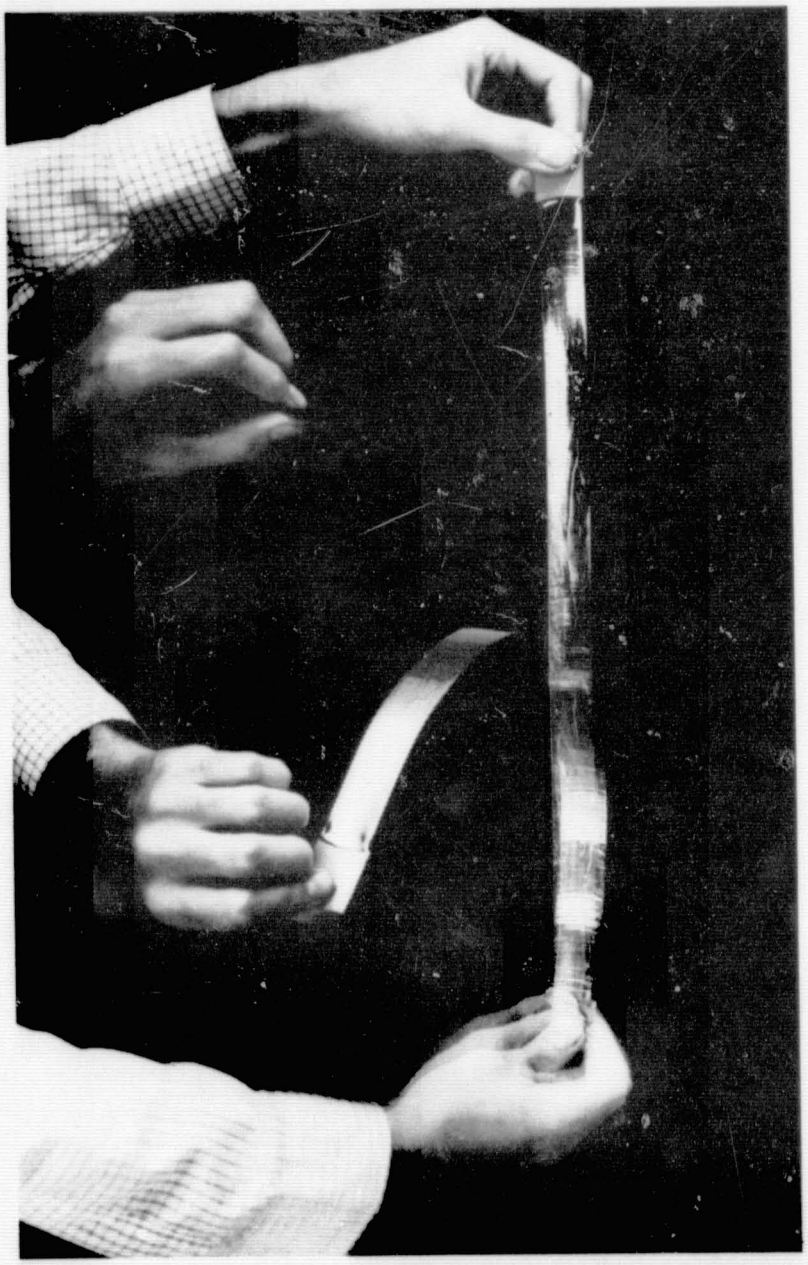

Figure 4. Multiple exposure photograph of flexible 90 micron thick 1" wide ESR ribbon

Electronic Performance and Dislocation Density

The primary tool used to characterize the electronic performance of ESR material from the perspective of thermal stress induced damage in our infra-red laser scanner, shown schematically in Figure 5 below.

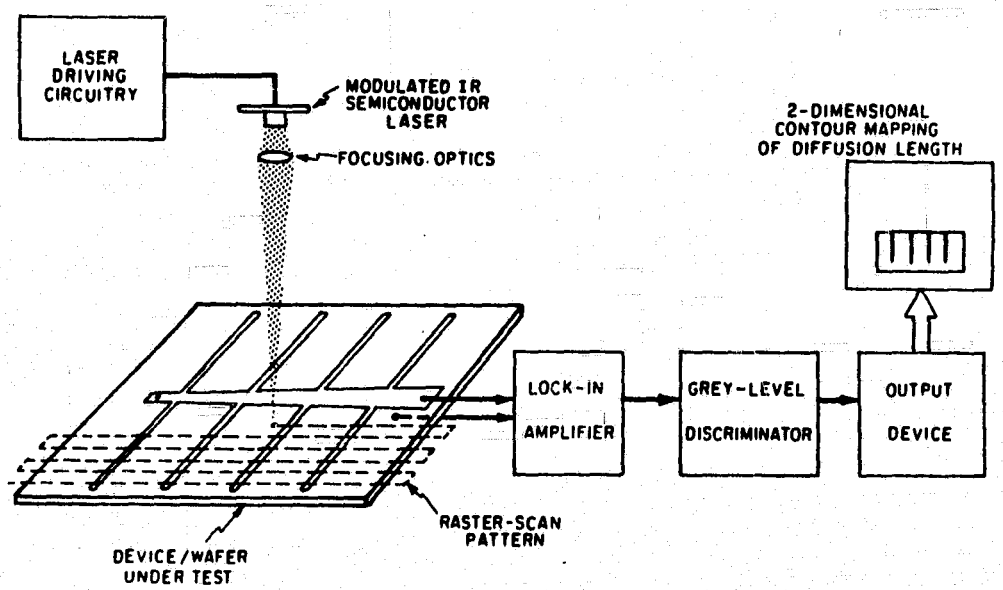

Figure 5 Schematic of infra-red laser scanner

This machine raster-scans the focused beam of a modulated semiconductor laser over the sample being tested. A lock-in amplifier is used to derive a dc voltage proportional to the component of the short circuit current of the sample at the modulating frequency. Since the short circuit current behavior at long wavelengths is related to the minority carrier diffusion length in the base of the material, this measured dc voltage is monotonically, but non-linearly related to the diffusion length of the material at the laser focus.

The voltage from the lock-in amplifier is directed to six comparators whose set points can be individually selected from ten different preset values which are chosen to correspond to specific diffusion lengths. The output of the comparators are analog summed to produce a signal which has seven discrete levels, including zero. This signal is used to generate a two-dimensional grey scale mapping of the diffusion length, with the grey scale densities corresponding to the six selected diffusion length values.

The laser scanner may be used on fabricated solar cells or on as-grown ribbon, utilizing an electrochemical junction technique. A similar electrochemical junction method is used to obtain large area averaged diffusion length measurements which are used independantly or to cross check the laser scanner results.

Figure 6 shows laser scans of 4 cm^2 ESR solar cells, with the simultaneously produced grey scale reference. These scans are representative of the best material produced to date. As may be seen, the scanner resolution is sufficient to resolve grain boundaries with good clarity (the laser spot size is approximately 25 microns in diameter). The large variations in performance from one area/grain to adjacent areas is typical of ESR material.

Figure 7 shows an electrochemical junction laser scan of a piece of 1" wide ESR ribbon oriented as if it were growing upward. Again, the resolution is sufficient to resolve grain boundaries. Figure 8 shows a similar scan on a sample of 2.2" wide ribbon. The small grain structure nucleated at the strings may be seen at the ribbon edges. The structure may be seen to grow larger as it moves toward the ribbon center. From these scans, one immediately can see that the performance of the material near the edges is certainly not worse than the performance of the material near the center.

Figure 8 is taken only about 8" from the seeding junction. It may be seen that the two sides of the ribbon have different structure. The right side is composed largly of twinned structure which is the result of the seeding orientation used (110 face, 211 growth direction). On the left hand side, the string structure has predominated. In general, it has been found that as growth continues, any structure imposed by the seed is eventually overwhelmed by the structure from the edges. Seeding has been done with single crystal seeds of several orientations, with polycrystalline seeds and with graphite.

The most important information derived from the laser scans concerns the origin of the reduced diffusion length. After scanning, these samples are etched to reveal dislocations and the dislocation densities are correlated to the scanner maps. Excellent correlation is observed between diffusion length and local dislocation densities. Thus, we see that thermal stress and resulting dislocations also controls the electronic performance of ESR ribbon. Such tests have also shown that twins are benign and may improve performance.

Conclusions - Future Effort

Future work will concentrate on better characterization of the cooling profiles present in the ribbon and better control of these profiles.

Also of great importance is the attainment of better thickness uniformity across the ribbon width and better control of melt level during growth. These efforts are currently underway. The alternative growth geometry of angled growth, wherein the growth interface is at a substantial angle to the growth axis, is also under active investigation. This method has the potential to vastly reduce the severity of the stress problem by reducing temperature gradients along the growth direction.

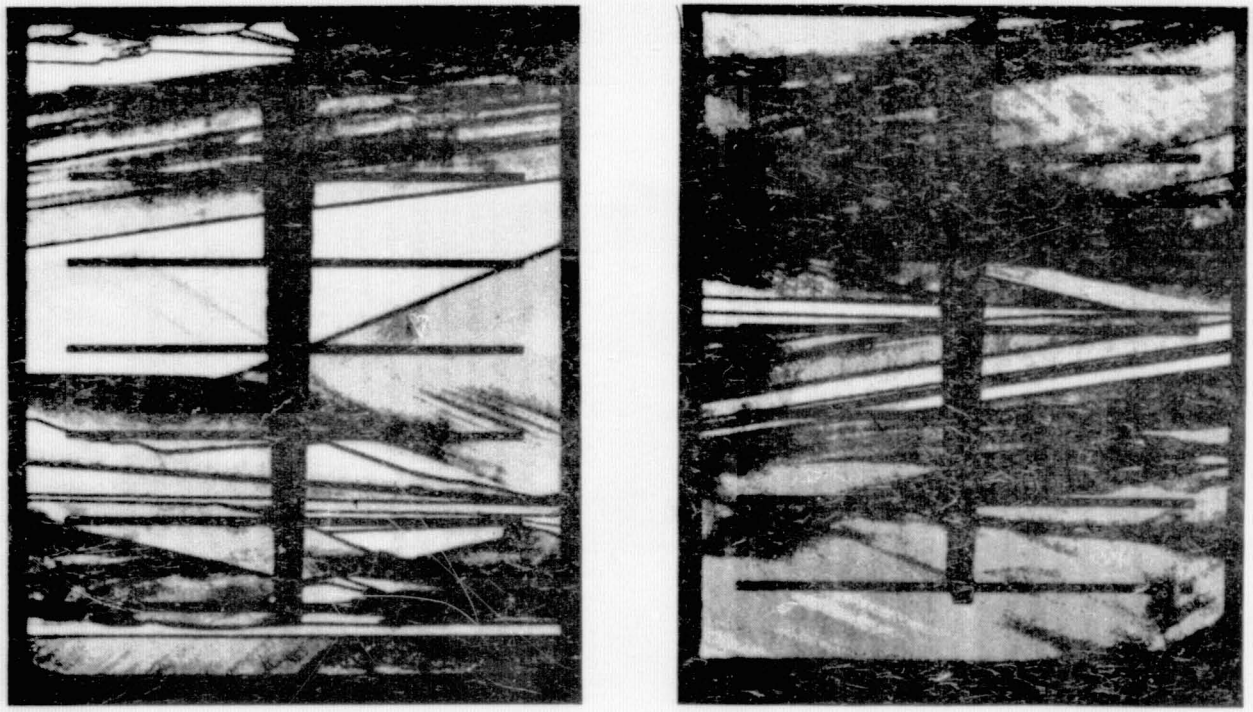

Diffusion length grey scale (μ)

15 20 30 40 50 80

Figure 6 Infra-red laser scans of 4 cm^2 ESR solar cells

Figure 7 Infra-red laser scan of 1" wide ESR ribbon. White represents best performance.

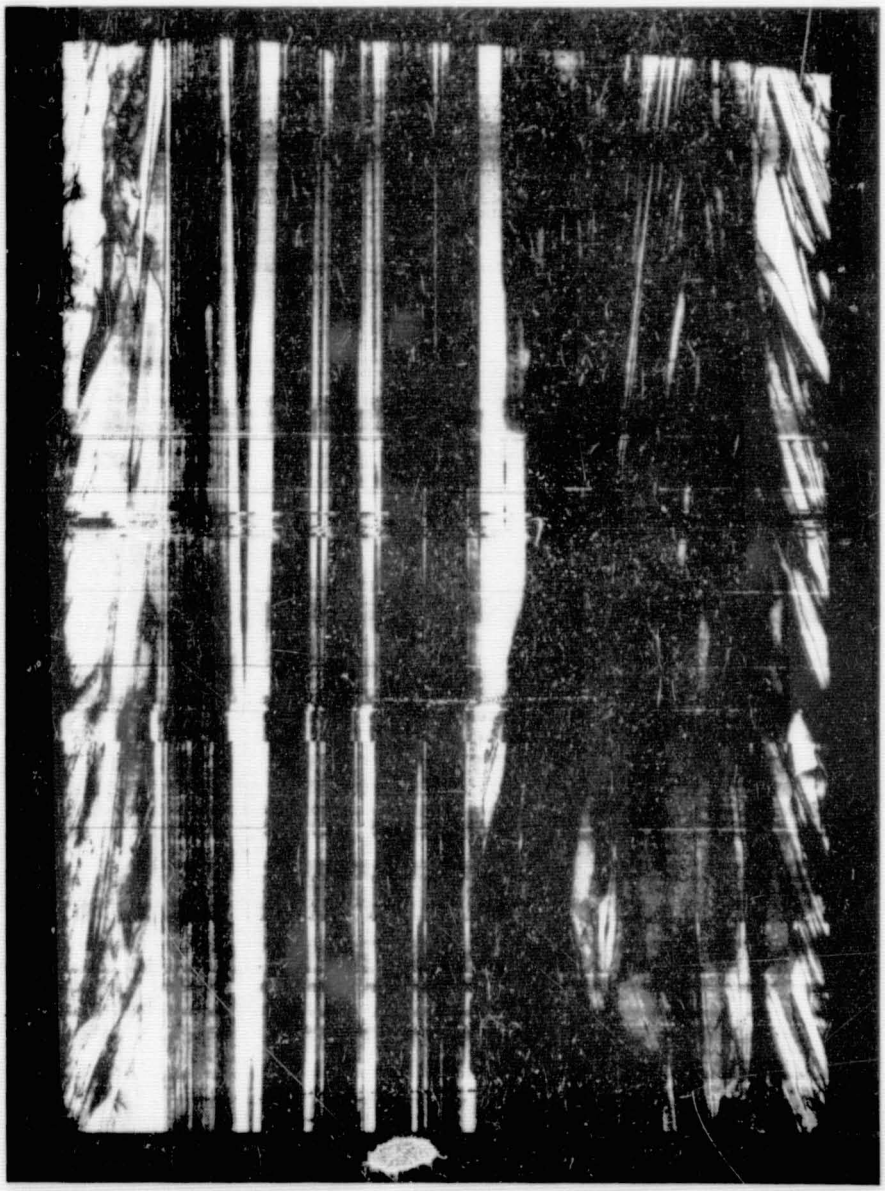

Figure 8 Infra-red laser scan of 2.2" wide ESR ribbon. White represents best performance.

DISCUSSION

LAMBROPOULOS: Would you have a rough estimate of the levels of the residual stresses you were getting in the ribbons?

SACHS: We have made no direct measurement of residual stresses. If you look up the breaking strain of silicon, we are often near it or above it. I would guess we are talking in units that I know, 5000 lb/in^2 or a little bit more, sometimes less also.

SMITH: What is your average growth speed in these samples?

SACHS: It depends entirely on thickness. We grow some very thin ribbon. There is an inverse relationship. The relationship between speed and thickness goes as $Vt^{1/2}$ = a constant. If you are growing at 6 centimeters a minute, you will get 50-µm-thick ribbon.

SMITH: Did you grow very slow? This was something that was mentioned yesterday as a way of getting rid of some of the residual stresses.

SACHS: Millimeters a minute. The problem is that to make the categorical statement that lower growth rate gives lower buckling confuses the issue of the thickness of the ribbon. If you grow a couple of millimeters a minute, you will have ribbon about one-eighth of an inch thick, maybe thicker. So it isn't really a useful exercise.

FAN: You mentioned the dislocation caused by stress. Do you have an idea at what point the dislocation occurred, at what stress level?

SACHS: I really wish I did.

FAN: What will happen if you have a slip or dislocation from the stress relief?

SACHS: I am assuming that is what happens and there are some other competing effects. Twins are another mechanism for stress relief, and the interaction between twins and dislocations is very interesting. Often a region that is twinned is not heavily dislocated, and that says to me that the twins have relieved some of the stress, and you don't need to dislocate any more in that region, and those regions can have very good performance as a result of that. That gives a clue, perhaps, as to where things are happening, but it is very hard to pin that down.

FAN: Do you want samples with a lot of twins so you have less stress?

SACHS: Maybe. The twins create other problems. Cleavage, for one. It is possible that that is a way to go.

REGNAULT: As you exercise further control to improve ribbon flatness and improve the thermal gradients above the melt to reduce the buckling, to

what extent did this lower the ±10° temperature control that you talked about at the first slide?

SACHS: Very little. There are two thermal zones in this type of ribbon growth, at least. One is the melt temperature, and the other is what you do to the ribbon above the interface. They are somewhat coupled, but very, very weakly.

REGNAULT: Is this ±10° strictly at the crucible and not at the meniscus height?

SACHS: It is at the point of measurement in the bottom of the crucible which, we hope, is well correlated to the bulk melt temperature, which is probably quite well related to the melt temperature at the base of the meniscus. Then you have about a quarter of an inch up until you get to the interface, which is obviously at the melting point. The temperature drop is probably happening primarily in that quarter of an inch. The bottom of the meniscus will be close to the bulk melt temperature, and the top will be at the melting point.

WARGO: You give as a major advantage of your process the fact that you get a segregation of impurities, but doesn't that preclude the steady-state growth where you have controlled incorporation of the wanted impurity, and also doesn't that make problematical the setting up of the process as a continuous process?

SACHS: The controlled impurity has a segregation coefficient near 1, namely boron, so as compared with 10^{-3}, 10^{-5}, it is a different ball game entirely. In terms of a continuous process, obviously if you are doing nothing else but putting melt in and taking it out in the form of ribbon, then after a couple of days of growth the levels will build up in the melt to the point where what you have going in is what you have coming out. There are other things that can be done. If you look at the volume of the melt, it provides a mechanism to concentrate impurities there, and there are ways to remove it. You don't have to stop every three feet and take it out. That is an issue to be faced but I think there are solutions to that.

LEIPOLD: Ray [Seidensticker], do you want to comment on that, since you have done some work there?

SEIDENSTICKER: Yes, in the melt replenishment of continuous growth which can be either the ESR, ESP, or web, where you do have a Czochralski-like segregation, the sort of impurity buildup you get will depend on how you replenish. There is a paper by me and Hopkins a couple of years ago that shows how this works out, and you can go for quite a while before you get deleterious buildup of unwanted impurities. Of course, this depends on whether you are replenishing it with relatively impure material, or relatively pure material. I will just make an added comment on the precluding growth. There are several possibilities. One is that you can use a very high segregation coefficient, obviously boron, and as you are replenishing it you just keep adding boron. There is another possibility, which is to use something that has a very low segregation coefficient.

You put in to begin with and just replenish it with pure material and most of it stays in the melt. You just draw a tenth of a percent or a hundredth of a percent of the material, so you can do it either way.

SACHS: Do you do that?

SEIDENSTICKER: We have. We have done it all sorts of ways.

SACHS: It seems to me that the resistivity variations in the grown ribbon might be substantial, depending on how much convection was in the melt.

SEIDENSTICKER: No. You have an advantage in your system because you are growing from a very high meniscus. It is a small volume. You have diffusion control. There is not much that is happening up in the meniscus. This is the sort of thing that Professor Chalmers was talking about. But it is somewhat isolated from the bulk of the melt, and in the bulk of the melt you have very good stirring, and how this works with the meniscus is a matter of the particular details of the system, but there are no real problems.

JEWETT: You have pointed out that your strain problem is going to be very sensitive to the thermal cooling profile. You also pointed out that you are presently having a melt level which is changing while you are pulling the ribbon and then finally that the initiation of a buckle means that you have then changed the shape of what you have pulled. It seems that your effort to produce low-strain material is going to be severely hampered until you do go to a continuous process where your melt level will be constant. Do have that in your immediate plans?

SACHS: Very immediate.

DILLON: What kind of dislocation densities are you finding, and what is your present electrical efficiency?

SACHS: Dislocation densities range from a low of 10^4 or lower, in some cases, up to 5×10^6.

DILLON: Where can you go in the future with respect to getting it uniform with respect to that density?

SACHS: I don't care if it is uniform and I don't think that matters. I want it all a little better. The bad areas in a solar cell contribute less current to the short-circuit current, but they don't do anything very significant to the solar-cell performance. Our voltages are very good and our fill factors are very good and our cells are current-limited. To answer the other part of your question, we have been making cells by a process that needs to be, and is being, improved. We make, on single-crystal, 12% and on our ribbon 10%. So we are making about 85% of the efficiency of single-crystal.

SCHWUTTKE: I would like to object to your remark that you don't care about the dislocation density or perfection or whatever. You also, if I understood right, said they don't contribute that much to the performance of the cell. Is this part correct?

SACHS: No. What I said was I don't care if it is not uniform across the surface.

SCHWUTTKE: Well, I care a lot, and I will tell you why. I would like to draw your attention to a paper published by Fred Lindholm and Randy Davis. They have shown that a 10% non-uniformity in minority carrier lifetime decreases your solar cell efficiency by 50%.

SACHS: Our fill factors are equivalent to what we see in Cz, namely 76 to 77. We have very deep junctions and that is why the currents are low. But our voltages are quite good--550 millivolts.

GIESSEN: In terms of the buckling, could one improve things by running some of the carbon fibers right through the center, having additional carbon fibers as a guide, or would that advantage be offset by additional nucleation from them?

SACHS: You would incur disadvantages and have no advantages.

GIESSEN: You would not eliminate buckling thereby, if they were taut?

SACHS: No. If you think about what the ribbon will look like when you do that, it would really be pretty ugly.

MILSTEIN: Listening to the discussion between Ray [Seidensticker] and you, it occurs to me that you may have a system that is a hybrid, in the sense that for rather wide ribbon you may have something approaching a quiescent capillary effect in the center of the ribbon, whereas the strings near the edge cause some turbulence, so that the effect of the segregation coefficient may not be constant across the width of the ribbon. It might be interesting to look for resistivity variations due to something like that.

SACHS: That is possible. I think the velocity of the strings is pretty low, so that it is not likely to be pumping a lot of melt around.

MILSTEIN: OK. But as you go up in growth rate, and as you go wider, so that effect, if it occurs, may be magnified.

WILCOX: I think we should keep in mind the possibility of having Marengoni or thermal-capillary-driven convection, which could be extremely important. If you have surface-tension gradients, due to temperature gradients and possibly composition gradients, it would give you a lot of convection, especially in a thin meniscus region, so there may be a lot of convection. I don't think we should automatically assume there is no convection.

SACHS: Right. And there has to be some thermal convection, because there is a temperature gradient in the meniscus.

WARGO: To reinforce Professor Wilcox, you have a very high surface-to-volume ratio in that meniscus region, compared with other bulk techniques--for example, Cz. In that case, and I would guess that even when it compares

to floating zone, the driving force for thermal capillary flows should be significant.

SACHS: I just want to point out that because the meniscus in ESR is high, about a quarter of an inch or so, there is, depending on the thickness, enough material for a couple of feet of ribbon in the meniscus. So it isn't all that small, although small compared to bulk techniques.

GRABMAIER: From your picture, the crystal quality in the middle of the ribbon is very high and very good, and less on the edge. Did you prepare cells from the middle area and also from the edge area and how high were the efficiencies?

SACHS: Yes, we have done that with mesa diodes, fabricated on a sample where the mesas run from center to edge. There is very little difference in performance.

GRABMAIER: Does that mean there is no influence of the grain size?

SACHS: No, it doesn't exactly mean that. If you remember the laser scans I showed of the as-grown ribbon, the intragrain performance inside the grain at the edges was very good but there were a lot of grain boundaries. So it's a tradeoff there. I don't know why the intragrain performance at the edge is as good as it is, and I have been wondering about that, perhaps having more grains around allows for some stress relief by a different mechanism. I think the reason the solar-cell performance comes out about the same is because you have good intragrain performance, but you have more grain boundaries, and they more or less cancel out.

GRABMAIER: Did you also try to pull two ribbons simultaneously?

SACHS: No, not yet.

RAVI: You have a lot of tradeoffs that may not all equalize each other. As I understand it, you have to control your thickness through your speed. You have to go fast to come up with decent thicknesses, decent meaning 5 or 10 mils or so, but if you grow fast you are going to get buckling, so in order to avoid buckling you will have to tailor your temperature profile above the interface. As you know, we have done a lot of work in trying to do just that. It is not easy. If you do that, under the best of circumstances, you probably will get a lot more dislocations and a lot more nonuniformity, because you will get a lot of creep. Juris [Kalejs] will talk about that later. So you have mutually incompatible requirements: thickness control which requires fast growth, fast growth which leads to buckling, controlled buckling leads to more dislocations, and so on. You can go around in a circle.

SACHS: I think that is one of the tradeoffs common to all vertical ribbon-growth techniques. I think controlling thickness by controlling speed is a big plus, it is a very easy way to do it, and a very dependable way to control thickness. I hardly think that that can be cast in the form of a liability. I think that the basic tradeoffs you have discussed, speed versus temperature profile and dislocation density, are the tradeoffs of

vertical ribbon growth. The differences between the techniques, in my opinion, concern the ease with which the growth itself may be performed. But I think above the interface they all have a great deal of resemblance.

CHALMERS: Haven't you missed a point in this last discussion? You can control the thickness by changing the melt temperature just as well as by changing the speed.

SACHS: You can. I think that is a little less desirable. I would perhaps rather control it, if I wanted an alternative to speed, by controlling heat removal from the ribbon.

RAVISHANKAR: Looking at your ribbons, it looks like the interface shape is pretty flat except for the very edges where it is concave. That's where, also, you have the nucleation problem. It looks like if you choose a fiber material with a different wetting angle with the silicon melt you might solve the problem. Have you thought about that?

SACHS: You have a lot of distance to go before you do that. The center is about one quarter of an inch or so and the edges are down significantly from that. The shape is controlled by the capillary requirements by integrating Laplace's equation from the top down. Changing that top boundary condition would change it a little but by that technique you will never get the edge meniscus to be above the center meniscus, I don't think.

LAMBROPOULOS: Have you observed from what point from the interface the buckles first start to form?

SACHS: Buckles don't happen like that. Observing them is not trivial at a growth rate of roughly an inch a minute, but I would say it is happening in the first few inches.

N84 28631

LOW ANGLE SILICON SHEET GROWTH: A REVIEW OF PROGRESS, PROBLEMS AND PROMISE.

H. E. Bates and D. N. Jewett

Energy Materials Corporation
So. Lancaster, MA.

Introduction

High growth rates are the key to a successful low-cost silicon ribbon technology. The approach typified by the Stepanov method, EFG and dendritic web suffers a fundamental limitation in this respect due to the manner in which the heat of fusion is lost from the solidification interface. This heat must be conducted along the grown ribbon for some distance before it can be dissipated. Thus the conduction path is limited to the cross-sectional area of the ribbon, since the solid-liquid interface is perpendicular to the pull direction. In contrast, "horizontal" ribbon growth is achieved by providing an extended solidification interface, parallel within a few degrees, to the pull direction. In this manner, the heat of fusion need only be conducted through the thickness of the ribbon and thence dissipated from the upper (solid) surface which comprises an area equal to the interface. This is illustrated schematically in Fig. 1.

The first description of a horizontal ribbon growth method was by Bliel in 1969, although it seems that the major advantages were not recognized at this time (1). Later, a group of Japanese workers applied the approach growth rates and good electrical properties (2,3).

The work reported here was begun in mid-1979, and has progressed to a third-generation system which is provided with automatic melt level control and liquid feed melt replenishment. This system has demonstrated growth of up to 15cm wide ribbon and continuous growth of ribbons as long as 120 meters. Areal productivity as high as $2.7m^2/hr$ has been demonstrated for a single 15cm ribbon, while typical values of approximately $1m^2/hr$ are obtained in the growth of 5cm ribbon.

Process Description

The ribbon growth apparatus consists of a water cooled aluminum jacketed furnace with insulated resistance heated zones operated in an argon ambient. Carbon plates support a shallow rectangular quartz crucible over four horizontal heating elements. The furnace has been configured for growth of a single ribbon from a 30 x 15cm crucible, and for growth from a 60 x 15cm crucible of either three 5cm wide ribbons or a single 15cm ribbon. The system is currently configured to

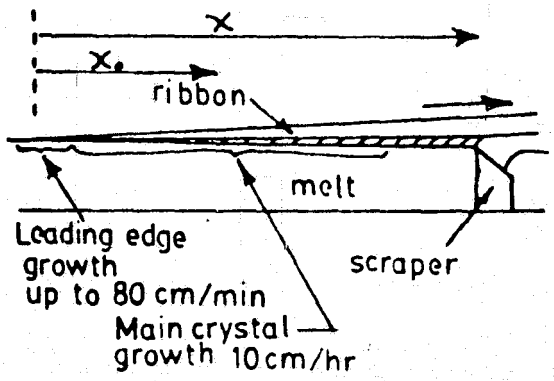

Figure 1. Schematic diagram of LASS process.

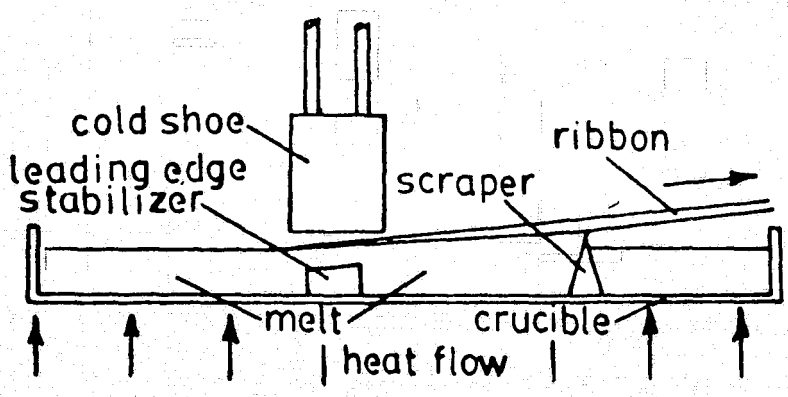

Figure 2. Schematic of LASS growth system.

grow a single ribbon of 5-10cm width from a 15 x 50cm crucible, the long axis of the crucible and the pull direction being coincident. The melt is replenished with liquid silicon from a fifth, melt-in zone, fed with solid chunk material. Melt level control is accomplished by a floating quartz cup linked to a magnetic proximity sensor, whose output signal activates a larger, motor-driven, quartz displacement cup.

Fig. 2 is a cross-sectional schematic of the growth zone. Temperature fields in the melt are modified by thermal impedances and a cold shoe that promotes growth at the leading edge. Thus the leading edge becomes a constantly renewed seed that grows in the thickness direction as the ribbon is pulled across the melt surface. Ribbon thickness is therefore a function of bulk growth rate, downward, and linear pull rate. Typical values of the bulk growth rate range from 15 to 20cm/hr. The meniscus is detached from the bottom surface of the ribbon by the "scraper". The elevation of the scraper above the melt level raises the meniscus to provide increased stability to the ribbon edges.

Ribbon growth is initiated by introducing a seed through a set of motor-driven rollers into the furnace until it contacts the melt. The cold shoe is lowered into position and the cooling gas flow increased. The seed is withdrawn slowly to initiate growth and then pull speed is increased gradually as gas flow and temperature are adjusted. Once steady growth has been obtained, sections of ribbon are scribed and broken off as pulling continues.

The process is quite stable; continuous growth of as long as four hours have been achieved, and it is quite tolerant of abrupt variations in pull speed. A very notable feature is the complete absence of residual stress under all combinations of ribbon width, thickness and pull rate. No afterheater is used and no particular attention has been given to the thermal environment of the ribbon after it passes the scraper.

An empirical study of ribbon thickness vs. pull speed was done on ribbons grown from 27 experimental runs and compared to the behavior predicted by two models of horizontal ribbon growth. Ribbon thickness was computed as an average from measured weight, width and length of ribbon sections. The dashed line in Fig. 3 is a straight line logarithmic fit to these data. The solid lines are values computed from Zoutendyk's (4,5) analysis, where if ΔT_L is positive the melt is hotter than melting point, and if ΔT_L is negative the melt is supercooled.

Kudo's model predicts thicker ribbon at slow growth speeds and thinner ribbon at fast growth speeds than we experimentally observed, with a cross-over point at about 40cm/min. This is

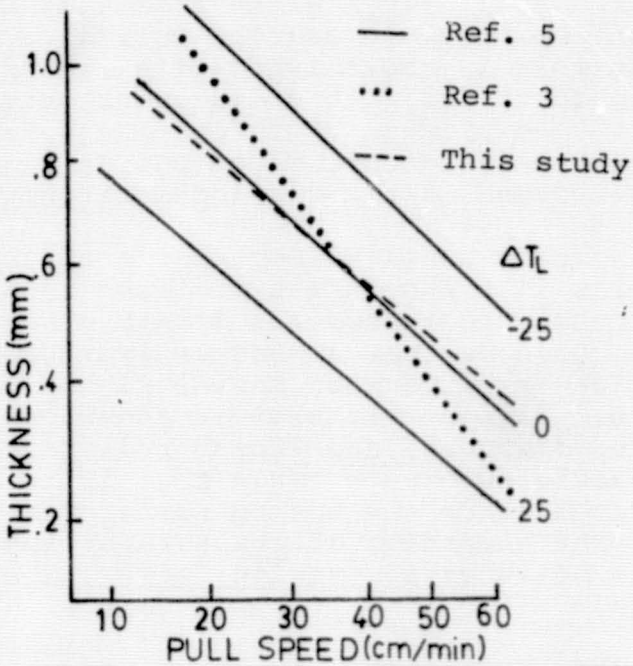

Figure 3. Variation of ribbon thickness with pull speed. Solid lines represent varying degrees of melt undercooling: $T_L = T_L - T_{MP}$

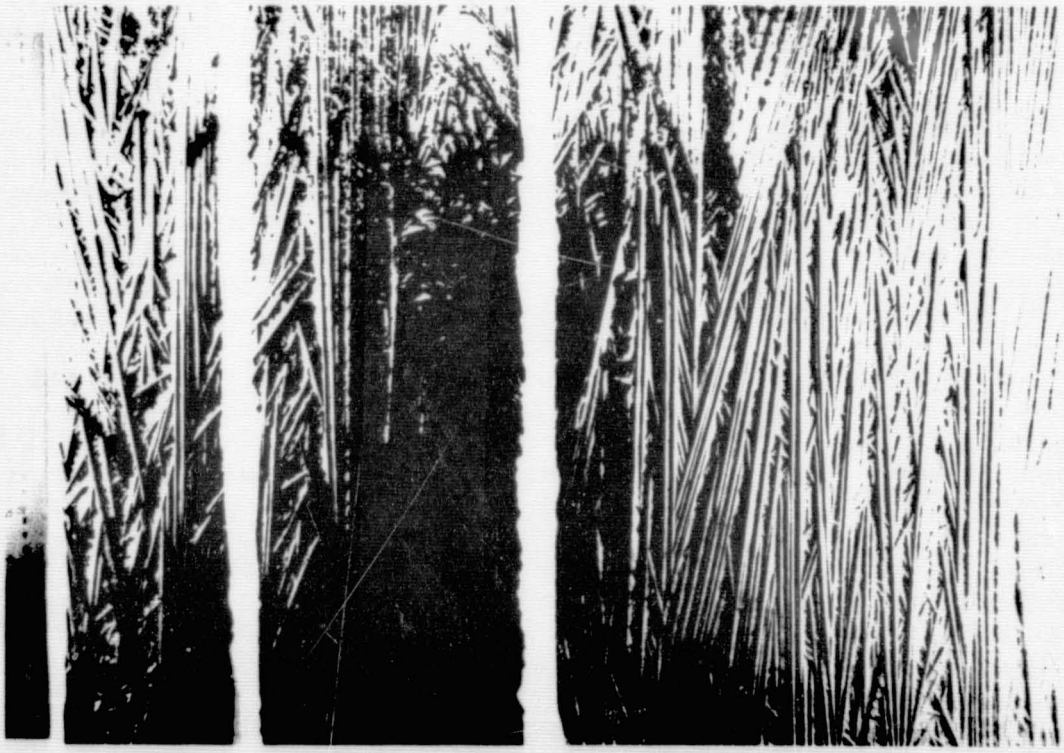

Figure 4. Top surfaces of random dendritic ribbons of various widths: 35, 55, and 150mm.

also true of Zoutendyk's model, only much less so, and it is interesting that the cross-over is at approximately the same point. The agreement amongst the two models and experimental data is quite remarkable, given the various simplifying assumptions of the models and the complexity of the real system. Two major assumptions, uniformity of cooling of the ribbon surface and an isothermal melt with no convection, seem unlikely to be realized in practice. Nonetheless, our experiments seem to agree substantially with the modelling attempts.

LASS Ribbon Characteristics

Silicon ribbon has been grown reproducibly by the LASS process at rates from 10-60cm/min.; a maximum rate of 85cm/min. has been achieved. Ribbon thickness is typically in the range of 0.5 to 1mm; a minimum thickness of 0.35mm has been attained. The ribbon width is controlled by the cold shoe dimensions and thermal control elements. The maximum ribbon width has been 150mm, while typically widths 50 to 65mm are grown.

Two main types of structure have been found to occur in LASS ribbon. These are, respectively, random and aligned dendritic. The former is characterized by a somewhat rough top surface composed of more or less random intersecting dendrites that have grown within ±30-40° of the gross ribbon growth direction. The top surface appearance of this material is shown in Fig. 4. The top surface roughness of random dendritic material is on the order of 0.2-0.5mm with large primary dendrites and finer secondaries that fill the interstices. The bottom surface of thinner ribbon (0.4-0.5mm) tends to be somewhat irregular, while that of thicker material (0.5-1.0mm) is quite smooth. On a microscopic scale, as seen in Fig. 5, the material is polycrystalline with twins and a few high angle grain boundaries. Twin bands are usually associated with the peaks and valleys of the dendrites.

The structure of aligned dendritic ribbon is a regular array of dendrites parallel to the growth direction. The peak-to-peak spacing of the dendrites varies from less than 1 to 3mm. The top surface relief of this structure is from 0.1-0.3mm. Fig. 6 shows a polished and etched cross-section of a ribbon comprised of aligned dendrites. The density of twins and twin lamellae varies substantially; closely spaced dendrites typically exhibit higher twin densities. High angle boundaries are seen only rarely in this material. Similarly, very few dislocation pits are seen, other than occasional clusters of pits which we believe result from entrapment of small droplets of liquid. X-ray examination of this type of ribbon has revealed the orientation to be as shown in Fig. 7. The <110> direction typically lies 20°-30° off the surface normal, while the growth directions observed have been either <210> or <211>.

Figure 5. Cross-section of random dendritic ribbon. Sirtl etch.

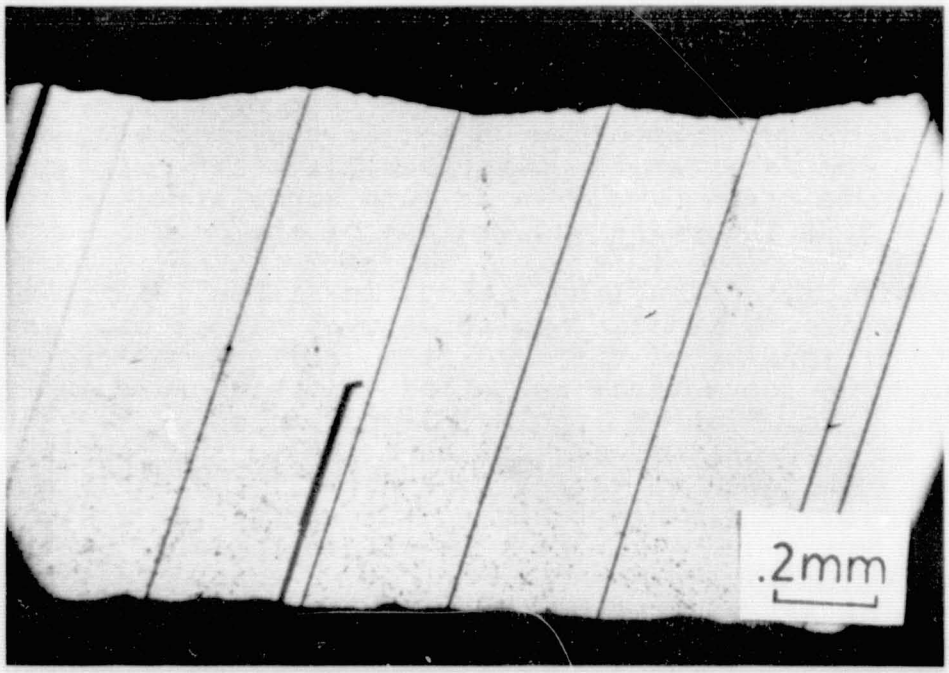

Figure 6. Cross-section of aligned dendritic ribbon. Sirtl etch.

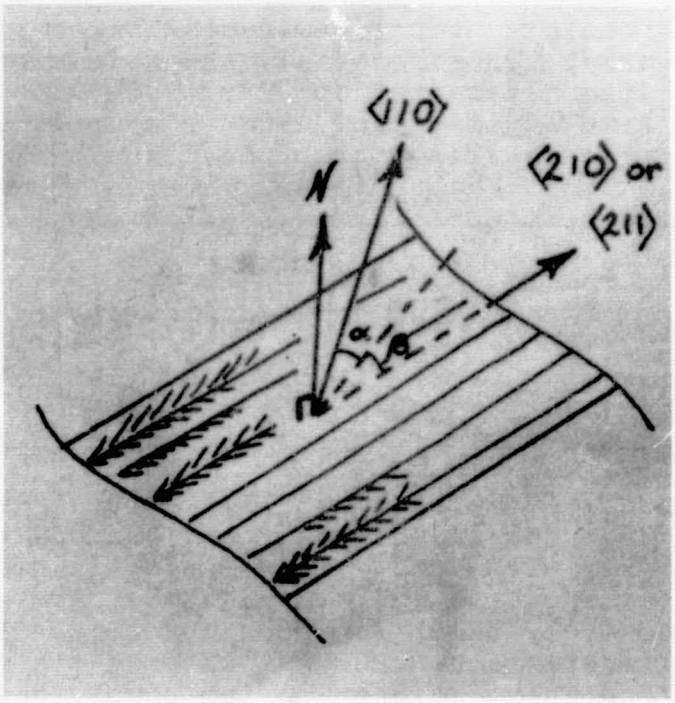

Figure 7. Typical orientations observed by X-ray examination of aligned dendritic ribbon.

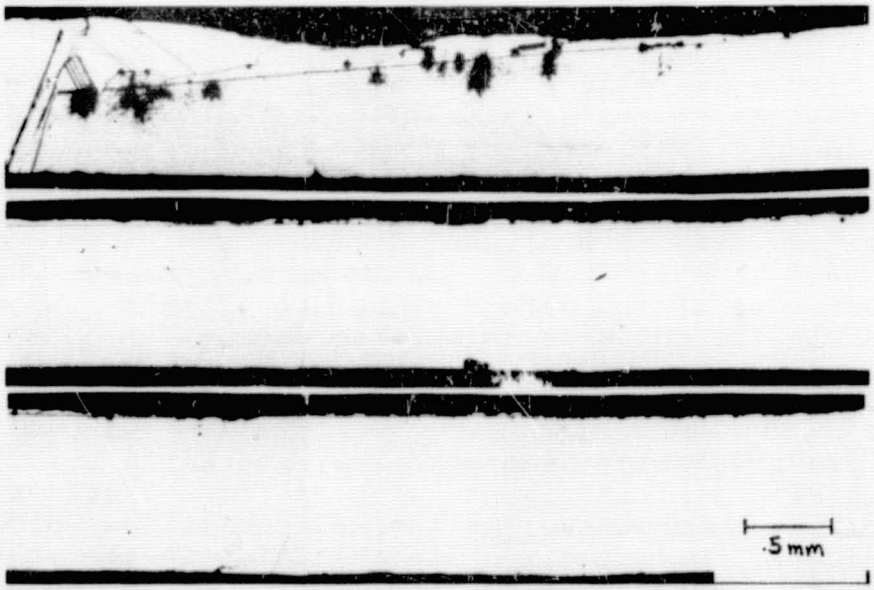

Figure 8. Cross-section of twin-stabilized planar morphology. Bounding random dendritic material is seen at top left. Dark areas are dislocation clusters due to liquid entrapment.

A third morphology, termed twin-stabilized planar, has been grown recently. This material, shown in cross-section in Figure 8, comprises a facetted upper surface with very slight relief, a twin lamella lies just under the upper surface, and the bulk of the ribbon, below the twin plane, is without structure. Laue photographs of this material show the ribbon plane to be (111) with the <112> direction generally close to the growth direction.

Examination of adjoining areas of twin-stabilized planar and random dendritic material in the EBIC mode, with an Al Schottky barrier showed very little recombination in the TSP area while significant recombination was observed in the random material, particularly in the interdendritic areas. (6)

Very limited amounts of material have been grown with a planar leading edge, as indicated by the absence of the twin lamellae associated with dendrites. Typically, this planar material has been grown at pull rates below 20cm/min which has led to excessively thick ribbon. The thick ribbon has tended, due to interaction with the guidance system, to disturb the growth geometry at the leading edge, thus disrupting the conditions leading to a planar interface.

Ribbons have been generally grown from boron-doped melts in the range of 0.5-2Ω-cm. Surface photovoltage measurements of the minority carrier diffusion length have yielded values from less than 10 to 85μm. The low end of these values can typically be attributed to contamination of the melt during experimental manipulations.

The best solar cell efficiencies obtained to date on LASS material have been greater than 12% AMI on $16cm^2$ cells. These cells were fabricated by phosphorus diffusion on 1Ω-cm boron-doped blanks prepared from random dendritic material by lapping, polishing and etching. The cell processing was not optimized, and, indeed, the performance of these cells seems to have been limited by low shunt resistance. No apparent effects of the defect structure of LASS ribbon have been found in the solar cells made to date.

Discussion

The process, while demonstrating remarkable stability in the growth of dendritic ribbon, also at times displays a susceptibility to uncontrolled thermal variations which has been attributed to convective instabilities in the melt. Variations in the temperature distribution of the melt, both spatially and temporally can be inferred from the variability of the dendrite growth directions in the random dendritic material, and from the behavior of the leading and lateral edges of the ribbon. A variety of effects may be at work here,

including the bulk flow of melt replenishing the growth interface, forced convection due to the motion of the solid ribbon over the liquid, natural convection from surrounding areas of the crucible and surface tension gradient-driven flows (Marangoni effect) toward the solid ribbon. The magnitudes and interactions of these various flows are extremely difficult to predict or observe, thus we feel that a potential solution to control this situation may lie in producing a controlled circulation of the melt which will dominate the other, uncontrolled flows.

"Horizontal" growth also poses a particular set of problems for maintaining adequate ribbon flatness. Gravity does not serve as an aligning force here as it does in vertical pulling techniques. Rather, the ribbon is supported as a more or less flexible beam between some supporting/guiding surface and the meniscus. Perturbations of the ribbon are not particularly well restrained by the liquid and are thus easily transmitted to the leading edge as a change in the effective pull angle. This results in a grown-in deviation from straightness for a length roughly equal to the duration of the perturbation. This deviation tends to reproduce itself when it reaches the support/guidance surface. Lacking damping effects, this process will continue ad infinitum. However, it appears possible to use the flexibility of the ribbon itself to decouple the interaction of perturbations at the one end of the system from the growth process at the other.

The central problem in the development of the LASS process is control of the ribbon's leading edge. The shape of the leading edge determines the nature of the top surface of the ribbon and, indirectly, the thickness. The latter result is observed in the growth of dendritic material, where the top surface relief of the dendrites is mirrored in the bottom surface becoming rough as the ribbon thickness is reduced below about 0.5mm. Thus, to produce a ribbon of economic thickness with two smooth surfaces, it is clear that the leading edge must be smooth and straight. This requires that the melt near the leading edge must not be undercooled and must be uniform and stable in temperature. Suppression of melt undercooling will be best accomplished by improved control of the impingement of the cooling gas onto the solid ribbon. Glicksman has calculated that for thin leading edges temperature differences of only a few degrees through the solid can produce stable growth of a planar interface at velocities approaching 1cm/sec. (7) It is apparent that realizing the appropriate heat flow conditions will produce significant improvements in ribbon quality without reducing the process advantages.

Notwithstanding the problems touched on above, the principal feature of the LASS process, the extended growth

interface, which provides high growth speeds and low bulk growth rates and which decouples the thermal conditions leading to growth from the gradients in the fully formed ribbon as it cools, represents a major opportunity to achieve a very low cost silicon sheet formation technique. The capabilities of the process demonstrated to date serve to indicate this potential.

Acknowledgements

The financial support of a substantial part of the work reported here by Department of Energy funding under an initial Jet Propulsion Laboratory contract and subsequent Solar Energy Research Institute contracts is gratefully acknowledged. We also thank Dr. Joseph B. Milstein, of SERI, for his enthusiastic support and stimulating discussions.

References

(1) C. Bliel, Journal of Crystal Growth, 5 99 (1969)
(2) T. Kayonagi, Proceedings Twelfth IEEE Photovoltaic Specialists Conference, 1976, p. 627
(3) B. Kudo, Journal of Crystal Growth, 50 247 (1980)
(4) J. Zoutendyk, Journal of Applied Physics, 49 3927 (1978)
(5) J. Zoutendyk, Journal of Crystal Growth, 50 83 (1980)
(6) Y. S. Tsuo, private communication, June 1983
(7) M. E. Glicksman and P. W. Voorhees, Journal of Electronic Materials, 12 161 (1983)

DISCUSSION

WARGO: What is your melt depth?

BATES: One centimeter.

WARGO: Do you make any active temperature control to control the heat transfer?

BATES: Yes, we do. The 24-inch-long crucible is spread out over four heaters, so we do have the ability to control the temperature of the melt that is being fed up to the growth zone.

WARGO: Is that the controlling factor for controlling the edge stabilization?

BATES: Yes and no. The control of the edges in the past has also been severely hampered by the mechanical instability of unflat ribbon because when the ribbon does this, increases and decreases the size of the meniscus, the thing basically acts like a diaphragm pump, and we have seen this in bench tests with model fluids. It is quite phenomenal, what it can do in comparison with the other flows that happen just as a consequence of pulling the ribbon over the surface of the melt, and removing stuff and replenishing at the same time.

SUREK: The process of this twin-stabilized growth does not have anything to do with the process taking place at the leading edge? Is that right?

BATES: Those that you saw, that is correct. I think when it is growing in the center of the ribbon and is growing full width it does have something to do with the leading edge. In fact, that long section that is spread out to full width grew underneath the shoe at 40 centimeters a minute.

CISZEK: Regarding the leading edge, can you see it at all in any of your experimental arrangements from the top view? And could you describe how you think it looks from the different modes of growth: random dendrite, aligned dendrite and others?

BATES: In the case of the random dendrites, they grow towards each other, they grow out, they conflict, they pinch each other off, and the interface is not smooth. It's relatively irregular over a scale of perhaps two to three millimeters. The parallel dendrites have a very regular interface.

WARGO: Concerning active attempts at heat transfer control, have you ever thought about magnetic-field melt stabilization, and which direction you would put it?

BATES: Yes, we certainly have. From what I understand of the effect, no matter which way you impose it, it will essentially increase the viscosity of the melt. I would say for convenience's sake we would impose it vertically.

SESSION V: STRESS/STRAIN EFFECTS IN RIBBON

O. Dillon, Chairman

PRECEDING PAGE BLANK NOT FILMED

N84 28632 D18

MATHEMATICAL MODELLING OF HIGH-SPEED RIBBON SYSTEMS: A CASE STUDY OF EDGE-DEFINED FILM-FED GROWTH*

Hisham M. Ettouney and Robert A. Brown
Massachusetts Institute of Technology
Cambridge, MA 02139

ABSTRACT

Finite-element numerical analysis is used to solve the coupled problem of heat transfer and capillarity which describes low and high speed silicon sheet growth in meniscus defined systems. Heat transfer models which neglect the details of convective heat flow in the melt are used to establish operating limits for an EFG system in terms of the growth rate, die temperature and the static head acting on the meniscus. The predicted sensitivity of crystal thickness to growth velocity is in good agreement with experimental results taken at Mobil Solar Energy Company. Details of convective heat transfer in the melt are shown to become important only at high growth rates or for materials with low thermal conductivities.

1. INTRODUCTION

The development of growth processes for silicon ribbons used in photovoltaic cells has reached the crucial stage where the engineering optimization of each technique with respect to crystal quality and areal growth rate will determine its economic feasibility. Mathematical modelling can play an important role in this optimization by differentiating the operating characteristics for different geometries and by supplying details of the process, e.g. melt/solid interface shape, temperature profiles and dopant distributions, which impact on crystal quality. The limits on growth rate and sheet thickness as well as the degree of crystalline perfection and compositional homogeneity attainable in meniscus-defined configurations for ribbon growth depend on the interactions between the temperature field in the melt and crystal and the shapes of the melt/gas and melt/solid interfaces. Each interaction is described by the solution of detailed mathematical models for heat and mass transport and meniscus shape.

This paper describes the development and systematic numerical solution of such models of edge-defined film-fed growth (EFG). We concentrate on analysis of transport phenomena in the plane of the ribbon thickness. Hence, we implicitly assume that the thickness of the ribbon is reasonably constant across the width of the sheet and that effects of the edges do not propagate far in the width dimension. The numerical analysis is based on finite element approximations of the field variables combined with newly developed iteration schemes [1,2] for solving the free-boundary problem caused by the unknown shape of the molten zone.

* Research supported by the Mobil Solar Energy Company and the JPL Flat Plate Solar Array Project sponsored by the U.S. Department of Energy.

In general, heat transfer in meniscus defined growth systems depends on conduction and on convection due to the velocity field in the melt. In EFG, the motion of the melt is driven by the upward motion of the growing sheet and perhaps by surface-tension differences caused by axial temperature variations [3,4]. Almost all previous heat transfer models neglect the details of the melt velocity [5-7] in the ribbon cross-section and account for convection by using a uniform velocity in the growth direction; only Kalejs et al. [8] have included the velocity field in their calculations of melt/solid interface shape in EFG. Although this simplification is valid for low growth rates and conductive melts (like silicon) it may fail for models of high speed systems like the Low Angle Silicon Sheet Growth (LASS) technique of Jewett and Bates [9]. The importance of the melt velocity in predicting the operation of high speed growth systems is established in Section 5.

Accounting for the interaction of heat transfer and capillarity in meniscus-defined ribbon growth leads to predictions of the variation of ribbon thickness with operating parameters, such as growth velocity and ambient temperature. This interaction is inherently a two-dimensional process; changes in heat transfer move the melt/solid interface which in turn adjusts the meniscus, the thickness of sheet and the shape of the melt through which heat transfer takes place. One-dimensional models of heat transfer cannot capture this interaction and so cannot predict the operation of meniscus-defined growth systems. We have reported detailed finite element analysis of the operation of a prototype EFG system in another publication [2] and those results are highlighted in Section 3. In Section 4, results of calculations are compared directly to experimental measurements of thickness as a function of growth speed obtained by J.P. Kalejs at Mobil Solar Energy Company [10].

2. MATHEMATICAL MODELS AND FINITE ELEMENT METHODS

We model EFG of silicon sheets with thickness $2\tilde{t}$ which are continuously pulled at velocity V_s from the graphite die shown in Fig. 1. The die has the same dimensions as the one used in the calculations reported in [2,7]. The melt/solid and melt/gas interfaces are denoted by the curves $\tilde{h}(\tilde{x})$ and $\tilde{f}(\tilde{y})$, respectively. The equations describing heat and momentum transfer in EFG are also tabulated in Fig. 1 and the dimensionless groups are tabulated in Table 1. These equations are listed in dimensionless form with lengths scaled with the half-width of the die $L^*=2\tilde{\ell}_3$, temperature with the reference $T^*=1783K$ and velocity with $V^*=V_s$. In this equation set we have omitted surface-tension driven flows caused by temperature variations along the meniscus which may be significant (see [4]) if the melt/gas interface is free of surface films. We have also neglected changes in meniscus shape due to variations in capillary pressure with temperature and to normal viscous stress; both effects are small for silicon growth of thin sheets, but may be important for more viscous melts with lower surface tensions [11]. With these simplifications, the meniscus shape depends only on gravity as represented by the Bond number (B) and the height of the die top above the melt level, which we refer to as the static head $\tilde{h}_{eff}$.

The shapes of the meniscus and melt/crystal interface determine the shape of the melt and so are coupled to heat transfer through it. The junction between the meniscus and the melt/solid interface is described by the

HEAT TRANSFER IN CRYSTAL

$$Pe_s\, \underline{e}_y \cdot \nabla T_s = \nabla^2 T_s \qquad (1)$$

MELT/SOLID INTERFACE

$$T_m = T_s = T_\ell \qquad (2)$$

$$\hat{\underline{N}} \cdot \nabla T_\ell - (k_s/k_\ell)\, \hat{\underline{N}} \cdot \nabla T_s = Pe_\ell S(\hat{\underline{N}} \cdot e_y) \qquad (3)$$

$$\underline{v} \cdot \hat{\underline{t}} = Pe_\ell (\underline{e}_y \cdot \hat{\underline{t}}) \qquad (4)$$

$$\hat{\sigma}(\underline{v} \cdot \hat{\underline{N}}) = Pe_\ell (\underline{e}_y \cdot \hat{\underline{N}}) \qquad (5)$$

MELT

$$Re\, \underline{v} \cdot \nabla \underline{v} = -\nabla p + \nabla^2 \underline{v} \qquad (6)$$

$$\nabla \cdot \underline{v} = 0 \qquad (7)$$

$$Pe_\ell \underline{v} \cdot \nabla T_\ell = \nabla^2 T_\ell \qquad (8)$$

MENISCUS

$$2\tilde{W} = B(y + H_{eff}) \qquad (9)$$

$$\underline{v} \cdot \underline{N} = 0 \qquad (10)$$

DIE

$$\nabla^2 T_d = 0 \qquad (11)$$

ALL EXTERNAL SURFACES

$$-\underline{N} \cdot \nabla T_i = Bi_i\, (T_i - T_\infty(y)) + R_i\, (T_i^4 - T_\infty^4(y)) \qquad (12)$$

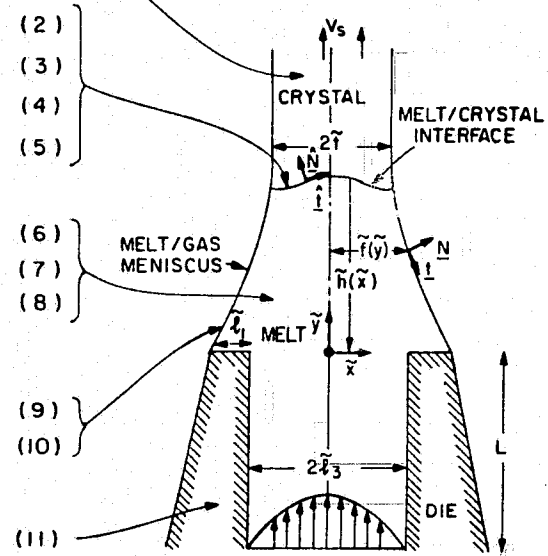

Figure 1. Mathematical formulation of heat and momentum transport which describe EFG systems in cross-section.

equilibrium wetting angle ϕ_o for growth of a uniform sheet [12]

$$df(h(t))/dy = \sin\phi_o \quad , \tag{13}$$

where t is the dimensionless half-thickness of the sheet $t \equiv \tilde{t}/L^*$. The shape of the meniscus couples directly to the height of the molten zone and to the thickness of the crystal sheet through the shape of melt/solid interface which enters as a limit in eq. (13).

The meniscus shape is also influenced by the wetting conditions at lines of contact between the melt and die. We assume that the melt partially wets the die material (graphite is used in EFG of silicon) and that the three-phase contact line between melt, die and gas pins along the outer edge of the die. This condition is only valid when the apparent contact angle at the edge falls between limits dictated by the equilibrium contact angle between graphite and molten silicon and the shape of the die. These limits are laid out in [2] and are not exceeded by any menisci calculated here.

Heat transfer between the surfaces of die, melt and crystal with the ambient is by a combination of convection and radiation, as modelled by eq. (11). The heat transfer surroundings in a real EFG system are composed of radiation shields, coolers and after heaters (see refs. 13 and 14) which can only be precisely modelled by detailed calculation of the view factor along the surface of the system. We do not attempt this, but instead use an ambient temperature distribution $T_\infty(y)$ which reflects the environment. The operating diagrams predicted in Section 3 were computed for a uniform ambient temperature $T_\infty(y) = T_\infty = 0.2$. The comparison with experiment described in Section 4 was carried out with the ambient temperature distribution measured by Kalejs and Bell [14].

The importance of convective heat transfer is measured in eq. (8) by the Peclet Number $Pe \equiv V^*L^*/\alpha_\ell$. For low speed silicon sheet growth $Pe = O(10^{-2})$ and conduction is the dominant mode of heat transfer in the melt. Then the momentum and continuity equations (4,5) need not be solved because convective heat transfer is well approximated by a uniform velocity field which has been corrected to account for the tapering of the mensicus:

$$\underline{v} = 2f(h(t))\underline{e}_y \quad , \quad y < 0 \quad , \tag{14a}$$

$$\underline{v} = (2f(h(t))/f(y))\underline{e}_y \quad , \quad 0 < y < h(x) \quad , \tag{14b}$$

where $\underline{e}_y$ is the unit vector in the y direction. The velocity field described by eq. (14) has been used to generate the operating diagram in Section 3. The accuracy of this approximation is examined as a function of Peclet number in Section 5.

Equations (1-14) describe a complex nonlinear free-boundary problem for the temperature, velocity and pressure fields, and the shapes of the melt/gas and melt/solid interfaces. In a series of papers [1,2,11,15] we have developed finite element methods which are especially tailored for approximating field variables and iterating for self-consistent interface shapes. Two types of algorithms have been devised. The first iterates successively be-

tween the solution of the thermal problem in melt, crystal and die and the calculation of the two interface shape until convergence is achieved in all unknowns. This successive iteration scheme is easily adapted to complicated heat transfer surroundings and is the basis for the calculations presented in Sections 3 and 4, as well as the calculations presented in [2].

When the interaction between meniscus shape and heat transfer is severe many successive iterations are required for convergence. A more effective solution technique is based on using Newton's method to solve the entire equation set simultaneously for the field variables and interface shapes. We have developed this approach for meniscus-defined growth following the guidelines in [1]. The convergence characteristics of the successive approximation and Newton iterations are compared in Fig. 2a for calculations with the conduction dominated heat transfer model. Newton's iteration demonstrated the typical [1] quadratic convergence rate while the successive iteration scheme converged only linearly. The more rapid convergence of Newton's method translates into a factor of three savings in computer cost, as demonstrated on Fig. 2b by calculations for a range of static heads $H_{eff} \equiv \tilde{h}_{eff}/L^*$. As H_{eff} is increased the crystal thickness becomes more sensitive to meniscus height and the coupling between heat transfer and melt shape is enhanced. The number of successive iterations increased with increasing H_{eff} , whereas the number of Newton iterations stayed almost constant.

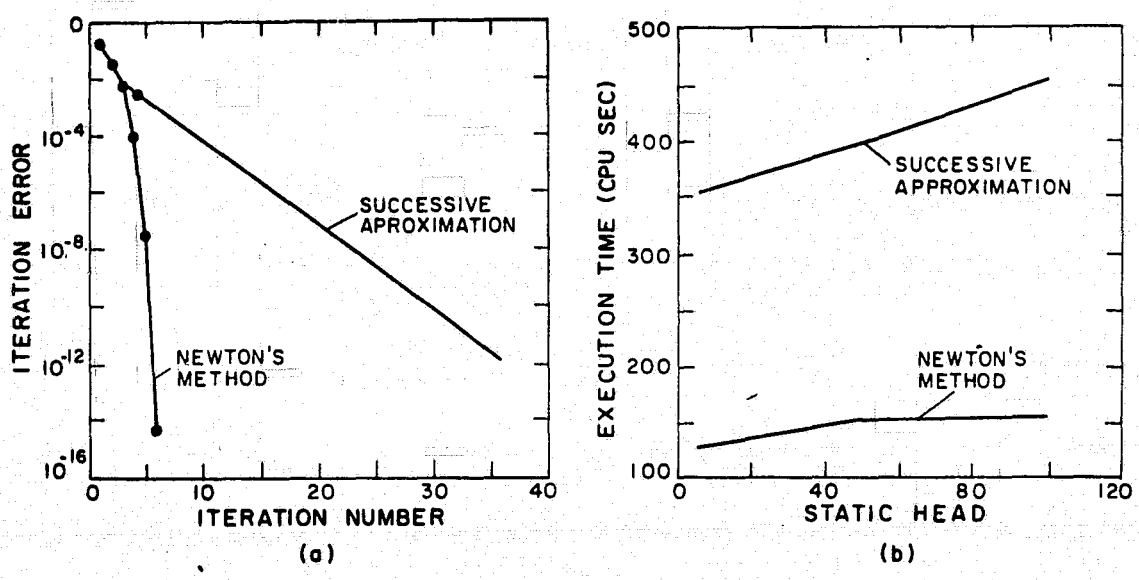

Figure 2. Comparison of convergence and computational effeciency of successive approximation and Newton methods for solving conduction dominated EFG model: (a) convergence with iteration number; (b) execution times in cpu seconds as a function of the dimensionless static head H_{eff} .

Besides giving more rapid convergence Newton's method forms the basis for numerical algorithms for tracking families of solutions in parameters and for determining parametric sensitivity and temporal stability. These methods are developed in the publications [16,17] and are demonstrated for meniscus-defined growth in Section 3.

3. OPERATING LIMITS FOR SILICON EFG SYSTEM

The thermophysical properties for Si in Table 2 give the dimensionless groups in Table 1 and, have been used to study the sensitivity of the model EFG system to growth rate (V_s), die set-point temperature ($\tilde{T}_o$) and static heat ($\tilde{h}_{eff}$). These calculations have been presented in detail in [2] and are only reviewed here.

Increasing the pull speed while holding the set-point temperature $\tilde{T}_o$ constant causes melt to solidify farther from the die and decreases the crystal thickness so that the meniscus shape satisfies the Young-Laplace equation (9) and the wetting condition (13). The shapes of the melt predicted for V_s between 1 and 4 cm/min and $\tilde{T}_o$ = 1763 K are shown in Fig. 3 .

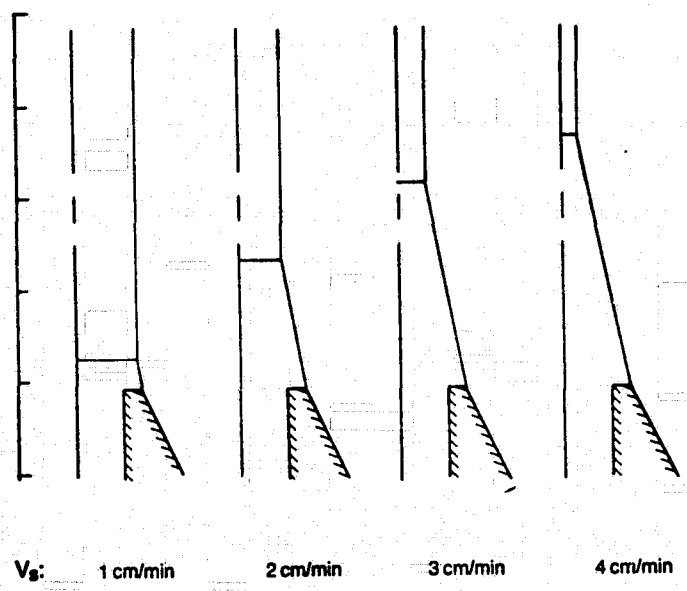

Figure 3. Calculated meniscus and ribbon shapes for the effect of increasing growth rate at the constant set-point temperature $\tilde{T}_o$ = 1763 K.

The narrowing of the crystal restricts the area for axial heat conduction and causes increased temperature gradients at the melt/crystal surface. For the systems shown in Fig. 3, the axial gradient in the melt at y=h(0) increases from 772 to 849 K/cm with changes in V_s between 1 and 4 cm/min. Decreasing the set-point temperature at constant speed lowers the melt height and increases the crystal thickness. This sequence is shown schematically on Fig.

4 for V_s = 3 cm/min.

Calculations for the variation of crystal thickness with growth speed are summarized on Fig. 5 for set-point temperatures between 1713 and 1793 K. Three different types of operating limits are evident. First, increasing V_s with $\tilde{T}_o$ held constant decreases the ribbon thickness until unreasonably thin ribbons are produced. The lower dashed line on Fig. 5 represents the maximum growth rate if $2\tilde{t}$ = 0.01 cm is the lowest useful ribbon thickness. Low growth

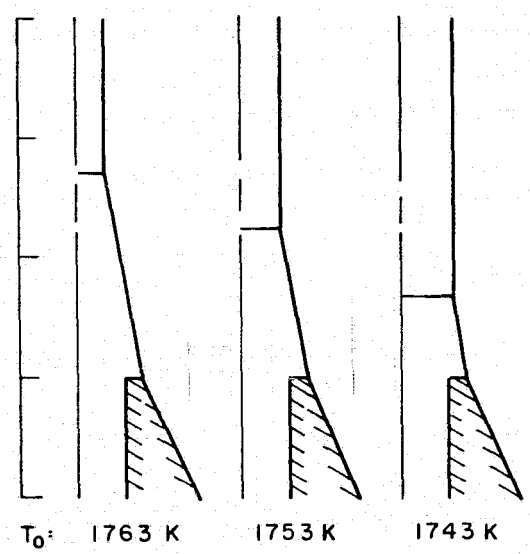

Figure 4. Calculated meniscus and ribbon shapes for the effect of decreasing set-point temperature at the constant growth rate V_s = 3 cm/min .

rates are not attainable for all values of $\tilde{T}_o$. Lowering V_s at constant $\tilde{T}_o$ lowered the melt/solid surface towards the die. Unless adequate sensible heat was available in the melt solidification occurred at the die top ($2\tilde{t}$ = 0.030 cm) and growth stopped. Calculations with $\tilde{T}_o$ = 1793 and 1783 K allowed a stationary ribbon and melt.

Continually changing the die temperature along with the growth rate as dictated by horizontal lines across Fig. 5 gives a strategy for increasing growth rate at constant thickness $2\tilde{t}$. Under these conditions the height of the melt is unchanged and the axial temperature gradient at the melt/solid interface decreases with increasing V_s. Then the maximum attainable pull rate is limited by thermal supercooling of the melt near the solidification front which leads to a breakdown of the crystal morphology. The dashed

operating curve for $\tilde{T}_o$ = 1713 K denotes that the melt was supercooled for all values of V_s.

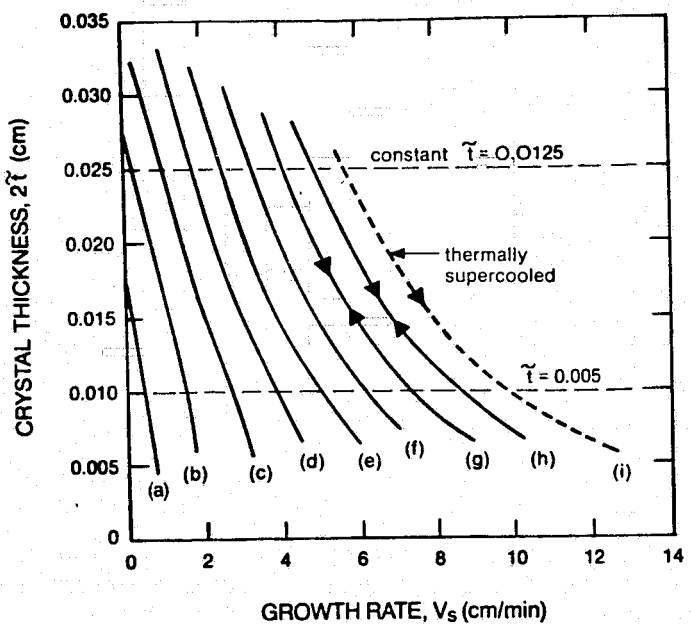

Figure 5. Operating curves of crystal thickness as a function of growth rate for nine set-point temperatures and h_{eff} = 0.5 cm. The dashed operating curve indicates combinations of $\tilde{T}_o$ and V_s for which the melt is thermally supercooled: the arrows give the direction of changing V_s for decreasing the interfacial temperature gradient in the melt. The set-point temperature varies from (a) 1793 to (i) 1713 K in 10K increments.

The height of the melt pool with respect to the die top h_{eff} is another parameter which is available experimentally for controlling crystal thickness. As described by the Young-Laplace equation (7), increasing h_{eff} increases the curvature of the meniscus and decreased $\tilde{t}$. This behavior is shown on Fig. 6 for V_s = 2.0 cm/min and $\tilde{T}_o$ = 1753 K where results were calculated using the Newton iteration method and by introducing an artificial arc-length parameter for stepping along the family of solutions [16]. Introducing arc-length in place of the more conventional parameter $\tilde{h}_{eff}$ allows calculation of solution families which are not single-valued in the static head but instead turn back to lower values of $\tilde{h}_{eff}$. Figure 6 shows that this is the case for these growth conditions. No steady solutions exist beyond the critical value $\tilde{h}_{eff} = \tilde{h}^c_{eff} \approx 9.2$ cm. Elementary arguements originating from linear stability analysis [17] show that the steady shapes which exist on the dashed portion of this operating curve are unstable. Sample shapes of molten zones computed at points along the curve on Fig. 6

are displayed on Fig. 7.

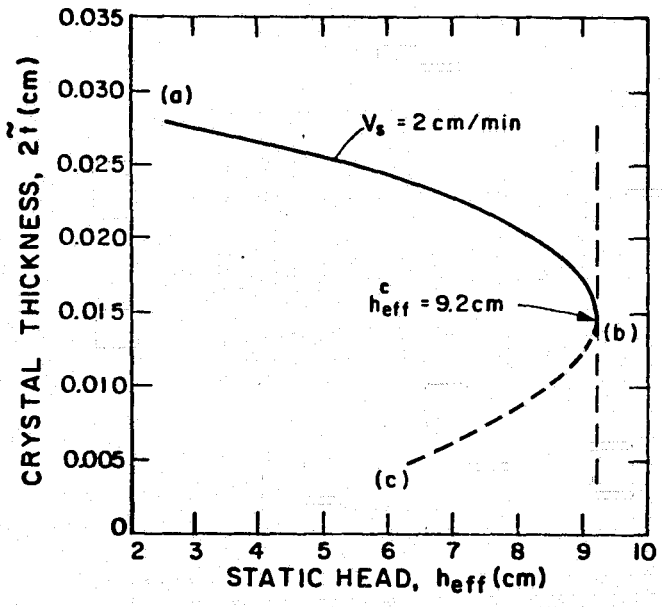

Figure 6. Effect of static head on growth rate for V_s = 2.0 cm/min and $\tilde{T}_o$ = 1753 K.

4. COMPARISON WITH EXPERIMENTS

The predictions of the dependence of crystal thickness on pull speed and thermal operating conditions are an ideal starting place for comparing the calculations with experiments. We have attempted to do this using recent data for the dependence of $2\tilde{t}$ on V_s taken at Mobil Solar Energy Company by J.P. Kalejs and his colleagues [10]. Their data was for a 4 cm wide ribbon grown from a $2\tilde{\ell}_3$ = 0.05 cm thick graphite die and showed considerable non-uniformity of thickness across the width of the ribbon. We have attempted to fit the data taken from the righthand side of the ribbon. All thermophysical properties have been assumed to be constant with temperature except for the thermal conductivity of the solid which varies as [18]

$$k_s(\tilde{T}) = k_s\tilde{T}_m/\tilde{T} \quad , \tag{14}$$

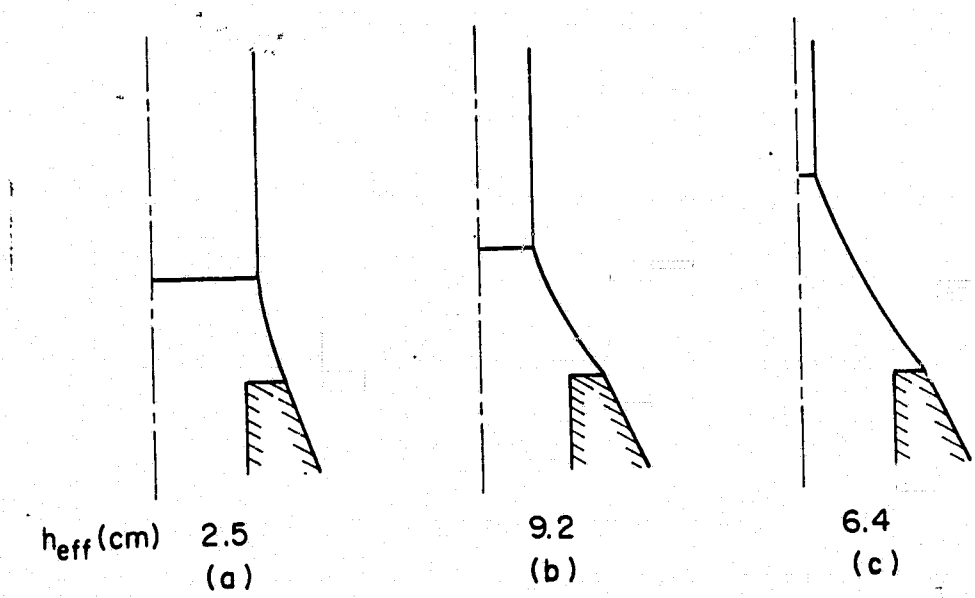

Figure 7. Calculated meniscus and ribbon shapes along the operating curve shown on Fig. 6.

The surroundings of the EFG system used in these measurements included a radiation shield adjacent to the die top, a water-chilled cooler near the melt and an after-heater along the crystal surface. We have approximated the ambient temperature profile which results from these sources, sinks and shields by combining the ambient temperature profile measured by Kalejs and Bell [14] for the surroundings above the die top with a linear temperature rise across the radiation shield to the temperature $\tilde{T}^{\circ}_{\infty}$. This profile is shown in Fig. 8 in the dimensionless form scaled with $\tilde{T}^{*}$ = 1783 K. The static head was measured experimentally to be 4 cm.

Two unprescribed temperatures remain; the set-point temperature at the base of the die and the temperature of the radiation shield $\tilde{T}^{\circ}_{\infty}$. We have used these temperatures as variables to fit the variation of crystal thickness with velocity. Results of the fit are shown on Fig. 9 for $\tilde{T}_{o}$ = 1727 K and $\tilde{T}^{\circ}_{\infty}$ =1733 K. The excellent agreement between the calculation and experiment is extremely sensitive to the value selected for the die temperature $\tilde{T}_{o}$ which controls the amount of sensible heat entering the die, but is relatively unaffected by $\tilde{T}^{\circ}_{\infty}$. For example, changing $\tilde{T}_{o}$ to 1714 shifted the operating path for $\tilde{T}^{\circ}_{\infty}$ = 1733 K to the dashed curve shown in Fig. 9. Hence, less than a one percent change in $\tilde{T}_{o}$ lead to a twenty percent variation in the ribbon thickness at a given growth rate. Conversely, changing $\tilde{T}^{\circ}_{\infty}$ to 1961 K for $\tilde{T}_{o}$ = 1727 K changed the crystal thickness at V_s = 4 cm/min from $2\tilde{t}$ = 0.01 cm to

$2\tilde{t}$ = 0.0082 cm , a twelve percent shift.

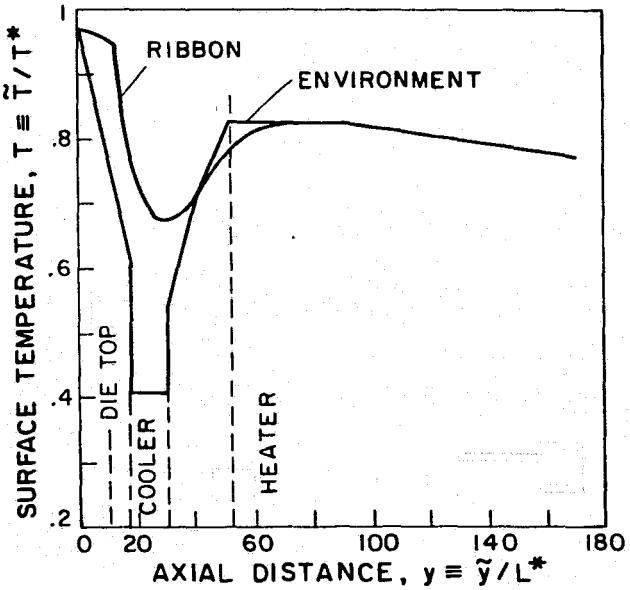

Figure 8. Ambient temperature profile taken from Kalejs and Bell [1] and used for comparison which experimental measurements of ribbon thickness. The unknown lower shield temperature $\tilde{T}^{\circ}_{\infty}$ as an adjustable parameter for fitting the calculations to the experiments. The calculated temperature profile along the center of the melt and ribbon is also shown.

The temperature gradient along the center of the crystal evaluated at the melt/solid interface is also plotted in Fig. 9 and shows the same increase with pull speed observed for the uniform ambient conditions. The temperature profile computed along the ribbon center is shown on Fig. 8 and agrees well with the profile computed by Kalejs and Bell [14].

5. EFFECT OF CONVECTIVE HEAT TRANSFER AT HIGH PULL SPEEDS

Equation (8) shows that at high Peclet Numbers $Pe_{\ell} \equiv V^*L^*/\alpha_{\ell}$, the details of the velocity field in the melt will have a marked effect on convective heat transfer and hence on the operating limits predicted for EFG. The effect of convective heat transport is demonstrated by comparing predictions of crystal thickness for Si and Al_2O_3 growth by EFG from models using the approximate velocity profile eq. (14) and the full solution of the momentum and continuity equations (6) and (5). Both materials have been grown from the same die geometry (ℓ_3 = 0.025 cm); the thermophysical properties for the die corresponds to graphite for the Si system and to molybdenum for Al_2O_3 growth. The thermophysical properties for both die/melt/crystal com-

binations are listed in Table 2.

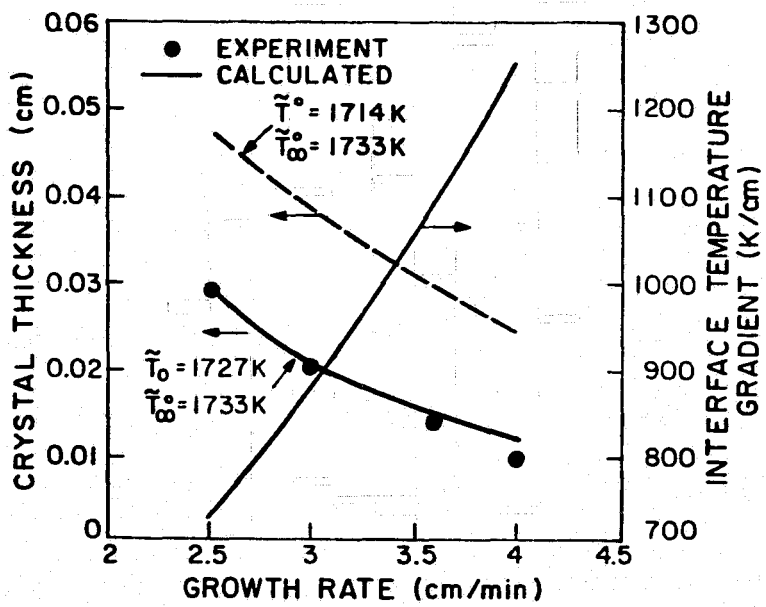

Figure 9. Comparison of experimental measurements and finite-element calculations of ribbon thickness versus pull speed. The interfacial temperature gradient predicted by the calculations is also shown.

Thickness versus pull rate diagrams for the two systems are summarized on Fig. 10 for speeds between 0 and 6 cm/min. Obviously, neglecting the details of the velocity field is a good assumption for silicon growth, but poor for Al_2O_3 . The thermal diffusivity of Al_2O_3 melt ($\alpha_\ell \simeq 0.026$ cm^2/sec) is ten times smaller than that of Si ($\alpha_\ell \simeq 0.264$ cm^2/sec . This difference causes convection to be ten fold more important in the Al_2O_3 system.

Although in this example the influence of convective heat transport has been amplified by reducing the thermal diffusivity of the melt, exactly the same result is expected by more generally increasing the Peclet number in the melt by either increasing the capillary width of the die or by increasing the characteristic velocity of the melt V*. The factor of ten increase in growth rates for horizontal growth such as LASS [9] will cause convective heat trasport to be of similar importance to the Al_2O_3 system. Convective heat trans port will be of similar or greater importance in any system where fluid flow driven by buoyancy or surface-tension gradients are more intense than the growth velocity.

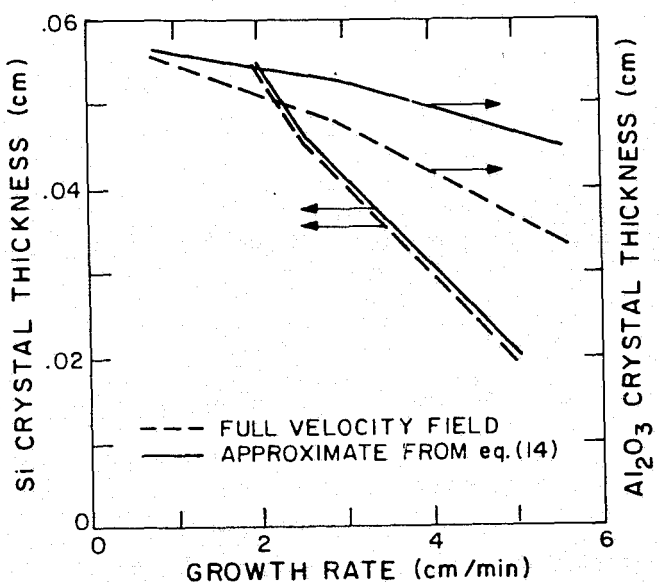

Figure 10; Effect of convection on thickness versus pull speed predictions for Si and Al_2O_3 growth.

6. DISCUSSION

Detailed modelling of meniscus-defined growth techniques is now feasible and leads to new insights into the operation and limitations of ribbon growth methods. New operating limits have been identified which result from interactions of heat transfer in melt and crystal with capillarity through the shape of the static meniscus. For example, the maximum accessible value for the static head h_{eff} predicted in Fig. 6 marks the loss-of-existence of a steady solution which simultaneously conserves heat and satisfies the Young-Laplace equation and wetting condition. This limit cannot be predicted from either heat transfer or capillarity alone.

Whether or not the steady state growth configurations predicted here are attainable in an experimental system depends on the stability of these states to small (and sometimes large) perturbations in operation. The finite-element/Newton algorithm mentioned here is the foundation for linear stability analysis and for complete dynamic simulation; results of its application

will be reported later.

The comparison between calculations and experiment, although limited to crystal thickness, give confidence that the physics essential to EFG is being captured quantitatively. Further comparisons are needed for a variety of thermal operating conditions and should be extended to include melt/solid interface shape and lateral segregation of a dopant. Both are pointwise properties of the melt/crystal interface and provide a much more stringent test for the calculations.

REFERENCES

1. H.M. Ettouney and R.A. Brown, J. Computat. Physics 49, 118 (1983).
2. H.M. Ettouney, R.A. Brown and J.P. Kalejs, J. Crystal Growth 62, 230 (1983).
3. D. Schwabe, A. Schramann, F. Priesser and R. Deder, J. Crystal Growth 43, 305 (1978).
4. H.M. Ettouney and R.A. Brown, J. Appl. Physics submitted (1983).
5. J.C. Swartz, T. Surek and B. Chalmers, J. Electron. Mater. 4, 255 (1975).
6. H.M. Ettouney and R.A. Brown, J. Crystal Growth 58, 313 (1982).
7. H.M. Ettouney, R.A. Brown and J.P. Kalejs, J. Crystal Growth submitted (1983).
8. J.P. Kalejs, L.-Y. Chin and F.M. Carlson, J. Crystal Growth 61, 473 (1983).
9. D.N. Jewett and H.E. Bates, this Proceedings.
10. J.P. Kalejs, Stress Studies in EFG, DOE/JPL, 956312/83/02.
11. H.M. Ettouney and R.A. Brown, Int. J. Heat Mass Transfer, in preparation.
12. T. Surek and B. Chalmers, J. Crystal Growth 29, 1 (1975).
13. F.V. Wald, in: Crystal Growth, Properties and Applications, Vol 5 (Springer. Berlin, 1981).
14. J.P. Kalejs and R.D. Bell, this Proceedings.
15. C.J. Chang and R.A. Brown, in Numerical Properties and Methodologies in Heat Transfer, Ed. by T.M. Shih, Hemisphere Press, New York, 1983.
16. L.H. Ungar and R.A. Brown, Phil. Trans. R. Soc. Lond. A306, 347 (1982).
17. Y. Yamaguchi, C.J. Chang and R.A. Brown, Proc. R. Soc. Lond. A. submitted (1983).

Table 1. Dimensionless Groups for Modelling Si Ribbon Growth: $L^* \equiv 2\ell_3 \simeq 0.025$ cm, $T^* = 1783$ K.

Dimensionless Group	Characteristic Value
Biot Numbers, $B_i = hL^*/k_i$, $i=\ell,s,d$	0
Radiation Numbers, $R_\ell \equiv \hat{\sigma}\varepsilon_i L^* T^{*3}/k_\ell$	7.2×10^{-4}
Melting Temperature, $T_m \equiv \tilde{T}_m/T^*$	0.95
Stefan Number, $S \equiv \Delta H_f/C_{p_s} T^*$	1.0
Bond Number, $B \equiv gL^{*2}\Delta\rho/\sigma$	2.1×10^{-3}
Static Head, $H_{eff} \equiv h_{eff}/L^*$	20
Ambient Temperature, $T_\infty \equiv \tilde{T}_\infty/T^*$	0.2
Reynolds Number, $Re \equiv \rho V^* L^*/\mu$	0.5
Density Ratio, $\hat{\sigma} \equiv (\rho_s/\rho_\ell)$	1.0

Table 2. Thermophysical Properties for Silicon and Al_2O_3 Systems.

Property	Si	Al_2O_3
Melt		
Thermal Conductivity, k_ℓ (W/cm K)	0.64	0.1
Density, ρ_ℓ (g/cm^3)	2.42	3.05
Specific Heat, c_{p_ℓ} (J/g K)	1.00	1.26
Emissivity, ε	0.64	0.9
Viscosity, μ (g cm/sec)	0.01	0.01
Crystal		
Thermal Conductivity, k_s (W/cm K)	0.22	0.1
Density, ρ_s (g/cm^3)	2.30	4.00
Specific Heat, c_{ps} (J/g K)	1.00	1.26
Emissivity, ε	0.64	0.9
Interfaces		
Melting Temperature, $\tilde{T}_m$ (K)	1683	2316
Latent Heat, ΔH_f (J/g)	1800	1046
Melt Contact Angle with Die, ϕ_d	30°	26°
Melt/Gas Surface Tension, γ (dynes/cm)	720	700
Melt/Crystal Growth Angle (orientation)	11°	17° (<0001>) 35° (<1010>)
Property	**Graphite**	**Molybdenum**
Die		
Thermal Conductivity, k_d (W/cm K)	0.43	0.84
Density, ρ_d (g/m^3)	2.1	10.2
Specific Heat, c_{pd} (J/g K)	1.7	0.4

DISCUSSION

WARGO: Because of some heat-reflector diagrams and data that I am going to show tomorrow, I would like to know how you would optimally design that reflector so as to produce those thermal boundary conditions to optimize your growth?

BROWN: The calculation really doesn't know it is a reflector. It knows that there is a set temperature-boundary condition that goes between the temperature on that side of the shield to the other in a linear way. So the details of the reflector, angle of incidence and things like that, are not in there. The details of radiation are important in the things that are missing.

SUREK: I think in the seeding condition at zero velocity, you are probably restricting yourself too much, because there the meniscus condition does not need to be satisfied.

BROWN: That's true. If I am absolutely at zero, I don't have to. But if I approach zero in a smooth way, I do.

SUREK: I think you have very nice quantitative comparisons to data, looking at velocity-thickness relations. When you extend this to the interface shape, it is going to be a lot more critical what the exact details of that environment temperature are, because even though the vertical conduction is well described by the transport problem that you are solving, the details of the interface shape are going to be very critically dependent on not just an average environment temperature, but the details of that environment. So I would not put too much faith in actually doing anything more than a qualitative analysis.

The question is: I don't recall exactly how you brought in the bottom boundary condition to contact the die, and how you brought in limits to the operating conditions based on that. Could you show that again?

BROWN: At the bottom, we pin the meniscus on the outer edge of the die. You cannot bring both the angle and the pinning condition in, you have to decide on one or the other.

SUREK: But that is going to limit you in meniscus height well before you reach a thickness of zero, because at some point you will not be physically able to satisfy a contact pinning condition at the edge of the die. In fact, the meniscus will pull in from the outer edge to the inner edge.

BROWN: That is why we have that curve of a contact angle versus S the height, but what you will find is that none of our calculations fall outside the Gibbs angles, so there is no tendency for it to run in, for our operating conditions. Certainly if you decoupled the capillary problem you could get it to do it. But with the heat transfer in our system, it won't.

MILSTEIN: You pointed out that if you defined a minimum thickness of ribbon that you care to grow, you then have a limiting region of temperature that you can deal with. In raising the temperature to go after mixing in the upper region in the die, you begin to run into a problem in terms of your growth velocity, which you also want to maximize from a productivity point of view. Have you any data that might tell us where the regime lies where you can have high productivity until you get mixing, or do you get segregation?

BROWN: The mixing issue relies very sensitively on this issue of surface-tension-driven flows. If you say that there is no driving force for a shear flow on that surface, the amount of mixing that you are going to get in any sense is very small. In a realistic EFG system, if you have the surface-tension differences that you would have for pure silicon, as is being measured by Steve Hardy at NBS; you would have appreciable convection in the melt. In the sense of our calculations, we are at a steady state. K_{eff} in our system is 1, so you can mix it as much as you want and you still get K_{eff} of 1.

ABBASCHIAN: Are you assuming any thickness for the interface between the solid and liquid? How are you releasing the latent heat?

BROWN: I am releasing it along a line.

ABBASCHIAN: So you are assuming zero thickness.

BROWN: Yes.

ABBASCHIAN: All the pictures we have seen and all the other evidence has shown that crystals cannot grow in a zero thickness, and you have dendrites that are shooting. There is a region that is usually called a mushy zone and it is in that region that all the heat is being released.

BROWN: What I am trying to measure is not dendritic growth but the EFG system, and I don't believe the EFG system has a mushy zone. I think it is a well-defined melt zone.

ABBASCHIAN: Also, I note that you had calculated temperature gradients around 500°C per centimeter. Don't those seem to be fairly high? In directional solidification, one does not reach such high temperature gradients.

BROWN: Remember the scale of the system you are working with here. This is a tiny, tiny system. This is a system on the order of 0.025 centimeters high. So to get a 500° gradient, I don't need much of a temperature difference. I can get that temperature gradient out of a 10° temperature difference.

ABBASCHIAN: Even when they try to grow wires of small diameters, they cannot reach 400° to 500°C per centimeter.

BROWN: There is an interesting point there, and I think Juris [Kalejs] will touch on more. The way to get those numbers down in our calculations is

to have a light piping mechanism to get heat out of the interface by something other than conduction.

ABBASCHIAN: For a comparable system, I would look for what people have done in electric slag remelting or continuous casting where they see lateral segregation, and they model those based on the fluid flow at the interface in the mushy zone, no matter how small it is, and get the results based on that. They see the same effects during continuous casting--that you can change the shape of the segregation by changing the fluid flow in the mushy zone.

BROWN: Let me just say that if you modeled it that way, you would be missing the physics.

DILLON: Have you done any calculations on the temperature profile perpendicular to the view that is on the screen?

BROWN: No. That is an interesting question. If you say that you have a slowly varying temperature distribution, then obviously in these cases the ribbon is not of constant thickness in the lateral direction across the width. If you have a slowly varying temperature distribution across the die face, then these calculations we have hold at every cross section. So that problem, to us, is really an engineering problem and not a mathematical problem. The problem that is still of concern is the actual edge where the meniscus swings all the way around and joins from the other side. That is truly an inherently three-dimensional problem.

DILLON: But as an engineer wanting to calculate the buckling, I want to know how that is varying in that direction too.

BROWN: Just tell me what the temperature gradient there is and I will just do it in little sections and it will work.

PETRICK: When you compared your analytical results with the data from Mobil, there were two temperatures that were unknown. One of them was on the bottom of the shield, and the other was at the die. You had to back-calculate these before your data matches up. Are you going to measure these temperatures to see if your model agrees with the measurement?

BROWN: There are two things to do that I think are fairly straightforward. One is to look at a parametric sensitivity to make sure we can't get anything we want by changing those temperatures a few degrees. Now, preliminary calculations say that if we change the die set-point temperature, the whole curve shifts from left to right. So that is a very finite parameter, and you are going to get a unique value out of it. The other parameter is not so clear, the shield temperature, and we are going to have to look at that as a parametric sensitivity study. What we really need is more data for this system operating at the same set-point temperature, and growing at different speeds, and perhaps different static heads.

PETRICK: These apparently were steady-state runs. Is your model amenable to conversion to a transient case for determining what happens at the beginning of a run?

BROWN: Yes, it is amenable but it increases the computation time. Our approach is to do stability first. First thing to do is to look at sensitivity coefficients, basically time constants. Obtain the case for linear stability first and then, if you see some interesting behavior, or you find specific places you want to look at transient phenomena, then go in and spend the money.

N84 28633 D19

An Improved Analysis of the Thermal Buckling of Silicon Sheet

O. W. Dillon, Jr. and R. DeAngelis
University of Kentucky
Lexington, KY

INTRODUCTION

One of the problems that presently occurs when one tries to produce wide and thin silicon sheet is buckling (rippling). Buckling occurs in all of the processes presently being investigated for their potential in mass producing wide silicon sheet for use in making solar cells. It is a fact that the processes which produce good ribbon 2 cm in width do not yield the same quality product at 10 cm in width. Buckling develops precisely because the sheets are "wide" and very very thin.

This paper considers the buckling of very thin cantilever plates due to temperature variations in the axial direction (i.e. along the length). The method used in the analysis follows the general procedures of Reissner and Stein [1]. It is very similar to a series of reports by Mansfield [2] who considered the case where the temperature varied in the width direction. The problem considered is an idealization of those encountered in processes for making large amounts of thin silicon sheet for large solar cell applications.

We demonstrate below that axial temperature variations cause very thin plates to buckle in a torsional mode.

We assume the particular variation of the stress function in the width direction and thereafter the analysis is "exact". We consider here only the case where all material properties and the plate thickness are constant.

The present analysis develops a better analytical model of thermal buckling of cantilever plates by incorporating two important improvements.
(I) The mid plane stresses prior to buckling are better approximated.
(II) The temperature field is generalized.

The present analysis assumes an elastic material and a constant modulus of elasticity. With these assumptions the thermal buckling phenomena is governed by (see p. 432 of Boley and Weiner [3])

$$D\nabla^4 w = N_{xx}\, w_{xx} + N_{yy}\, w_{yy} + 2N_{xy}\, w_{xy} \tag{1}$$

and

$$\nabla^4 F + \alpha E t \nabla^2 T = 0 \tag{2}$$

where w is the transverse deflection, F is the stress function and $w_{xx} = \frac{\partial^2 w}{\partial x^2}$, $w_{yy} = \frac{\partial^2 w}{\partial y^2}$, $w_{xy} = \partial^2 w/\partial x \partial y$ and T is the temperature. The stress function F is related to the midplane forces N_{xx}, N_{yy} and N_{xy} via.

$$N_{xx} = \frac{\partial^2 F}{\partial y^2}$$

$$N_{yy} = \frac{\partial^2 F}{\partial x^2} \tag{3}$$

$$N_{xy} = -\frac{\partial^2 F}{\partial x \partial y}$$

The parameters α, E, t and $D = \frac{Et^3}{12(1-\nu^2)}$ are the coefficient of thermal expansion, Young's modulus, plate thickness and plate stiffness respectively.

It is unlikely that convenient exact solutions to Eqs. (1) and (2) can be found. To aid in obtaining high quality approximate solutions, it is noted that Eqs. (1) and (2) are equivalent to a <u>variational</u> formulation given by

$$U = \frac{1}{2}\iint D\{(\nabla^2 w)^2 + 2(1-\nu)\left((\frac{\partial^2 w}{\partial x \partial y})^2 - \frac{\partial^2 w}{\partial y^2}\frac{\partial^2 w}{\partial x^2}\right)\}dA$$

$$+ \frac{1}{2}\iint\{N_{xx}(\frac{\partial w}{\partial x})^2 + N_{yy}(\frac{\partial w}{\partial y})^2 + 2N_{xy}\frac{\partial w}{\partial x}\frac{\partial w}{\partial y})\}dA \tag{4}$$

and

$$U^* = \frac{1}{2}\iint\frac{1}{E}\{(\nabla^2 F)^2 + 2(1+\nu)\left((\frac{\partial^2 F}{\partial x \partial y})^2 - \frac{\partial^2 F}{\partial x^2}\frac{\partial^2 F}{\partial y^2}\right)\}dA$$

$$+ t\iint\alpha T\ \nabla^2 F\ dA \tag{5}$$

where the integration is to be over the plate area.

Equations (1) and (2) are generated by the application of the variational calculus and the conditions that

$$\delta U = 0 \tag{6}$$

and

$$\delta U^* = 0 \tag{7}$$

i.e. that the functionals U and U* be minimized.

The temperature during sheet growth varies in the axial, or x, direction and very little in the width or y direction. Hence we assume that

$$T = T(x) \tag{8}$$

Pre Buckling Stress Field

Based on the stress function in Boley and Weiner (p. 323), we assume that the stresses are self equilibrated in the width direction but we seek improvements in the axial direction. That is we assume *

$$F = (c^2 - y^2)^2 f(x) \tag{9}$$

and seek improvements in f(x). Equation (5) now becomes

$$U^* = \frac{1}{2}\int_0^L \{\frac{256}{315}(f'')^2c^9 + \frac{153.6}{105} ff''c^7 + \frac{128}{5} f^2c^5 + \frac{665.6}{105} c^7(f')^2 + \frac{32}{15} E\alpha Tf''c^5t\}\, dx \tag{10}$$

where $(\ )' \equiv \frac{d(\ )}{dx}$ and we have used Poisson's ratio of 0.30. Standard calculus of variations procedures and Eq. (7) yield

$$c^4f'''' - 6c^2f'' + 31.5f = -1.3125\ \alpha EtT'' \tag{11}$$

The general solution of Eq. (11) is

$$f = fp + e^{\infty x/c}[A_1\cos(Bx/c) + B_1\sin(Bx/c)] + e^{-\infty x/c}[C_1\cos(Bx/c) + D_1\sin(Bx/c)] \tag{12}$$

where

$$\infty + Bi = \sqrt[4]{126}\, e^{i\lambda},\ 2\lambda = \tan^{-1}(\sqrt{22.5}/3). \tag{13}$$

The particular solution f_p in Eq. (12), actually reflects the particular temperature field that is imposed on the plate. The boundary conditions are

*The coordinate system used is shown in Fig. 1.

$$f = 0 \text{ and } f' = 0 \tag{14}$$

at x = 0 and x = L in order that the ends of the plate be traction free. These conditions determine A_1 - D_1 in Eq. (12) once f_p is known.

We consider in detail below three specific temperature fields:

$$\begin{aligned} &\text{I} \quad T'' = T_o'' = \text{a constant} \\ &\text{II} \quad T = T_o e^{-Nx} \\ &\text{III} \quad T = T_1 e^{-Mx} \cos(2\pi x/\ell) \end{aligned} \tag{15}$$

Each of these admit exact particular solutions of Eq. (11), namely.

$$\begin{aligned} f_p &= -\infty E t To''/24 \\ f_p &= \frac{-\infty E To N^2 (1.3125) t}{N^4 c^4 - 6N^2 c^2 + 31.5} e^{-Nx} \end{aligned} \tag{16}$$

$$f_p = [A_q \cos(2\pi x/\ell) + B_q \sin(2\pi x/\ell)] e^{-Mx} \tag{17}$$

where A_q and B_q are determined by the differential equation (11) and are given in Appendix A. The boundary conditions Eq. (14) then determine the constants A_1 - D_1 in Eq. (12) in terms of the temperature field (T_o'', T_o and T_1) and geometric parameters (c and L). The numerical calculations for A_1 - D_1 are readily done on a home computer which can solve four simultaneous equations. For long plates double precision may be required to obtain good results for A_1 and B_1. Typical results for the stress function f for the case where T_o'' = a constant are shown in Fig. 2. It is noted that the results for the case where c = 1 cm, can be thought of as the particular solution (i.e. f = 1.0) together with an "end correction" in order to satisfy the boundary condition. However the solution for the case where c = 3 cm is all "end correction" and is not well approximated by f = - 1.0.

In fact for wider plates the maximum stress itself decreases as the plate gets wider. Typical results are shown for T_o'' = constant in Fig. 3.

EFG temperature profile

By using superposition of solutions like those given in Eqs. (12) and (16) we obtain still more general solutions. Specifically we approximated a typical temperature profile given in the literature for the EFG process (designated Profile B below) to be:

$$T = 437e^{-1.36x}\cos\pi x - 317e^{-.47x}\sin(\tfrac{\pi}{2}x + \tfrac{\pi}{6}) + 1157e^{-.066x} \qquad (18)$$

The first term in Eq. (18) reflects the rapid cooling region, while the second term is the reheating region used to reduce the residual stresses. The temperature and its second derivative are shown in Fig. 4. The second derivative is seen to be very small beyond x = 3 cm.

The particular solution, for the stress function f_p, associated with this profile is [for c = 3 cm]:

$$f_p = \alpha Et[e^{-1.36x}(.415408\cos\pi x + .406419\sin\pi x)$$

$$- e^{-.47x}(.141385\cos\tfrac{\pi x}{2} + 1.531262\sin\tfrac{\pi x}{2})$$

$$- e^{-.066x}(.211565)] \qquad (19)$$

Combining Eqs. (12) and (19) and then using boundary conditions Eq. (14) yields [numbers given are to be multiplied by αEt]

$$A_1 = -5.09931 \times 10^{-4} \qquad C_1 = -0.0619478$$

$$B_1 = 1.409923 \times 10^{-3} \qquad D_1 = 2.88095$$

These numbers were determined on a home computer and more significant figures were retained than are shown above. The resulting stress function f(x) is shown in Fig. 5. The largest stresses for this profile are near x = 1 cm but those near x = 2.5 cm are also substantial. Results containing basically this same observation have previously been made from the examination of computer outputs. However the question remains as to which of the large stresses is most damaging insofar as buckling is concerned.

BUCKLING

We began this study by assuming the buckled shape to be

$$w = (W_0 + yW_2)(x^2 - x^3/3L) \qquad (20)$$

The strain energy, Eq. (4), was evaluated and minimized using $\frac{\partial U}{\partial W_0}$ and $\frac{\partial U}{\partial W_2}$. This resulted in $W_0 = 0$, indicating that problems where the stresses are self equilibrated and given by Eq. (9) do not buckle by bending but rather by torsion since $W_2 \neq 0$.

This can be seen by an examination of the last integral in Eq. (4). The last two terms are clearly zero when w = w(x) only and the first term

can be written as $\int_0^L (\frac{\partial w}{\partial x})^2 \int_{-c}^{c} N_{xx}\, dy\, dx$ which vanishes due to the thermal stresses being self equilibrated.

Having established that torsion is the mode of buckling when thermal stresses are the sole cause we generalized Eq. (20) to

$$w = yW_1(x) \tag{21}$$

That is we also use the Kantorovich method to determine the differential equation for torsional buckling. Using Eqs. (9) and (21), Eq. (4) becomes

$$U = \frac{1}{2}\int_0^L D[\frac{2c^3}{3} W''^2 + 4c(1-\nu)W'^2]dx + \frac{16c^5}{15}\int_0^L (fW'^2)dx + \frac{16}{30}c^5 \int_0^L (f''W^2 + 2f'WW')dx \tag{22}$$

The variation of the last term in Eq. (22) is identically zero. Minimizing U in the usual way then yields

$$\frac{D2c^3}{3} W'''' - \underline{4cD}(1-\nu)W'' - \frac{32}{15} c^5 \frac{d}{dx}(fW') = 0 \tag{23}$$

Integrating Eq. (23) and defining

$$\phi = W' \tag{24}$$

one obtains

$$\phi'' + [-\frac{4.2}{c^2} - \frac{3.2c^4}{Dc^2} f]\, \phi = C_4 \tag{25}$$

where C_4 is a constant which can be shown to be zero from the natural boundary conditions associated with Eqs. (6) and (22). Eq. (25) is the main new result of this paper. Clearly if $f > 0$ no torsional buckling develops. Even if $f < 0$, there is a "window" of temperature fields which keep the terms in [ ] negative and hence prevent buckling. On the other hand once the stresses gets larger and c becomes larger as well, thermal buckling will develop. The appropriate boundary conditions for the cantilever plate are

$$\phi'(0) = 0 \text{ and } \phi(L) = 0 \tag{26}$$

Eq. (25) can be rewritten as

$$c^2\phi'' + 3.2\,[-1.3125 + k^2 g(x)]\phi = 0 \tag{27}$$

where $k^2 = c^4 T^*/D$ and $-T^*$ is a parameter which characterizes the magnitude of the stress function f while g(x) represents its spatial variation.

Eq. (27) has nontrivial solutions which satisfy the boundary conditions, Eq. (26), only for discrete values of k^2. Depending on how the data is given, the lowest value of k^2 which causes the solution of Eq. (27) to satisfy Eq. (26) defines a critical temperature, a plate width or a plate thickness.

Wang [4] contains a series solution for an equation somewhat like Eq. (27). However due to the complicated shape of g(x), numerical methods are used here.

We have used a fourth order Runge-Kutta method on a home computer to solve Eq. (27) by an iterative process to give values for k^2 which satisfy Eq. (26). We usually use $\phi(0) = 0.10$ [but this is not essential] and change k^2 until $\phi(L) = 0$ is satisfied to better than 0.0001. Typical results are shown in Fig. 6.

It is useful to examine the solution of Eq. (25) when f is a constant. Then

$$\phi = A \sin(\omega x/c) + B \cos(\omega x/c) \tag{28}$$

where $\omega^2 = -4.2 - 3.2c^4 f/D$. The boundary conditions, Eq. (26) implies $A = 0$ and $\omega L/c = \pi/2$, so that for this case

$$- f_{cr} = [1.3125 + (\pi c/2L)^2/3.2]D/c^4$$

when $c/L = 1/6$, the term in brackets is [1.3125 + .02142]. In other words there is not much difference between the temperature values where the term in [ ] vanishes in Eq. (27) and where buckling actually occurs. Incidentally using the exact value of f for the case where $T_0'' =$ constant in Eq. (27) yields [ ] = 1.414 for $c/L = 1/6$. As c/L increases there is a larger gap between where the [ ] vanishes and buckling occurs. At a value of $c/L = 1/2$ and $T_0'' =$ constant, the entire [ ] term = 2.255 in Eq. (27).

Incidentally the $\cos(\omega x/c)$ shape is not a bad approximate shape for ϕ when c/L is moderate (say > 1/2) and the temperature field is such that $T_0'' =$ constant.

Approximate Method

It is sometimes useful to have an approximate solution for f(x). For this purpose the last term in Eq. (10) can be rewritten as

$$\frac{32}{15} \alpha E t c^5 (fT'') .$$

In view of the shape of f(x) such as that shown in Fig. 2 [for c = 3 cm] we choose the approximate solution for f to be of the form

$$f = Bx(L - x) \tag{29}$$

Eq. (10) then becomes

$$U^* = \frac{1}{2}\{B^2Lc^5(\frac{1024c^4}{315} + \frac{512c^2L^2}{315} + \frac{128L^4}{150}) + \frac{B32}{15}\alpha E\, t\, c^5L^3T^{**}\} \tag{30}$$

where $T^{**}L^3 = \int_0^L T''x(L-x)dx$. Hence the condition that $\partial U^*/\partial B = 0$ yields

$$\frac{BL^2}{4} = -\frac{\alpha E\, t\, T^{**}}{22.5(\frac{1024c^4}{315L^4} + \frac{512c^2}{315c^2} + \frac{128}{150})} \tag{31}$$

for the maximum value of the stress function. For the approximate deflected shape we assume

$$W = A\cos(\pi x/2L) \tag{32}$$

Since the variation of the last term in Eq. (22) is identically zero, we use only the first line in that equation. This becomes

$$U = \frac{cA^2}{L}\{D(\frac{\pi^4c^2}{96L^2} + \frac{(1-\nu)\pi^2}{4}) + \frac{16\pi^2c^4BL^2}{60\ 4.5049816}\} \tag{33}$$

Hence the condition that $\partial U/\partial A = 0$ leads to an approximate value of B to be

$$\frac{BL^2}{4} = -\frac{D(\frac{c^2}{L^2}\frac{\pi^4}{96} + (1-\nu)\frac{\pi^2}{4})}{\frac{16}{15}(.2219765)} \tag{34}$$

Combining Eq. (31) and (33) yields the critical temperature condition as

$$T^{**} = \frac{164.13D}{c^4\alpha Et}(\frac{1024c^4}{315L^4} + \frac{512c^2}{315L^2} + \frac{128}{150})(1 + .5875\frac{c^2}{L^2}) \tag{35}$$

For cases where the temperature and c are specified, Eq. (35) can be rearranged to give the critical thickness as

$$t_{cr}^{2} = \frac{c^4 \alpha T^{**}}{15.0301\left(\frac{1024c^4}{315L^4} + \frac{512c^2}{315L^2} + \frac{128}{150}\right)\left(1 + .5875\,\frac{c^2}{c^2}\right)} \tag{36}$$

RESULTS

The main result of the analysis section of this report is that cantilever plates subjected to axial temperature fields buckle in a torsional mode at a value of k^2 which is obtained by the solution of Eq. (27) subject to Eq. (26). Results for several temperature profiles and plate widths are given in Table I.

TABLE I

Temperature Profile

	$T_o'' = 24$	A	B	C
c = 1	1.414	.13463		.699
c = 2	1.833			
c = 3	2.777	3.267	5.265	1.726
c = 4	4.867	8.141		

Values of k^2 (when L = 6 cm)

Approximate values for k^2 can be deduced from Eq. (36).

To this writer the most unexpected result of the analysis is that k^2 for Profile B is (roughly) twice that for Profile $T_o'' = 24$. and three times that of Profile C (when c = 3 cm). This can be understood in hindsight by again looking at Eq. (27) and seeing what part of the total length makes the [ ] > 0 as is necessary for buckling to occur. The "effective length", ℓ^*, i.e. that length where $|k^2 g| > 1.3125$ can be read from the graphs for f(x). The results for c = 3 cm are

Profile $T_o'' = 24$ $\quad f^* = \frac{1.3125}{k^2} = .473 \quad \ell^* = 3.2$ cm

Profile A $\quad f^* = \frac{1.3125}{3.267} = .402 \quad \ell^* = 1.4$ cm

Profile B $\quad f^* = \frac{1.3125}{5.265} = .249 \quad \ell^* = 1.15$ cm

Profile C $\quad f^* = 1.3125 = .760 \quad \ell^* = 3.1$ cm

It is relatively easy to convert the mathematical results into physical feeling by noting how easy it is to twist a sheet of paper. The last term in Eq. (22) represents the contribution of N_{yy} and N_{xy} and since its variation is zero [due to the boundary conditions on f] only N_{xx} really affects the buckling. Due to Eq. (9) the axial "stresses" N_{xx} is given as

$$N_{xx} = 4(3y^2 - c^2)f \tag{37}$$

And since $f < 0$ for buckling to occur the center ($y = 0$) is in tension and the outer edges are in compression and twice as large as those at the center. The wider the plate the larger are those compressive stresses.

Our calculational procedure has (usually) been to fix the plate width c because the particular solutions depend on it. If the temperature profile is also assumed fixed (say Eq. (18)), then k^2 is determined on a home computer. Once this value (for a fixed L which is here taken as 6 cm) is known, the definitions of D, f, k^2 etc. can be manipulated to give the critical thickness t_{cr} as

$$t_{cr}^{\ 2} = \frac{\alpha c^4 12(1-\nu^2)T^{***}}{k^2} \tag{38}$$

where $T^{***} = 1$ when the temperature field is fixed and therefore included in f. It is noted that this result is dimensionally correct, because T^{***} and k^2 are not, in fact, dimensionless. The numbers shown in Table I for k^2 have been converted to critical thicknesses (using $\alpha = 4.5 \times 10^{-6} = \alpha$ @ 1000°C). The results are shown in Table II.

TABLE II

Thermal Profile	$T_o'' = 24$	A	B	C
	t_{cr}(mm)	t_{cr}(mm)	t_{cr}(mm)	t_{cr}(mm)
c = 1 cm	.059	.1911	-	.084
c = 2 cm	.207			
c = 3 cm	.379	.349	.275	.480
c = 4 cm	.508	.393		

Critical Plate Thicknesses

The value of critical plate thickness at c = 3 cm is .275 mm = 10.8×10^{-3} inches is a very reasonable value illustrating the value of the analysis despite neglecting plastic effects and variable elastic modulus. It is also noted that this is the thinest plate for c = 3 cm.

In the above tables temperature Profile A is

$$T(x) = 1157e^{-.063x} + 478e^{-.8x} \cos \pi x$$

while profile B is given by Eq. (18) and profile C is the sum of two exponentials

$$T(x) = 1000e^{-.063x} + 435e^{-.5x} .$$

The stress functions associated with these profiles are compared in Fig. 7.

APPENDIX A Coefficients in Eq.(17)

We write Eq.(11) as

$$c^4 f'''' - 6f''c^2 + 31.5f = [R\cos(2\pi x/\ell) + S\sin(2\pi x/\ell)]e^{-mx}$$

where

$$R = (n^2 - m^2)\, T_1(1.3125\alpha Et/c^2)$$

and

$$S = -2\, nm\, T_1(1.3125\alpha Et/c^2)$$

$$n = Mc$$

$$n = 2\pi c/\ell$$

Using the particular solution, Eq.(17), and matching coefficients, we find that

$$A_1 A_q + A_2 B_q = R$$

and

$$-A_2 A_q + A_1 B_q = S$$

where

$$A_1 = (m^2 - n^2)^2 - 4m^2n^2 - 6m^2 + 6n^2 + 31.5$$

$$A_2 = 4mn[3 - m^2 + n^2]$$

The coefficients in Eq.(17) are therefore

$$Aq = \frac{RA_1 - SA_2}{A_1^{\,2} + A_2^{\,2}}$$

$$Bq = \frac{RA_2 + SA_1}{A_1^{\,2} + A_2^{\,2}}$$

<u>Example</u>: $M = 1.36$ $T_1 = 437$ $c = 3$ $\ell = 2$ $\therefore$ $m = 4.08$ $n = 3\pi = 9.424778$

$$A_1 = -240.0234$$

$$A_2 = 11563.6205$$

$$R = 4599.97\alpha Et$$

$$S = -4901.16\alpha Et$$

$$Aq = .4154077\alpha Et$$

$$Bq = .4064195\alpha Et$$

Hence the boundary conditions at x = 0 become

$$A_1 + C_1 = -.415\ 4077\alpha Et$$

$$\alpha A_1 + BB_1 - \alpha C_1 + BD_1 = -2.135550\alpha Et$$

The boundary conditions at x = L are more complicated but basically the same idea. Hence one finds the coefficients A_1 - D_1 and ultimately the stress field just prior to buckling.

Acknowledgements

The authors appreciate the help of JPL personnel for calling our attention to this problem. We also greatly appreciate the help of Mrs. Laura Cottingham in preparing the manuscript.

References

1. Reissner, E. and Stein, M. "Torsion and Transverse Bending of Cantilever Plates, N.A.C.A.T.N. 2369, June 1951.

2. Mansfield, E. H., "Bending, Buckling and Curling of a Heated Thin Plate," Proceedings of the Royal Society, A, vol. 268, pp. 316-327, 1962.

3. Boley, B. A. and Weiner, J. H. "Theory of Thermal Stresses," Wiley and Sons, New York, N.Y. (1960).

4. Wang, C. T., "Applied Elasticity" McGraw Hill, New York, N.Y. (1953).

Figure 1

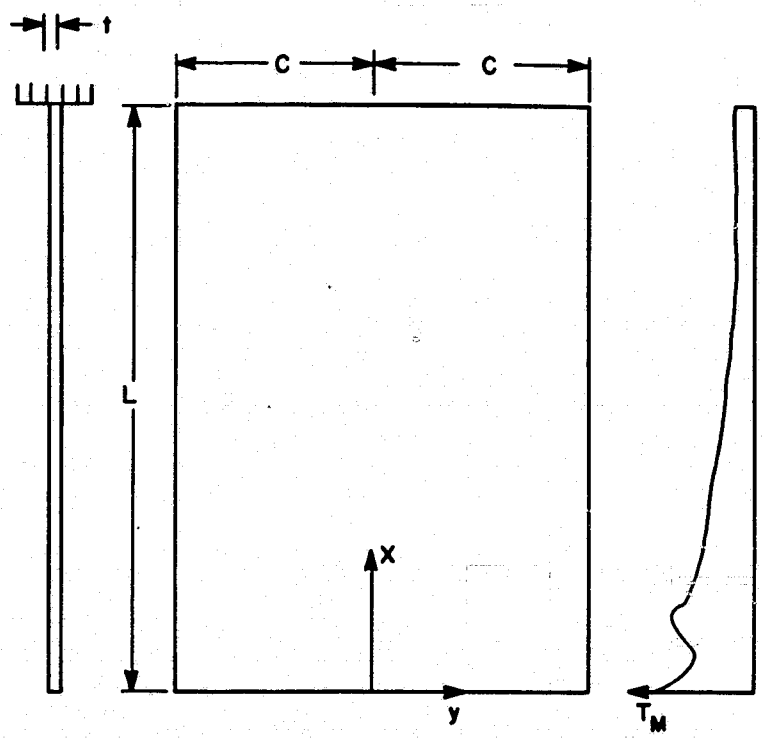

Figure 2

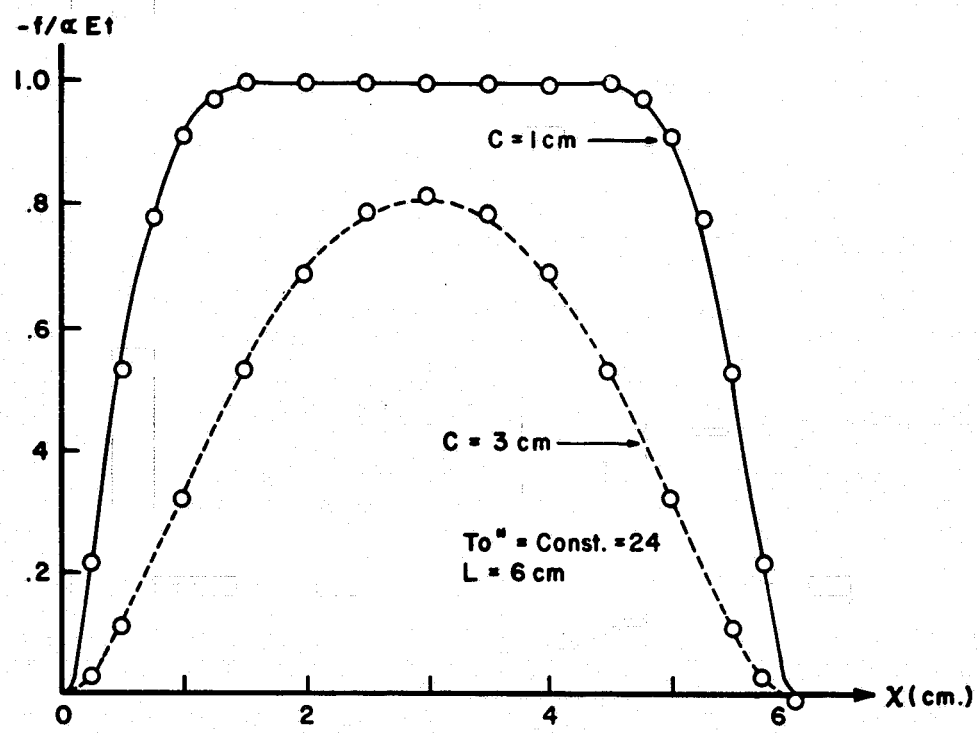

Figure 3

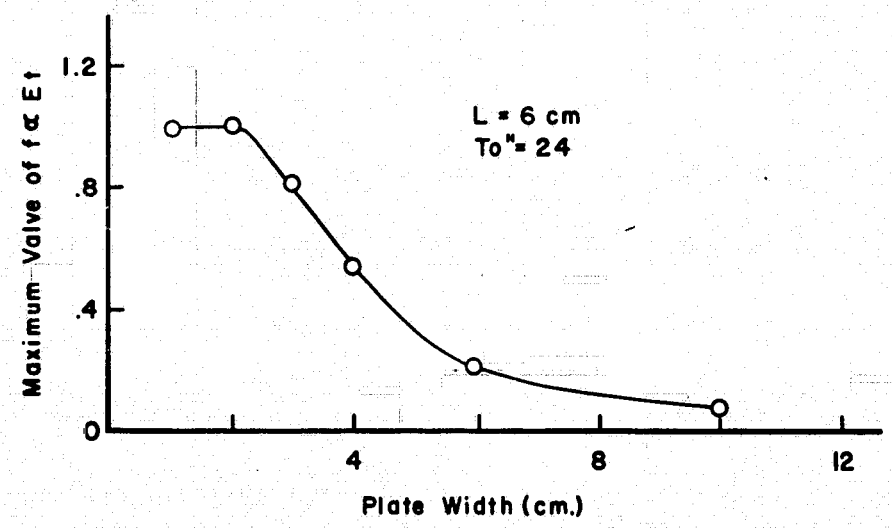

Figure 4

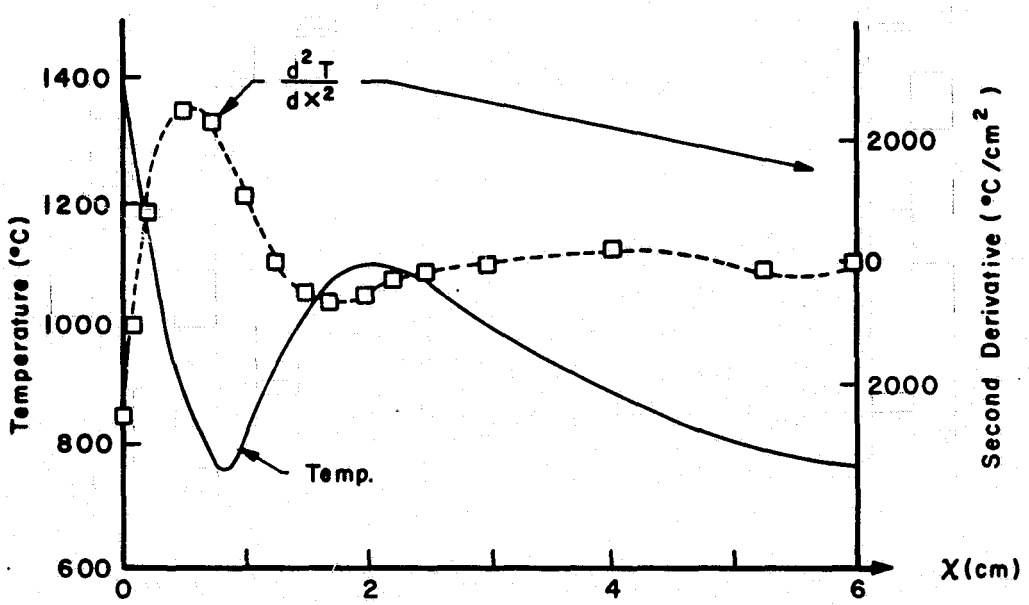

Figure 5

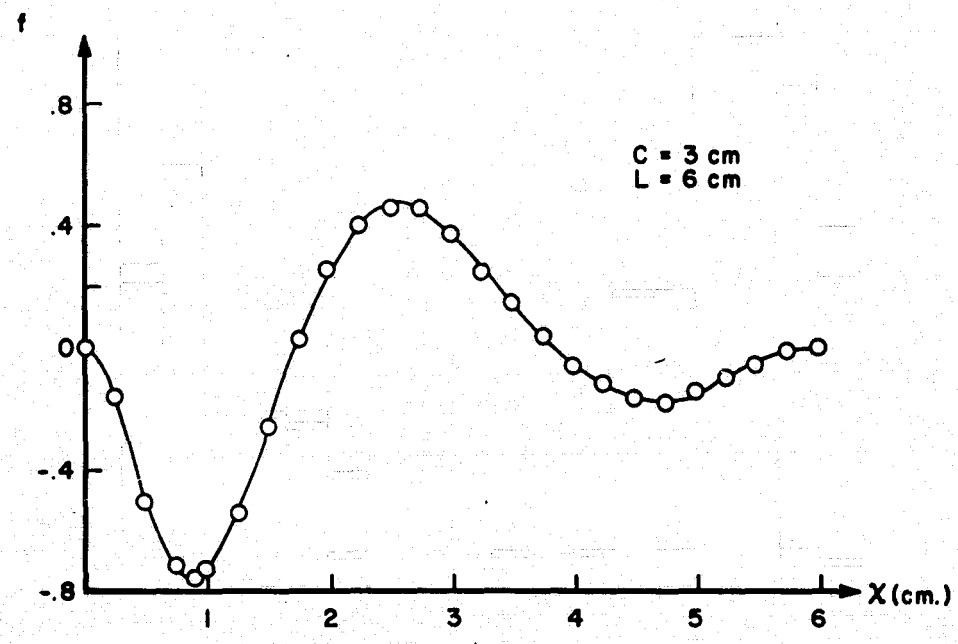

Figure 6

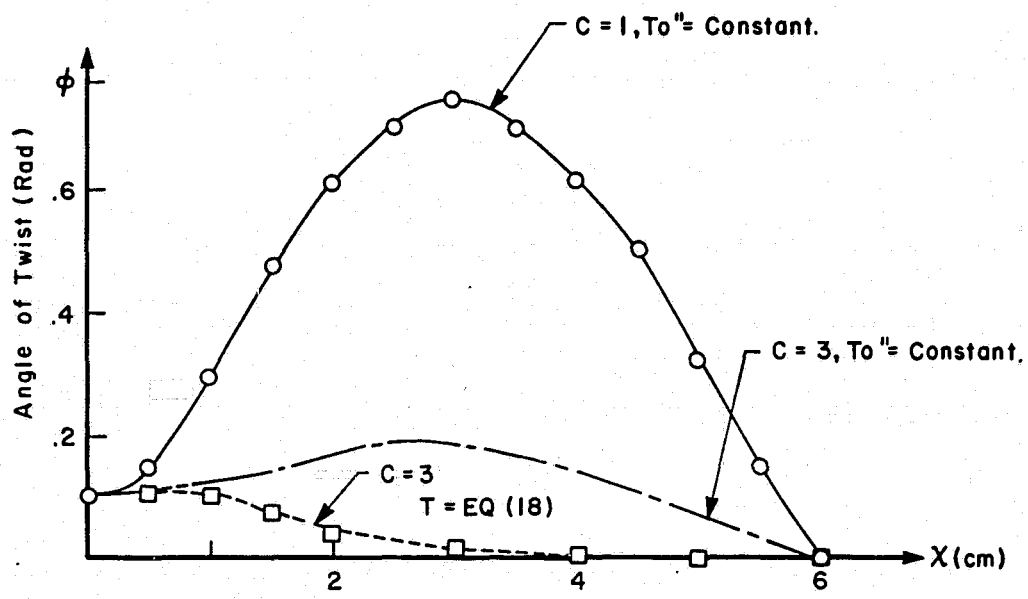

Figure 7

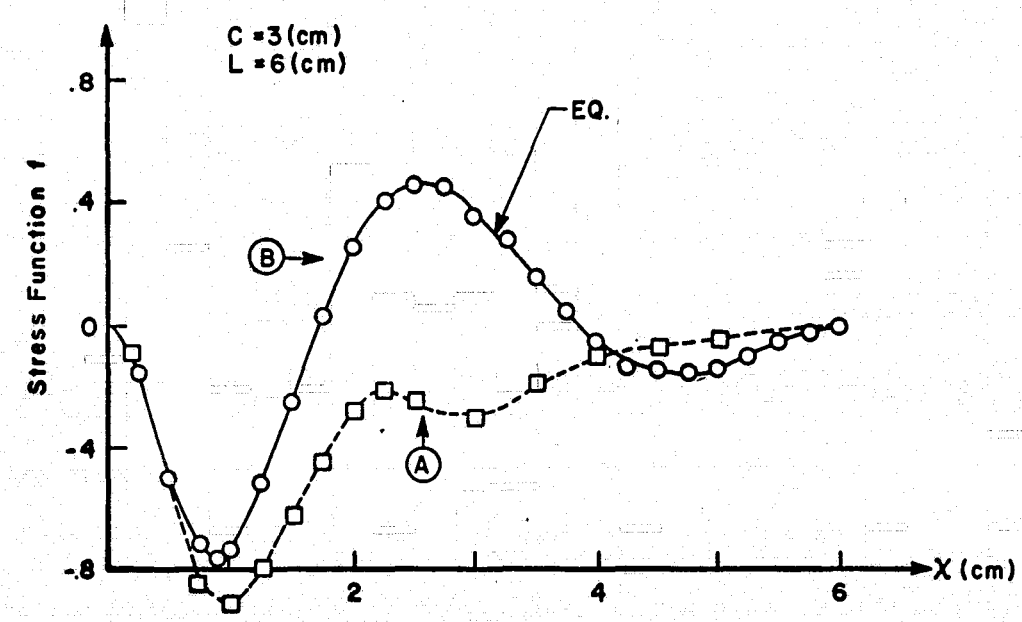

DISCUSSION

WILCOX: I have a fairly extensive comment. If you use your theory and apply it to ribbon or any other crystal at room temperature, the crystal is isothermal, and you predict no stress and no buckling, so it is clear that there is a good deal more involved than just thermal stress, and that is plastic deformation. I would like to describe to you what really happens when you grow a crystal. It may be easiest to think in terms of Czochralski growth because you don't have any buckling at high temperatures. In growing a Czochralski crystal, the outside cools before the inside, so at the growth temperature, or just below the growth temperature, the outside is under tension and the inside is under compression but plastic deformation can occur, and in the limit completely relieves the stress so that you have a grown-in strain. As you cool the crystal down, you go beyond the plastic temperature, and plastic deformation can no longer occur. At room temperature, the temperature is uniform, you no longer have the thermal strain introduced, but you have a residual stress because of the relaxation that occurred at high temperature. Now you have a complete stress reversal where the surface of the crystal is under compression and the interior is under tension. As you correctly pointed out, that is what gives you buckling. In the case of a ribbon, things are a good deal more complicated because you can get buckling at high temperature as well as plastic deformation and if you are going to understand the physics of the process, you can't throw out the plastic deformation. You have to consider the entire temperature cycle; otherwise it is an impressive exercise, but it is really not telling you what is going on.

It is easy to think of plastic deformation when you have a material with dislocations in it, but what gives you the residual stress when you don't have dislocations? I would answer that it has got to be point defects. There are two possibilities; one is that the thermal stress of high temperature causes the point defects to move around to try to relieve it. The other possibility is that if you are growing with a curved interface, you actually have a stress applied to the growth interface and the growth interface is going to incorporate point defects, vacancies, impurities, as best it can, to try and minimize the stress at the growth temperature. And then those get rapidly frozen in, and you get a stress reversal again.

CHALMERS: I have seen a lot of buckled ribbons, and buckling is clearly of two types, which I would describe as center buckling and torsional buckling. In torsional buckling the ribbon twists alternately in two directions. That seems to me to be inevitably the result of the edge being in compression and the center in tension, which is the reverse of the condition you are describing. This way you can make the edge a bit longer than the center, which is what it wants to do. The opposite type, center buckling, has no torsion; the center goes in and out compared with the edges and that must be the result of the center being in compression and the edges in tension. Is this correct?

DILLON: I thought a lot about that, too. The bending modes, when they come in, have to be a result of the nonuniformity of the temperature in the width direction. The temperature here is a function of x only, which says that it can only buckle in the torsional mode. The other one, if it buckles in any other way, has to be due to the temperature being nonuniform in the y direction.

CHALMERS: I wonder if that is correct. The buckling that seems to be important, that everybody is trying very hard to avoid, is the center buckling, in which the edges have been in tension and the center has been in compression.

DILLON: I would agree with you, except I will go back to the statement that in order for the thing to buckle in any other mode, it has to come from the temperature being nonuniform in the y direction. It can be a very small temperature, but it has to happen that way.

CHEN (JPL): Would you describe the buckling that we observe as wavy? You are only assuming that it is a compression. It is a first-mode type of buckling.

LEIPOLD: The assumptions you started out with in terms of material characteristics are rather restrictive, especially when you operate at high temperatures. How much complication is it going to introduce to include more realistic assumptions as far as what material properties do with temperature, and so on?

DILLON: I have made some first stabs at taking exponential variations in temperature or material properties that lead to the same kind of equations. Since the deformations are permanent deformations, you have to include the plasticity, but assuming a variable modulus, it will not be that difficult.

LEIPOLD: That the plastic component has to be included is valid but I have two comments. One is that plastic deformation will allow a reduction in the applied stress that you are using before the onset of buckling. Second, it will allow that buckling to become permanent in terms of a permanent deformation included in the material after the buckling but I don't agree that the analysis is a priori invalid because it is elastic.

SEIDENSTICKER: We have seen examples of both torsional and nontorsional buckling. Which mode you happen to actually arrive at is very sensitive to the exact constraints you place on the system. Also if you do have a residual stress present, this will modify any of the stress fields, and once a buckling deformation has occurred, then this may or may not result in additional residual stress. It depends very much on the specific details of what happens in plastic deformation. Once you have that done, this will depend on what you see after the crystal is grown. The sort of thing that Oscar [Dillon] is discussing is that you would end up with a flat crystal. It wouldn't be buckled any more.

N84 28634 D20

THE EFFECT OF CREEP ON THE RESIDUAL STRESSES GENERATED DURING SILICON SHEET GROWTH

J. W. Hutchinson and J. C. Lambropoulos
Division of Applied Sciences, Harvard University
Cambridge, Mass. 02138

1. INTRODUCTION

The modeling of stresses generated during the growth of thin silicon sheets at high speeds is an important part of the EFG technique since the experimental measurement of the stresses is difficult and prohibitive. The residual stresses arising in such a growth process lead to serious problems (such as buckling or fracture) which make thin Si ribbons unsuitable for fabrication. A previous attempt [1] at modeling of the stress distribution in Si ribbons, although providing considerable insight, lacked two important components: on the one hand it neglected the effect of the steady-state growth velocity V on the residual stress distribution since it addressed the static thermoelastic problem; on the other hand, the aforementioned solution modeled the ribbon as purely elastic. Such a constitutive behavior is unrealistic because at high temperature (close to the melting point) Si exhibits considerable creep which significantly relaxes the residual stresses.

The object of this paper is to address the effect of creep on the residual stresses generated during the growth of Si sheets at high speeds. Some results concerning the effect of the steady-state velocity V on the stresses as well as some aspects of the effect of creep are reported elsewhere [2]. Thus, only the basic qualitative effect of creep will be reported here.

It must be pointed out that the constitutive behavior of Si at high temperatures is not precisely known. Although the constitutive law applicable to temperature dependent secondary creep is used here, the appropriateness of steady-state creep is questionable. Thus, the results presented here must be viewed as preliminary and qualitative indications of what is to be expected rather than precise predictions of the actual stresses present in experimentally grown Si ribbons.

Part 2 of this paper presents the formulation of the field equations applicable to the growth of thin Si ribbons. It includes a brief discussion of the boundary conditions and of the constitutive law used. Part 3 treats the basic aspects of the finite element method which was used to solve numerically the field equations. It must be noted that due to the material non-linearity of Si an analytical solution is essentially impossible. Part 4 presents some of the results of a representative solution which corresponds to a temperature profile and a growth velocity used in practice. Both the physical model and the results are discussed in Part 5. The essence of the solution is outlined and the basic assumptions are critically discussed. Several suggestions regarding future work are also presented.

The overall basic conclusions are outlined in Part 6.

2. FIELD EQUATIONS

A ribbon of negligible thickness and of width $2H$, extending from $x_2 = -H$ to $x_2 = +H$, emerges from the solid liquid interface at $x_1 = 0$ and is pulled in the positive x_1-direction with the uniform velocity V. The ribbon is subject to a known temperature distribution $T(x_1, x_2)$ which is assumed independent of time. The basic features of $T(x_1, x_2)$ are that it starts from the melting temperature of Si at $x_1 = 0$ and that it decreases with a very steep gradient (≥ 1000 K°/cm) near $x_1 = 0$. The $x_1 = \infty$ end of the ribbon is at room temperature. For temperature distributions symmetric about the x_1-axis, it is sufficient to consider only the domain $0 \leq x_2 \leq H$, as shown in Fig. 1.

Denoting by v_i the components of the velocity, the strain rates $\dot{\varepsilon}_{ij}$ are found by

$$\dot{\varepsilon}_{ij} = (v_{i,j} + v_{j,i})/2 \tag{1}$$

The stress rates $\dot{\sigma}_{ij}$ obey the equilibrium equations

$$\dot{\sigma}_{ij,j} = 0 \quad , \quad \dot{\sigma}_{ij} n_j = \dot{T}_i$$

which take the equivalent variational form

$$\int_A \dot{\sigma}_{ij} \delta v_{i,j} dA = \int_S \dot{T}_i \delta v_i dS \tag{2}$$

where A and S denote the domain and its boundary respectively. Assuming conditions of plane stress the only non-zero stresses are σ_{11}, σ_{12} and σ_{22}. The boundary conditions are shown in Fig. 1. The boundary conditions on the sides $x_1 = \infty$, $x_2 = 0$ and $x_2 = H$ are easily understood, but the b.c. on the side $x_1 = 0$ deserve some comments: When the solidifying material accretes at zero stress $\sigma_{22} = 0$ at $x_1 = 0$, then the traction rate b.c. at $x_1 = 0$ are $\dot{\sigma}_{11} = \dot{\sigma}_{12} = 0$. However, when the initial stress $\sigma_{22}(x_1 = 0, x_2)$ is non-zero, the proper b.c. at $x_1 = 0$ is

$$\dot{\sigma}_{11} = 0 \quad , \quad \dot{\sigma}_{12} = -V \partial \sigma_{22}(0, x_2)/\partial x_2 \tag{3}$$

Equations (3) are simple consequences of equilibrium. Hence, they provide no information about the correct distribution of σ_{22} at $x_1 = 0$. The

proper specification of $\sigma_{22}(0,x_2)$ requires additional understanding of the physical process of solidification which is not available at this time. For the rest of this paper it will be assumed that $\sigma_{22}(0,x_2) \equiv 0$. A physical argument in favor of this assumption is that dislocations are generated at a sufficient rate at $x_1 = 0$ so as to relieve the compressive σ_{22} stress at the interface [3]. Further mechanical arguments in favor of $\sigma_{22}(0,x_2) = 0$ are available [4]. Nevertheless, further work is being done to assess the influence of non-zero $\sigma_{22}(0,x_2)$ on the resultant residual stresses.

Under the assumption of steady-state quasi-static motion, the material derivative $\dot{\phi}$ of any field quantity ϕ is related to the spatial variation of ϕ by

$$\dot{\phi} = V\partial\phi/\partial x_1 \tag{4}$$

The total strain rate $\dot{\varepsilon}_{ij}$ (given by Eqn. (1)) is the sum of the elastic $\dot{\varepsilon}^{el}_{ij}$, thermal $\dot{\varepsilon}^{th}_{ij}$, and creep $\dot{\varepsilon}^{c}_{ij}$ strain rates. These components are given by:

$$\begin{aligned} \dot{\varepsilon}^{el}_{ij} &= \frac{1+\nu}{E}\dot{\sigma}_{ij} - \frac{\nu}{E}\dot{\sigma}_{kk}\delta_{ij} \\ \dot{\varepsilon}^{th}_{ij} &= \alpha(T)\dot{T}\delta_{ij} \end{aligned} \tag{5}$$

$$\dot{\varepsilon}^{c}_{ij} = \dot{\varepsilon}^{c}_{ij}\ (T\ ,\ \text{stress history, internal parameters}) \tag{6}$$

where ν is the Poisson's ratio, E is the Young's modulus (both temperature independent) and $\alpha(T)$ is the temperature dependent thermal expansion coefficient. Equation (6) provides the constitutive law of the creep part of the total strain rate. It is a quite involved expression in general. Here it is assumed that the primary (or transient) part of $\dot{\varepsilon}^{c}_{ij}$ is negligible and that the only contribution to $\dot{\varepsilon}^{c}_{ij}$ is the one due to temperature dependent secondary (or steady-state) creep. Furthermore, it is assumed that $\dot{\varepsilon}^{c}_{ij}$ depends on the stress through a power law relation, i.e.

$$\dot{\varepsilon}^{c}_{ij} = Cf(T)(\sigma_e/\mu)^{n-1}\, s_{ij} \tag{7}$$

where C , n are material constants, μ is the shear modulus, $s_{ij} = \sigma_{ij} - \frac{1}{3}\sigma_{kk}\delta_{ij}$, and $\sigma_e^2 = 3s_{ij}s_{ij}/2$. The function of temperature f(T) is given by

$$f(T) = \exp(-Q/RT)/T \tag{8}$$

Q being a measure of the activation energy. In principle, more accurate

creep descriptions can be modeled; however, the available data for Si do not appear to justify a more involved description at this point.

Several experiments on the creep behavior of Si have been reported [5-9]. A creep law expression of the form of Eqn. (7) and compatible with all the data could not be found. In fact, it seems that the constants Q and n (varying from 2 to 11) are stress and temperature dependent [2, 10]. In the present paper we adopt the values $n = 5$ and $Q = 496$ kJ/mol which are representative of creep at intermediate stress levels with an activation energy typical of self-diffusion [2]. The constant C is chosen so as to produce a shear strain rate $\dot{\gamma}^c = 10^{-4} s^{-1}$ at a temperature of 1300 K° and at the stress level $\tau = 10^{-3}\mu$.

Thus, the field equations describing the physical model are: Eqn. (1) expressing compatibility; Eqn. (2) with the proper b.c. expressing equilibrium; Eqn. (4) expressing steady-state motion; and Eqns. (5), (7) which express the constitutive behavior of the material.

3. FINITE ELEMENT SOLUTION

In the finite element method (FEM) used here the domain under interest is partitioned into elements and the values of the velocity at the nodal points become the primary unknowns. The vector of nodal velocities $\underset{\sim}{q}$ satisfies

$$\underset{\sim}{K}\underset{\sim}{q} = \dot{\underset{\sim}{P}}^{th} + \dot{\underset{\sim}{P}}^{c} \tag{9}$$

where $\underset{\sim}{K}$ is the (known) global stiffness matrix and $\dot{\underset{\sim}{P}}^{th}$, $\dot{\underset{\sim}{P}}^{c}$ are vectors of equivalent body forces due to the thermal and creep strain rates respectively. Equation (9) is solved iteratively since the $\dot{\underset{\sim}{P}}^{c}$ term contains a non-linear term as shown in Eqn. (7).

The FEM has been used to solve other steady-state problems in elastic-plastic [11] and non-linear visco-elastic fracture mechanics [12] and, hence, its application will not be further described except in order to mention that knowledge of $T(x_1,x_2)$, of the pull velocity V and of the material properties allows the calculation of σ_{ij} , $\dot{\varepsilon}_{ij}$, $\dot{\varepsilon}^c_{ij}$ and v_i as functions of x_1 and x_2 .

The temperature profile used is taken to be independent of x_2 . Its x_1 variation is shown in Fig. 2. This profile is representative of a temperature distribution in a thin ribbon in which cooling elements and an afterheater have been attached [2]. Beyond $x_1 = 3$ cm the profile is linear until it reaches room temperature at $x_1 = 20$ cm.

The ribbon is modeled with a half-height $H = 4$ cm and a length L extending from $x_1 = 0$ to $x_1 = 20$ cm. The length is sufficient to insure that the field quantities have attained their steady-state values by the

time the temperature has reached the room value. The steady-state pull velocity V is taken to be 6 cm/min and the material parameters of Si were chosen as

$$\nu = 0.3 \quad , \quad E = 165 \text{ GPa}$$

$$\alpha(T) = 2.552 \times 10^{-6} + 1.95 \times 10^{-9} T - 9.0 \times 10^{-15} T^2$$

The choice of the material parameters concerning the creep part of the constitutive law were already mentioned in the previous part.

A characteristic partition of the domain used in the FEM calculation is shown in Fig. 3. For the calculations to be reported here, the dimension Δx_2 was chosen to be uniform for all the elements and equal to 0.05H. The horizontal extent Δx_1 varied from $2.5 \times 10^{-3} H$ near the interface $x_1 = 0$ to $6.25 \times 10^{-2} H$ at the room temperature end of the ribbon. In total 5480 elements covered the domain 20 of which spanned the vertical and 274 the horizontal direction. The relevant equation (9) was solved iteratively on a VAX-780 computer. A representative solution required 5-10 iterations lasting a total time of 10-20 CPU minutes.

4. RESULTS

Before presenting some indicative results it should be pointed out that the results must be regarded as preliminary and qualitative due to the uncertainty in the constitutive law used. Most of the features of the results to be presented are common to other solutions in which different temperature profiles and pull velocities were input.

Figures 4, 5 present the stress distribution on the centerline $x_2 = 0$ of the ribbon for the elastic and the creep solution. By elastic is meant the constitutive law of Eqn. (7) with $C = 0$. Figure 6 gives the variation of the residual stresses $\sigma_{11}(x_1 \to \infty, x_2)$ with distance from the centerline. In Fig. 7 plots of the creep strain rates on the centerline $x_2 = 0$ are presented. Finally, Fig. 8 gives the variation of the creep strain rates with distance from the centerline at the location $x_1 = 0.3$ cm.

5. DISCUSSION

The results presented in Figs. 4-8 are indicative of what is to be expected when creep is allowed to relax the elastic stress distributions. In another paper [2] more extensive results were presented. These results included various creep strain rate intensities, temperature profiles and pull velocities. However, the main features are the same: The peak values of all stress quantities are significantly relaxed. With reference to Figs. 4, 5 it is seen that the peaks in the σ_{11} , σ_{22} distributions occur within 0-4 cm from the solid-liquid interface. Hence, it is concluded that stress relief mechanisms (such as buckling) are more likely to occur in the

hot end of the ribbon. Partial experimental verification of this conclusion has been reported in [10] in which a scribe and split technique was used to estimate the residual stresses which were found to be in the range of 10 to 30 MPa. These values compare well to the results for the residual stresses shown in Fig. 6. However, it should be emphasized that, although creep significantly relaxes elastic stresses, the details of the stress relief are very sensitive to the details of the temperature profile employed.

With reference to Fig. 7 it is seen that a steep rise in the creep strain rates occurs within a few millimeters from the interface. Furthermore, beyond several centimeters from the interface the creep strain rates become negligible. From the plot in Fig. 8 of the creep strain rates vs. distance from the centerline at a small distance from the interface it is concluded that the outer boundaries of the ribbon are elastic whereas the center part is undergoing creep at a significant rate. This is probably a manifestation of a stress-free edge effect.

The general conclusions presented above constitute only a small part of the applicability and usefulness of the numerical solution. The effect of several important design parameters (pull velocity, temperature distribution) can be easily explored. However, there are two important questions regarding the formulation of the field equations: (a) what is a proper constitutive law for Si at high temperatures? and (b) what are the proper boundary conditions at the solid-liquid interface?

The nature of these questions classifies them within the scheme of a complete research effort in the mechanics of solidifying bodies put forth by O. Richmond [4]:

(i) Accurate measurement of mechanical behavior at high temperatures and appropriate stresses

(ii) development of elastic-viscoplastic constitutive models that describe this behavior.

(iii) Development of computational methods for solving the resulting boundary value problems, and

(iv) experimental evaluation of the predictions of the model used under appropriately controlled laboratory conditions.

6. CONCLUSIONS

The effect of creep deformation on the residual stresses generated during silicon sheet growth has been examined with the help of the finite element method. The FEM was used to calculate stresses and creep strain rates for a representative temperature profile consisting of cooling and afterheating elements and for a typical pull velocity of 6 cm/min. It is found that creep significantly relaxes residual and peak stress levels and it is concluded that any realistic calculation of residual stress and deformation should necessarily include the effect of creep.

Since several important questions have not been definitively answered,

the results presented should be regarded as qualitative indications of what the effect of creep is rather than as actual and complete solutions to the Si sheet growth problem.

The two areas that need further work are:

(a) the development of a constitutive law for Si applicable to high temperatures and to the level of stresses found close to the interface, and

(b) the understanding of the physics of solidification with special reference to the boundary condition appropriate to the solid-liquid interface.

In the present calculation the constitutive law used was that of temperature dependent secondary creep and the boundary condition used was based on the assumption that the material solidifies at zero normal stress.

The design aspects of the finite element scheme have not been investigated in this paper. However, the FEM allows great freedom in specifying various design parameters (pull velocity, temperature profile) and examining their effect on the residual stress distributions. The FEM also allows the choice of the constitutive law or of the boundary conditions used and thus permits the investigation of the effect of these theoretical factors on the residual stresses.

ACKNOWLEDGEMENTS

The authors gratefully acknowledge helpful discussions with Professor B. Chalmers and with Drs. Kalejs and Bell from Mobil Solar Energy Corporation. Further, the authors would like to gratefully acknowledge the financial support of the Jet Propulsion Laboratory Flat Plate Solar Array Project (subcontract 956312) sponsored by the U. S. Department of Energy.

REFERENCES

[1] Gurtler, R. W., J. Crystal Growth, 50 (1980), p. 69.

[2] Lambropoulos, J. C., Hutchinson, J. W., Bell, R. O., Chalmers, B., and Kalejs, J. P., Plastic Deformation Effects on Stress Generated During Silicon Sheet Growth at High Speeds, to be presented at the 7th International Conference on Crystal Growth (ICCG-7) in Stuttgart, September 1983.

[3] Chalmers, B., private communication, 1983.

[4] Richmond, O., in Modelling of Casting and Welding Processes, eds. H. D. Brody and D. Apelian, Met. Soc. AIME, 1981.

[5] Siethoff, H., and Schröter, W., Scripta Met., 17 (1983), p. 393.

[6] Yonenaga, I., and Sumino, K., Phys. Stat. Sol. (a), 50 (1978), p. 685.

[7] Suezawa, M., Sumino, K., and Yonenaga, I., Phys. Stat. Sol. (a), 51 (1979), p. 217.

[8] Frost, H. J., and Ashby, M. F., "Deformation Mechanism Maps", Pergamon Press, 1982.

[9] Myshlyaev, M. M., Nikitenko, V. I., Nesterenko, V. I., Phys. Stat. Sol. (a), 36 (1969), p. 89.

[10] Kalejs, J. P. et al., Third Quarterly Report DOE/JPL 956312/83/03 (April 1983), unpublished.

[11] Dean, R. H., and Hutchinson, J. W., in Fracture Mechanics, ASTM-STP 700, p. 383, Philadelphia, 1980.

[12] Hui, C. Y., Doctoral Dissertation, Division of Applied Sciences, Harvard University, 1981.

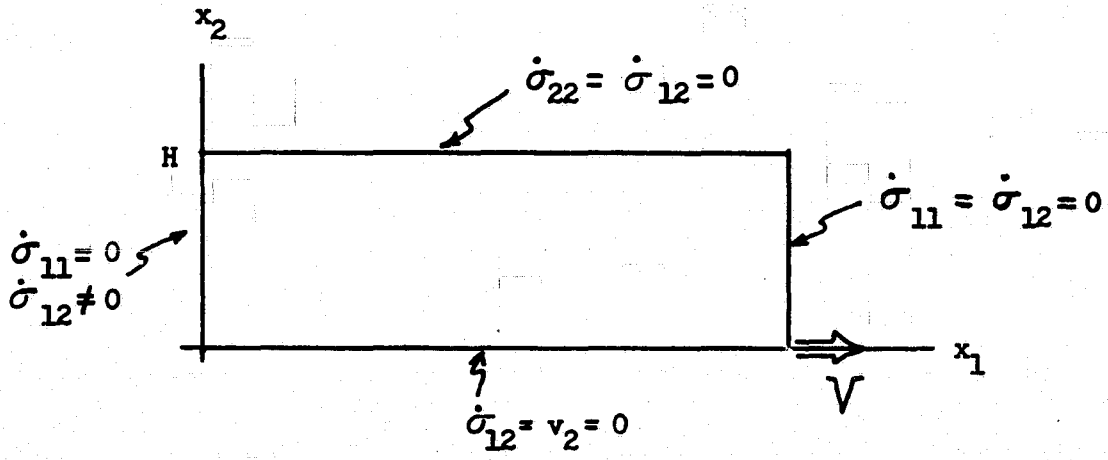

Figure 1: The geometry and boundary conditions of the Si ribbon growth problem.

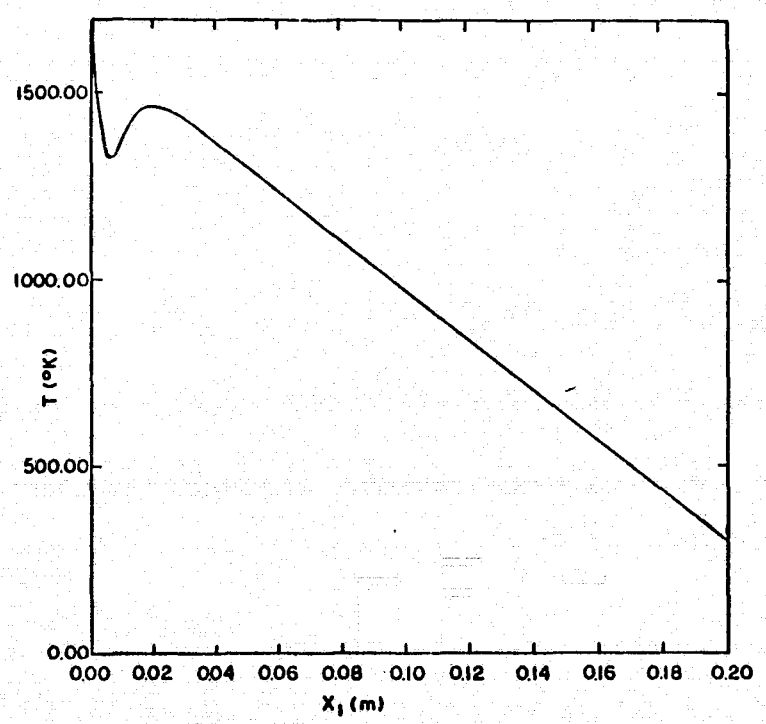

Figure 2: Temperature profile $T(x_1)$ used in the finite element calculation.

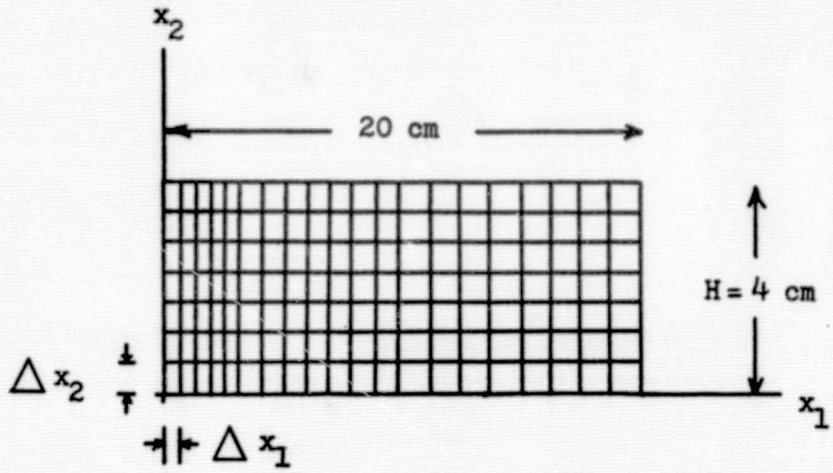

Figure 3: Representative FEM grid.

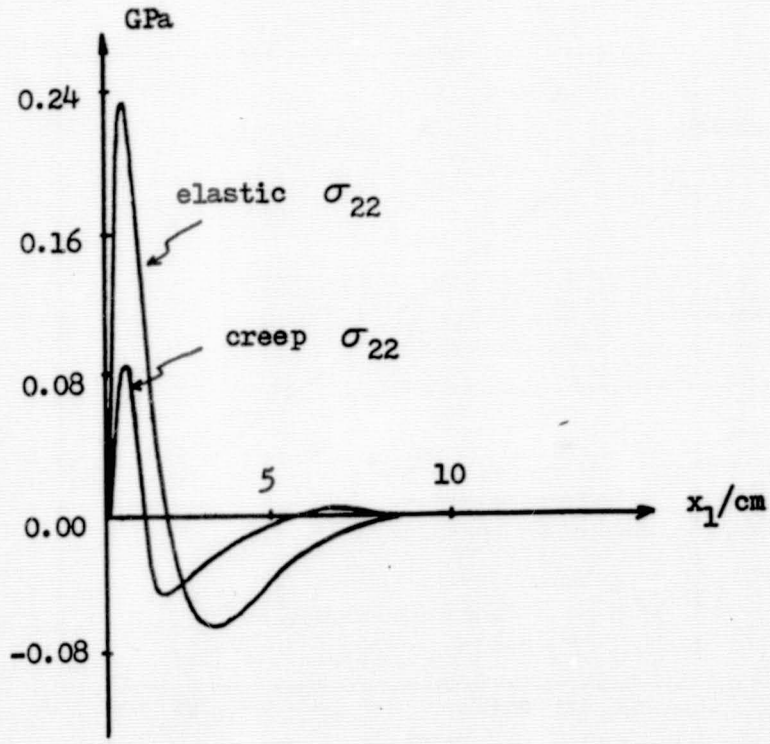

Figure 4: Stresses $\sigma_{22}(x_1,0)$ for the elastic and creep solutions.

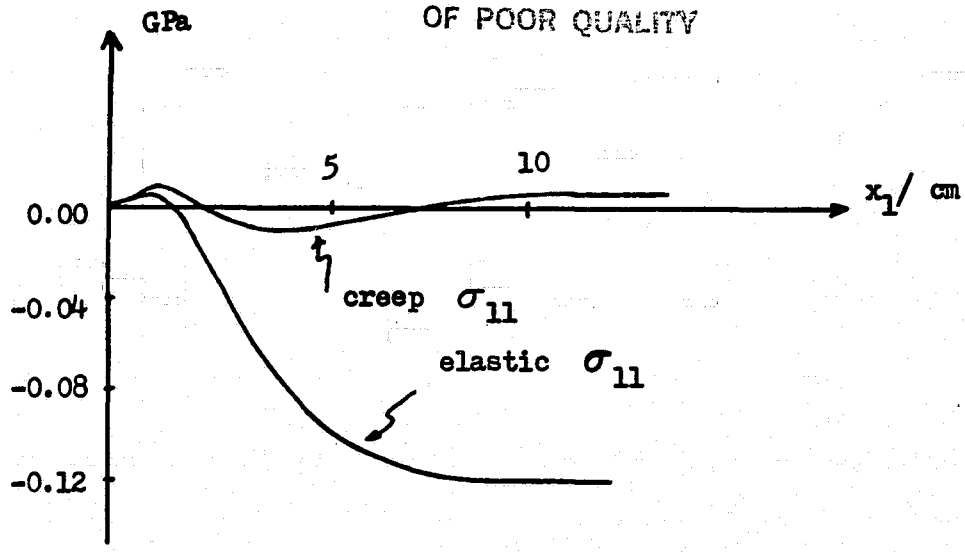

Figure 5: Stresses $\sigma_{11}(x_1,0)$ for the elastic and creep solutions.

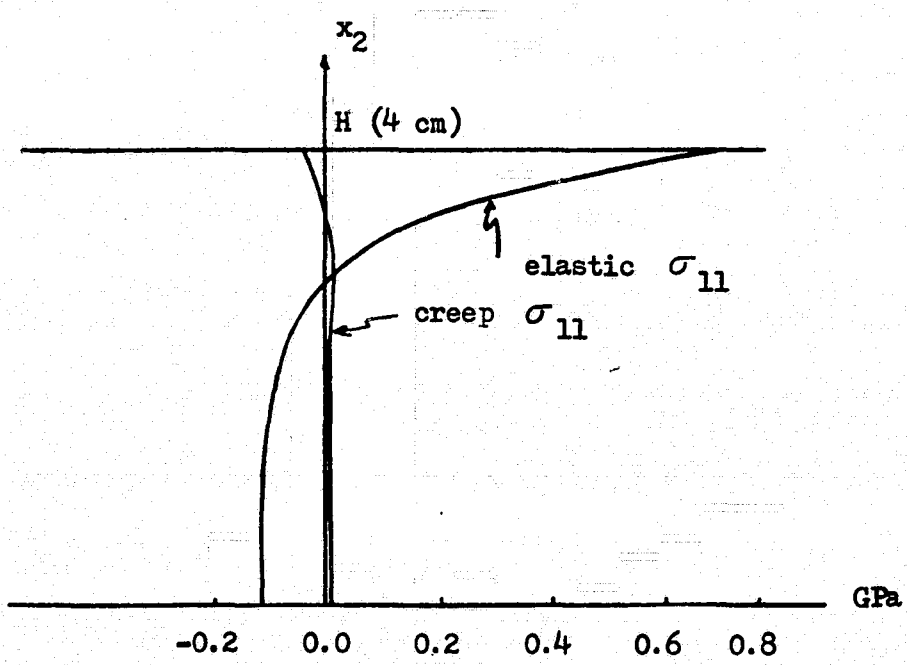

Figure 6: Residual stresses $\sigma_{11}(x_1 \to \infty, x_2)$ for the elastic and creep solutions.

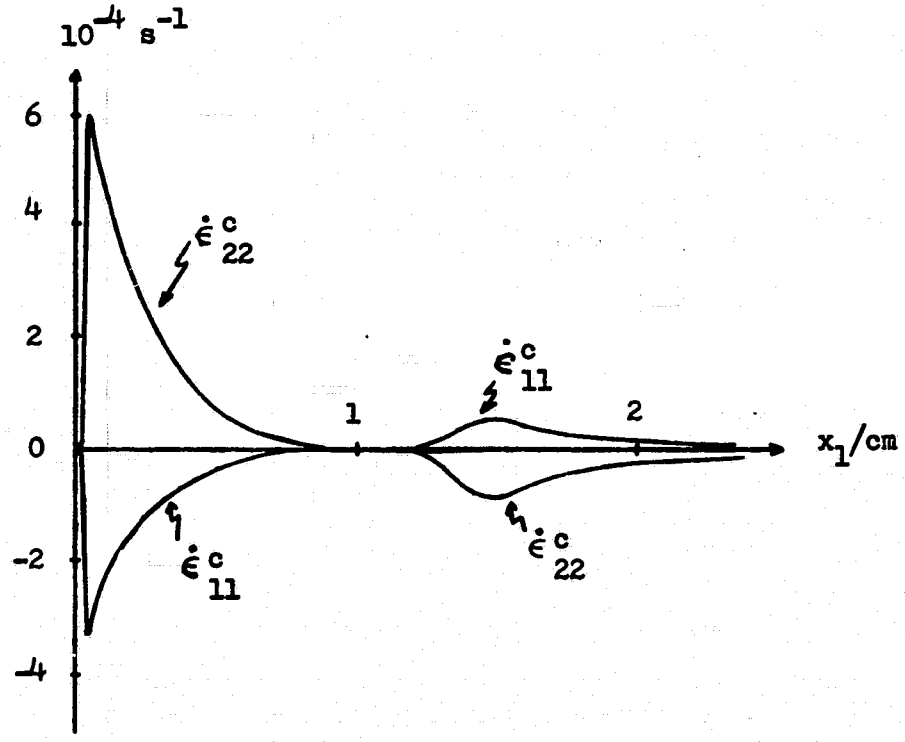

Figure 7: Plots of creep strain rates $\dot{\varepsilon}^c_{11}(x_1,0)$ and $\dot{\varepsilon}^c_{22}(x_1,0)$.

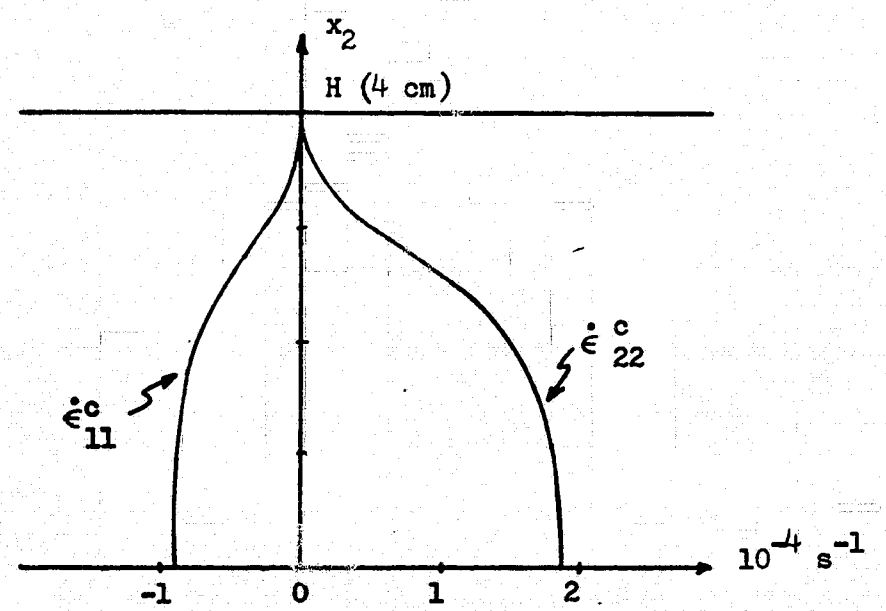

Figure 8: Plots of creep strain rates $\dot{\varepsilon}^c_{11}(x_1 = 0.3 \text{ cm}, x_2)$ and $\dot{\varepsilon}_{22}(x_1 = 0.3 \text{ cm}, x_2)$.

DISCUSSION

CHALMERS: The difficulty is that there is no steady state. The stress does not remain constant; neither does the temperature, although there is steady-state for the ribbon as a whole. Any individual part of the ribbon is going through a wildly fluctuating series of stresses, and the temperature is doing the same sort of thing at a different rate, and I am not even clear what kinds of experiments I would have done. It is a problem that will never be solved by writing down any equation of a kind that you started off with. This will simply be inappropriate because it inherently assumes that the temperature is remaining constant and the stresses are remaining constant.

The second point that I think is very important, and this really refers to the previous talk as well, is to recognize the major effects of the relaxation. I think the reason you can get the second type of buckling is that in the early stages, if you have a sub-buckling stress that would give you torsional buckling, you relax that, and then later the stresses are reversed and you can get the other type of buckling without any transverse temperature variations at all.

WILCOX: If I understood you correctly, you said that you really only considered the effect of a longitudinal temperature gradient. I guess, in essence, you are assuming that the stress due to longitudinal gradients is much larger than that due to temperature gradients through the thickness of the film. Did you actually check that with any calculation to see if that was a good assumption?

LAMBROPOULOS: This is a two-dimensional calculation. We just didn't input any transverse variation of the temperatures.

WILCOX: But did you check to see if that was a good assumption? I know that is what you did, but is that a good thing to do? Because we know that thermal stress comes when your temperature gradient is not constant, and your longitudinal temperature gradient over a large portion of the ribbon tends to be pretty constant, whereas across the thickness of the ribbon you always have nonconstant gradients. You have to, because the temperature goes through a maximum in the center of the ribbon. I believe it is small but one should still do the calculation to see if it is important or not. Have you done that?

LAMBROPOULOS: Yes.

WILCOX: What happens if you take the solid-liquid interface as being nonplanar? How much difference is that going to make to the stresses you get?

LAMBROPOULOS: We haven't done any calculations on nonstraight interfaces. This could be modeled also using the finite elements method.

AST: What value of n did you use for the stress exponent?

LAMBROPOULOS: Five.

AST: Since you have it in your program, did you grind it through with some other value to see how sensitive it is?

LAMBROPOULOS: I have also used another value of 3.6, and because it is very nonlinear, the results are very sensitive to the exponent being used. Also they are very sensitive to the exponential factor involved there.

SUREK: I don't understand either your point or Professor Chalmers' point as to what is really wrong with steady-state. Assuming you are in a coordinate system, every part of the ribbon goes through the same temperature profile. It will have a steady-state stress distribution, a steady-state strain rate at a given position in that temperature profile. I am assuming thicknesses and things like that are constant. What is the problem?

CHALMERS: A ribbon is not a point in space, and it goes through these various temperatures, and undergoes various stresses, and is not in steady state at any point.

SUREK: But the ribbon going through the temperature profile is in steady state. Assuming these equations are correct, and there is a fixed temperature profile the ribbon goes through, somewhere out in that room temperature the ribbon is going to come out with a residual stress, which the equations are going to predict.

CHALMERS: Where I think that is wrong is that if you want to predict the strain rate at a given temperature and a given stress, you have to know the previous history of that particular piece of material. That is why using the steady-state assumption does not work. That assumption is that it has always been at the same temperature and the same stress, and therefore that bit of material is at its steady state, and it is not.

SUREK: But every point of that ribbon, not in the moving frame but in the fixed frame, is at a fixed stress condition, which changes if you fix yourself with a part of the ribbon and take it through the moving frame. It is still steady state. I don't understand what the problem is.

DILLON: [To Chalmers] There could be some question of how long it does take before you develop to steady state. Was not that your point yesterday?

SUREK: Another question is, have you tried a simpler temperature profile? There are a lot of experimental data also at Mobil Solar where, just taking a ribbon through a simple cooling profile, they know it comes out with a very high residual stress and the ribbon shatters. In fact, have you tried to see what you predict under a simple cooling profile?

LAMBROPOULOS: Yes. I think Dr. Kalejs is commenting on the experimental results. He is more familiar with them.

BROWN: You mentioned the inappropriateness of the boundary conditions at the melt-solid interface. Would you conjecture on what kind of form you think may be appropriate, or what things you think have to be accounted for to get the physics right?

LAMBROPOULOS: It seems to me that the boundary condition around the interface will have to deal with how liquid really attaches itself to the interface and how it solidifies at that point. It seems to be more involved than just saying that a strip of liquid is being taken from the liquid and just moved across, and becomes suddenly solid and contracts or expands.

SACHS: As someone who wants to grow ribbon, what I would really like is an instruction book on how to synthesize the temperature profile rather than an analysis of temperature profiles that happen to be used. In other words, what is the ideal temperature profile, assuming that we can construct anything that you can write down?

LAMBROPOULOS: The goal of my presentation today was to show just what the effect of creep is and then if you want to use this miracle scheme in order to develop the proper temperature profile, it would take a lot of computer work and especially a lot of interactive work, with which I am not really familiar.

MILSTEIN: I think Ellie [Sachs] is touching on a very important point, and that is that when you attempt to grow a particular material, I think it is in error to say "I have this furnace and I am going to oblige the material to conform to the boundary conditions that exist in the furnace." I think the correct approach to the problem is to say what boundary conditions must exist to grow this material successfully and then put the burden on the person constructing the furnace and running the experiment to meet those boundary conditions. It seems to me that the theoretical analysis should really go in that direction, as opposed to trying to explain why some experiment fails.

AST: First of all, I think that is the kind of calculation that has to be done, and second, I want to make a comment about the steady state or the equilibrium that may clarify some confusion. When you work with steady-state creep laws, you assume basically a dynamic equilibrium between the generation of dislocations and the annihilation of dislocations. Basically, it no longer becomes dependent on the history of the specimen, because work hardening is just balanced by annealing. This is a basic underlying phenomenon of secondary-state creep. This has nothing to do with your calculations; they really have to be done as a first step. What worries some people who think about equilibrium in this whole problem is, do you ever get to this point where work hardening just balances the annealing effects to a point that the thing goes to what material scientists would consider steady state? The other comment is, it is really very important that somebody looks at the boundary condition between the liquid and the solid, because of the form of your creep law. Almost everything happens dramatically at very high temperatures, and these high temperatures are very close to the interface, so it becomes very sensitive. Somebody should really look at what is going on there, because basically it happens very close to the interface.

LAMBROPOULOS: What we are trying to do is model different nonzero initial stresses, to see how it would affect the zones. But this doesn't necessarily mean that we know how to model it.

AST: Then I think it is valid.

LEIPOLD: Just one quick comment, following up on Dieter [Ast]'s comments, and that is the fact that you are probably still in the very first stages of creep. What seriously concerns me about neglecting transient creep is that in fact it may be the whole ball game.

WARGO: How applicable or easily modified is your technique to, say, a cylindrical-type coordinate system? (Being a Czochralski grower.) The guys down at Bell Labs, Andy Jordan in particular, did a real nice treatment for predicting stresses and strains in gallium arsenide in looking at the defect density, and they found they were off by some additive factor and I am not sure they included creep in their treatment. Do you think you could change your numerical scheme to handle cylindrical coordinates?

LAMBROPOULOS: Yes. Actually, this is one very flexible feature of the finite-element method. You can change the form of the general feature of the geometry very easily without having to do that much work on it.

WARGO: A final comment. I think, in that condition, since you have such an enormous effect of interface morphology in Czochralski-grown gallium arsenide on defect structure, that you are going to have to take that into more careful consideration.

N84 28635

EXPERIMENTAL ASPECTS OF THE STUDY OF STRESS GENERATING MECHANISMS IN SILICON SHEET GROWTH*

J.P. Kalejs and R.O. Bell

Mobil Solar Energy Corporation
16 Hickory Drive, Waltham, Massachusetts 02254, U.S.A.

ABSTRACT

Experimental work in support of stress analysis on silicon sheet grown at high speeds is being carried out through examination of the growth behavior and defect structure of 10 cm wide ribbon produced by the EFG technique. Parameters under investigation include the ribbon temperature field, the high temperature creep response of silicon, and approaches to measurement of the residual stress.

INTRODUCTION

A numerical analysis technique has been recently developed to allow calculation of stress distributions with plastic deformation for steady-state growth of silicon sheet. This approach is described in detail in another paper [1]. It is desired to test the analysis through development of a model that can be used to predict the stress distribution in the sheet and to guide system design toward achievement of minimum stress configurations. Progress in the main areas of study is described below.

RIBBON TEMPERATURE FIELD STUDIES

A. Heat Transfer Modeling

Calculation of temperature distributions in ribbon grown at high speeds requires a comprehensive heat transfer model and specification of a number of material parameters. The restrictions placed on means to achieve temperature profiles leading to low stress configurations in silicon with respect to the latter are generally not discussed extensively in favor of detailed examination of the influence of environmental temperature boundary conditions. Particular emphasis is placed here on examining the role of material constants.

*This work is being carried out for JPL under Subcontract No. 956312 of the JPL Flat Plate Solar Array Project sponsored by the U.S. Department of Energy.

Our initial attempt at calculating ribbon temperature profiles for an EFG cartridge system for 10 cm wide ribbon growth has included consideration of heat transfer effects in the solid only. Ribbon environment temperature boundary conditions for this region of the EFG cartridge system have been extensively characterized. A representative calculated ribbon profile is shown in Fig. 1. This is obtained on the basis of radiative heat exchange between the plane ribbon and its enclosure walls (in three dimensions) representing cartridge components of known surface temperatures. The enclosure is represented schematically in the inset in Fig. 1. Temperatures in portions of the ribbon enclosure that represent gaps in the walls that radiate to a generally much cooler environment are interpolated. The accuracy of the profiles for a given environment temperature distribution is likely to be limited by uncertainties in some of the material constants for silicon. The most important of these are the solid thermal conductivity, the surface emissivity, and the absorption coefficient for radiation in the solid. Assumptions made in the heat transfer model for the solid include: Allowance for light transmission by photons with energies less than that of the band gap; incorporation of a wavelength dependent emissivity and absorption coefficient which are determined by free carrier absorption; and use of a temperature dependent band gap energy and thermal conductivity.

A sensitivity analysis has included examination of the effects on the temperature profile and its second derivative caused by variations in the temperatures of the enclosure walls and in the values of some material constants. Representative results of this analysis are given in Figs. 1 and 2 and in Table I. All the calculations reported here are for a 300 μm thick ribbon.

An uncertainty associated with the absorption coefficient can be inferred from the literature [2,3] (Fig. 3). If the solid is transparent in the infrared, heat transfer by long wavelength radiation from the interface can augment heat transfer along the ribbon. However, in silicon the free carrier absorption becomes very high near the melting point making the solid opaque, but still semi-transparent at lower temperatures. The lower absorption coefficient decreases the spectral emissivity, thus decreasing the net heat flux from the face of the ribbon. The overall effect in silicon is to decrease the thermal gradient at the interface. Table II shows the effect on the first and second derivative for conditions ranging from the black body case to that of no free carrier absorption beyond the band gap.

Variations in enclosure wall temperatures at the plane of the interface and in the afterheater region do not impact greatly on the value of the second derivative of the temperature profile near the interface (Fig. 2 and Table I). However, profile changes in regions of the sheet greater than about 1 cm from the interface, even though they are smaller, may have comparable impact on stress because this is a region of lower creep.

Calculated stress profiles for an elastic ribbon have been discussed in another paper [1]. These reflect the changes in the second derivative produced by the temperature boundary conditions in variations of both the high temperature σ_{yy} stress component as well as the residual stress (σ_{xx}). These results are in qualitative agreement with analysis done for RTR [4] and web [5] growth configurations. In particular, high values of the second derivative of the temperature profile at the interface are also found in these analyses, and thus are not specific to the system configuration (boundary conditions) but reflect the material properties of silicon. The most significant result, then, is the fact that large values of the second derivative at the growth interface temperature accompany profiles with the high interface gradients generally required to sustain high speed (> 4 cm/min) growth of sheet in a vertical mode. This occurs more as a result of the material property values for silicon than because of the presence of specific environment temperature distributions. We conclude that the only way the curvature can be reduced is by reduction in the interface gradient, such as by supplying extra heat input at the ribbon surfaces, which then concurrently reduces the maximum sustainable growth speed in the system.

Heat transfer by radiation of the latent heat released at the interface during growth has not been included in the calculations. In principle, this could be done by considering its absorption, reradiation and internal reflection in the solid. The effect on the temperature profile curvature near the interface is not expected to be great. This represents only a small fraction of the released heat and could at most reduce curvature by a few percent by preferentially heating up regions of the solid removed from the interface.

We have also examined the effect of lateral (width dimension) heat transfer. It has been suggested that such horizontal isotherm shaping may be used to counteract the effects of the vertical temperature profile and reduce the effective stresses. Preliminary work suggests that horizontal isotherm shaping may be able to influence stresses 1 cm or more from the interface, but will have little impact near the interface. This is the case because achievement of large horizontal gradients in practice will be limited by finite conductivity and a need to maintain a nearly horizontal interface. For example, for an imposed ribbon surface flux corresponding to a 100°C temperature difference in the enclosure wall between the ribbon center line and its edge, the temperature difference in the ribbon itself is only 55°C, and the maximum horizontal gradient is 35°C/cm (300 μm thick ribbon).

The influence of heat transfer in the region below the growth interface; i.e., in the meniscus and the die top, has not yet been investigated. A heat transfer model capable of accounting for meniscus effects on the interface region temperature field is under development for EFG [6]. This will allow more detailed study to be made of the effect of increasing meniscus height on interface heat transfer and on the temperature distribution of the solid.

B. Temperature Field Measurement

A program is underway to develop a high resolution temperature sensor utilizing optical fibers that can be used to monitor ribbon temperatures during growth. The basic thermometry uses a combination of Al_2O_3 and quartz fibers, and has been developed for use up to 2000°C with high sensitivity [7]. The detector system and probe have been constructed and calibrated and are being tested in the ribbon growth environment.

The temperature measurement is made by taking the ratio of the radiation emitted into the fiber optics cavity at two wavelengths. Application of Planck's formula for radiation allows the temperature to be calculated once this ratio is measured. The two wavelengths chosen for the measurement are 0.6 and 0.7 μm. It is necessary to ensure that the incident radiation from the high temperature source to be measured dominates at the chosen wavelengths within the fiber optics circuit. To achieve such conditions has been a problem up to now. Initial tests of a probe placed in the afterheater region of the cartridge have been carried out. This probe was first calibrated at room temperature using a tungsten ELH light source and a spectral radiometer. At the temperatures of the measurement, 900-1100°C, too much stray radiation appeared to be admitted to the fiber optics circuit, and the probe results did not reproduce cartridge temperatures measured with a thermocouple. A second probe is being constructed that will be placed in a cooler region of the cartridge near the cold shoes to attempt to reduce the effects of stray radiation.

CREEP LAW AND DEFECT STUDIES

A. Creep Effects on Stress

The creep strain-stress relation applicable to the case of high speed silicon sheet growth is not known. Several forms of the constitutive law for secondary creep have been used in the stress modeling to date [8,9]. They represent a considerable range of creep intensities and dependences on stress and temperature. These are given in Table III. This large variation appears to be a consequence of differences in magnitude of stresses, of strain, of strain rate and of temperature used in obtaining the experimental data. The data suggest that the creep intensity and its dependence on stress and temperature are particularly strong functions of the strain rate magnitude. From a practical standpoint, not only the temperature but the rates at which strain and stress increase in the course of sheet movement through the high temperature gradient in the neighborhood of the interface are relevant to specification of appropriate creep constitutive relationship.

Comparison of the stress analysis results and experimental observations on 10 cm wide ribbon indicates that the highest creep rates modeled are most compatible with stress manifestations in the ribbon grown. Residual stress magnitudes, as measured by a scribe and split technique, range from about 1 to 30 MPa in ribbon grown under different

conditions. Under optimum growth conditions, residual stress in the 10 cm ribbon is of the order of 1 to 5 MPa. This level does not change measurably with speed in the range from 2.5 to 4.5 cm/min investigated, yet ribbon buckling does become more severe. The buckles are permanent, not elastic deformations, and appear to be essentially "frozen in" by high temperature stress relief. Stress levels increase in ribbon grown with lowering of afterheater region temperatures.

The sheet temperature profiles used in the stress analysis to date all lead to much larger elastic stresses, of the order of 200 MPa. These are sufficient to result in severe buckling and ribbon fracture. Thus, creep is required in the present model to account for the lower residual stress levels observed experimentally for EFG cartridge growth.

The stresses associated with buckling in the present growth mode likely are dominated by σ_{yy}, which has its peak value within about 1 cm of the interface. σ_{yy} peak values in a solid with creep remain much greater than those for σ_{xx} for all conditions modeled, and also do not undergo the large variations with creep intensity observed in σ_{xx}. The large interface second derivatives of the temperature (viz., as in Fig. 2) do not allow creep to play a significant role in preventing build-up of the high temperature buckling stress in this case once a given growth speed is exceeded.

The residual stress σ_{xx} is greatly reduced in the presence of creep in the 10 cm cartridge with its active afterheater in comparison to stresses calculated for the profile where the interface gradient is maintained but the afterheater region profile is linearized [1]. This shows that at the growth speeds and creep intensities modeled, the main contribution to residual stress arises from the high interface region curvature. This is subsequently annealed out via creep relaxation in the afterheater region of the cartridge; thus, the result that the residual stress is relatively sensitive to the details of the afterheater region profile. The σ_{yy} peak magnitude is understandably most closely related to the interface region curvature in the temperature profile, and does not vary greatly with afterheater region profile changes.

To date, only a qualitative level of understanding has been achieved regarding the effect of creep on sheet stress. Further knowledge of the creep law at high temperatures is critical for confirmation of the stress model at a quantitative level. An indirect approach to obtaining this information is being evaluated with the study of silicon material creep response and defect structure generated during high temperature ($\geq 1100^{\circ}C$) four-point bending tests. This work is discussed next.

B. Defect Generation During Creep

Defects generated in single-crystal silicon by applied stress have been most extensively studied below about $1100^{\circ}C$. Less information is available on the creep response of silicon in the temperature region of $1200-1400^{\circ}C$, and no studies of defect structure have been reported. At

the lower temperatures, cross slip is the most common mode of stress relief at low to moderate strain rates and stresses. There is some evidence that slip continues to dominate stress relief at 1300°C [10].

At this point, it is not known conclusively which of the defect structures observed in ribbon is generated through stress relief and which arises at the growth interface. A further complication arises in the study of EFG ribbon because of inhomogeneous and high levels of impurities, particularly carbon. These may act as local centers for stress concentration and inhibit defect motion.

Examination of 10 cm wide ribbon cross sections has shown particular dislocation structures occur in patterns which suggest that they most probably originate from stress relief. These defect features are illustrated in the cross-sectional micrographs in Figs. 4 and 5. They appear to be non-randomly distributed with respect to the ribbon width, and most frequently occur near the ribbon center line, also corresponding to the location of peak σ_{yy} values. These highly dislocated regions are often bounded by even more intense dislocation bands (e.g., Fig. 5). Their width is generally of the order of the ribbon thickness, but two or three such areas are often observed closely spaced within a region spanning several ribbon thicknesses. These very intensely dislocated regions could originate from shear stress instabilities that result in rapid multiplication of dislocations in highly localized regions. What may be earlier stages of formation of the regions of intense dislocations are shown in Figs. 4(a) and (b). The former suggests a defect pattern similar to that observed to result from cross slip. These latter configurations are more often seen in thicker regions of the ribbon, toward the edges. However, extended regions of slip, such as shown in Fig. 4(a), have been observed very infrequently in 10 cm wide ribbon.

Four-point bending at high temperatures has been chosen as an indirect means by which to attempt to determine the nature of the creep law that may be applicable to describe stress relief in high speed sheet growth. A test apparatus has been constructed from graphite for use up to the melting point of silicon. The goal of these studies ideally is to arrive at an understanding of the strain rate and stress conditions needed to reproduce in initially defect-free silicon aspects of the defect structure observed in as-grown ribbon.

RESIDUAL STRESS MEASUREMENT

Knowledge of the residual stress distribution in the sheet is required for verification of the stress analysis model. The calculations predict that the residual stress is very sensitive to details of the temperature profile and may have a complicated width distribution. The method of scribing and splitting ribbon can yield only an average stress magnitude at the ribbon edge: $\sigma = EW/2R$, where W is the ribbon width and R the radius of curvature for the ribbon strip after splitting. The measurement and interpretation are further complicated by thickness

nonuniformities that may influence creep response and buckle formation. An obvious perturbation appears because of thick ribbon edges. Thus, quantitative evaluation of the stress distribution is required particularly to understand the impact of edge effects.

Two approaches being evaluated for feasibility are a modification of the above method, the multiple-finger cutting approach, and a laser interferometric technique. In the former, the cutting of strips or fingers of ribbon, of the order of a few mm in width, along the growth axis, allows application of the above formula to a narrower region of the ribbon. Laser cutting methods are at present being explored to improve accuracy and flexibility of forming strips.

The second approach is being evaluated at the University of Illinois [11]. This uses analysis of the deformation mode of a rectangular sample subjected to out of plane stress to back calculate the sample residual stress. Laser interferometry is used to map out the topology of the sample before and after the deformation. A mathematical formalism has been developed that allows calculation of local stresses on a point-by-point basis for all locations in the sample.

Initial application of this method has been to circular and rectangular (10 x 5 cm^2) CZ wafers subjected to an in-plane load to simulate residual stress (see Fig. 6). It has been shown that the applied load P can be calculated from the measured deflections to an accuracy of about 100 kPa. Work is underway to apply this method to ribbon. Problems that are anticipated arise from the more irregular and inhomogeneous material and from the perhaps much more complicated stress distributions present.

SUMMARY

Considerable advances in understanding of the role of creep in high speed silicon sheet growth have been made in application of stress modeling results to analysis of 10 cm wide EFG ribbon growth. At present, only qualitative trends in sheet stress distributions with system and material parameters have been established. Experimental work is in progress in areas of temperature field specification, of high temperature creep studies, and of residual stress measurement in order to obtain information that can allow testing of the model on a quantitative level. Among the findings of the study so far are:

1. Evidence that high creep levels need to be operative in order to account for the reduced residual stress levels, lower than those characteristic of an elastic solid, which are observed in 10 cm wide ribbon grown in an EFG cartridge system.

2. The material constants of silicon impose significant constraints on heat flow conditions that contribute to producing large interface values of the second derivative of the temperature profile, hence the high

temperature buckling stress σ_{yy}, under conditions necessary to maintain high speed growth (i.e., large interface gradients).

Reduction of the buckling stress requires careful manipulation of temperature profiles over a very narrow spatial extent of the order of a few mm from the growth interface. A broader implication of the analysis, even at the present qualitative level, is that all vertical silicon ribbon buckle-free growth may already be creep limited at speeds of the order of 3 cm/min. This occurs because it is very difficult to adjust environment temperatures to significantly change the interface region temperature profile curvature without compromising the growth speed capability, on account of material properties of silicon which fix conditions of axial heat transport.

REFERENCES

1. J.W. Hutchinson and J.C. Lambropoulos, paper presented in this Research Forum.

2. Yu. I. Ukhanov, Soviet Physics - Solid State, 3, 1529 (1962).

3. S.M. Sze, Physics of Semiconductor Devices (Wiley - Interscience, New York), p. 25 (1969).

4. R.W. Gurtler, J. Crystal Growth, 50, 69 (1980).

5. R.G. Seidensticker and R.H. Hopkins, J. Crystal Growth, 50, 221 (1980).

6. R.A. Brown, paper presented at this Research Forum.

7. R.R. Dils, J. Appl. Phys., 54, 198 (1983).

8. M.M. Myshlyaev, V.I. Nikitenko and V.I. Nesterenko, phys. stat. sol., 36, 89 (1969); H.J. Frost and M.F. Ashby, "Deformation Mechanism Maps for Ceramics", Cambridge University Publication CUED/C/MATS/TR.79, May 1981.

9. H. Siethoff and W. Schröter, Scripta Met., 17, 393 (1983).

10. H. Siethoff, private communication.

11. A.T. Andonian and S. Danyluk, to be published.

FIGURE CAPTIONS

Fig. 1. Temperature distribution of the environment and in a 300 μm thick ribbon. The base plate temperature was 1500°C.

Fig. 2. Variation of second derivative of sheet vertical temperature profile with distance from interface for cases reported in Table I.

Fig. 3. Absorption coefficient as a function of wavelength and temperature in silicon as given in Ref. 2: ①, and Ref. 3: ② (see also Table II).

Fig. 4. Cross-sectional micrographs of 10 cm wide ribbon grown at 2.6 cm/min and afterheater temperature T_A = 900°C: (a) Ribbon thickness t = 0.41 mm (magnification X56.6); (b) ribbon thickness t = 0.42 mm (magnification X70.4).

Fig. 5. Cross-sectional micrographs of 10 cm wide ribbon grown at 2.6 cm/min and afterheater temperature T_A = 1000°C; ribbon thickness is: t = 0.15 mm for (a), and t = 0.21 mm for (b). Magnification is X70.4.

Fig. 6. Schematic of clamping and loading geometry for measurement of sample response to load F with given in-plane stress P.

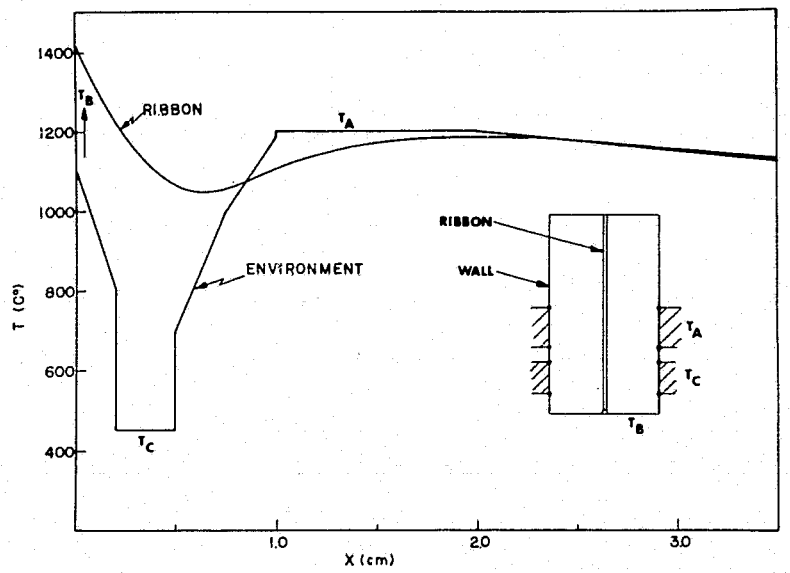

Figure 1

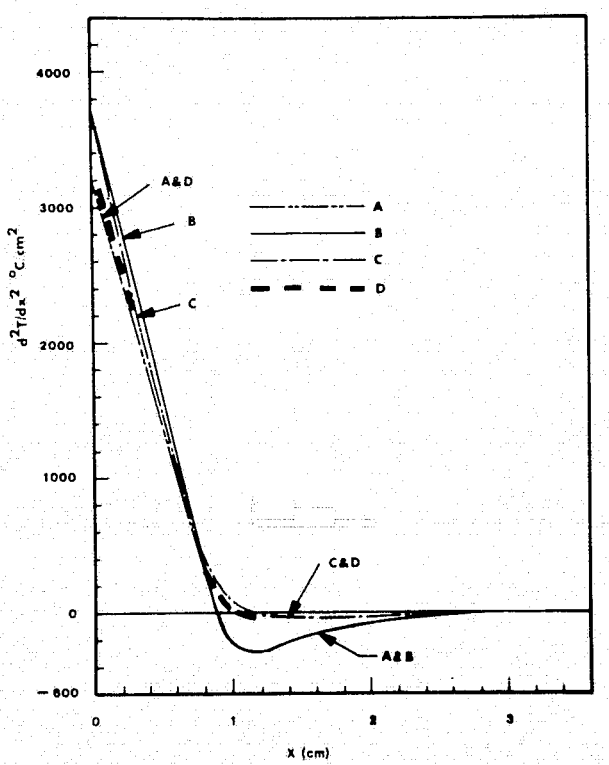

Figure 2

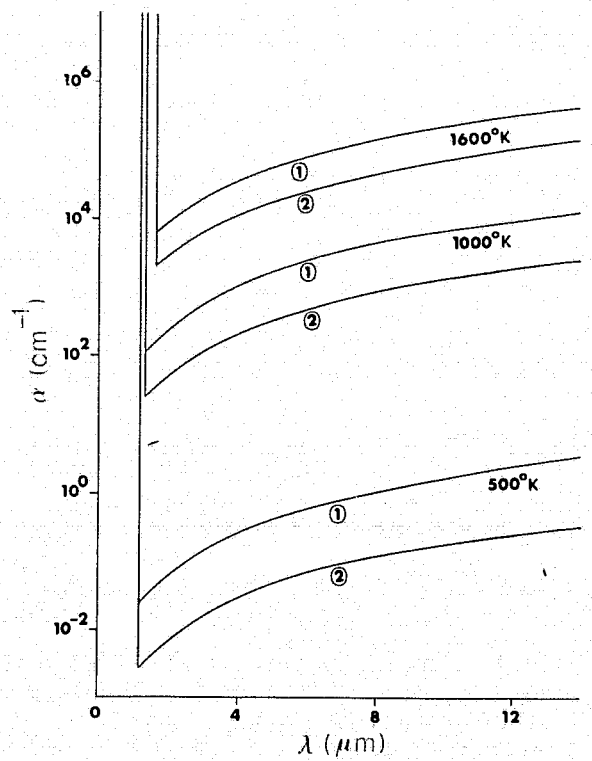

Figure 3

C-5

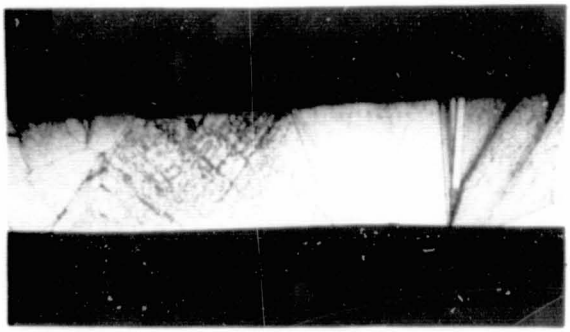

(a)

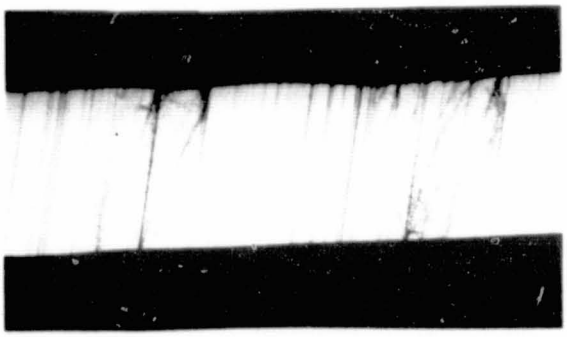

(b)

Figure 4

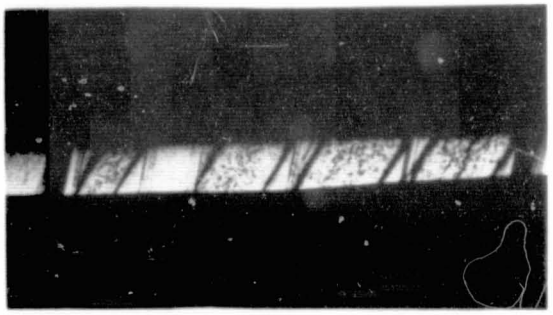

(a)

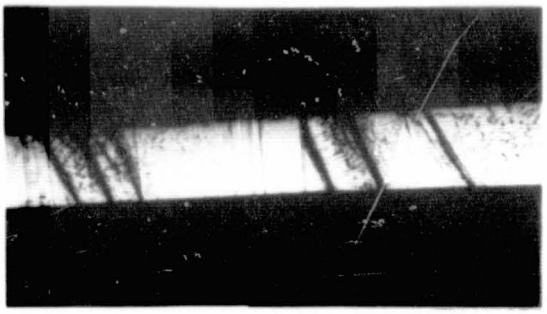

(b)

Figure 5

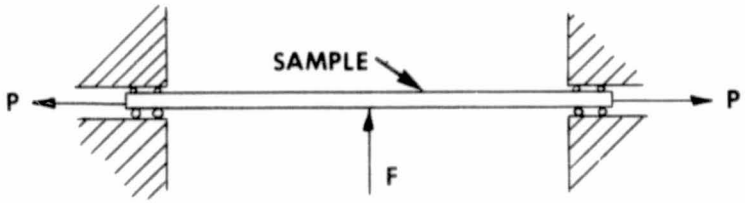

Figure 6

Table I. Thermal Conditions Used In Modeling. Ribbon Thickness is 300 μm, Growth Speed V = 0.

	Curve A	B	C	D
T_B, Base Plate Temperature	1500°C	1200°C	1200°C	1500°C
T_C, Cold Shoe Temperature	450	450	400	400
T_A, Afterheater Temperature	1200	1200	960	960
$dT/dx\|_{x=0}$, Vertical Gradient	1310	1370	1490	1427

Table II. Effect of Optical Absorption Beyond the Energy Gap on First and Second Derivative of the Temperature. In the Expression for α, T is in °K, λ in μm and $E_g = 1.194 - 2.79 \times 10^{-4}$ T. Radiation from the Interface is Neglected. Environmental Temperature is that of Case C in Fig. 2 and Table I.

Case	α (cm^{-1}) for $E_\lambda < E_g$	$\frac{dT}{dx}$ (°C/cm)	$\frac{d^2T}{dx^2}$ (°C/cm^2)
Black Body	∞	1610	4290
(1) Ref. 2	$1.36 \times 10^{-2}\ \lambda^2 T^2 \exp(-5803\ E_g/T)$	1490	3745
(2) Ref. 3	$2.71 \times 10^{-6}\ \lambda^2 T^3 \exp(-5803\ E_g/T)$	1365	3475
No Free Carrier	0	730	1460

Table III. High Temperature Creep Laws Used in Modeling.

$$\dot{\varepsilon}^c_{ij} = C\,[\exp(-\beta/T)/T]\,(\sigma_e/\mu)^{n-1}\,S_{ij}$$

Reference	C $(GPa\text{-}s)^{-1}$	β (°K)	n	$\dot{\varepsilon}$ (s^{-1})*
Myshlyaev et al. (8) "Low Creep" Condition	1.05×10^{29}	59,760	5	1×10^{-6}
"High Creep" Condition	1.05×10^{31}	59,760	5	1×10^{-4}
Siethoff and Shröter (9)	5.85×10^{22}	41,800	3.6	41×10^{-4}

*Calculated strain rate for $\tau/\mu = 10^{-3}$ and T = 1300°K.

DISCUSSION

MAYO: Is the laser interferometer sensitive to shears? Can you detect shear strengths? Or are you just looking at normal strains?

KALEJS: I am not sure. I think we will be measuring a residual stress, which averages the stress through the ribbon thickness so it is likely we can't pick that out. I may be wrong in this, but I think we can only measure σ_{xx}, the compressive or tensile side of σ_{xx}.

MAYO: Being an X-ray man, my natural question would be, why don't you use some simple X-ray techniques for measuring residual strains? They are well known.

KALEJS: We have often thought about this, but one of the problems is that our material is quite inhomogeneous. Have you tried that, Marty [Leipold]?

LEIPOLD: Yes. A number of years ago we did support a small program on use of the bond technique for determination of residual stresses. We found, specifically in EFG, that while it could be done, it was not a practical approach for making a large number of measurements, as they need to do.

DILLON: Marty, was it a question of sensitivity, you couldn't pick out differences?

LEIPOLD: You could find differences, yes. I don't remember whether the level of sensitivity was sufficient for their purposes, but it was not a useful technique as a measurement tool related to an experimental growth program.

KALEJS: Is your level of sensitivity about 1 mPa, would that be fair?

MAYO: It has a 10 ppm sensitivity with 5 μm resolution.

LEIPOLD: In the multifinger sectioning, has anyone ever looked at the twist of the fingers, as well as the horizontal deflections, as an attempt to look at any residual shear stresses?

KALEJS: I think Ellie Sachs can answer that. He actually did the initial experiments at Mobil Solar in looking at the various twists and turns, and he did in fact find wonderful patterns, which we could not interpret at the time without any kind of a model.

SACHS: That technique, as I did it back then, was really limited by equipment availability. We were waxing wafers down and dicing them and dewaxing them; it was an incredible pain in the neck, and I would hope that by using your laser, you are going to have a lot better time.

KALEJS: We will need not only to do that, but also to compare the multifinger scribing to the laser interferometry method, because I am sure that we will find, in each of those approaches, things we can't explain.

LEIPOLD: I would be very careful about taking deformation measurements on pieces of ribbon as being the right numbers to use in constitutive equations, because I am sure you are bending the ribbon in one direction rather than in the other direction, which in fact may be what is happening. Your material is directional. I would suggest not using Czochralski, because you don't want to have the problem of dislocation nucleation to contend with. You want material that is dislocated.

KALEJS: I would certainly welcome any advice on how to do it. One of the quick experiments is just to hang a piece of Czochralski silicon in the furnace and yank it out and see what happens. Basically, I think that the answer is going to be in reproducing very high strain rates, and that will lead us in the right direction in deciding on what the constitutive law of creep response is.

SACHS: Did you mention that you thought that your thermal buckling stresses were really happening in the first couple of millimeters from the interface?

KALEJS: Yes.

SACHS: What is the wavelength of those buckles?

KALEJS: I think from the talk we heard about buckling, I would hate to think anybody would try to predict what kind of wavelength you might get. However, I do think that the buckles appear to be frozen in at room temperature, that they occur at high enough temperatures to have appreciable creep.

SACHS: But when you do, if you grow thinner ribbon and you do see the buckles, are the wavelengths of the order of millimeters?

KALEJS: No. I don't think you could get a wavelength on the order of millimeters.

SACHS: No, I don't think so either, that is what I am getting at. If your buckles are on the order of centimeters, then don't you have to worry about stresses over regions of the order of centimeters?

KALEJS: The σ_{yy} stress does extend over about 2 centimeters. I think that the wavelength is on the order of 2 to 4 centimeters.

SACHS: So then why should one focus on what it is at 2 millimeters?

KALEJS: I think that unless you reduce the second-order derivative at the interface, which really determines the rate of increase of this buckling stress, you are not going to reduce the peak value either. So that is where you have to operate with your temperature boundary conditions. Unfortunately, the conclusion is that no matter what you do, the material constants of silicon just do not allow you to do very much with radiative environmental heating.

SACHS: So are you basically making a scaling argument, and are you saying they are really bad at 2 millimeters and if we reduce it there, we will be reducing everywhere else too?

KALEJS: No. You have to worry about what happens in the after-heater region, obviously. The second-order derivatives for certain temperature profiles are large in the after-heater cool-down region, and if, in fact, the creep is inadequate there, you will get stress due to that region. I think that is a complication that in practice we have never been able to separate out. By taking out the after-heater region, and recalculating the stress profiles, we find, in fact, that all these numbers go up, particularly the residual stresses. So the conclusion is, at least tentatively, that by far the major contribution to the residual stress comes from the high-temperature region, σ_{yy}, which has not been annealed out in the after-heater.

MORRISON: Have you measured the effect on device efficiency of the generation of these highly deformed regions?

KALEJS: It is just recently that these have come to my attention. I think they appeared in people's micrographs before, but I don't think anyone ever looked at them and realized that they had some kind of a special distribution. They were, in fact, rather anomalous in relation to the rest of what we call steady-state structure.

SUREK: How do you support your conclusion from this distribution of σ_{yy} under high creep conditions that you do have buckling occurring in the first couple of millimeters? I don't see it from the calculated σ_{yy}.

KALEJS: What would you conclude?

SUREK: It seems to be tensile.

KALEJS: Yes, it is tensile. That's right.

SUREK: Why would the ribbon want to buckle under that tensile stress?

KALEJS: I guess the idea would be that if you stretch it across the width, that you are actually pulling material from above. It also creates some kind of a buckle--a dimple.

SUREK: What do you mean? This is already the calculated existing steady-state stress that occurs under the assumed constitutive laws that were in the model. I don't see why the ribbon would want to buckle under a tensile stress in the first centimeter from the interface.

KALEJS: They say that one possible mode is if you stretch it, the material moves in from above and creates some kind of dimple.

SUREK: It is already stretched. I mean, this is the steady-state stress condition existing in the ribbon. Why would it want to buckle to relieve that tensile stress, instead of just going on to zero stress at some distance away?

KALEJS: I am afraid I don't know how a buckling theoretician would answer that. I am afraid I can't answer it.

MILSTEIN: You made a comment about having a furnace. I would also point out that your first conclusion is that you've run into fundamental conditions that are applied on the system by the material, and I think that is the point I was driving at.

KALEJS: At a growth speed of 1 to 2 centimeters per minute, I have not seen any calculated temperature profile with low second-order derivatives at the interface, and I would think at those speeds you don't see the effects of creep because creep is fast enough to prevent the buckling.

MILSTEIN: There are material properties that you have to take into account. You have just stated that there are certain properties that appear not to be particularly dependent on the conditions that you might consider being applied. What I am suggesting is, if those properties of materials can be deduced, you can then say what is required is the following set of conditions, A, B, C, D. One then attempts to build a system that matches the conditions so deduced.

KALEJS: Yes. It is clear that you can probably reduce the magnitude of the second-order derivative by putting heat back into the ribbon, but you have to do it without appreciably reducing the gradient at the interface and compromising the speed. That's where the trick, I think, is. The model can't tell you that it can or can't be done, but it appears that with manipulations in temperature boundary conditions, we can do it while maintaining steady-state growth conditions. We are really stuck with second-order derivatives that are too high, even at 3 centimeters per minute. I'm not sure how we can decide whether σ_{yy} in fact is a buckling stress, but there is a high-temperature, high-stress component that arises even with creep. Whatever it does, I think, is something of great interest and significance.

REGNAULT: Wherever the curvature (of the interface) would be highest, I would expect the dislocation density to be quite high. Have you ever looked at that with X-ray topography or defect etching?

KALEJS: To my understanding, Harry Rao (MSEC) is going to talk a bit more about the actual defect distributions in EFG ribbon tomorrow. I don't think anyone has ever done width-dependent studies in EFG ribbon.

REGNAULT: If there is a curvature, there must be a dislocation density that would be occurring that would cause these ribbons to remain in this curvature after they are cooled down. I was just wondering if you ever looked at anything like that?

KALEJS: No one has ever looked for them. People have generally looked at the inhomogeneities in the ribbon, and I certainly don't think there is any evidence right now to support the idea that there are any long-range residual stresses in ribbon. That is just a conjecture that comes out of the modeling. It could be that, because of the inhomogeneity, and all the parallel boundary structure, and the carbon and other defects, the

long-range stresses are all, at some point, totally wiped out by creep. So what you get at room temperature is a whole lot of localized small strain centers that have no relationship to the macroscopic stress distribution that might have caused it. There is no evidence to say that we do have a macroscopic stress distribution in the ribbon at room temperature.

REGNAULT: Do these structures occur at areas of maximum radius in the ribbon, or are they in relatively flat areas of the ribbon?

KALEJS: Relatively flat areas. Not only that, but I find that they occur preferentially near the center of the ribbon. There are also two side lobes that are located roughly halfway between the edge and the center of the ribbon, where there are a few more of these, but I must say that I have only looked at about a dozen ribbons or so, under different growth conditions. There are some trends, but there are certainly not enough data to say what they are.

RAO: To answer your question, Bill [Regnault]. I have looked at the cross sections of ribbons where the buckle is and did not find any significant increase in dislocation densities either on the side of it or in the center of it.

N84 28636

CONTROL OF THERMAL STRESS IN DENDRITIC WEB GROWTH

R. G. Seidensticker
Westinghouse R&D Center
Pittsburgh, Pennsylvania

J. S. Schruben
University of Akron
Akron, Ohio

1. Introduction

The temperature distributions present during the growth of ribbon crystals generate stresses which can adversely affect the growth or perfection of the material.[1,2,3] Several different effects can occur depending on the magnitude and distribution of these stresses, and in the most general case the observed phenomena are the result of complex interactions of a number of mechanisms. In many instances, however, one mechanism predominates to such an extent that somewhat simplified distinction can be made between the various effects. We shall follow this course in the present discussion, and hence must make some rather arbitrary definitions based on observed behaviour in dendritic web growth.

We shall use the term residual stress to indicate the lattice stresses present in a grown ribbon which shows no obvious macroscopic deformation such as ripple, bow, or twist. The importance of these stresses depends on their magnitude; if they are large enough, the crystal may be prone to fracture under the action of modest external forces during device fabrication processes. In some instances, the dislocations associated with the lattice strain may have undesirable effects on the properties of a device made using the ribbon. On the other hand, if the strain is small enought, no apparent difficulties will result, and the associated residual stress levels are "acceptable."

Another thermal stress effect which we will consider is buckling of the crystal during growth, by which we mean a relatively sudden deformation of a previously flat ribbon. After buckling has occurred, the crystal may have a residual deformation in the form of ripples, twist, bow, etc., but in some instances a crystal which obviously deformed during growth may return to an undeformed condtion when removed from the growth furnace and may even show negligably small residual stress. The importance of the buckling phenomena is two-fold: first buckled ribbon is difficult to grow by the dendritic web process and second, permanently buckled web crystals are unsuitable for device fabrication. Control of buckling is of particular importance for the dendritic web process since the critical conditions for buckling depend strongly on the ribbon dimensions and hence the ability to grow wide, thin crystals depends on reducing those thermal stress factors which cause the buckling to occur.

2. Control of Thermal Stress

In the development program for the dendritic web process, a key philosophy has been the concept of reducing the thermal stresses during

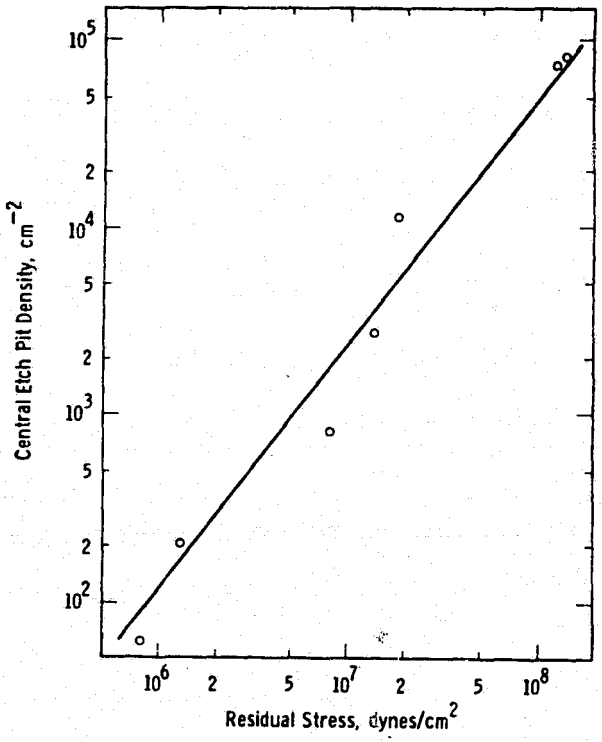

Figure 1. Measured residual stress in dendritic web crystals versus central etch pit density.

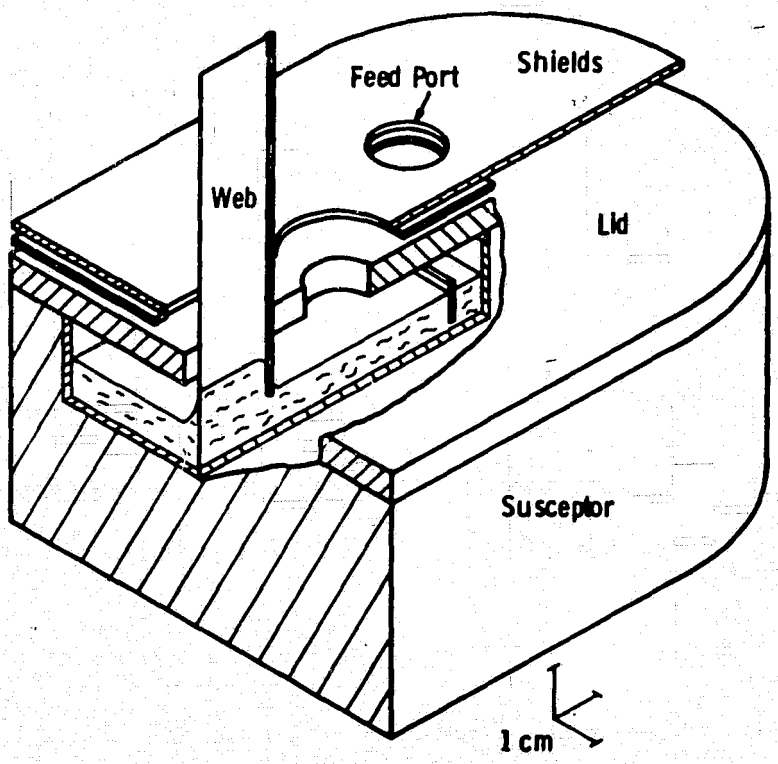

Figure 2. Schematic representation of dendritic web growth configuration.

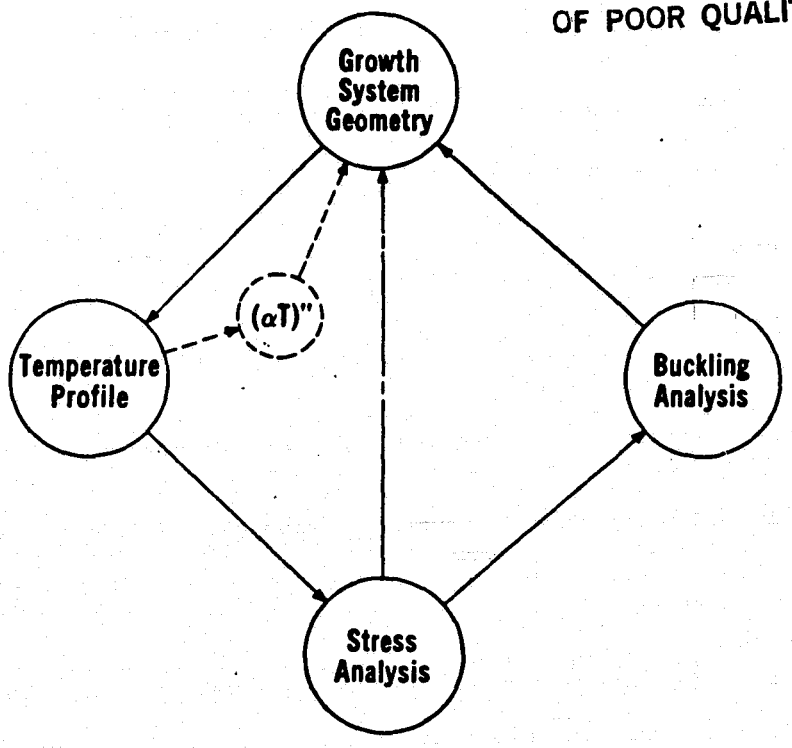

Figure 3. Application of models to growth system design.

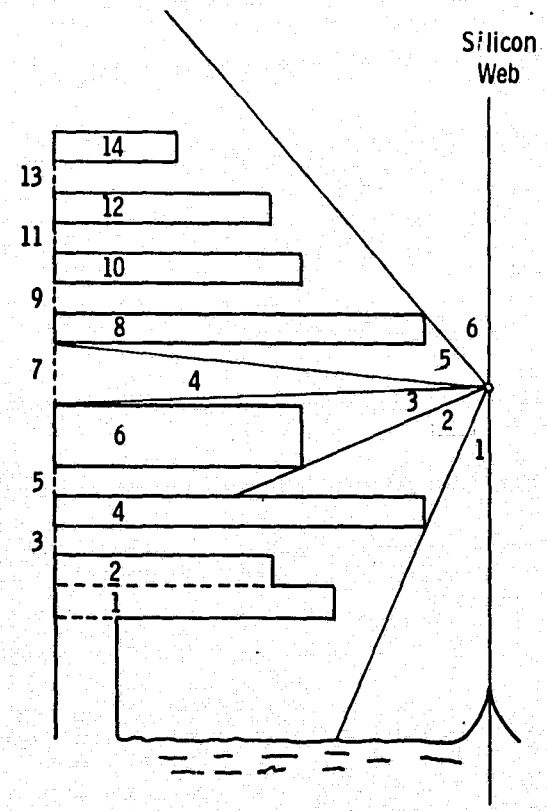

Figure 4. Viewing regions from a point on the web.

growth to a non-zero but "acceptable" level. Gurtler[2] has pointed out that the temperature distribution required to have zero thermal stress is physically unrealizable. However, it is not necessary to have zero thermal stress during growth to have acceptable properties in the crystal. Dendritic web crystals have been grown which apparently have no (or at least unmeasureably small) residual stress. Further, there is apparently a direct relation between residual stress and dislocation density as shown in Figure 1, so that such "zero stress" stress ribbon are also "zero-dislocation" crystals by semiconductor standards. Since dislocations tend to persist in crystals once formed and since dendritic web can hardly be growing under zero thermal stress condition, we must conclude that there is some finite "yield stress" below which little, if any plastic deformation occurs in the silicon lattice.[2] Such an argument drastically oversimplifies the real visco-elastic mechanisms, but provides a simplified working definition for "acceptable" stress in the design, analysis and development of improved growth configurations.

The rapid decrease in temperature along the length of the growing web crystal suggests that most of the plastic deformation and dislocation generation occurs within a few centimeters of the growth interface. Further from interface where the crystal can be more reasonably considered to be elastic, large thermal stresses can also be generated. Such stresses would be undetected in the cold crystal when they were of a magnitude to cause macroscopic deformation of the growing ribbon. For a given set of ribbon dimensions it is relatively straight forward to calculate the stress magnitude at which buckling would occur thus providing another definition of an "acceptable" stress distribution.

The design task is thus to create a thermal environment for the growing web which will produce a temperature profile generating such "acceptable" stresses. The process is evolutionary in nature: the properties of a proposed configuration of lids and shields, such as shown in Figure 2, are evaluated and by parametric variation, guidelines for new configurations are established. The evaluation of the configuration and its variations is carried out using several computer models which will be described more fully later. The initial model computes a ribbon temperature profile based on the temperatures and dimensions of the lids and shields. This temperature distribution is then used as the input for the second model which computes the thermal stresses. These thermal stresses in turn form the input for the third model which evaluates the critical buckling conditions. Iterations of the design can be made on the basis of the results from any stage in the modeling process as shown in Figure 3. In the case of the temperature model, judgements are based on the second derivative of the temperature-thermal expansion product, $(\alpha T)''$, rather than the temperature proper. As the final step in the process, hardware is fabricated and the real growth parameter can be compared with the modeling predictions.

3. Models

The three models used in the program to reduce the thermal stress problems in dendritic web growth are all slightly different in character. The first, which calculates a temperature profile along the ribbon, uses a numerical integration procedure to arrive at a solution of the heat flow equation involved. The second model employs finite element techniques to

calculate the thermal stresses in web crystal. The final model, also uses the finite element approach to solve the critical buckling stress problem which is formulated as an eigenvalue problem.

3.1 Temperature Model

Determining the temperature profile along a growing dendritic web crystal is the starting point for all subsequent stress analysis. For our analysis we chose a model based on the following assumption. First, we assumed that a one dimensional analysis would be adequate to delineate the major features of thermal stress generation. We tested cases with curved isotherms and found that the effect on stress was secondary, in agreement with Morrison, et al.[1] Second, we assumed that all heat transfer was by radiation. Subsequent analysis showed that the significant stresses occurred at ribbon temperatures greater than 1200°K where gas conduction effects are negligible relative to radiation transfer. Finally, we assumed that the width of the ribbon was large relative to the slot dimensions in the thermal elements. This assumption permitted relatively simple forms for the geometric view factors.

Using these assumptions, we devised appropriate numerical solutions for the heat flow equation in a moving coordinate system, viz.

$$\rho V C_p \frac{dT}{dx} = \frac{d}{dx}\left(\frac{a}{T}\frac{dT}{ax}\right) - \frac{2Q}{b} \qquad (1)$$

where ρ = density of silicon (solid) = 2.30 gm/cm^3
V = web pull velocity
a = thermal conductivity coefficient = 318 W/cm
C_p = specific heat = .9811 J/gm
b = ribbon thickness
Q = heat loss from one side of web

Two particular tasks were addressed in arriving at the solution of this equation. The first was finding an appropriate form for Q, the radiation exchange of the ribbon with its environment: the second was finding a stable integration routine for Equation 1.

Calculation of the radiation interchange was accomplished by developing a subroutine which determined which elements were "seen" at any position on the ribbon as shown in Figure 4. The geometrical view factor could then be evaluated for each element so that the total irradience could be determined. The effect can be seen Figure 5 in a typical plot of $(\alpha T)''$, one of the forms of output from the program.

Development of a stable integration routine was required by the non-linear character of Equation 1 when the fourth power temperature law is used for radiation transfer. At the growth front, x = 0, the temperature is specified, but the slope must be determined by iteration so that temperature approaches the ambient at large distances, e.g. 30 cm. Even using double precision calculation does not always insure convergence and in those instances "backward integration" can be used wherein the integration process is begun at a large distance and iterated to give T_m at x = 0. Ideally the two integration routines could be spliced to give a convergent solution over

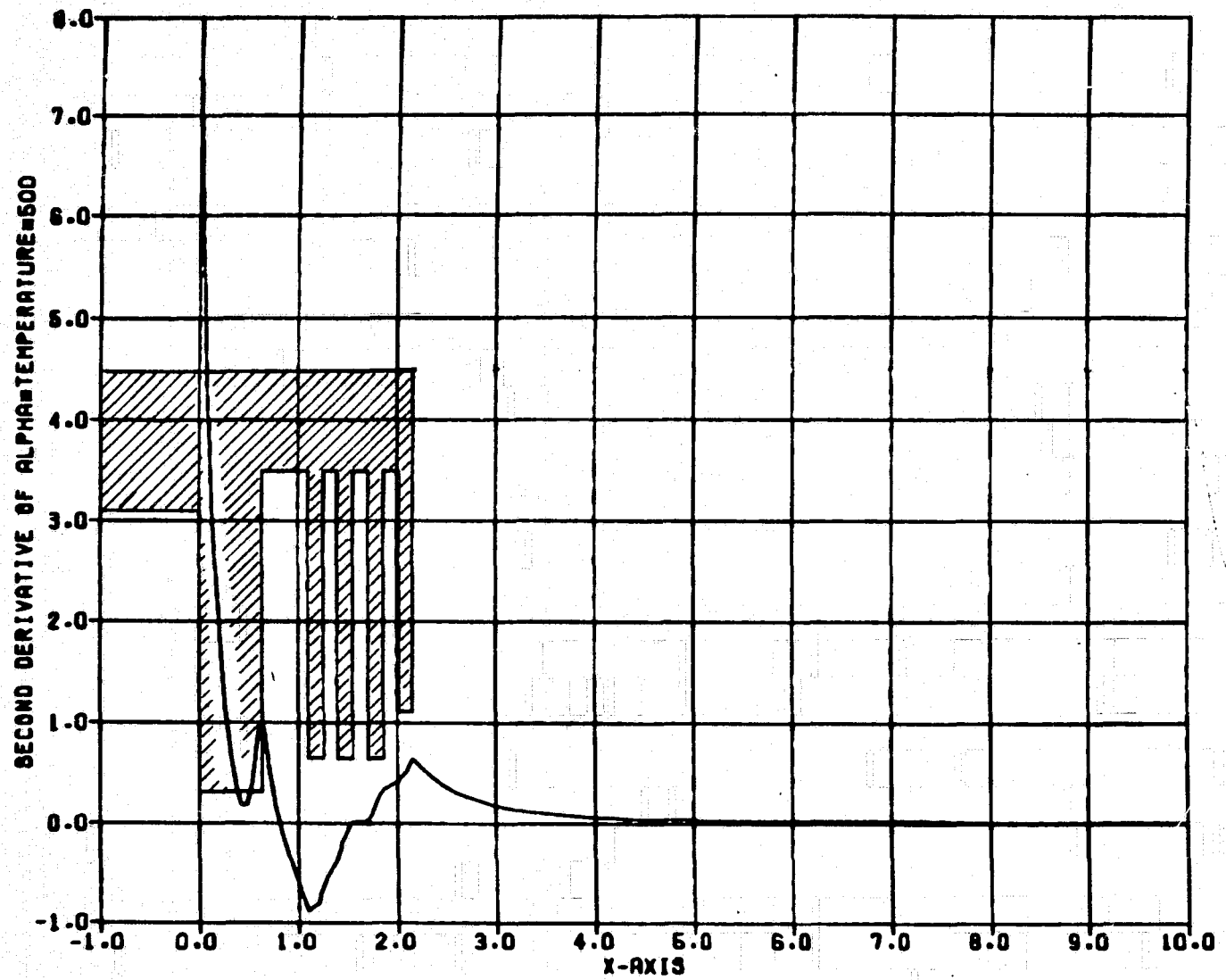

Figure 5 Representative (αT)" plot. Lid and shield geometry shaded.

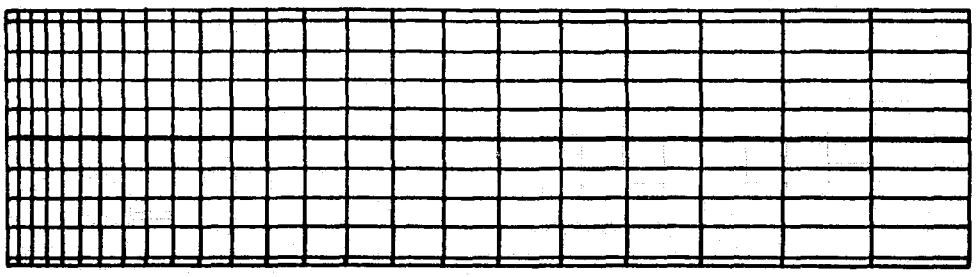

Figure 6. Variable spacing finite element mesh.

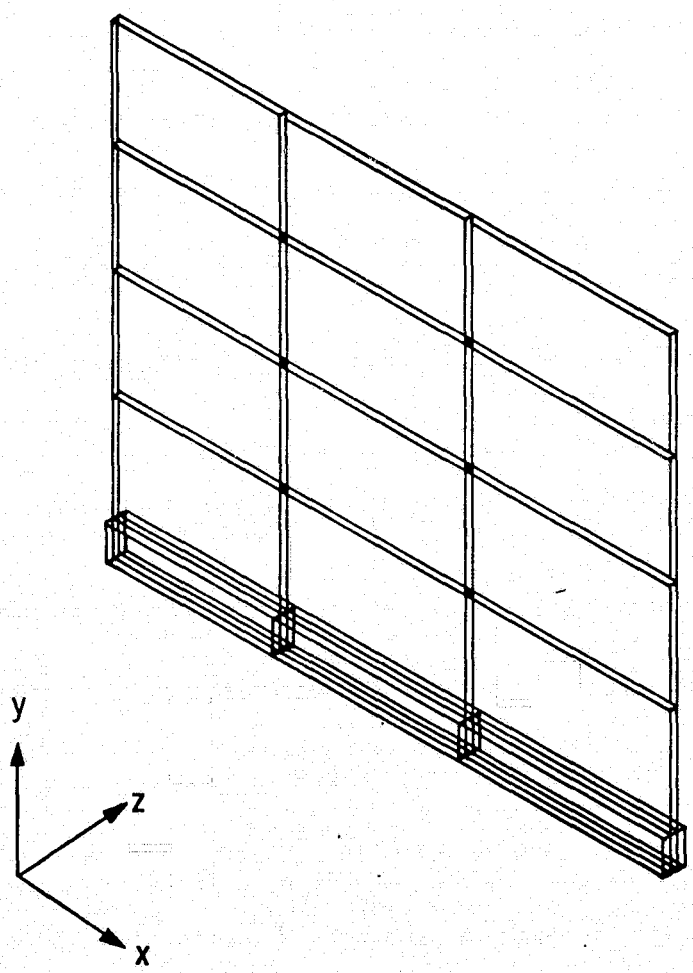

Figure 7. Three-dimensional finite element mesh.

the whole range.

Measurement of ribbon temperatures to the required accuracy in magnitude and position is very difficult so that a test of the validity of the temperature calculations must be done by more indirect means. The first test involves the relationship of ribbon thickness to pull velocity, essentially a test of T' at x = 0. In practice it has been found that the agreement between predicted and observed velocity is better than one percent, well within experimental error. The second test is even more indirect and involves the remaining models as well, that is the agreement of predicted buckling with observed buckling. There, too, the agreement is very good, so that for its purpose, the temperature model is more than adequate.

3.2 Stress Model

The thermal stresses in the ribbon are calculated by a finite element analysis which uses the temperature distribution from the previous model as input data. Two slightly different models are used depending on the end use of the output from the calculations: a two dimensional analysis is used if only the stress distribution is desired while a full three dimensional analysis is performed if a buckling analysis is anticipated. Both models use a variable mesh size along the length of the ribbon so that greater resolution is obtained near the growth front where temperature and stress are varying most rapidly. The elements are sized as a geometric progression with the final elements eight times as long as the initial ones. A diagram of the two dimensional mesh is shown in Figure 6, and a portion of the three dimensional mesh in Figure 7. For improved computational accuracy at reasonable computation times, higher order elements are used for the mesh: cubic elements for the two dimensional mesh and quadratic for the three dimensional calculations. The cubic elements have two additional nodes on the element edges, while the quadratic elements have one additional node; temperatures must be specified at all nodes.

Strips of many sizes have been modeled, however a more or less "standard" model represents the first ten centimeters of a 2.7 cm wide ribbon. The use of a "standard" model permits ready comparison of different growth system designs and the dimensions chosen are realistic. The aspect ratio of the model is also reasonable so that the free boundary assumption (zero normal stress) used at the ribbon end of the mesh (where the modeled section has been "detached" from the balance of crystal) does not significantly perturb the stress fields in regions of interest. Free boundaries are also assumed for the growth front and edges of the strip, while the centerline of the crystal is a symmetry plane (zero normal displacement U_y).

Finally, the following numerical constants are used for the calculation. The thermal expansion is assumed to be temperature dependent of the form $\alpha = \alpha_0 + \alpha_1 T$ where $\alpha_0 = 2.8192 \times 10^{-6}$ and $\alpha_1 = 9.789 \times 10^{-10}$ K^{-1} are derived from the lattice parameter measurements of Hall.[5] Young's modulus is taken as 1.9×10^6 Mdyn/cm^2 and Poisson's ratio as 0.2.[6]

The analysis itself is done using the Westinghouse WECAN numerical analysis code on a CDC7600 computer. The output gives a tabulation of the various stress components at each node of the mesh as well as isostress

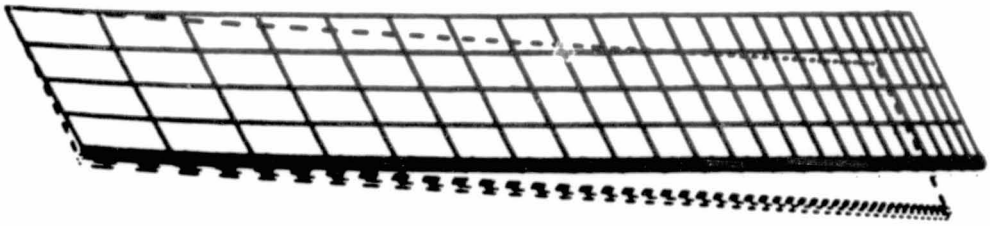

Figure 8A. Calculated buckled web shape.

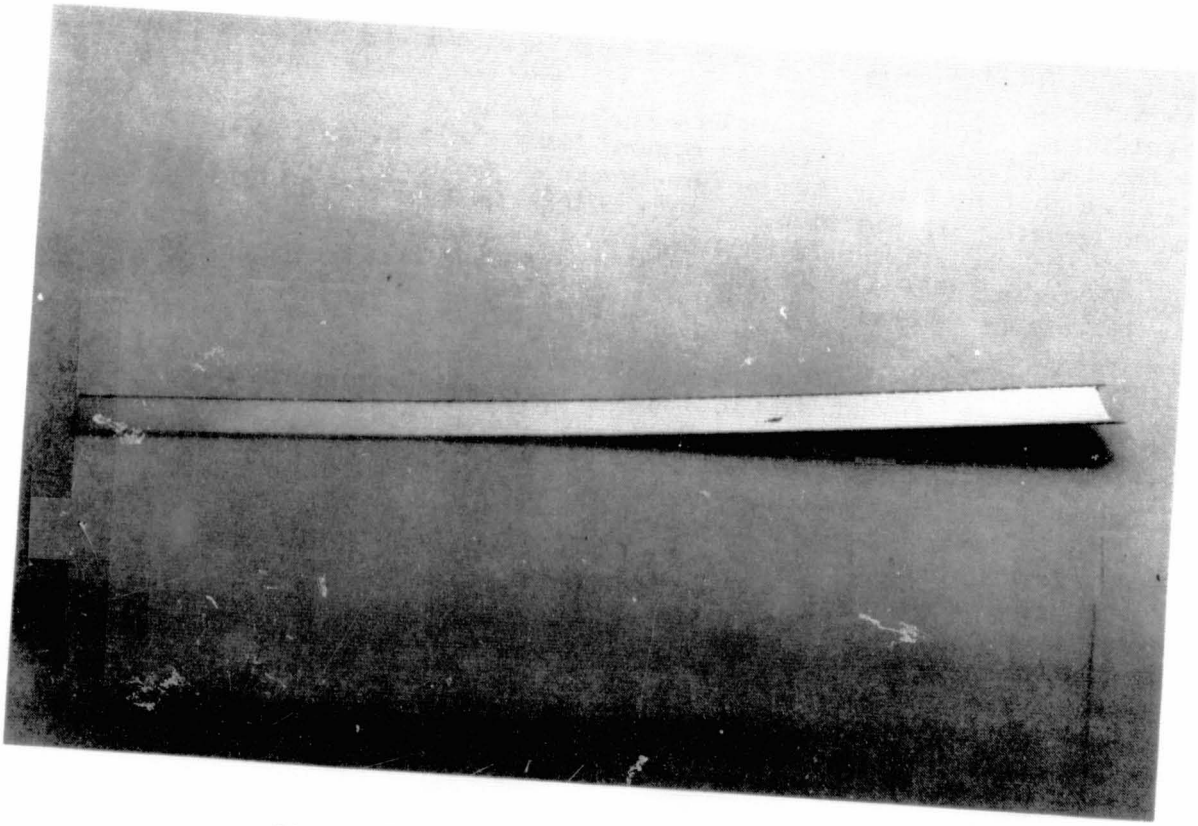

Figure 8B. Photograph of buckled web.

contours. A useful adjunct for the present purposes is a plot of selected stress values along the ribbon centerline and edge.

3.3 Buckling Model

In their turn, the stresses from the three dimensional stress model of the previous section serve as the input data for a model that calculates the critical buckling conditions for a growing web crystal. The use of the stress results from a strictly elastic calculation is justified for two reasons. First, in many instances, the residual stress measured in a ribbon just prior to buckling is very small. Second, the buckling predictions of the model are in good agreement with observed growth behavior.

Once the stresses are specified for each node of the mesh, the buckling problem can be specified as an eigenvalue equation[7]

$$[K]\ \{\Delta\} = \lambda[S]\ \{\Delta\} \qquad (2)$$

where [K] is the conventional stiffness matrix which depends on the dimensions and elastic constants of the ribbon; $\{\Delta\}$ is the eigenvector representing the (unknown) displacements of the ribbon from flatness; [S] is the stress matrix; and λ the eigenvalue. The output of the model gives one or more values for λ, as desired, and the associated eigenvectors $\{\Delta\}$. An example of a typical predicted shape for a buckled ribbon is shown in Figure 8A. This can be compared with the permanently buckled web crystal shown in Figure 8B.

Mathematically a number of both positive and negative eigenvalues can be found; for our purposes, only the smallest positive eigenvalue is significant. If $\lambda > 1$, it implies that all the stresses must be increased by the factor λ for buckling to occur. Conversely if $\lambda < 1$, then all the stresses must be diminished by the factor λ for the ribbon to remain flat during growth. In practice, several widths (and/or thicknesses) of web are modeled and the critical dimensions for $\lambda = 1$ are obtained by power law interpolation. Although extrapolution must sometimes be used, especially for low stress configuration, caution must be exercised in interpreting the results since not all the stress components vary by the same power low. The ability to calculate several combinations of widths and thicknesses permits the demarcation of a stability boundary separating width-thickness regions in which the web will either grow as a flat ribbon or will deform.

4. Results and Conclusions

Prior to the use of the models discussed in this paper, the design of lid and shield configurations for dendritic web growth was essentially an empirical art. The most successful design developed at that time was the J98M3 configuration which could produce web crystals up to 28 mm wide at 150 μm thickness. The calculated $\Delta\sigma_x$ (σ_x(center)-σ_x(edge)) for this configuration is shown in Figure 9 for comparison with two newer designs, J460 and J483 developed with the aid of the models. The substantial reduction of the "far" stress peak in the newer designs has substantially increased the width at which crystals can be grown without buckling.

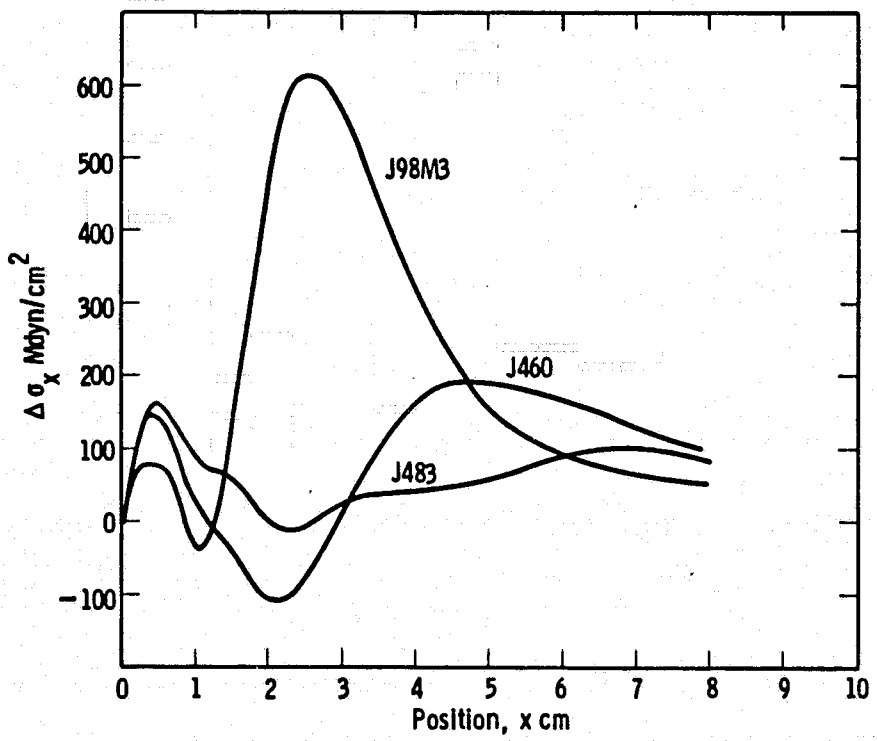

Figure 9. Delta x-stress for three web growth geometries.

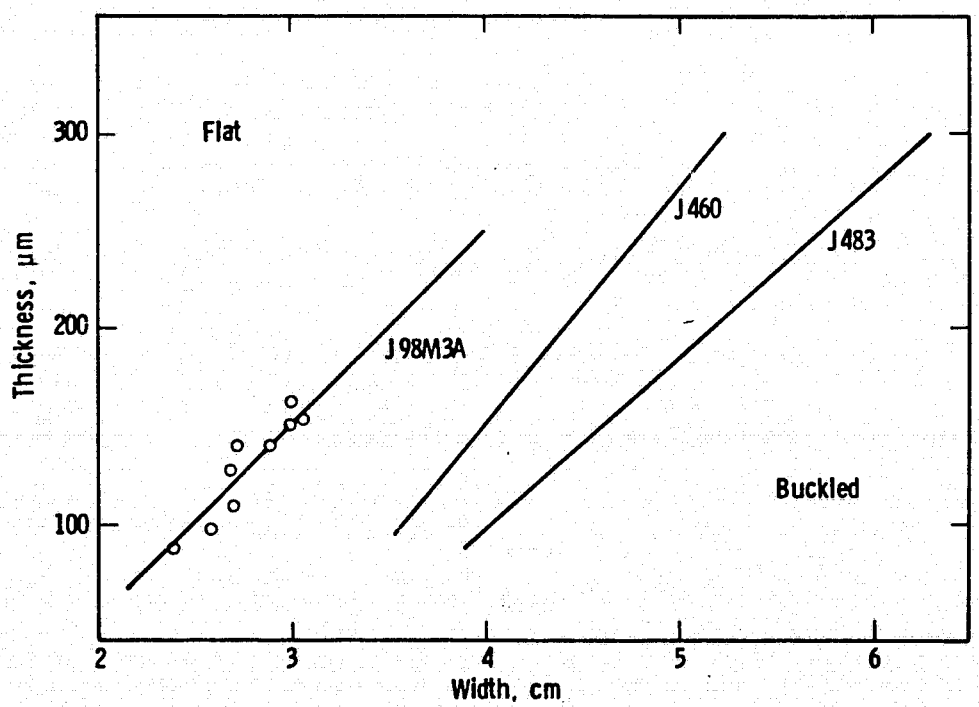

Figure 10. Buckling predictions for the configurations of Figure 9.

The buckling model calculations confirm these expectations of wider crystal growth as shown in Figure 10. The solid lines are based on the model calculations of the width and thickness for which $\lambda = 1$, that is they separate regimes of flat and buckled growth. In the case of the J98M3 curve, the points represent observed ribbon dimensions at which deformation occurred. The excellent agreement for that case provides substantial validation that the models we have assembled provide an adequate representation of the stress generation by our growth systems.

The curves representing the lower stress configurations tend to give more conservative estimates of the buckling conditions. In the low stress cases $\lambda >> 1$ even for the widest ribbon that can be reliably modeled using our present finite element mesh. Thus, some form of extrapolation is required to determine the dimensions for which $\lambda = 1$. The curves for the J460 and J483 configuration were generated using a power law extrapolation based on narrower, high stress cases. For the reasons previously cited, this extrapolation procedure tends to understimate the critical widths and thus leads to a conservative estimate of the buckling behavior. Increasing the size of the finite element mesh would improve the accuracy of the buckling analysis for these wide, low stress ribbons and for future cases, the models may be reformulated.

In summary the use of temperature, stress, and buckling models has been a powerful technique for improving the design of growth configurations for silicon dendritic web.

5. Acknowledgements

This work was supported by the Department of Energy through the Flat Plate Solar Array Project administered by the Jet Propulsion Laboratory of California Institute of Technology. We would also like to acknowledge the support and assistance of our colleagues at the Westinghouse Research Laboratories, especially Dr. E. Kothmann for providing the initial development of the temperature model and members of the Analytical Mechanics Department for formulating the WECAN analysis of the finite element stress and buckling models.

References

1. A. D. Morrison, K. V. Ravi, C. V. Hari Rao, T. Surek, D. F. Bliss, L. C. Garone and R. N. Hogencamp. Annual Report. ERDA/JPL 954355/76-11 (1976). p. 41.

2. R. W. Gurtler, J. Crystal Growth 50,69 (1980).

3. R. G. Seidensticker and R. H. Hopkins, J. Crystal Growth 50, 221 (1980).

4. R. G. Seidensticker, in Crystals, 8. H. C. Freyhardt, Ed. Springer-Verlag, (Berlin, Heidelberg, New York, 1982).

5. R. O. A. Hall, Acta Crist. 14, 1004 (1961).

6. Yu. A. Burenkov and S. P. Nickanorov, Fiz. Tver. Tela 16, 1496 (1974). trans. in Sov. Phys.-Solid State 16, 963 (1964).

7. W. G. Carson and R. E. Newton, AIAA Journal, 7, 527 (1969).

DISCUSSION

SEKERKA: Rather than go through an iterative procedure, suppose you set the problem up in terms of a problem like you would for the calculus of variations and attempt to minimize some figure of merit, let's say, some maximum second derivative or some integrated second derivative. Have you tried that approach?

SEIDENSTICKER: There are lots of things that one can do to obviously change the mechanical geometry and the thermal temperature geometry. Since we use inductive heating, it is not just a simple radiation transfer. If you want to cool them down you can put some little slits around the edge, etc.

SEKERKA: Sure, but I meant to use a finite number of shields reasonably spaced. Let's leave the spacing out for a moment, and decide what set of temperatures they ought to have to minimize the second derivative, to minimize the buckling mode.

SEIDENSTICKER: It is a reasonable thought.

KALEJS: From that last graph, you had a plot of constant-thickness results. The fact that you go to different shield designs implies that the temperature field has to be changed somehow as you change the design, but if you grow constant thickness with web growth you must also be changing the speed. Were those results all at constant speed?

SEIDENSTICKER: Pretty much so. The growth velocity is sensitive to the details of the thermal system very near the interface, in the first centimeter or two. But the thermal stress, which I have called on some occasions, a far peak, the Δ_x stress that occurs out three to six centimeters above the interface, is not very dependent on that. This is one of the things we are looking at now. We have reduced this far peak stress, and we are now going back to see if we can do a little bit with the stresses near the interface. I think that one has to recognize the very simple mathematical problem, which is that when you get the ribbon far away from the growth front that you are not losing very much heat because you are at room temperature; therefore, the second derivative is zero and it is pretty much at constant temperature, and therefore the first derivative is zero. All you have to do is take a spatial integration of the second derivative all the way up to the interface to find the first derivative and the first derivative is of course related to the growth velocity. So you somehow have to have the integral of the second derivative over the whole region come out about the same.

KALEJS: You don't think those results reflect a gradual lowering speed?

SEIDENSTICKER: No. It is not gradual. As a matter of fact, the J460, with a wide low-stress growth, is a little bit faster than the J98.

KALEJS: So you have done it maintaining the same ribbon thickness?

SEIDENSTICKER: We have maintained the same ribbon thickness and, as a matter of fact, made it a little thinner. There is not that much difference.

KALEJS: Have you entertained the idea that the creep results are hidden because the particular orientation of the material and the stresses are all swept into your central plane, which I understand is really highly defected?

SEIDENSTICKER: The twin planes do form a barrier for dislocation motion so that you do get pileup there. Czochralski people say that less than a thousand per square centimeter is dislocation-free, and that's about where we get a lot of our crystals. We have looked at surface etch-pit counts, because that is simple and easy to do. We have looked at cross-sectioned etch-pit counts and we have done X-ray topographs and there just aren't very many dislocations there.

SHIH: You have taken into account the material property variation of the thermal expansion coefficient. I wonder if you can make a comment on the Young's modulus variation effect?

SEIDENSTICKER: Well, there are some Russian papers that we used for Young's modulus and this particular one seems to agree fairly well with some unpublished local results.

SHIH: You have mentioned the finite element method you used in your computer, called WECAN. It is my understanding your elements are cubic-block-type elements and I wonder why you didn't use a plate-type element, especially for the buckling analysis?

SEIDENSTICKER: For buckling you have to have a three-dimensional mesh.

SHIH: I know. I just wondered why you used a cubic-block type, not a plate-type element. In a plate-type element you can take three dimensions into consideration.

SEIDENSTICKER: I am not an expert in any way in finite element analysis. The analysis was a package program in the analytical mechanics group who did the work.

SHIH: Can your computer code take the varying Young's modulus into account?

SEIDENSTICKER: Yes, the computer code could put it in. Just a small variation over the temperature range of interest. In that case we could use a second derivative of α_e for our rough analysis.

SHIH: From a comparison of your experimental results and your analysis, it seems that they agree very well, but you have shown a buckling mode from the analysis. This looked like a beam-type buckling mode. It is a very-long-wave-type buckling mode, and from the experimental observations, I can see, most of your production has shown a very-short-wave-type buckling mode, and these two buckling modes are totally different. For a different type of buckling mode I expect you will get a different kind of eigenvalue. I wonder why you can get a very good critical temperature?

SEIDENSTICKER: I'm not sure I completely understand your question. Let me just make the remark that after buckling occurs during growth, what happens then, as far as the frozen end wiggling or not is concerned, is a very complex question, and we haven't even addressed it.

SHIH: This is a very complex situation, but the problem is, if I have a different kind of buckling mode I can have different kinds of eigenvalues. If you do an analysis, and you get different eigenvalues, this implies different buckling modes. Conversely, if the two buckling modes are totally different, I expect the eigenvalues will be quite different, too. I was just wondering why you can get a very good result between your analysis and your experiment?

SEIDENSTICKER: The result here is the lowest eigenvalue, the first-order mode for the symmetric, and I am very anxious to get back and look at the antisymmetric buckling now.

MORRISON: I wondered if you would describe your experience using this predictive process on the new growth setup that you are operating in experimental mode today with the variable geometry?

SEIDENSTICKER: I can't give you very much data on that except that it seems to behave normally and doesn't have any residual stress, even though it is faster.

MORRISON: Have you run a series of iterative analyses and then run a series of ribbons with different geometries and related predictions of the model to the results of the growth runs?

SEIDENSTICKER: We have run several, yes.

MORRISON: And you have got a match? Can you tell us how well they match or anything?

SEIDENSTICKER: Well, we still need more experimental data. One of the questions that one asks is always "How well you are calculating temperature, how do you know that you are getting the right results?" We look at the thickness velocity and we find that the velocity at which we grow, say, 150-μm-thick web, ends up within a percent or so of what we measure, which says that the initial slope is good. The buckling seems to be pretty good, which says that the second derivative is good and that is really all that I care about the temperature. As far as the dynamic system goes, there seems to be nothing particularly out of order.

MORRISON: Your analysis predicts at what width of ribbon the onset of buckling occur for any system? Am I right?

SEIDENSTICKER: That is basically patterned after the J460, so that should be in the 5-centimeter range.

MORRISON: If the model predicts when the onset of buckling takes place, has the model predicted when the onset of buckling would take place in this multiple run or in this variable-parameter run, have you seen the onset of buckling?

SEIDENSTICKER: The data that we have so far is that the velocity/thickness fits. The stress is another matter. We do not have enough data on that yet.

CHALMERS: I would like to return the discussion to a very simple-minded level. You mentioned, I think, that one of the buckling modes was a simple bend of the ribbon without any twist. I can't imagine any system of tension and compression within the ribbon itself that could possibly make it do that.

SEIDENSTICKER: If you consider, for example, that the center of the ribbon is in compression, and the edges are in tension, the center of the ribbon would like to expand and the edges would like to contract. It has a complex curve. Or if it is the other way around, you get the inside of the torus.

SESSION VI: LASER RECRYSTALLIZATION

J. Fan, Chairman

PRECEDING PAGE BLANK NOT FILMED

N84 28637 D23

HIGH SPEED CRYSTAL GROWTH BY Q-SWITCHED LASER MELTING

A.G. Cullis
Royal Signals and Radar Establishment,
Malvern, Worcs. WR14 3PS, England

1. INTRODUCTION

During the last few years there has been great interest in the modification of the structural and electrical properties of semiconductors by processing with short radiation pulses obtained from Q-switched lasers. The way in which these modifications are accomplished involves hitherto unachievably high heating and cooling rates. This processing has revealed novel crystal growth and high speed resolidification phenomena that have marked out a new area of fundamental research. It is this area of rapid advance that will be the focus of the present paper, with particular reference to the behaviour of semiconductor Si. The vigorous activity in this area is particularly clearly documented in a number of conference proceedings (see, for example, Appleton and Celler [1] and Narayan et al [2]).

The annealing process typically employs short (∿1-100nsec) pulses of radiation in or near the visible region of the spectrum. Q-switched ruby and Nd-YAG lasers are commonly used and these are sometimes mode-locked to reduce the pulse length still further. Material to be annealed can be processed with a single large area radiation spot although it is often necessary to render the laser beam spatially uniform and to eliminate local energy density fluctuations [3]. Alternatively, a small (∿10-100μm) radiation spot size can be used and a large sample area is covered by overlapping irradiated regions by means of a scanning process [4]. However, this latter method may give rise to small-scale annealing nonuniformities.

2. FUNDAMENTALS OF ANNEALING PROCESS

Many experimental investigations have given information about the mechanism by which Q-switched laser annealing occurs. Much early work [4-7] indicated that transient surface melting played a central role, although an alternative annealing mechanism was proposed [8], this being based upon the postulated presence of a dense, long-lifetime plasma of photoexcited carriers. However, the latter was not supported by time-dependent optical reflectivity measurements at various wavelengths [9] and the transient melting model has been confirmed by other subsequent studies. Indeed, as further described in section 4, a range of important dopant segregation phenomena strongly indicate that melting occurs [10,11]. Most recently, independent time-resolved measurements of several different Si physical properties have provided final confirmation [12-16]. Time-resolved Raman scattering measurements [17] have also been shown [18] to be in accord with the transient melting model.

The behaviour of the laser-induced molten surface layer has been modelled by computer heat-flow calculations. Typical results [19,20] for a Q-switched

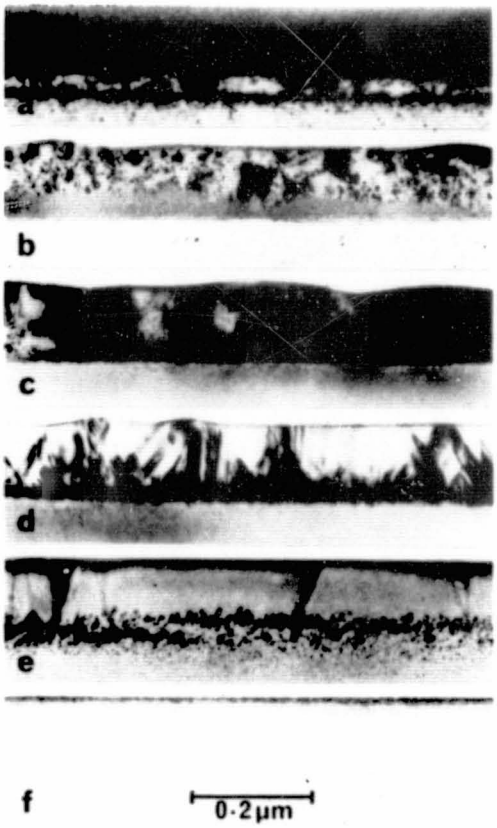

Figure 1 : TEM images of cross-sections of (001) Si implanted with $4x10^{15}$ 150keV-As^+/cm^2 a) as-implanted, b) $0.20J/cm^2$, c) $0.35J/cm^2$, d) $0.85J/cm^2$, e) $1.00J/cm^2$ and f) $1.20J/cm^2$. (After Cullis et al [29].)

laser pulse of a few tens of nanoseconds duration show that, with a beam energy density above the surface melting threshold, after melt formation commences the liquid layer thickness increases rapidly while substantial irradiation continues. The velocity of the liquid-solid interface often lies in the range 5-10m/s and the melt quickly reaches its maximum depth which may be as great as ∿1μm depending upon beam energy density. Resolidification next takes place with a liquid-solid interface velocity typically in the range 1-5m/s, as has been verified by direct measurements [21] of transient conductivity behaviour. The latter velocity is a particularly important parameter since it controls the behaviour observed during resolidification, which in turn determines the characteristics of the final solid phase. The resolidification interface velocity can be varied over a wide range by changing the background temperature of the substrate material [22] or by altering the laser pulse length [23,24]. This velocity control gives the important ability to test the application of crystal growth models to the many, diverse observations that have been made.

3. LATTICE DISORDER REMOVAL AND MODIFICATION

Q-switched laser annealing research has focused most intensively on the recrystallization of ion implantation damage in Si [4-6,25,26]. The extent of penetration of the laser-induced melt is particularly important [27] and the nature of the defect transitions observed at moderate energy densities of irradiation depends upon the character of the initial ion-induced lattice disorder. If ion implantation has led to the formation of an amorphous surface layer, annealing with typically 30ns ruby laser pulses can yield residual defects ranging from polycrystals to dislocation networks, though a pulse with a high enough energy can give single crystal free of extended defects [28]. The various structure transitions are shown particularly clearly by cross-sectional transmission electron microscope (TEM) work [29], as illustrated in Fig. 1 for an As^+ ion-implanted layer. A low energy density radiation pulse of just $0.2J/cm^2$ partially melts the amorphous layer, the outer region of which then resolidifies as polycrystalline material since it is not in contact with the underlying crystal matrix (Fig. 1b). With increasing energy density of irradiation, the amorphous Si is melted to the crystal interface. However, resolidification continues to give material of poor crystal quality up to

$\sim 0.7 J/cm^2$ and there is good evidence that the transient melt at the position of deepest penetration is significantly undercooled - see section 5. Nevertheless, at $0.85 J/cm^2$ (Fig. 1d) the melt temperature has risen sufficiently to give epitaxial recrystallization upon the underlying crystal. However, the reformed single crystal layer still contains many defects, principally inclined microtwin lamellae. For an energy density of $\sim 1 J/cm^2$ the melt actually just penetrates the crystal matrix although an irregular buried band of point defect clusters still remains in the annealed crystalline layer. Occasional V-shaped dislocation pairs originate in the defect band. Ultimately, when the energy density of the irradiating pulse is increased to $1.2 J/cm^2$, the transient melt removes all the dense surface damage produced by implantation so that resolidification yields high quality epitaxial recrystallization and a Si layer free of all extended crystallographic defects (Fig. 1f).

If initial ion implantation gives only a buried defect cluster damage band, the polycrystal transitions described in the above sequence do not occur. In this case, the most prominent defects to be produced occur when the melt front, at deepest penetration, intersects the damage band [30] and dislocation pairs are nucleated in the interfacial region. Once again, of course, all extended defects can be eliminated from the annealed layer by much deeper melting with a sufficiently high energy density laser pulse.

Pulses of Q-switched laser radiation can also be used to recrystallize Si layers deposited on various substrates. Amorphous layers deposited on single crystal Si substrates can exhibit excellent epitaxial recrystallization under suitable irradiation conditions [31,32]. However, if free-volume is present in the initial layers void formation can occur upon annealing. If an as-deposited layer is actually single crystal but contains epitaxy-related defects, these can be substantially modified by transient laser melting. For epitaxial Si on sapphire where the initial layer contains arrays of inclined microtwin lamellae, laser-melting down to the hetero-interface can partially suppress twin growth during recrystallization of the Si although many dislocations are introduced into the annealed single crystal material [33].

Studies have also been carried out on the effects of laser annealing upon diffusion-induced defects in Si. Small dislocation loops introduced by P-diffusion can be removed by laser melting and, indeed, the depth of melting itself has been measured by observations of this phenomenon [34]. When extended dislocations are present in the initial material they can change their shape in the annealed, resolidified region and dislocation splitting reactions of a complex nature can occur [35].

4. TRAPPING AND SEGREGATION OF DOPANTS

When the conventional dopants such as B, P and As are implanted into Si crystal they can be incorporated almost exclusively onto substitutional lattice sites by laser annealing [4,36]. In fact, even if dopants exhibit a particularly low equilibrium solubility in solid Si, the speed of the resolidification interface during annealing is great enough to physically trap nonequilibrium high concentrations of the impurities on lattice sites [37-43]. This process increases the effective interfacial segregation coefficient (k') of a dopant and has been observed in a number of cases, including those of In, Sb, Bi, Pt and C in Si [25,27,36,44-47]. The dopant solubility enhance-

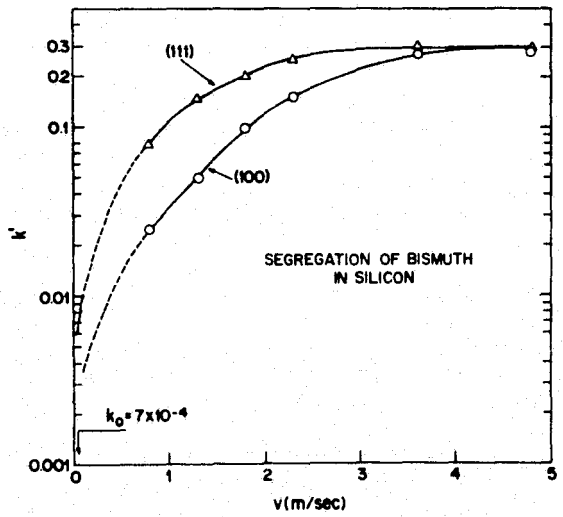

Figure 2 : Interface segregation coefficient for Bi in Si as a function of velocity and crystallographic orientation. (After Baeri et al [47].)

ments that can be achieved are sometimes extremely large: in the case of Pt in Si the maximum solubility is almost three orders of magnitude greater than the equilibrium level [25]. The impurity trapping phenomenon also exhibits a dependence upon the crystallographic orientation of the irradiated Si surface [47]. This is demonstrated for Bi in Si in Fig. 2 where it is clear that, for recrystallization interface velocities of up to about 4m/s, trapping is more pronounced for (111) Si than for (001) Si. This is likely to be at least in part a consequence of the greater undercooling expected to be associated with a (111) Si interface moving at any given velocity (see also section 5). The supersaturated solid solutions formed by solute trapping are, of course, metastable. However, in the case of C in Si, layers supersaturated by about two and a half orders of magnitude require temperatures of ~1000°C for rapid impurity precipitation to take place [46].

If an exceptionally large concentration of a low solubility dopant is present in a laser annealed layer not all (and in some cases very little) of the impurity is substitutionally trapped in the solid. One consequence often observed is that a large amount of the impurity segregates out to the sample surface [10,44,48]. This phenomenon is analogous to that which occurs during the process of zone refining. However, the lateral distribution of the segregated material is also often not uniform. Indeed, the precipitate phase can occur as microscopic channels which form the boundaries of minute crystalline Si cells. This effect has been observed for a number of implanted dopants in Si [44] and has been shown to be due to the occurrence of constitutional supercooling in the resolidifying transient-melt [11,22]. Calculations [49,50] employing morphological stability theory [51] have shown that the experimental observations can be accounted for in a quantitative manner. A typical segregation cell structure given by laser annealed In^+ ion implanted Si is shown in Fig. 3. Channels of metallic In form the cell walls and it is clear that the cell dimensions depend sensitively upon the velocity of the recrystallization interface. The Figure demonstrates that as the velocity of the interface is changed from 4 to 2m/s (using substrate temperature control) the cell size changes from ~450Å to 850Å [49].

It is important to note that not all low solubility dopants give segregation cell structures of the type just described. If the impurity has only a low solubility in even molten Si precipitation can occur in a more uniform manner before resolidification is complete. This is the case for excess implanted C in Si where some segregation towards the surface is evident [46]. However, implanted Ar in Si is so extremely insoluble that precipitation in the form of gas bubbles can take place at an early stage in the melting sequence so

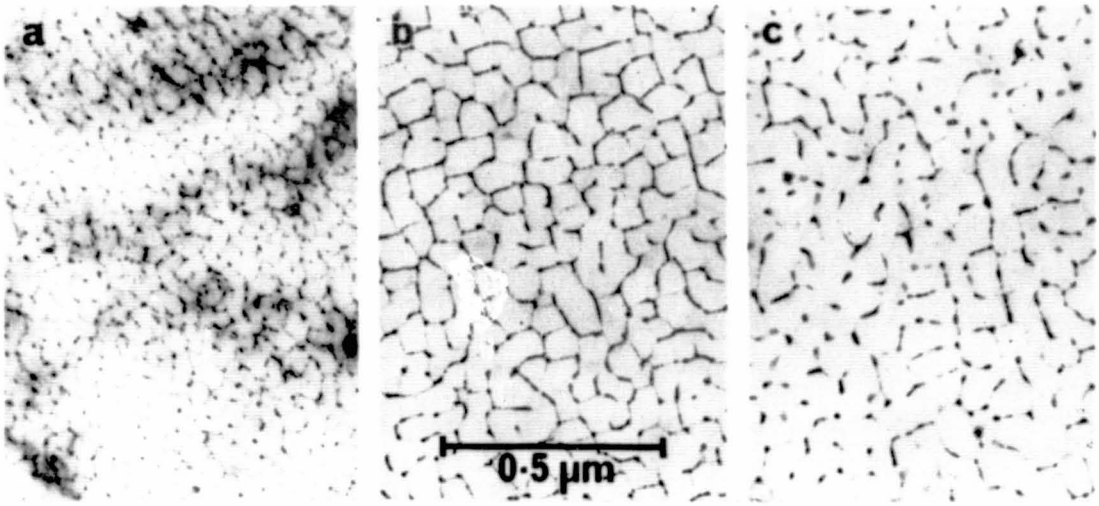

Figure 3 : TEM images of (001) Si implanted with $3x10^{15}$ 170keV In^+/cm^2 and annealed at $1.5J/cm^2$ (ruby, 30ns). Note dependence of cell size on substrate background temperature: a) 77°K, b) 300°K and c) 410°K. (After Cullis et al [49].)

that the final bubble depth distribution is similar to the initial Ar implant distribution [11].

A method other than ion implantation that has been used to introduce large quantities of impurities into Si is the direct laser alloying of deposited metal films. Laser melting a deposited Pt layer on Si once again results in the formation of segregation cells due to melt supercooling [52]. Similar cell formation has been observed [53] after the laser alloying of Co and Mo films on Si and other, larger cells ascribed to melt convection effects in non-uniformly irradiated areas were also identified.

5. ULTRA-RAPID SOLIDIFICATION PHENOMENA

Transient annealing with Q-switched laser radiation has revealed a range of new high-speed, liquid-phase crystal growth phenomena. The preceding sections were primarily concerned with work involving resolidification interface velocities in the range 1-5m/s. However, even higher velocities can be achieved by use, especially, of short laser pulse lengths and short wavelength radiation. Important results in this regime were obtained by groups at Harvard [54] and IBM [55]. These workers were first to demonstrate that at exceptionally high quench rates achieved, for example, using mode-locked laser pulses initially crystalline Si is rendered amorphous. In this case, the resolidification interface velocity is so high that atomic re-ordering cannot occur.

The conditions required for the formation of amorphous material have been quantified in studies [56] which employed large-area uniform 2.5ns laser pulses of ultra-violet radiation. For (001) Si, Figs. 4a and b demonstrate that a very thin (~100Å) amorphous surface layer is produced just above the threshold for melting (about $0.15J/cm^2$) and that the thickness of the amorphous material initially increases as the radiation energy density is raised. However, above $\sim 0.3J/cm^2$ amorphization abruptly ceases to occur and, instead,

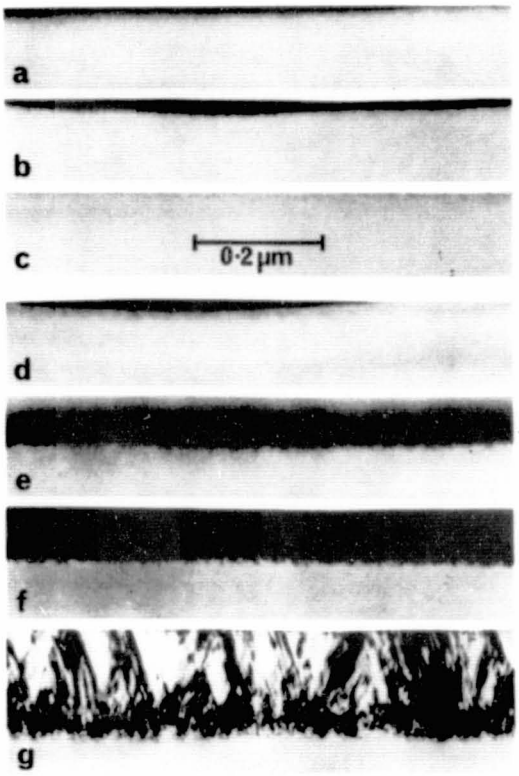

Figure 4 : TEM images of cross-sections of Si layers irradiated with 2.5ns 347nm pulses: (001) Si - a) 0.20J/cm^2, b) 0.27J/cm^2 and c) 0.40J/cm^2 ; (111) Si - d) 0.20J/cm^2 , e) 0.5J/cm^2 , f) 0.55J/cm^2 and g) 0.9J/cm^2. (After Cullis et al [56].)

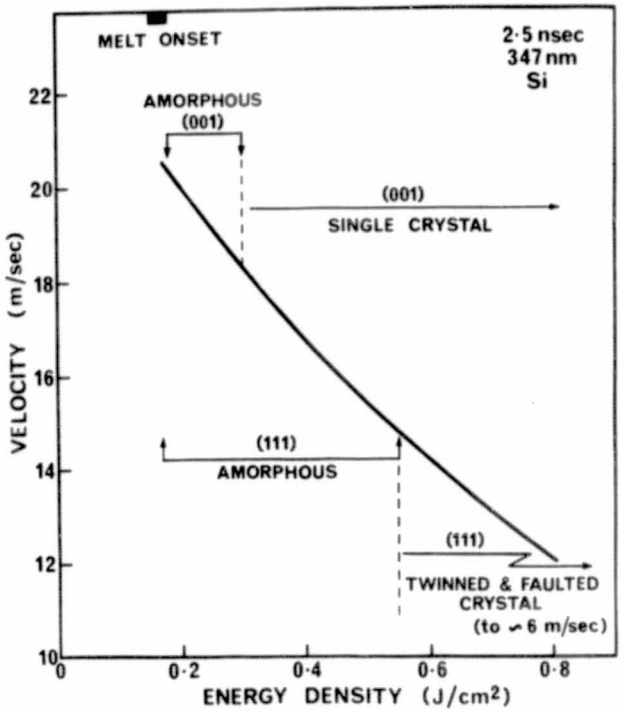

Figure 5 : Computed peak velocity of 1412°C isotherm as a function of pulse energy density showing surface melting threshold and orientation-dependent amorphization and defect formation regimes. (After Cullis et al [56].)

high quality single crystal free of extended defects is formed (Fig. 4c). This behaviour is to be contrasted with that exhibited by (111) Si. For material of the latter orientation surface amorphization begins at low energy densities as before (Fig. 4d). However, amorphous Si continues to form up to ~0.55J/cm^2, with thicknesses of up to ~800Å due to the deeper melting (Fig. 4f). Furthermore, although for irradiation above this energy density crystalline material is produced, the annealed layer is heavily defective and contains many inclined microtwin lamellae (Fig. 4g). With further increase in radiation energy density (almost up to the damage threshold) or increase in the pulse length the defect density is reduced.

It is interesting to note that the amorphous Si produced by rapid quenching is structurally similar to that produced by conventional means (for example, by ion implantation) and it is essentially impurity-free [56,57]. However, under more extreme conditions of irradiation surface oxidation can occur [58].

The various defect transitions described above are summarized in Fig. 5, which also shows the relationship of the radiation energy density to the computed velocity of the 1412°C isotherm (normal melting temperature) [56]. It is

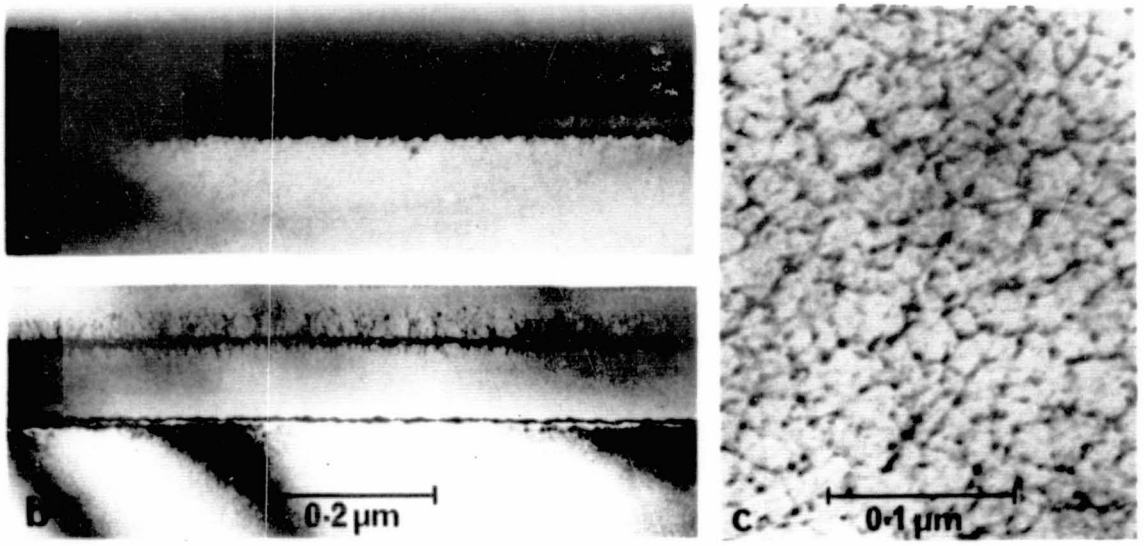

Figure 6 : TEM images of (001) Si implanted with 10^{16} 170keV-In^+/cm^2 and annealed at $0.40J/cm^2$ (ruby, 2.5ns, 77°K substrate): a) cross-section showing as-implanted layer, b) cross-section showing In segregation band in amorphous layer, c) plan-view showing segregation cell structure. (After Cullis et al [68].)

immediately clear that the energy density thresholds which were identified previously can be taken to correspond to thresholds in the resolidification velocity. Thus, higher velocities are needed for the formation of an amorphous solid on (001) Si ($\gtrsim$18m/s) than on (111) Si ($\gtrsim$15m/s). While crystalline material is formed below these thresholds, profuse defect nucleation occurs specifically on (111) Si for resolidification interface velocities down to about 6m/s. The different maximum recrystallization velocities of (001) and (111) Si are also very apparent after the fast laser melting of ion implanted Si [59].

The curve given in Fig. 5 represents an approximation [60] since the velocity computation did not take into account undercooling which is likely to occur in the transient melt. The formation of an amorphous solid will be possible when the undercooling at the resolidification interface falls below the melting point of that phase. This concept is consistent with the relative ease of formation of amorphous Si on (111) surfaces since, due to the difficulty of plane nucleation on this crystal orientation, its associated undercooling during resolidification would be larger than for (001) Si crystal. Furthermore, it has been theoretically predicted [61,62] that amorphous Si should undergo a first order melting/solidification phase transition a few hundred °C below the crystal melting temperature. Some experimental measurements support this proposition [63-65] but the issue remains rather contentious [66].

Further information about the melting and solidification behaviour of amorphous Si can be obtained when very short laser pulses are used to rapidly anneal pre-existing amorphous layers (formed, for example, by ion implantation) [67,68]. Indeed, explosive recrystallization events have been observed under suitable conditions [68]. However, intriguing sub-threshold behaviour also occurs. Figure 6b shows an In^+ ion implanted layer which initially had a uniform

structure. Extremely short-term melting with a low energy density, 2.5ns, ruby laser pulse appears to give a very undercooled transient liquid which resolidifies directly back into an amorphous state while the implanted In segregates into a narrow band actually within the amorphous layer [68]. Further confirmation that a normal melt is formed during this very fast annealing sequence is given by the observation of a cell structure in the segregation band (Fig. 6c), which almost certainly is due to the occurrence of constitutional supercooling in the resolidifying liquid. This is thought to be the first observation of impurity segregation during the direct solidification of an amorphous phase and the accompanying diffusion behaviour indicates that amorphous Si is not, for example, simply a glassy state [68].

Experiments of the type just described give considerable insight into the fundamental nature of amorphous Si. When considered together with the wide-ranging basic research outlined earlier in this article, it is evident that studies of laser annealing phenomena are leading to most important advances in the areas of high-speed solidification and crystal growth.

6. ACKNOWLEDGEMENTS

The author is indebted to colleagues at RSRE, Bell Laboratories (Murray Hill, USA) and the University of Catania (Italy) for their collaboration in those items of work mentioned above which were carried out in the author's group at RSRE.

REFERENCES

[1] Appleton, B.R. and Celler, G.K., Laser and Electron-Beam Interactions with Solids (North Holland, New York, 1982).
[2] Narayan, J., Brown, W.L. and Lemons, R.A., Laser-Solid Interactions and Transient Thermal Processing of Materials (North Holland, New York, 1983).
[3] Cullis, A.G., Webber, H.C. and Bailey, P., J. Phys. E: Sci. Instrum., 12, 688 (1979).
[4] Celler, G.K., Poate, J.M. and Kimerling, L.C., Appl. Phys. Lett. 32, 464 (1978).
[5] Baeri, P., Campisano, S.U., Foti, G. and Rimini, E., Appl. Phys. Lett. 33, 137 (1978).
[6] White, C.W., Christie, W.H., Appleton, B.R., Wilson, S.R., Pronko, P.P. and Magee, C.W., Appl. Phys. Lett. 33, 662 (1978).
[7] Auston, D.H. Surko, C.M., Venkatesan, T.N.C., Slusher, R.E. and Golovchenko, J.A., Appl. Phys. Lett. 33, 437 (1978).
[8] Van Vechten, J.A., Tsu, R. and Saris, F.W., Phys. Lett. 74A, 422 (1979).
[9] Nathan, M.I., Hodgson, R.T. and Yoffa, E.J., Appl. Phys. Lett. 36, 512 (1980).
[10] Baeri, P., Campisano, S.U., Foti, G. and Rimini, E., Phys. Rev. Lett. 41, 1246 (1978).
[11] Cullis, A.G., Webber, H.C., Poate, J.M. and Chew, N.G., J. Microsc. 118, 41 (1980).

[12] Stritzker, B., Pospieszczyk, A. and Tagle, J.A., Phys. Rev. Lett. 47, 356 (1981).
[13] Larson, B.C., White, C.W., Noggle, T.S. and Mills, D., Phys. Rev. Lett. 48, 337 (1982).
[14] Liu, J.M., Yen, R., Kurz, H. and Bloembergen, N., Appl. Phys. Lett. 39, 755 (1981).
[15] Lowndes, D.H., Jellison, G.E. and Wood, R.F., in Laser and Electron-Beam Interactions with Solids, Appleton, B.R. and Celler, G.K., eds. (North Holland, New York, 1982) pp. 73-78.
[16] Takai, M., Sato, Y., Murakami, K., Gamo, K., Minamisono, T. and Namba, S., in Laser and Electron-Beam Interactions with Solids, Appleton, B.R. and Celler, G.K., eds. (North Holland, New York, 1982) pp. 91-96.
[17] Compaan, A., Aydinli, A., Lee, M.C. and Lo, H.W., in Laser and Electron-Beam Interactions with Solids, Appleton, B.R. and Celler, G.K., eds. (North Holland, New York, 1982) pp. 43-48.
[18] Wood, R.F., Lowndes, D.H. and Giles, G.E., in Laser and Electron-Beam Interactions with Solids, Appleton, B.R. and Celler, G.K., eds. (North Holland, New York, 1982) pp. 67-72.
[19] Baeri, P., Campisano, S.U., Foti, G. and Rimini, E., J. Appl. Phys. 50, 788 (1979).
[20] Wood, R.F. and Giles, G.E., Phys. Rev. B23, 2923 (1981).
[21] Galvin, G.J., Thompson, M.O., Mayer, J.W., Hammond, R.B., Paulter, N. and Peercy, P.S., Phys. Rev. Lett. 48, 33 (1982).
[22] Cullis, A.G., Webber, H.C., Poate, J.M. and Simons, A.L., Appl. Phys. Lett. 36, 320 (1980).
[23] Bloembergen, N., in Laser-Solid Interactions and Laser Processing - 1978, Ferris, S.D., Leamy, H.J. and Poate, J.M., eds. (Amer. Inst. Phys., New York, 1979) pp. 1-9.
[24] Baeri, P., Poate, J.M., Campisano, S.U., Foti, G., Rimini, E. and Cullis, A.G., Appl. Phys. Lett. 37, 912 (1980).
[25] Kachurin, G.A., Pridachin, N.B. and Smirnov, L.S., Sov. Phys. Semicond. 9, 946 (1976).
[26] Khaibullin, I.B., Shtyrkov, E.I., Zaripov, M.M., Galyautdinov, M.F. and Zakirov, G.G., Sov. Phys. Semicond. 11, 190 (1977).
[27] Bertolotti, M., Vitali, G., Rimini, E. and Foti, G., J. Appl. Phys. 50, 259 (1979).
[28] Tseng, W.F., Mayer, J.W., Campisano, S.U., Foti, G. and Rimini, E., Appl. Phys. Lett. 32, 824 (1978).
[29] Cullis, A.G., Webber, H.C. and Chew, N.G., Appl. Phys. Lett. 36, 547 (1980).
[30] McMahon, R.A., Ahmed, H. and Cullis, A.G., Appl. Phys. Lett. 37, 1016 (1980).
[31] Lau, S.S., Tseng, W.F., Nicolet, M-A., Mayer, J.W., Eckardt, R.C. and Wagner, R.J., Appl. Phys. Lett. 33, 130 (1978).
[32] Bean, J.C., Leamy, H.J., Poate, J.M., Rozgonyi, G.A., Sheng, T.T., Williams, J.S. and Celler, G.K., Appl. Phys. Lett. 33, 227 (1978).
[33] Cullis, A.G., Webber, H.C., Chew, N.G., Hill, C. and Godfrey, D.J., in Microscopy of Semiconducting Materials 1981, Cullis, A.G. and Joy, D.C., eds. (Inst. Phys., Bristol, 1981) pp. 95-100.
[34] Narayan, J., Appl. Phys. Lett. 34, 312 (1979).
[35] Narayan, J. and Young, F.W. Jr., Appl. Phys. Lett. 35, 330 (1979).
[36] White, C.W., Pronko, P.P., Wilson, S.R., Appleton, B.R., Narayan, J. and Young, R.T., J. Appl. Phys. 50, 3261 (1979).

[37] Cahn, J.W., Coriell, S.R. and Boettinger, W.J., in Laser and Electron-Beam Processing of Materials, White, C.W. and Peercy, P.S., eds. (Academic Press, New York, 1980) pp. 89-94.
[38] Jackson, K.A., Gilmer, G.H. and Leamy, H.J., in Laser and Electron-Beam Processing of Materials, White, C.W. and Peercy, P.S., eds. (Academic Press, New York, 1980) pp. 104-109.
[39] Wood, R.F., Appl. Phys. Lett. 37, 302 (1980).
[40] Aziz, M.J., J. Appl. Phys. 53, 1158 (1982).
[41] Campisano, S.U., Appl. Phys. A30, 195 (1983).
[42] Gilmer, G.H. and Broughton, J.Q., in this proceedings volume (1984).
[43] White, C.W., in this proceedings volume (1984).
[44] Cullis, A.G., Poate, J.M. and Celler, G.K., in Laser-Solid Interactions and Laser Processing - 1978, Ferris, S.D., Leamy, H.J. and Poate, J.M., eds. (Amer. Inst. Phys., New York, 1979) pp. 311-316.
[45] White, C.W., Wilson, S.R., Appleton, B.R. and Young, F.W. Jr., J. Appl. Phys. 51, 738 (1980).
[46] Cullis, A.G., Series, R.W., Webber, H.C. and Chew, N.G., in Semiconductor Silicon 1981, Huff, H.R., Kriegler, R.J. and Takeishi, Y., eds. (Electrochem. Soc., Pennington, 1981) pp. 518-525.
[47] Baeri, P., Foti, G., Poate, J.M., Campisano, S.U. and Cullis, A.G., Appl. Phys. Lett. 38, 800 (1981).
[48] White, C.W., Narayan, J., Appleton, B.R. and Wilson, S.R., J. Appl. Phys. 50, 2967 (1979).
[49] Cullis, A.G., Hurle, D.T.J., Webber, H.C., Chew, N.G., Poate, J.M., Baeri, P. and Foti, G., Appl. Phys. Lett. 38, 642 (1981).
[50] Narayan, J., J. Appl. Phys. 52, 1289 (1981).
[51] Mullins, W.W. and Sekerka, R.F., J. Appl. Phys. 35, 444 (1964).
[52] Poate, J.M., Leamy, H.J., Sheng, T.T. and Celler, G.K., Appl. Phys. Lett. 33, 918 (1978).
[53] Van Gurp, G.J., Eggermont, G.E.J., Tamminga, Y., Stacy, W.T. and Gijsbers, J.R.M., Appl. Phys. Lett. 35, 273 (1979).
[54] Liu, P.L., Yen, R., Bloembergen, N. and Hodgson, R.T., Appl. Phys. Lett. 34, 864 (1979).
[55] Tsu, R., Hodgson, R.T., Tan, T.Y. and Baglin, J.E., Phys. Rev. Lett. 42, 1356 (1979).
[56] Cullis, A.G., Webber, H.C., Chew, N.G., Poate, J.M. and Baeri, P., Phys. Rev. Lett. 49, 219 (1982).
[57] Liu, J.M., Yen, R., Donovan, E.P., Bloembergen, N. and Hodgson, R.T., Appl. Phys. Lett. 38, 617 (1981).
[58] Liu, Y.S., Chiang, S.W. and Bacon, F., Appl. Phys. Lett. 38, 1005 (1981).
[59] Cullis, A.G., Webber, H.C. and Chew, N.G., in Microscopy of Semiconducting Materials 1983, Cullis, A.G., Davidson, S.M. and Booker, G.R., eds. (Inst. Phys., Bristol, 1983) pp. 167-172.
[60] Thompson, M.O., Mayer, J.W., Cullis, A.G., Webber, H.C., Chew, N.G., Poate, J.M. and Jacobson, D.C., Phys. Rev. Lett. 50, 896 (1983).
[61] Spaepen, F. and Turnbull, D., in Laser-Solid Interactions and Laser Processing - 1978, Ferris, S.D., Leamy, H.J. and Poate, J.M., eds. (Amer. Inst. Phys., New York, 1979) pp. 73-83.
[62] Bagley, B.G. and Chen, H.S., in Laser-Solid Interactions and Laser Processing - 1978, Ferris, S.D., Leamy, H.J. and Poate, J.M., eds. (Amer. Inst. Phys., New York, 1979) pp. 97-101.
[63] Baeri, P., Foti, G., Poate, J.M. and Cullis, A.G., Phys. Rev. Lett. 43, 2036 (1980).

[64] Donovan, E.P., Spaepen, F., Turnbull, D., Poate, J.M. and Jacobson, D.C., Appl. Phys. Lett. 42, 698 (1983).
[65] Webber, H.C., Cullis, A.G. and Chew, N.G., Appl. Phys. Lett. 43, 669 (1983).
[66] Kokorowski, S.A., Olson, G.L., Roth, J.A. and Hess, L.D., Phys. Rev. Lett. 48, 498 (1982).
[67] Rozgonyi, G.A., Baumgart, H., Phillipp, F., Uebbing, R. and Oppolzer, H., in Microscopy of Semiconducting Materials 1981, Cullis, A.G. and Joy, D.C., eds. (Inst. Phys., Bristol, 1981) pp. 85-94.
[68] Cullis, A.G., Webber, H.C. and Chew, N.G., Appl. Phys. Lett. 40, 998 (1982).

DISCUSSION

FAN: You have a 15 m/s region between amorphous and crystalline. Do you always get either amorphous or crystalline regions or do you get polycrystalline?

CULLIS: It is a sharp transition. You either get amorphous or you get single-crystal, and absolutely never get polycrystalline.

MILSTEIN: When you were discussing the indium implanted in amorphous silicon and then remelting, I was puzzled as to why the indium does not segregate out. Does it find interstices or something?

CULLIS: You are puzzled by the position of the band. Well, so were we, initially. What we think is that the solidification is very fast. You are talking about a total melt dwell time of less than 10 nanoseconds. The indium cannot diffuse very far, and it happens that the peak of the projected range of the initial implant is about halfway through the layer. So you don't expect the indium to move far from there. It is forced to stay near there. What happens is that as solidification occurs from the bottom, amorphous material forms. Some of the indium is swept forward, but the solidification temperature of the melt with the high indium concentration, falls dramatically, so the solidification slows. Ultimately, you get so much indium at this point. It is almost like metallic indium, and that melts at 150°C, and the surface of this layer, which had a lower indium concentration to start with, really is at such a low temperature with just a low indium concentration, it starts solidifying there and it comes banging in from that side.

MILSTEIN: I agree with you, but if you are growing from an indium-silicon mixed system and you do have this molten material at some exceedingly low temperature, it doesn't take a lot of thermal energy to keep it molten. Why ought the process not go on in terms of, essentially, a zone migration of the indium as a solvent?

CULLIS: Maybe it does. The only question is, over what distance, because the cooling rate is so high the heat just flows out of the whole region in 10 to 20 nanoseconds. If you consider temperature-zone migration, you could probably work out how far they could go and, it might be like 2 Å. It is possible that is what is happening, but I think it is the scale that is the problem there.

WILCOX: I have always thought of amorphous solids as being nothing but supercooled, superviscous melts. What is the difference between amorphous silicon and supercooled molten silicon?

CULLIS: Molten silicon is essentially metallic. The amorphous solid silicon is a semiconductor. One can see straightaway that coordination has to change. Therefore, if you consider taking the molten silicon and maintain its coordination, get it thicker and thicker and thicker, something happens. Actually, the solid formation point, because the coordination

must change. It isn't just like a slow setting of a glass. It was certainly postulated that it was likely a first-order phase transition for that reason, originally. I think Bagley certainly thought of it like that.

WILCOX: Is there evidence for that?

CULLIS: In the results that I tried to present about amorphous, I implied that the diffusion behavior we see of the impurity during the resolidification of an amorphous layer indicates that it is not the setting of a glass that is occurring. In other words, you would expect all the atoms to just set where they fall, essentially, if that were happening. We can actually see segregation occurring during that solidification. It doesn't look at though it is a glass transition.

WHITE: The amorphous layers you are forming on either (100) or (111), are you melting deeper than the thickness of the amorphous layer you are forming, and if so, how much deeper? And if so, why? Because the high solidification velocity should be just after the melt front turns around.

CULLIS: In both cases, we are melting deeper. In the (111) case, if we form an 800-A-thick layer, we melt maybe 1000 Å, and 80% goes amorphous. In the (111) case, if we melt 600 Å at 0.3 joules per square centimeter, we just about form an amorphous layer about 100 Å thick on the surface. What this is saying is that velocity is important, but we think that the undercooling is also important, and there is a time for that to build up. In the (111) case, because of the low crystal-growth rate, the rate of release of latent heat is so slow, a little bit of crystal grows but the temperature is falling madly so amorphous material can form after only 200 Å of crystal is grown. On the (100), it bombs away at 15 m/s, and holds off the temperature for longer, so you get more crystal growing.

WHITE: The twinning that you see on (111) crystals in the velocity range from 7 or 8 up to 14 or 15 m/s, what is that due to?

CULLIS: If you think about the (111) surface, certainly you can put that in two sorts of rotational twins. If you drive that surface madly and try to make it recrystallize, you cool it fast and try to give it the maximum growth rate. It will grow for a short time, but then, rotational twinning defects are going to build up, and as soon as rotational twins grow laterally and meet there is a horrible mass at the boundary where they actually meet, and the incline twins just take off from there.

N84 28638

High-Quality Silicon Films Prepared by Zone-Melting Recrystallization

C. K. Chen, M. W. Geis, B-Y. Tsaur, and John C. C. Fan
Lincoln Laboratory, Massachusetts Institute of Technology
Lexington, Massachusetts 02173-0073

I. INTRODUCTION

In recent years, substantial efforts have been directed toward the development of a technology for producing high-quality single-crystal Si films on insulating substrates [1-4]. These efforts have been motivated by the potential of thin-film devices for achieving higher packing density, speed, and radiation resistance than bulk devices. One of the most promising SOI approaches is zone-melting recrystallization (ZMR), in which the grain size of a polycrystalline Si film on an insulating substrate is greatly increased by the passage of a narrow molten zone. ZMR was initially proposed in 1953 as a possible technique for producing large-grain or single-crystal films of ZnS [5]. The technique was used by several investigators in the 1960's to produce films of Ge [6] and InSb [7,8] with electron mobilities close to bulk values and grain sizes of several hundred micrometers. Despite these promising results, interest in ZMR waned until the recent advent of laser, electron-beam, and strip-heater recrystallization of Si films [1-4]. Currently, in addition to ZMR, high-dose oxygen implantion, oxidation of porous Si, vapor-phase lateral epitaxy, and solid-phase lateral epitaxy are being investigated for producing thin Si films on insulating substrates [9].

In this paper we will describe details of the graphite-strip-heater ZMR technique being developed at Lincoln Laboratory, report the material properties of the ZMR films, and present an overview of SOI device results. Although our ZMR work is primarily motivated by integrated circuit applications, this work evolved in part from earlier research on laser crystallization of thick amorphous GaAs and Si films, which was undertaken with the goal of producing low-cost photovoltaic materials [10]. Our understanding of the ZMR growth process and its effect on the properties of the recrystallized films (typically 1 μm thick) may contribute some insight to a general understanding of the rapid recrystallization of Si for solar cells. In addition, the possibility of adapting ZMR for solar cell fabrication will be considered at the conclusion of the paper.

II. ZMR BY THE GRAPHITE-STRIP-HEATER TECHNIQUE

The ZMR technique recently developed at Lincoln Laboratory [11,12] utilizes two graphite strip heaters, as shown in Fig. 1. The sample, which is placed on the stationary lower heater, consists of a fine-grained Si film on an insulating substrate or layer, together with an encapsulation layer. The inset of Fig. 1 shows a cross section of a typical sample, with a 1.0-μm-thick thermally grown SiO_2 layer on a Si wafer, a 0.5-μm-thick

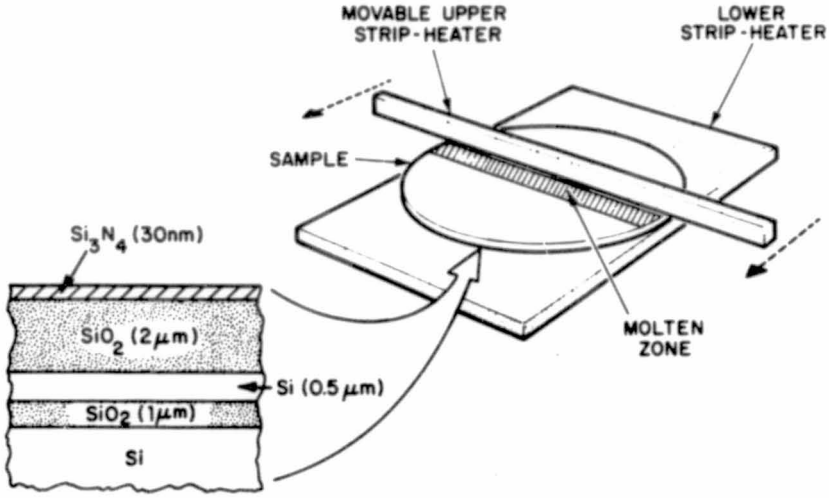

Fig. 1. Schematic diagram of sample and strip heaters used in zone-melting recrystallization of Si films.

poly-Si layer deposited by low-pressure chemical-vapor deposition (LPCVD), a 2-μm layer of CVD SiO_2 and a 30-nm layer of sputtered Si-rich Si_3N_4. The lower strip heater is used to heat the sample to a base temperature of 1100 - 1300°C, generally in a flowing Ar gas ambient. Additional radiant energy, provided by the movable upper strip heater, is used to produce a narrow molten zone in the poly-Si layer (mp of Si = 1410°C). The molten zone is then translated across the sample by scanning the upper heater, typically at ~1 mm/sec, leaving a recrystallized Si film. Films on three-inch-diameter wafers can be recrystallized over their entire surface. The thicknesses of the SiO_2 and Si layers, the composition of the encapsulation layer, the molten zone velocity, and the shape and position of the upper heater relative to the sample and lower heater all have a strong effect on the morphology and crystallography of the recrystallized films.

In InSb ZMR, encapsulation layers were found to enhance the quality of the films [7]. In ZMR of Si with the strip-heater technique, an encapsulation layer is necessary to prevent agglomeration of the molten Si zone. We have found that a composite SiO_2/Si_3N_4 encapsulant is effective in preventing agglomeration [13,14], although the role of the Si_3N_4 is not well understood. As shown in Fig. 2, in the absence of Si_3N_4 the capping SiO_2

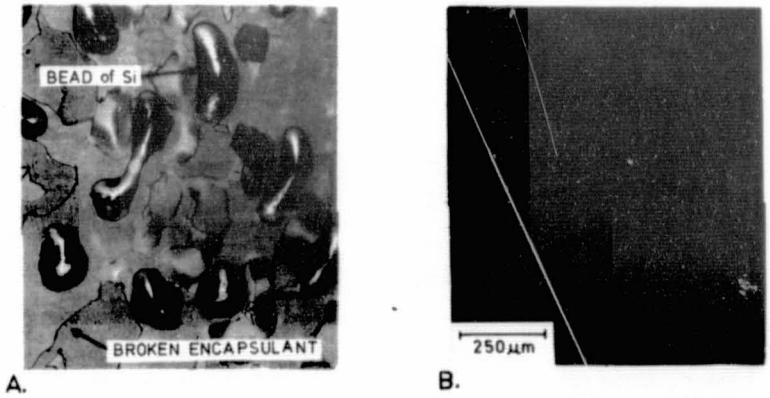

Fig. 2. Photomicrographs of zone-melting-recrystallized Si films encapsulated with (a) SiO_2 only (b) composite SiO_2/Si_3N_4 cap.

layer breaks up during ZMR and the Si film forms many droplets, whereas smooth films are obtained with the SiO_2/Si_3N_4 cap [15]. We have found that

a cap with the SiO_2 and Si_3N_4 layers in reverse sequence is also effective in preventing agglomeration. In addition, a cap layer of Si_3N_4 less than 6 nm thick, without an SiO_2 layer, has been found to enhance the melt stability and improve the surface morphology of Si films on SiO_2 substrates during laser recrystallization [16]. These observations suggest that in samples with Si_3N_4, N may be incorporated in the SiO_2 layer or may be present at the Si-SiO_2 interface during recrystallization, enhancing the wetting of SiO_2 by molten Si. (Although N was not detected either in the SiO_2 cap or at the Si-SiO_2 interface by Auger analysis [17], a monolayer or submonolayer of N at the Si-SiO_2 interface, which could significantly alter the wetting characteristics of the molten Si, would be below the Auger detection limit, ~0.1 atomic %.) Another possibility is that the Si_3N_4 layer simply enhances the mechanical strength of the 2-μm-thick SiO_2 layer.

III. FILM TEXTURE

The ZMR Si films contain highly oriented crystals [18]. Figure 3(a) is a high-magnification optical micrograph showing the starting end of a

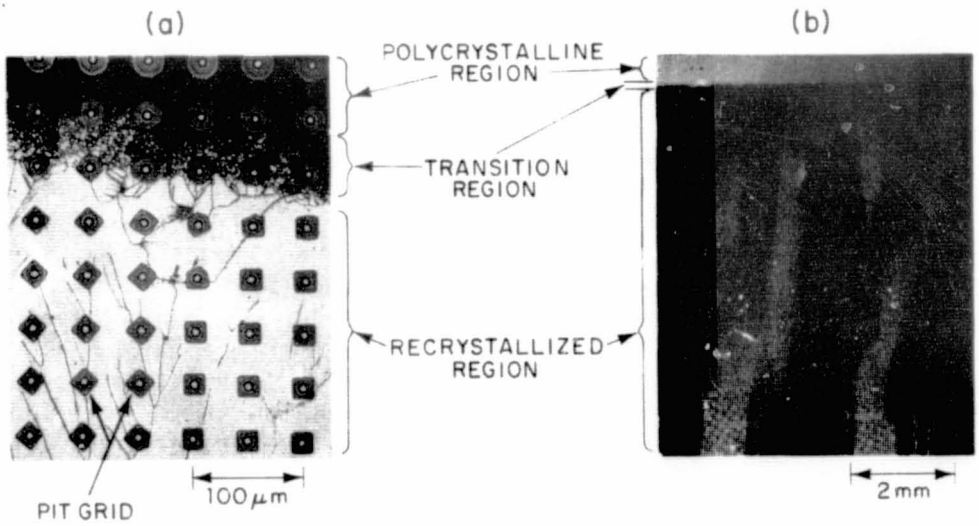

Fig. 3. Photomicrographs of the starting end of a recrystallized Si film. A grid array of etch pits has been etched into the film, which has also been etched to reveal the grain boundaries and sub-boundaries. Reflection from the etch pit facets makes crystals with different orientations stand out distinctly. (a) High magnification, (b) low magnification.

recrystallized film that has an etch pit grid [19] and has also been etched to delineate grain boundaries and other defects. Three areas are discernible: an area of very fine grained Si that was not melted, a transition region with larger grains, and an area where the Si film was completely melted and recrystallized. The square shape of the pits indicates <100> texture, and the diagonals to the pits are parallel to the <100> direction in the plane of the substrate. Away from the transition region there are two large grains, both with <100> texture, that are rotated relative to one another by about 45° in the plane of the substrate. Figure 3(b) is a micrograph showing a larger area of the same recrystallized

sample. The variation in the light intensity makes the individual grains stand out distinctly. The figure shows that the grains originate in the transition region. Within a few millimeters of this region, grains that have <100> texture and their <100> axes close to the scanning direction of the upper strip heater dominate the film.

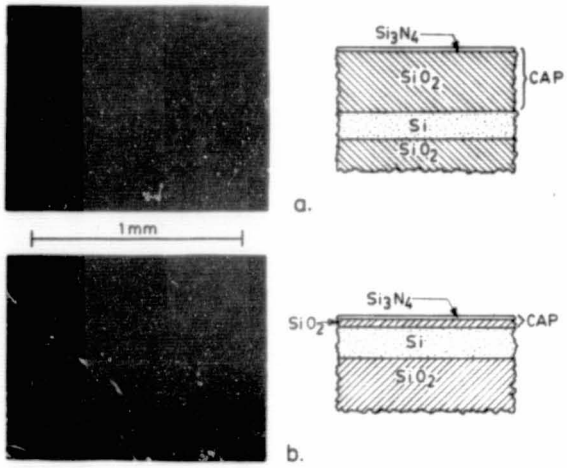

Fig. 4. Photomicrographs of recrystallized Si films with SiO_2/Si_3N_4 encapsulant in which the SiO_2 layer was (a) 2 μm thick, (b) 0.2 μm thick. In both cases the Si_3N_4 layer was 30 nm thick.

In addition to preventing agglomeration, the encapsulation layer also serves to produce a smooth surface morphology and to induce <100> texture in the recrystallized films. The former aspect is illustrated in Fig. 4 which shows optical micrographs of recrystallized Si films for two thicknesses of SiO_2 in the capping layer. For 0.2-μm SiO_2, the Si film is highly faceted, whereas it is smooth for 2-μm SiO_2. Clearly, the thicker SiO_2 cap is mechanically stronger and therefore more effective in maintaining a smooth surface.

Under the recrystallization conditions described above, the encapsulation layer induces a predominantly <100> texture in the recrystallized films. Several possible explanations for this texture [20] are based on the assumption that the interfacial energy between Si and SiO_2 is lowest for the <100> planes, making the <100> texture the most energetically favorable. If the growth of the ZMR film is seeded, other textures can occur. For example, we have fully melted a 0.5-μm-thick poly-Si film over a SiO_2 layer in which parallel slit openings were provided down to a <111> oriented Si substrate; upon solidification, the Si film had a <111> texture. However, if a <100>-

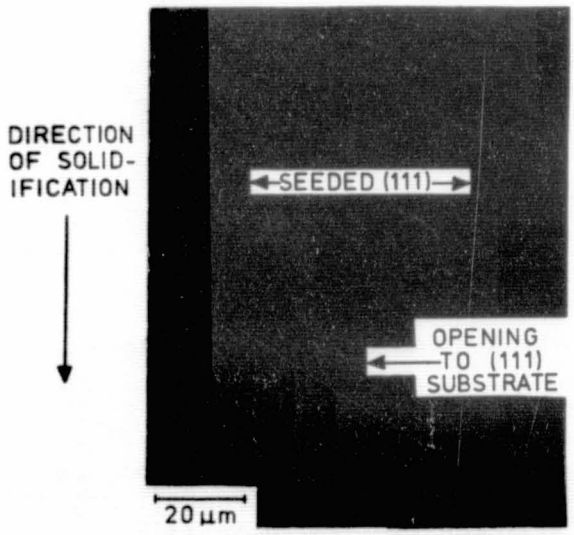

Fig. 5. Photomicrograph of recrystallized Si film, showing that growth from a <111>-textured seed is rapidly eliminated by growth from <100>-textured seeds. Etch pits indicate crystal texture and orientation. Note the approximate 6-fold symmetry of the portions of the pits located in the region recrystallized from the <111> seed.

texture seed and a <111>-texture seed both contact the same melt, then the <100> texture displaces the <111> texture, as shown in Fig. 5.

The texture of ZMR films also depends upon the speed of zone motion and the thickness of the poly-Si layer. As shown in Fig. 6, the fraction of the

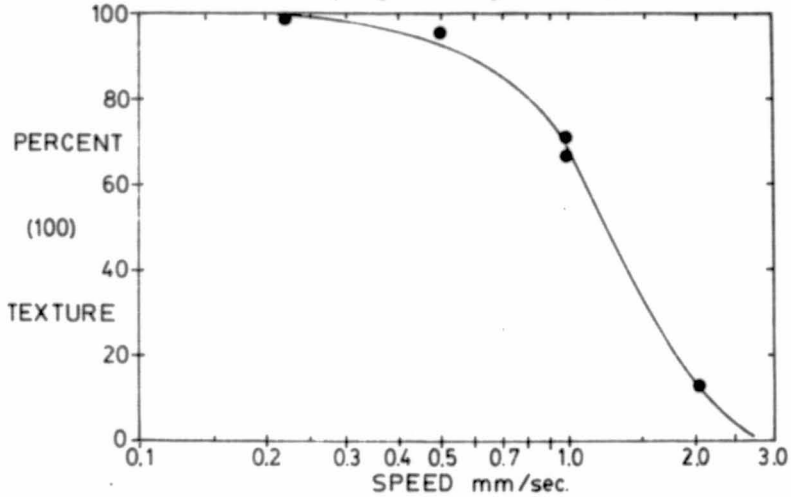

Fig. 6. Fraction of a recrystallized film having <100> texture as a function of the speed of zone motion. Data were obtained by analyzing the shapes of etch pits located along a line parallel to transition region and about 4 mm in front of it.

recrystallized film with <100> texture decreases with increasing zone speed. Films not exhibiting <100> texture are generally heavily twinned and appear dendritic, suggesting substantial undercooling of the melt at higher speeds. As the thickness of the poly-Si layer is increased, the degree of texturing decreases, consistent with the proposals that texturing is the result of the orientation dependence of Si/SiO_2 interfacial energy.

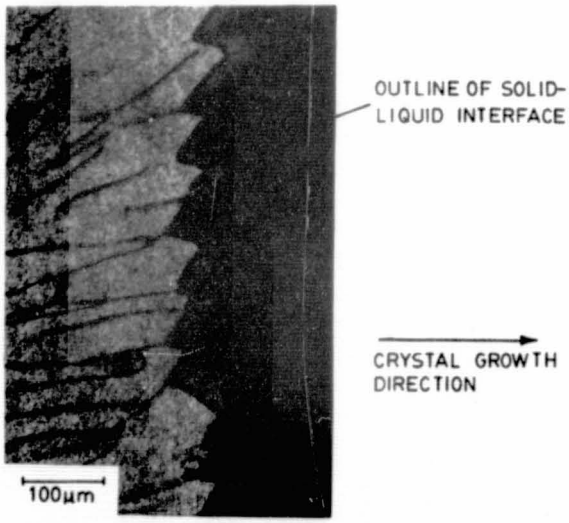

Fig. 7. Photomicrograph of recrystallized Si film that was quenched by a He gas jet during zone melting.

IV. GRAIN BOUNDARIES AND SUB-BOUNDARIES

In unseeded films recrystallized by zone melting, we can distinguish two types of crystallographic boundaries: grain boundaries and subgrain boundaries (or sub-boundaries). The number of grains and the deviation of their in-plane orientations from <100> decrease with distance from the transition region. Films with a single grain can be obtained by seeding from a single-crystal substrate [21], by cross-seeding [18], or by zone melting through planar constrictions [22], but in all cases the sub-boundaries remain.

Sub-boundaries, which consist primarily of dislocation arrays [23], have crystallographic misorientations of one degree or less. They originate at the interior corners of the faceted growth front, as illustrated by the optical micrograph in Fig. 7. To obtain this micrograph, the molten zone was rapidly quenched with a jet of He gas

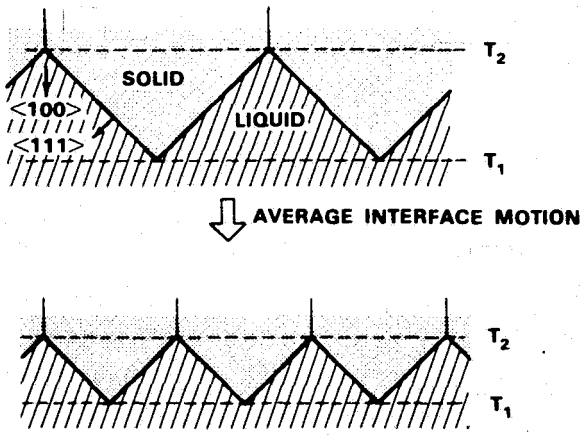

Fig. 8. Schematic of the liquid-solid interface, showing the dependence of the sub-boundary spacing on temperature gradient.

in order to delineate the solid-liquid interface at the trailing edge of the zone. Etching studies of the sample have shown that the growth front facets are close to <111> planes [20]. Because the average growth occurs in the <100> direction and the angle between <111> facets is crystallographically fixed, the spacing between the sub-boundaries is determined by the distance to which the facets extend into the melt [24], as illustrated in Fig. 8. This distance is equal to the separation between the temperature isotherms T_1 and T_2, which are characteristic of faceted growth. This growth occurs by the addition of atoms at ledges or steps that sweep rapidly across the facets. Under steady state conditions, T_2 is the temperature at which new ledges are generated at a rate such that the forward advance of the facets matches the zone scanning velocity, while T_1 is a higher temperature (slightly below the melting point of Si) at which growth along the <111> plane has a component of velocity in the <100> direction that is equal to the scanning velocity. Since the distance between the T_2 and T_1 isotherms is inversely proportional to the temperature gradient in the scanning direction, the sub-boundary spacing decreases as this gradient increases.

The temperature gradient is affected by a number of parameters. Increasing the scanning speed causes a reduction in the gradient, which results in an increase in the sub-boundary spacing, as shown in Fig. 9. This effect is illustrated in Figs. 10(a) and (b), which are optical micrographs showing sub-boundaries in 0.5-μm-thick Si films recrystallized at 0.2 and 2.0 mm/sec, respectively. The sub-boundary spacing cannot be increased indefinitely by simply increasing the scan speed, because at very high speeds dendritic growth occurs and control of the texture and orientation of the recrystallized film is reduced.

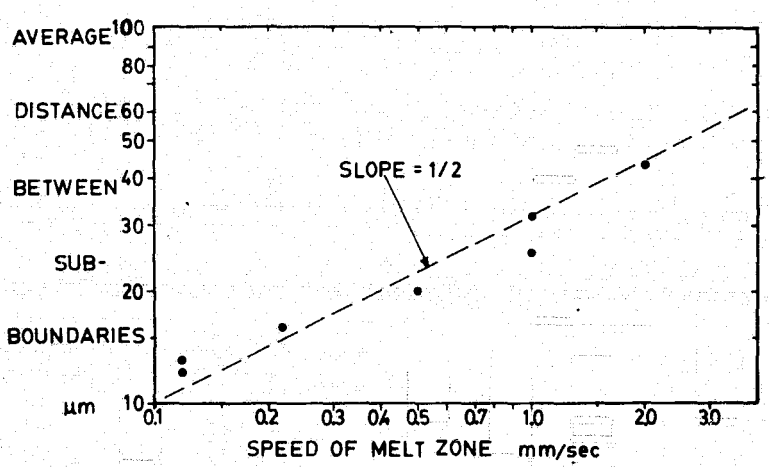

Fig. 9. Plot of the average spacing between sub-boundaries as a function of molten zone speed. These data are for <100> textured material only. At a zone speed of 2 mm/sec only about 10% of the film has <100> texture.

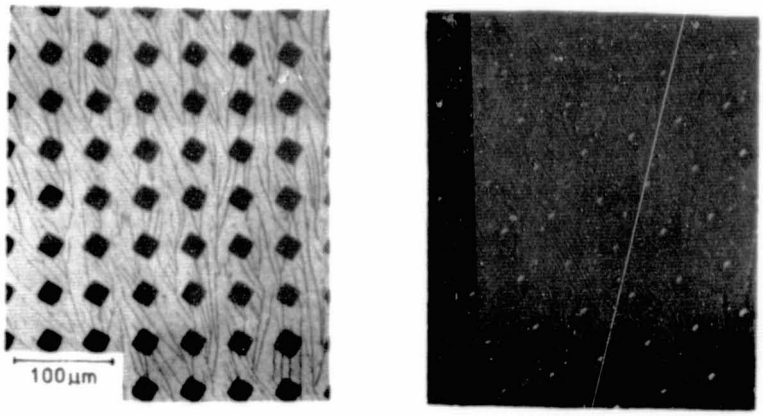

Fig. 10. Photomicrographs showing sub-boundaries in 0.5-μm-thick Si films recrystallized at speeds of (a) 0.2 mm/sec and (b) 2 mm/sec.

The shape of the upper strip heater and the separation between the sample and the upper heater affect the profile of the power incident on the Si film [25]. Figure 11 shows calculated curves of incident power versus distance on the sample surface for several different heater-sample separations and for two different heater shapes. The power has been normalized at position x = 0, directly beneath the heater. The calculations take into account the angle subtended by the heater at the sample as well as the angle at which the radiant energy is incident on the sample surface. The curves show that the incident power profiles (and thus the temperature gradient) become sharper with decreasing heater-sample separation and with smaller vertical dimension of the heater. Consistent with this result, smaller sub-boundary spacing has been observed for reduced heater-sample separation.

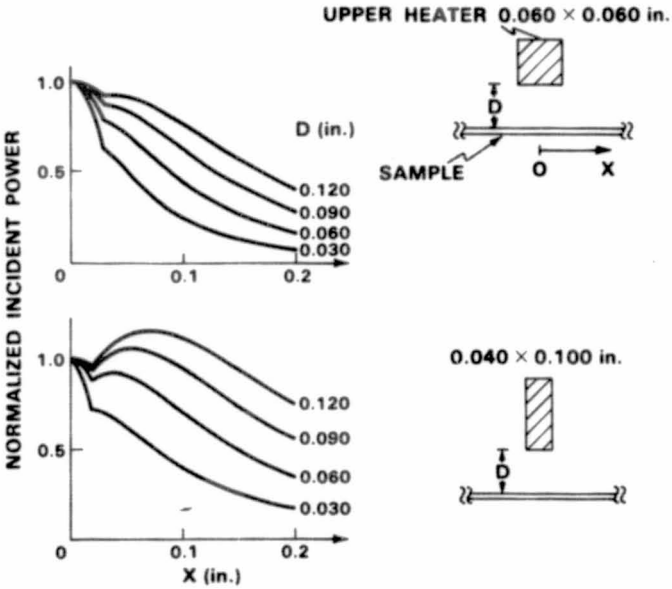

Fig. 11. Power incident on a sample from the upper strip heater as a function of position x along the sample surface. D is the heater-sample separation.

The temperature gradient at the growth interface also depends on the heat dissipation from the Si film, which is a function of the sample structure, the ambient atmosphere, and the thermal contact between the sample and lower heater. Increasing the thickness of the Si film increases the total heat of fusion which must be dissipated, and increasing the thickness of the underlying SiO_2 layer reduces the rate of heat dissipation to the substrate; both result in a decreased temperature gradient and hence an increased sub-boundary spacing (see Fig. 12). Similarly, using an ambient atmosphere with a higher thermal conductivity (He instead of Ar)

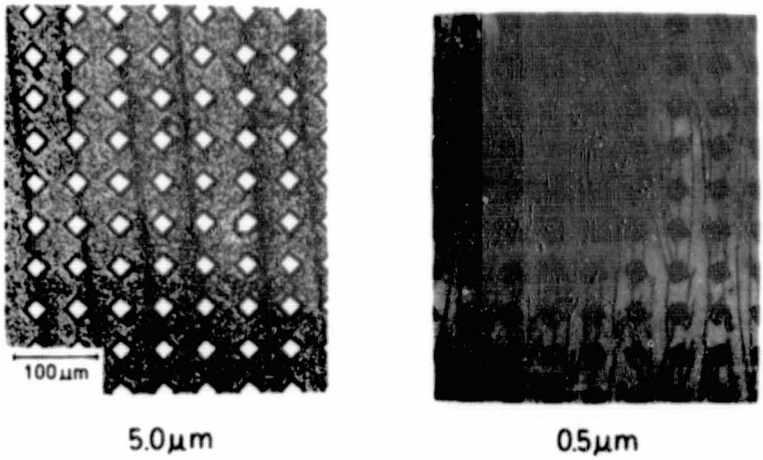

A

Fig. 12. Dependence of sub-boundary spacing on Si film thickness. (a) optical micrographs showing sub-boundaries in two Si films, 5 and 0.5 µm thick. The 5-µm-thick films had a rough surface after CVD, and the cap retained some of this roughness after recrystallization. (b) Plot of the average spacing between sub-boundaries as a function of Si film thickness.

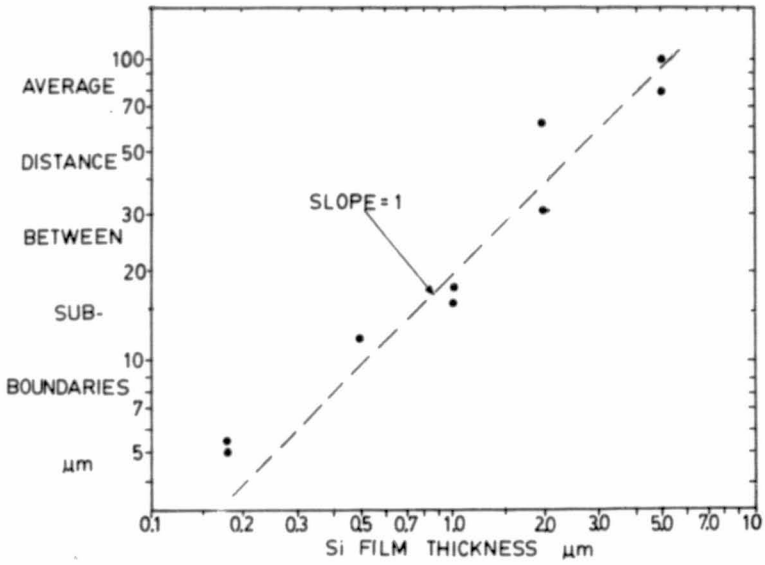

B

will increase the rate of heat dissipation from the molten zone. This occurs not only by improving direct gas conduction and convection heat transfer from the thin film, but also by improving the thermal contact between the underlying substrate and lower strip heater. This minimizes the temperature rise of the substrate due to heating from the upper strip heater, and hence results in an increased temperature gradient.

Several methods have been proposed to reduce the sub-boundary density, including repeated melting and solidification [26] and patterning the Si films into stripes and islands [27]. We have investigated a technique for entraining sub-boundaries by the use of photolithographically defined patterns that modulate the solidification front [24]. The localization of sub-boundaries at well defined positions would allow devices to be fabricated in the defect-free zones between the sub-boundaries.

Since the sub-boundaries originate at the interior corners of the faceted growth front, sub-boundaries can be entrained by controlling the positions of the facet intersections. This can be accomplished by spatially

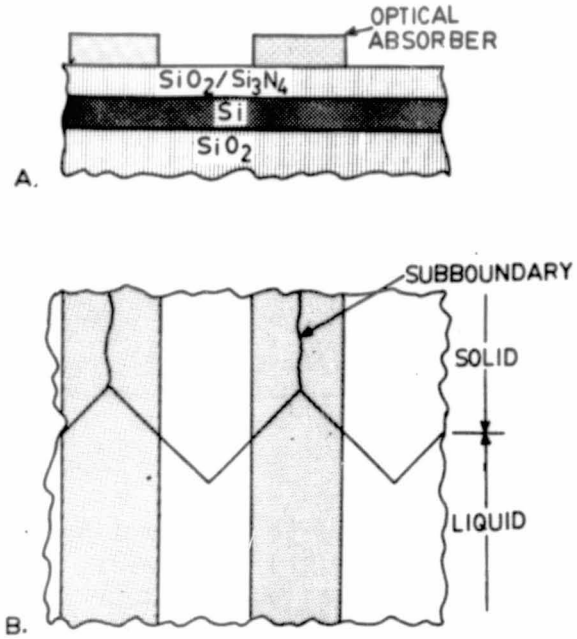

Fig. 13. Schematic diagrams of (a) cross section of sample with grating of optical absorber stripes on top of encapsulation layer (b) entrainment of sub-boundaries under the middle of the optical absorber stripes.

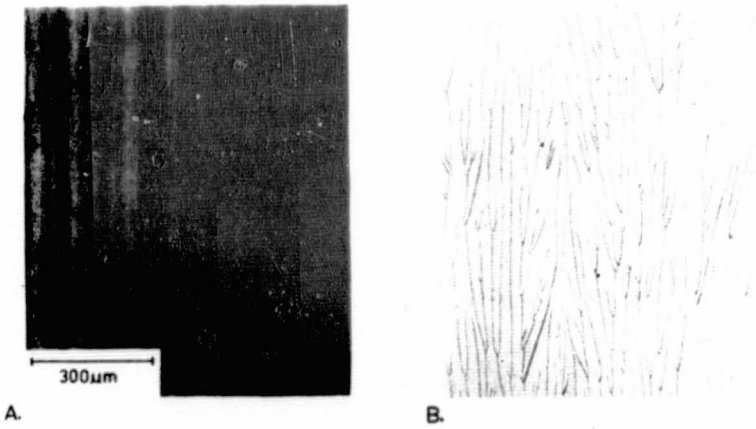

Fig. 14. (a) Sub-boundaries in Si film recrystallized with grating of carbonized photoresist stripes on top of encapsulation layer. (b) Sub-boundaries in control film recrystallized without absorber grating.

modulating the temperature at the liquid-solid interface by forming a grating above the Si film that locally enhances the absorption of the radiation incident from the upper heater, as shown schematically in Fig. 13. Since the Si is hottest under the middle of each absorbing stripe, it will be the last to freeze, and the interior corners of the growth front and hence the sub-boundaries align with the middle of the absorbing stripes. Results obtained by using carbonized photoresist as an optical absorber are shown in Fig. 14(a), where an absorber grating pattern of 50 μm wide stripes with 100 μm period was deposited on a standard encapsulated layer. The Si between the entrained sub-boundaries is free of dislocations, as determined by chemical etching, and no carbon contamination was detected by Auger analysis. Figure 14(b) shows a typical pattern of sub-boundaries from a control sample without the grating pattern.

Figure 15 illustrates the use of a grating of thin Si stripes imbedded in the encapsulation layer to achieve entrainment. Because of the high reflectivity of Si at the temperatures used in ZMR, in this case the sub-boundaries are entrained between the stripes.

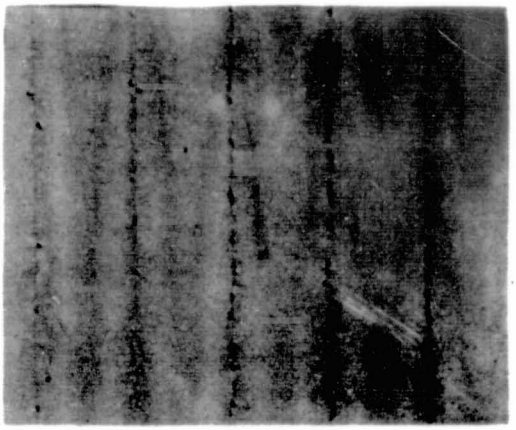

A.

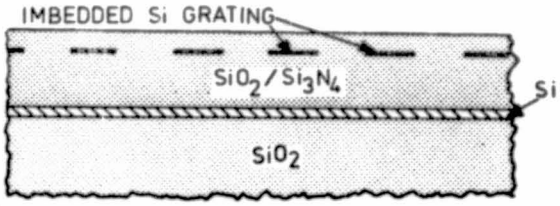

B.

Fig. 15. (a) Sub-boundaries in Si film recrystallized with grating of Si reflector stripes imbedded in encapsulation layer (b) Schematic cross-section diagram of sample with imbedded Si reflector stripes.

VI. TOPOGRAPHIC IMPERFECTIONS

Zone-melting-recrystallized Si films exhibit several types of topographic imperfections. One type is wafer warpage, which must be minimized because of the stringent flatness requirements imposed by photolithographic processes used in VLSI fabrication. We have measured [25] wafer flatness with a high-angle-of-incidence laser interferometer, which gives a fringe pattern that provides a topographic map of the sample surface, with each fringe corresponding to a constant height contour. Before recrystallization, the overall warp, peak to valley, of a 2-inch-diameter sample placed on a vacuum chuck is typically 2-4 μm, as shown in Fig. 16. This warp is comparable to that for a bulk Si wafer after device processing. To maintain this degree of flatness for recrystallized samples, well controlled heating rates and temperature profiles are necessary. After recrystallization, the samples remain relatively flat over most of the surface but show a few high points giving rise to a total warp of over 25 μm, as shown in Fig. 17(a). We have found that such high points result from imperfections that protrude from the back side of the wafer and prevent it from conforming to the flat surface of the vacuum chuck. When these imperfections are removed by mechanically lapping the back side of the sample, the overall warp decreases dramatically to less than 8 μm [Fig. 17(b)]. To simulate the effects of high-temperature device processing, the sample

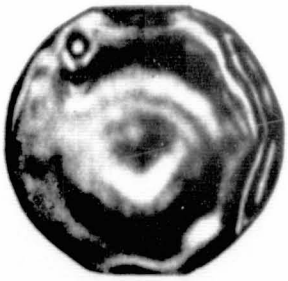

WARP < 4 μm
2 μm/FRINGE

Fig. 16. Interference pattern showing the flatness of an SOI sample before recrystallization.

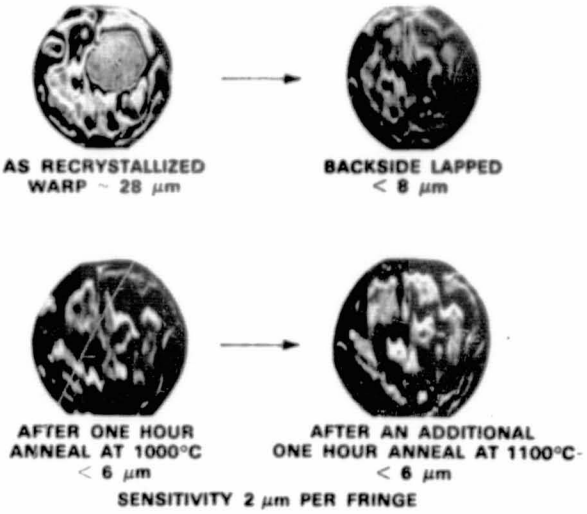

Fig. 17 Interference patterns showing the flatness of SOI sample: (a) as recrystallized; (b) backside lapped; (c), (d) after high-temperature anneals.

was then annealed for one hour at 1000°C and for another hour at 1100°C. The overall flatness was actually slightly improved, to less then 6 μm warp [Figs. 17(c) and 17(d)]. Similar results have been obtained for three-inch-diameter wafers, with total warp reduced to less than 8 to 12 μm.

Another type of topographic imperfection is the surface protrusion, as shown in the scanning electron micrographs of a recrystallized SOI film (see Fig. 18). Protrusions are believed to result from the volume expansion

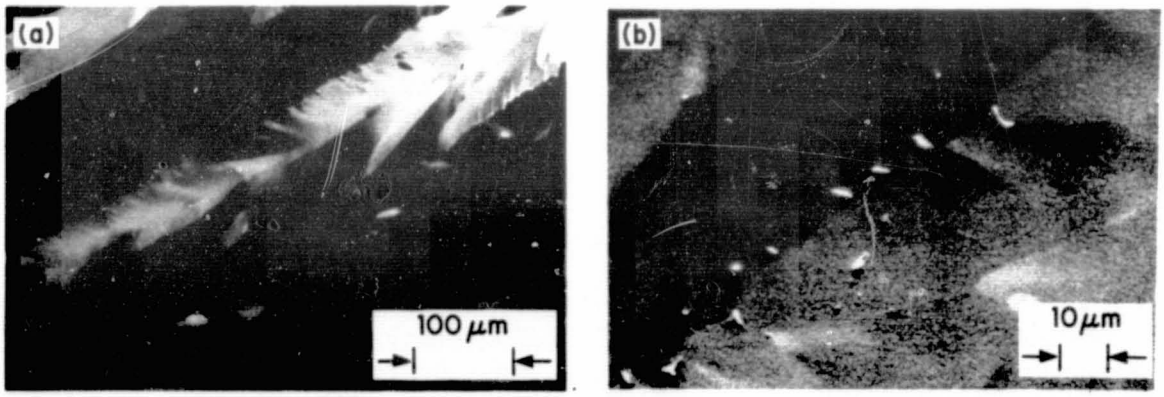

Fig. 18. (a) Micrograph of recrystallized Si film taken with a scanning electron microscope operated in the backscattering mode. The Si_3N_4/SiO_2 cap has been removed. (b) Magnified view of a small area of the film showing protrusions.

occurring during the solidification of liquid Si pools which remain after the liquid-solid interface has passed. Auger profiling studies have shown that the elemental composition of the protrusions is the same as that of the surrounding Si film [28]. Protrusions generally lie along sub-boundaries,

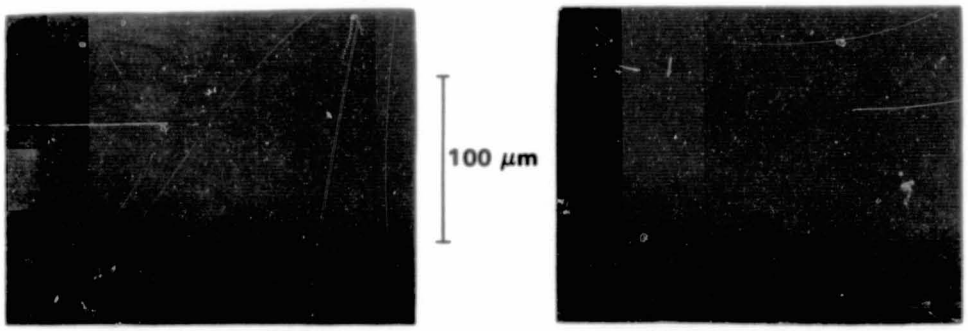

Fig. 19. Photomicrographs of recrystallized Si films illustrating the correlation between protrusion density and sub-boundary spacing.

and their density increases with increasing sub-boundary spacing (Figs. 19 and 20). Both of these observations can be understood in terms of the model developed earlier to explain sub-boundary formation [24]. The sub-boundaries form at the trailing intersections of the <111> facets, where liquid pools of Si, if any, would be trapped as the melt front advances. A sharper temperature gradient, which results in a smaller sub-boundary spacing, also stabilizes the liquid-solid interface against small thermal fluctuations that would give rise to protrusions, and hence decreases the protrusion density. With sharper temperature gradients, two-inch-diameter SOI films nearly free of protrusions have been obtained.

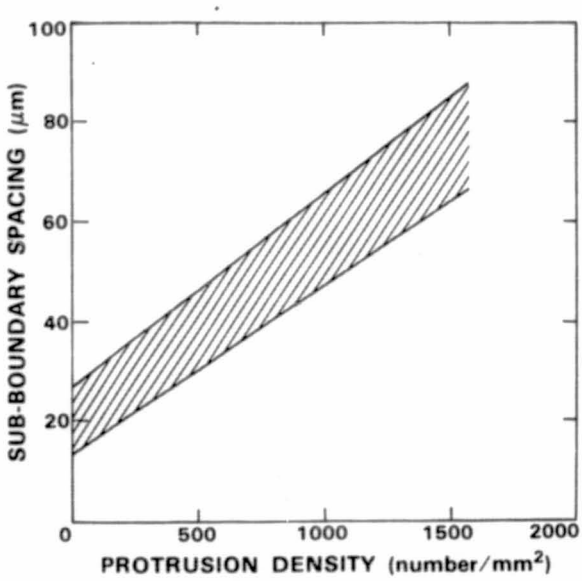

Fig. 20. Plot of sub-boundary spacing vs protrusion density. Data points for 85% of the samples examined fall in the shaded region.

VII. MOS DEVICES AND CIRCUITS

The electrical characteristics of ZMR Si films have been extensively studied [29-34]. Thin-film resistors and n-channel MOSFETs have been used [31] to evaluate the majority carrier transport properties. The sub-boundaries, which are the predominant defects in the material, have very little effect on majority carrier transport and MOS device performance. N-channel MOSFETs with electron transport parallel or perpendicular to the sub-boundaries show nearly identical surface electron mobilities. This is consistent with measurements on thin-film resistors, which indicate that the sub-boundary trapping state density is low enough that sub-boundaries do not produce a large potential barrier to impede carrier transport. The grain boundaries in the films, however, have been found to cause a significant reduction in conductivity and degradation of MOSFET performance [35].

The most important application of SOI materials is in high-density and high-speed integrated circuits. Higher packing density can be achieved because of the simplicity of device isolation, and higher operating speeds result from the reduction in parasitic capacitance. As we have previously reported [29,32], both n- and p-channel MOSFETs fabricated on recrystallized Si films exhibit electrical characteristics comparable to those of single-crystal Si devices. To carry out a more critical evaluation of the ZMR SOI films for integrated circuit applications, we have designed and fabricated a CMOS test circuit chip [34]. The test chip, based on a 5 μm design rule, contains n- and p-channel transistor arrays, ring oscillators, inverter chains, and various test devices for process control. Approximately 100 test chips were fabricated on each of three wafers.

To evaluate the uniformity of the SOI films we have investigated the performance of the n- and p-channel transistor arrays, each consisting of approximately 500 parallel transistors. The overall yield of functional arrays exceeds 90% when obvious fabrication defects (determined by microscopic inspection) are discounted. Assuming that each of the failed arrays contains only one defective device, the transistor failure rate is $\sim 2 \times 10^{-4}$. The operating characteristics of the functional transistor arrays are quite uniform from chip to chip, with a variation of less than ± 5%.

Measurements have also been made on the 31-stage ring oscillators fabricated on the test chips. The yield is similar to that for the transistor arrays. The typical characteristics of a functional oscillator at $V_D = 5$ V are a switching delay time and dissipated power of 2 ns and 0.13 mW per stage, respectively, for a power-delay product of 0.26 pJ. The operating speed can be attributed to the high carrier mobilities in the recrystallized Si films and the reduced parasitic capacitance of the SOI structure.

VIII. CONCLUSION

A zone-melting recrystallization technique using graphite-strip heaters has been developed. A composite Si_3N_4/SiO_2 encapsulating layer prevents agglomeration of the molten Si film, insures a smooth recrystallized surface, and induces a strong <100> texture. The recrystallized films contain widely spaced grain boundaries, which can be eliminated by several techniques, and many sub-boundaries within each grain. In addition, the films are susceptible to some topographic imperfections. The overall wafer warpage has been substantially reduced, approaching the stringent flatness requirements needed for VLSI applications. The protrusion density and sub-boundary spacings, which are inversely correlated, can be understood in terms of the temperature gradient at the liquid-solid interface during recrystallization.

We have performed extensive electrical measurements on the recrystallized films. The majority-carrier transport properties of ZMR Si films are comparable to those of single-crystal Si and are essentially unaffected by the presence of sub-boundaries, the predominant defect in the films. High yields of good quality transistor arrays and ring oscillators have been obtained for CMOS test chips.

Although the Si films we have prepared by ZMR are too thin for conventional solar cells, the ZMR technique using graphite strip heaters may be adaptable for solar cell applications. In an effort [36] to achieve this objective, much thicker Si films (5 - 50 μm) are being recrystallized and characterized for solar cells. Two approaches are being explored in that work, one in which the Si is recrystallized on conducting substrates and the other in which all electrical contacts are made on the top surface of films on insulating substrates. Alternatively, the use of unconventional techniques such as light trapping [37] might make it possible to fabricate efficient cells with films comparable in thickness to those we have prepared. We note that the scan rate employed in ZMR with graphite strip heaters, 1 mm/sec, is comparable to that used in various Si ribbon growth processes. For a 3-inch-wide substrate, this rate corresponds to an area recrystallization rate of 45 cm/min. Because of the ready scalability of graphite systems, we expect that our ZMR technique can be scaled to achieve even higher area production rates.

ACKNOWLEDGEMENT

The authors acknowledge the expert technical assistance of M. J. Button, M. C. Finn, R. W. Mountain, and P. M. Nitishin, and helpful discussions with R. L. Chapman, D. J. Silversmith, H. I. Smith, and A. J. Strauss. This work was sponsored by the Department of the Air Force and the Defense Advanced Research Projects Agency.

REFERENCES

1. Laser and Electron Beam Processing of Materials, edited by C. W. White and P. S. Peercy (Academic Press, New York, 1980).

2. Laser and Electron Beam-Solid Interactions and Material Processing, edited by J. F. Gibbons, L. D. Hess, and T. W. Sigmon (North Holland, New York, 1981).

3. Laser and Electron Beam Interactions with Solids, edited by B. R. Appleton and G. K. Celler (North Holland, New York, 1982).

4. Laser-Solid Interactions and Transient Thermal Processing of Materials, edited by J. Narayan, W. L. Brown, and R. A. Lemons (North Holland, New York, 1983).

5. British Patent 691,335, "Improvements in or Relating to Methods of Making Luminescent Screens," E. Leitz, May 13, 1953.

6. J. Maserjian, Solid-State Electron. 6, 477 (1963).

7. A. R. Billings, J. Vac. Sci. Technol. 6, 757 (1969).

8. W. J. Williamson, J. Vac. Sci. Technol. 6, 765 (1969).

9. See J. Cryst. Growth for an issue devoted to SOI technology (to be published, 1983).

10. J. C. C. Fan, H. J. Zeiger, and P. M. Zavracky, Proceedings of the National Workshop on Low Cost Polycrystalline Silicon Solar Cells, Dallas, May 1976, T. L. Chu and S. S. Chu, eds. (Southern Methodists University, Dallas, 1976), p. 89.

11. M. W. Geis, H. I. Smith, D. A. Antoniadis, D. J. Silversmith, J. C. C. Fan, and B-Y. Tsaur, Electronic Materials Conf., Santa Barbara, CA, 1981; and J. C. C. Fan, M. W. Geis, B-Y. Tsaur, IEDM Technical Digest (Washington, DC, 1980), p. 845.

12. J. C. C. Fan, B-Y. Tsaur, R. L. Chapman, and M. W. Geis, Appl. Phys. Lett. 41, 186 (1982), and reference therein.

13. E. W. Maby, M. W. Geis, Y. L. LeCoz, D. J. Silversmith, R. W. Mountain and D. A. Antoniadis, IEEE Electron Dev. Lett. EDL-2, 241 (1981).

14. We note that encapsulants prepared by different CVD processes have also been effective. See for example H. W. Lam, R. F. Pinizzotto, S. D. S. Malhi, and B. L. Vaandrager, Appl. Phys. Lett. 41, 1083 (1982).

15. M. W. Geis, J. Vac. Sci. Technol. A 1, 716 (1983).

16. T. I. Kamins, J. Electrochem. Soc. 128, 1824 (1981).

17. J. C. C. Fan, B-Y. Tsaur, and M. W. Geis, J. Cryst. Growth (to be published).

18. M. W. Geis, H. I. Smith, B-Y. Tsaur, J. C. C. Fan, E. W. Maby, and D. A. Antoniadis, Appl. Phys. Lett. 40, 158 (1982).

19. K. A. Bezjian, H. I. Smith, J. M. Carter, and M. W. Geis, J. Electrochem. Soc. 129, 1848 (1982).

20. M. W. Geis, H. I. Smith, B-Y. Tsaur, J. C. C. Fan, D. J. Silversmith, and R. W. Mountain, J. Electrochm. Soc. 129, 2812 (1982).

21. J. C. C. Fan, M. W. Geis, and B-Y. Tsaur, Appl. Phys. Lett. 38, 365 (1981).

22. H. I. Smith, H. A. Atwater, and M. W. Geis, Meeting of the Electrochemical Society, Montreal, Canada, May 9-14, 1982, Extended Abstracts, p. 257.

23. R. F. Pinizzotto, H. W. Lam, and B. L. Vaandrager, Appl. Phys. Lett. 40, 388 (1982).

24. M. W. Geis, H. I. Smith, D. J. Silversmith, and R. W. Mountain, J. Electrochem. Soc. 130, 1178 (1983).

25. C. K. Chen, M. W. Geis, B-Y. Tsaur, R. L. Chapman, and J. C. C. Fan, Electronic Materials Conference, Burlington, VT (1983).

26. K. A. Jackson and C. E. Miller, J. Cryst. Growth 42, 364 (1977).

27. H. J. Leamy, Ref. 3, p. 459.

28. Unpublished results.

29. B-Y. Tsaur, M. W. Geis, J. C. C. Fan, D. J. Silversmith, and R. W. Mountain, Appl. Phys. Lett. 39, 909 (1981).

30. B-Y. Tsaur, J. C. C. Fan, M. W. Geis, D. J. Silversmith, and R. W. Mountain, IEDM Tech. Digest (Washington, DC, 1981), p. 232.

31. B-Y. Tsaur, J. C. C. Fan, M. W. Geis, D. J. Silversmith, and R. W. Mountain, IEEE Electron Dev. Lett. EDL-3, 79 (1982).

32. B-Y. Tsaur, M. W. Geis, J. C. C. Fan, D. J. Silversmith, and R. W. Mountain, Ref. 3, p. 585.

33. B-Y. Tsaur, J. C. C. Fan, and M. W. Geis, Appl. Phys. Lett. 41, 83 (1982).

34. B-Y. Tsaur, J. C. C. Fan, R. L. Chapman, M. W. Geis, D. J. Silversmith, and R. W. Mountain, IEEE Electron Dev. Lett. EDL-3, 398 (1982).

35. E. W. Maby and D. A. Antoniadis, Appl. Phys. Lett. 40, 691 (1982).

36. Private communication with H. I. Smith, Department of Electrical Engineering and Computer Science, M.I.T.

37. E. Yablonovitch and G. Cody, IEEE Trans. Electron. Devices ED-29, 300 (1982).

DISCUSSION

JOHNSON: What surprised me about the work is that all the subgrain boundaries seem not to be very electrically active. It is contrary to what is normally found in all the polycrystalline material that people have looked at. They tend to be always the worst boundaries. The crystallographic twin-related boundaries may or may not be electrically active. Can you make any comment on that?

CHEN: I think they certainly are electrically active for minority carrier devices. For the MOSFETS and the CMOS circuits, they are majority carrier devices, in which case they have very little effect. I had mentioned that, for example, a microsecond lifetime had been measured for the electron carriers, and this was in the as-recrystallized without any kind of entrainment schemes or anything, and for very thin silicon films. We expect that we can entrain the sub-boundaries and build devices in between; then, of course, it is no longer a problem.

WARGO: How far do you think you can push the entrainment process? How far away can you get your cell boundaries?

CHEN: It depends upon what kind of thermal gradient you can get. If you can get a very shallow thermal gradient, you can, in principle, continue to separate the sub-boundaries. Basically, the problem is, if you try to entrain the sub-boundaries at a very large separation, the thermal gradients are amenable to small sub-boundaries facing, they will just form in between. The question really is, how well can you control the thermal gradients, and I can't answer that yet.

ABBASCHIAN: Regarding the texture, I see no difference in what you are seeing with what people have seen in casting, and what they call columnar growth or columnar grains. Next to the chilled mold you have equiax grains, then you see the columnar grains, which are mostly oriented in <110> or <100> direction depending on the material, and that is similar to what you have. I suggest you check on that.

The second thing is, of course, they use columnar grains in contrast with texture, which is used in cold working and hot rolling. When you solidify a casting, you have grains that are oriented. They are elongated and they are oriented in a certain direction, and those are called columnar grains, which is similar to what you have.

FAN: Let me answer this. They are not exactly the same, because if you do not have the SiO_2 cap, the crystallized region does not orient itself vertically. It is random. It is only with SiO_2 cap that it has texture.

ABBASCHIAN: If you do not have an SiO_2 cap, the crystals are being nucleated toward the top; then you don't develop the columnar grains. So, in order to form the columnar grains, you have to prevent heterogeneous nucleation, and that's what it is like in casting. Your subgrain boundary spacing is again similar to what other people call dendrite arm spacing or

cellular spacing, which should be proportional to the temperature gradient or the growth rate or the cooling rate, whichever you feel like using.

LEIPOLD: Did you observe an upper limit to the rate of crystallization?

CHEN: No. I did not. I pushed it up to 5 millimeters per second, and I was still able to see the same kinds of characteristics that you see here. Problem-wise, it gets a little bit more difficult to control.

LEIPOLD: I was concerned with any changes in the shape of the crystallization front as one got to the higher-speed regime.

CHEN: You see sub-boundaries and protrusions attached.

CISZEK: Do you see a proportional increase in the subgrain angle as you try to separate these subgrains, and roughly what kinds of magnitudes do these subgrain boundaries have for misorientation angle?

CHEN: Misorientations are roughly up to a degree.

CISZEK: Do they increase as you increase in spacing?

CHEN: I don't think that study has actually been done.

SCHWUTTKE: I would like to comment on your grain boundaries and your remark that you do majority carrier devices, and so you are not interested in the recombination.

CHEN: I didn't say I wasn't interested.

SCHWUTTKE: I think if you go to a high packing density you will observe that your leakage currents are caused by your grain boundaries. Even if you use majority carrier devices, this would be a limiting factor for high packing densities.

FAN: We have made MOSFETs with a channel length low-order, to about 2 μm, with no problem.

SCHWUTTKE: You stay within the good area.

FAN: We have to eliminate them for a large density.

CHEN: For really high packing densities you have to put them either where you know where they are, or eliminate them completely.

N84 28639 D25

NONEQUILIBRIUM CRYSTAL GROWTH DURING LASER ANNEALING OF SILICON*

C. W. White
Oak Ridge National Laboratory
Oak Ridge, TN 37830

I. INTRODUCTION

In pulsed-laser annealing of silicon, the deposition of energy from the laser into the near-surface region leads to melting followed by liquid-phase-epitaxial regrowth from the substrate.[1-5] The velocity of the interface during solidification can be several meters/sec.[11] At these velocities, recrystallization of the melted region takes place under conditions that are far from equilibrium at the interface. Several studies[6-10] have shown that implanted or deposited Group III, IV, or V impurities can be incorporated into substitutional lattice sites as a result of pulsed-laser annealing even when the dopant concentration greatly exceeds the equilibrium solubility limit. Here we review the systematic studies of dopant (Group III, IV, or V) incorporation into silicon as a result of pulsed-laser annealing. At low concentrations, dopant profiles measured after laser annealing can be compared to model calculations for redistribution by liquid-phase diffusion in order to determine the interfacial distribution coefficient (k').[6] At high concentrations there is a limit (C_S^{max}) to dopant incorporation into substitutional lattice sites.[6] The mechanisms[9] which limit dopant incorporation will be discussed as well as the dependence of k' and C_S^{max} on crystal orientation. Finally, measurements[12,13] of interface temperatures, temperature profiles, and thermal gradients during rapid solidification will be summarized.

II. EXPERIMENTAL

Group III, IV, or V impurities were implanted into both (100) and (111) Si to doses in the range of 10^{15}–10^{17}/cm^2. The implant energies were chosen to give a projected range of ∿800 Å. Laser annealing was carried out in air using either a pulsed ruby (6934 Å, 12 x 10^{-9} s) or pulsed XeCl laser (3080 Å, trapezoidal pulse shape, ∿35 ns full width at half maximum). Under these conditions, regrowth velocities up to ∿6 m/s were achieved during solidification. Analysis of the implanted samples was carried out using RBS-ion channeling measurements to determine the dopant profiles and substitutional concentrations as a function of depth. Selected crystals were examined by transmission electron microscopy (TEM) to determine the microstructure in the near-surface region.

III. DOPANT INCORPORATION AT LOW CONCENTRATIONS

For Group III, IV, or V dopants at low concentrations, the dopant is trapped into substitutional lattice sites as a result of pulsed-laser annealing in the absence of any cell formation or dopant precipitation. In these cases, the interfacial distribution coefficient (defined as $k' = C_S/C_L$ where C_S and C_L are dopant concentrations in the solid and liquid phase at the interface) can be determined by comparing measured dopant profiles after

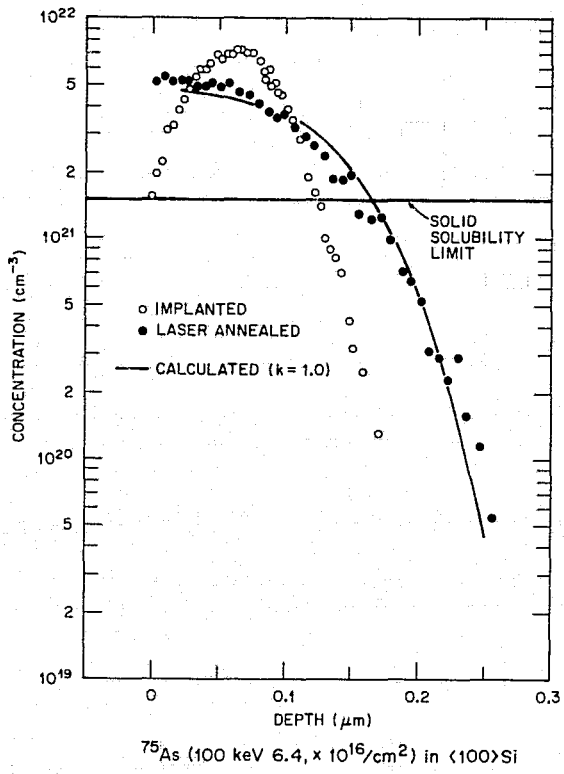

Fig. 1. Dopant profiles for ^{75}As (100 keV, 5.4 x 10^{16}) in (100) Si compared to model calculations. From Ref. 6.

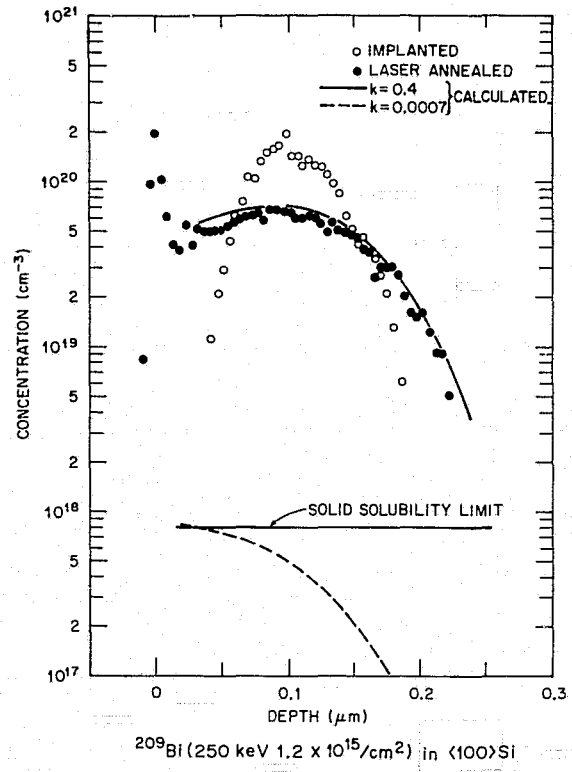

Fig. 2. Dopant profiles for ^{209}Bi (250 KeV, 1.1 x $10^{15}/cm^2$) compared to model calculations. From Ref. 6.

laser annealing to model calculations for dopant redistribution by liquid-phase diffusion during solidification.[6] In the calculations k' is treated as a fitting parameter and the best fit value for k' during solidification is determined by least squares analysis. Figure 1 shows an example for the case of ^{75}As in (100) Si. Following laser annealing, RBS-channeling measurements show that As is >95% substitutional in the lattice even though the concentration exceeds the solubility limit by a factor of 4 in the near-surface region. This demonstrates the formation of a supersaturated alloy as a consequence of high speed solidification. The solid line in Fig. 1 is a profile calculated assuming that k' = 1.0. The agreement with the experimentlly measured profile after laser annealing (solid circles) is excellent. The value determined for k' is considerably higher than the equilibrium value (k_0 = 0.3).

Figure 2 shows similar results for ^{209}Bi in (100) Si. During solidification, approximately 15% of the implanted Bi is zone refined to the surface, but that remaining in the bulk is substitutional in the regrown lattice even though the concentration exceeds the solubility limit by almost two orders of magnitude. The dopant profile can be fit with a value for k' = 0.4, which is much higher than the equilibrium value (7 x 10^{-4}). If solidification occurred under conditions of local equilibrium at the interface, the dotted profile would result and essentially all of the Bi would have zone refined to the surface. The large departure from conditions of local equilibrium at the interface is brought about by the very rapid regrowth velocity achieved during pulsed laser annealing (V ∿ 4.5 m/s in the case of Fig. 1 and Fig. 2).

TABLE I
Comparison of distribution coefficients under equilibrium (k_0) and laser annealed (k') regrowth conditions.

Dopant	k_0	k'
B	0.80	1.0
P	0.35	1.0
As	0.30	1.0
Sb	0.023	0.7
Ga	0.008	0.2
In	0.0004	0.15
Bi	0.0007	0.4

Table I summarizes[9] values for k' determined as described above for several impurities in silicon compared to equilibrium values (k_0). Values for k' were determined at a growth velocity of 4.5 m/s except in the cases of B, P, and Sb where a velocity of 2.7 m/s was used. In every case $k' > k_0$ which reflects the nonequilibrium nature of this high speed liquid-phase-epitaxial regrowth process. The increased values for k' relative to k_0 demonstrate that at these velocities solute atoms do not exchange a sufficient number of times across the interface to establish their equilibrium concentrations in the solid and liquid phases before being permanently incorporated into the solid. This process is referred to as solute trapping.

IV. DEPENDENCE ON GROWTH VELOCITY

Values for k' depend on growth velocity[14-16] as demonstrated in Fig. 3. Growth velocities of 1.5, 4.5, and 6.0 m/s were achieved by ruby laser annealing with the substrate held at 650 K, 300 K, and 100 K respectively.

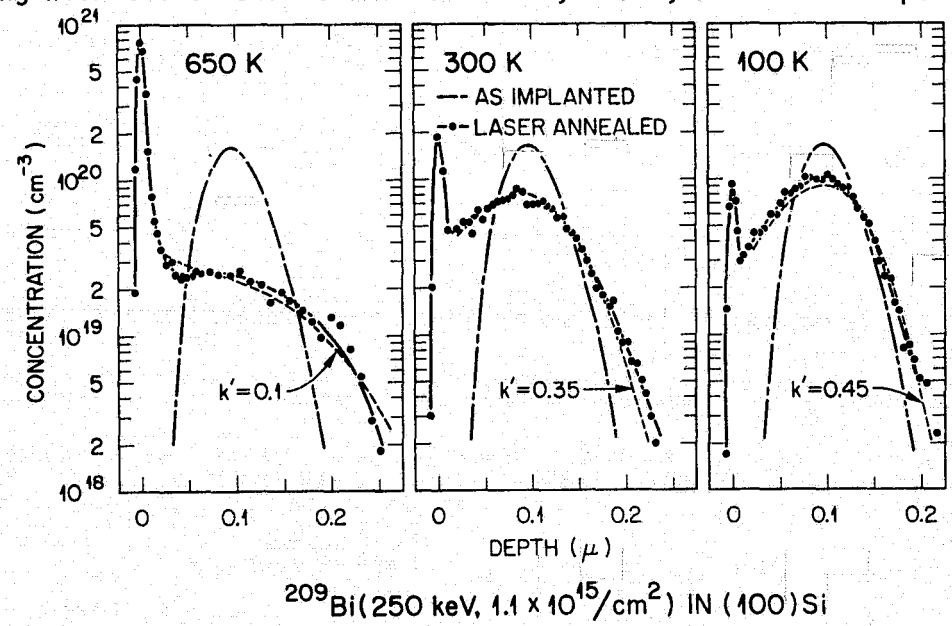

Fig. 3. Profiles for ^{209}Bi (250 KeV, 1.1 x 10^{15}/cm^2) in (100) Si Ruby laser annealed at different temperatures. From Ref. 16.

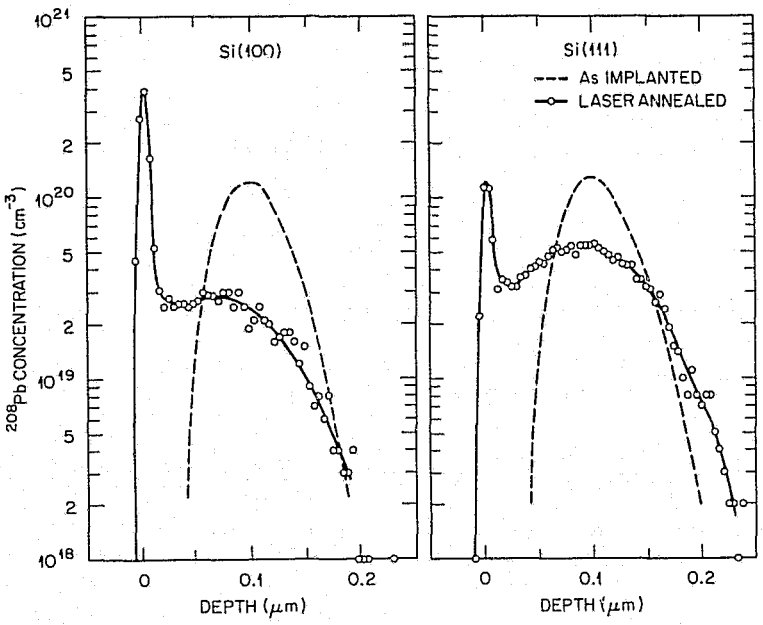

Fig. 4. Profiles of ^{208}Pb (250 keV, 8.8 x 10^{14}/cm^2) in (100) and (111) Si following Ruby laser annealing (1.3 J/cm^2).

At the lowest velocity ~55% of the Bi is zone refined to the surface and the value determined for k' is 0.10. At the highest velocity only 5% is zone refined to the surface and the value for k' is 0.45. The dependence of k' on growth velocity demonstrated in Fig. 3 is expected because as V ⟶ 0, k' ⟶ k_0. A dependence of k' on growth velocity has been reported for the case of In in silicon,[17] and a similar dependence should be observable for all Group III, IV, and V impurities in silicon.

V. DEPENDENCE ON CRYSTAL ORIENTATION

In certain velocity ranges, the value for k' is dependent on crystal orientation.[18] An example is shown in Fig. 4 for the case of ^{208}Pb in (100) and (111) Si. The implanted crystals were laser annealed under identical conditions (Ruby, 1.3 J/cm^2, 12 x 10^{-9} s, V ~ 4.5 m/s) but considerably more Pb is retained in the bulk of the (111) crystal. This implies that the value for k' is greater in the (111) case even though the growth velocity is the same. A dependence of k' on crystal orientation has been observed in the case of Bi, In, Ga, Sn, and Pb in silicon.

The dependence of k' on crystal orientation has been attributed to a larger interfacial undercooling on the (111) surface, compared to the (100) surface.[19] As discussed in Ref. 20, growth velocity depends on the fraction of sites available for crystallization and the interfacial undercooling. For the (111) surface, the fraction of sites available for crystallization is less than that on the (100) surface. Consequently, the interfacial undercooling must be greater on the (111) surface in order to have the same growth velocity. Estimates indicate that interfacial undercoolings up to several hundred degrees might be expected.[19] Using time resolved x-ray diffraction techniques, it has become possible to measure interface temperatures and thermal gradients during rapid solidification.[12,13] The results of these measurements will be discussed in the next section.

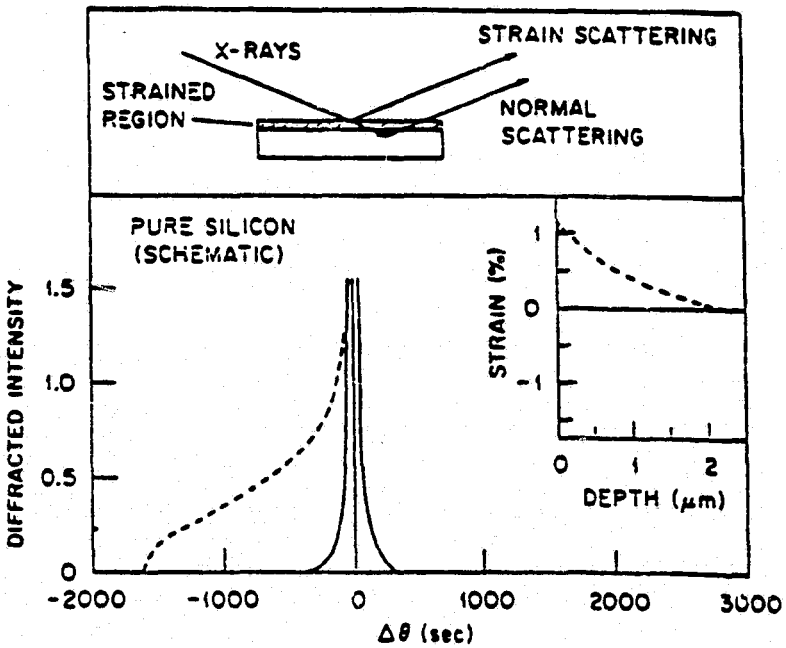

Fig. 5. Schematic representation of the scattering geometry (upper) and the extended Bragg scattering (lower) expected from the near surface strains. From Ref. 13.

VI. MEASUREMENTS OF INTERFACE TEMPERATURES, TEMPERATURE PROFILES, AND THERMAL GRADIENTS DURING RAPID SOLIDIFICATION

In crystal growth at any velocity, knowledge of the interface temperature, temperature profile and the thermal gradients is essential in order to characterize the growth process. These quantities are extremely difficult to measure experimentally and the measurement problems are compounded during rapid solidification because the time scale is so short. Recent experiments[12,13] have shown that these quantities can be measured with nanosecond time resolution using time resolved x-ray diffraction techniques. Here we summarize the measurement technique and the results.

Figure 5 illustrates schematically the idea behind the experiment. The upper part illustrates the scattering geometry for the case of a thick crystal with a thin thermally expanded surface layer (such as that produced as a result of the absorption of laser energy). The lower part illustrates schematically the expected x-ray scattering near a Bragg reflection for such a crystal. The solid line indicates the Bragg scattering from the unstrained substrate while the dotted line illustrates the extended scattering expected in the vicinity of the Bragg reflection arising from the thermal strain distribution indicated in the insert. The lattice parameter in the strained region is different from that of the bulk thus accounting for the extended Bragg scattering. The strain distribution in the near-surface region can be determined from the extended Bragg scattering "rocking curve" depicted in Fig. 5 using dynamical x-ray diffraction theory. The rocking curve illustrated in Fig. 5 is measured on a point by point basis using single pulses of radiation from a synchrotron source. Each point on the rocking curve must be measured at a fixed time delay after the firing of

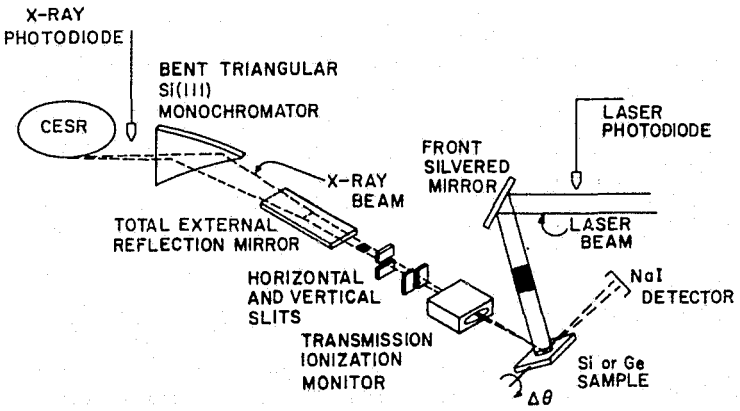

Fig. 6. Experimental apparatus (schematic for time-resolved x-ray diffraction studies.

the laser in order to provide a measurement of the time resolved rocking curve (and therefore a time resolved strain distribution). The time resolved temperature profiles are determined from thermal expansion analysis of the near-surface strains. This technique has been used to determine temperature profiles to a depth of several microns in the crystal during laser annealing.[13]

The experimental set-up for the experiment is illustrated schematically in Fig. 6. Single pulses of 1.5 Å x-rays (∿0.1 ns pulse duration time, 2.5 μsec separation between pulses, ∿25,000 x-ray photons per pulse) are incident on the Si crystal as shown. Pulses from the Q-switched Ruby laser (15 ns time duration) were synchronized with the x-ray pulses using coincidence circuits and variable time delays. After the firing of the laser, the multichannel analyzer was gated on to measure the diffracted photons from the following x-ray pulse. Since only 1–10 diffracted photons per pulse were expected, repeated measurements at each angle and delay time were required. The time delay between the laser pulse and the probing x-ray pulse was determined directly using an oscilloscope to measure the time delay between the outputs of the two photodiodes corrected for differences in cable lengths. The time resolution achieved was ±3 ns and was determined by the timing jitter in the firing of the laser.

Figure 7 shows Bragg x-ray scattering profiles near the (111) reflection on (111) oriented silicon measured at 20 ns, 55 ns, and 155 ns following a ruby laser pulse of 1.5 J/cm^2. The x-ray scattering intensity resulting from the laser pulse ranges out to ∿450 s for the 20 ns and 55 ns

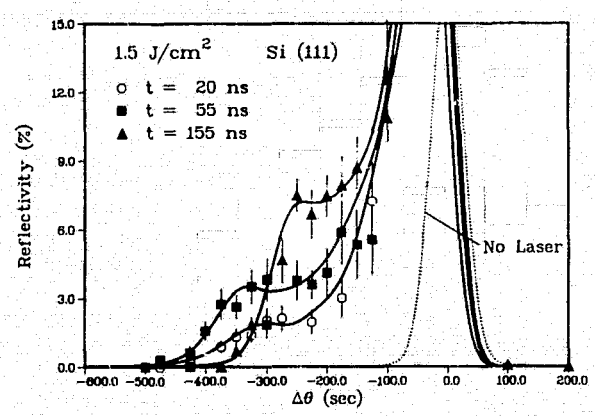

Fig. 7. Time resolved x-ray scattering measured near the (111) Bragg reflection on (111) oriented silicon. From Ref. 13.

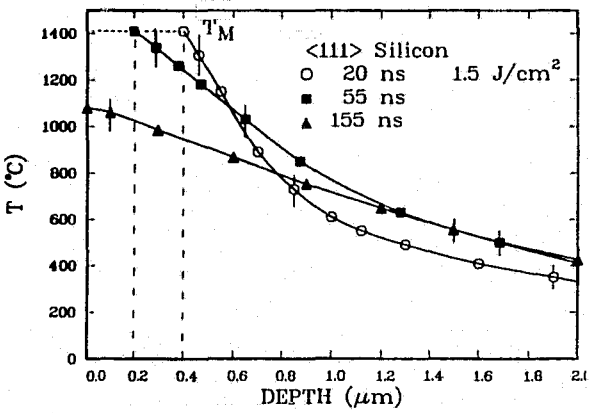

Fig. 8. Temperature profiles in (111) silicon obtained by fitting x-ray scattering calculations to measurements shown in Fig. 7. From Ref. 13.

cases, but only to ∿375 s for the 155 ns case. This implies a lower temperature at 155 ns and the greater scattering intensity implies a shallower thermal gradient at this time. The temperature profiles in the crystalline part of the sample corresponding to the same delay times are shown in Fig. 8. In this figure, depth is measured from the crystal surface. Temperature profiles in Fig. 8 are measured in the crystalline part of the sample below the liquid layer because it is only the crystalline part of the sample which gives rise to x-ray diffraction. The depth of the liquid-solid interface can be determined (roughly) by comparing the (measured) absorbed laser energy to the energy contained in the crystalline part of the sample (calculated from the temperature profile). The difference between these energies must be contained in the liquid layer and from this the approximate melt depth can be determined.

In Fig. 8 at 20 and 55 ns at the temperature at the liquid-solid interface, reaches the melting point of silicon to within the uncertainty of the measurements (±75°C). At 20 ns the melt front is penetrating into the crystal while at 55 ns solidification of the melted region is taking place. These results show that superheating of the solid during melting and interfacial undercooling during recrystallization are less than 75°C, for the laser conditions used ($V \sim 3$ m/s). Thermal gradients in the near-surface region are of the order of 10^7°C/cm at 20 and 55 ns and the gradient is considerably less at 155 ns. For the results shown in Figs. 7 and 8, recrystallization of the melted region is complete at 100 ns (as determined from measurements of the time resolved optical reflectivity). This accounts for the fact that the surface temperature at 155 ns is less than the melting point and the thermal gradients are considerably smaller than those at earlier times.

Results similar to those shown in Fig. 8 were obtained also using (100) silicon. Consequently the x-ray diffraction results clearly show that temperatures at or near the melting point are reached during pulsed-laser annealing, but interfacial undercooling during regrowth (or superheating of the solid during melting) must be less than 75°C for the laser conditions used. Faster growth velocities and/or more precise measurements of temperatures will be required to determine the interfacial undercooling during rapid solidification. Such measurements are in progress and will be reported at a later date.

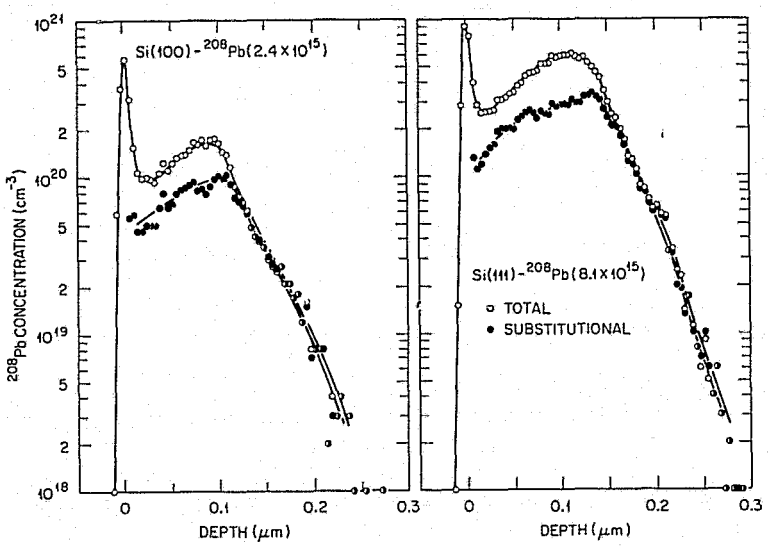

Fig. 9. Limitations to the incorporation of ^{208}Pb (250 keV) into (100) and (111) silicon as a result of ruby laser annealing. Regrowth velocity is ∿4.5 m/s.

VII. DOPANT INCORPORATION AT HIGH CONCENTRATIONS; MAXIMUM SUBSTITUTIONAL SOLUBILITIES (C_S^{max})

There is a maximum concentration (C_S^{max}) above which the dopant is no longer incorporated into substitutional lattice sites for a given growth velocity.[6] Examples are shown in Fig. 9 for the case of ^{208}Pb in (100) and (111) Si. Following laser annealing (Ruby, 1.3 J/cm^2), RBS-ion channeling measurements were used to measured the total and substitutional concentrations as a function of depth. Up to a concentration of 1×10^{20} for (100) Si and ∿3×10^{20} for (111) Si the total and substitutional concentrations are indistinguishable. In the near surface region where the concentration exceeds these values, the total and substitutional concentrations differ considerably. These values are the maximum substitutional concentrations (C_S^{max}) which can be incorporated into (100) and (111) Si at this growth velocity (∿4.5 m/s). Values for C_S^{max} have been determined[9] for nine Group III, IV, or V impurities in both (100) and (111) silicon at a growth velocity of 4.5 m/s. The results are summarized in Table II and compared with equilibrium solubility limits. The last column in Table II indicates the mechanism that limits substitutional solubility. These mechanisms are discussed in the next section.

VIII. LIMITATIONS TO SOLUBILITY

Substitutional solubility appears to be limited by four mechanisms.[9] These are (1) thermodynamic limitations, (2) lattice strain, (3) interface instability during regrowth and (4) dopant precipitation in the liquid. Predictions of thermodynamic limits to dopant incorporation in silicon have been made by Cahn.[21] The basic idea is that the solidus and liquidus lines intersect at one point on the Gibbs free energy diagram. This limits the solid composition which can be formed from the liquid since there is no barrier to nucleation of the solid phase. The locus of these points plotted on the phase diagram defines the T_0 curve which is the limit to dopant incorporation even at infinite growth velocity.

TABLE II
Substitutional solubilties in silicon achieved by recrystallization at 4.5 m/s

DOPANT	C_s^o (cm^{-3})	C_s^{max} (cm^{-3}) (100) Si	C_s^{max} (cm^{-3}) (111) Si	COMMENT
As	1.5×10^{21}	6.0×10^{21}	6.0×10^{21}	Thermodynamic limit
Sb	7.0×10^{19}	2.0×10^{21}	2.0×10^{21}	Cell formation
Bi	8.0×10^{17}	4.0×10^{20}	8.6×10^{20}	Precipitation Cell formation
Ge	5.0×10^{22}	6.0×10^{21}	$>1.2 \times 10^{22}$	Cell formation on (100)
Sn	5.5×10^{19}	9.8×10^{20}	1.4×10^{21}	Cell formation
Pb	---	1.0×10^{20}	3.0×10^{20}	Precipitation Cell formation
B	6.0×10^{20}	2.0×10^{21}	2.0×10^{21}	Mechanical strain
Ga	4.5×10^{19}	4.5×10^{20}	7.2×10^{20}	Cell formation
In	8.0×10^{17}	1.5×10^{20}	4.5×10^{20}	Cell formation
Tl	---	---	---	Coherent precipitation

Substitutional solubilities achieved during laser annealing are much higher than equilibrium solubility limits,[6] but in only one case do we appear to have reached Cahn's predicted limits. For the case of As in Si, the value measured for C_s^{max} is independent of velocity in the range of 2 to 6 m/s and is independent of crystal orientation. Figure 10 shows results for XeCl laser annealing (6 m/s) for high dose implants of ^{75}As into (100) and (111) Si. In each crystal, As is measured to be substitutional up to a concentration of $6 \times 10^{21}/cm^3$. Above this concentration epitaxial growth stops and the near-surface region is observed by TEM to contain polycrystalline regions, small amorphous regions and As precipitates. The line of

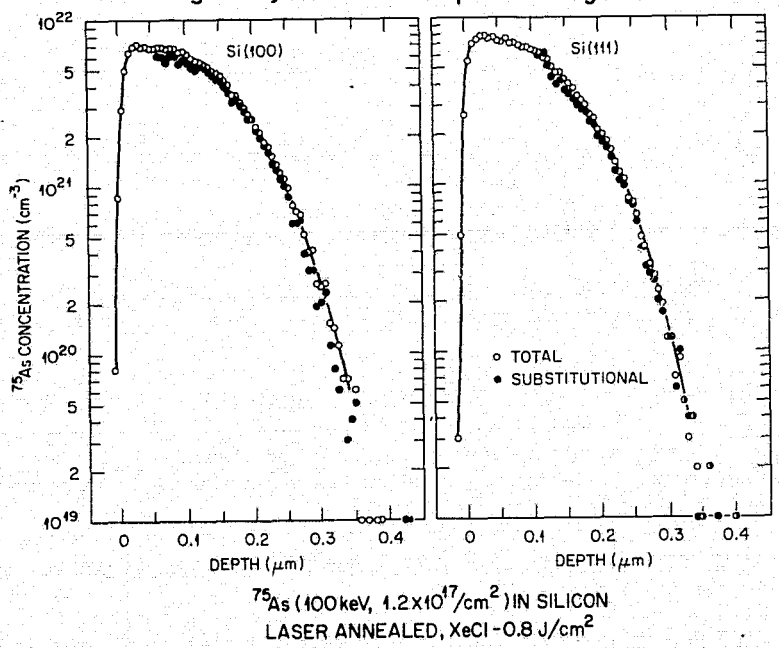

Fig. 10. Limitations to the incorporation of As in (100) and (111) silicon as a result of laser annealing. Regrowth velocity is ∿6.0 m/s. From Ref. 9.

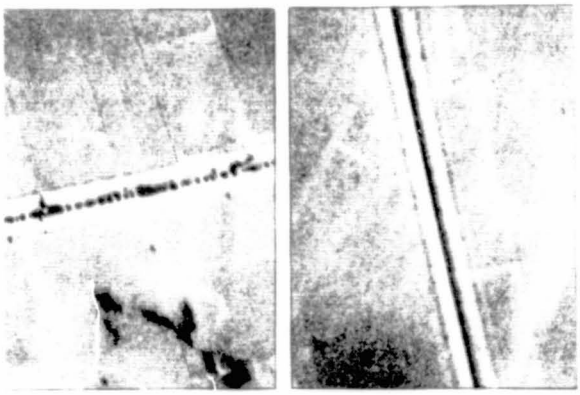

Fig. 11. Cracks in the near-surface region of high dose boron implanted silicon following laser annealing. Ref. 16.

demarkation between the epitaxially recrystallized region and the defective region is quite sharp. Based on the fact that this limit is independent of velocity and crystal orientation we conclude that the thermodynamic limit has been reached.

For the case of B in Si, strain in the implanted region after laser annealing provides the limit to dopant incorporation.[16] The strain results from the one dimensional lattice concentration which occurs when B is incorporated into the lattice during recrystallization.[22] When the strain exceeds the fracture strength, cracks will develop in the implanted region as shown in Fig. 11. The cracks are observed to be ~1 μm wide x 1 μm deep and extend the entire length of the sample (~1 cm). Cracks will develop whenever the boron concentration exceeds ~4 at.%. At lower concentrations, the annealed region is strained but cracks do not develop.

Maximum substitutional solubilities for several impurities (Ga, In, Ge, Sn, Sb, Bi, and Pb) are limited by interface instability which develops during regrowth. The instability leads to lateral segregation of the dopant into the walls of a cell structure in the near-surface region. An example is shown in Fig. 12 for the case of In in (100) Si. Up to a concentration of 1.5–2.0 x $10^{20}/cm^3$, the In is highly substitutional following laser annealing. Above this concentration the nonsubstitutional In is localized to the cell walls (Fig. 12 right) which penetrate to a depth of ~1000 Å. Both the concentration at which the instability develops and the resulting cell size can be predicted[23] with reasonable accuracy by using the Mullins and Sekerka perturbation theory of interface instability[24] modified to account for the large deviations from equilibrium during regrowth. Values determined for k' in the case of Ga, In, Ge, Bi, and Pb are larger for (111) crystals than for the (100) case at equivalent growth velocities. The larger values for k' in (111) crystals imply that higher concentrations can be trapped into the solid before interface instability occurs. This accounts for the fact that C_s^{max} is larger for these impurities in the (111) case (see Table II).

A few of the impurities listed in Table II (Bi, Pb, Tl) are immiscible in liquid silicon. Consequently at low growth velocities these impurities will precipitate in the liquid if the time available for nucleation and growth of precipitates is long enough. Precipitates formed in the liquid will be frozen into the solid during solidification. Figure 13 shows this for Bi in silicon at growth velocities of 1.5 m/s (13a) and 0.7 m/s (13b).

CONCENTRATION PROFILE

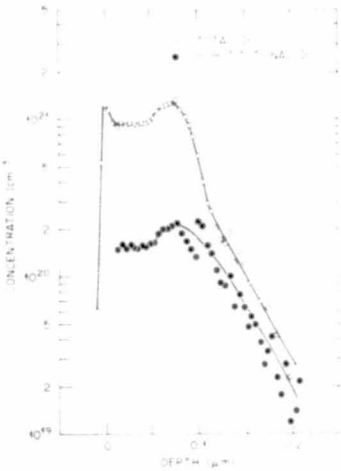

MICROSTRUCTURE

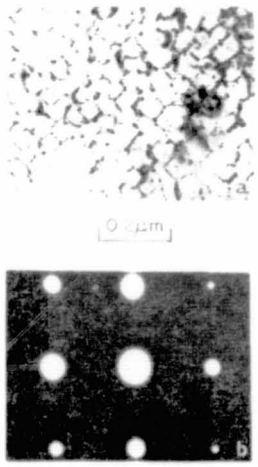

Fig. 12. Profiles and microstructures for ^{115}In (125 keV, 1.3 x $10^{16}/cm^2$) in (100) Si following ruby laser annealing. From Ref. 16.

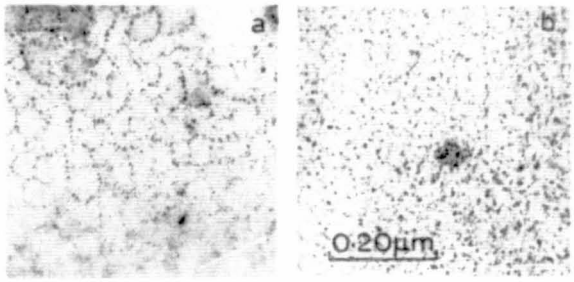

Fig. 13. Microstructures in the near-surface region of (100) Si implanted by ^{209}Bi (250 KeV, 1.4 x $10^{16}/cm^2$) and ruby laser annealed to give rise to growth velocities of (a) 1.5 m/s and (b) 0.7 m/s. From Ref. 8.

At the lower growth velocity the annealed region contains a uniform dispersion of precipitates. At the high velocity a cell structure is observed, with the walls being decorated by precipitates. At velocities greater than 3 m/s only the cell structure is observed with little or no indication of precipitates. The value of k' for Bi, Pb, and Tl is less than unity and each is immiscible in liquid Si. Consequently at low growth velocities, dopant precipitation will limit substitutional solubility but at higher velocities interface instability will dominate.

IX. CONCLUSIONS

Laser annealing of ion implanted silicon has provided very fundamental information on high speed nonequilibrium crystal growth processes. During the rapid liquid-phase-epitaxial regrowth process, implanted Group III, IV, and V impurities can be incorporated into the lattice at concentrations that exceed equilibrium solubility limits by orders of magnitude. Interfacial distribution coefficients (k') have been determined for a wide variety of impurities in silicon. Values for k' far exceed equilibrium values (k_0) and can be functions of growth velocity and crystal orientation. Limits to substitutional solubility which can be achieved by laser annealing have been established and insight has been gained into the mechanisms which limit substitutional solubility. Measured solubility limits are approaching thermodynamic limits to diffusionless solidification.

REFERENCES

*Research sponsored by the Division of Materials Sciences, U.S. Department of Energy under contract W-7405-eng-26 with the Union Carbide Corporation.

1. Laser-Solid Interactions and Laser Processing-1978, (ed. by S. D. Ferris, H. J. Leamy and J. M. Poate, American Institute of Physics, New York), 1979.
2. Laser and Electron Beam Processing of Materials, (ed. by C. W. White and P. S. Peercy, Academic Press, New York), 1980.
3. Laser and Electron-Beam Solid Interactions and Materials Processing, (ed. by J. F. Gibbons, L. D. Hess and T. W. Sigmon, North Holland, New York), 1981.
4. Laser and Electron Beam Interactions with Solids, (ed. by B. R. Appleton and G. K. Celler, North Holland, New York), 1982.
5. Laser-Solid Interactions and Transient Thermal Processing of Solids, (ed. by J. Narayan, W. L. Brown, and R. A. Lemons, North Holland, New York), 1983.
6. WHITE C.W., WILSON S.R., APPLETON B.R., and YOUNG F.W., J. Appl. Phys. 51 (1980) 738.
7. STUCK R., FOGARASSY E., GROB J.J., and SIFFERT P., Appl. Phys. 23 (1980) 15.
8. WHITE C.W., Ref. 4, p. 109.
9. WHITE C.W., ZEHNER D.M., NARAYAN J., HOLLAND, O.W., and APPLETON B.R., Ref. 5, p. 287.
10. FOGARASSY E., STUCK R., SIFFERT P., BROUTET F., and DESOYER J.C., Ref. 5, p. 311.
11. GALVIN G.J., THOMPSON M.O., MAYER J.W., HAMMOND R.B., PAULTER N., and PEERCY P.S., Phys. Rev. Lett. 48 (1982) 33.
12. LARSON B.C., WHITE C.W., NOGGLE T.S., and MILLS, D.M., Phys. Rev. Lett. 48 (1982) 337.
13. LARSON B.C., WHITE C.W., NOGGLE T.S., BARHORST J.F., and MILLS D.M., Appl. Phys. Lett. 42 (1982) 282.
14. CULLIS A.G., WEBBER H.C., POATE J.M., and SIMONS A.L., Appl. Phys. Lett. 36 (1980) 320.
15. BAERI P., POATE J.M., CAMPISANO S.U., FOTI G., RIMINI E., and CULLIS A.G., Appl. Phys. Lett. 37 (1981) 912.
16. WHITE C.W., APPLETON B.R., STRITZKER B., ZEHNER D.M., and WILSON S.R., Ref. 3, p. 109.
17. POATE J.M., Ref. 4, p. 121.
18. BAERI P., FOTI G., POATE J.M., CAMPISANO S.U., and CULLIS A.G., Appl. Phys. Lett. 38 (1981) 800.
19. GILMER G.H., Ref. 5, p. 249
20. SPAEPEN F. and TURNBULL D., p. 15 in Laser Annealing of Semiconductors, ed. by J. M. Poate and J. W. Mayer, Academic Press, New York, 1982.
21. CAHN J.W., CORIELL S.R., and BOETTINGER W.J., Ref. 2, p. 89.
22. LARSON B.C., WHITE C.W., and APPLETON B.R., Appl. Phys. Lett. 32 (1978) 801.
23. NARAYAN J., J. Appl. Phys. 52 (1981) 1289.
24. MULLINS, W.W, and SEKERKA, R.F., J. Appl. Phys. 35 (1964) 444.

DISCUSSION

FAN: Why is germanium so anomalous?

WHITE: Germanium is completely soluble in silicon and the best we could ever do there is one. The interface goes unstable before you can get to there, in the (100) case. In the (111) case, we have gone up to concentrations as high as $10^{22}/cm^3$. We are putting the germanium in by ion implantation and we are sputter-limited. We cannot get any more in. That is the best you will ever do on that. Possibly in deposited layers on (111) you might do better.

SESSION VII: MATERIAL CHARACTERIZATION

K. Ravi, Chairman

PRECEDING PAGE BLANK NOT FILMED

N84 28640

STRUCTURAL CHARACTERIZATION OF SOLAR SILICON

D.G.Ast
Mat.Sci.& Eng.; Cornell University; Bard Hall
Ithaca, N.Y. 14853. USA.

1. Introduction

Compared to single crystal silicon, as grown solar silicon generally contains large residual stresses and numerous structural defects. During subsequent processing, the defect structure can undergo further changes since at the high temperatures required for diffusion, dislocations are sufficiently mobile to rearrange themselves in patterns which reduce long range residual stresses. This process, which is similar to the polygonization of strained metals, has no counterpart in single crystal silicon. Finally, many of the solar silicon materials are grown from graphite dies and crucibles and therefore contain carbon concentrations in excess of 1E18. The interactions between carbon, crystal defects, intrinsic point defects, oxygen and diffusing dopants has not been studied to any degree since this problem does not arise in integrated circuit technology.

The presence of a limited number of structural defects is not necessarily detrimental to solar cell performance. In single crystal silicon, for example, lifetimes are higher in moderately dislocated material (1E3 to1E5 dislocations/sqcm) than in dislocation free material (Melliar-Smith 1977). In general, defects can both degrade (by providing recombination sites) and improve (by gettering of impurities) the electrical properties of solar cells. The nature of the grown in defects, their interactions with chemical impurities and intrinsic point defects, and subsequent changes in the defect structure during processing must be understood if cell performance is to be improved further.

2. Structural Characterization Techniques

2.1. Chemical etching and optical microscopy

The advantages of etching are simplicity, sensitivity, and the ability to rapidly evaluate large areas. Disadvantages are the inability to resolve closely spaced defects and the frequently obscure relation between etching features and the atomic structure of defects. The basic principle of silicon etches is to oxidize silicon into SiO[2], using an agent such as nitric or chromic acid and then to dissolve the oxide with hydrofluoric acid (see Tuck 1975). Sites at which the lattice is strained, such as dislocations, or sites of different composition, such as impurity agglomerates, are etched at different rates. The size of the etching features can be controlled by changing the etch concentration and/or etching time. In practice, conditions are selected such that the feature size exceeds the resolution of the microscopic examination technique. Because of this "chemical magnification" optical microscopy can resolve defects of atomic dimensions.

Early etching solutions, e.g. Sirtl and Adler (1961), achieved high sensitivity only on specific planes or were, when isotropic, very slow (Dash 1956). Secco (1972) developed an etch with good sensitivity on all crystallographic planes. The Wright etch (Wright Jenkins 1977) is also sensitive on all crystal planes and yields etch pits which are crystallographically defined rather then the round or elliptically shaped etch pits obtained with the Secco etch. An etch which consistently develops mounds rather then pits. and works on all planes except {111} has been described by Seiter (1977). Since solar materials are usually polycrystalline. the Wright etch is generally the best choice.

An example of an anisotropic etch is demonstrated in Fig. 1a, which shows twin bands in heat exchange method (HEM) silicon. The orientation of the matrix is ~{111} and the twin band orientation is {115}. The etch (a diluted Sirtl) is strongly anisotropic and reveals details on {111} but not on {115}. Thus, scratches are visible on {111} but not on {115}. That the scratches exist on the {115} surface is indicated by the smooth continuation of most of the matrix scratches on either side of the twin bands. The {221}/{221} second order twin joints at the intersection of the first order twin bands are also not etched. The corresponding EBIC images, Figs 1b and 1c will be discussed later.

2.1.1. The relationship between etching features and defect structures

A comparison of the appearance of crystal defects etched with various solutions can be found in the article by Wright Jenkins (1977) and a useful schematic diagram can be found in the article by Rozgonyi (1981). In Sirtl or Wright etched specimens, dislocation etch pits have the symmetry of the surface plane, e.g. twofold on {110}, threefold on {111}, fourfold on {100}.

Unlike dislocations and stacking faults, the nature of point defect clusters cannot be easily identified by etching. Saucer pits in single crystal silicon have only recently been shown to originate from heavy metal precipitates (Stacy et al 1982). Pits similar to these saucer pits are also observed in some solar materials, such as edge defined film fed growth (EFG) ribbons, see Fig. 2, or web (not shown) but the nature of the defects is unknown. It is possible that the defects are heavy metal complexes (Mo has been observed by Rutherford backscattering on web surfaces, Cunningham and Palmstrom 1982). It is also possible that the saucer pit like etching features may involve carbon complexes. In single crystal silicon, carbon interacts with oxygen (Bean and Neman 1972. de Kock and van de Wijgert 1981) metallic impurities such as gold (Hill and Van Iseghem 1977), and promotes nucleation of intrinsic point defects (Foll et al 1977) and oxygen (Shimura et al 1980). An interesting feature of carbon/intrinsic point defect complexes is that they tend to be strain free and therefore invisible in the transmission electron microscope. In the case of the saucer like EFG pits mentioned above. no corresponding TEM features could be observed. The absence of TEM contrast is reminescent of B swirl defects (Petroff and deKock 1976. Foll and Kolbesen 1975), which are believed to be carbon-point defect agglomerates. When defects occur in dense groupings, e.g. microtwins, optical microscopy underestimates their density. This efffect is iluustrated in Fig. 3, about 100 twin boundaries are present within the field of view of about 10 µm. Determination of the twin density of a material by optical microscopy would severely underestimate the density of defects present.

An example of the ambiguity of the interpretation of seemingly simple etching features is the identification of long, straight, linear boundaries with traces compatible with {111} boundary planes. Such boundaries are commonly identified as first order coherent twin boundaries. an assignment which is correct most of the time. However, such traces can also originate from asymmetric second order, e.g. {111}/{115} twin boundaries (see section 5). In principle, all higher order twins of the form {111}/{HKL} could be mistaken as first order twins. However, it appears that {111}/{115} is the only combination which occurs relatively frequently.

Etching of semiconductors can be carried out in the presence of a DC voltage, in which case the process is referred to as cathodic or anodic etching (Deines et al 1979, Foll 1980). A grain boundary which is electrically active has a different electrical potential than the matrix. This potential difference offers, in principle, a method of preparing TEM specimens in which only electrically active boundaries are etched (Foll 1980). The possible application of cathodic etching in the automated counting of electrically active defects by optical imaging analyzers should be investigated.

The staining of beveled p-n junctions makes use of the built-in junction potential to delineate the junction location. The technique is useful in studies of bulk diffusion versus grain boundary diffusion, and was first used by Queisser (1963) to show the absence of enhanced diffusion along coherent twin boundaries. The technique has been used to study enhanced diffusion along grain boundaries in solar materials (Cheng and Shyu 1982).

A very useful etch in the preparation of TEM specimens of p-n junctions is one the discussed by Bogh (1971). This etch has a much higher dissolution rates for n type than for p type material and does not attack p+ layers.

Infrared microscopy of silicon has been used to study the precipitation in transition metal doped EFG ribbons (Cretella 1982). Defects which would be otherwise invisible, can be viewed by decorating internal defects with fast diffusers such as copper (Dash 1956, 1958). Cu decoration on EFG is being carried out in an effort to answer the question if B-swirl like agglomerates exist in this material.

2.2. Electron microscopy

2.2.1 Scanning electron microscopy.

2.2.1.1 Specimen current mode.

In this mode, the current flowing between the specimen and ground is used to modulate the intensity of the CRT display. This current is composed of the current carried by the incident beam minus the current carried away from the specimen by backscattered primary and secondary electrons. The specimen current varies slightly with crystallographic orientation, an effect which can be used to accurately determine the orientation of small grains in polycrystalline solar materials by rocking the beam about a fixed spot (Van Essen et al 1971). The resulting "electron channeling pattern" is analogous to Kikuchi or Kossel patterns. Since electron channeling is a dynamical effect it is very sensitive to crystalline perfection. Channeling patterns

have been used for the non-destructive assessment of the crystalline perfection of silicon on sapphire and could also be used to study the emitter layers of solar cells.

2.2.1.2 Secondary electron imaging.

In the secondary electron imaging mode (SEI), low energy electrons emerging from the specimen are collected, and used to form the image. Most of the secondary electrons originate within the first few atomic layers from the surface, and escape with energies of 2 to 3 eV. The resolution is approximately equal to the beam diameter, or about 5 nm in a modern instrument. The secondary electron image carries information on the surface topography, since electrons emitted from recessed areas are less likely to reach the offside mounted detector.

2.2.1.3 Backscattered electron imaging mode.

The number of backscattered electrons, defined as electrons with energies >50 eV, depends on specimen orientation. surface topography and chemical composition of the specimen. To highlight topological or compositional variations, some SEM's, such as the JEOL 733, use two solid state detectors, arranged symmetrically on either side of the specimen. The difference and sum of the two detector outputs corresponds roughly to a slanting illumination. emphasizing topology, and a flat illumination emphasizing compositional differences, respectively. Fig. 4 shows a chemically polished specimen containing Fe related precipitates imaged in the SEI (a), topo (b) and compo (c) modes. Since the precipitates protrude slightly above the surface. they are visible in the topo mode. Note that twinned regions are visible in the SEI and compo mode. but not in the topo mode.

Line and planar defects which locally bend lattice planes can be imaged in a SEM in a "TEM like" manner by choosing an orientation close to a Bragg condition, using electron channeling patterns for alignment. To obtain useful contrast. an SEM fitted with a field emission gun and an energy filter for back scattered electrons is required (Pivatal et al. 1977, Morin et al 1979). The technique is capable of resolving defects with a resolution of about 10 nm located up to 100 nm below the surface. Its chief advantage is that it is non-destructive and does not require any specimen thinning. The technique may be, therefore, useful to study shallow junction solar cells.

2.2.1.4 X-ray imaging mode

The intensity and energy of characteristic x-rays emitted from the specimen yields information on the chemical composition of the specimen. With corrections for absorption, fluorescence and atomic number effect, accuracies of about 1% can be achieved. The technique is most sensitive to high atomic number elements where a concentration of 0.1% or lower can be detected in the region probed by the electron beam. If the impurity is present in the form of precipitates, much lower volume concentrations can be detected. The technique is less sensitive for lighter elements, since Auger processes increase at the expense of x-ray emission, and also because the beryllium window on the detector becomes more absorbent at lower energies. Light elements can be detected with windowless energy dispersive detectors or by wavelength dispersive spectroscopy.

2.2.1.5 Electron beam induced current mode.

In this mode. carriers generated by the incident electron beam in a small volume. called the generation volume. are used to form the image. The shape of the generation volume is determined by the scattering of the incident electrons and is roughly spherical, of radius Rp (see the chapter by R.Bell). At practical beam voltages (5 to 30 KV), Rp varies between 0.5 and several µms in size. The injected current is collected at a nearby p-n or Schottky barrier junction and used, after amplification, to modulate the intensity of a CRT display scanned synchronously with incident beam. A low input impedance amplifier is commonly employed, in which case the EBIC current corresponds to the short circuit current of the cell. Thus. the EBIC image is basically a map of the variation of the short circuit current. Regions of low efficiency (e.g. defects) therefore appear dark. Superimposed over this image is a faint "backscattered image", since the EBIC current is related to the number of electrons entering the crystal; i.e. all effects which increase the fraction of back scattered electrons will reduce the EBIC current. Contrast features which are visible in the backscattered image will also be visible in the EBIC image. Therefore, the backscattered image should be checked if unusual features appear in the EBIC image. The fact that the "backscattered" component of the EBIC image has a higher resolution than the EBIC image (especially if the latter is taken at a high voltage), is occasionally useful in separating the contribution of the two images.

Usually, the specimen is mounted in such a way that the collecting junction is perpendicular to the incident electron beam (plan view mode). Occasionally, however, it is useful to view the specimen end on. This mode corresponds to cross-sectional EBIC of solar cells and can be used to study the junction formation, see Fig. 5, which shows a cross sectional EBIC image of a processed EFG cell. Minority carrier diffusion lengths can be determined by measuring the collected current as a function of distance from the collecting plane (Jastrzbeski et al 1975). The minority carrier diffusion coefficients can be obtained from time domain measurements, either in the single shot mode (Ioannou 1980) or by periodically blanking the beam (Fuyuki and Matsunami 1981).

At typical beam voltages each incident electron generates about 500 to 1000 electron-hole pairs. High beam currents can cause local movements of the Fermi level as well as the formation of micro plasmas and should be therefore avoided in defect studies (at least as long as one does not want to exploit these feature to measure e.g. the density of states of a defect, or the electrical field in the vicinity of a defect). The injected carriers move by drift in the junction region by diffusion in the emitter and base region (neglecting field arsing from doping gradients). Since quantitative theories of EBIC contrast are available only for the diffusion case. is important to establish that such conditions exist before a quantitative interpretation of EBIC results is attempted.

In solar cells the junction depth is typically about 0.3 to 0.7 µm, and the depletion layer is between 1 and 2 µm deep. Since the range of 10 to 20 KeV electrons is between 1 and 3 µm (undesirable) drift field conditions can easily exist under common operating conditions.

At high voltages, high doping levels and shallow junctions, the majority of carriers are injected into field free material and move by diffusion. The contrast of linear and planar defects has been calculated by a variety of authors (Donolato 1983, Marek 1982, Zook 1983) for the plan view mode. These calculations show that the resolution of EBIC depends on the geometry of the defects studied. For linear defects, the resolution is roughly comparable to the size of the generation volume. For planar defects, the resolution is roughly equal to the minority carrier diffusion length. Convenient mathematical expressions are available for the EBIC contrast of dislocations (Donolato and Klann 1980) and grain boundaries (Donolato 1983, Marek 1982, Zook 1983), which can be used to derive the minority carrier diffusion length and the recombination velocity from measurements of the EBIC current in the vicinity of the defects. When using these expressions, it should be noted that the definition of the surface recombination velocity used by Zook (1983) differs by a factor 2 from that of Donolato (1983). The integral representation chosen by Zook for the Bessel function converges much faster than that given by Donolato and is therefore much more convenient in numerical evaluations. Finally, when programming these expressions, it is useful to remember that all arguments pertain radians, rather than in degrees. In practice the largest errors in L and s arise from the uncertainty of the background level, the choice of which can introduce an error of 30% or more.

EBIC line scans of grain boundaries are frequently asymmetric, both in regard to the background and the decrease of the EBIC current as the boundary is approached, see Fig. 6, which shows a line scan across a 5.5° tilt boundary of a silicon bicrystal grown at JPL. The reason for this asymmetry are generally not well understood. Grains of different orientation can easily be distinguished in EBIC micrographs, as shown in Fig. 7, which shows a section of HEM material. In such a case, the asymmetry is due to the different back ground at either side of the boundary, but this effect can be ruled out for Fig. 6. In addition, the profiles themselves are usually asymmetric in the sense that they yield different lifetimes in adjacent grains, even when the different background at either side of the boundary is properly taken into account. This is effect is not understood at present. The asymmetric profiles could be caused by asymmetric probing beams, (for which reason the specimen should be rotated by 180° and the measurement repeated) or different types and concentrations of defects on either side of the boundary. Different dislocation densities are commonly observed on different sides of boundaries in EFG ribbons, see Fig. 8. On an atomic scale, grain boundaries are frequently asymmetric (see section 4). In particular, grain boundaries frequently emit microtwins to one side only. Finally, in cast specimens with multiple nucleation sites, microsegregation can occur, with more segregation occurring in large grains than in small grains.

The electronic energy levels of defects can be determined by moving the Fermi level relative to the defect levels by changing the temperature or injection conditions. Thermal movement of the Fermi level has been used by Kimmerling et al (1977) to determine the electronic energy level of a contaminated stacking fault. Shallow levels in EFG have been quantitatively determined from temperature dependent EBIC measurements by Hanoka and Bell (1981). The frequency dependence of the EBIC contrast has been used by Ourmazd et al (1981) to study recombination at dislocations. The frequency dependence of the EBIC contrast contains information of the density of states

and should be further studied, e.g. on grain boundaries.

2.2.2. Transmission electron microscopy

Compared to optical microscopy, the advantages of TEM are high spatial resolution and the ability to derive quantitative information on the detailed crystallographic nature of the defects; e.g. Burgers vectors of dislocations. For more details see e.g. Hirsch et al (1977), Thomas and Goringe (1979) and Spence (1981).

The penetrating power of electrons in silicon is approximately 1 μm at 100 Kev and 5-10 μm at 1 MeV. Thin specimens are therefore required for transmission electron microscopy, particularly in high resolution studies. Thin areas are found in the vicinity of tapered holes etched into the material by a variety of techniques, e.g. argon ion milling. The areas examined by TEM are very therefore very small and many specimens must be inspected before statistically significant results can be obtained. TEM investigations of junction regions are especially difficult, since a single defect penetrating a junction can have a pronounced effect on the electrical properties. In such investigations, auxiliary methods such as etching or EBIC must be used to preselect the areas of interest.

The resolution of TEM depends on the imaging conditions and the specimen thickness. Weak beam images (Cockayne 1972) can separate dislocations which are about 2 nm apart. In the lattice imaging mode, the the image generated corresponds to a projection of the crystal structure along the incident beam direction. A quantitative analysis of lattice images requires image computations, see e.g. Spence (1981). Limitations of the technique are that the specimens must be extremely thin in order to reduce multiple scattering. Only images of defects which are imaged end-on can be easily interpreted. Fortunately, in silicon, a large number of dislocations and grain boundaries meet this requirement. In silicon, the <110> direction is both the preferred line direction of dislocations, and the direction in which the lattice has the largest open channels. A projection of the silicon lattice along a <110> direction is shown in Fig. 9. The resolution of commercially available microscopes is insufficient to resolve the closely spaced pairs of atoms in Fig. 9. The "white dots" observed in lattice images of silicon most frequently correspond to the open six-sided channels. However, reversed image contrast can occur under certain imaging conditions, particularly in thicker specimens. A lattice image of a microtwin is shown in Fig. 10. Microtwins can terminate inside the crystal in a variety of ways, see Fig. 10 b which shows both {112}/{112} boundaries and "peeling off" of individual layers terminating in partial dislocations.

The scanning transmission electron microscope (STEM) combines the features of a conventional TEM with those of a scanning electron microscope. However, much higher resolution can be achieved in the SEM mode because of the smaller probe size (~ 1 nm) and because beam spread is reduced in the thin foils used in TEM.

The highly convergent probe formed in STEM's can be used to obtain convergent beam patterns which contain crystallographic information on small volumes (Steeds 1979). Elemental analyses of small volumes can be carried out by energy dispersive spectroscopy, EDS, (Goldstein 1979) and electron energy

loss spectroscopy, EELS, (Joy 1979, Silcox 1979, Leapman et al 1981).

In addition to the STEM mode. the instrument can also be operated in conventional TEM and secondary electron imaging modes. In summary, a variety of microstructural analysis can be carried out by STEM. including surface topographical studies by SEI. structural investigations by TEM and chemical analysis by EDS and EELS.

When semiconductors are investigated, the STEM can be operated in the EBIC and CL modes. However, because of the small volumes probed, the collected signals are weak, and the signal to noise ratio is low unless phase sensitive detection techniques are used. The technique has been applied to the study of defects in GaAs by Petroff (1982).

3.Structural defects in silicon

3.1 Point defects.

The atomistic nature of the high temperature equilibrium point defect and its charge state in silicon is controversial, and vacancies (Shaw 1975), interstitials (Seeger and Chik 1968) and models which assume an equilibrium between vacancies and interstitials (Sirtl 1977) have been proposed. The latter model predicts that the presence of carbon will shift the equilibrium towards the interstitial side. Graphite crucible grown silicon should therefore contain a higher fraction of highly mobile point defects than regular silicon. This prediction is in agreement with various observations on EFG material to be discussed later. Indirect evidence. mostly from observation of B-swirls, suggests that interstitials form complexes with carbon. The composition of these complexes is such that no strain develops, and therefore depends on the internal strains in the matrix.

3.2 Line defects.

Silicon has the crystal structure of the diamond cubic lattice. which is an fcc Bravais lattice with a basis of two atoms at 000 and 1/4 1/4 1/4. Glide dislocations in bulk silicon have Burgers vectors of the type a/2<110>. Since the diamond lattice consists of two interpenetrating fcc lattices, displaced relative to one another by a/4 [111], two kind of dislocations can be constructed which are known as the glide and shuffle set (Hirth and Lothe 1982). The difference between these two types of dislocations consists in the termination of the extra half plane. which is shown schematically in Fig. 11. Experimentally it is very difficult to determine whether dislocations in silicon belong to the glide or shuffle set. By comparing experimental lattice images to computer simulated images Olsen and Spence (1981) determined that the 30° a/6<112> Schockley partial belonged to the glide set. The conversion of glide to shuffle set dislocations via the absorption and emittance of point defects is discussed e.g. by Alexander (1979). Dislocations in silicon have a preferred line direction of <110>, since the Peierls energy is lowest in that direction. Dislocations formed at high temperatures have a more irregular line direction than those formed at low temperatures. which tend to adhere more rigidly to <110>. This tendency can be used as a guideline in deciding at what stage of the growth process dislocations are introduced into the material.

Three different possible combinations of <110> Burgers vectors and line directions exist. and dislocations with <110> line directions are therefore either screw, 60° or edge type. Possible atomic configurations of these dislocations are discussed by Hornstra (1958) and by Hirsch (1982). Glide dislocations in silicon are of the 60 or screw type. The stacking fault energy in silicon is relatively low, about 69 mJ/m (Foll and Carter 1979), and most dislocations are therefore dissociated into a/6 <112> Shockley partials. Dislocations in twin boundaries in silicon are mostly a/6 <112> type dislocations.

Low angle grain boundaries can contain complex dislocations with large Burgers vectors. These complex dislocations, first investigated by Bourret and Desseaux (1979), can form by the interaction of different glide dislocations, and have been discussed by Foll and Carter (1979) and Carter (1982). Examples of dislocations in low angle tilt boundaries are given in section 4.

3.3 Grain Boundaries in Silicon

Grain boundaries with misorientations up to ~ 20° can be modelled as arrays of discrete lattice dislocations. Such boundaries are referred to as low angle grain boundaries. Boundaries which share a large fraction of common lattice sites are commonly referred to as low boundaries, where is the reciprocal fraction of common lattice sites of the two interpenetrating lattices (Bollmann 1970). In this notation. the coherent first order twin boundary is a Σ =3 boundary and boundaries created by consecutive twinning operations such as second and third order twin boundaries are termed Σ =9 and Σ =27 boundaries, respectively. Small deviations from these low Σ boundaries are taken up by secondary dislocations which play a role similar to those of regular dislocations in low angle grain boundaries. A given Σ boundary can have many different boundary planes but experimentally it is found that symmetric boundary planes with a high density of coincident sites are preferred (Cunningham et al 1982d).

Studies on the structure of polycrystalline silicon indicate that the majority of grain boundaries are <110> tilt boundaries. These boundaries are either low angle. (Cunningham 1982, Cunningham and Ast 1982), or Σ =3. 9 or 27 boundaries (Cunningham et al 1982d, Fontaine and Rocher 1980. Rocher et al 1981, Yang et al 1980. Armstrong et al 1980).

The structure of a particular grain boundary in silicon or germanium appears to be independent of the way it was created. The structure of low-angle <110> tilt boundaries has been studied in melt grown bicrystals of germanium, Bourret and Desseaux (1979), in hot-pressed bicrystals of silicon, Carter, Rose and Ast (1981) and in chemically vapor deposited (CVD) silicon. Cunningham (1982) and the dislocation structure of these boundaries is found to be very similar. The atomic structure of second order, or Σ =9 coincidence, boundaries has been studied by Krivanek et al (1977), Bourret et al (1981), and Vaudin et al (1983) and again are found to be independent of the formation mechanisms.

The following discussion will be confined to <110> tilt boundaries since these are the only ones of importance in solar silicon. Twist boundaries are rarely found but can be made by sintering of single crystal wafers (Foll and

Ast 1979, Vaudin and Ast 1982). The results presented below were obtained from a study of the boundaries in CVD silicon serving as feedstock for RTR ribbons. The material had a grain size of about 1 um and a <110> texture and was deposited at 1100 °C. The high deposition temperature resulted in a higher and "more annealed" grain structure than that of standard CVD silicon.

3.3.1 Low-Angle [1$\bar{1}$0] Tilt Boundaries.

Most dislocations in low-angle tilt boundaries are of edge character, since the sum of the Burgers vectors of the dislocations comprising the boundary must be perpendicular to the tilt axis and parallel to the boundary plane normal, Hirth and Lothe (1982).

Bourret and Desseaux (1979) and Bourret et al (1981) have identified dislocations with Burgers vectors a [111], a/2 [112], a [001] and a/2 [110] in melt grown bicrystals of germanium and Carter et al (1981) have identified dislocations with Burgers vectors a[001] and a/2[112] in hot-pressed bicrystals of silicon. These dislocations have also been observed in low angle [110] tilt boundaries in CVD silicon by Cunningham (1982) and Cunningham and Ast (1983).

Fig. 12 (a) shows a 10 [110] tilt boundary. The grain boundary plane has different orientations in different sections and the character of the dislocations changes accordingly. The enlargements of the different boundary regions show the nature of the dislocations in more detail, Figs. 12 (b)-(d). For a further discussion it is convenient to introduce the concept of the median lattice, Frank (1950). The median lattice is identical in structure and halfway in orientation between the crystal lattices at either side of the boundary, and will be indicated by the subscript m. Between A and B, Fig. 12 (b), the boundary is symmetric, (110)m, and consists of an array of pure edge a/2 [110] Lomer dislocations. Between B and C, Fig. 12 c, the boundary plane is asymmetric, (111)m, and contains dislocations with Burgers vectors a [111], which are dissociated into three Frank partials, a/3 [111], separated by intrinsic and extrinsic stacking faults. a/2 [110] dislocations occasionally introduce facets into the (111)m boundary plane. Between C and D the asymmetric boundary plane. (112)m, consists of dislocations with the E rgers vector a/2 [112], which are dissociated into a Frank partial, a stair-rod, a/3 [001], and a Shockley partial, Fig. 12 d. The dissociation widths are very narrow since the boundary dislocations are tightly spaced. The dissociation scheme is shown more clearly in Fig. 13. which is taken from a tilt boundary with a smaller misorientation angle. shown in Fig. 13 b. The configuration of the dislocations in this boundary are consistent with a model that assumes that the boundary has migrated during cool down. Changes of the boundary plane requires the introduction of new dislocations into the boundry, see 3.3.1. As the boundary moves, the a/6[112] and a/3[111] move by glide and climb, leading to anomalously widely dissociated intrinsic and extrinsic stacking faults.

3.3.2 Twin related boundaries

Since the [110] plane in silicon has two mirror planes. two possibilities exist for the location of a symmetric grain boundary plane, independent of the misorientation. The two symmetric boundary planes for a [110] tilt boundary correspond to (110) and (001) in the median lattice. It was suggested by

Hornstra (1959) that <110> tilt boundaries with a {110} median lattice boundary plane could be constructed without broken bonds. Recent comparison of Hornstra's models with lattice images of the Σ =9 boundary in germanium (Krivanek et al 1977, Bourret et al 1981) and the Σ =9 and Σ =27 boundaries in silicon, (Vaudin et al 1983) have shown the validity of these models. Fig. 14 is a lattice image of a Σ =27 boundary, (110)m in silicon, together with a superimposed model of the boundary. Good agreement exists between the experimentally observed structure and the model. The structure of boundaries with a (001) median lattice boundary plane, which include the (112) incoherent twin boundary, appear to be more complicated. Fontaine and Smith (1982) and Vlachavas and Pond (1981) experimentally determined different values for the rigid body translation associated with the incoherent (112) twin boundary. Recent computer calculations by Pond et al (1983) suggest the existence of two energetically favorable structures. Cunningham and Ast (1983) have observed three different structures for the (112) twin boundary in silicon.

Asymmetric boundaries are also observed in polycrystalline silicon. Recent results by Koch and Ast (1982) and Dianteill and Rocher (1983) suggest that greater recombination of minority carriers occurs at macroscopically asymmetric boundaries than at symmetric boundaries. On an atomistic scale, asymmetric grain boundaries frequently dissociate into faceted structures consisting of symmetric grain boundary sections (Cunningham et al 1982d). Examples of this process are shown in Figs. 15 and 16. In Fig. 15, a Σ =27 boundary is dissociated into a Σ =9 boundary and a faceted Σ =3 boundary, and in Fig. 16 a Σ =9 boundary is dissociated into two Σ =3 boundaries. In both cases dissociation occurs only in those sections where the undissociated boundary plane would have had an asymmetric configuration.

The above results emphasize the need to characterize the nature of defects in polycrystalline silicon, on the scale of nanometers, before a comparison of electrical properties of grain boundaries can be made with confidence. All electrical characterization techniques average over large (μm) sections of grain boundaries. On a microscopic scale, the structure of the boundary can vary significantly over such a distance, as shown above. Correlation of macroscopic electrical characterization techniques such as AC spectroscopy, DLTS and EBIC with TEM is therefore inconclusive unless the boundary is structurally characterized along the entire region probed by the electrical measurement.

4. Electrical Properties of Defects

The relationship between structural defects and the efficiency of solar cells is not obvious. Lower defect densities do not necessarily result in better cells, and materials with a high density of structural defects can be processed into cells of rather high efficiency. One reason for this seemingly puzzling behavior is the dual role of structural defects. Lattice defects can act as recombination centers for minority carriers, and as gettering sites for chemical impurities. A illustrative case of the latter occurs in solar cells prepared from corner sections of HEM material. This material contains a high density of impurities since it is the last section to solidify. A solar cell fabricated from such a material shows high collection efficiency only in close proximity of grain boundaries. Fig. 17 shows a light induced current (LIBC) scan of such a cell, and Fig. 18 shows the corresponding optical image. A TEM analysis shows that the grain boundaries are heavily decorated and are

surrounded by denuded (precipitate free) regions, see Fig. 19. The decrease in collection efficiency at the boundary itself is more then offset by the increased collection in its vicinity, with the result that the collection efficiency is highest in the boundary region.

In solar cells, defects which cross the depleted layer are more troublesome than similar defects in the base region, decorated defects being particularly damaging. Thus, the presence of defects in the base, even though reducing the minority carrier lifetime, can be beneficial if these defects act as strong gettering centers for the depletion layer. The detailed nature of the defect structure in the junction and base regions, and the optimization of cell efficiencies through processing is the subject of current microstructural research. A difficulty in such studies is that the electrical activity of a defect can change without visible changes in microscopic appearance, presumably by interacting with impurity atoms and intrinsic point defects.

In the following section, the electrical activity of individual lattice defects (local electrical activity) and their influence on the overall efficiency of the solar cell (global activity) will be discussed. The application of EBIC to the study of the defect structures of dendritic web and EFG silicon is given in sections 5.1 and 5.2 respectively.

4.1.1 Electrical activity of point defects and point defect clusters.

In the discussion of point defects it is useful to differentiate between chemical impurities (especially transition metals), intrinsic point defects (vacancies and interstitials), and dopants such as phosphorous. The role of impurities is discussed later. The role of intrinsic point defects and their interaction with carbon and oxygen is very complex and can not be discussed here in any detail. It appears fairly certain that carbon is complexed with interstitials and that these complexes tend to be strain free and not electrically active. Treatments which increase the concentration of interstitials (such as the diffusion of posphorous) increase the interstitial fraction and might lead to strained complexes which are then electrically active (see Goesele and Ast 1983). However, more information is needed to establish the validity of such a model. Experiments such as emitter push effect and copper decorations should provide such information.

4.1.2 Electrical activity of dislocations.

The electrical activity of dislocations has been studied principally by EBIC (Ourmazd and Booker 1979, Ourmazd et al 1981) and by the correlation of EBIC with high voltage electron microscopy (Blumtritt et al 1979, Strunk and Ast 1980a). These investigations show that the recombination efficiency of dislocations increases with increasing edge component of the Burgers vectors (screw vs. 60°, see Ourmazd 1981), and also depends on the dissociation state (Ourmazd 1979), the amount of decoration (Blumtritt et al 1979) and the jog content (Ast et al 1982). Theoretical models of the electrical activity of dislocations are usually based on a broken bond model and do not take into account the presence of impurities. Presently, it is not clear if clean dislocations (clean to the extent that the gettered impurities do not play a role in the electrical activity) exist in silicon. Investigations of the electrical activity of emitter misfit dislocations which pass close to strong gettering centers show a reduction in the electrical activity (Pasemann et al

1982). This result suggests that even dislocations which appear to be free of impurities in TEM may be decorated with impurities on a level not observable by microscopic examination (Kittler and Seifert 1981). However, it is conceivable that results obtained on emitter misfit dislocations are not necessarily representative of the dislocation behavior in the bulk, since phosphorus diffusion is known to getter impurities. Investigations of the correlation between dislocation density and minority carrier lifetime show that the lifetime is one to two orders of magnitude higher when the dislocations are introduced by deformation. rather than grown in (see Vink et al 1978). This observation can be rationalized with the absence of a Cottrell atmosphere in deformation induced dislocations. Another factor which appears to influence the electrical activity of dislocations is the dissociation width. Plots of the dissociation width of dislocations versus increasing edge character show a large scatter, for reasons which are not well understood. (Gomez et al 1975). Experimentally, it is found that dislocations which are generated at high stresses and low temperatures (Wessel and Alexander 1979), are strongly electrically active (Sullivan and Ast 1981). Finally, both theory and experiment suggest that kinks and jogs are sites of enhanced electrical activity (see section 5.1).

4.1.3. Stacking faults and other planar defects.

The electrical activity of planar defects varies greatly, and depends on the atomic structure, the presence of intrinsic or extrinsic grain boundary dislocations, and the segregation of impurities. These factors have only been studied extensively for coherent twin boundaries. Clean dislocation free coherent twin boundaries and stacking faults are not electrically active (Strunk et al 1981; Ourmazd et al 1981). Most dislocations in coherent twin boundaries are electrically active. although dislocations are occasionally observed which do not show any discernable EBIC contrast (Strunk et al 1981). These dislocations tend to be straight and oriented in <110> directions. Decorated stacking faults, see Fig. 20 showing a decorated stacking fault in HEM material are always strongly electrically active (Kimmerling et al 1977). Carbon, with a high bond energy, is unlikely to segregate at stacking faults since only impurities which lower the stacking fault energy segregate to stacking faults or twins (Suzuki segregation), and carbide precipitates (such as SiC) have never been observed at stacking faults. The electrical activity of other grain boundaries has been studied to a much lesser extent. As a general rule, twin related symmetric grain boundaries with [110] tilt axis are less electrical active than boundaries with a macroscopically asymmetric orientation (Koch and Ast 1982, Dianteill and Rocher 1983). This effect can be easily seen in HEM specimens which develop large macroscopic twins, see Fig. 1a. The second order {221}/{221} twin boundary at intersecting bands of equal thickness is not electrically active (see Fig. 1 b,c) but shows electrically activity when bands of unequal thickness are joined, i.e. when the boundary takes on a macroscopic asymmetric element. Such comparisons show that the symmetric {112}/{112} first order twin boundary can only be very weakly electrically active (Koch and Ast 1982). These observations can be rationalized with structural models which show that symmetric [1$\bar{1}$0] tilt boundaries can be constructed without broken bonds, whereas broken bonds are generally present in asymmetric boundaries. However, more research is needed to establish the validity of the broken bond hypothesis since impurity decoration is an alternative possibility. A comparison between AC admission spectroscopy results and TEM shows that the spacing of secondary dislocations

is comparable to the average distance between trapping sites (Werner and Strunk 1982). However, this conclusions rests on the assumption that the structure of the grain boundary in the large area probed by the electrical measurement is identical to the structure in the small area probed by TEM. In general, this is a safe assumption only for twin related boundaries, and even there the dislocation content of the boundary can vary with position (Strunk and Ast 1980a). In non-twin related boundaries, the electrical activity of a boundary usually varies with position (Cheng and Shyu 1981. Seager 1982).

In solar materials, the correlation between etching features and bulk electrical properties (conversion efficiency, minority carrier diffusion length, majority carrier mobility) is not well established, even though modern image processing methods allow rapid acquisition of numerical data. Studies of ubiquitous crystallization process (ucp) silicon with automated quantized optical microscopy show no discernable correlation between the solar cell efficiency and the dislocation density (Natesh et al 1983). In view of the complex role of defects, the inhomogeneous defect distribution, the different impact of defects on the emitter, junction and base region, the absence of simple correlations is, perhaps, not surprising.

4.2 Passivation of defects by hydrogenation.

The electrical activity of structural defects in solar silicon can be reduced by hydrogenation (Ast and Sullivan 1979, Seager et al 1980, Hanoka et al 1983). An example of hydrogen passivation is shown in Fig. 21. The dark area in Fig. 21a contains dislocation loops, formed in a scratched and annealed specimen. It can be seen that these dislocations, introduced at a low temperature and a high stress are very more electrically active than the grown in dislocations visible in the background. The strong electrical activity is most likely caused by an unusually large dissociation width (Dislocations generated at low temperatures and high stresses tend to be widely separated). Fig. 21b shows that hydrogenation in a glow discharge reduces the electrical activity of these dislocation loops to a level comparable to that of the grown in dislocations, allowing individual loops to be resolved.

Hydrogenation experiments are commonly carried out at temperatures between 350 and 450° C. Thermal introduced changes in the minority carrier lifetime (Graff et al 1973) must therefore be separated from hydrogenation effects if the latter effect is to be studied properly (Sullivan 1983).

5. The Defect Structure of Solar Silicon Material

5.1.Dendritic Web

The growth mechanisms for dendritic web silicon ribbon have been described previously by e.g. Seidensticker (1977). The resulting ribbon has a <111> surface normal whereas <110> is observed in most other ribbon materials.

The general features of the defect structure of web ribbon are (i) a bulk dislocation density of 1E4 to 1E5 cm^{-2}, and (ii) a number of twin planes lying parallel to the ribbon surface and located near the mid plane of the ribbon. Fig. 22 shows a typical etch pattern observed at the surface of web ribbons.

The etch pits delineate the traces of two different {111} glide planes, suggesting that the corresponding dislocations were introduced into the material by plastic processes. The dislocation density varies over the width of the ribbon with a maximum of about 1E5 cm^{-2} at the center and decreasing by an order of magnitude toward the dendrites.

Near the twin boundaries, located in the central region of the web ribbon, high densities of dislocations have been observed. These dislocations have been discussed previously by Cunningham et al (1982a) and are thought to be responsible for the slightly reduced efficiencies of web solar cells as compared to standard dislocation free Czochralski cells. The dislocations at the twin planes can be studied by TEM but specimen preparation is difficult. A more convenient method for observing these dislocations has been used by Sporon-Fiedler and Ast (1982), who polished the ribbon down parallel to the twin plane, and used EBIC to examine the dislocations. Since it is impossible to polish the specimens exactly parallel to the twin planes, a small bevel invariably develops. This geometry allows several twin planes to be observed simultaneously, and also the determination of the dislocation densities on different twin planes. Fig. 23 shows an optical micrograph of such a specimen where the traces of 5 twin plane intersections with the surface can be seen. The EBIC micrograph, Fig. 24, shows that a variety of dislocations reside in the boundaries. Hexagonal networks of dislocations can be seen and also many long straight dislocations. Analysis by TEM shows that the hexagonal network consists of near screw, a/6<112> dislocations in the boundary, and that the long straight dislocations are most likely Lomer-Cottrell locks (Cunningham et al 1982a). The EBIC observations show that the twin planes nearest the ribbon surface invariably contain the highest density of dislocations. This observation supports the conclusion that most of the dislocations are introduced by plastic processes. The twin boundaries therefore act as sinks for the dislocations which are generated at the surface, or at the dendrites, and glide in the ribbon due to thermal stresses. On intersecting the twin boundaries, the dislocations are effectively trapped. The process can be thought of as internal gettering of dislocations. It is conceivable that the high conversion efficiencies of cells fabricated from web ribbons is due to effective trapping of dislocations at the twin planes. No similar process is possible in ribbons with a <110> surface normal.

Fig. 25 shows a higher magnification EBIC image of the hexagonal network. Close inspection shows that there is enhanced contrast at alternate dislocation nodes. The threefold symmetry of hexagonal loops is a consequence of the fact that each dislocation introduces a step in the boundary. Carter and Foll (1980) have shown that for an hexagonal network of dislocations in a twin boundary, three of the nodes must contain unit jogs. The EBIC contrast is consistent with the hypothesis that jogs are sites of enhanced electrical activity (for more details see Ast et al. 1982). This observation demonstrates that the correlation of EBIC with structural characterization can yield information on defects too small to be directly resolved by TEM.

5.2 Defect Structure of EFG Ribbons

5.2.1 As grown defect structure of EFG ribbons.

The defect structure of EFG ribbons has been studied by Strunk et al (1982a), and by the group at Mobil (for a summary see Wald, 1981). Most of

the ribbons have a <110> surface normal, a <112> growth direction and contain mainly twin boundaries which lie perpendicular to the surface and parallel to the growth direction. This geometry has been termed the "equilibrium" or "steady state" defect structure (see Wald, 1981) since it invariably develops during ribbon growth, regardless of the orientation of the seed crystal. In addition, the ribbons contain dislocations, of densities 1E3 to 1E5 cm , and higher order twin boundaries. Random high angle boundaries, i.e. high angle boundaries which are not twin related, are rarely observed. This defect structure is very similar to that of the CAST ribbons studied by Yang et al (1979).

Several boundaries of the equilibrium structure are characterized by strong electrical activity, as shown in the EBIC micrograph of Fig. 26. It is often observed that boundaries are electrically active only at certain regions along their length. Correlation of EBIC with TEM shows that intermittent EBIC contrast can be due to at least two different mechanisms (Cunningham et al 1982b). The EBIC contrast in Fig. 27 is due to dislocations in twin boundaries whereas the dotted contrast in Fig. 28 arises from sections of incoherent twin boundaries. The strong EBIC contrast of linear boundaries lying parallel to the coherent boundaries may therefore be due to a high density of dislocations in the twin boundary or to long sections of higher order twins boundaries. A third possible mechanism, segregation of impurities to selected regions of the grain boundary has never been observed in EFG ribbons.

As shown by Cunningham et al (1982c), the occurrence of sections of incoherent twin boundaries produced by intersections of coherent {111} twin boundaries is very common in many solar silicon materials, such as RTR, EFG, SOC, and HEM. A related mechanism is shown in Figs. 29 (a) and (b). These EBIC and TEM micrographs were taken from an RTR ribbon. The EBIC contrast is due to dislocations in the boundaries, but the dislocations are connected by stacking faults, which are electrically inactive and therefore not visible in the EBIC micrograph. The process by which these defects were introduced is very likely different from that responsible for introducing individual dislocations.

A puzzling feature of as grown EFG ribbons is that carbon precipitation has never been observed by TEM, despite the high carbon content of the material. Graff et al (1977), who studied precipitation in high carbon CZ single crystal silicon noted that "the most striking fact is the absence of carbon in the precipitates analysed". Kolbesen and Muehlbauer (1982), who studied the influence of carbon on the performance of high voltage two and three terminal devices, also failed to find SiC precipitates. The reader should consult this reference for further details on possible factors controlling the presence and absence of SiC. It appears that carbon is either dispersed throughout the material, possibly decorating dislocation cores and boundaries (Rocher et al 1980) or exists in the form of strain free agglomerates with intrinsic point defects. The latter is also suggested by the fact that strain free B-swirls, whose nucleation is related to carbon, develop into strained defects when subjected to treatments which increase the interstitial concentration, i.e. oxidation.

5.2.2. Effects of processing on the defect structure of EFG ribbons.

It is well known that processing of single crystal silicon can change the configuration of existing defects, and can introduce new defects, such as stacking faults, dislocations and precipitates. This fact suggests that defect rearrangements and the creation of new defects may also play an important role in the processing of solar silicon.

The effects of a 30 min PH3 diffusion on the defect structure of EFG ribbons have been reported by Cunningham and Ast (1982). Dislocation helices are formed in the diffused region due to the absorption of point defects, as shown in Fig. 30. The supersaturation ratio calculated from the pitch of these spiral is generally in the order of 100 except in one case where the supersaturation ratio was in excess of 1E5 (this case is being checked further). Similarly coiled dislocations (and supersaturation ratios) have been observed in the vicinity of junctions in single crystal silicon by Strunk et al (1980b) who explained their formation by the absorption of silicon self interstitials created by the diffusion of phosphorous. Another effect observed in processed EFG ribbons is the formation of boundaries, as shown in Fig. 31. After solidification, the ribbons quickly cool below the temperature where dislocation motion can take place easily (~700°C). The duration of the 30 min. processing step is long compared to the cooling time and stress relief can therefore easily occur. In the present case this stress relief occurs by dislocation multiplication and glide. Since a low-angle boundary reduces the strain field of a configuration of dislocations it is not surprising that such low-angle boundaries are found in many of the processed ribbons. Dislocation nodes in such low-angle boundaries act as nucleation sites for small precipitates (see section 5).

The above results show some of the effects of processing on the structure of EFG ribbons. Similar effects may occur in other solar materials. The nature of this effect will depend on the pre-existing defect structure, residual stresses and impurities.

5.2.3 Impurities in EFG Ribbons.

Hopkins et al (1980) have studied the effects of various metallic impurities on the electrical properties of solar cells and defined "acceptable" impurity contents below which the conversion efficiencies were not seriously affected. In many instances, these concentrations are exceeded, especially in ribbon technologies with no impurity rejection into the melt. Internal gettering of impurities by oxygen precipitates and back side damage is extensively practiced in the fabrication of integrated circuits. Internal gettering in solar cells by lattice defects is an important topic of structural characterization.

5.3. Precipitation in EFG Ribbons

Small, ~10 nm, precipitates frequently form at the dislocation nodes of processed induced networks, see section 5.2.2., as shown in Fig. 32. The size of these precipitates is compatible with the diffusion coefficients of either carbon or oxygen.

Larger precipitates (~1μm) are occasionally observed in processed ribbons, Fig. 33. The size and shape of these precipitates indicates that they are most likely formed in the melt and incorporated into the ribbons

during growth, rather than forming as a result of the high temperature diffusion process. Energy dispersive spectroscopy shows that the precipitates contain a variety of metallic impurities including Fe. Mo, Cr, Ni and Ti, see Fig. 33 b. Wavelength dispersive spectroscopy shows that the precipitates also contain carbon. In EFG ribbons, these precipitates are always surrounded by dislocations, Fig. 34, whereas such dislocations are never observed in similarly grown Nonagon material. A possible explanation for this difference is that the slower cooling rate of Nonagon material favors stress relief by point defect migration, rather than by the creation and movement of dislocations. A feature of EFG ribbons which is presently not understood is the absence of conventional misfit dislocations in the emitter layer. The effect is appears to be related to carbon but the details of the process are not established.

In recent experiments on EFG ribbons, the melt has been intentionally doped with Fe (Cretella 1982) which subsequently precipitates in the central plane of the ribbon. It has been found that such doping with Fe increases the efficiency relative to undoped ribbons. Fig. 35 shows a secondary electron image of a colony of such precipitates after etching down to the central plane of the ribbon. X-ray mapping reveals that the precipitates contain Fe. No other metallic impurities were detected. The precipitates contain only Fe, in contrast with undoped processed ribbons where significant amounts of Ni, Ti, Cr and Mo are observed. This observation suggests that Fe-C-Si complexes form in the melt and that the other impurities are "gettered" during processing. The dense dislocation networks around the precipitates can aid such a process by pipe diffusion along the dislocations. The precipitates are frequently associated with grain boundaries, and seem to be related to the frequent faceting of nearby coherent twin boundaries, see Fig. 36. Such facetting is extremely rare in regular (non transition metal doped) EFG specimens. These observations are compatible with a model which assumes cusps are formed at the solid liquid interface, in order to minimize the surface energy, see Fig. 37. Once a precipitate is attached to such a cusp it temporarily disturbs the equilibrium defect (i.e. cusp) spacing of the ribbon, and nearby cusps move laterally. This lateral movement introduces facets in the coherent twin boundaries attached to the cusps.

6. Concluding remarks

The aim of solar silicon research is to improve the conversion efficiencies of solar cells. A similar objective exists in single crystal silicon used for device fabrication. Here the aim is to improve the yield through the purposeful introduction of defects into electrically inactive regions of the wafer. The analogy suggests that improved solar cell efficiencies can be obtained through the manipulation of the defect structure. Knowledge of the structure and electrical properties of individual defects, as well as an understanding of the interaction of the various defects with each other, and point defects, is therefore required.

Compared to the extensive literature available on single crystal silicon, defect research in solar silicon is still in its infancy. In addition, the controlled manipulation of the defect structure of solar materials is more difficult, since the defect structures are built in, rather than carefully introduced, and no electrically inactive regions exist in a solar cell. An

optimum trade off will exist between the decrease in the minority carrier diffusion length by recombination at defects, e.g. in the base. versus their gettering activities in nearby layers, e.g. the junction. Ribbon technologies in which the defects are arranged in planes parallel to the junction, such as web, will be more suitable for a such trade off.

No agreement exists on the configuration of the high temperature intrinsic point defect in silicon. In most solar materials the situation is further complicated by the presence of high carbon concentrations. Since carbon is an unwanted impurity in single crystal silicon, its concentration is kept as low as possible. The precipitation of carbon and its interaction with other defects has therefore not been studied extensively, except for its role as a nucleation site for oxygen precipitation and the formation of B swirls. Tentative evidence suggests that the presence of carbon results in a higher concentration of mobile point defects capable of relieving stress. Point defects in dispersed form cannot be easily resolved by microscopy, regardless of resolution, since in a specimen of finite thickness (eg. 10 nm) many atomic layers contribute to the image. Excess concentrations of point defects can, however, be detected by indirect means, such as the coiling of originally straight dislocations and the formation of precipitates.

Microstructural characterization is likely to contribute most to improvement of those materials which have a complex and unstable defect structure, and whose growth technology is relatively well developed so that empirical correlation between growth conditions and electrical characteristics are available. Materials such as dendritic web, with a relatively simple defect structure, are less likely to benefit from such investigations. Materials in the early stages of development are less suitable, since the growth conditions are frequently not reproducible and alternative defect arrangements cannot therefore be generated reproducibly.

Future structural investigations of complex solar materials are likely to concentrate on an evaluation of the gettering abilities of defect structures in the base and their effects on junction quality. The structure of passivating surface layers prepared by the implantation of low energy hydrogen layers (Hanoka et al 1983) is likely to be another area of emerging research.

Acknowledgements

Many useful discussions were held with F.Wald, J.Hanoka, U.Kalejs, U. Goesele, H.Strunk and C.B.Carter. The results presented here were obtained in collaboration with past and present members of the Materials Science Department at Cornell, including H.Foll, B. Cunningham, H.Strunk, M.Vaudin, R.Gleichmann, D.Lillienfeld, T.Sullivan, F.Stafford, F.Sporon-Fiedler, and T.Koch. The authors would like to thank these co-workers for their considerable input into our present understanding of the subject.

Financial support is acknowledged from DOE 76ER02899, DOE/JPL 956046 and Mobil Solar Corporation.

REFERENCES

Alexander, H., 1979, J. de Physique 40, Colloque C 6, 7.

Armstrong, R.W., M.E. Taylor. G.M. Storti and S.M. Johnson, 1980. 14 th IEEE Photovoltaic Specialists Conference. San Diego, 1/7/80-1/10/80. p. 191.

Ast. D.G., B.Cunningham and H.P.Strunk, 1982, in : Grain Boundaries in Semiconductors. Proc. Mat. Research. Soc, Boston, 1981. eds H.J.Leamy, G.E.Pike and C.H.Seager (North - Holland, New York) p. 167.

Ast. D.G. and T. Sullivan. 1979, "Preparation of Schottky Diodes for EBIC Investigations of Grain Boundary Passivation in Si Ribbons", JPL Report 956046-No.3, 1979.

Bean A.R. and R.C. Neman. 1972. J. Phys. Chem. Solids 33. 255.

Blumtritt,H., R.Gleichmann, J. Heydenreich and H. Johansen. 1979, phys.stat.sol. (a) 55, 611.

Bogh, A., 1971. J. Electrochem. Soc. 118, 401.

Bollmann, W. 1970, Crystal Defects and Crystalline Interfaces (Springer, Berlin).

Bourret, A. and J.Desseaux, 1979, Phil. Mag. A39, 405, 413.

Bourret, A., J. Desseaux and C. D'Anterroches, 1981. in: Proc. Conf. Microscopy of Semiconducting Materials, Oxford, 1981. eds H.G.Cullis and D.C.Joy (Institute of Physics, Bristol), Inst.Phys.Conf.Ser.60, p.9

Carter, C.B. ,1982, in: Grain Boundaries in Semiconductors, Proc. Materials Research Soc., Boston, 1981. eds. H.J. Leamy, G.E.Pike and C.H. Seager, (North Holland, New York) p.33

Carter,C.B. and H.Foll, 1980. in Dislocation Modelling of Physical Systems, eds M.F.Ashby ,R.Bullough, C.S.Hartley and J.P.Hirth (Pergamon Oxford) p. 554.

Carter,C.B., J.Rose and D.G.Ast. 1981. in: Proc. Conf. Microscopy of Semiconducting Materials, Oxford, 1981. eds. A.G.Cullis and D.C.Joy (Institute of Physics, Bristol) Inst.Phys.Conf.Ser.60, p.153.

Cheng, L.J. and C.M. Shyu, 1981. Semiconductor Silicon 1981. eds. H.R. Huff, R.J. Kriegler and Y. Takeishi (The Electrochemical Society, Princeton N.J.),p. 390.

Cheng, L.J. and C.M.Shyu, 1982, to be published in the Proceedings of the 1982 Materials Research Society Meeting, Oct 1982, Boston Mass (North Holland)

Cockayne, D.J.H.,1972. Z.Naturforsch. 27a. 452.

Cretella, M., 1982, Private communication.

Cunningham, B., 1982, in: Proc. Elec. Microcs. Soc. Amer., Washington, 1982, ed. G.W.Bailey (Claitor, Baton Rouge) p.434.

Cunningham, B. and D.G.Ast. 1982 , Spring 1982 Meeting, Montreal, Extended Abstracts Vol 82-1. (The Electrochemical Society, Princeton NJ) p.109.

Cunningham, B., and D.G.Ast. 1983. to be published.

Cunningham, B. and A. Palmstrom, 1982, unpublished.

Cunningham, B., H.Strunk and D.G.Ast. 1982a, J. Electrochem. Soc. 129, 1089.

Cunningham, B., H.Strunk and D.G.Ast. 1982b, Appl. Phys. Lett. 40, 237.

Cunningham,B., H.Strunk and D.G.Ast. 1982c, in: Grain Boundaries in Semiconductors, Proc. Materials Research Soc., Boston, 1981. eds. H.J.Leamy, G.E.Pike and C.H.Seager (North-Holland, New York) p.51.

Cunningham, B., H.P. Strunk and D.G.Ast. 1982d, Scripta Met. 16. 349.

Dash,W.C., 1956. J. Appl. Phys. 27, 1193.

Dash, W.C., 1958, J. Appl. Phys. 29, 705.

Deines. J.L, J.W.Philbrick, M.R.Poponiak and D.B.Dove. 1979, Appl. Phys. Lett. 34, 746.

de Kock, A.J.R., 1970. Appl.Phys.Lett 16. 100.

de Kock, A.J.R. and W.M. van de Wijgert. 1981. Appl.Phys.Lett. 38,888.

Dianteill, C., and A. Rocher, 1983. to be published in the Proceedings of the 1983 Conference on the Microscopy of Semiconducting Materials, Oxford, (Inst.Phys.Conf.Series))

Donolato, C., 1983. J. Appl. Phys. 54, 1314.

Donolato, C. and H. Klann, 1980. J. Appl. Phys. 51, 1624.

Foll, H., 1980, Appl. Phys. Lett 37. 316 ; also J. Electrochem. Soc. 127.1925

Foll, H. and D.G.Ast. 1979, Phil. Mag A. 40, 589.

Foll, H. and Carter, 1979, Phil. Mag. 40, 497.

Foll, H., U.Goesele. and B.O.Kolbesen. 1977. Semiconductor Silicon 1977. eds H.R.Huff and E.Sirtl, (The Electrochemical Society, Princeton NJ), p. 565

Foll,H. and B.O.Kolbesen. 1975. Appl. Phys. 8, 319.

Fontaine, C. and A.Rocher, 1980. Journal of Microscopy 118, 105.

Fontaine,C. and D.A.Smith, 1982, Appl. Phys. Lett. 40, 153.

Frank,F.C., 1950, Report of the Symposium on the Plastic Deformation of Crystalline Solids, Carnegie Inst. of Technology, Pittsburg, 1950, p.150.

Fuyuki T., and H. Matsunami, 1981. J. Appl. Phys. 52, 3428.

Geis, A.W., H.I.Smith, B.T.Tsaur, J.C.C.Fan, G.W.Maby, D.A.Antoniadis Appl. Phys. Lett., 1982, 40, 158.

Goesele U. and D.G.Ast. 1983. to be published as a JPL Report.

Goldstein,J.I., 1979, Principles of Thin Film X-Ray Microanalysis, in: Introduction to Analytical Electron Microscopy, eds. J.J.Hren. J.I.Goldstein and D.C.Joy (Plenum Press, New York) ch.3.

Gomez, A., D.J.H. Cockayne, P.B.Hirsch and V.Vitek, 1975, Phil.Mag. 31, 105.

Graff, K., H. Peiper and G. Goldbach, 1973. Semiconductor Silicon 1973. eds. H.R. Huff and R.B. Burgers, (The Electrochemical Society, Princeton) .p 170.

Graff, K., J.Hilgarth and H. Neubrand, 1977, Semiconductor Silicon 1977, eds.H.R.Huff and E.Sirtl, (The Electrochemical Society, Princeton N.J.) p.575.

Hanoka, J.I. and R.O. Bell, 1981. Ann. Rev. Mater. Sci. 1981. p. 353.

Hanoka J.I., C.H. Seager, D.J. Sharp, and J.K.G. Panitz, 1983. Appl. Phys, Lett 42, 618.

Hill, M.J, and P.M. Van Iseghem, 1977, Semiconductor Silicon 1977, eds. H.R. Huff and E.Sirtl (The Electrochemical Society, Princeton NJ) p. 715

Hirsch, P., 1982, Defects in Semiconductors, eds.J.Narayan and T.Y.Tan. Proc. Materials Research Soc. Conf, Boston, 1981. (North Holland, New York) p. 257.

Hirsch,P., A.Howie, R.B.Nicholson, D.W.Pashley and M.J.Whelan, 1977, Electron Microscopy of Thin Crystals, 2nd ed. (Krieger, Malabar).

Hirth,J.P. and J.Lothe, 1982, Theory of Dislocations, 2nd ed. (Wiley-Interscience. New York).

Hopkins, R.H., J.R. Davis, R.Rohatgi, R.B.Campbell, P.D.Blais, P.Rai-Choudhury, R.E. Stapleton, H.C. Mollenkopf and J.R. Cormick, 1980, Effects of Impurities and Processing on Solar Silicon Cells, DOE/JPL Report 9543331-9, Vol. 2

Hornstra,J., 1959, Physica 25, 409.

Hornstra, J. 1958, J.Phys.Chem. Solids 5, 129

Ioannou, D.E., 1980. J.Phys. D, 13, 611.

Jastrzbeski L., J. Lagowski and H.C.Gatos, 1975, Appl. Phys. Lett 27,537.

Jewett, D.N., H.E.Bates and J.W. Locher, 1982, Spring Meeting 1982, Electro-

chemical Society, Montreal, Extended Abstracts, Volume 82 - 1, p. 108.

Joy,D.C., 1979, The Basic Principles of Electron Energy Loss Spectroscopy, in: Introduction to Analytical Electron Microscopy, eds. J.J.Hren. J.I.Goldstein and D.C.Joy (Plenum Press, New York) ch.7.

Kimmerling L.C., H.J.Leamy and J.R. Patel, 1977. Appl. Phys. Lett. 30, 217.

Kittler M., and W. Seifert. 1981. phus.stat.sol. (a) 66, 573.

Koch T, and D.G. Ast. 1982, An EBIC Study of HEM Polycrystalline Silicon, DOE/JPL Report 956046-2, May 1982.

Kohn.J.A., 1958, Amer. Mineralogist 41. 778.

Kolbesen B.O and A. Muehlbauer, 1982, Sol. State Electronics 25, 759.

Krivanek,O.L., S.Isoda and K.Kobayashi, 1977. Phil. Mag. 21, 1253.

Leapman R.D., L.A.Grunes. P.J.Fejes and J.Silcox, 1981.in: EXAFS Spectroscopy: Techniques and Applications, eds. B.K.Teo and D.C. Joy (Plenum Publishing Co. NY 10013) p. 217 - 239.

Marek, J., 1982, J. Appl. Phys. 53. 1454.

Melliar-Smith,C.M., 1977. Treatise on Material Science and Technology, Vol 11, p.47 (Academic Press, New York)

Menzel, E. and E. Kubalek, 1979, Scanning Electron Microscopy/1979/I SEM Inc., AMF O'Hare. Il 60666, USA. p. 297.

Morin, P., M.Pitaval, B.Besnard and G. Fontaine. 1979, Phil.Mag. A, 40,511

Natesh,R,., G.B.Stringfellow, A.V. Virkar, J. Dunn and T. Guyer, 1983. Analysis of Defect Structure in Silicon, Final Report. DOE/JPL 955676-1.

Olsen, A. and J.C.H. Spence. 1981. Phil. Mag. 43. 945.

Ourmazd, A., and G.R. Booker, 1979, phys.stat.sol (a) 55,771.

Ourmazd, A., E.Weber, H. Gottschalk, G.R. Booker and H. Alexander, 1981. Proc. Conf. Microscopy of Semiconducting Materials, Oxford, 1981. Inst.Phys.Conf.Ser. No 60: Section 1; 1981. p. 63.

Pasemann, L., H. Blumtritt and R. Gleichmann, 1982, phys.stat.sol (a) 70. 197.

P.M. Petroff, 1982 in: Defects in Semiconductors, Proc. Materials Research Conf., Boston 1981 ,eds. J.Narayan a. T.W.Tan. (Noth Holland New York) p.457.

Petroff,P.M. and A.J.R.de Kock, 1976. J. Cryst. Growth 36. 4.

Pivatal M., P.Morin, J.Bandry, E.Vicario and G. Fontaine, 1977. Electron Microscopy 1977, Vol 1. Proceedings of the Workshop on

Analytical Microscopy (ITT Research) p. 439.

Pond, R.C., D.J.Bacon and A. Bastaweesy, 1983. to be published in the Proceedings of the Conf. on Microscopy of Semiconducting Materials, Oxford 1983 (Inst.Phys.Conf.Series).

Queisser H.J., Shockley Transistor Corporation, 1963, Final Report. AF 30(602) 2556.

Rocher, A., C. Fontaine and C. Dianteill, 1981. Microscopy of Semiconducting Materials, Inst. Phys. Conf. Ser. No 60, p. 289.

Rocher A., C. Fontaine, M.Oberlin, J. Goma. C. Burggraf, J.P. Deville. M. Aucoutier and A. Chari, 1980, 14th IEEE Photovoltaic Specialist Conference. San Diego. 1/7/80-1/10/80. p. 1192.

Rozgonyi, G.A. ,1981. Semiconductor Silicon 1981. eds H.R.Huff, R.J.Kriegler and Y.Takeishi, The Electrochemical Society (Princeton NJ) Vol 81-5, p. 494 Fig. 12.

Seager, C.H., 1982, J. Appl. Phys. 53. 5968.

Seager, C.H., D.S. Ginley and J.D.Zook, 1980. Appl. Phys. Lett 36, 831.

Secco d'Arragano,F., 1972, J. Electrochem. Soc. 119, 948.

Seeger A. and K.P. Chick, 1968, phys. stat. sol. 29, 455.

Seidensticker, R.G., 1977, J. Cryst. Growth 39, 17.

Seiter, H.,1977, Semiconductor Silicon 1977, eds. H.R.Huff and E.Sirtl (The Electrochemical Society, Princeton NJ) p. 187.

Shaw, D., 1975, phsy.stat.sol. (b) 72,11.

F.Shimura, H. Tsuya and T. Kawamura, 1980, Appl. Phys. Lett. 37,483

Shyu, C.M. and L.J.Cheng, 1982, Grain Boundaries in Semiconductors. Proc. Materials Research Society Meeting 1981, Boston, 1981. eds. H.J.Leamy, G.E.Pike and C.H.Seager, (North Holland, New York), p 131.

Silcox, J., 1979, Analysis of the Electronic Structure of Solids, in: Introduction to Analytical Microscopy, Eds. J.J.Hren. J.I.Goldstein and D.C. Joy (Plenum Press, New York) Chapter 10.

Sirtl,E. and A.Adler, 1961, Z. Metallk. 52, 529.

Sirtl, E., 1977, Semiconductor Silicon 1977. eds. H.R.Huff and E.Sirtl, (The Electrochemical Society, Princeton N.J.) p. 4.

Spence, J.C.H., 1981 Experimental High Resolution Electron Microscopy (Claredon, Oxford).

Sporon-Fiedler F. and D.G.Ast. 1982, An EBIC Study of Dislocation Networks

in Unprocessed and Processed Web Silicon Ribbon, JPL/DOE Report 956046-2. May 1982.

Stacy, W.T., D.F. Allison and T.-C. Wu, 1982, J. Electrochem. Soc. 129, 1128.

Steeds,J.W., 1979, Convergent Beam Electron Diffraction, in: Introduction to Analytical Electron Microscopy, eds. J.J.Hren. J.I.Goldstein and D.C.Joy (Plenum Press, New York) ch.15.

Strunk H., B.Cunningham and D.G.Ast.1980a ,Defect Structure of EFG Silicon, DOE/JPL Report 954852-6.

Strunk, H. and D.G.Ast.1980a, 38th Ann. Proc.Electron.Microscopy.Soc.Amer. ed. G.W.,Bailey, p.332.

Strunk, H. and D.G.Ast. 1980b, The Structure of RTR Silicon Ribbons, DOE/JPL 954852-4, April 1980.

Strunk,H., B.Cunningham and D.G.Ast. 1981. in: Defects in Semiconductors, Proc. Materials Research Soc., Boston, 1980, eds. J.Narayan and T.Y.Tan (North-Holland, New York) p. 297.

Strunk,H., U.Goesele and B.O.Kolbesen. 1980b, J. Microscopy 118, 35.

Sullivan T.D., and D.G.Ast. 1981. Defects in Semiconductors, Proc. Materials Research Soc., Boston, 1980, eds. J.Narayan and T.Y.Tan (North Holland, New York-Amsterdam-Oxford) p. 303.

T.D. Sullivan, 1983. MS Thesis, Cornell University.

Thomas,G. and M.J.Goringe, 1979, Transmission Electron Microscopy, (Wiley-Interscience, New York).

Tuck, B., 1975, J.Mater.Sci. 10, 321.

Van Essen, C., E.M.Schulson, R.M. Donaghy, 1971. J. Mater. Sci. 6, 213.

Vaudin, M.D., and D. G. Ast. 1982 to be published in the Proceedings of the Materials Research Conference 1982, Boston, (North Holland).

Vaudin,M.D., B.Cunningham and D.G.Ast. 1983. Scripta. Met. 17, 191.

Vink, A.T., C.J.Werkhoven and C.v.Opdorp, 1978, Semiconductor Characterization Techniques, eds. P.A.Barnes a. G.A. Rozgonyi, Electrochemical Society, Proc. Volume 78-3 (Princeton, N.J.), p. 273.

Vlachavas, D and R.C.Pond, 1981. in: Proc. Conf. Microscopy of Semiconducting Materials, Oxford 1981. eds. A.G.Cullis and D.C.Joy (Institute of Physics, Bristol) p.159

Wald F.V., 1981, in Crystals: Growth, Properties and Applications 5 (Springer Verlag Berlin Heidelberg) p.147-198.

Werner, J. and H.Strunk, 1982, J. de Phys., colloque 10, C1-89.

Wessel K., and H. Alexander, 1977, Phil. Mag. 35, 1523.

Wright Jenkins, M., 1977, J. Electrochem. Soc., 124,757

Yang,K., G.H.Schwuttke and T.F.Ciszek, 1980, J. Cryst. Growth 50, 301.

Zook, J.D., 1983, Appl. Phys. Lett. 42, 602.

Figure Captions

Fig.1 a) Optical micrograph of an etched HEM silicon specimen. Anisotropic etch does not reveal scratches in twin bands or second order twin boundary. The corresponding EBIC image is shown in b). Details of two twin joints are shown in c), optical micrograph (top) and EBIC image (bottom). The symmetric {221}/{221} twin boundary is not electrically active. The small incoherent section of the =3 boundary in the top left corner is clearly visible in the EBIC image.

Fig.2 Optical micrograph showing saucer pit like etching features in an EFG ribbon.

Fig.3 Transmission electron micrograph of closely spaced twin boundaries in silicon.

Fig.4 Scanning electron micrographs of Fe precipitates in a silicon sample. a) SEI b) topo and c) compo modes.

Fig.5 Cross-sectional EBIC picture of a processed EFG cell. The junction is the narrow bright band. Adjacent to the junction are the top metall contact and the the silicon base.

Fig.6 EBIC scan across a 5.5° tilt boundary in a silicon bicrystal; {100} median plane. <110> tilt axis. Crystal grown at JPL.

Fig.7 EBIC micrograph showing variations in contrast of grains with different orientations.

Fig.8 Etched EFG ribbon showing different dislocation densities in adjacent grains.

Fig.9 Projection of the silicon lattice along <110>.

Fig.10 Lattice image of microtwin in silicon. b) illustrates various different termination possibilities of microtwins.

Fig.11 Schematic drawing of glide (5-6) and shuffle (2-3) set dislocation in silicon (from Hirth and Lothe 1968). The projection is [110].

Fig.12 Lattice image of a 10 [110] tilt boundary in silicon. b), c), and d) are enlargements of the boundary between AB, BC, and CD respectively.

Fig.13 Lattice image of a dissociated a/2[112] edge dislocation in silicon. b) Location of the dislocation in a boundary which most likely migrated during cooling.

Fig.14 Lattice image of a symmetric Σ =27 boundary in silicon with a model of the proposed structure superimposed. The largest dots in the lattice correspond to the largest open channels in the model.

Fig.15 Lattice image of a dissociated Σ =27 boundary. Arrows denote one of the products of the dissociation which is a coherent twin boundary.

Fig.16 Lattice image of a dissociated $\Sigma=9$ boundary. Note that the symmetric regions of the boundary are not dissociated.

Fig.17 LBIC scan of a HEM solar cell. The base material is from a corner section opposite the seed crystal. High collection efficiency occurs only along grain boundaries.

Fig.18 Optical image of the same HEM solar cell as in Fig. 17

Fig.19 TEM image showing heavily decorated grain boundary section in HEM.

Fig.20 Decorated stacking fault in HEM material.

Fig.21 EBIC micrographs showing the passivation of dislocations a) before and b) after hydrogenation treatment.

Fig.22 Optical micrograph of dislocation etch pits on the surface of a web silicon ribbon.

Fig.23 Optical micrograph of a beveled and etched web silicon specimen. revealing multiple twinning planes located in the mid plane of the ribbon (upper section).

Fig.24 EBIC micrograph of dislocations in a twin boundary in web silicon.

Fig.25 Higher magnification micrograph of hexagonal network visible in Fig. 18 Enhanced EBIC contrast is observed at alternate nodes.

Fig.26 EBIC micrograph of an EFG ribbon showing long straight sections of electrically active grain boundaries.

Fig.27 Dotted EBIC contrast from dislocations in coherent twin boundaries.

Fig.28 Dotted EBIC contrast due to sections of incoherent {111}/{115} boundaries. Top, EBIC image; bottom, optical micrograph.

Fig.29 a) EBIC micrograph of dislocations in twin boundaries in RTR silicon ribbon b) corresponding TEM micrograph showing the nature of the defects giving rise to the dotted EBIC contrast.

Fig.30 Helical dislocations in the junction region of a PH[3] diffused EFG ribbon.

Fig.31 TEM micrograph of a low angle boundary in the base region of a processed EFG ribbon. The letter I and E refer to intrinsic and extrinsic dislocations, respectively.

Fig.32 TEM micrograph of a small precipitate found at a dislocation node in processed EFG ribbbon.

Fig.33 Large precipitates in an EFG ribbon. Left. STEM image, right. SE image. b) EDX spectra of one precipitate.

Fig.34 TEM micrograph showing dislocations around one of the precipitates shown in Fig. 32.

Fig.35 Secondary electron image of an Fe precipitate colony, found in an EFG ribbon which was grown from an intentionally doped melt.

Fig.36 TEM micrograph showing faceting of twin boundaries in a region close to the Fe precipitate.

Fig.37 Schematic of the interaction of the solid liquid interface with a precipitate formed in the graphite die.
a)The precipitate particle. formed by the impurity gradient in the die approaches the liquid (L) to solid (S) interface.
b) After the particle reaches the solid liquid interface. the equilibrium spacing changes temporarily.
c) After incorporation of the particle, the original equilibrium spacing is restored.

Figure 1a

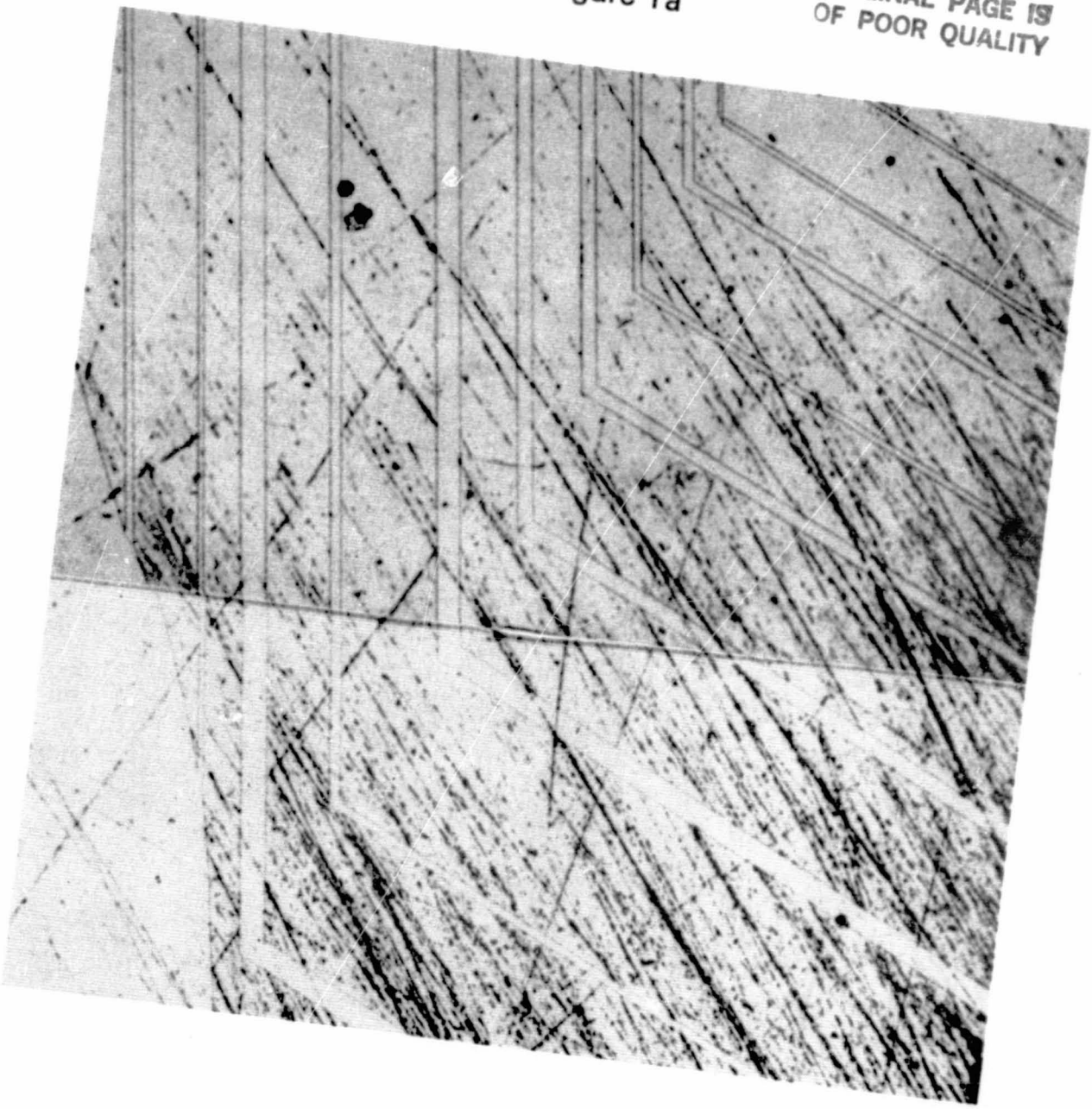

Figure 1b

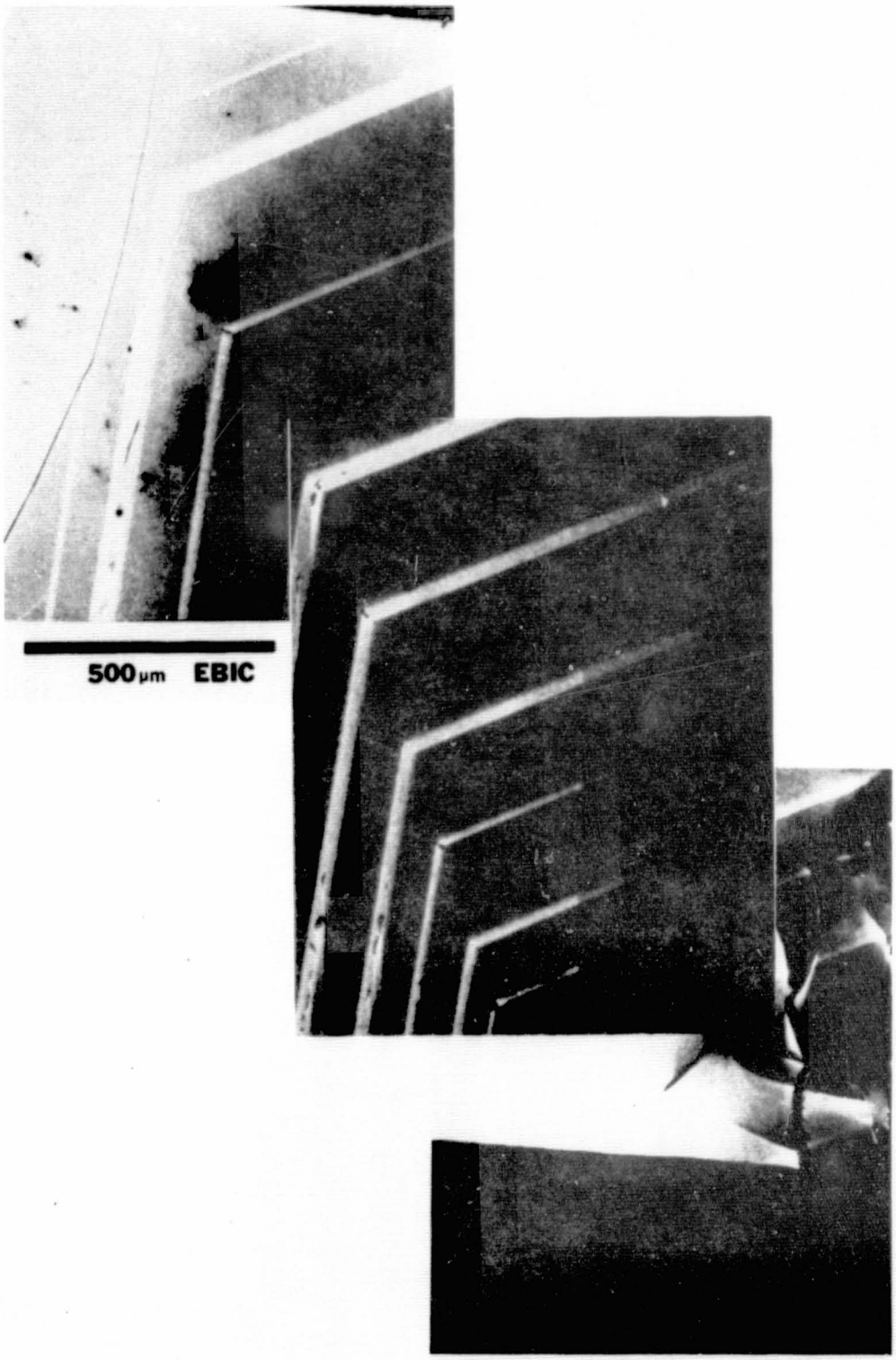

Figure 1c

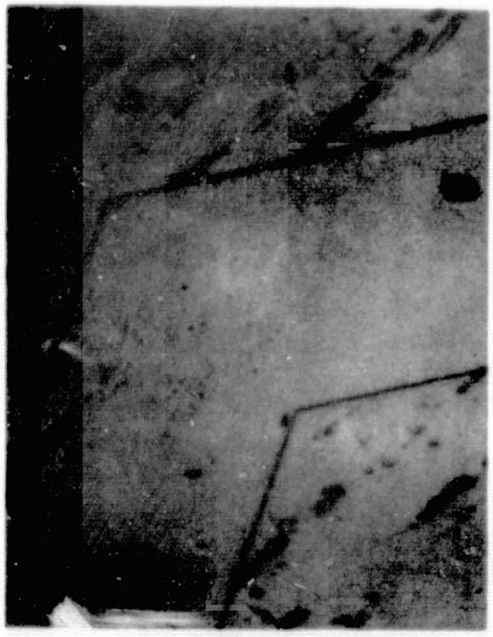

20 μm

20 μm

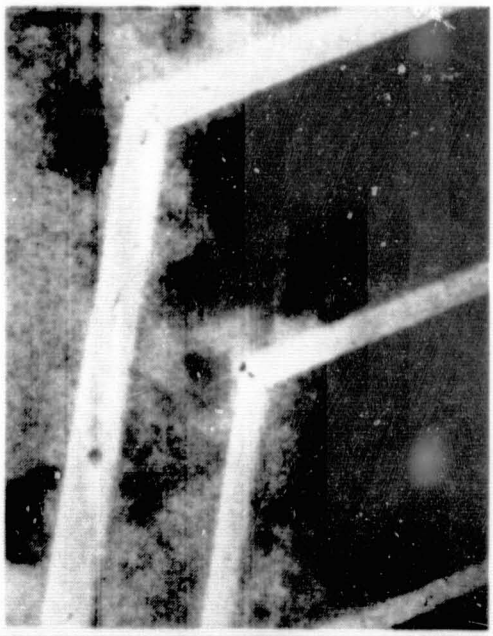

100 μm EBIC

Figure 2

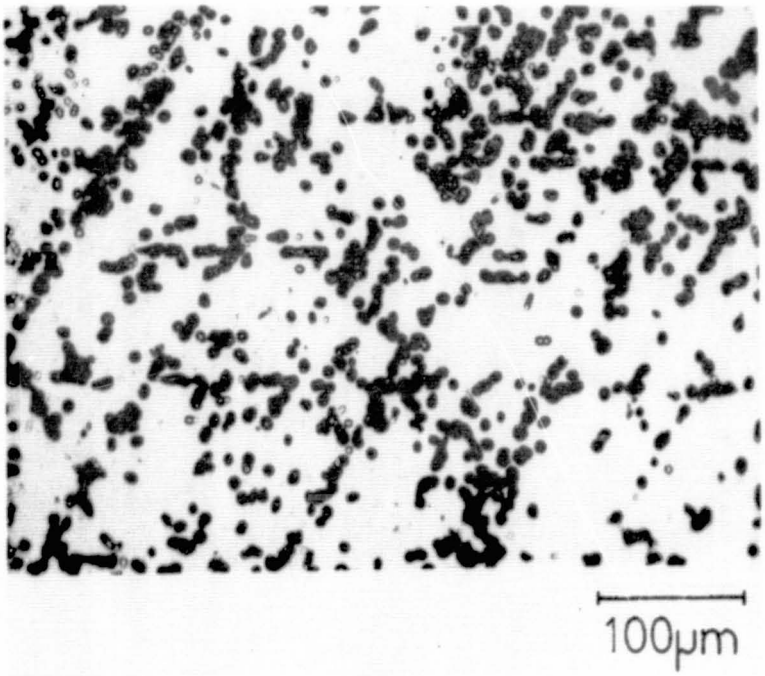

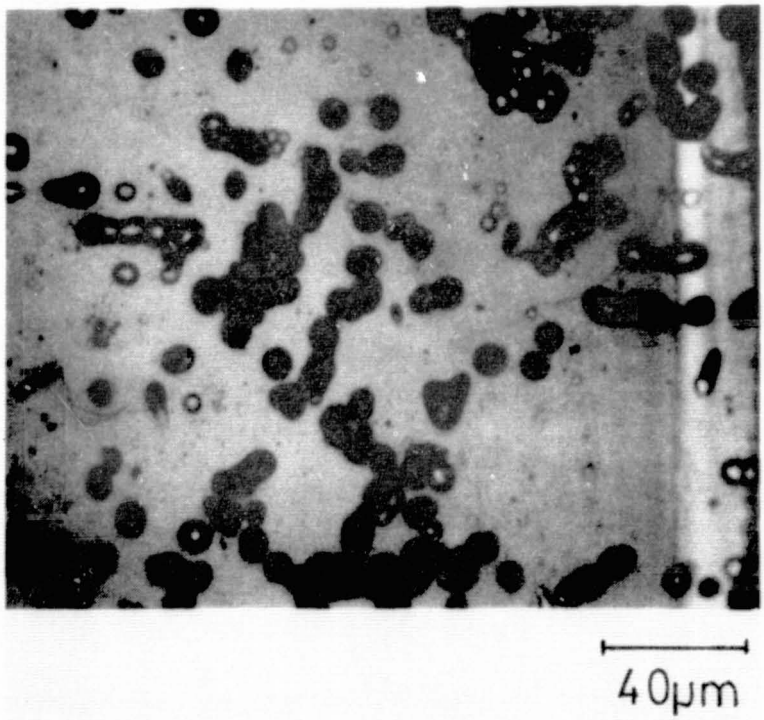

Figure 3

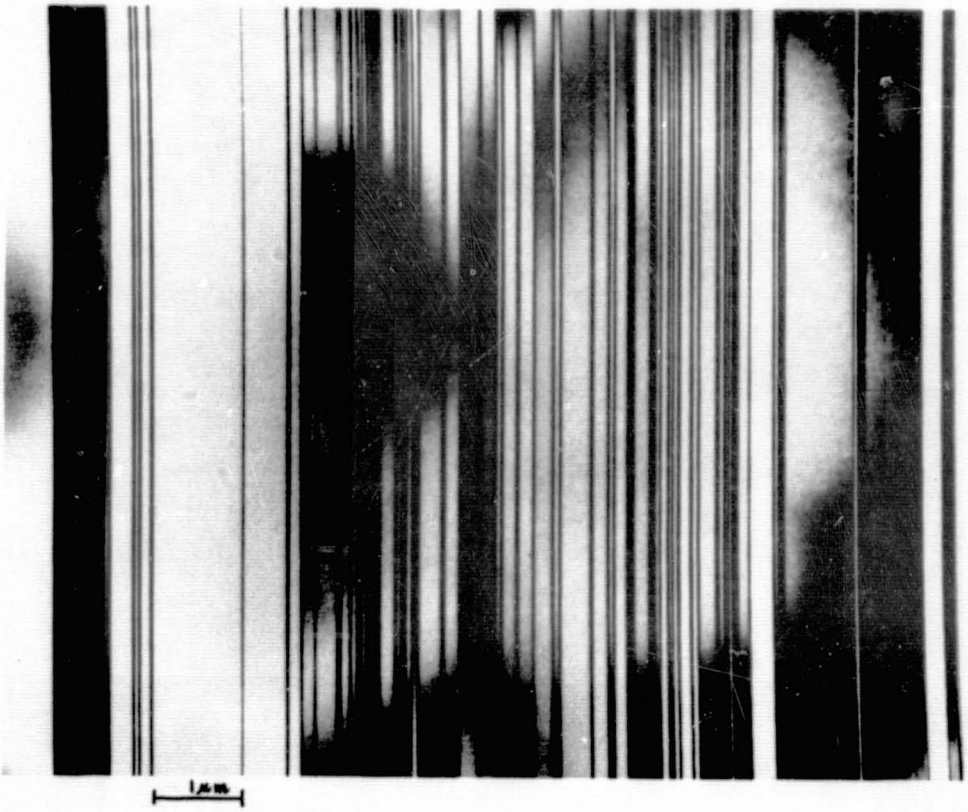

Figure 4a

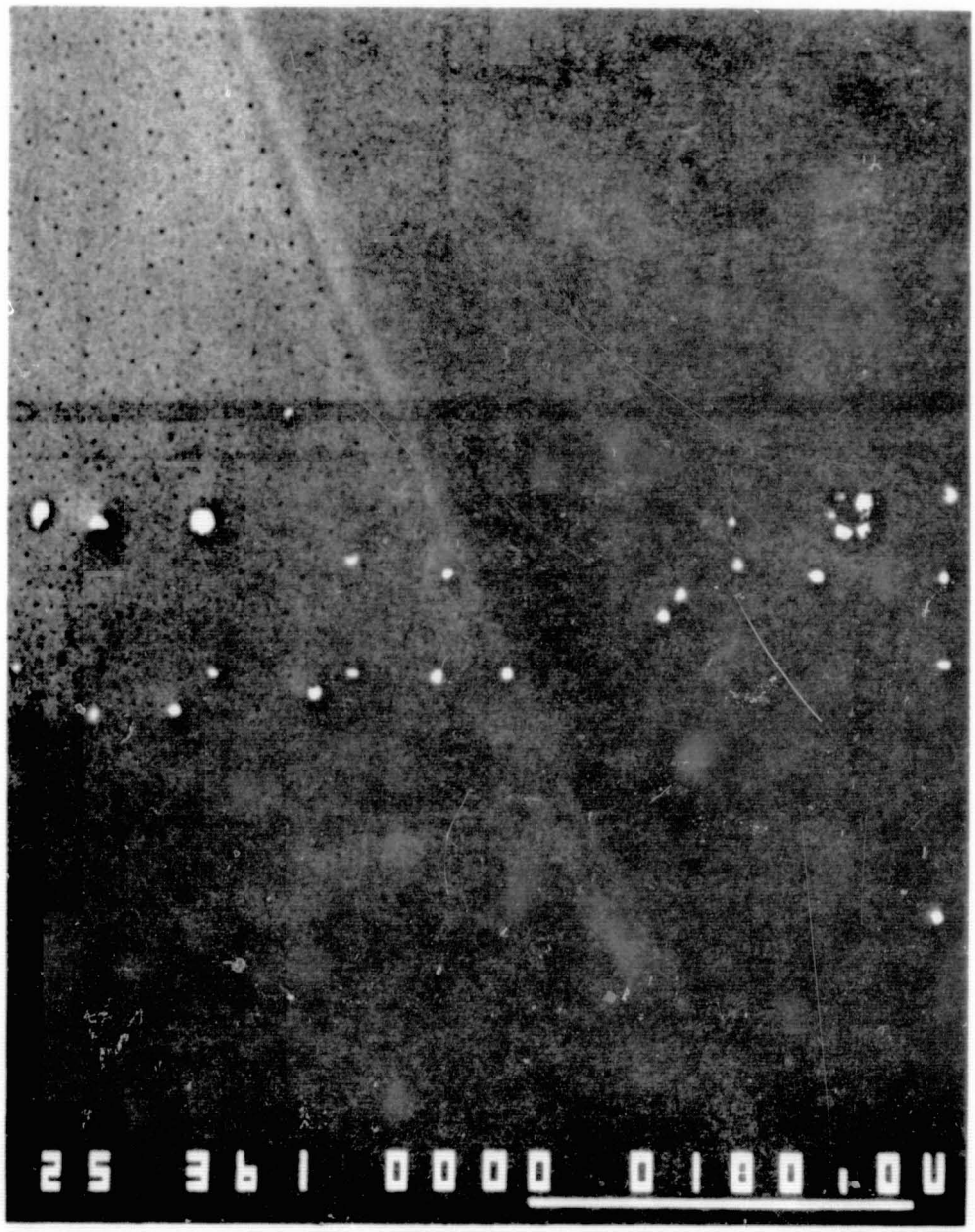

Figure 4b

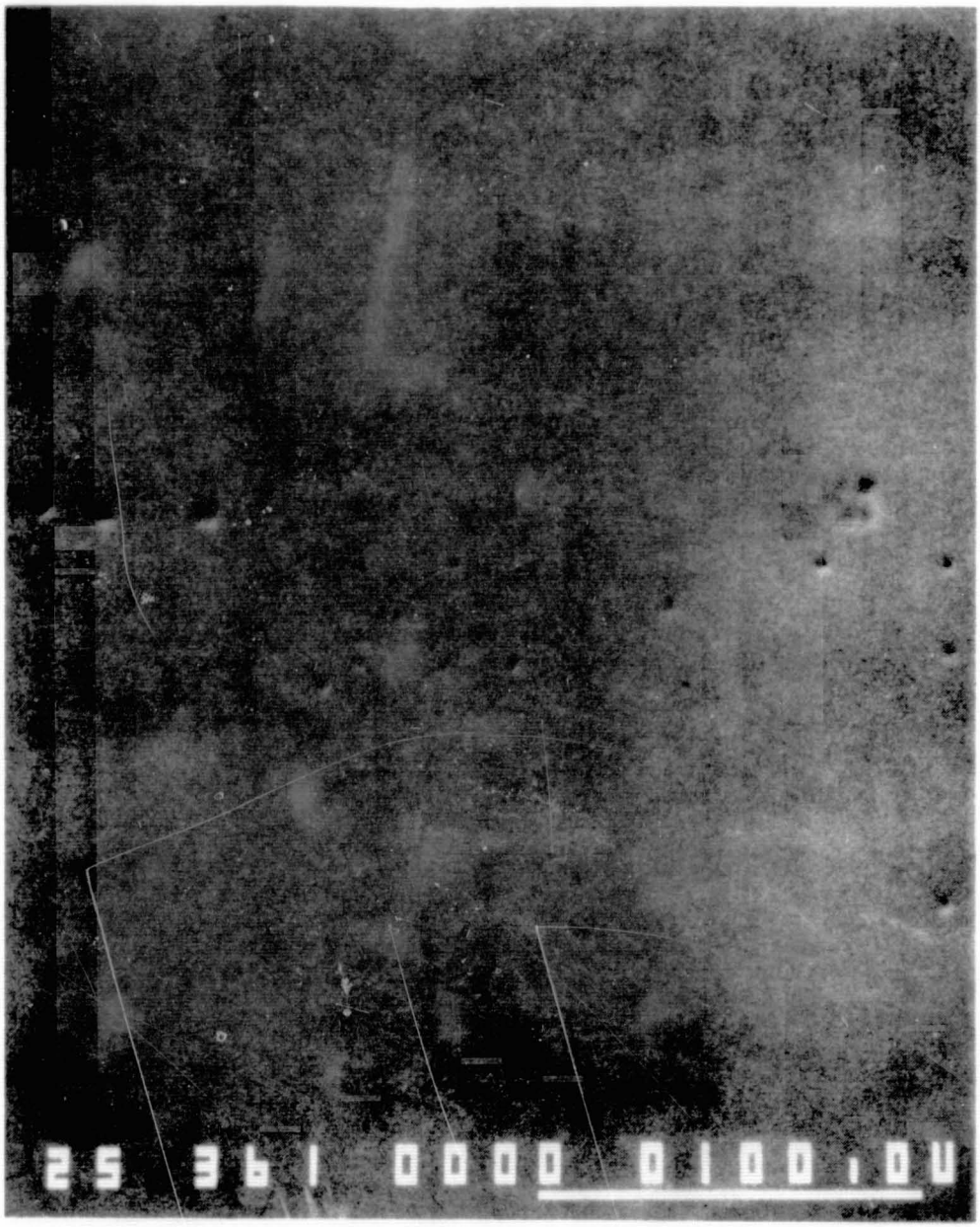

Figure 4c

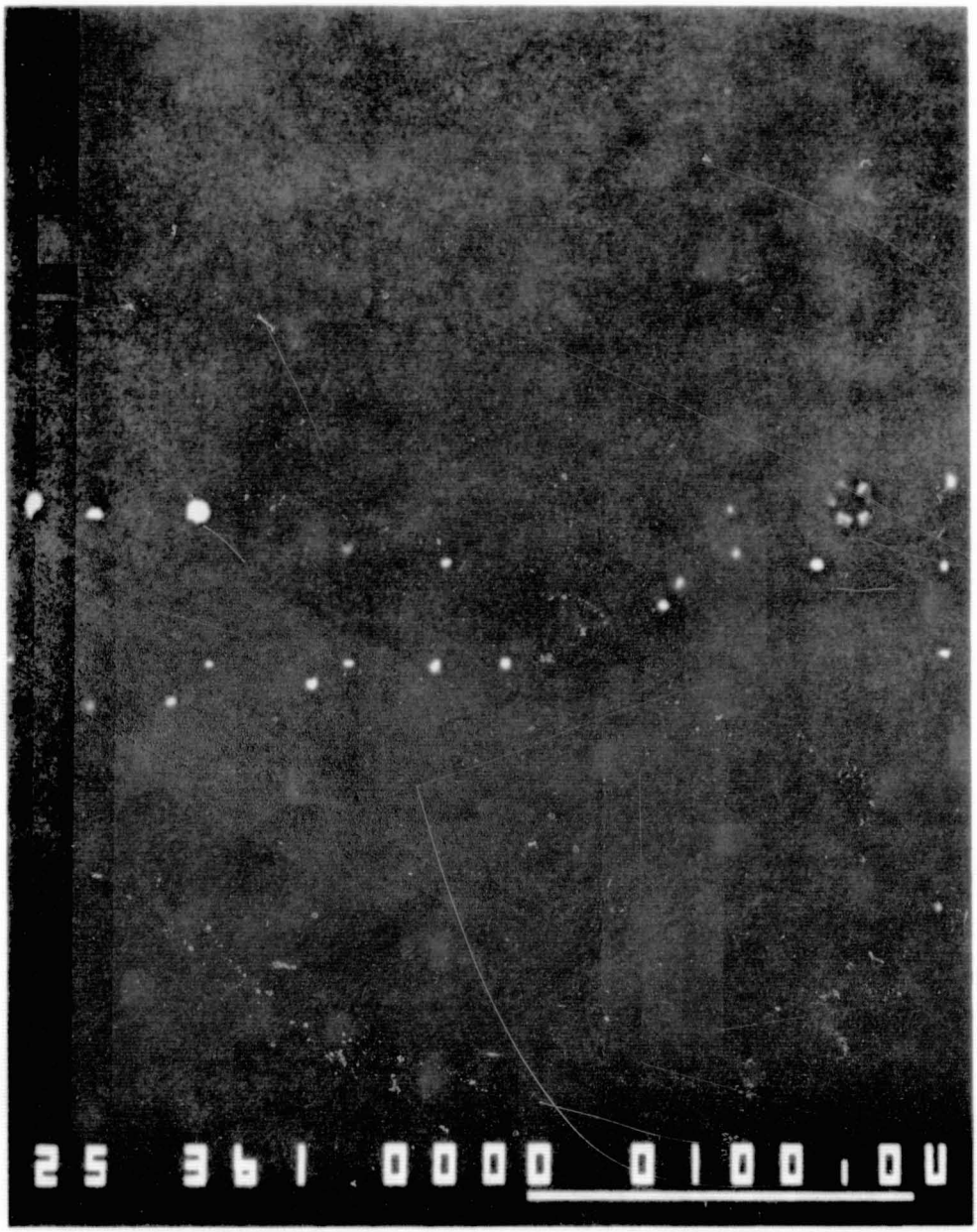

Figure 5

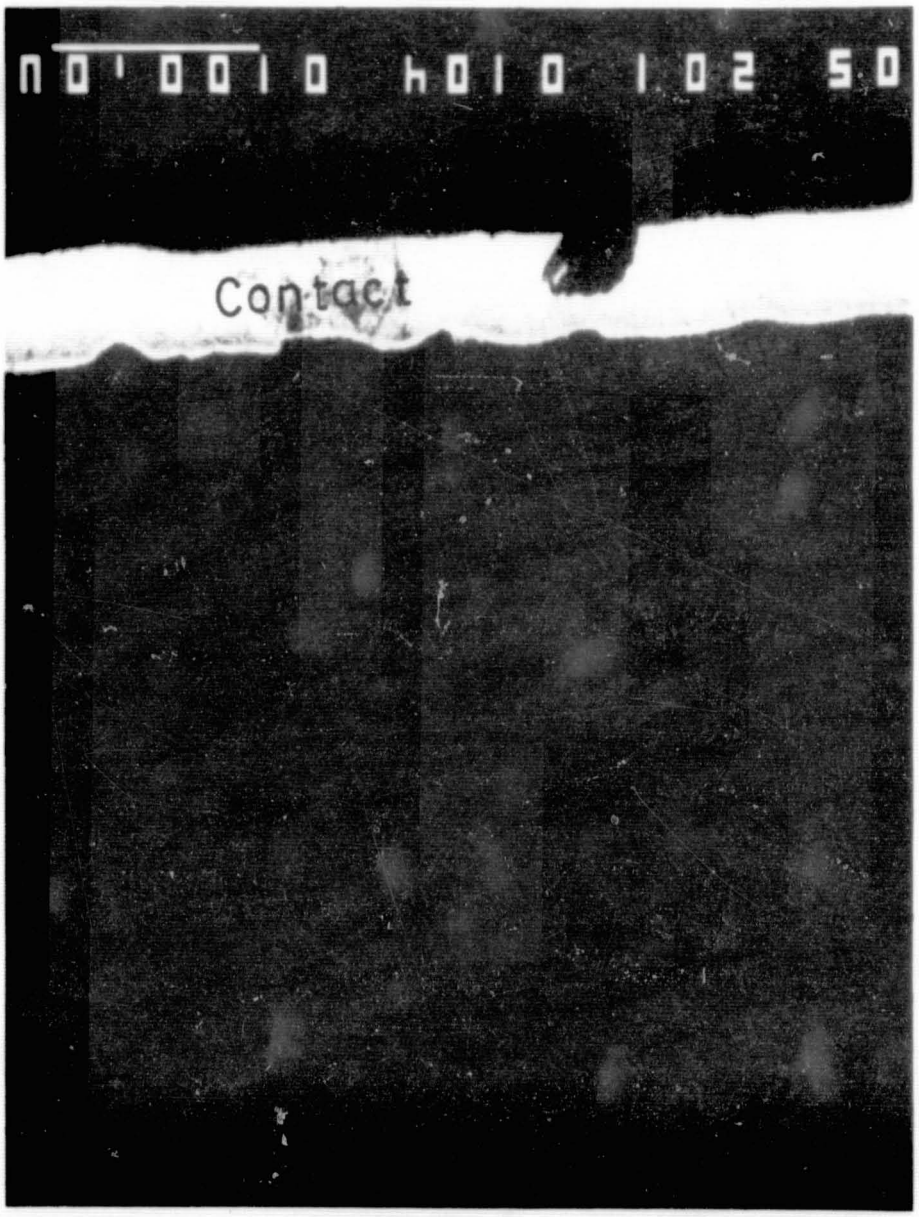

Figure 6

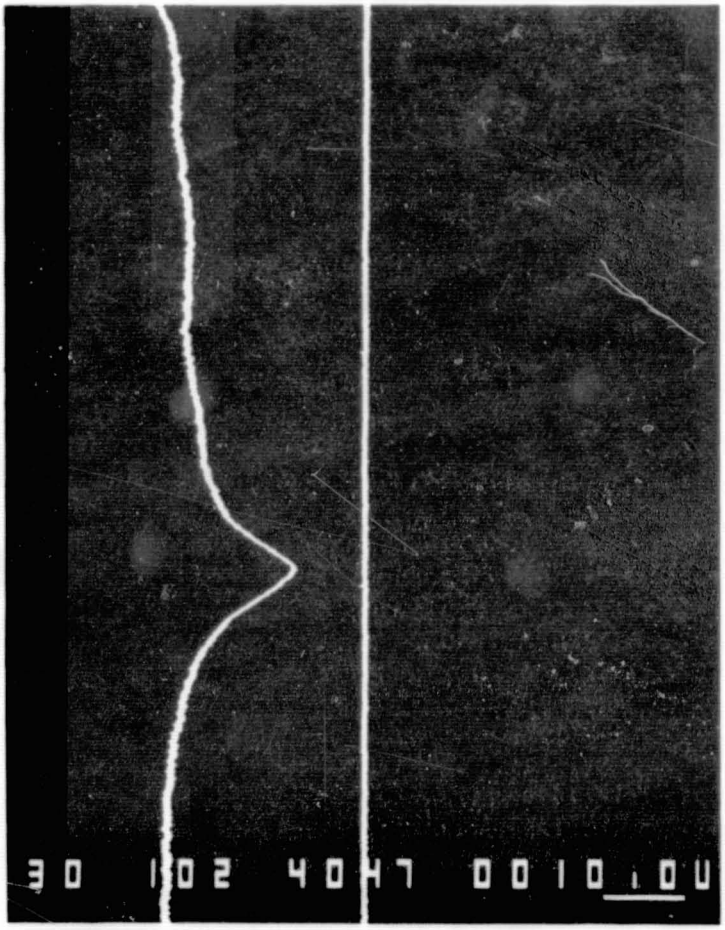

Figure 7

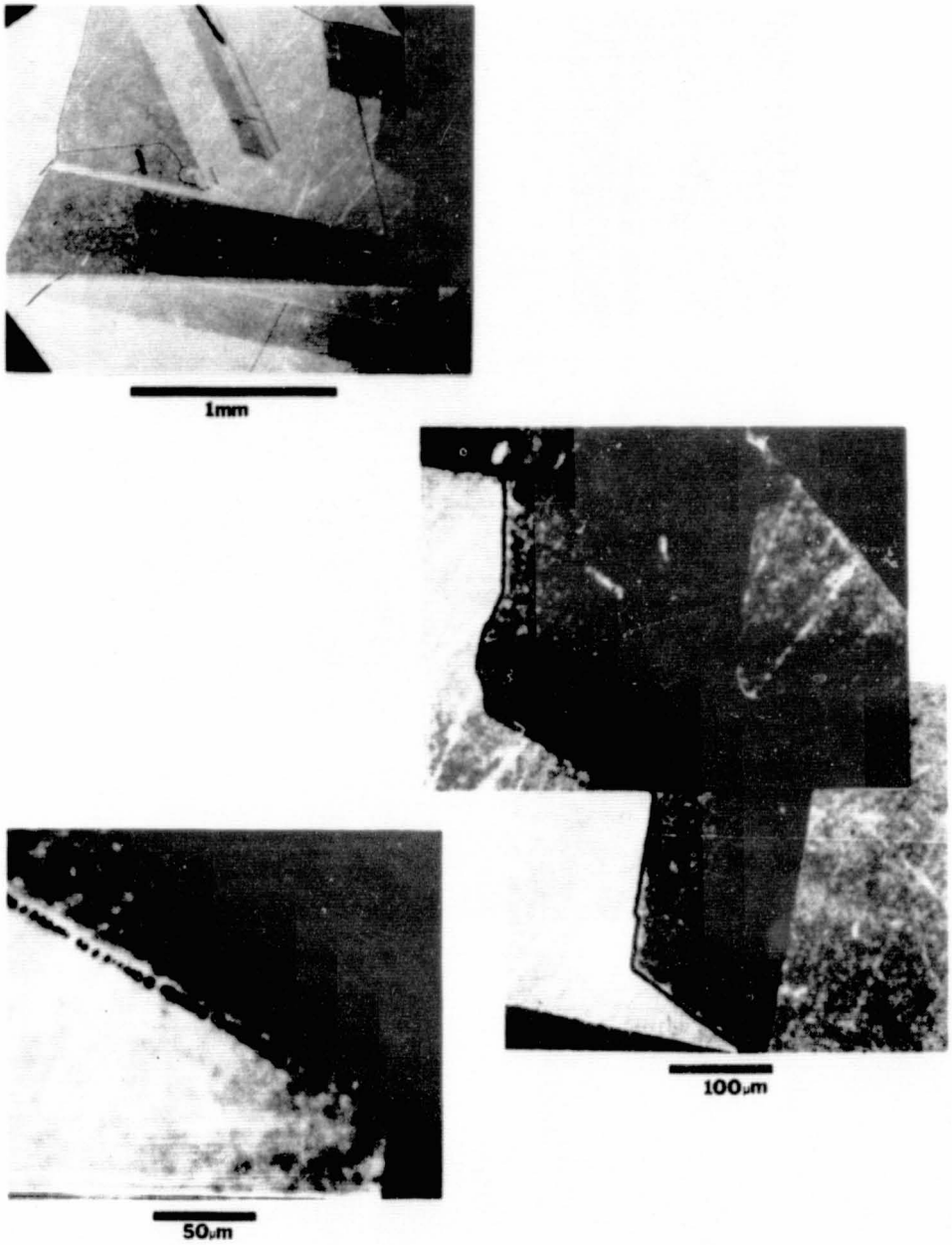

Figure 8

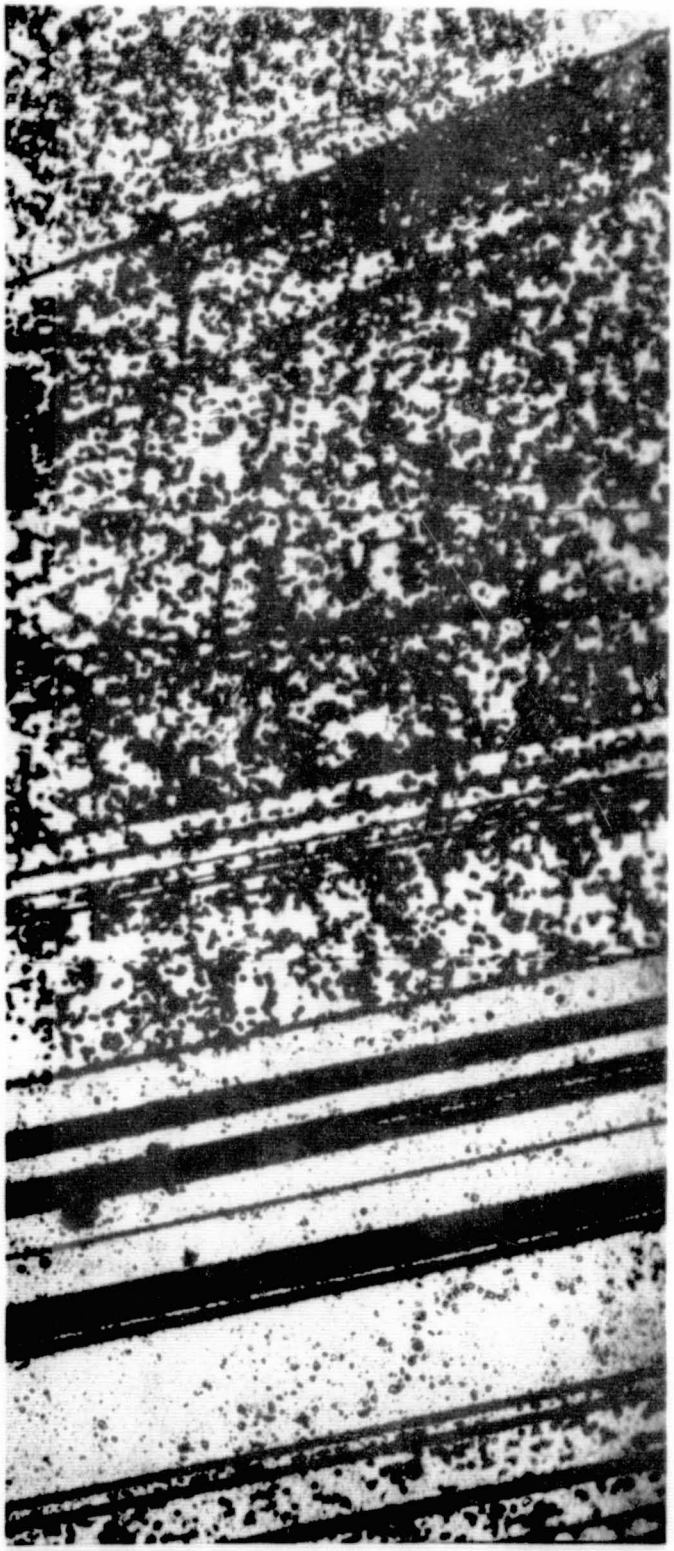

100μm

Figure 9

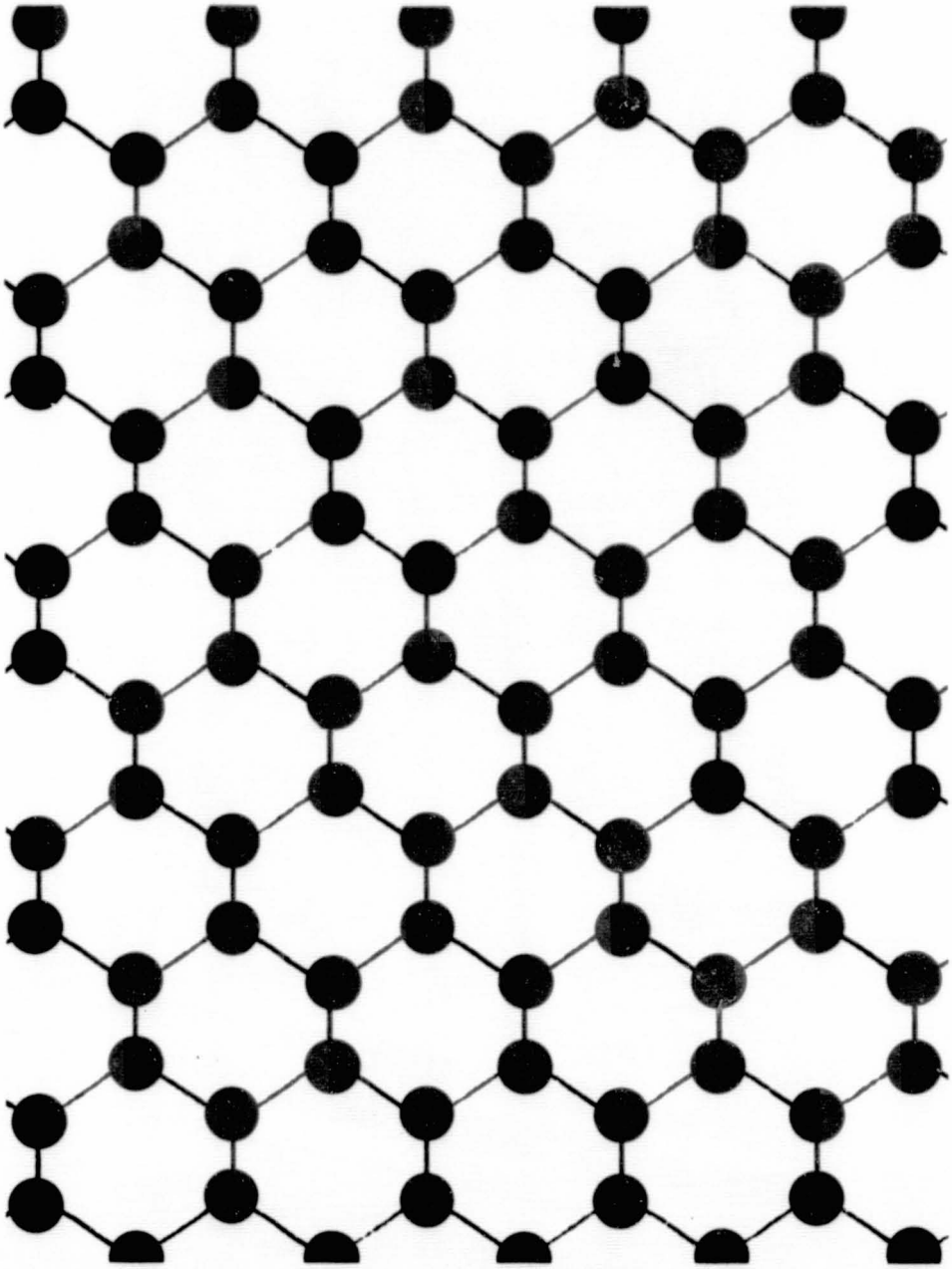

Figure 10

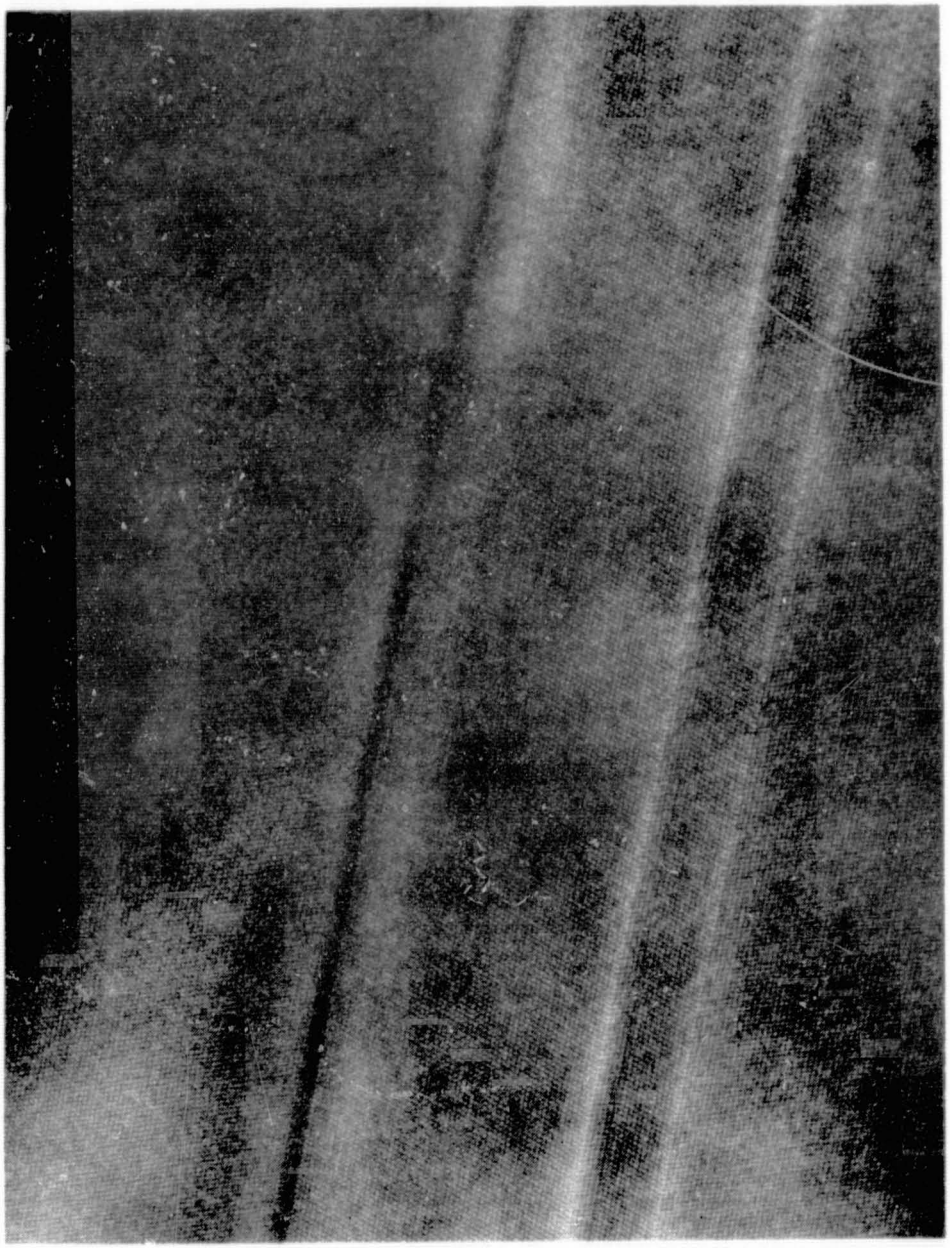

Figure 10b

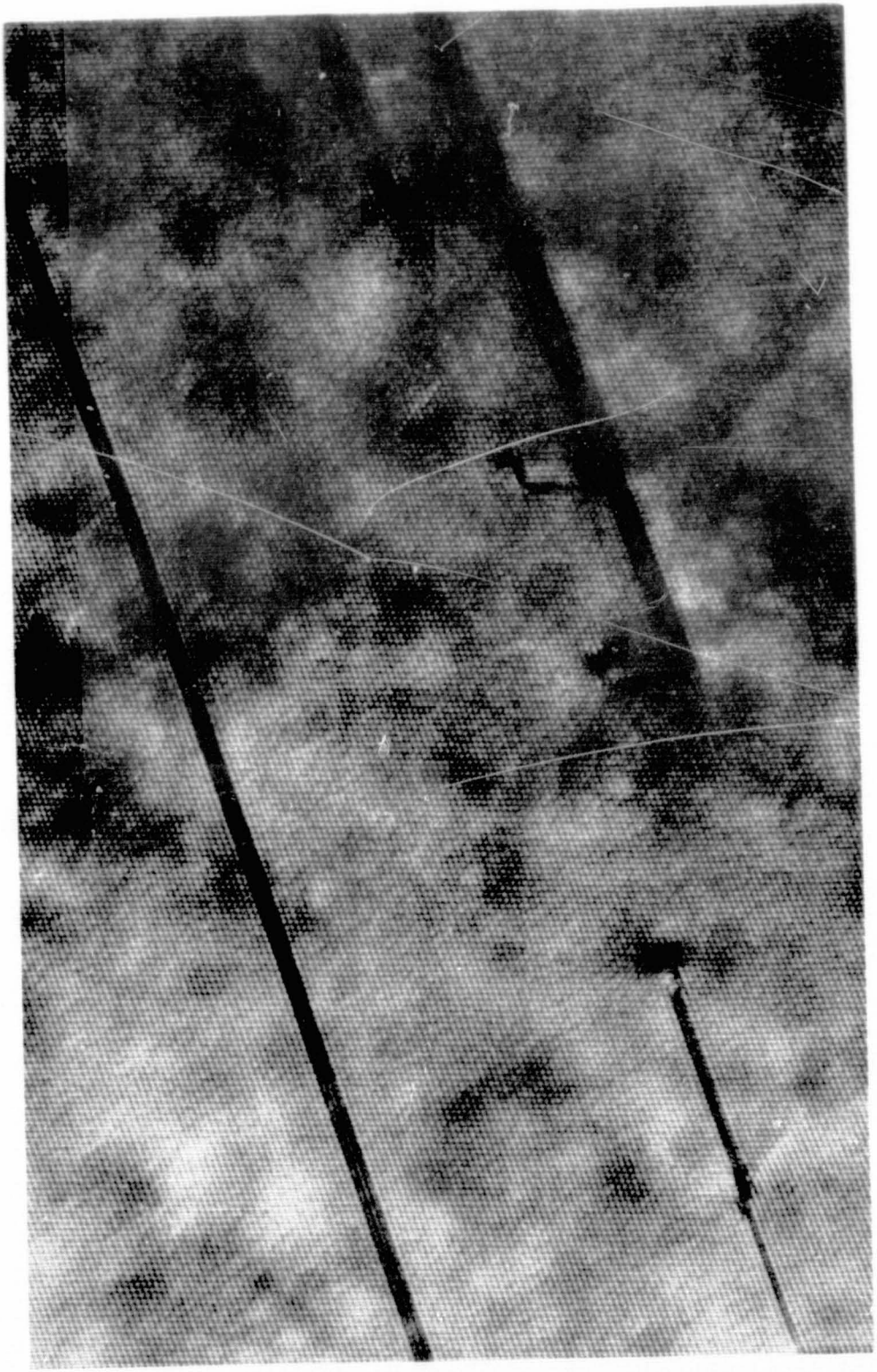

Figure 11

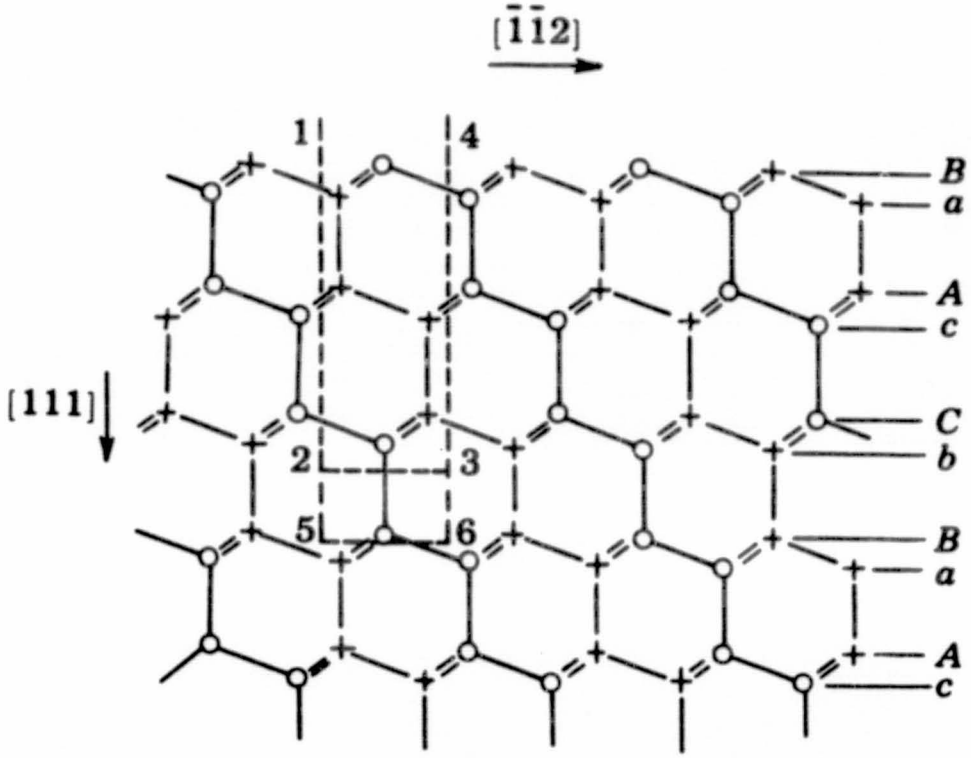

Figure 12

Figure 12b

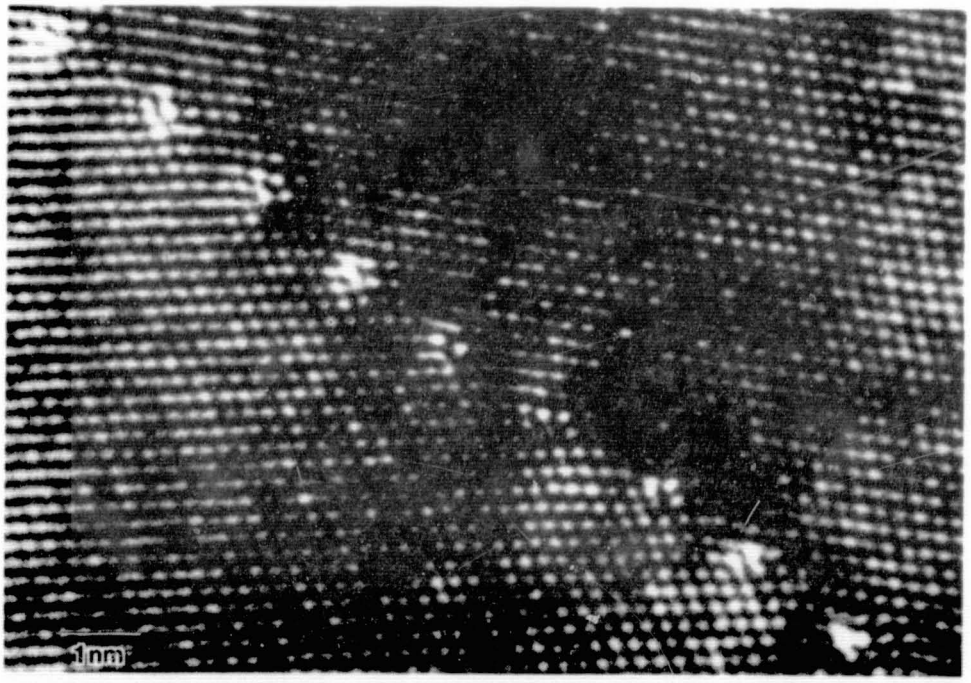

Figure 12c

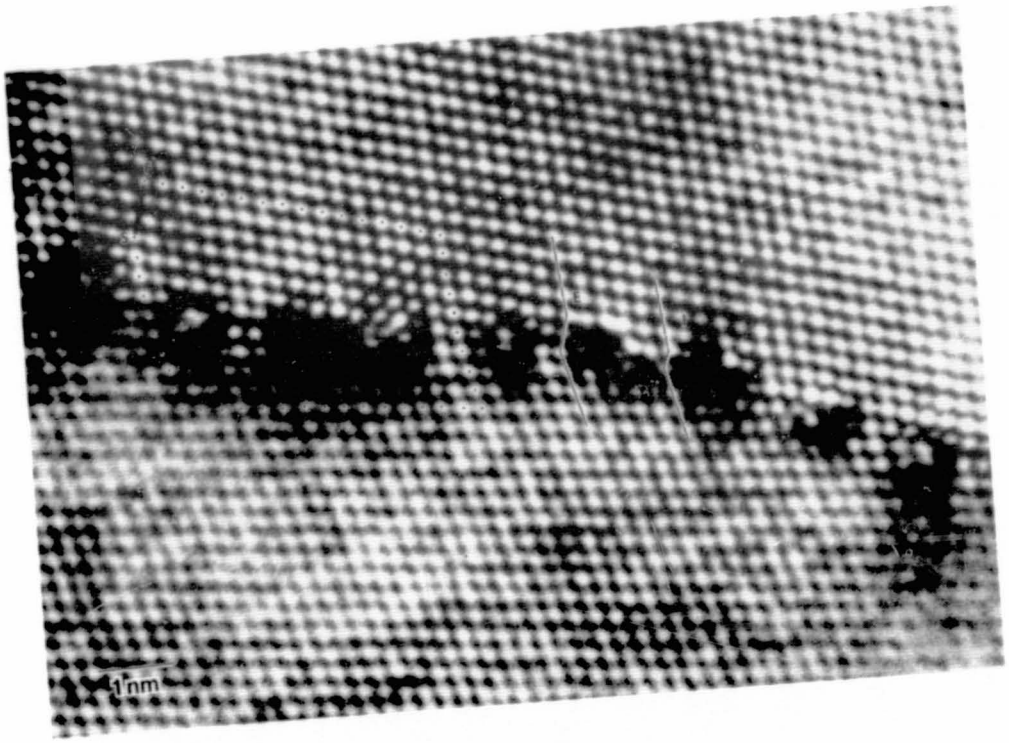

Figure 12d

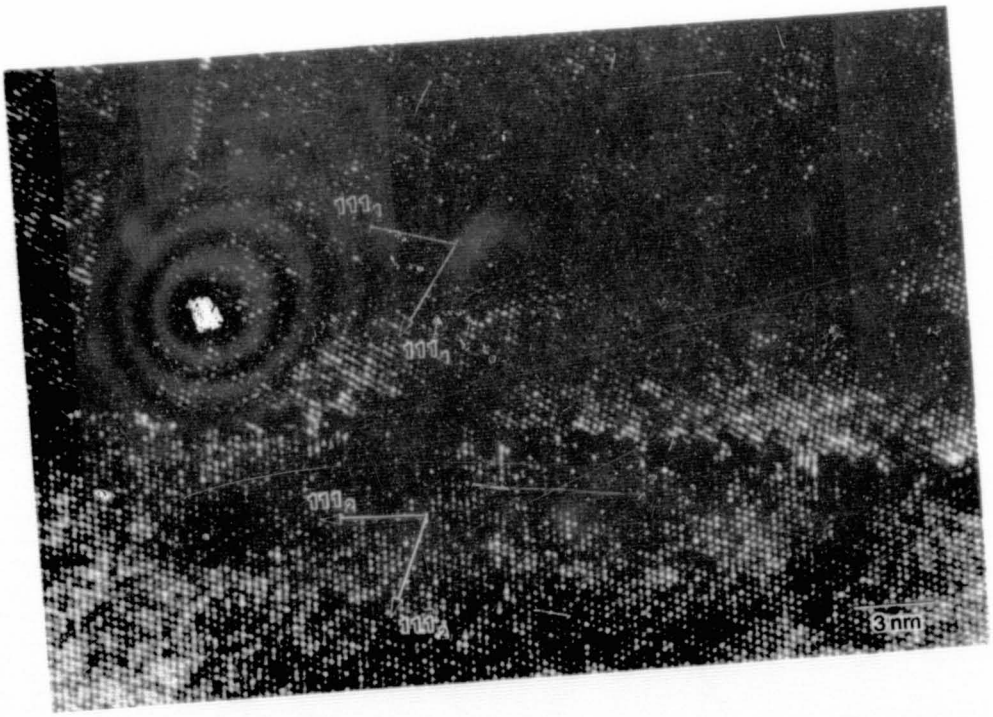

Figure 13

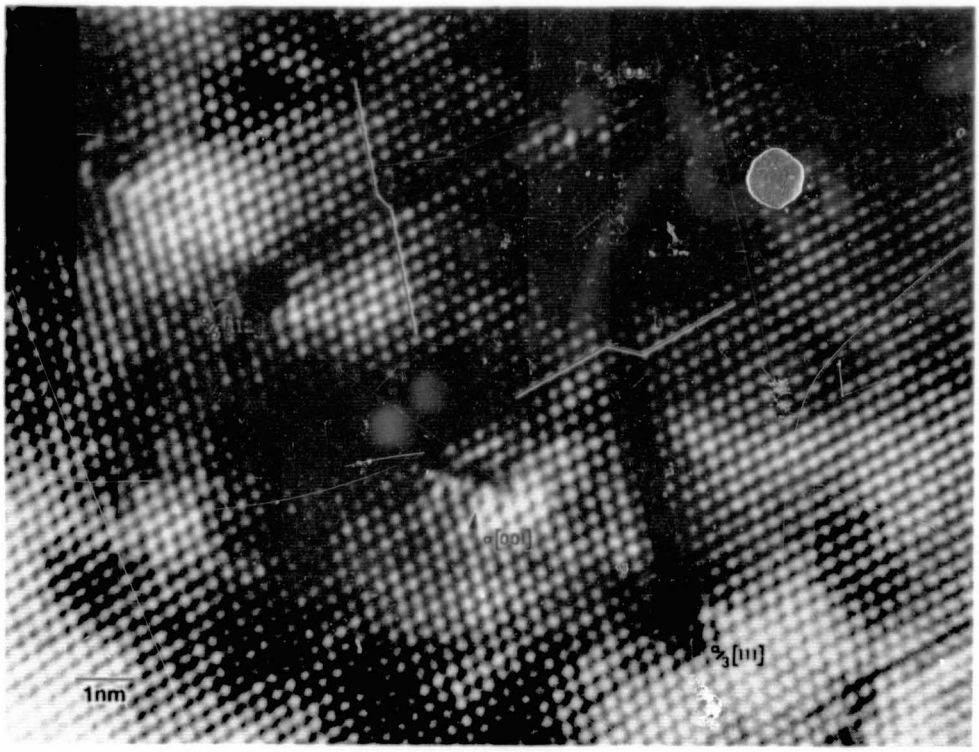

Figure 13b

Figure 14

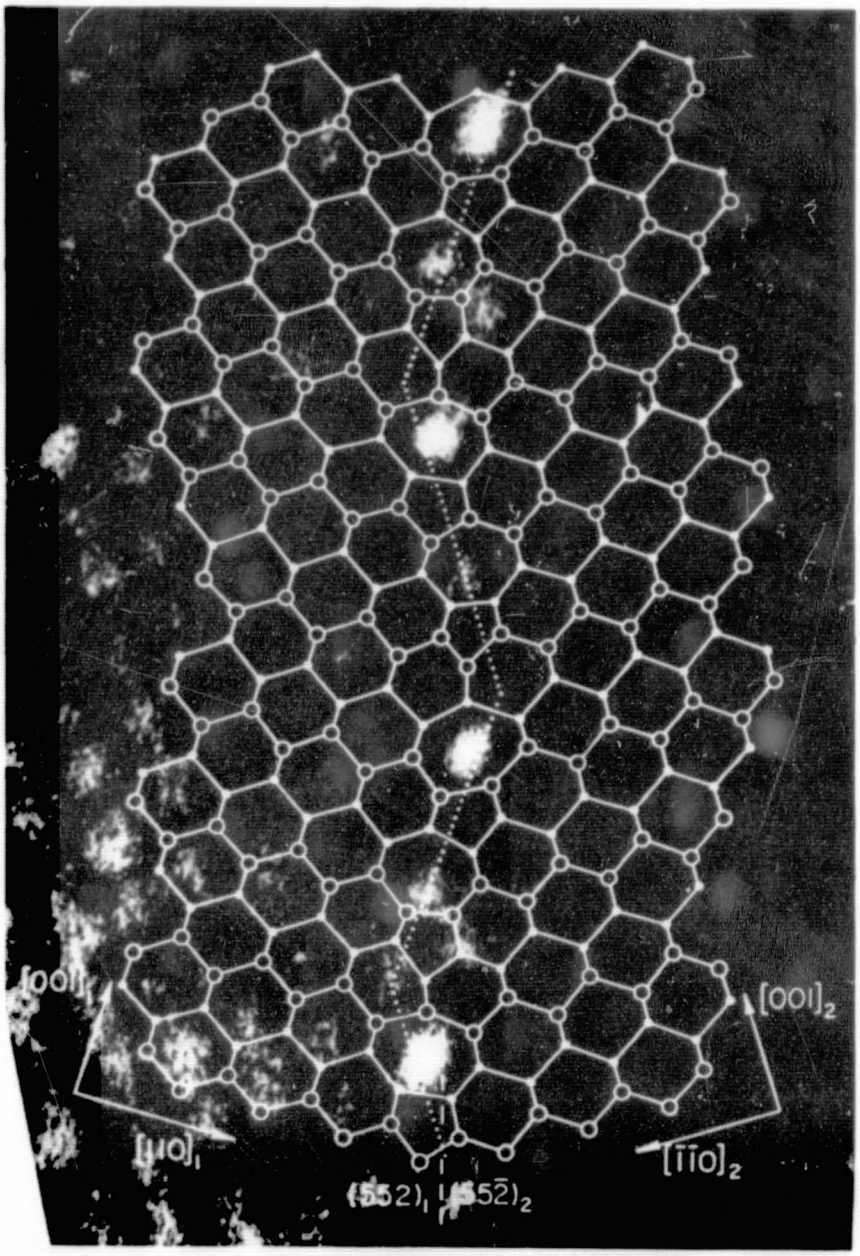

Figure 15

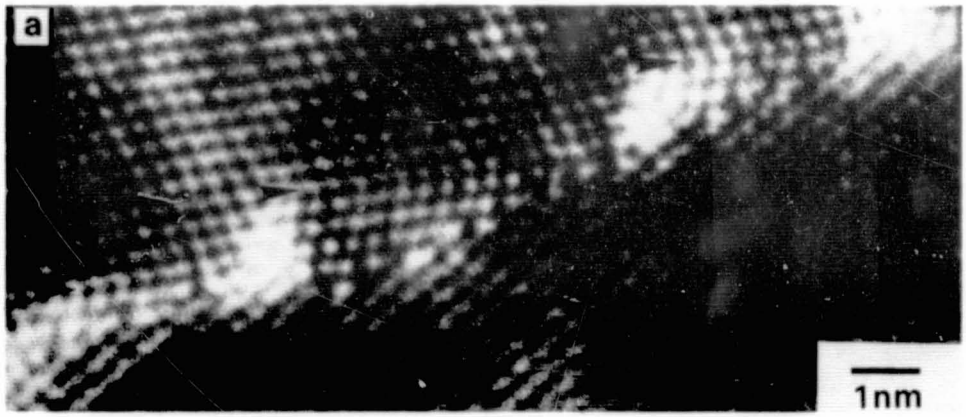

Figure 16

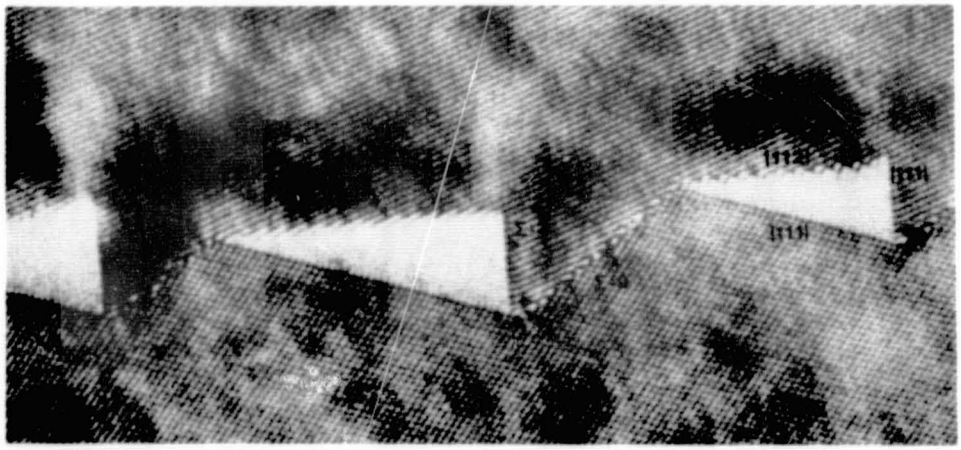

Figure 17

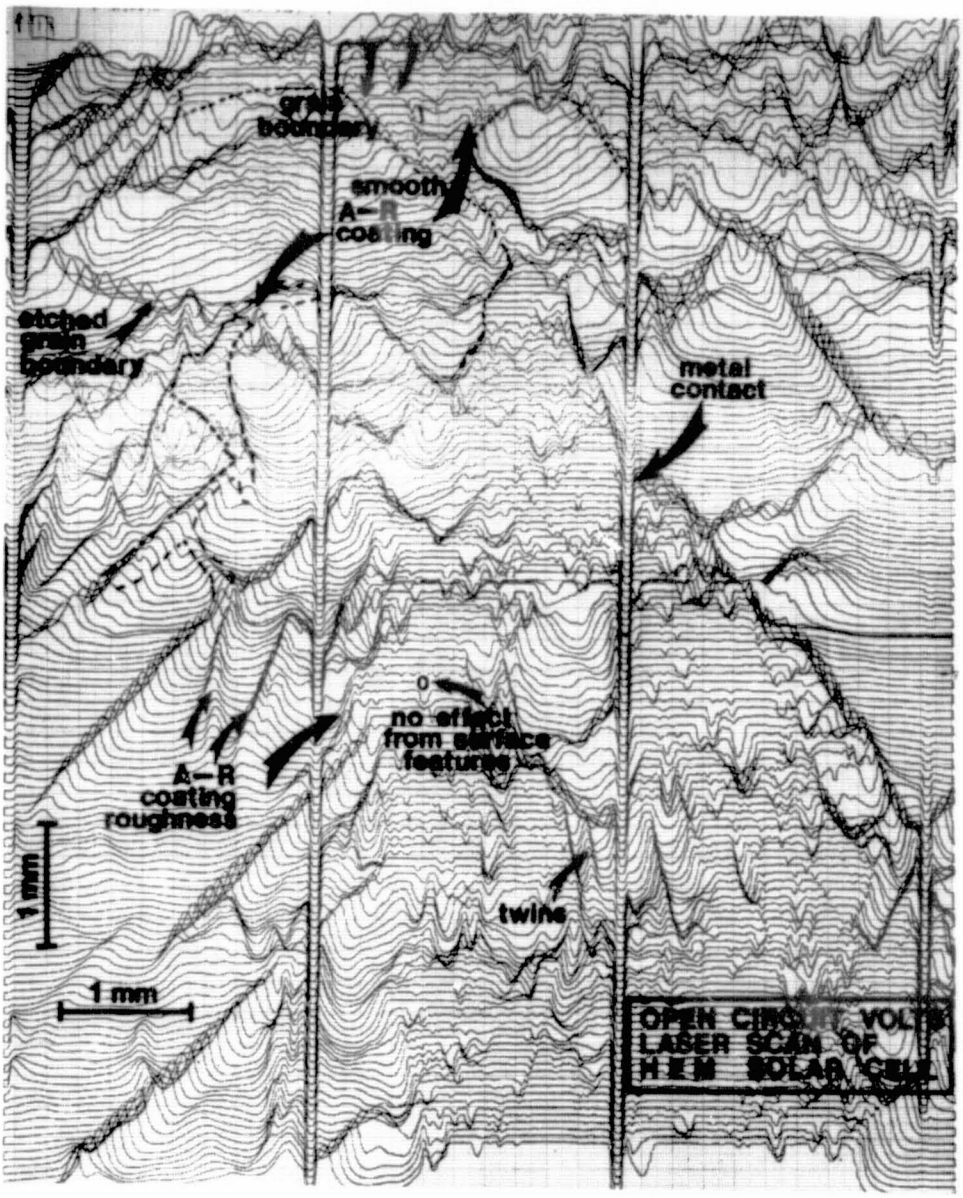

Figure 18

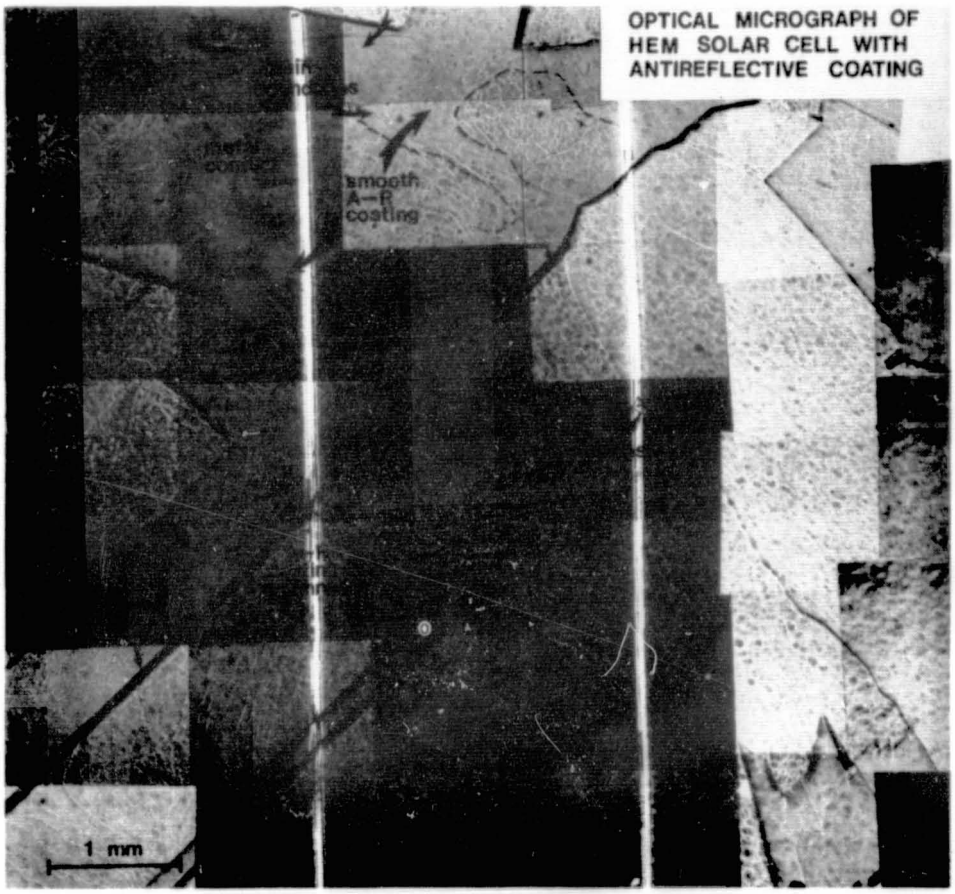

Figure 19

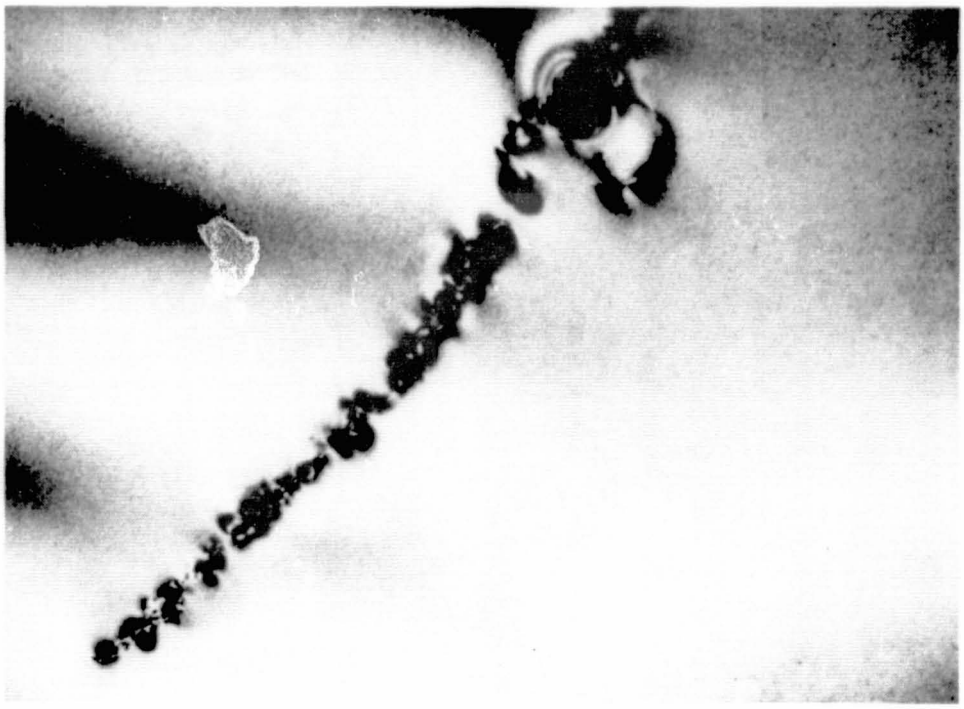

Figure 20

Figure 21a

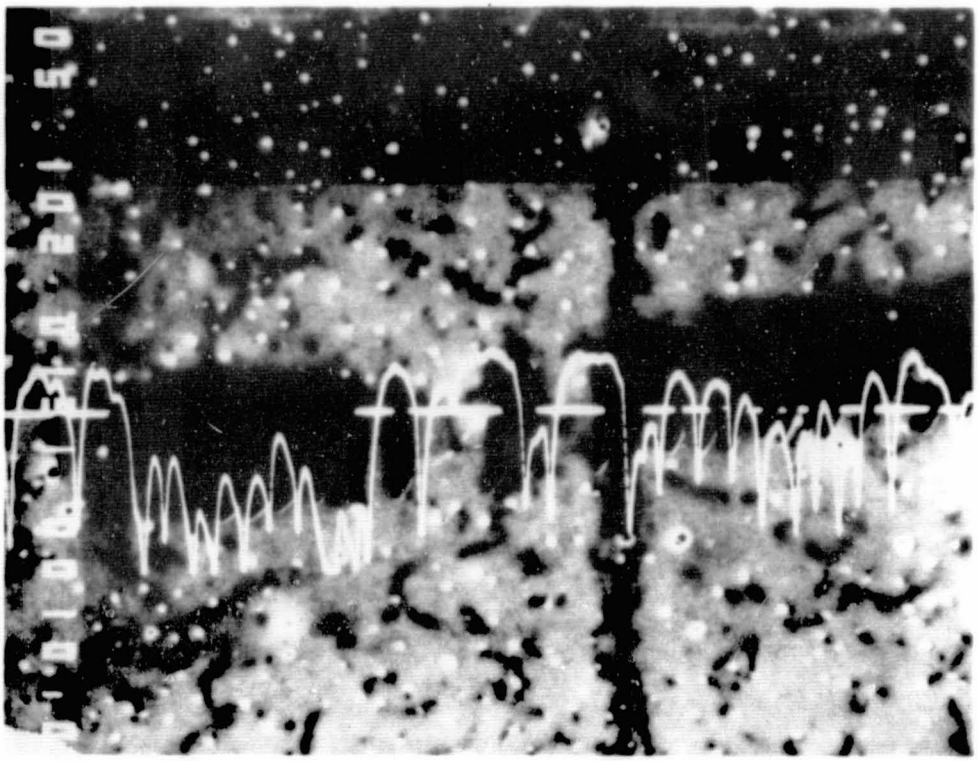

Figure 21b

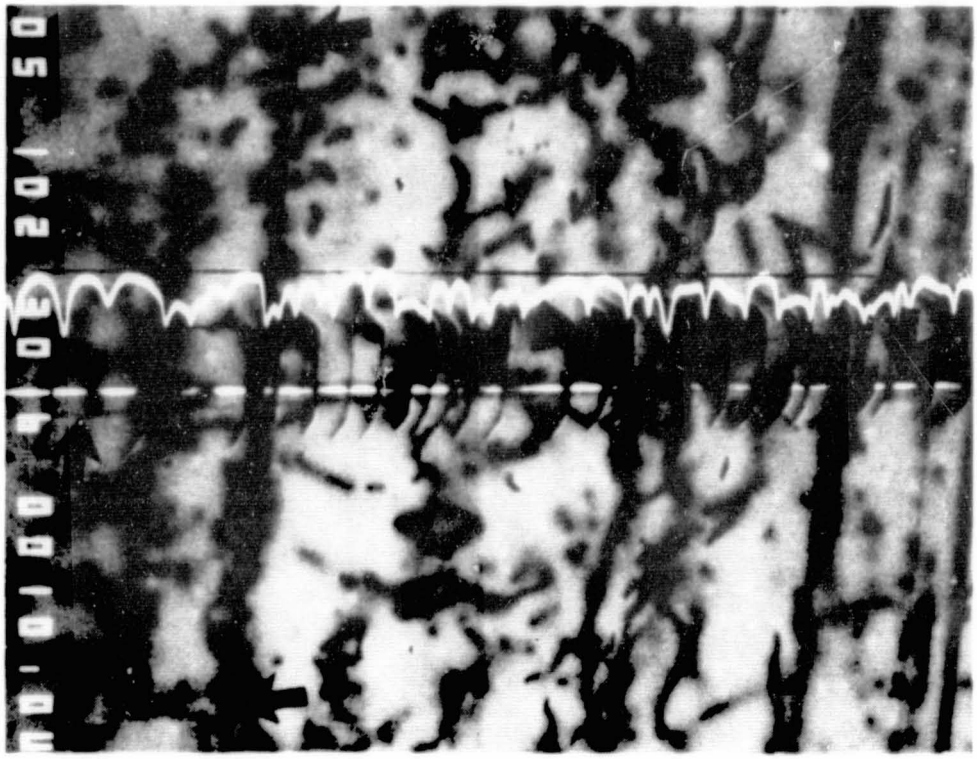

Figure 22

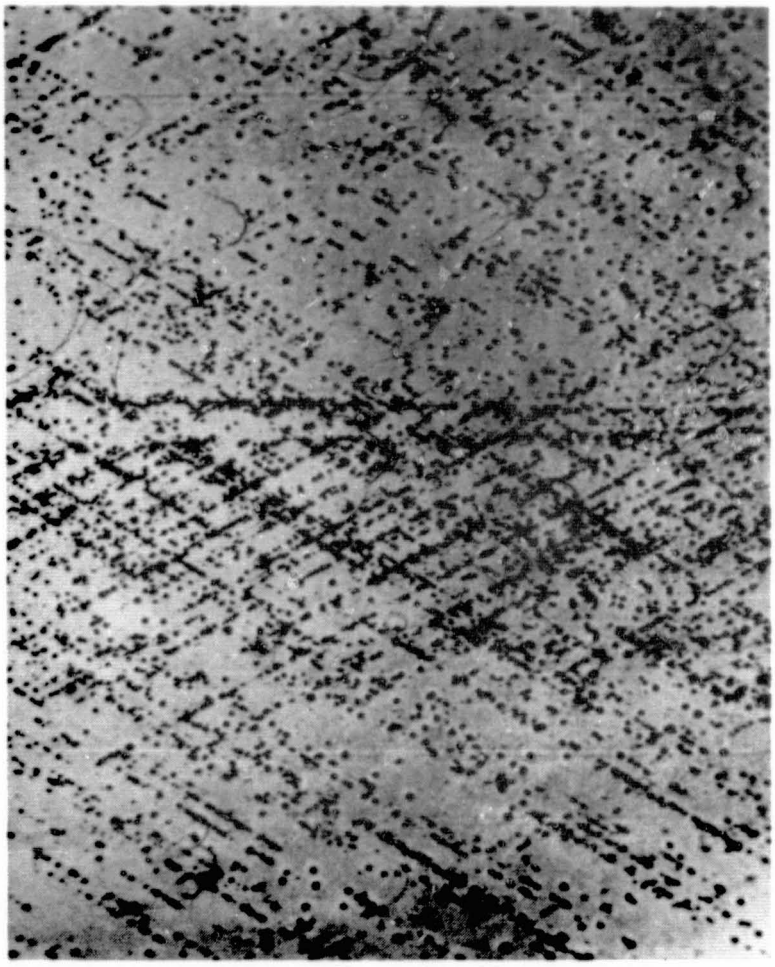

Figure 23

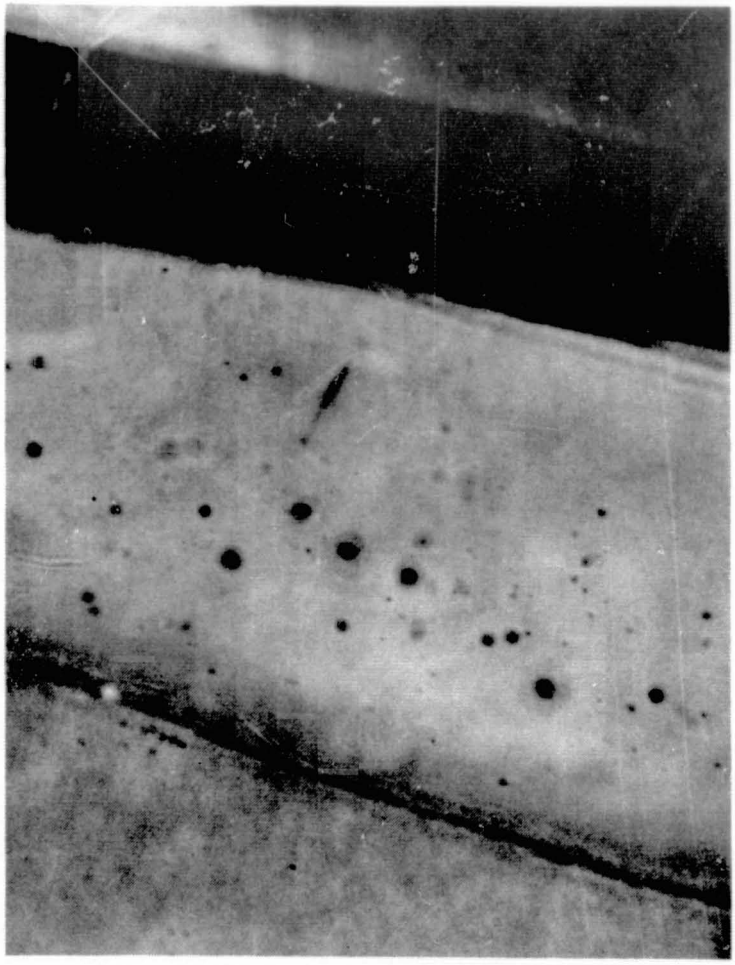

Figure 24

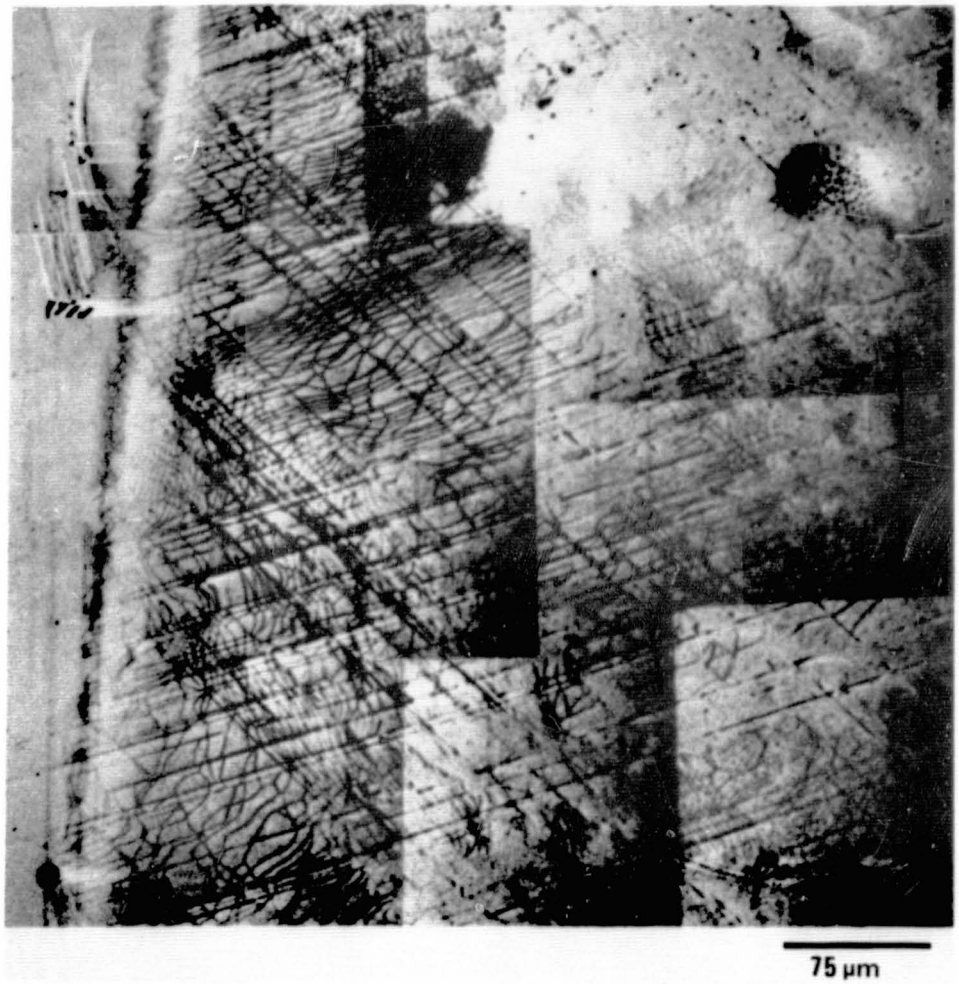

Figure 25

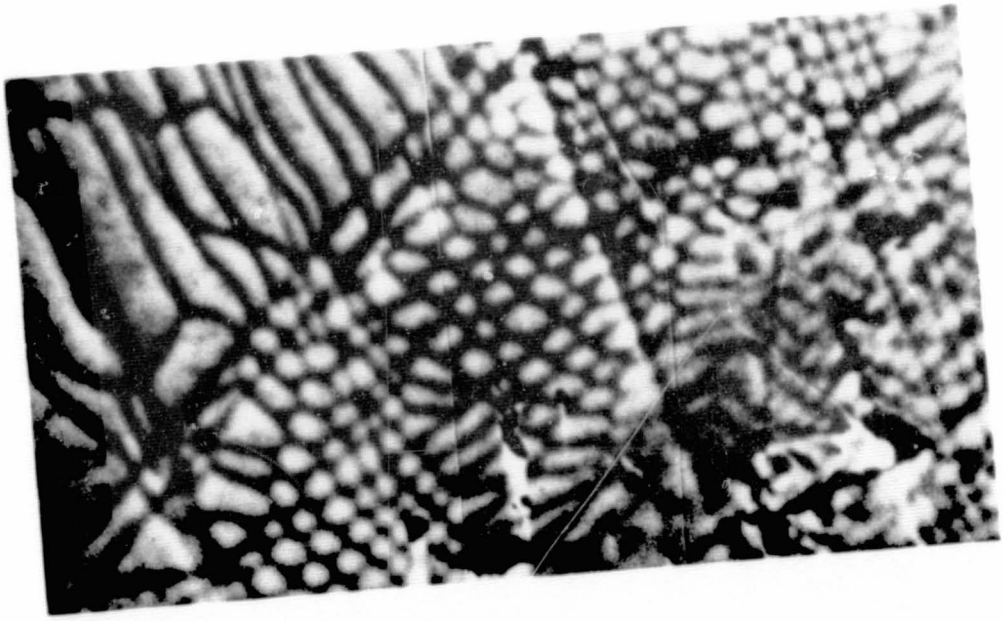

Figure 26

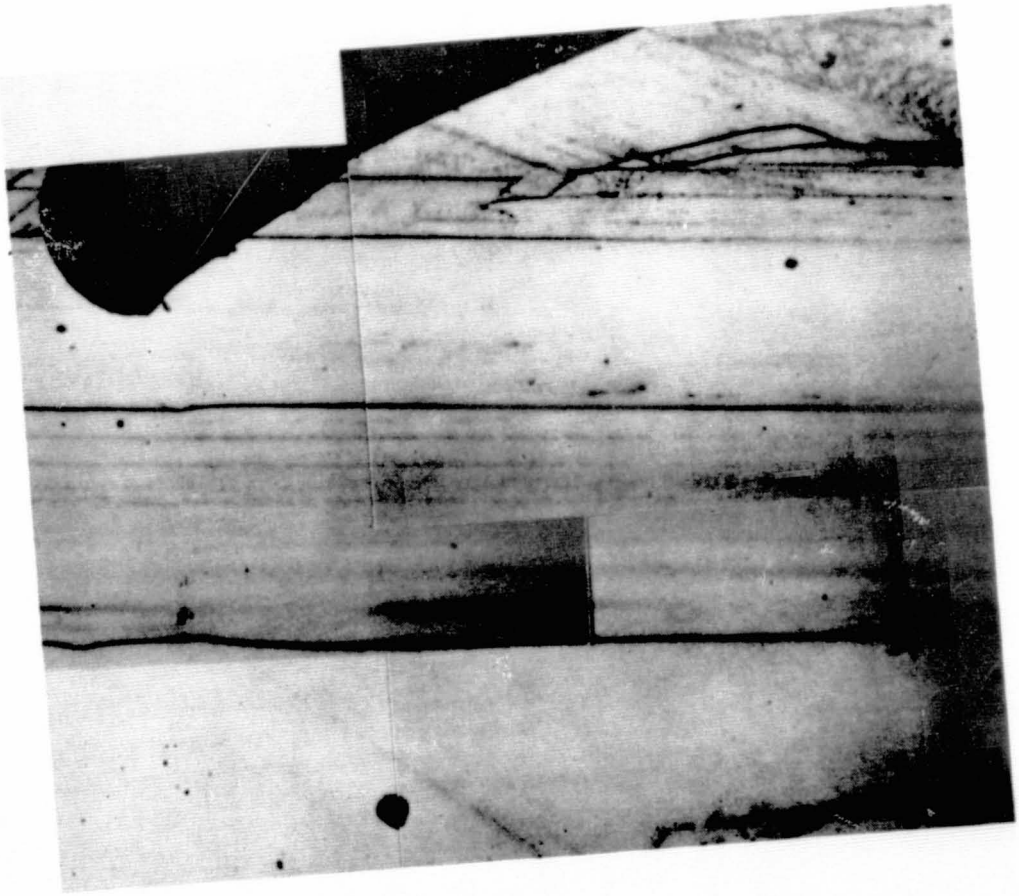

Figure 27

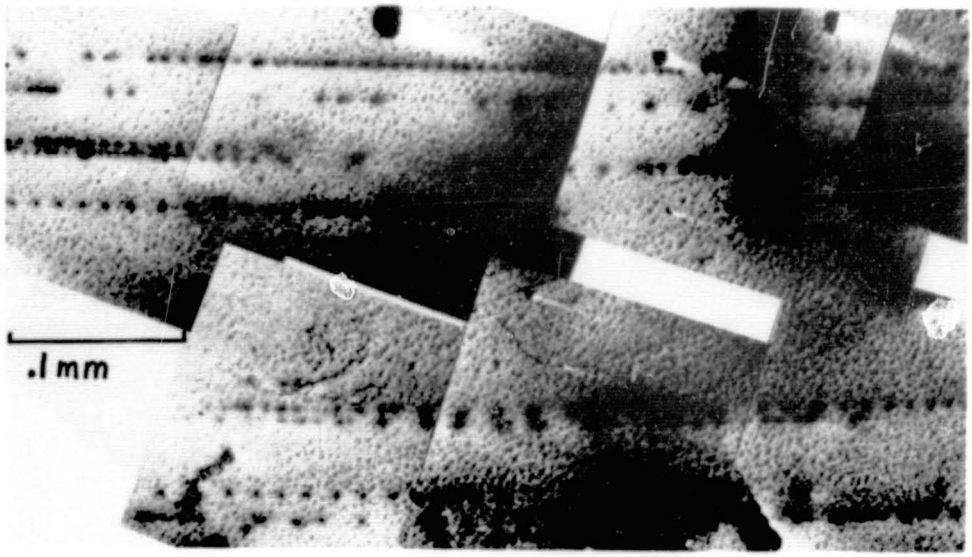

Figure 28

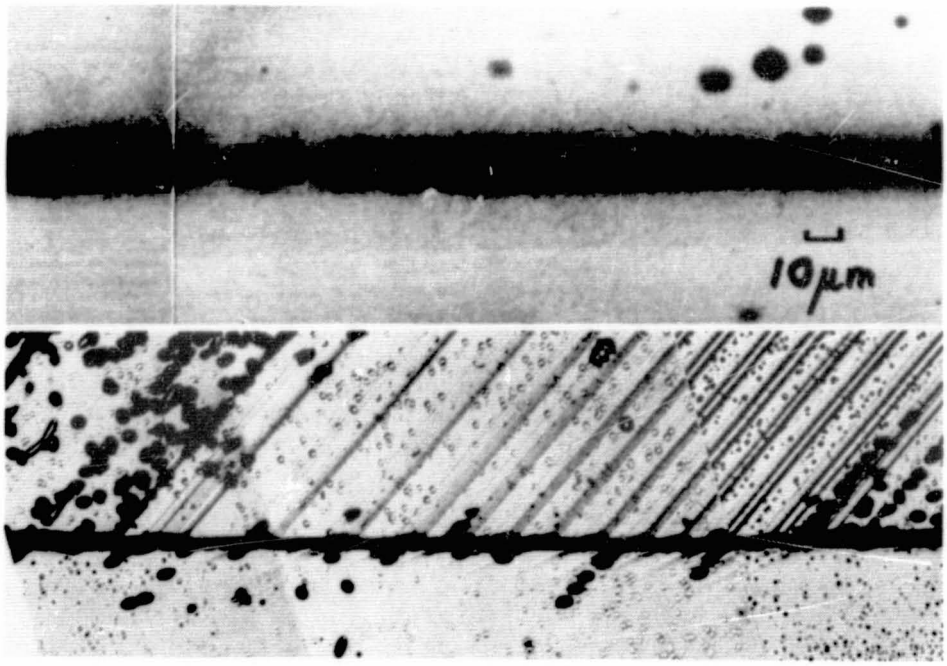

Figure 29

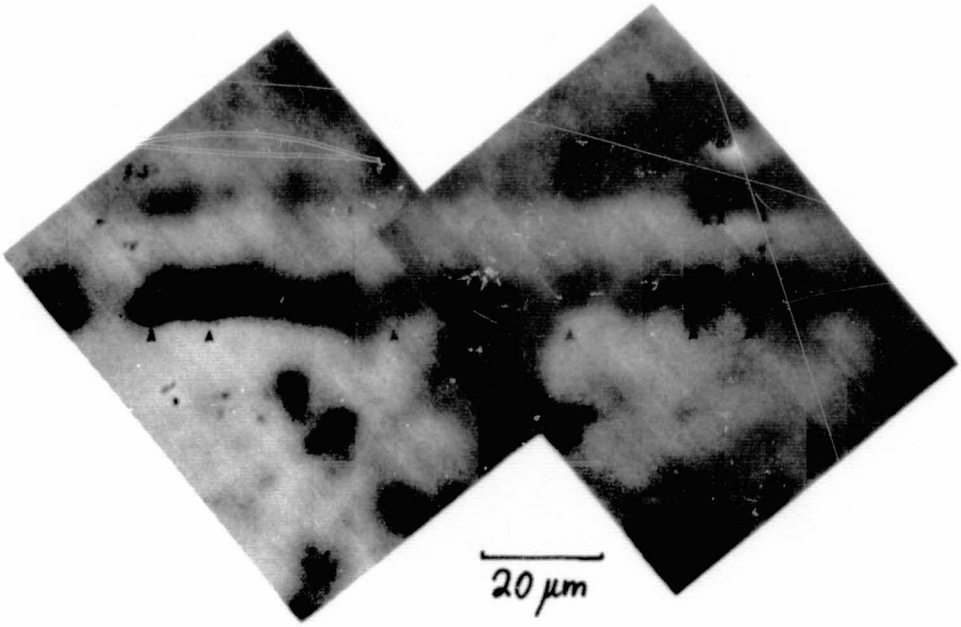

Figure 29b

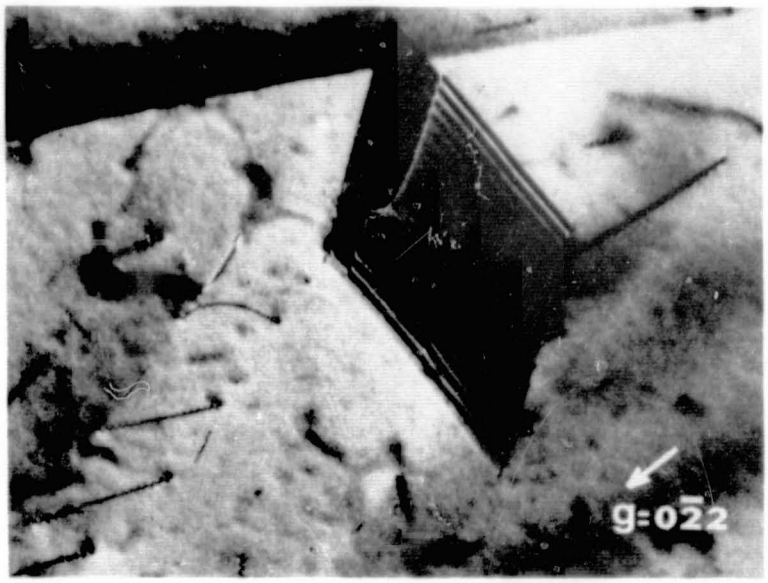

Figure 30

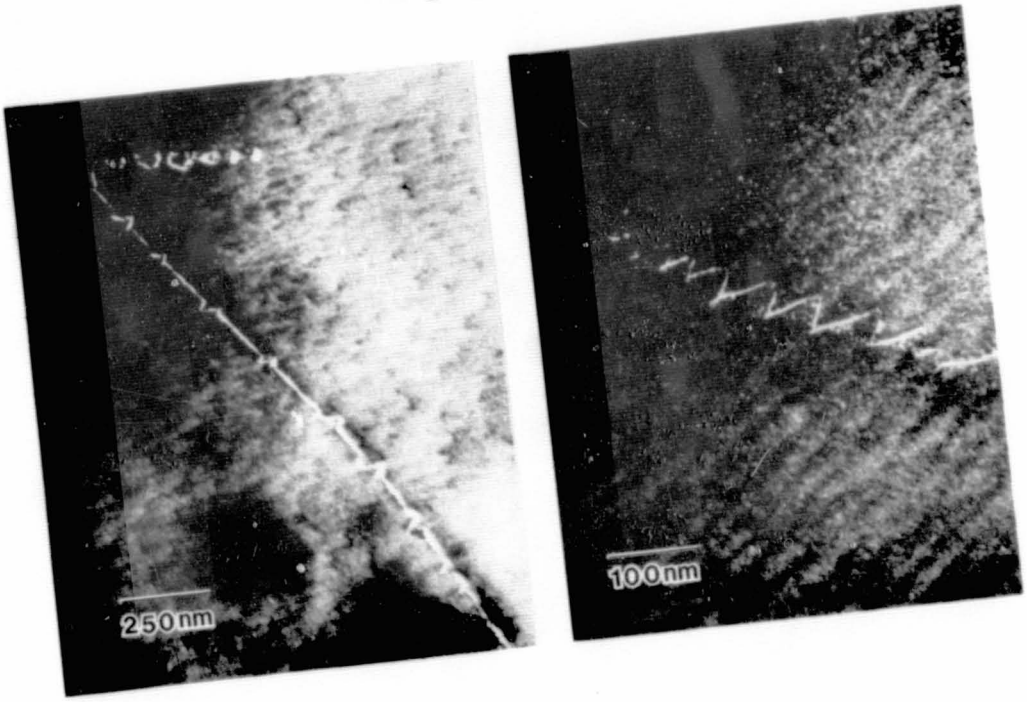

Figure 31

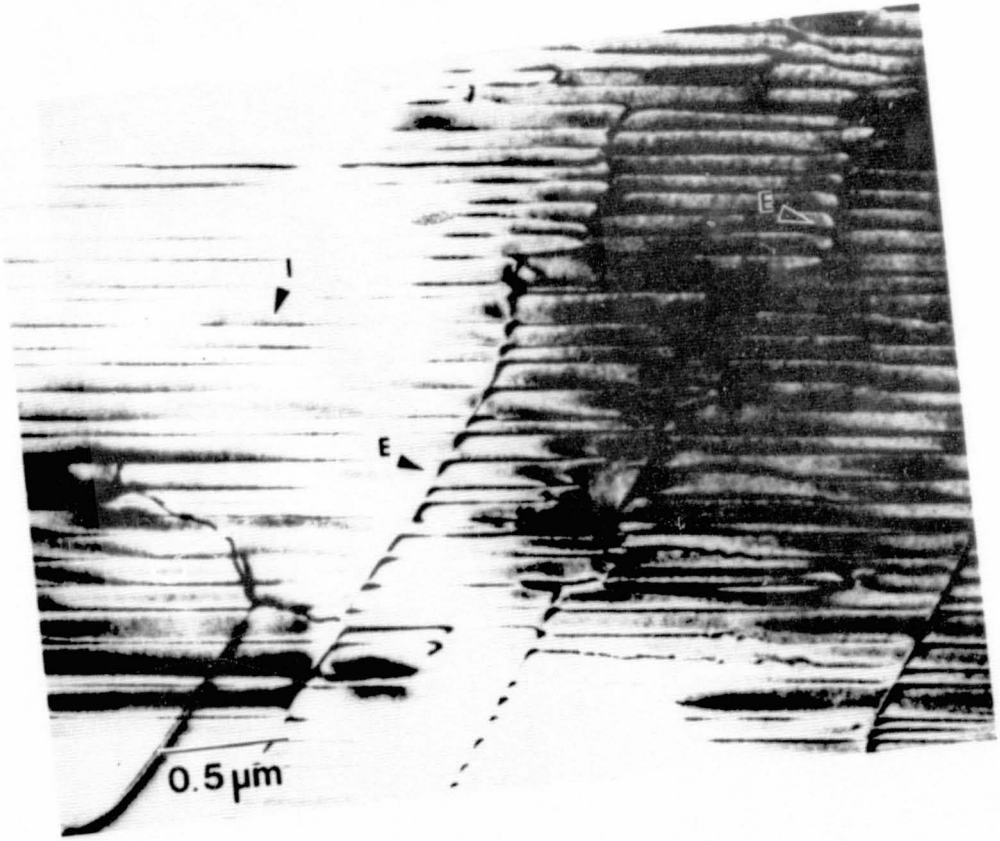

Figure 32

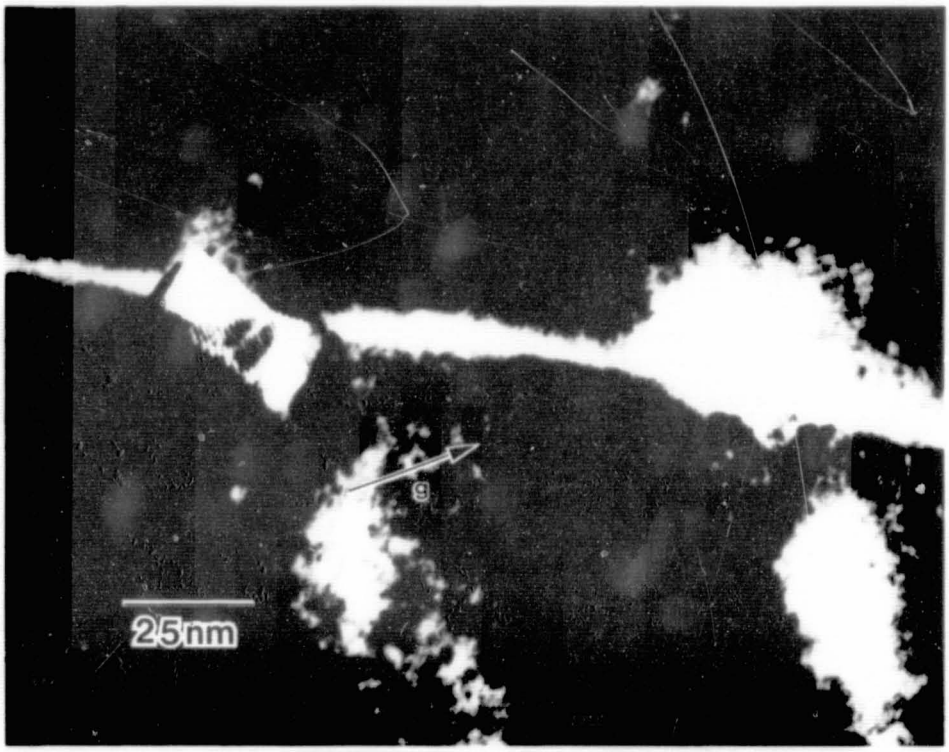

Figure 33

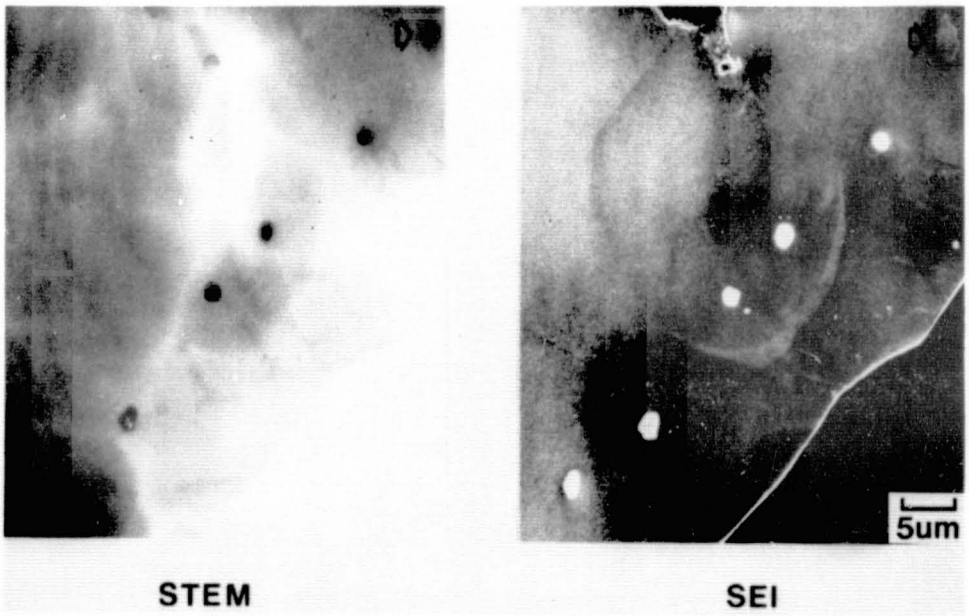

Figure 33b

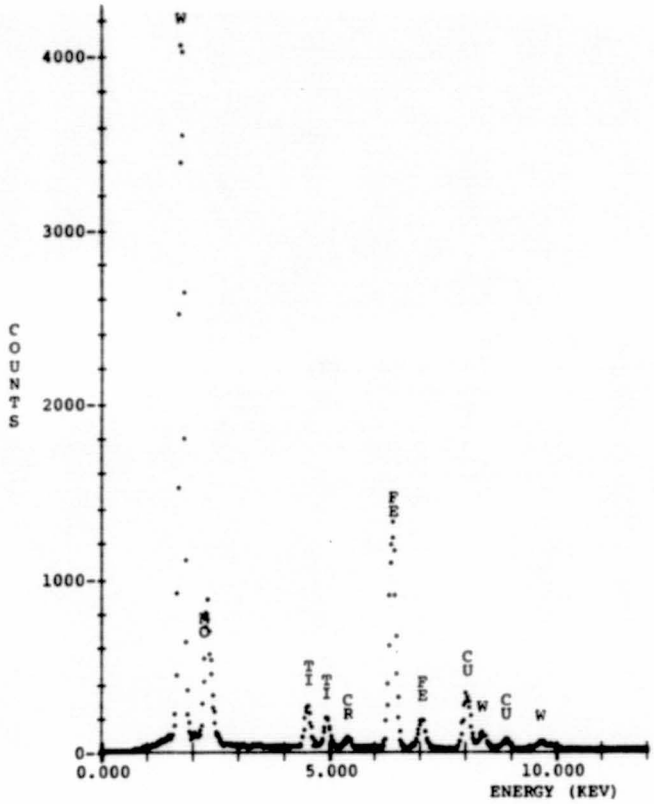

Figure 34

Figure 35

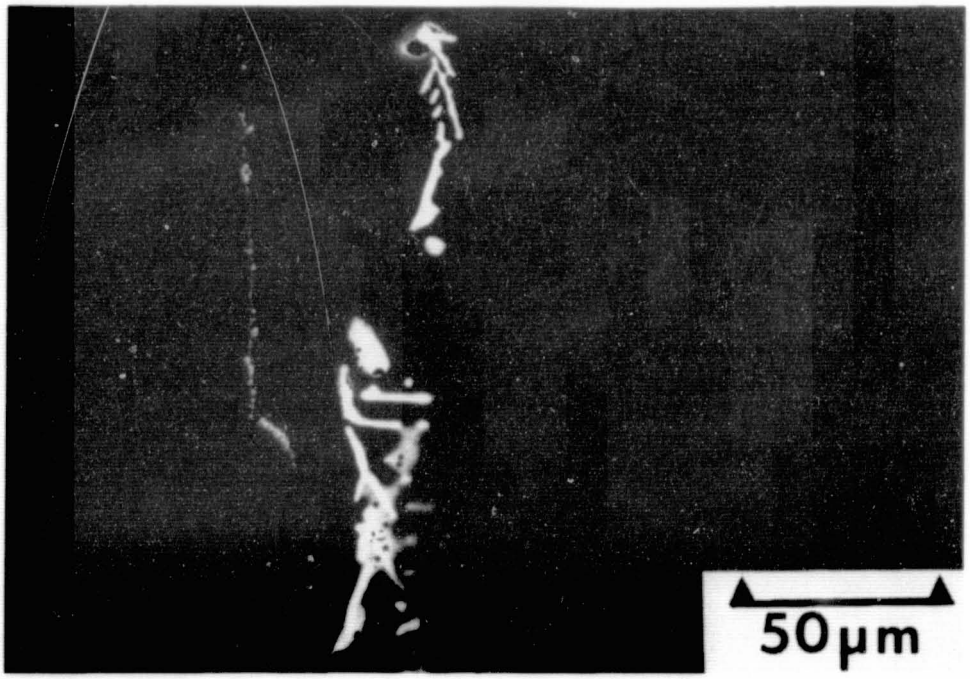

Figure 36

Figure 37a

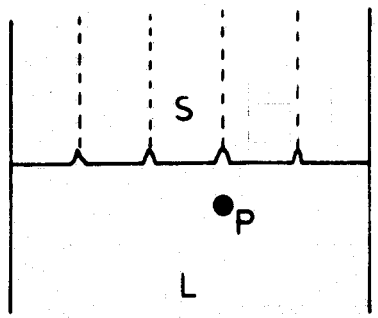

Figure 37b

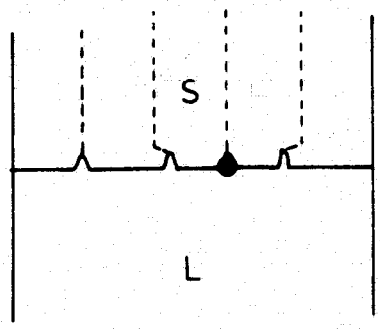

Figure 37c

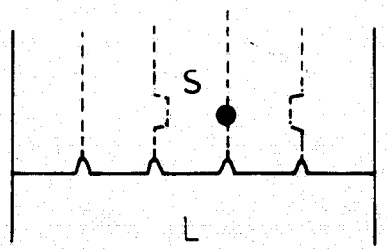

DISCUSSION

FAN: In the last slide you showed misfit dislocations in the emitter. Is that because the doping levels are different, or the doping species cause misfits?

AST: We have never seen misfit dislocations in emitters of EFG material. If the emitters are really 0.6-0.7 µm thick, we should really see misfit dislocations, but we don't. Why we don't see them is something we don't understand. If you read the literature, all these dual diffusion things with arsenic together with phosphorus, or boron together with aluminum, they don't get misfit dislocations. So you can make models about the possible role of carbon. Or maybe it is rather trivial. Maybe the junctions are really 0.3 µm thick. I get conflicting statements from Mobil how deep the junctions are. Maybe that is why we don't see them. The fact is we have never seen one, although we think that occasionally they make one which is 0.7 µm thick, so we should see them.

FAN: You say the misfit dislocation should be there because the different doping species should cause a misfit?

AST: No, just a misfit from the phosphorus. They go up to 10^{20} or so.

SCHWUTTKE: Regarding misfit dislocations: you generate them if you generate by your diffusion, a certain volume strain. Originally, misfit dislocations occurred early in the transistor manufacturing process. Two things were different. First of all, the diffusion process was done differently than it is done today, so you ended up with a very high surface concentration of phosphorus because the diffusion was done at a much higher temperature. Today for solar cells they use a much lower temperature than we used when we discovered misfit dislocations, and then obviously the junction depth is very critical. It is our experience that if it is 0.3 µm, it is not deep enough. EFG is a highly strained material, so maybe the lattice is strained so that it already accommodates your phosphorus atom and that might compensate for the volume strain.

AST: All valid points. I should only say that not everything we get from Mobil is diffused at low temperatures. It may be trivial, but it may be profound. At the moment we simply don't know why we can't find them.

RAO: When you showed the electrical activity of dislocations in the EBIC image, you showed the dislocation where there is electrical activity and then you hydrogenated, and you said the electrical activity at the boundaries essentially decreased. Did you find any impurities at those boundaries where the electrical activity was, and then did you find any decrease in the impurity levels after hydrogenation? Why did they go down?

AST: In this particular case, these dislocations, which were introduced by scratching the specimen at room temperature and then annealing at 400°C so you got little dislocation loops that are basically very high-stress, low-temperature dislocations, and they have anomalously wide

dislocation-dissociation widths. We have not done the TEM on these samples, because it is difficult to find the same area. But from what we know from the literature, the electrical activities can be correlated with the dissociation widths. In general, we have never seen decorated dislocations in EFG or decorated grain boundaries. But that doesn't prove that the decoration doesn't exist, because if you calculate what you need for making a reasonable electrical activity on a dislocation, there is only one impurity atom every 100 atoms along the core. So all we can say is, there are no visible decorations in EFG, ever, that we have seen, but that doesn't prove that invisible decorations don't exist.

RAO: You showed that the precipitates had iron, copper, titanium, and so on, and then said if you look for carbon, you might find carbon. Did you?

AST: Yes. The precipitates are big, about 5 µm, so once you find them in the TEM, you can actually take them out and drag them over to a chilled, superprobe 733 which has a wavelength-dispersive X-ray spectrometer on it that goes down to carbon, and you can show there is carbon in these large precipitates.

CHALMERS: I didn't intend to imply that the very high proportion or percentage of impurities extended all the way down to the die, when I talked about 50% impurities. If there were precipitates, I was talking about within a micrometer or so of the interface, but nowhere else.

You observed the termination of some twins in the structure; if twins terminate, some must also initiate. If those initiations are similar to the terminations, I might suppose they happened within the crystal; if they are entirely different, I would like to conclude that they happened at the interface during growth.

AST: What initiates the twins as far as we can tell is that twins always come off from faceted boundaries. In other words, you know you find the second-order twin boundary in the material that is not totally symmetric, and these kinds of boundaries act as prolific emitters. That is the way it looks for twins. They emit partial dislocations, and the twin goes off. This is one of the more difficult questions: did the twins stop at the interface, did they all run into the boundaries and stop there, or were they emitted from the interface? So you need some feel and experience in looking at it. When the boundary emits the twin it doesn't do a little facet because it loses a little dislocation content, and you can see this fairly frequently. So that is where I think the twins originate.

LANE: Could you tell us a little about sample preparation and how it might affect what you see, if it does?

AST: You mean TEM or what? Silicon is wonderful material, because dislocations are immobile below 700°C, so you don't have great problems without effects, if you TEM in silicon. Some other materials, you may have problems, but not in silicon. It is just time-consuming. The biggest problem of TEM is it looks at very small areas, so if you ask

statistical results, or you deal with something for a small defect, it has a big influence, like a dislocation threading a junction, or something like this. It becomes very laborious and time-consuming. X-ray topography is much better suited for something like this. So it is a tradeoff. You get very detailed information but it is a lot of work. But all defects, in silicon, are not a big problem.

SCHWUTTKE: Actually topography is very dangerous. If you take what you see for granted, most of the time you are wrong, if you say the crystal is dislocation-free or defect-free, based on an X-ray topograph. I always recommend, before you run an X-ray topograph, I train my technicians--the first thing you do before we talk topography is learn how to etch the sample. Before you know how to etch the sample, look at it, then look under the microscope, and remember what you saw, then etch it. Once it is etched, and you know what the etch structure is like, then take an X-ray topograph. If you think there is an area that is defect-free in the X-ray topograph, go back to your etch pattern and see if this correlates with the X-ray topograph, and don't be satisfied at that. Then I say make a transmission electromicrograph, and if this shows that the area is defect-free, then I am sure that the crystal is perfect in this area. Actually, you cannot separate one technique from the other. It is a lot of sweat and blood and if Dieter [Ast] shows you these terrific electromicrographs, don't ask him how many hours he spends to get these things into the microscope.

WARGO: I was wondering, in the context of your discussion on dislocations, do you think you could speculate on how you can resolve a controversy in melt-grown cadmium telluride that has been around for a long time: whether the dislocations that are present in the cadmium telluride were introduced as a result of the liquid-solid phase transformation, or post-growth either in the anneal or during the processing? Is there any way you can separate the two? Or three, actually.

AST: First of all, I don't know anything about cadmium telluride. You should really ask Bob Sinclair. He does wonderful high-resolution microscopy on that stuff. The second point is: if you believe the literature, in principle, it can go about differentiating ingrown dislocations from glide-induced dislocation by the fact that plastic-deformation-induced dislocations don't have impurity atmosphere with it, because in introducing temperatures, except for copper or something like this, the usual impurity can't keep up with the moving dislocations. Many years ago a paper was published that studied the photoluminescence on dislocations in gallium arsenide, and it was shown that they got different spectra. They just had a little microscope, which was radiation-focused down into the dislocations that were pumped above the bandgap of light, and they looked at some bandgap of light coming out. It was shown that the spectra that you got on glide-induced dislocation and growth-induced dislocation were different. Dislocations in two-phase systems, like gallium arsenide, are generally much more electrically active than dislocation in silicon, because you screw up these A-B bonding schemes. It might be more difficult in a multicomponents system.

MILSTEIN: If the growth orientation of some of the samples can be preserved, in terms of your analysis, one might be able to take a look at the question that came up with regard to kinks along a boundary and the twin planes. Do the twins come off the kinks, or do you have the circumstance where you have twins in a material and a grain boundary, and the two happen to intersect then you produce the kinks? I don't know.

AST: This is one of the ideal things. You tell all these guys who actually do the work to keep track of the orientation of the specimen, but by the time you have a 3-millimeter little electric microscope, in many cases they have forgotten, then the image rotates further in the microscope because all these magnetic lenses rotate the image, of course. In principle it can be done. It just makes the work more difficult. The grain boundaries are wonderful things for basic studies, but I don't think they are the most critical things to study in a solar cell, if you just want to improve the solar-cell performance. You can study dislocations that pass very close to very strong gettering centers, and then if you study the EBIC contrast it can give you some clues if dislocation electrical activity is controlled by impurities or not, because if they run past very strong gettering centers, they get locally sucked clean and induce misfit locations. Things like this I think are more essential for improving the understanding of the solar cell at the moment.

N84 28641 D27

A HIGH-SPEED CHARACTERIZATION TECHNIQUE FOR SOLAR SILICON

V. Lehmann[1)], H. Föll, L. Bernewitz and J.G. Grabmaier
Siemens AG, Research Laboratories
Otto-Hahn-Ring 6, D-8000 Muenchen 83, FRG

ABSTRACT

High-speed crystal growth techniques demand high-speed characterization techniques to allow a timely feed-back of information to the crystal growers. The unique properties of the Si-electrolyte-contact (SEC) provide for an extremely fast and simple measurement of the light-induced photo-current for any piece of Si without lengthy preparation of the specimen. Electropolishing at high anodic current densities allows for in-situ generation of fresh surfaces whereas preferential etching of defects in various modes is possible at low current densities. In n-type Si a simple estimation of the minority-carrier diffusion length is possible in many cases. Laser-scanning enables local probing of the photocurrent and provides data about the homogeneity of a sample. The experimental realization of the method is described in detail and examples are given and discussed.

INTRODUCTION

Material analysts in the Siemens laboratories have been confronted lately with an unprecedented variety of "solar" Si specimens. Chunks of metallurgical Si from two carbo-thermic reduction furnaces /1/, poly- or single crystals grown from this material, "supported Web" (S-Web) /2/ specimens, Si-sheets made by sintering Si powder, Si-ribbons obtained by roller-quenching, and reference material from outside vendors were to be characterized as comprehensively as possible and, needless to say, as quickly as possible.

"Characterizing" a piece of solar Si usually calls for statements about basic morphological and structural properties (e.g. flatness, presence of microcracks, grain size, texture, dislocation density, inclusions and precipitates); electronic properties (conduction type, resistivity, carrier mobility, minority-carrier diffusion length L and life-time τ, density and type of deep levels), and ultimately solar-cell properties

1) Present address: Eupener Str. 135, D-5100 Aachen, FRG.
Please address correspondence to H. Föll.

(efficiency, open-circuit voltage U_{oc}, short-circuit current I_{sc} and fill-factor). For the potential user of solar Si, the short-circuit current I_{sc} is the most interesting material parameter because it is dominated by the bulk properties of the Si (the exact magnitude of U_{oc} and of the fill-factor are rather junction- and contact properties). I_{sc} is basically determined by the diffusion length L which in turn depends mostly on the concentration, the type, and the spatial distribution of recombination centers ("deep-levels"). Deep levels, finally, are created by impurities, by lattice defects (grain-boundaries, dislocations, precipitates) or by combinations of both. A grain boundary or dislocation is called "electrically active" if it is associated with deep levels and therefore acts as recombination center for minority carriers.

A quick, simple and reliable method that could provide I_{sc}-data and information about defects certainly would be most welcome. The Silicon-Electrolyte-Contact (SEC) can do just this; its mechanism and its application is the subject of this paper. Emphasize will be placed on the implementation of the technique. In order to provide easy reading for "silicon people", the necessary electrochemistry will be presented in semiconductor language rather than in electrochemical nomenclature. For more elaborate treatments of the electrochemistry of semiconductors the reader is referred to refs. /3-9/.

THE SI-ELECTROLYTE-CONTACT: BASIC PROPERTIES

In a first approximation, the SEC may be thought of as a Schottky-contact with an electrolyte substituting the metal. With a counter-electrode of arbitrary material (but preferably chemically inert) that "contacts" the electrolyte, a voltage may be applied and a current passed through the Si-electrolyte junction. The important differences to a proper Schottky-contact at this point are: i) There is a measurable cell- or battery-voltage U_o that depends on the properties of the Si, the counter electrode and the electrolyte, and ii) current flow is inherently tied to a chemical reaction. With HF-based electrolytes, the chemical reactions at the Si-electrode are the reduction and liberation of hydrogen-ions for the cathodic reaction (i.e. electron transfer from the Si to the electrolyte) and the dissolution of the Si for the anodic reaction (i.e. hole transfer from the Si to the electrolyte).

Fig. 1a shows typical U-I-characteristics for a mono-crystalline p-type sample with $\approx 0.5\ \Omega$ cm resistivity in 2.5 % HF and a particular set of experimental conditions that will be discussed later. The main features are:

i) The basic diode-characteristic is evident. For large reverse voltages, junction break-down occurs; for forward bias large currents flow (only limited by the resistivity of the electrolyte).

ii) Illumination produces a photo-current, carried by the light-generated minority carriers (i.e. electrons); the magnitude of which is proportional to the light intensity.

iii) Zero-current conditions are obtained when the applied voltage exactly compensates the built-in cell-voltage. The light-induced current is not superimposed on the dark-current for small voltages and thus does not induce a shift in the cell-voltage that would correspond to U_{oc} of a solar-cell.

iv) The forward-characteristic shows a peculiar structure with two current peaks, P_1 and P_2, and strong current oscillations for $U > U(P_2)$.

v) For current densities $J < J(P_1)$ a film exhibiting interference colors grows on the Si surface which is called the "porous Si layer" (PSL) /10-12/; if the current density is raised beyond $J(P_1)$ this layer peels off instantaneously.

What can be done with this? Firstly, the junction breakdown voltage at reverse-bias condition carries information about the resistivity of the sample. Secondly, the magnitude of the dark current provides a good measure of the surface quality of the sample. Third, illuminating the sample with a calibrated light-source produces a photo-current I_{Ph} which equals closely the I_{sc}-value of a solar-cell that were to be made from the sample. To give an example: Good single crystals illuminated under "air mass 1" (AM1) conditions (925 W/cm^2, spectral distribution corresponding to sun-light) produce about 30 mA/cm^2; "Silso" material yields $\approx$25 mA/cm^2 and metallurgical Si may be as low as 1 mA/cm^2. Fourth, if the specimen surface is poor, it may be electro-polished by raising the forward-voltage beyond $U(P_2)$. Finally, defects may be etched preferentially at forward current densities $\lesssim$1 mA/cm^2.

Before going into details, n-type Si needs to be discussed because it behaves very differently from p-type Si. Fig. 1b shows typical I-U-characteristics for n-type Si. Important points to note are:

i) With reference to p-type Si, the reverse- and forward-current regions are interchanged, but the chemical reactions are not. H_2 is still developed for the cathodic reaction (now forward-current region of the SEC) and the specimen dissolves in the anodic region.

ii) With light impinging on the Si, a photo-current flows in the anodic region. At very high light intensities the I-U-curve is similar to p-Si for anodic currents because of current limitation by the electrolyte. The photo-current, however, is not proportional to the light intensity but may be twice as high as the light-induced minority-carrier current.

iii) Electropolishing can only be achieved if the light intensity is high enough to allow for the current oscillations. Otherwise defect etching occurs as will be discussed later.

EXPERIMENTAL SET-UP

The experimental set-up comprises the electrolytic cell with the specimen holder, a pumping circuit for the electrolyte, light-source, potentiostat, and x-y-recorder. A description together with experimental details will be given in the appendix.

EXAMPLES OF MEASUREMENTS

p-type Si: Cathodic reactions

Fig. 2 compares I-U-characteristics of various Si specimens as they are obtained with Schottky-contacts (3 nm Cr, 5 nm Cu, 1 nm Cr, Al-grid, 18 mm^2 area) and, after removal of the metal layers in-situ by a short electropolishing treatment, with the SEC. The area in the latter case was 100 mm^2, the dark currents nevertheless were comparable to, or even smaller than the Schottky-contact case. The result from these and many other measurements is that the photo-induced current I_{Ph} can be measured quantitatively with the SEC-method. The possibility of repeated measurements with fresh surfaces produced by electropolishing is an additional advantage not available with other methods.

As already discussed, the SEC-method does not provide data about the open-circuit voltage U_{oc}. But this is no serious disadvantage because U_{oc} is mainly determined by the nature of the junction and thus by the technology used for its formation.

p-type Si: Anodic reaction

Electropolishing (i.e. etching of the sample to a mirror-finish) has already been discussed; it should be performed in the current-oscillation regime of the I-U-characteristics ($\approx$300 mA/cm^2 for [HF] = 2.5 %; cf. Fig. 1a). In contrast, very clear etching of defects is achieved for small current-densities around $\approx$500 $\mu A/cm^2$. In this current regime the lgI-U-characteristics often display classical diode-behaviour (i.e. $\lg I \propto U$ with proportionality factors typical for diffusion- or recombination-currents, cf. /13/). The etching of defects at low current densities has been described before by one of the authors /14/, but was then not well understood. It is still not well understood, but with the following items in mind, it is rather simple to produce etching patterns at least as good or superior to those obtained by the traditional chemical etches:

i) "Electrically active" defects are always etched below a certain critical current density (roughly 1 mA/cm^2); i.e. etch-pits or grooves are formed (cf. /14/). For good defect delineation a current-density x etching-time product of $\approx$(3-5) $mA.min.cm^{-2}$ is recommended. At very low current densities ($\lesssim$100 $\mu A/cm^2$) the etching behaviour may be complex.

ii) Whether or not electrically non-active defects are preferentially etched at somewhat higher current-densities as was stated in /14/ is an open question at present. Great care has to be exercised in judging if a grain-boundary was truly etched (i.e. a groove was formed) or if only a step was developed.

iii) For all current-densities, including rather large ones, the etching rate depends initially on the surface orientation which manifests itself by steps at grain-boundaries. The maximum step heights observed depend somewhat on the current-density but seem to remain constant after a certain time of etching.

iv) The colored layer always present at low current-densities partially obscures the etching pattern, partially enhances it (by showing different colors in different grains). It is easily removed by either raising the current-density J for a few seconds beyond $J(P_1)$ or by immersing the specimen for a few seconds in KOH!

The preferential etching effects must be closely related to the mechanisms of carrier-transport across the Si-electrolyte interface. In a first approximation, it can be envisioned that for low current-densities recombination currents at defects are larger than the diffusion-currents flowing in more perfect areas of the sample. This view is supported by the observation that etch-pits disappear rather suddenly if the current-density exceeds a certain value. In any case, preferential etching of defects using the SEC-method is tied to current transport mechanisms in defected junctions and thus should allow a deeper understanding of the correlation between etching behaviour and defect properties.

Notwithstanding the difficulties of a detailed interpretation of the preferential etching phenomena in p-type Si, it is a simple and straight-forward procedure to obtain high-quality etching-patterns that allow to determine grain-sizes, dislocation densities, presence of precipitates etc. Fig. 3 serves to illustrate the aforesaid. A major advantage in comparison to many purely chemical etching procedures lies in the fact that defects are always etched, irrespective of the surface orientation, and that qualitative judgements about the electrical activities of defects are possible.

n-type Si: Cathodic and anodic reactions

The cathodic current regime is rather uninteresting. The SEC is forward-biased; large currents flow; hydrogen is developed and not much can be learned about the Si specimen.

The anodic current regime corresponds to reverse bias of the SEC; the currents flowing therefore are interpreted as leakage currents (in the dark) or photo-currents with illumination. Since anodic current always go hand in hand with dis-

solution of the Si-electrode, the amount of Si locally dissolved is a direct measure of the time-integrated current flowing through that area.

As in the case of p-type Si, illumination induces a photocurrent. In contrast to p-Si, this photo-current is not identical with the light-induced minority-carrier current flowing to the Si surface, but is generally larger by a factor lying between 1 and 2. This phenomena is caused by an electron-injection process at the Si-surface which is triggered by the arrival of a hole and the concomitant breaking of a Si-Si bond. Much simplified, this process may be envisioned as follows: Surface atoms at the Si-electrolyte interface are tied with two bonds to the Si-crystal; the other two bonds are saturated with F^- ions. A hole arriving at the surface breaks one bond. The remaining one is either broken by another hole that happens to come along or, if that does not come to pass within a certain time, is broken by the injection of an electron into the Si. The free atom then enters the solution as SiF_2, an unstable species that immediately disproportionates according to

$$2\ SiF_2 \longrightarrow Si + SiF_4$$

or oxidises as follows

$$SiF_2 + 2\ HF \longrightarrow SiF_4 + H_2.$$

This process may also occur during the anodic dissolution of p-type Si at small current densities and probably plays a crucial role in the formation of the colored layer (PSL) formed for current densities smaller than $J(P_1)$.

Unfortunately, this electron-injection process makes direct measurements of the interesting quantity, the light-induced hole-current, very difficult. The injected electron-current has to be separated from the measured current and therefore has to be known. It is possible to "calibrate" a given experimental set-up (Fig. 4) but detailed measurements have not been attempted in the present work.

Preferential etching of defects now may be achieved either with the dark- or photo-current. Fig. 5 gives a rather spectacular example of a poly-Si sample that was grown from metallurgical Si and thus contains a high concentration of metallic impurities. Although nominally of 0.05 Ωcm n-type, it also contained a significant concentration of boron. The etching pattern obtained with the dark-current shows irregular features only loosely associated with the grain-structure of the specimen. Most likely, it mirrors the distribution of some metal that acts as generation center for minority carriers. The peculiar appearance of the etching pattern suggests that the main process governing the incorporation of the metal was constitutional supercooling of the Si melt.

Fig. 5b shows the etching pattern on an area adjacent to that shown in Fig. 5a, but now the current was light-induced. Since the photo-current in "bad" samples is sensitive to the width of the space-charge region which varies with the dopant concentration, the appearance of striations is understandable.

Of particular interest is the etching-profile across a grain-boundary. Since a portion of the minority carriers generated in the vicinity of a grain-boundary will recombine at the grain-boundary, the photo-current density around the grain-boundary is smaller than in the interior of the grain. The current increases with increasing distance from the boundary; the bulk-value will be reached at a distance roughly given by the minority-carrier diffusion length. Since the etching-profile mirrors the current-density profile, grain-boundaries, if etched with the photo-current, should appear as ridges with a basewidth of roughly twice the diffusion length. Fig. 6 proofs that this is indeed the case. The base-width of the grain-boundary ridges and the minority-carrier diffusion length (as obtained by the surface photo-voltage method) are in basic agreement.

Laser-scanning

As already mentioned, laser-scanning by simply moving the focussing lens is easily possible. The resolution is limited to a few 10 μm because of light-scattering in the plastic window and the electrolyte. A particular advantage is the possibility to perform a defect-etch in-situ after the laser-scan which often allows a direct correlation between the photo-current profile obtained and structural properties of the sample; Fig. 7 gives an example. The specimen was a single crystal of p-type, but partially compensated by phosphorus. The photo-current was small, due to the presence of metallic contaminants, and therefore sensitive to the width of the space-charge region. It is seen that photo-current maxima correspond perfectly to the striations revealed by a short etching at $\approx$500 μu/A/cm^2 and which therefore are interpreted as the maxima of the phosphorus distribution.

CONCLUDING REMARKS

The examples given demonstrate that the SEC does in fact provide a method for a "high-speed" characterization of solar Si. Some peculiarities of the method certainly do exist and some experience is needed for its proper application. But whoever has mastered chemical etching techniques and I-U-measurements can also handle the SEC. An initial effort is rewarded with a facility that can provide substantial data about a "raw" sample (e.g. broken off from a ribbon still being grown) within 15 min after it has been received.

There is also ample opportunity for more involved measurements utilizing the SEC. Suffice it to mention the possibility of measuring the dependence of I_{Ph} on the wavelength which may be used for diffusion-length determinations /15/, of deep-level spectroscopy /16/ and, with defined electropolishing steps between measurements, of carrier concentration profiling /17,18/. There is also much leeway for basic research: The etching behaviour of defects in both p- and n-type Si exhibits many particular features that wait for proper explanations. Moreover, the chemistry of the dissolution process, though much investigated, is far from being clear. The nature and the formation of the so-called porous Si-layer (PSL) still is not fully explained despite of its possible use in integrated-circuit technology (cf. /19/).

APPENDIX

EXPERIMENTAL DETAILS

The basic experimental set-up used for this investigation is shown in Fig. 8. Its main parts are the specimen holder and the electrolyte cell, the pumping circuit for the electrolyte, the light-source, the potentiostat and the x-y-recorder.

The specimen holder employed is depicted in Fig. 8b. It should allow an easy electrical contact to the back-side of the specimen, accommodate specimens of various sizes and shapes, define the sample area exposed to the electrolyte as precisely as possible and it should accommodate the reference electrode. It should not, above all, leak electrolyte to the sample backside and it should not obstruct too much the flow of the electrolyte. The specimen holder shown in Fig. 8b is a working compromise, better constructions are certainly possible. An interesting alternative, e.g., is described in ref. /20/; an other desirable option would be to rotate the specimen.

The electrolyte cell is a suitable container with fixtures that allow the insertion of the specimen holder, the counter electrode, and, if so desired, a thermometer and a pH-probe. It contains an inlet and outlet for the circulation of the electrolyte and a window to allow the illumination of the specimen. All parts of specimen holder, cell and pumping circuit in contact with the electrolyte should be HF-resistent; PVC or TEFLON are recommended.

Circulation of the electrolyte is essential for trouble-free measurements. A jet of electrolyte streaming against the specimen (via a suitable nozzle connected to the electrolyte inlet) insures that currents are not limited by diffusion of molecules to or from the electrode. More important, it removes hydrogen bubbles which otherwise could stick to the speci-

men and then obscure measurements of I_{Ph}. Fig. 9 shows the effect of pumping on the I-U characteristics of p-type Si. The jitter of the photo-current for the unpumped case is due to H_2-bubbles. In the anodic region marked differences occur because of current limitations for the unpumped case. Rotating the specimen or the use of an ultrasonic generator, however, may serve the same purpose as pumping.

The pumping circuit contains a TEFLON filter (10 μm) to remove small particles and dust from the electrolyte. This is advantageous if a focussed laser-beam is used as a light source. An intermediary container allows quick and easy adjustment of the electrolyte level irrespective of pressure differences in pump and filter by moving it up or down. As a pump, any HF-resistant pump strong enough to overcome the flow resistance of the circuit will do.

As electrolyte, HF in a concentration of ≈ 2.5 % by weight was chosen. Electrolytes containing no fluorides do not give satisfactory results; fluorine salt solutions, e.g. NH_4F in H_2O, are too current limiting for electropolishing. HF in much higher concentrations leads to inconveniently high currents (the height of the peaks P_1 and P_2 is proportional to the HF-concentration) in the anodic regime and concentrations below ≈ 2 % are too current-limiting. Very diluted HF, however, does not wet clean Si-surfaces very well. The addition of a wetting agent therefore is essential. In our experiments a few drops of a commercially available wetting agent for acidic environments ("Mirasol"; producer: Tetenal) proved sufficient for the purpose.

The light source used was a 150 W halogen lamp adjusted to give a homogeneous intensity within an area ≈ 5 cm in diameter. The intensity was adjusted to approximate AM1 conditions by placing a calibrated solar cell in the location of the specimen. As it was found that this intensity produced a photo-current of (30 + 2) mA/cm^2 in any good single crystal of p-type Si investigated (resistivities ranging from 0.1 Ω cm - 100 Ω cm), a 1 Ω cm sample was permanently mounted in a specimen holder and used as reference standard. Alternatively to homogeneous illuminations, a He-Ne laser-beam focussed to a spot size of ≈ 30 μm could be used. An inexpensive camera-lens (f = 100 mm) was used for focussing; "laser scanning" was achieved by simply moving the lens with a motor-driven table.

A few words about the potentiostat and the reference electrode: The former is essentially a device that keeps the voltage across the semiconductor-electrolyte junction at a constant, pre-determined value and supplies the current necessary to maintain this potential-difference. A built-in ramp generator allows to scan the junction voltage between pre-determined values and thus to record I-U-characteristics. As in any precision measurements of I-U-characteristics, the electrochemical equivalent of a "4-point-probe" configuration is used for the

measurements. Two current leads contact the sample backside and the counter-electrode and two potential probes measure the voltage. One is simply connected to the sample backside, the other one to a "reference electrode" that is located next to the specimen surface. This reference electrode not only eliminates the voltage drop across most of the electrolyte (which is normally nonlinear with the current) but serves as the reference point for the voltage scale. Since any electrode immersed in an electrolyte develops an electrochemical potential that varies with the electrode material, electrolyte composition, temperature, etc., an "ohmic" contact to the electrolyte is impossible. The difference between the electrochemical potentials of the Si-electrode and the reference electrode therefore is superimposed on the applied voltage and measurements are meaningful only if the potential of the reference electrode is constant and known. For very precise measurements therefore standard reference electrodes such as a saturated calomel electrode should be used, for the objective of this work, however, a simple Pt-wire will be adequate. The counter-electrode could be used as reference electrode, too. (Simplifying the set-up to a "2-point-probe"), but then the measured voltage will include the voltage drop in the electrolyte (quite significant at higher current densities) and unaccounted changes of the potential since the counter-electrode has to pass current and therefore cannot maintain a constant potential.

The potentiostat should be able to deliver about 1 A/cm^2 but should also allow measurements in the μA-region. Its voltage range should be large (e.g. -10 V - +10 V) and, considering the diode-character of the SEC, it should be fool-proof.

The samples should fit into the specimen holder, otherwise no restrictions concerning size or shape are necessary. Very irregular samples, or samples with holes (e.g. metallurgical grade Si or porous sintered Si) that would leak electrolyte to the backside contact, can also be simply contacted with an insulated wire (insulate the contact point with wax) and immersed into the electrolyte. The illuminated area then has to be defined by an aperture and high dark-currents may be encountered. The quality of the sample surface is of no importance since an electrically good surface (i.e. passing only small reverse currents) can always be obtained by electropolishing; this is demonstrated in Fig. 10. However, under-etching at the circumference of the rubber-seal may occur which often is accompanied by noticeable dark-currents. It is therefore good practice to etch unpolished samples before insertion in the specimen holder for a few minutes either in KOH (20 % at 80 ^{o}C) or in CP4.

The samples need to have an ohmic back-side contact which can be produced by the usual methods (e.g. evaporating and alloying Al in p-type Si). For "high-speed" measurements, it has been found sufficient to paste Ga and liquid Ga-In-eutec-

ticum on the sample backside in conjunction with some scratching. It is good practice to make two contact spots in this way and to measure the I-U-characteristics between them. This is easily done with the potentiostat; if an ohmic characteristic is obtained the contacts are good enough for measurements.

ACKNOWLEDGEMENTS

Discussions with Dr. H. Aulich, K. Geim and T. Salbert are gratefully acknowledged. Thanks are also due to G. Hoyler and W. Eckers for their able technical assistance.

This work has been supported under the Technological Program of the Federal Department of Research and Technology of the FRG. The authors alone are responsible for the contents.

REFERENCES

/1/ H.A. Aulich, K.-H. Eisenrith, W. Dietze, J. Schäfer, F.-W. Schulze and H.-P. Urbach; Proc. 4th E.C. Photovoltaic Solar Energy Conf., eds.: W.H. Bloss and G. Grassi (D. Reidel Publ. Comp.), 1982, p. 868
/2/ J.G. Grabmaier and H. Föll; these proceedings
/3/ "The Surface Chemistry of Metals and Semiconductors"; ed. H.C. Gatos (J. Wiley and Sons, Inc.), 1959
/4/ "The Electrochemistry of Semiconductors"; ed. P.J. Holmes (Academic Press, London and New York), 1962
/5/ E.A. Efimov and I.G. Erusalimchik: "Electrochemistry of Ge and Si" (The Sigma Press, Publ.), 1963
/6/ H.U. Harten in: Festkörperprobleme Vol. III; ed. F. Sauter (Vieweg u. Sohn; Braunschweig) 1964, p. 81
/7/ R. Williams; J. Vac. Sci. Technol. 13 (1976) 12
/8/ R.H. Wilson; CRC Critical Reviews in Solid State and Mat. Sciences (1980)
/9/ H. Gerischer in: Proc. NATO ASI Summer School, Vol. B69 (Plenum, New York), 1981, p. 199
/10/ Y. Arita and Y. Sunonara; J. Electrochem. Soc., 124 (1977) 285
/11/ Y. Arita; J. Cryst. Growth 45 (1978) 383
/12/ T. Unagami; J. Electrochem. Soc. 127 (1980) 476
/13/ S.M. Sze; "Physics of Semiconductor Devices" (John Wiley and Sons), 2nd edition, 1981
/14/ H. Föll; J. Electrochem. Soc., 127 (1980) 1925
/15/ A. Etchebery, M. Etman, B. Fotouhi, J. Gautron, J.-L. Sculfort and P. Lemasson; J. Appl. Phys. 53 (1982) 8867
/16/ R. Haak, C. Ogden and D. Tench; J. Electrochem. Soc. 129 (1982) 891
/17/ P.M. Tan; Phys. Stat. Sol. (a) 37 (1976) 439
/18/ C.D. Sharpe and P. Lilley; J. Electrochem. Soc. 127 (1980) 1918
/19/ K. Imai; Solid State Electr. 24 (1981) 159
/20/ T. Ambridge, J.L. Stevenson and L.M. Redstall; J. Electrochem. Soc. 127 (1980) 222

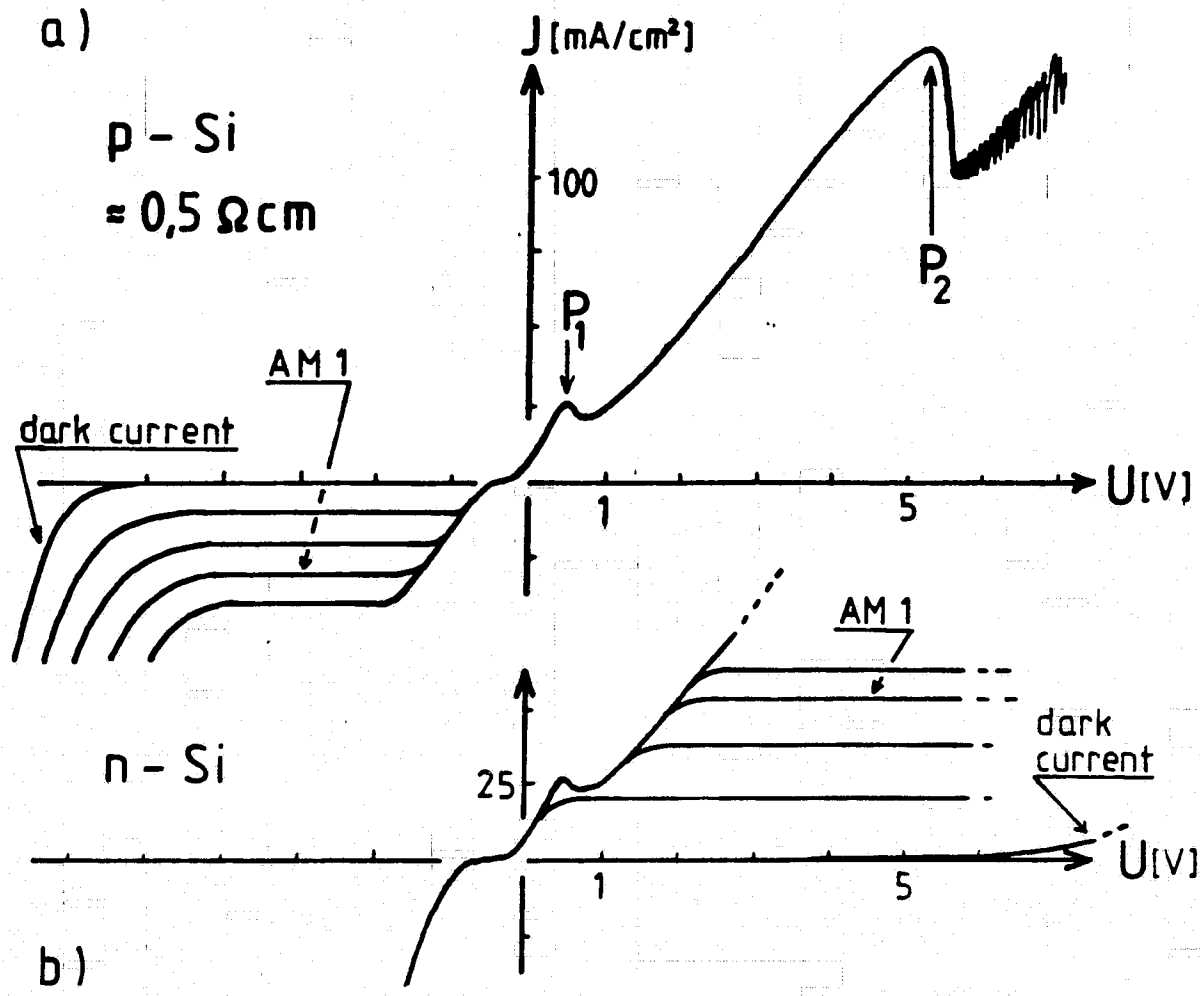

Fig. 1 Typical I-U-characteristics of ≈0.5 Ω cm p-Si (Fig. 1a) and for n-type Si (Fig. 1b) in a 2.5 % HF-electrolyte for various light intensities.

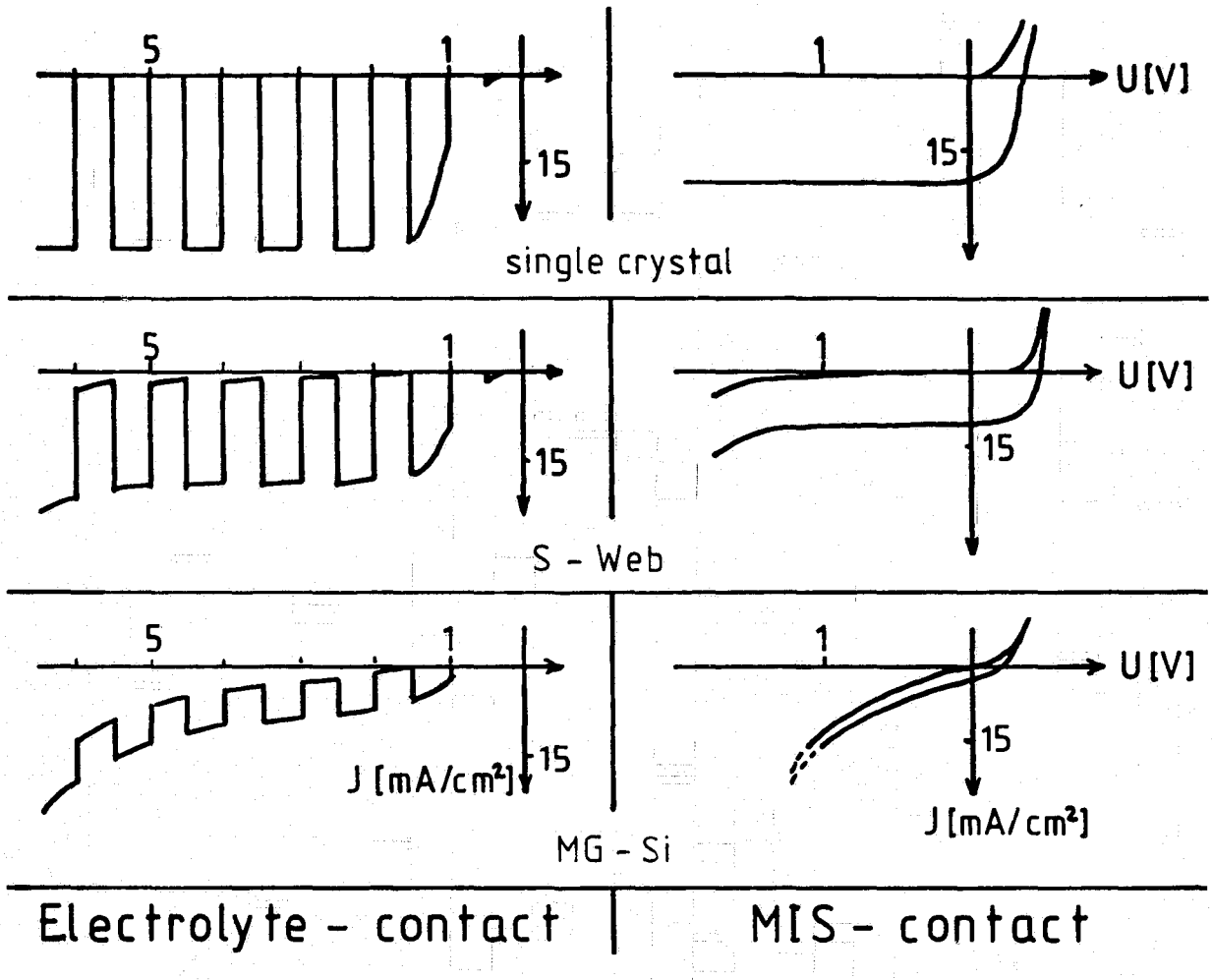

Fig. 2 Comparison between I-U-characteristics obtained with the SEC and with Schottky (MIS) contacts. The current densities in the MIS case are smaller because of light-loss in the metal layers.

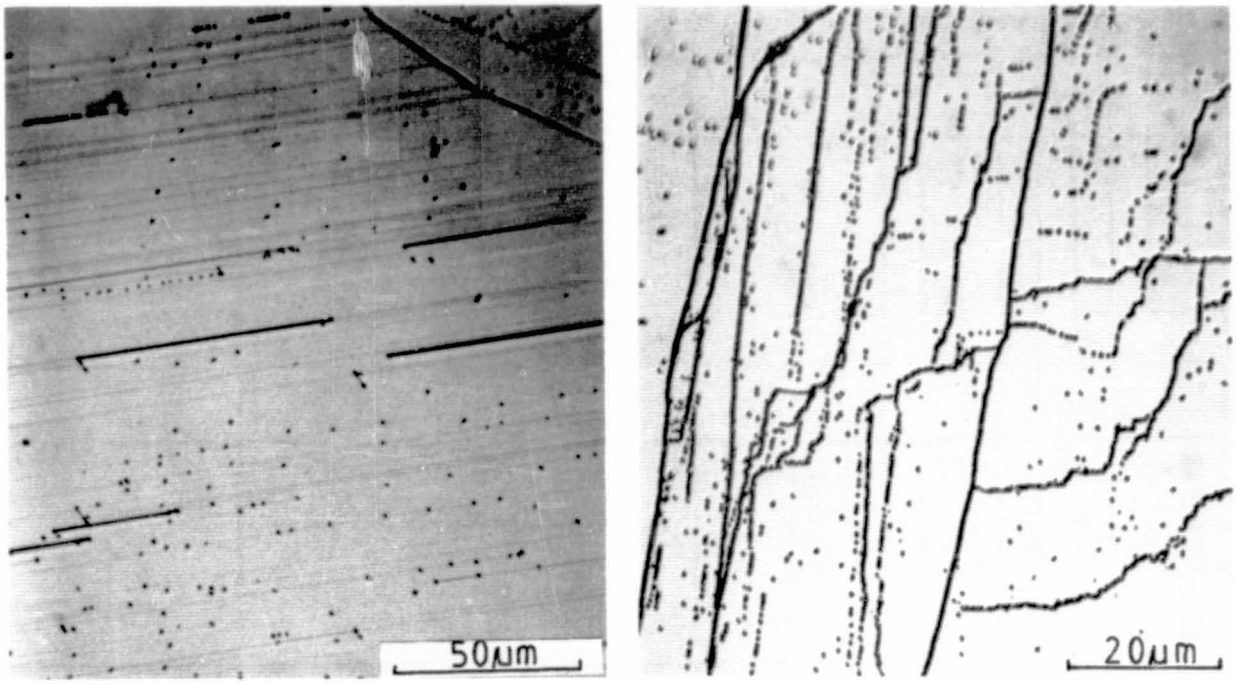

Fig. 3 Examples of etching-patterns obtained by anodic etching. The right-hand micrograph demonstrates pronounced differences in the etching behaviour of twin-related boundaries most likely related to differences in the electronic activity of the defects.

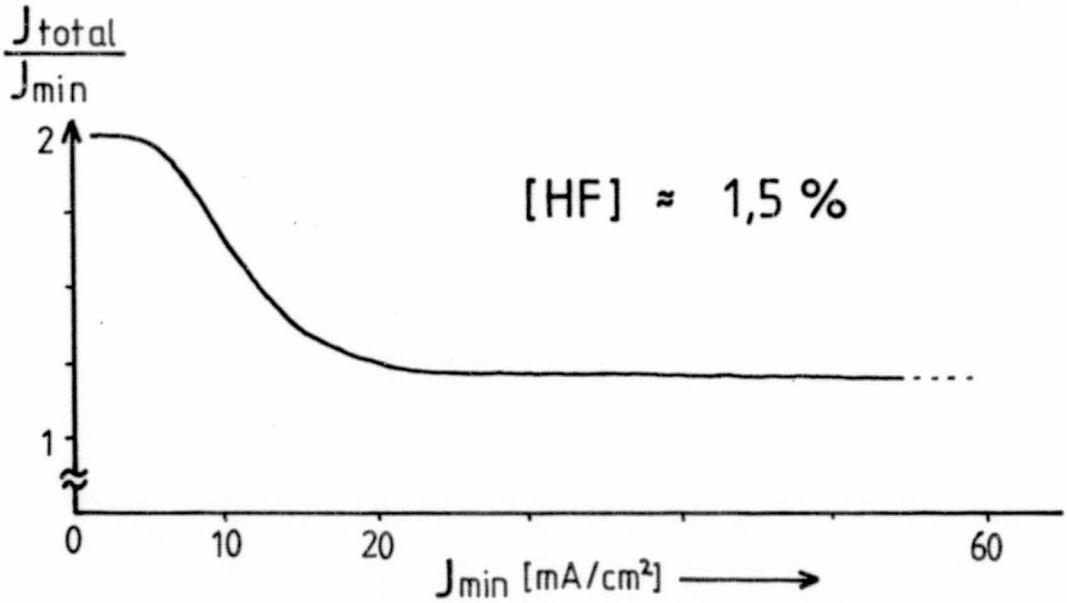

Fig. 4 Ratio of total current and minority carrier current vs. hole current for n-type Si in 1.5 % HF. The hole current was deduced from parallel measurements of the cathodic photo-current of a p-type sample.

a)

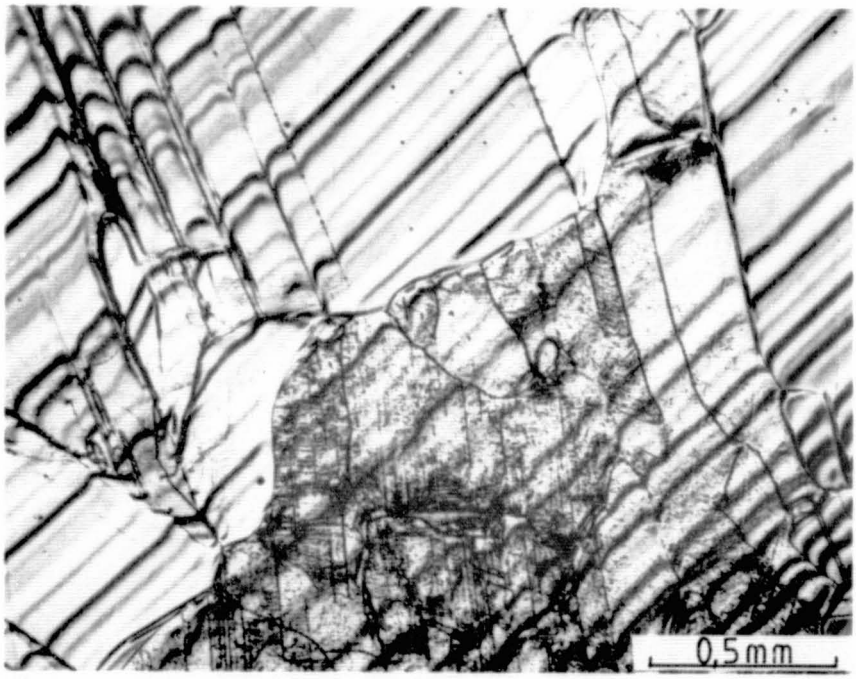

b)

Fig. 5 Etching pattern of n-type poly-Si obtained a) in the dark; b) with illumination.

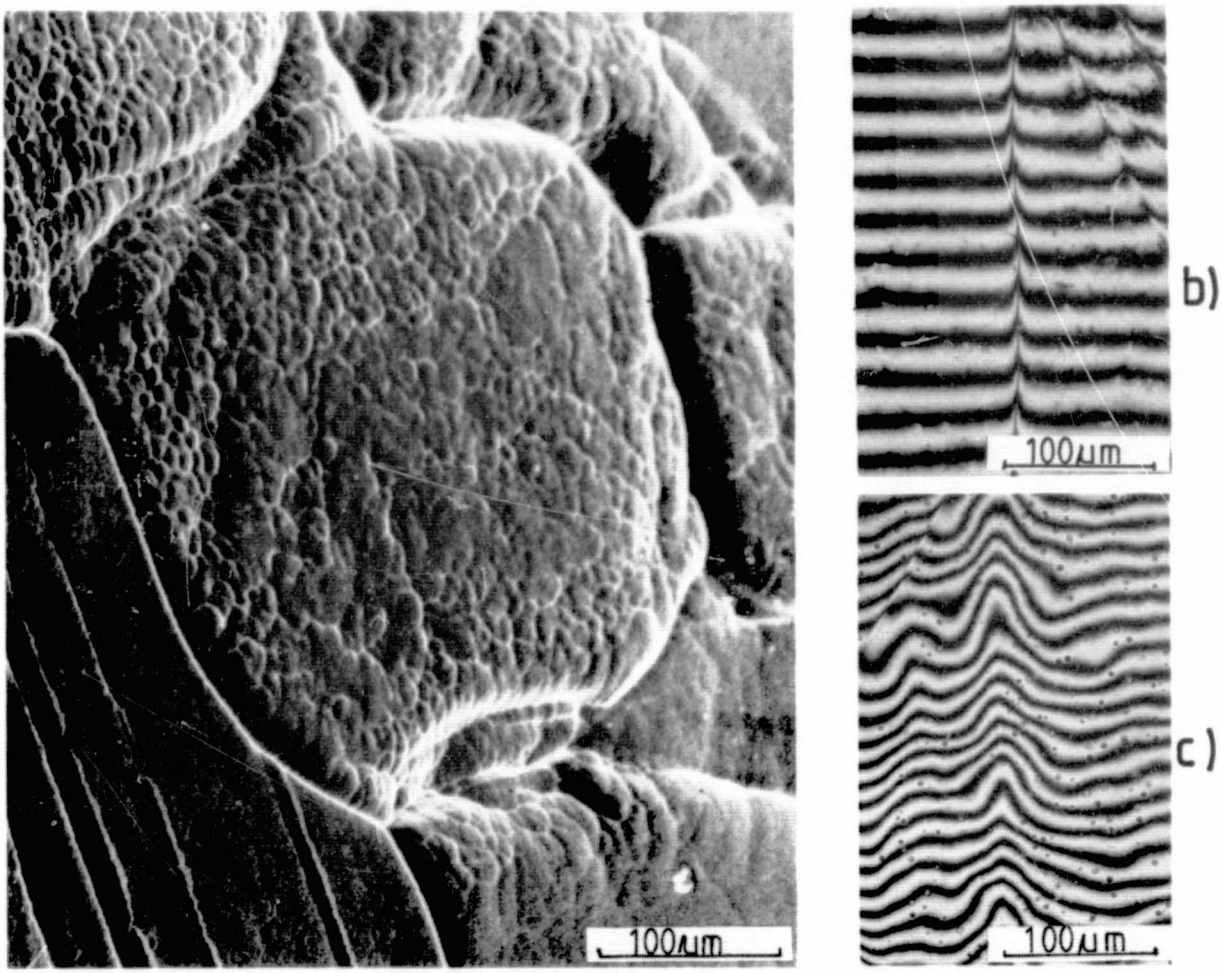

a)

Fig. 6 Etching profiles across grain-boundaries.
Fig. 6a shows a SEM-micrograph of an etched area;
Fig. 6b and 6c show interference fringes across grain-boundaries in specimens with diffusion-lengths of ≈ 3 µm and 25 µm, respectively.

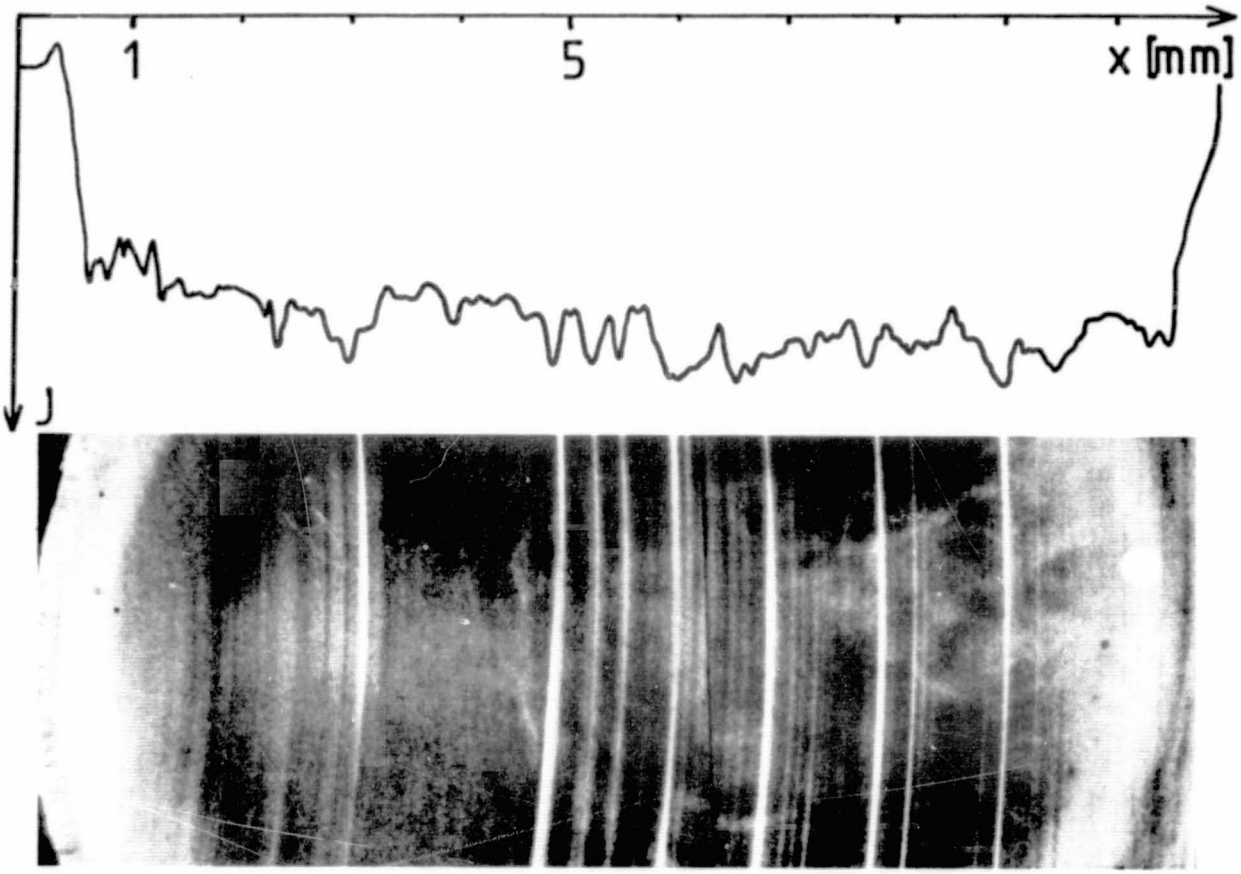

Fig. 7 Photo-current profile obtained by laser-scanning and corresponding etching pattern of a p-type single-crystal sample.

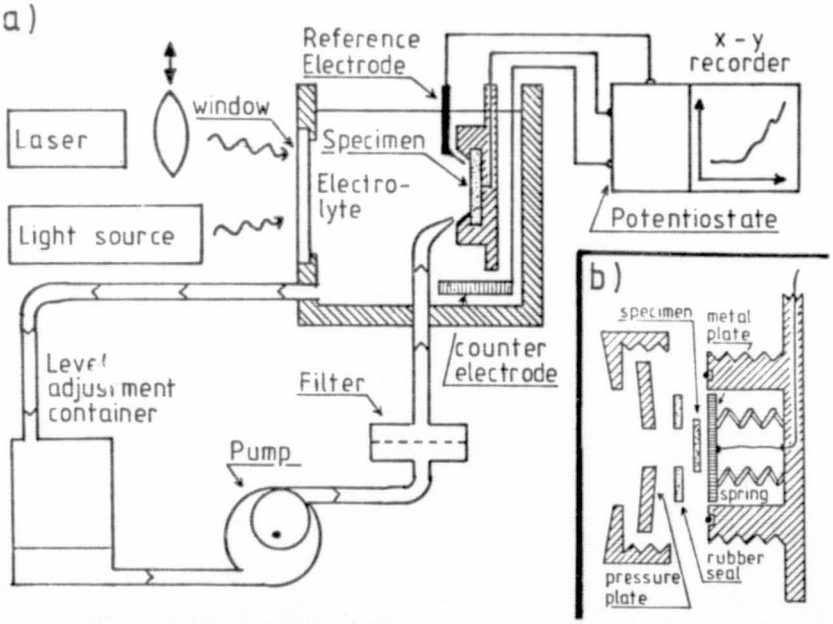

Fig. 8 Schematic drawing of the apparatus (Fig. 8a) and of the specimen holder (Fig. 8b).

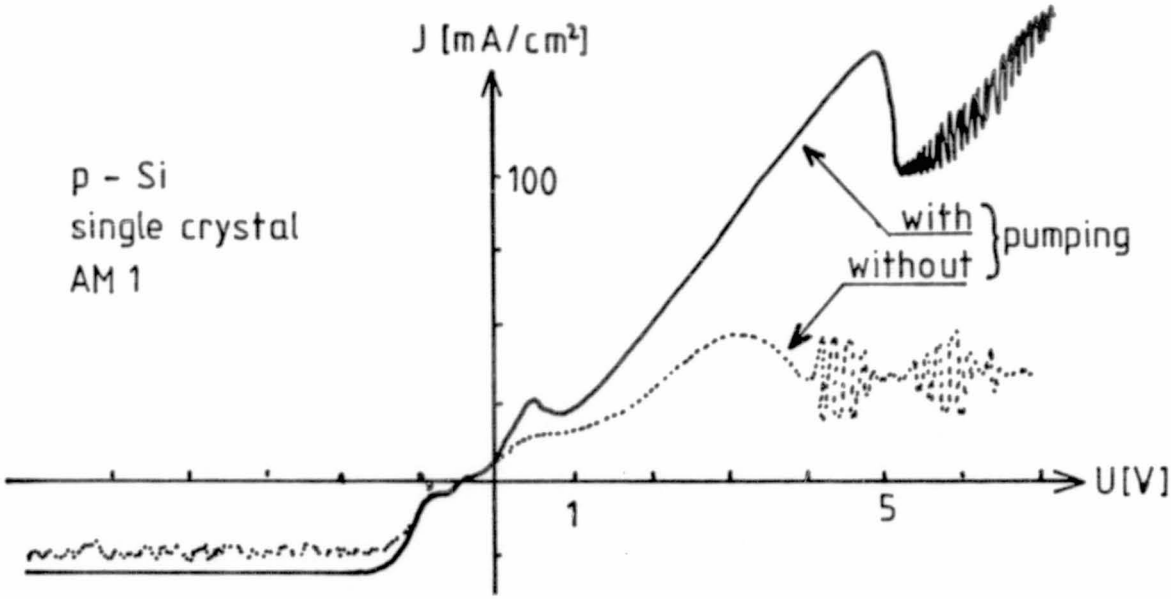

Fig. 9 I-U-characteristics of p-type Si obtained with and without circulation of the electrolyte.

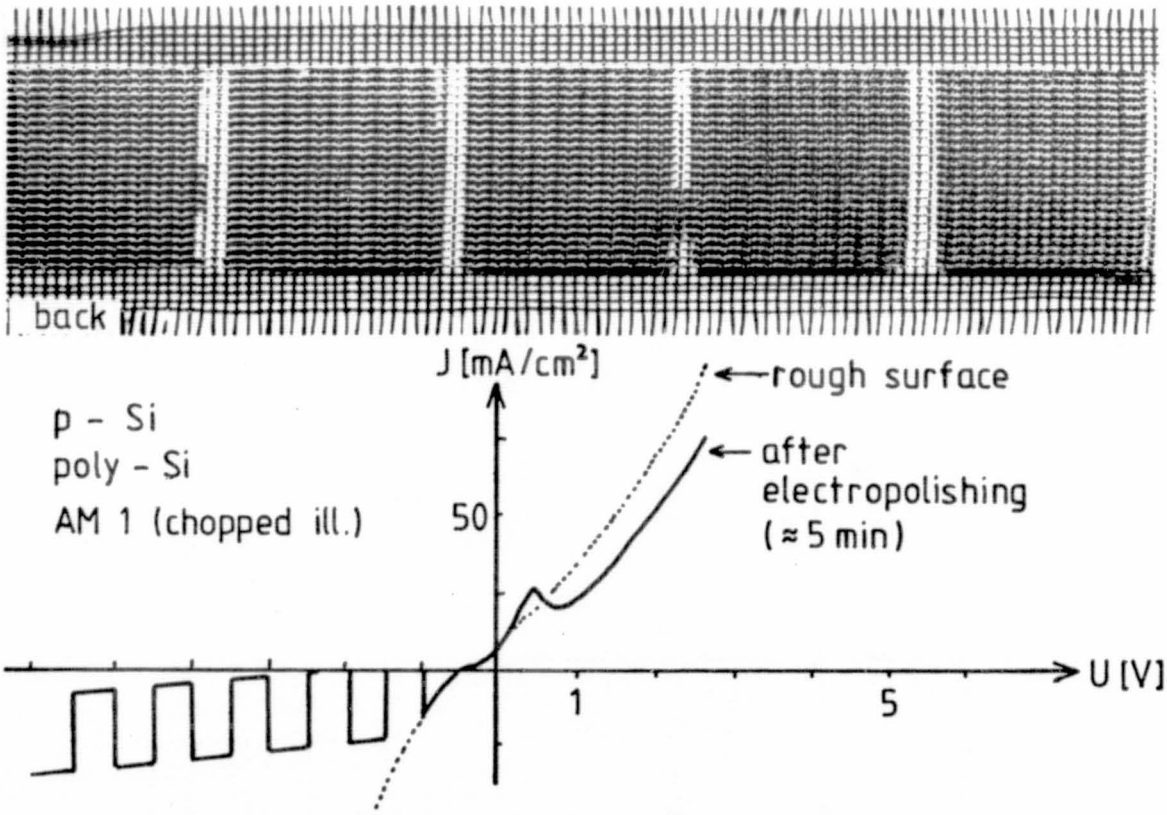

Fig. 10 I-U-characteristics of a sample with roughly ground surface before and after electropolishing.

DISCUSSION

JOHNSON: How do you make your contact to the back side of the wafer?

GRABMAIER: By evaporation or by pasting, with indium, gallium, and a little bit of aluminum. The best contacts are evaporated.

N84 28642

"DEFECTS IN HIGH SPEED GROWTH OF EFG SILICON RIBBON"

C.V. Hari N. Rao and Mary C. Cretella

Mobil Solar Energy Corporation
16 Hickory Drive, Waltham, Massachusetts 02254, U.S.A.

ABSTRACT

Silicon ribbons grown by the Edge-defined Film-fed Growth (EFG) technique exhibit a characteristic defect structure typified by twins, dislocations, grain boundaries and silicon carbide inclusions.

As growth speed is increased from less than 2.5 cm per minute, the structural details change. The major difference between the ribbons grown at speeds below and above 2.5 cm per minute is in the generation of a cellular structure at the higher growth speeds, observable in the ribbon cross section. The presence of the cross sectional structure leads, in general, to a reduction in cell performance. Models to explain the formation of such a cross sectional structure are presented and discussed.

INTRODUCTION

The Edge-defined Film-fed Growth (EFG) of silicon for terrestrial photovoltaic applications is the technology developed and practiced at Mobil Solar Energy Corporation. Silicon ribbons have been grown from both graphite crucibles and from fused silica crucibles at typical growth speeds of 2.5 cm per minute. In this paper, we will describe some of the phenomena observed during the growth of EFG ribbon and their impact on the material properties.

CRYSTAL GROWTH

The one feature of ribbons grown from melts is the defect structure, which is dominated by the presence of twins. Such a twinned structure has been observed in EFG ribbons, as well as in ribbons grown by the Ribbon Against Drop (RAD) process, the Ribbon to Ribbon (RTR) process, the Horizontal Ribbon Growth (HRG) process and others [1]. These twin densities range between 10^2 to 10^4 per cm in EFG ribbons. In addition, EFG ribbons exhibit high dislocation densities, 10^4-$10^6/cm^2$, similar to that exhibited by ribbons grown by many other growth techniques. Silicon material grown in the form of ingots, at solidification rates lower than those employed by the sheet growth methods, has, in addition, a classical polygonal grain structure [2].

PRECEDING PAGE BLANK NOT FILMED

The defect structure of ribbons grown by the EFG technique shows a dependence on purity of melt, speed and thickness. In the case of growth runs where the melt is "clean", the characteristic twin structure is observed through the thickness of the ribbon sample. For the same growth speeds, the introduction of impurities into the melt due to either the use of unpurified system components or due to accidents will result in a degree of structural breakdown and the increase of defect densities. In Fig. 1 are photomicrographs of the transverse (perpendicular to the growth direction) cross sections of ribbon samples showing the structural details through the thickness. Samples depicted in Figs. 1(a) and 1(b) were both grown at substantially the same speed, i.e., 2.0 to 2.3 cm/minute. The ribbon in Fig. 1(a) was from a "clean" growth run, while that shown in Fig. 1(b) was from a growth run where the graphite system components were not clean. As can be seen, the ribbon grown from the "unclean" run exhibits an increased defect density.

Growth of ribbons at high speeds (growth speeds greater than 2.5 cm per minute) requires the removal of the latent heat of crystallization from the growth interface at rates greater than would be possible by radiation into the growth ambient. Accelerated heat extraction at the interface can be effected via the use of water-cooled heat removal elements [3] which is the practice at Mobil Solar. A consequence of such increased rate of heat extraction is the introduction of stresses into the material. Alleviation of these residual stresses can be facilitated by the use of annealing afterheaters. Figure 2 is a representation of the temperature profile that the grown ribbon experiences. Figure 2(a) represents schematically, the ideal or desired temperature profile in such a cold shoe-annealing afterheater system, where the ribbon would experience a rapid cool-down followed by a linear cooling rate from approximately 1200°C. In practice, however, the ribbon undergoes a temperature excursion (shown in Fig. 2(b)), where a rapid initial cool-down is followed by a reheat before settling on a linear temperature gradient.

Ribbons grown at speeds greater than 2.5 cm/minute exhibit a subsurface structure often characterized by the presence of cellular grains. Figure 3 is a comparison of the transverse cross sections of ribbons grown at three different speeds: 3.7 cm/min, 4.5 cm/min and 5.6 cm/min, in the same growth run. All the ribbon sections examined were substantially the same thickness, ~200 μm. As can be seen from Fig. 3, ribbon grown at 3.7 cm/min shows an increase in the cross sectional defect density compared to that grown at ~2.0 cm/min (Fig. 1(a)); an increase in growth velocity causes an increase in the incidence of the subsurface or central grain structure. The fraction of the sample width with the central grain structure was examined in these ribbons and the data are:

Sample	Growth Speed (cm/min)	% of Width with Subsurface Structure	Average Thickness (μm)
16-126-1-1	3.7	5.4	203
16-126-1-4	4.5	7.2	212
16-126-1-8	5.6	48.8	212

Ribbon thickness seems to be a critical parameter governing the generation of the central grain structure. For the same growth speed, a decrease in ribbon thickness suppresses the formation of the central grain structure as shown in Fig. 4. Figures 4(a) and 4(b) are transverse cross sections of ribbons grown at two different speeds and, in each case, the thinner ribbon section is seen to be free of the central grain structure.

The central grain structure can be postulated to be the result of compositional inhomogeneities. As the ribbon is cooled, the solid-liquid interface acquires a shape shown in Fig. 5 as a result of the higher rate of heat extraction from the surfaces compared to the central region of the sample. An interface such as that shown in Fig. 5 leads to an inhomogeneous distribution of impurities, such as carbon and the transition metals, with a higher impurity concentration present in the center of the ribbon. The differences in temperatures are accentuated as the rate of heat extraction, required to attain higher speeds, is increased. As the growth rate is increased, the impurity gradient between the surface and the center of the ribbon also is exacerbated. The ribbon, initially under such conditions of impurity gradient, undergoes an anneal at ~1200°C as it travels through the afterheaters (Fig. 2(b)).

The quenched-in silicon self-interstitial concentration has been computed to be 2×10^{-6} cm^{-3} at $T = T_M$, with a self-diffusion coefficient of 2.49×10^{-6} cm^2/sec [4]. In the vicinity of the ribbon surface, the interstitials can outdiffuse to the surface sinks during annealing. On the other hand, the high carbon and other impurity concentration in the center of the ribbon leads to a high concentration of defects in the center portion of the ribbon. In fact, the central grain structure has not been observed to intersect the ribbon surfaces, and in all observations was found to be confined to the interior of the ribbon. These observations are consistent with the assumption that the self interstitials annihilate by migration to the ribbon surfaces and the shape of the growth interface is as depicted in Fig. 5.

To examine the interface shape during growth, ribbons were grown from a boron ($k_o = 0.8$; $k_{eff} = 1.0$) doped silicon melt contained in fused silica crucible at typical growth speeds of 2 cm/min. Progressively more boron dopant was added at specific intervals during the growth to achieve 5 Ω-cm, 1 Ω-cm, and 0.2 Ω-cm resistivity. It was expected that the boron concentration would remain constant through the ribbon thickness, while

contaminants like Al (k_o = 0.003), from the dissolution of the fused silica crucible, would superimpose a resistance profile which is responsive to the solid-liquid interface shape [5].

Careful spreading resistance data were obtained across the thickness of the samples, in the manner shown in Fig. 6. The resulting distributions measured through the ribbon thicknesses are shown in Fig. 7(a), (b), and (c). As can be seen from the profile of the 5 Ω-cm and 1 Ω-cm material, the impurities; e.g. Al, segregated to the center of the sample even at 2 cm/min growth speed. From these resistance profiles the liquid-solid growth interface can be assumed to have a shape akin to that shown in Fig. 5. At the 0.2 Ω-cm doping level ($B = 2 \times 10^{17}$ atoms/cc) the effect of the Al distribution is much diminished; however, there is no reason to assume that the growth interface shape has changed.

To examine the effect of speed on interface shape, ribbons were grown from a silicon melt with no added dopant, but contained in a fused silica crucible. The speed of growth was increased from 1.8 cm/min to 2.5 cm/min and to 3 cm/min. A displaced graphite die was used for growth. Spreading resistance data, taken at 10 μm step intervals across the thickness of the sample are shown in Figs. 8(a), (b) and (c). As observed earlier, impurity doping occurs from dissolution of the fused silica crucible. As can be seen, the inhomogeneous impurity distribution through the thickness is accentuated with an increase in growth speed. It is not unreasonable to expect that at higher growth speeds (4 cm/min and higher), if the thickness were a constant, impurity concentration through the sample thickness would be inhomogeneous, as proposed earlier. Figure 9(a) is a spreading resistance profile across the bevelled section of a sample grown at 3.5 cm/min. The sample was taken from a growth run where unpurified graphite components were used which introduced a high impurity concentration resulting in the formation of central grain structure in the ribbon. A periodic variation is seen in the spreading resistance, with low values of resistance coincidental with the position of the grains, shown in Fig. 9(b). In addition, the grains were found to be decorated with a second phase containing iron and other transition metals. These data further support the hypothesis that the central grain structure is a result of the interaction of the interface shape and inhomogeneous impurity distribution in the silicon ribbon which appears to lead, in the end case, to cellular growth.

These data suggest that the impurity distribution can be selected by a proper tailoring of the interface shape. For example, the impurities can be segregated to a particular position in the ribbon by an appropriate manipulation of the thermal and geometric gradients at the die top and with selection of the growth parameters of speed and thickness within the constraints imposed by residual stresses.

ELECTRICAL EFFECTS

Several studies [6,7,8] have reported on the electrical effects of the various defect types observed in EFG silicon ribbon and other sheet materials. Electron beam induced current (EBIC) data on (a) Schottky barriers fabricated on the as-grown material and (b) on finished cells allow correlations of the electrical activity of the as-grown defects and their response to solar cell processing. In general, it has been observed that twin boundaries do not act as recombination sites and that grain boundaries and dislocation arrays tend to reduce the local collection efficiency. This is depicted in Fig. 10(b) which is an EBIC image obtained on a section of as-grown P-type ribbon by fabricating an aluminum Schottky barrier. Fig. 10(a) is a photomicrograph of the surface of the sample and Fig. 10(c) is a portion of the same section of the sample after a preferential dislocation etch. Figure 10(d) is a magnified image of the portion of the sample marked "X", showing the details of the dislocation array that was found to be electrically active.

The presence of the electrically active defects leads to local variations in resistivity. Figure 11(a) shows a spreading resistance profile across the surface of a P-type ribbon grown at 2.0 cm/minute from a fused silica crucible; Fig. 11(b) and 11(c) respectively, are photomicrographs of the surface of the sample (unetched) and after a preferential dislocation etch. As can be seen, the grain boundary in Figure 11(c) shows a dramatic variation in the resistivity. This change in resistivity can be due to the segregation of impurities to the grain boundary site similar to that shown in the presence of the central grain structure (Fig. 9).

Growth of ribbons via the EFG technique has been practiced from melts contained in both fused silica crucibles and purified graphite crucibles. It has been reported [9] that a junction formation technique that employs gas phase diffusion (with PH_3 at 900^oC) yields cells with lower efficiency when the cells are fabricated on ribbons grown from a graphite crucible as compared to cells fabricated on material grown from fused silica crucibles. These data indicate the beneficial effects of the presence of oxygen in the as-grown ribbon.

A majority of the high speed ribbon growth experiments have involved growth from graphite crucibles, and these have exhibited low efficiencies of 7-9%. Oxygen can be introduced into these ribbons by the addition of oxygen bearing gases (such as CO_2) to the growth ambient in the vicinity of the solid-liquid interface [10]. Table I shows the solar cell data on a series of cells grown in a cartridge system from graphite crucibles. The data clearly indicate that controlled concentrations of CO_2 gas to the growth meniscus improves cell performance from ~9% to ~11% efficiency. Table II, however, shows the efficiency data of cells grown under similar conditions of CO_2 gas flow, but with the parameters adjusted so that the growth speed was 2 cm/min. It is possible that the higher efficiency (~12.5%) exhibited by these cells is a result of an improved defect structure; the improvement being brought about by a decrease in the

temperature gradient between the surface and the center portion of the as-grown ribbon at the solid-liquid interface. Unfortunately, no structural data was gathered on these cells. The role of oxygen or the effect of carbon in modifying the response of EFG ribbons to junction formation techniques is not well understood.

SUMMARY

The growth parameters of speed, thickness and thermal environment have been shown to affect the distribution of impurities through the thickness of the ribbon material. Although not discussed in this paper, similar distribution effects occur across the ribbon width.

The impurities and the impurity/defect interactions that result, have been shown to cause localized suppression of the current collection. Additional effects of oxygen, either introduced from the crucible material or the ambient (via CO_2), have been noted to perturb the solar cell performance.

REFERENCES

1. These processes described in "Shaped Crystal Growth", G.W. Cullen and T. Surek (eds.), North Holland Publishing Company, Amsterdam, 1980.

2. H. Fischer and W. Pschunder, 12th IEEE Photovoltaic Specialists Conference (New York: IEEE; 1976), p. 86.

3. B.H. Mackintosh, T. Surek, J.P. Kalejs, E.M. Sachs, S. Nagy, and F.V. Wald, IEEE Photovoltaic Specialists Conference (New York: IEEE; 1978), p. 350.

4. H. Foll, V. Gosele and B.O. Kolbesen, J. Crystal Growth, 40, 90 (1977).

5. J.P. Kalejs, G.M. Freedman, and F.V. Wald, J. Crystal Growth, 48, 74 (1980).

6. K. Yang, C.H. Schwuttke and T.F. Ciszek, "Shaped Crystal Growth", G.W. Cullen and T. Surek (eds.), North Holland Publishing Company, Amsterdam, 301 (1980).

7. C.V. Hari Rao, R.O. Bell, M.C. Cretella, J.C. Ho, F.V. Wald and K.V. Ravi, 13th IEEE Photovoltaic Specialists Conference (New York: IEEE; 1978), p. 1213..

8. B. Cunningham, H.P. Strunk, and D.G. Ast, Appl. Phys. Lett., 40, 237 (1982).

9. K.V. Ravi, R.C. Gonsiorawski, A.R. Chaudhuri, C.V. Hari Rao, C.T. Ho, J.I. Hanoka and B.R. Bathey, 15th IEEE Photovoltaic Specialists Conference (New York: IEEE; 1981), p. 928.

10. B.H. Mackintosh, J.P. Kalejs, C.T. Ho, and F.V. Wald, Third E.C. Photovoltaic Energy Conference, ed. W. Palz (Dordrect: D. Reidel; 1980), p. 553.

FIGURE CAPTIONS

Fig. 1. Photomicrographs of transverse cross sections of silicon ribbons: a) grown in a clean system; b) grown in a system with unpurified graphite components. Growth speed was 2.0-2.3 cm/min from melt contained in fused silica crucibles.

Fig. 2. Schematic of (a) ideal and (b) experimental vertical temperature profiles for high speed cartridge ribbon growth.

Fig. 3. Photomicrographs of transverse cross sections of silicon ribbons showing the subsurface structure as a function of growth speed.

Fig. 4. Photomicrographs of transverse cross sections of silicon ribbon grown at speeds of 3.7 and 4.5 cm/min showing the subsurface structure as a function of thickness.

Fig. 5. Schematic of the solid-liquid interface shape during EFG of silicon ribbon.

Fig. 6. Schematic showing spreading resistance probe paths in the cross sections of silicon ribbon. Probe spacing used is 25 μm at stepping intervals of 10 μm. Surfaces are prepared with a final chemical/mechanical polish using 30% Syton HT* as the abrasive.

Fig. 7. Spreading resistance probe measurements showing the impurity distribution through the thickness for various boron doping levels. Resistances are given relative to the minima (taken as 1X).

Fig. 8. (a) Spreading resistance probe measurements on silicon ribbon cross sections showing the distribution of impurities as a function of growth speed. No dopant was added; impurities were introduced to the melt through dissolution of the final silica crucible. From left to right growth speeds are 1.8, 2.5, and 3.0 cm/min. Resistances are given relative to the minima (taken as 1X). (b) Schematic of solid-liquid interface shapes related to the impurity distributions shown in (a).

*Syton is a registered trade name of the Monsanto Company.

Fig. 9. Spreading resistance probe measurement (a) through a bevelled section of silicon ribbon containing central grain structure as shown in the photomicrograph (b). The arrow indicates the probe path. Low resistance regions occur around the grain boundaries. Note the presence of a second phase surrounding the grains. Magnification by bevelling is 20X.

Fig. 10. Photomicrographs of an area of a silicon ribbon surface. (a) Surface after etching in 4 pts (70%) HNO_3: 1 pt (49%) HF for 30 seconds. (b) EBIC image of the same area obtained using an Al Schottky barrier. (c) Portion of same area (note increase in magnification) after etching in Sirtl etchant (5MCrO_3 in 12NHF) to reveal defects. Arrows A, B and X indicate recombination boundaries. (d) Higher magnification image of boundaries B and X.

Fig. 11. (a) Spreading resistance profile across a section of Syton polished silicon ribbon surface showing large variation in carrier concentration. (b) Photomicrograph of polished surface showing probe traces. (c) Photomicrograph after etching in Sirtl etchant. Arrow indicates boundary region corresponding to high carrier concentration in probe trace.

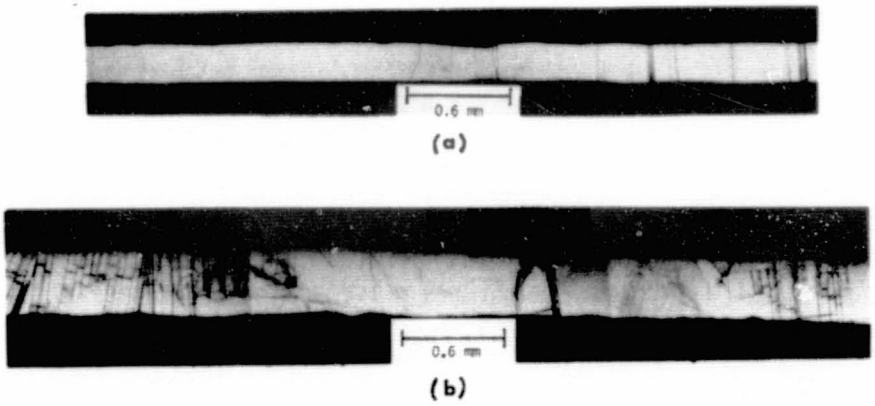

Figure 1

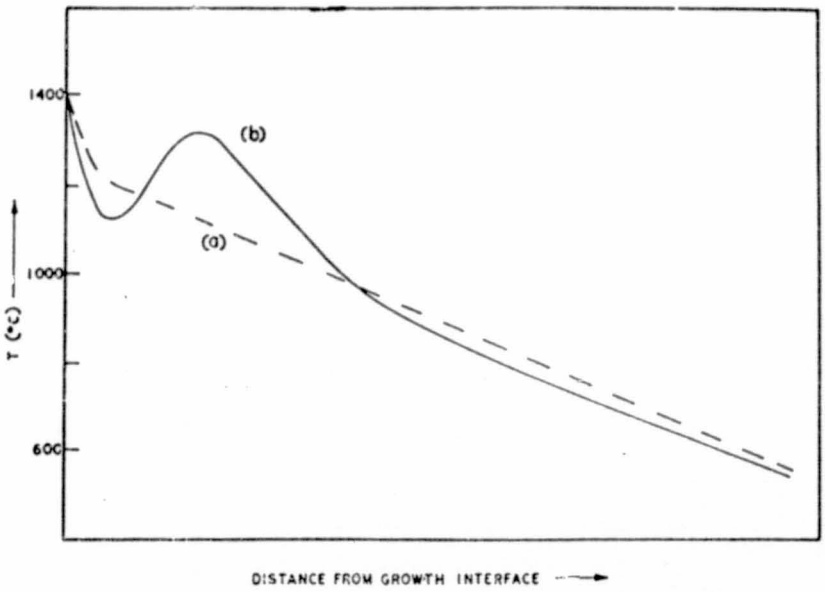

Figure 2

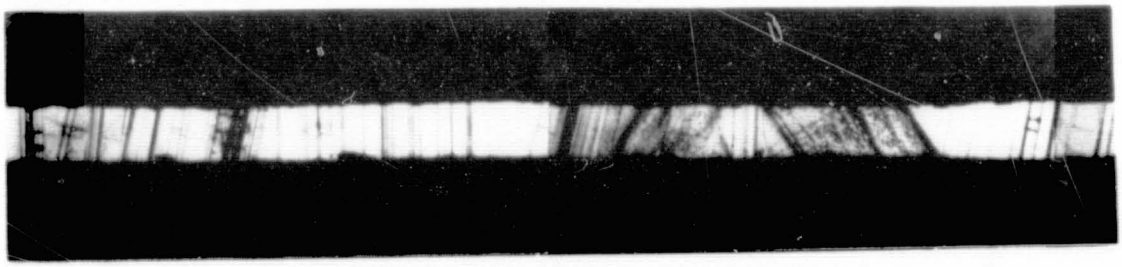

GROWTH SPEED = 3.7 CM/MIN.

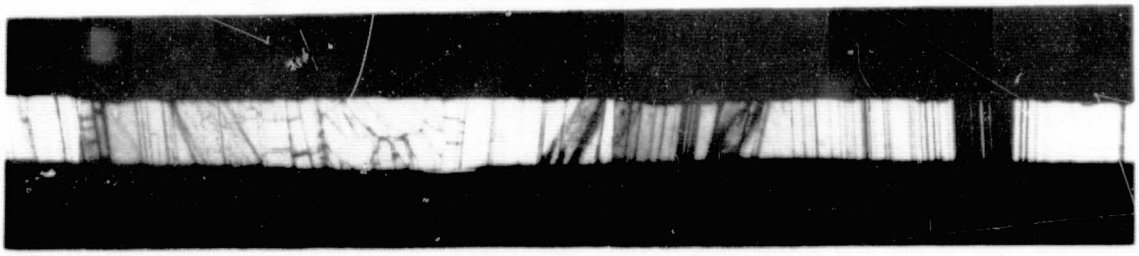

GROWTH SPEED = 4.5 CM/MIN.

GROWTH SPEED = 5.6 CM/MIN.

Figure 3

GROWTH SPEED = 3.7 CM/MIN.

THICKNESS = 203 μM

THICKNESS = 336 μM

GROWTH SPEED = 4.5 CM/IN.

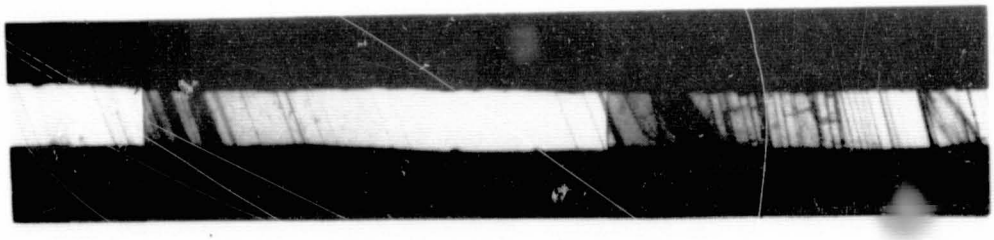

THICKNESS = 212 μM

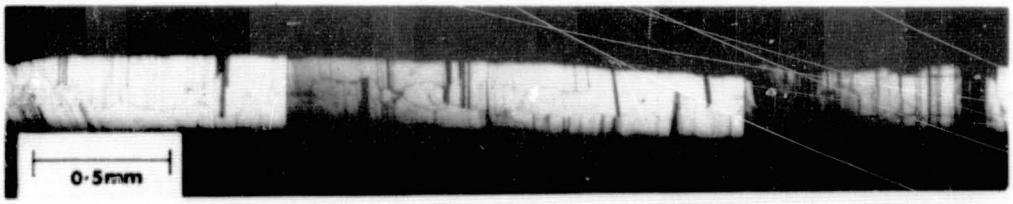

THICKNESS = 274 μM

Figure 4

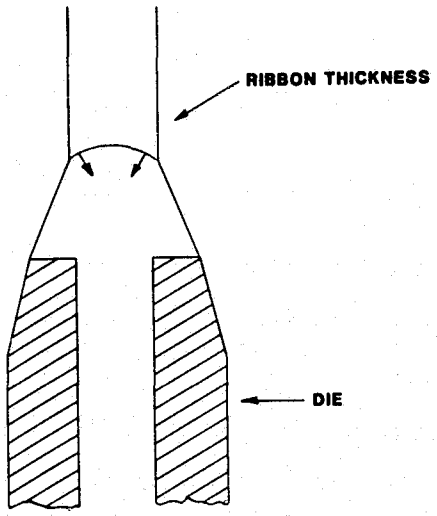

Figure 5

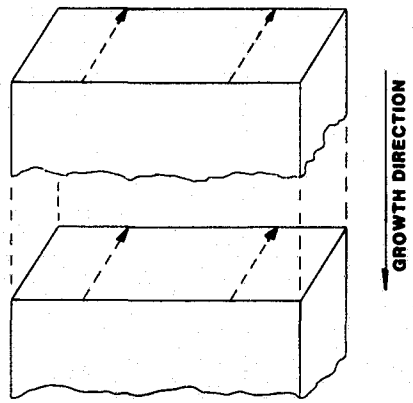

Figure 6

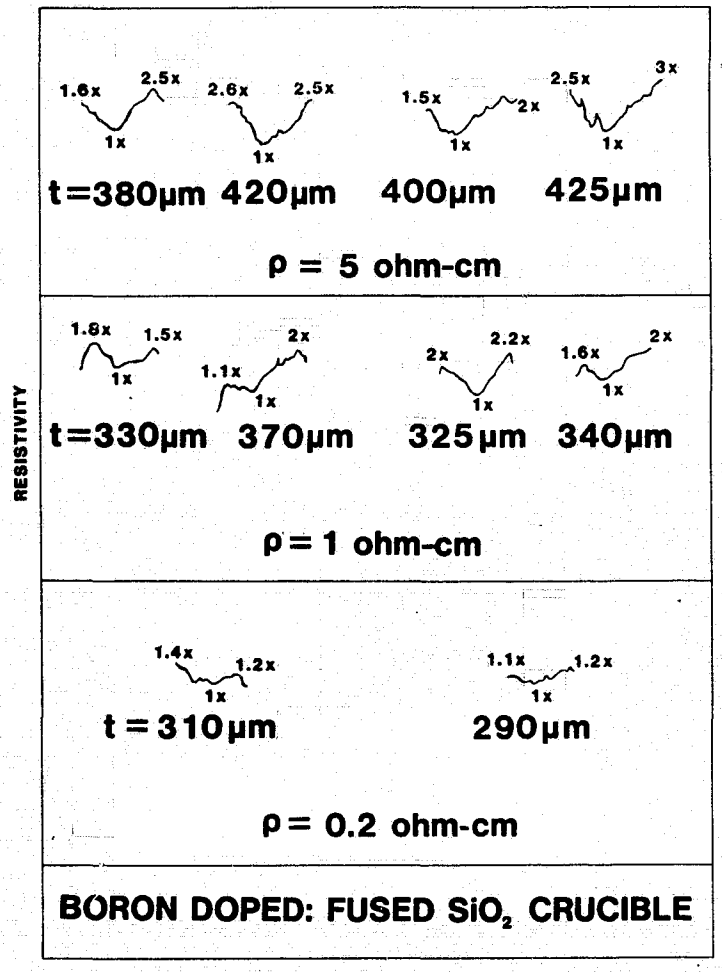

Figure 7

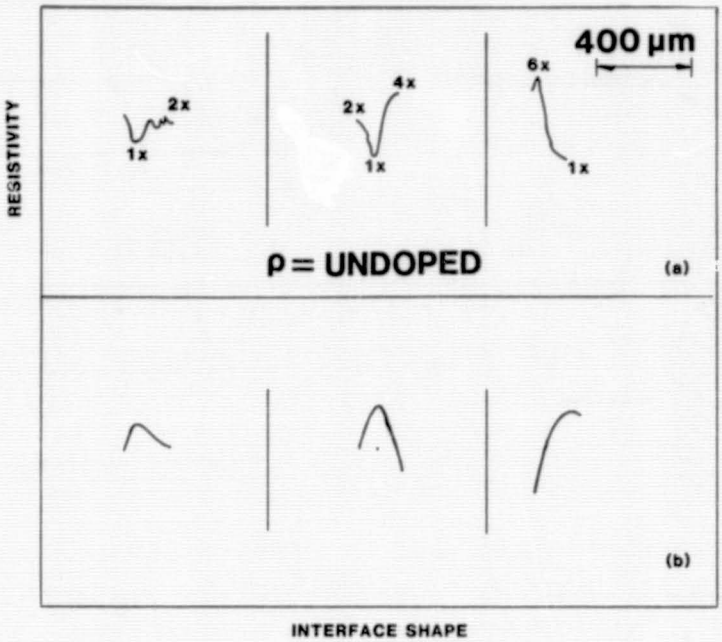

Figure 8

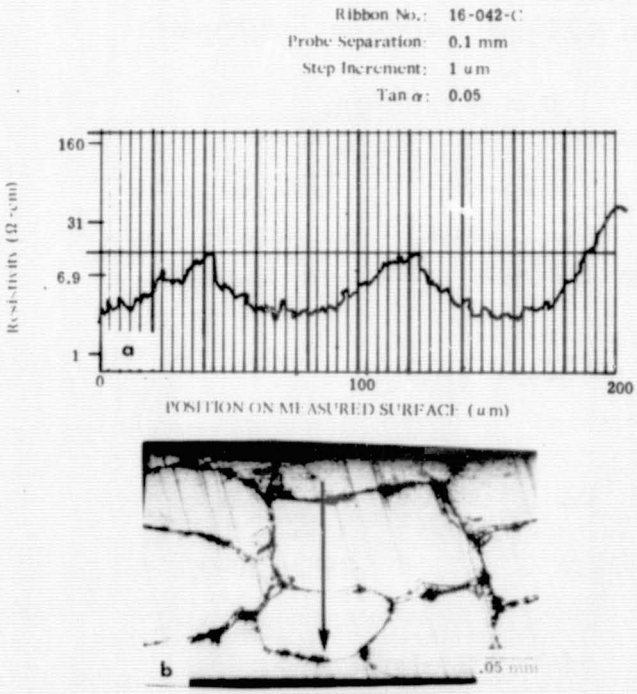

Figure 9

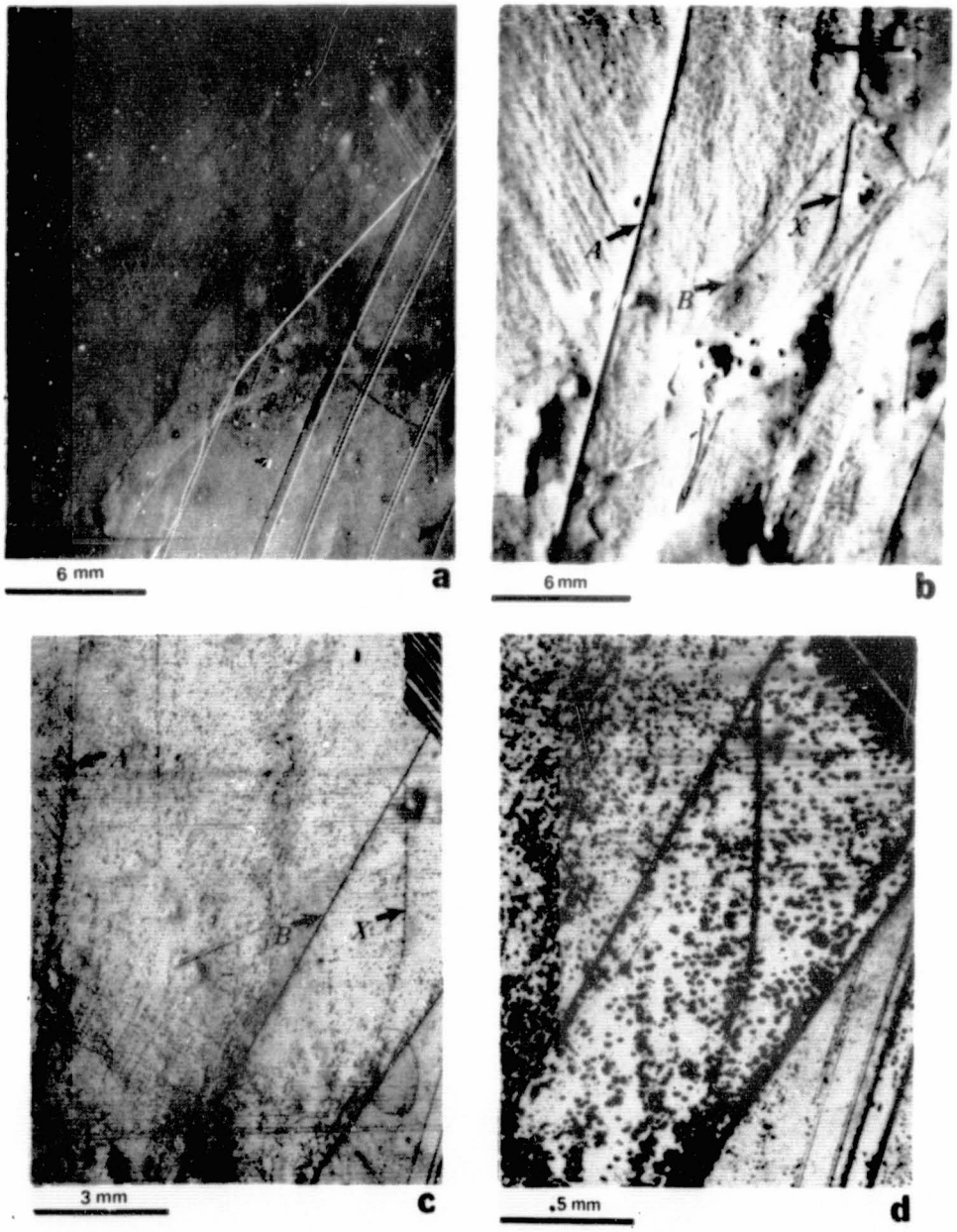

Figure 10

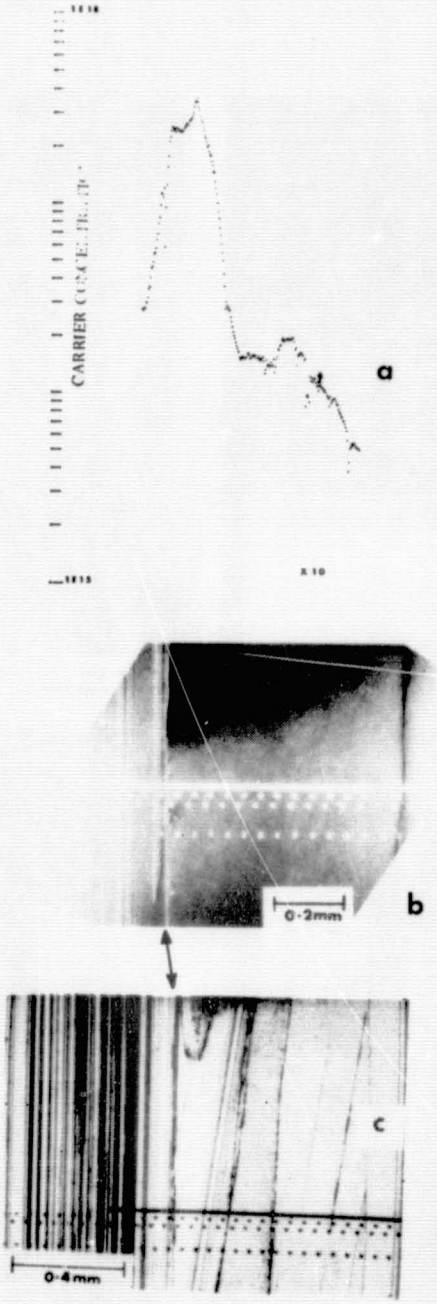

Figure 11

ORIGINAL PAGE IS
OF POOR QUALITY

Table I. Efficiencies (AM1) of Solar Cells Fabricated on Ribbons Grown from a Graphite Crucible at MSEC, With and Without CO_2 Gas in the Ambient Near the Growth Interface. Growth Speed = 3.5 cm/minute.

Ambient Condition	J_{sc} (mA/cm²)	V_{oc} (V)	FF	η (%)
CO_2 Off	22.2	.523	.738	8.7
	18.7	.499	.723	6.8
	22.7	.530	.732	8.9
	18.9	.501	.731	7.0
	23.1	.534	.760	9.4
CO_2 On	28.0	.570	.721	11.6
	28.8	.580	.698	11.8
	28.1	.574	.717	11.7
	26.4	.562	.695	10.4
	26.9	.565	.730	11.2
	27.5	.573	.727	11.6
	26.3	.560	.730	10.4
	27.3	.573	.714	11.3
	26.1	.562	.739	11.0
	26.1	.560	.741	10.9
	25.2	.555	.738	10.4
	26.2	.563	.765	11.4

Table II. Efficiencies (AM1) of Solar Cells Fabricated on Ribbons Grown from a Graphite Crucible at MSEC, With CO_2 Gas in the Ambient Near the Growth Interface. Growth Speed = 2.0 cm/minute.

CELL NUMBER	AREA (cm^2)	I_{rv} (mA/cm^2)	V_{oc} (V)	I_p (mA)	I_{sc} (mA/cm^2)	FF	P (mW/cm^2)
60	49.68	0.02	0.557	1498	33.06	0.724	13.34
61	49.68	0.02	0.549	1449	32.24	0.728	12.90
62	49.68	0.02	0.552	1460	32.42	0.718	12.85
63	49.68	0.03	0.566	1475	33.00	0.737	13.77
64	49.68	0.00	0.562	1571	33.47	0.753	14.17
65	49.68	0.15	0.547	1405	32.02	0.719	12.59
66	49.68	0.13	0.552	1422	32.32	0.723	12.88
67	49.68	0.07	0.555	1541	33.41	0.734	13.62
68	49.68	0.18	0.562	1442	32.34	0.725	13.18
69	49.68	0.12	0.546	1502	33.09	0.718	12.97
70	49.68	0.12	0.552	1517	33.29	0.719	13.21
Mean values for 123 cells:							
	49.68	0.13	0.551	1416	31.95	0.710	12.52

DISCUSSION

MILSTEIN: You were describing the effects of glass-doped and phosphene-doped materials, and made the comment that in materials grown in quartz crucibles versus graphite crucibles, the effect seemed to reverse. There have been other studies, such as work at Motorola by Ming Liaw, dealing with the slagging of metallurgical silicon melts, typically using oxide slags. What is observed is that the impurities segregate into the oxide to a rather large extent. I wonder whether, when you do an oxide-phosphorus diffusion, partially what you are also doing is depleting the near-surface region of some metallic impurity, perhaps, and conversely when you grow from an oxidic crucible you are doing the same thing to the entire melt; therefore, when you see the phosphine reaction, it is better because the material is cleaner throughout.

RAO: It is possible, but while you are growing the material you could be doing some kind of slagging, so you are removing those impurities in the slag. Now, coming back to the CVD phosphorus diffusion, one should not find the effect of that in the long-wavelength region, which is the red response, and that is where the improvement in diffusion lengths come in. So it is difficult to call it a near-surface effect, when the gettering is happening deeper in the bulk of the material.

MILSTEIN: I was simply thinking of it as a near-surface effect because you have the glass on the surface, and you would imagine that if it acts as a sink you are going to have the standard diffusional relationships.

RAO: If one uses that argument, then it is still difficult to explain what's happening way in the bulk of the material.

N84 28643

Electrical and Structural Characterization of Web Dendrite Crystals

G. H. Schwuttke

Scottsdale, AZ 85261

Abstract

Minority carrier lifetime distributions in silicon web dendrites are measured. Emphasis is placed on measuring areal homogeneity of lifetime, show its dependancy on structural defects, and its unique change during hot processing. The internal gettering action of defect layers present in web crystals and their relation to minority carrier lifetime distributions is discussed. Minority carrier lifetime maps of web dendrites obtained before and after high temperature heat treatment are compared to similar maps obtained from 100 mm diameter Czochralski silicon wafers. Such maps indicate similar or superior areal homogeneity of minority carrier lifetime in webs.

Introduction

Recently, calculations have been made which show that the presence of areal inhomogeneity of minority carrier lifetime in silicon wafers can devastate solar cell efficiency (1). For instance, it was shown that for no more than 5% of the solar cell area being inferior compared to the rest of the cell area, solar cell efficiency can be as poor as it would be if the entire area would be of inferior quality (1). Thus areal homogeneity of minority carrier lifetime is an important requirement for high efficiency solar cells.

This paper reports measurements of minority carrier lifetime "distributions" made on silicon web dendrite sections. Such measurements are compared to similar data obtained from 100 mm diameter Czochralski silicon wafers.

Structural Aspects of Silicon Web

A brief description of the as-grown web geometry and dislocation structure is needed to describe our electrical measurements clearly. For detailed results we refer to the original papers on web growth (2) and dislocation structures (3-5).

The web surface is parallel to the (111) plane, and the web pulling direction is ⟨112⟩. A cross-section of web shows its most prominent structural feature: multiple twin lamellae in the center of the web covered by two thick (100 μm) surface layers which are also in twin relation.

Dislocations in web are generated through "melt entrapment" caused by "wing" growth along the dendrites (2). Propagation of such dislocation depends on the curvature of the solid-liquid interface of the web during growth. An interface curvature of concave downward concentrates the dislocations in the

center of the web [2]. Webs grown with a straight interface concentrate the dislocations in the fillet region. Thus the web grows free of any dislocations [3, 4]. Most webs of today contain bundles of very long dislocations parallel to <112> piled up against the twin planes in the center. In addition, annealed web contains large area stacking faults lying in (111) planes parallel to the surface. These large faults give rise to complex contrast phenomena and intricate arrays can be observed in x-ray transmission topographs after annealing [5]. Common defect structures present in silicon web are summarized in Table I.

Minority Carrier Lifetime Measurements in Web

Silicon web dendrite sections were evaluated through minority carrier lifetime "mapping" using 1.5 mm diameter MOS capacitors. The total number of MOS capacitors per web section was 300. The MOS dots were arranged into 15 rows. The dendrites were included into the evaluation. The dimensions of the web sections were 2 inches long and 32 mm wide. The webs were evaluated after each oxidation cycle (15 min wet-110 min dry-15 min wet at 1000°C). Three or four consecutive oxidation cycles were used. Minority carrier lifetime maps of the total web section were obtained after each oxidation cycle by measuring the lifetime under each capacitor as described by Fahrner & Schneider [6]. Subsequently, the lifetime was computer plotted versus its position on the web surface. Local lifetime degrading defects revealed by such lifetime maps were analyzed by advanced characterization techniques. For the measurements web sections were selected according to perfection. The web dendrites to be MOS processed were free of slip dislocations which can result from buckling stresses during crystal growth. The selected webs contained all the characteristic defects listed in Table I.

A result typical for the web sections surveyed is shown in Figure 1. This figure summarizes the influence of high temperature heat cycles on minority carrier lifetime. The lifetime data are displayed in 6 maps. Each map represents a matrix of 300 capacitor dots. The maps on the left side of the figure carry the label oxidation 1 to 3 and represent the lifetime data obtained after the first, second, and third oxidation cycle. The devices were obviously stripped before every successive oxidation step. The z-scale represents the measured lifetime values in microseconds. The range of lifetime data present on the web section is also included in the label. For instance, the minimum lifetime obtained at a specific location (capacitor) after the first oxidation was 0.274 microseconds. The maximum lifetime is 207 microseconds. The lifetime map shows a relatively smooth plateau. Noteworthy is, that this plateau extends over the total web section surveyed. Accordingly, this web is of excellent crystal quality and compares well with the best Czochralski silicon as available today. Interesting is a comparison of the maps obtained after the first, second and third oxidation. The lifetime plateau obtained after the second oxidation is well above the one obtained after the first oxidation and the same is true for the third oxidation. The third plateau is a little bit lower than the second one. Using Czochralski wafer quality as a standard, the material obtained after the third oxidation shows a very uniform lifetime distribution.

The maps on the right side of Figure 1 are labeled DECREASE or INCREASE. The DECREASE map shows the degradation of lifetime as a result of the second or third oxidation cycle. The INCREASE map shows the area where the lifetime increased after the third oxidation relative to the first oxidation. These maps show clearly the improvement of lifetime as a result of oxidation. This improvement is fairly uniform and covers practically the total web area. Decreases in lifetime occur only along the dendrites, the fillet region or along the edges where the web section was cut by the dicing saw. This result is unique and relates to the special crystal structure of the "perfect" web. The defect planes, sandwiched between the perfect web surface layers, provide for "internal" gettering during high temperature heat cycles. Thus a substantial improvement in minority carrier lifetime can result. These measurements are compared to similar measurements made on 100 mm Czochralski silicon wafers and presented in the following.

Minority Carrier Lifetime Measurements in Czochralski Silicon

Recently, we conducted an evaluation of 100 mm diameter Czochralski silicon wafers as available from major vendors throughout the world. The evaluation concentrated on minority carrier lifetime mapping as described for the web crystal. Four consecutive oxidation cycles were used. The MOS dot matrix consisted of 25 times 25 MOS capacitors of 1.5 mm diameter. A result typical for the evaluated Czochralski wafers is shown in Figure 2. The lifetime data shown in Figure 2 are displayed in 4 maps. The maps on the left carry again the oxidation number. The data obtained after the first oxidation indicate excellent wafer quality. The map has a plateau at approximately 250 to 300 microseconds and extends practically across the total wafer area. This wafer represents silicon of the best quality. Nevertheless, successive oxidation results in steady degradation of lifetime. This is seen by comparing the maps obtained after the first and fourth oxidation.

Interesting are the DECREASE and INCREASE maps shown on the right of Figure 2. The DECREASE map confirms that degradation occurs uniformly across the total wafer area. After the fourth oxidation cycle small lifetime increases are observed only at 9 locations. In all other areas lifetime degraded substantially.

Discussion and Summary

The data given in Figures 1 and 2 are representative of "perfect" web and Czochralski silicon wafers. We note a basic difference between these two materials. Oxidation increases generation lifetime in web but decreases the same lifetime in Czochralski material. The decrease in lifetime in Czochralski wafers correlates with the precipitation phenomena of oxygen in silicon [7].

The large extent to which areal inhomogeneities exist in todays silicon is not well known. However, uniform minority carrier lifetime distributions are a prerequisite to high performance solar cell technology. Solar cell efficiency in excess of 15% for large area single crystal silicon cells will be very difficult to achieve without proper control of minority carrier lifetime distributions during large scale manufacturing.

References:

1. F. A. Lindholm, et al, Solid State Electronics, 23, 967, (1980).
2. S. O'Hara & A. I. Bennett, J. Appl. Phys., 35, 409, (1964).
3. S. O'Hara & G. H. Schwuttke, J. Appl. Phys., 36, 2475, (1965).
4. T. N. Tucker & G. H. Schwuttke, Appl. Phys. Letter, 9, 219, (1966).
5. E. S. Meieran & I. Blech, J. Appl. Phys., 38, 3495, (1967).
6. W. Fahrner & C. P. Schneider, J. Electrochem. Soc., 123, 100 (1976).
7. G. H. Schwuttke, Semiconductor Industry Association (SIA) Lecture, Stanford University, Palo Alto, CA, September 1981.

Table I

GROWTH CHARACTERISTICS	WEB
SEEDING	WELL CONTROLLED
SURFACE ORIENTATION	<111> WELL CONTROLLED
GROWTH DIRECTION	<112> WELL CONTROLLED
THICKNESS	AS LOW AS A FEW MICRONS THICK HAS BEEN GROWN
WIDTH ACHIEVED	~ 40 mm
HANDLING EASE	STRENGTH THROUGH DENDRITES DENDRITE REMOVAL CAN BE A PROBLEM
CONTINUOUS GROWTH	YES (30 mm WIDTH)
TWIN PLANES	PARALLEL TO SURFACE; APPROX. IN THE MIDDLE OF THE WEB (CAN ALSO BE GROWN WITH TWIN PLANES ONLY IN DENDRITES)
TWINS	SIMPLE TWINS: INFLUENCE ON ELEC. PROPERTIES NOT SHOWN, ASSUMED TO BE SMALL IF ANY.
DISLOCATIONS	PARALLEL TO <112> DIRECTION; CLOSE TO TWIN PLANES. ELECTRICAL ACTIVITY NOT DEMONSTRATED. (NO SEM EBIC). ASSUMED TO BE LOW (HIGH EFF. CELLS 15% AMI). DENSITY 10^4 - $10^6/cm^2$.
STACKING FAULTS	LARGE AREA OF LOWER-COTTRELL TYPE, ELECTRICAL ACTIVITY NOT KNOWN, ASSUMED TO BE LOW, IF ANY. NO EBIC MEASUREMENTS HAVE BEEN MADE.
GRAIN BOUNDARIES	NORMALLY NOT PRESENT IF GROWN UNDER CONTROLLED CONDITIONS. TOO HIGH A GROWTH RATE CAN LEAD TO GRAIN BOUNDARIES.

C-7

Figure 1

Web Dendrite Silicon Lifetime Distribution Data

Oxidation 1

NO. OF OXIDATIONS: 1
DATA RANGE: .2740 207
Z-SCALE: MICROSECONDS

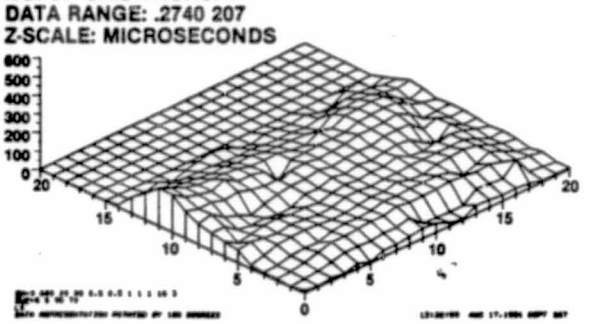

Decrease 1 to 2

OXIDATION NUMBERS: 1 2
DATA RANGE: .5000 200
Z-SCALE: MICROSECONDS

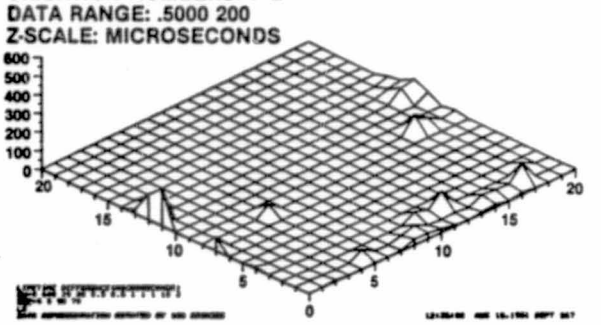

Oxidation 2

NO. OF OXIDATIONS: 2
DATA RANGE: .2120 608
Z-SCALE: MICROSECONDS

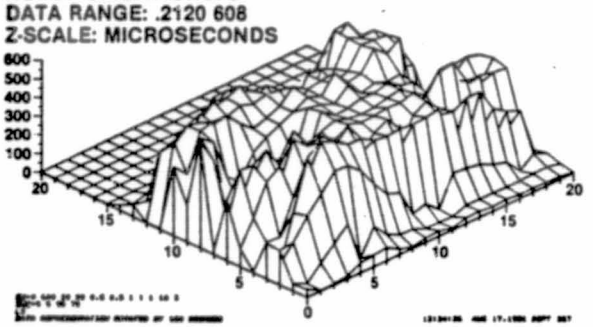

Decrease 1 to 3

OXIDATION NUMBERS: 1 3
DATA RANGE: .1000 163
Z-SCALE: MICROSECONDS

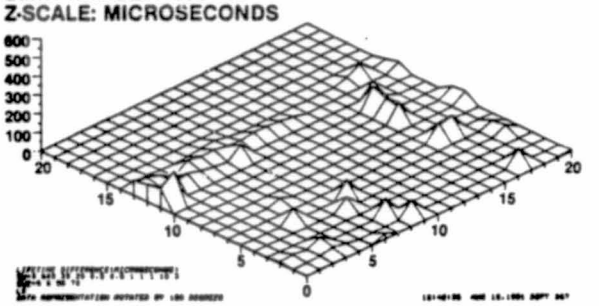

Oxidation 3

NO. OF OXIDATIONS: 3
DATA RANGE: .1810 452
Z-SCALE: MICROSECONDS

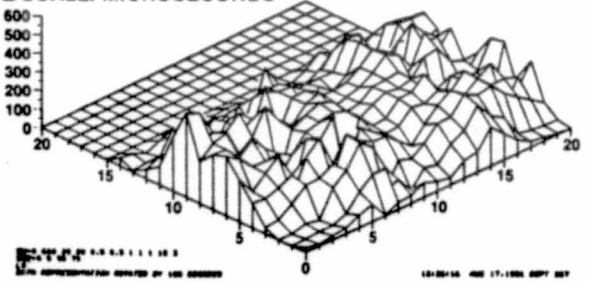

Increase 1 to 3

OXIDATION NUMBERS: 1 3
DATA RANGE: .1810 305
Z-SCALE: MICROSECONDS

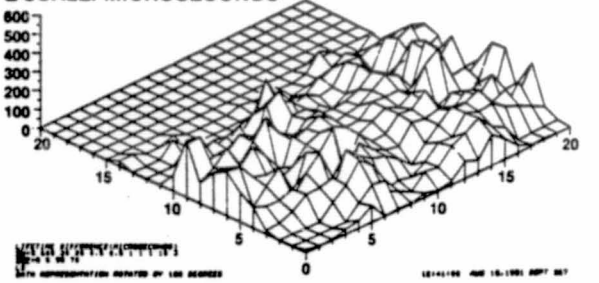

Figure 2

Lifetime Data Distribution Map
Vendor B

Oxidation 1

NO. OF OXIDATIONS: 1
DATA RANGE: 4.0000 478
Z-SCALE: MICROSECONDS

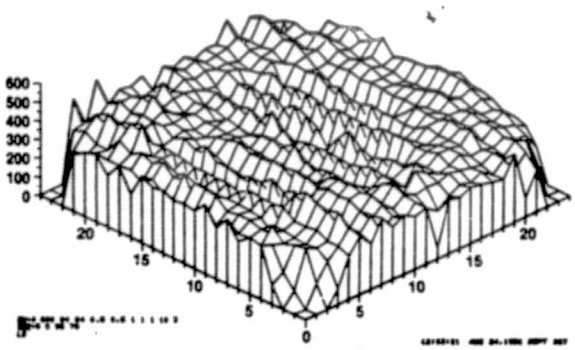

Decrease

OXIDATION NUMBERS: 1 4
DATA RANGE: 7.0000 442
Z-SCALE: MICROSECONDS

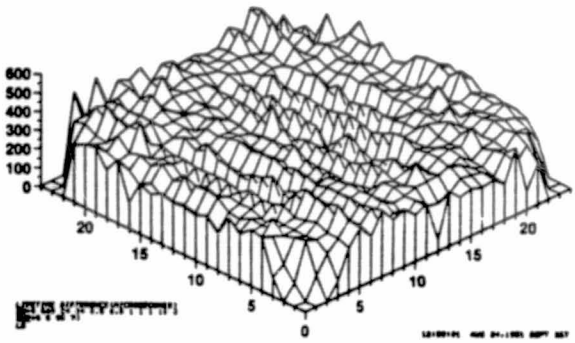

Oxidation 4

NO. OF OXIDATIONS: 4
DATA RANGE: .5300 129
Z-SCALE: MICROSECONDS

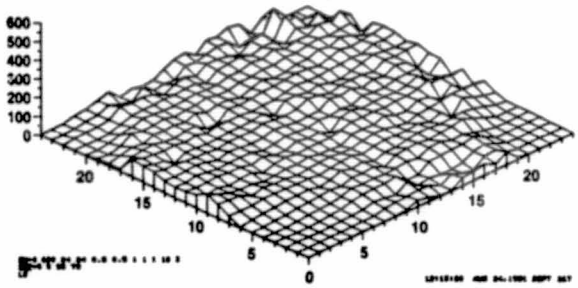

Increase

OXIDATION NUMBERS: 1 4
DATA RANGE: 2.0000 48
Z-SCALE: MICROSECONDS

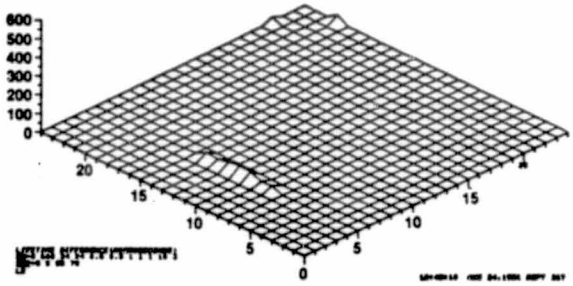

DISCUSSION

AST: During your oxidation treatment, it actually spends more time at high temperature than when it is growing. It has a unique gettering structure. All that this shows is that the central twin plane is a better gettering plane than the usual back-side damage. People are improving their back-side damage all the time. There is something more fascinating to this, because the standard web cells actually have dislocations that thread the junctions all the time.

SCHWUTTKE: These are not standard webs. These are webs that have dislocations, due to buckling stresses.

AST: But the standard web has dislocations that go through, and still has 15% or 16% efficiency. The trick must be, because a clean dislocation in a junction doesn't do anything, that the central twin planes, Lomer-Cottrells, or whatever, are such strong gettering centers that they suck the dislocations, which go with the junction, clean. If EFG also develops these low-angle tilt boundaries in the base, they don't look as appealing as gettering centers like the web, but it develops something that also connects as a gettering center. The great trick of web is that it has this unique structure of the (111).

SCHWUTTKE: I think the internal gettering comes naturally, if you deal with web, and it does not with Czochralski. You also have internal gettering in Czochralski crystals if you know what to do. The semiconductor industry has become very knowledgeable in producing what we call a denuded zone, and then we have a centrally located high-oxygen concentration layer. The first vendor I showed you used a centrally located oxygen layer for internal gettering. Only the oxygen layer does not withstand the continuous heating, due to the high oxidation the wafer experiences, if you do semiconductor processing. Then you encounter oxygen precipitation, and then you generate dislocation loops, and they start to penetrate into the denuded zone and they destroy the minority carrier lifetime in the important area. You are obviously correct--the inherent property of the web dendrite is summarized as follows: you have two perfect thick twin lamella. This is the area where you build your devices, be it a solar cell or be it a semiconductor device. In the middle you have the defect layer, which provides natural gettering, and I think that is something nature is giving you free.

KALEJS: If this twin plane is there, how would it affect back-surface-field enhancement of solar-cell properties? Somehow, with all the JPL-reported material processing in web, it appears that when people do talk about back-surface-field enhancement of solar cell properties, you do appear to see it in web. Do you think then that the internal gettering plane really does not impede these effects?

SCHWUTTKE: I have no direct measurements to prove how active that internal layer is. It is a defect layer, and if it is gettering, then it will be doing something. If you ask my opinion, I think that the solar web

material is good for an 18% cell. It is as good as the best Czochralski. Why don't we have an 18% web dendrite solar cell today? I think that relates directly to the manufacturing problems in producing high-quality stuff. I have not looked at Westinghouse material since I did this evaluation, but I see they have made considerable progress in widths and in removing impurities, in which case gettering would be of less significance. The web dendrite offers you very clean material. Even better than Czochralski. In terms of impurity distribution, the web is superior to the Czochralski wafer. It doesn't have the microsegregation phenomena. The web can fulfill very tight resistivity specs. The disadvantage it has today for VLSI is that it is of <111> orientation.

MILSTEIN: If you look at some of the analysis that Rohatgi has done at Westinghouse, I think the major feature that is considered in terms of increasing efficiency is trying to reduce the surface recombination, and in the region of the twin plane, at least based on the modeling, there seem to be zero effect. It doesn't act like there is anything electrically going on there.

CISZEK: Were any of those comparisons of vendors made on float-zone material, and if not, how would you speculate float-zone material might compare?

SCHWUTTKE: Float-zone material was not evaluated. Float-zone is missing the internal gettering. You have to use extra gettering to maintain the purity, etc.

AST: There must also be something to the thickness of the web, because any kind of minority carrier that you generate below the twin plane in order to be collected has got to go through the twin plane before it reaches the junction, and these dislocations in the twin planes, which we have studied a lot with EBIC, are definitely recombination centers. If you get too many of these guys in the twin plane, you will lose some of the long-wavelength response in these solar cells.

SCHWUTTKE: We are dealing with a planar arrangement of dislocations, so the electrical activity of a dislocation is anisotropic. Any carrier that will come up this way sees a planar arrangement, and so the capture cross section for him is very low. If we are dealing with dislocations in the same direction, then the capture cross section is very high.

BELOUET: Do you have any idea of the position of the twin planes across the thickness along the ribbon length?

SEIDENSTICKER: The twin planes can be almost anyplace. You can have it where it actually has gone through the surface. The usual condition is that the twin plane is approximately centered, and up to maybe a micrometer out of a hundred or something of that sort.

SCHWUTTKE: This seems to be a self-stabilizing affair. If the process is very controlled, the twin plane stays or positions itself very neatly. If the process gets out of control and they get buckling stresses, the twin plane can even outcrop, come to the surface and the whole structure deteriorates. Some web dendrite has seen buckling stresses, and I have

not shown you these topographs. You then, definitely, may have a high density of slip dislocations which interact. I call this a bad web dendrite crystal.

MORRISON: I would like to remind people that Koliwad showed Li-Jen Cheng's latest EBIC work on slip dislocation arrays in web dendrite. The most significant thing about those photographs is, those are low-temperature EBIC pictures, of electrical activity that was not observed at room temperature. This may be something that exists in other materials that have been evaluated at room temperature and they were just a property that was never recognized.

SCHWUTTKE: This EBIC picture looks very much like the X-ray topographs I take of material that will give you this particular recombination. Obviously you are dealing with dislocation, mainly slip, introduced by buckling, etc.

N84 28644 D30

REAL-TIME X-RAY DIFFRACTION: APPLICATIONS TO MATERIALS CHARACTERIZATION

Ronald G. Rosemeier
Brimrose Corporation of America
Baltimore, Maryland 21236

I. INTRODUCTION

With the high speed growth of materials it becomes necessary to develop measuring systems which also have the capabilities of characterizing these materials at high speeds. One of the conventional techniques of characterizing materials has been x-ray diffraction. Film which is the oldest method of recording the x-ray diffraction phenomenon is not quite adequate in most circumstances to record fast changing events. Even though conventional proportional counters and scintillation counters can provide the speed necessary to record these changing events they lack the ability to provide image information which may be important in some types of experimental or production arrangements. A selected number of novel applications of using x-ray diffraction to characterize materials in real-time will be discussed. Also, device characteristics of some x-ray intensifiers useful in instantaneous x-ray diffraction applications will be briefly presented.

II. REAL-TIME X-RAY DIFFRACTION EXPERIMENTAL ARRANGEMENTS

Applications of real-time x-ray diffraction (1), (2) in the characterization of materials can be easily achieved in both laboratory and production arrangements with the availability of portable image x-ray intensifiers. Real-time x-ray diffraction has found application in materials characterization in the field of all x-ray topography techniques, orientation, identification of grain boundaries and subgrain goundaries, direct observation of lattice rotation and bending, grain boundary migration, and flash x-ray applications, to mention a few.

X-ray topography provides a method of assessing both macroscopic and microscopic observation of strain fields caused by defects in single crystal and polycrystalline materials (3),(4),(5) and epitaxial films (6). All x-ray topography systems with real-time image x-ray intensification (2),(7),(8) provide a useful tool of ascertaining macroscopic quality of materials instantly with a spatial resolution of 100 um. In the developmental electronic materials field, real-time x-ray topography can be used as a screening technique of poor materials before undergoing costly processing (2).

A schematic of one type of double crystal camera is the asymmetric crystal topography (ACT) technique (7),(8) shown in Fig. 1. In this particular system an x-ray intensifier is placed at the image position for viewing of the topographic image in real-time. In Fig. 2 is a real-time (220) surface reflection topograph of an individual grain within a polycrystalline wafer of cast silicon (9). The topographic image was observed in real-time with Cu radiation at 45 kV and 32 mA in the double crystal arrangement. The absence of images in the inside portion of the grain in the vertical direction are (111) twin volumes of

a different orientation from the bulk of the grain and do not satisfy the Bragg condition. Image intensification is routinely used by the author with all conventional topography systems as both an alignment tool and as a method of assessing macroscopic quality of crystalline materials.

Real-time x-ray diffraction can find usefulness in the most simple of the techniques, the Laue method. In Fig. 3 is a schematic of a Laue arrangement used in conjunction with an image x-ray intensifier. In Fig. 4 is a real-time Laue transmission pattern of a 1 mm thick sapphire single crystal obtained at 40 kV and 32 mA with Cu radiation. Using a modification of this technique in Fig. 3 the crystal can be translated linearly which can allow the change in orientation of the crystal to be monitored along its length. Also, precise positions of grain boundaries and macroscopic quality of crystalline structures (e.g. identification of subgrain boundaries, twins, rotation, axes, strain, etc.) can be determined.

Similarly, real-time x-ray Debye-Scherrer arrangements can also be set up as shown in Fig. 5. Fig. 6 illustrates a real-time x-ray Debye-Scherrer transmission pattern of a brass foil obtained at 40 kV and 32 mA using Cu radiation. The rolling texture within the material is demonstrated in the photograph. Using a similar arrangement annealing experiments could be performed in situ to measure effects upon the texture in the grain structures. Also, experiments can be conducted to study real-time phase changes in a material system.

In order to study how single crystal aluminum materials behave during uniaxial tensile deformation, crystallographic orientations obtained from transmission Laue patterns were observed in situ (10,(11). The use of an image x-ray intensifier system developed by Reifsnider and Green (11) permitted Laue transmission x-ray diffraction patterns to be recorded with a motion picture camera at rates as fast as 24 frames per second. In Fig. 7 is an experimental configuration for observing Laue transmission patterns in real-time during tensile deformation. In Fig. 8 is a sequence of Laue x-ray patterns observed in real-time during various stages of tensile strain. In Figs. 8.0 through 8.26 lattice rotation first occurs, which is evidenced by the formation of two ellipses of Laue spots which reach approximately the same size. Lattice rotation approximately ceases from Fig. 8.26 and gross plastic deformation occurs which is illustrated by increased asterism in the individual Laue spots.

In a relatively simple design and a system extremely easy to use, Green(12) developed a method which permits absolute measurement of grain boundary positions at temperature as well as being able to observe in situ fast moving boundaries. The basic components of the system as shown in Fig. 9 are as follows. A continuous spectrum x-ray beam which is slit collimated is incident along the entire length of the test specimen. This beam is interrupted by a wire grid just prior to impingement on the test specimen. The sample is supported vertically in a furnace maintained at the temperature required for grain boundary migration. The various diffracted x-ray beams pass out of the furnace into the image x-ray intensifier system. Figure 10 illustrates a sequence of x-ray diffraction Laue patterns as a function of time in the furnace. Each of these line segments is interrupted at regular intervals as a results of the fiducial screen placed in the incident x-ray beam. When the grain boundary moves the set of line segments decreases in length as shown. A similar configuration could also be designed to study solidification behavior by monitoring liquid-solid interfaces in various materials systems. For example, the solid region will produce a defined x-ray pattern whereby the liquid or amorphous region will not produce a defined x-ray pattern.

For special cases involving very rapid events, flash x-ray systems have been designed incorporating image x-ray intensifiers. Green (13), (14) developed a flash x-ray system which enabled x-ray diffraction patterns to be recorded from shaped charge jets. The system illustrated in Fig. 11 consists of a 150 kV flash x-ray generator and an electro-optical system incorporating an image intensifier tube as a detector. In Fig. 12 is shown a transmission flash x-ray diffraction pattern of an aluminum shaped charge jet obtained with a single 150 kV x-ray pulse of 70 ns duration. Analysis of the pattern indicated that the jet consisted of a particulate solid, with a grain-sized distribution ranging from about 1 mm to about 0.01 mm. The diameter of the outer ring of the diffraction pattern agreed with the theoretical calculation of the diameter of the (200) diffraction ring for an aluminum powder irradiated by MoKα x-rays.

III. IMAGE X-RAY INTENSIFIER CHARACTERISTICS

With all these techniques, image x-ray intensifier devices play a major role in allowing fast changing events to be recorded. An excellent review of the various electro-optical systems for dynamic display of x-ray diffraction images was presented by Green in 1971 (15). In Fig. 13 is a three stage portable image x-ray intensifier (PIXI) with a 40 mm input x-ray window, unity magnification, 100 um spatial resolution and gains of the order of 240,000. Physical dimensions are 31 cm x 9.5 cm dia. and weighs 2.2 Kg. In Fig. 14 is a microchannel plate (MCP) inverter tube miniature image x-ray (MINIX) intensifier with a 50 mm input window, 40 mm output viewing window, 100 um spatial resolution and gains of the order of 40,000. Physical dimensions are L-11cm x W-9cm x D-8 cm and it weighs 0.9 Kg. In some experimental or production arrangements where size is a limitation this unit can be used.

IV. CONCLUSIONS

Real-time x-ray diffraction experiments with the incorporation of image x-ray intensification have been shown to add a new dimension in the characterization of materials. The uses of real-time image intensification in laboratory and production arrangements are quite unlimited and their application depends more upon the ingenuity of the scientist or engineer.

V. ACKNOWLEDGEMENTS

Funding for part of this work has come from Brimrose Corporation of America. The author would also like to especially thank Professor Robert E. Green, Jr. from the Johns Hopkins University whose systems he has discussed and for supplying both technical information and copies of original figures.

VI. REFERENCES

(1) R.G. Rosemeier and R.E. Green, Jr., "A New Miniature Microchannel Plate X-ray Detector for Synchrotron Radiation," Nuclear Instruments and Methods, 195, (1982) p. 299.

(2) R.G. Rosemeier, "Real-Time X-ray Topography: Applications to Bulk HgCdTe Materials," (1983) to be published in the Journal of Vacuum Science and Technology.

(3) R.G. Rosemeier, R.W. Armstrong, S.M. Johnson, G.M. Storti, and C.Cm.Wu, "Polycrystalline X-ray Topography and Photoresponse of Grains or Grain Boundaries in Polysilicon," 15th IEEE Photovoltaic Specialists Conf., (1981) p. 1331.

4. S.M. Johnson, R. W. Armstrong, S.M. Johnson, G.M. Storti, H.C. Lin, and W.F. Regnault, "An Enhanced Photoresponse at Dislocation Subgrain Boundaries Revealed by X-ray Topography of Polysilicon Solar Cells," Grain Boundaries in Semiconductors, Eds,. C.H. Seager, G.E. Pike, and H.J. Leamy, (N.Y., North Holland) (1981) p. 179.
5. R.G. Rosemeier, K.C. Yoo, and S.M. Johnson, "Polycrystal X-ray Topography (PXT) of a Silicon Solar Cell," Materials Letters, 1 (5,6) (1983) p.194
6. G.H. Schwuttke and V.Sils, "X-ray Analysis os Stacking Fault Structures in Epitaxially Grown Silicon", J. Applied Physics, 34 (1963) p. 3127.
7. R.G. Rosemeier, R.E. Green, Jr.,and R.H. Baughman, "Asymmetric Crystal Topography of Macroscopic Diacetylene and Polydiacetylene Single Crystals," J. Applied Physics, 52, (12), (1981) p. 7129
8. R.G. Rosemeier, "ACT, Berg-Barrett and Lang X-ray Topographic Methods," University of Maryland, Electron Microscope Central Facility Newsletter, Issue 8 (1981) p. 9
9. Material provided by Semix, Inc., Gaithersburg, MD
10. N.R. Joshi and R.E. Green, Jr., "Continuous X-ray Diffraction Measurement of Lattice Rotation During Tensile Deformation of Aluminum Crystals," J. Materials Science, 15 (1980) p. 729
11. K. Reifsnider and R.E Green, Jr., "Dynamic X-ray Diffraction Study of the Deformation of Aluminum Crystals," Transactions of the Metallurgical Society of AIME, 245 (1969) p. 1615
12. R.E. Green, Jr., "An Electro-Optical X-ray Diffraction System for Grain Grain Boundary Migration Measurements at Temperature," Advances in X-ray Analysis, 15 (1972) p. 435
13. R.E. Green, Jr., "First X-ray Diffraction Photograph of a Shaped Charge Jet," Rev. Sci. Instrum., 46, 9 (1975) p. 1257
14. J.A. Dantzig and R.E. Green, Jr., "Flash X-ray Diffraction Systems," Advances in X-ray Analysis, 16 (1973) p. 229
15. R.E. Green, Jr., "Electro-Optical Systems for Dynamic Display of X-ray Diffraction Images," Advances in X-ray Analysis, 14, (1971) p. 311

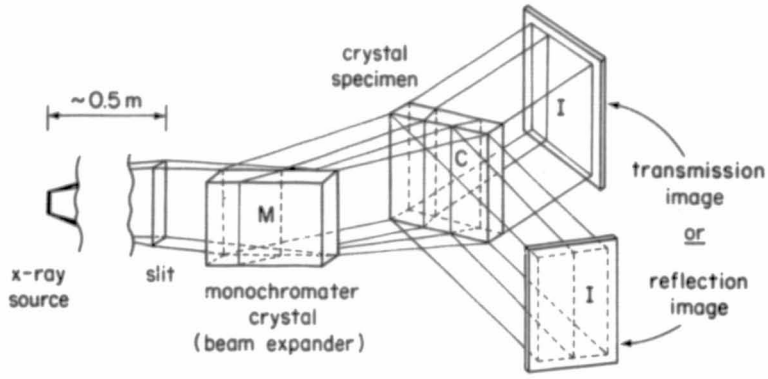

Fig. 1 Schematic of the Double Crystal Asymmetric Crystal Topography (ACT) System Illustrated in Both the Surface Reflection and the Transmission Mode. Ref. (2)

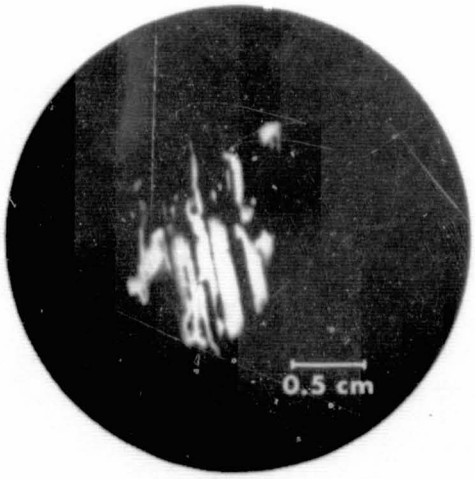

Fig. 2 A Real-Time (220) ACT Surface Topograph of an Individual Grain Within a Cast Polysilicon Semix Wafer. Ref. (1)

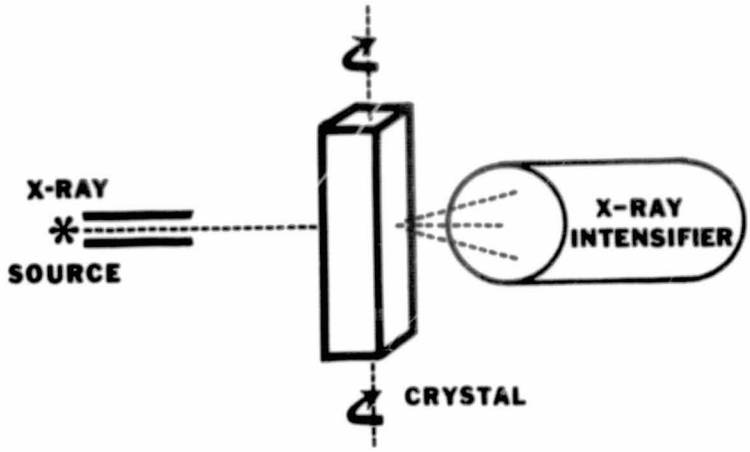

Fig. 3 Illustration of a Real-Time X-ray Laue Transmission Arrangement.

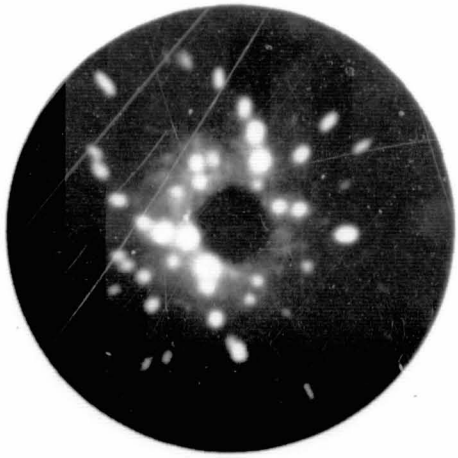

Fig. 4 Real-Time Laue Pattern of a Sapphire Single Crystal Illustrating the Two-Fold Symmetry.

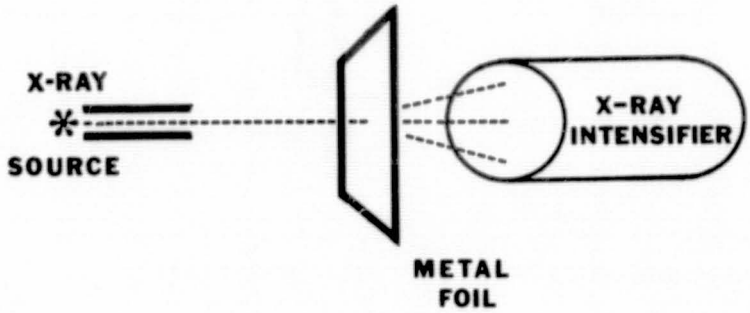

Fig. 5 Experimental Arrangement for Observing Real-Time X-ray Images From Fine Polycrystalline Materials.

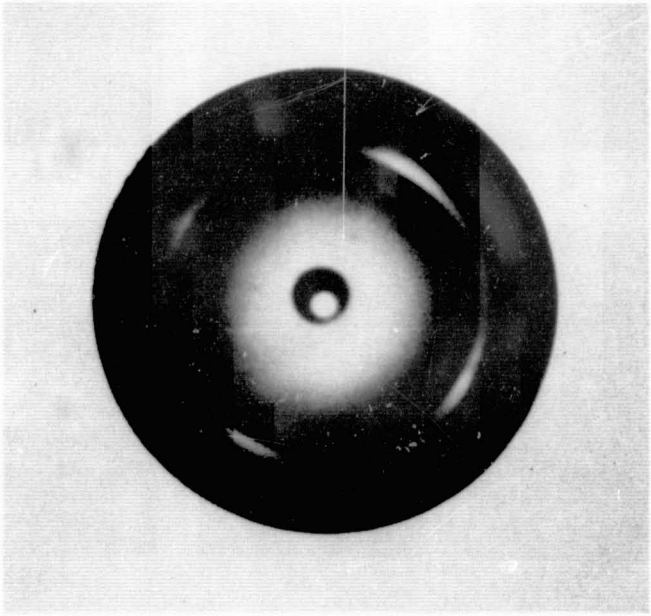

Fig. 6 Real-Time Photograph of X-ray Debye-Scherrer Transmission Pattern from a Rolled Brass Foil. Ref. (1)

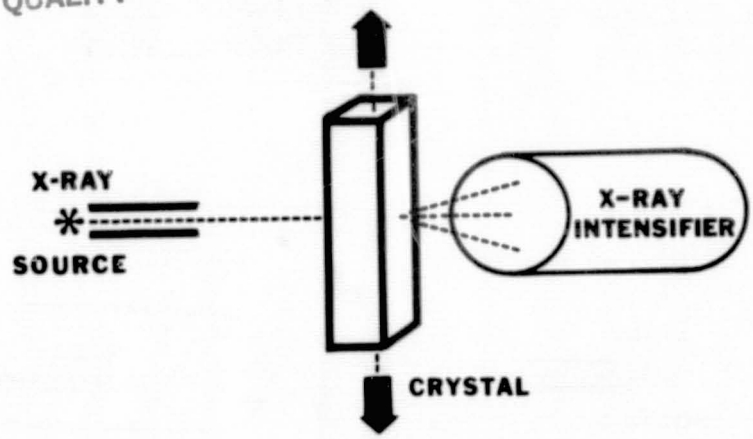

Fig. 7 Schematic of an In Situ Experimental Arrangement to Observe Deformation of Single Crystal Materials.

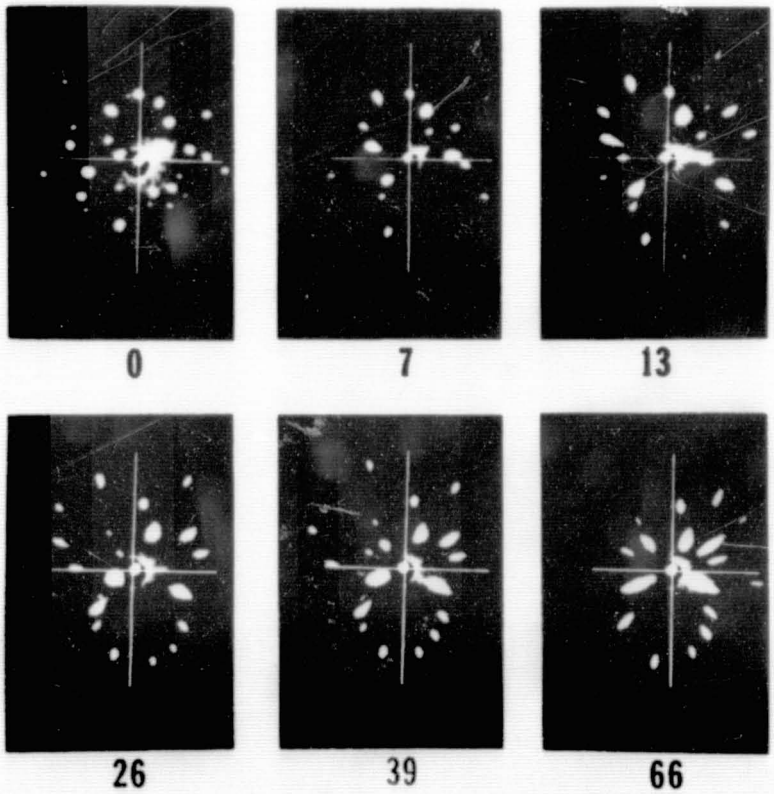

Fig. 8 Laue X-ray Transmission Motion Picture Frames at Various Stages of Tensile Strain as Labelled. Ref. (10)

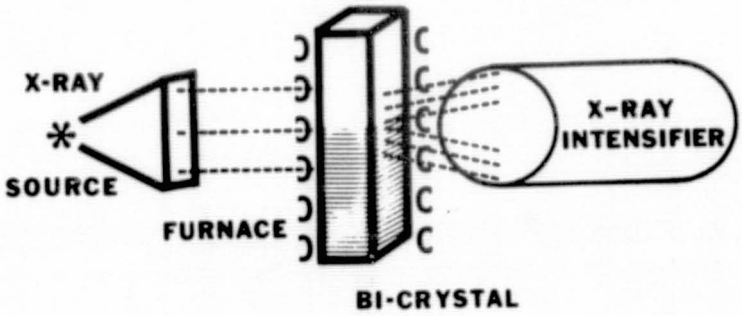

Fig. 9 "Experimental Configuration of In Situ Grain Boundary Migration Experiment"

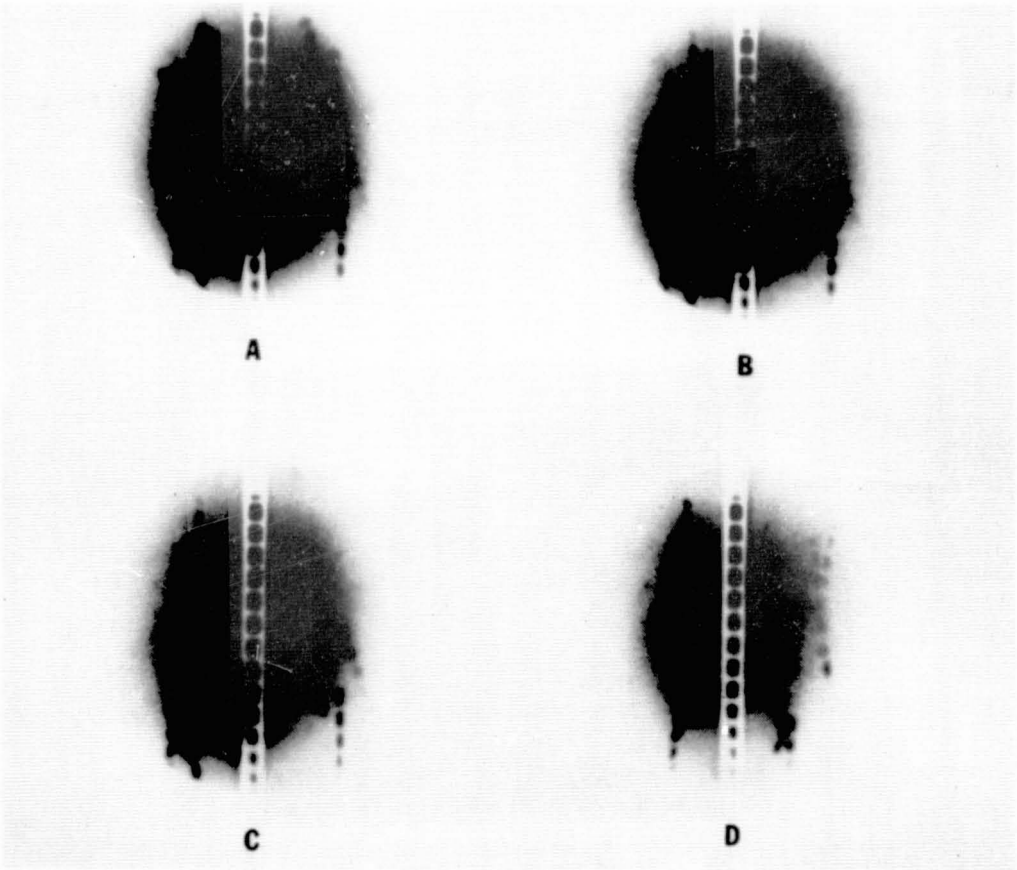

Fig. 10 Real-Time X-ray Laue Transmission Pictures Taken at Various Stages of Grain Boundary Migration. Ref. (12)

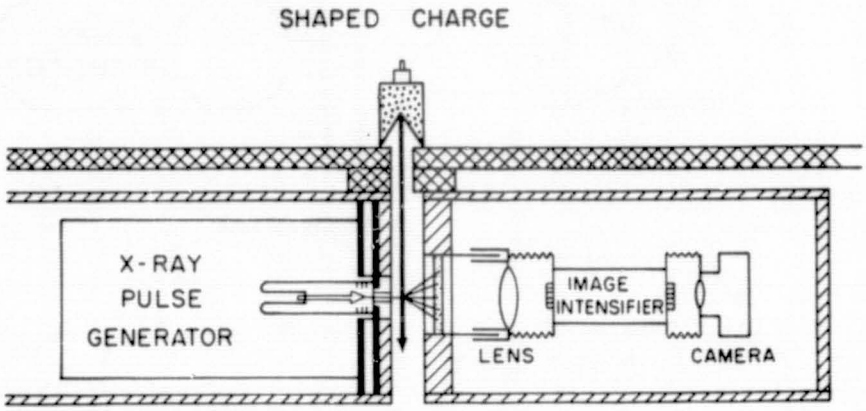

Fig. 11 Schematic Flash X-ray System For Recording X-ray Diffraction Patterns From Shaped Charge Jets. Ref. (13)

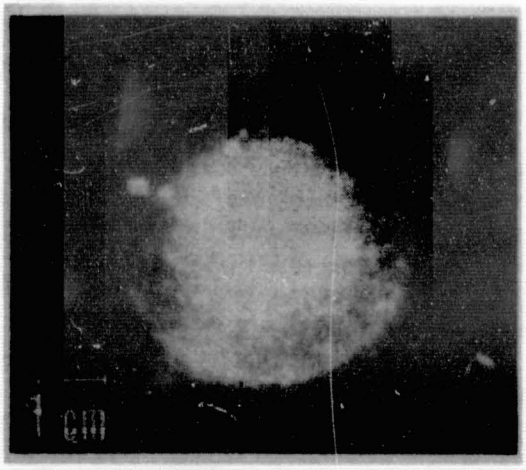

Fig. 12 X-ray Diffraction Pattern of Aluminum Shaped Charge Jet. Ref. (13)

Fig. 13 Three-Stage Portable Image X-ray Intensifier (PIXI). Ref. (1)

Fig. 14 A Micro-Channel Plate Miniature Image X-ray (MINIX) Intensifier. Ref. (1)

DISCUSSION

CISZEK: How easy is it to see individual dislocations, if you were trying to observe a diffraction topography image?

ROSEMEIER: There are tradeoffs between film and using real-time X-ray image intensification. First of all, image intensification is not meant to be used as a quantitative tool for assessing dislocation densities in a material. It is mostly used in laboratory arrangements for doing alignments of diffraction images. We have had some instances where we were able to look at mercury cadmium telluride materials and use it as a screening operation as the first step in a production assembly. We take the material and pick a random orientation, and then look at a substructure. If it is poor, you get rid of it. If it is good, then you put it along the step of the production line and use more sophisticated techniques. Basically, it is an alignment tool, up to this time.

MILSTEIN: In 1978, at the first European Crystal Growth Conference, Ruxneller from Phillips showed some work he had done on X-ray diffraction processes on LEC-encapsulated gallium arsenide indium phosphide in the furnace. He observed, using that technique, the loss of zero D structure with widening the crystal. The technique is even doable under those conditions. He took great pains to look for the fiber he was looking for.

MAYO: My question is probably a follow-up on your comment. One of the points that has come up in this discussion the last few days is that people would like to study the melt-solid interface in real time. Do you feel that real-time topography perhaps can be combined with synchrotron radiation? It might offer advantages over optical techniques. Granted, logistics would be horrendous, but are the advantages worthwhile?

ROSEMEIER: I agree. For example, if you were interested in setting up some type of experimental arrangements, you would probably want to use initially some low-melting-temperature materials. At the Brookhaven Synchrotron Facility, Dr. John Bellelo is setting up a dedicated X-ray synchrotron topography facility, where experiments are going to be done where he will be able to observe dislocation movements in materials in real time. One of the things that make that possible is, we have a very intense X-ray source to look at. As a result, you will be able to use film quicker and at the same time develop improved imaging systems.

AST: Chikawa has used X-ray diffraction techniques to look at the solid-liquid interface in silicon and has seen the incorporation of liquid droplets, and I think a group in Stuttgart also has an X-ray topography system that they apply to crystal growth. These are both rotating-anode machines.

ROSEMEIER: The first fellow to do X-ray time diffraction was Bob Green from Johns Hopkins University. He was working with RCA at that time. Chikawa came over to the United States and he stayed a week with Bob Green going through RCA. Five years later they built a topography system where they

they are able to look at individual dislocations in material. They are setting up arrangements to quality control electronic material before it goes into the expense of processing arrangements.

SESSION VIII: INGOT GROWTH AND CHARACTERIZATION

R. Lane, Chairman

PRECEDING PAGE BLANK NOT FILMED

LANE: We are getting into the ingot growth section now, and I thought just to help us get into the mood, I would show you this picture. This is Czochralski's apparatus. Although the apparatus is perhaps a little archaic to us, his concept was very interesting, and quite appropriate to what we are trying to do here. He had molten metal in a graphite crucible and dipped a glass rod into the metal. He used lead or tin or something like that, and he rubbed the glass rod on some metal, to try to get the glass rod to stick to the metal, and then he began to pull. He learned that he could pull a thin filament of metal up, and then he could lower the temperature and pull faster and faster. So he learned a lot of the basic principles of Czochralski growth in this experiment. But I think the interesting thing, which is very appropriate to this conference, is that Czochralski was trying to measure the maximum growth rate of metals. He was not interested in growing single crystals. So I am not sure why we call it the Czochralski method, except that certainly he was aware of the several important principles in pulling, and that is probably why some people insist on calling it the Teal-Little method, because Teal and Little were the ones who rotated the crucible, and rotated the seed, and so forth.

PRECEDING PAGE BLANK NOT FILMED

N84 28645

X-RAY TOPOGRAPHIC METHODS AND APPLICATION TO ANALYSIS OF ELECTRONIC MATERIALS

William E. Mayo, Hung Y. Liu and Jharna Chaudhuri
Rutgers University
Piscataway, New Jersey 08854

ABSTRACT

X-ray topographic methods have proven to be of great use in characterizing microelectronic materials. The Lang and Berg-Barrett techniques have long been used for visualizing gross structural defects such as twins and misfit dislocations. As a result, these methods are routinely applied to the study of growth induced defects in electronic materials prepared by a variety of methods.These techniques, although useful, yield an incomplete description since they provide no information about the overall stress state in the material. To this end, three supplementary x-ray techniques new to semiconductor applications will be discussed. These are the Computer Aided Rocking Curve Analyzer, the Divergent Beam Method and a new method based on enhanced x-ray flourescence. The first method is used for quantitative mapping of an elastic or plastic strain field while the other two methods are used only to measure elastic strains. The divergent beam method is used for measuring the full strain tensor while the microfluorescence method is useful for monitoring strain uniformity. These methods will be discussed in detail and examples of their application will be presented. Among these are determination of the full strain ellipsoid in state-of-the-art LPE deposited III-V epitaxial films; mapping of the plastic strain concentrations in tensile deformed Si; and quantitative determination of damage in V_3Si due to ion implantation.

INTRODUCTION

X-ray topographic methods have long been used as a nondestructive tool for relatively low resolution examination for crystal perfection. It has proven to be suitable for characterizing and mapping lattice defects in crystalline materials, and is most useful when the defect concentration is low. Quite often topography is used to supplement information obtained by other methods which have inherently higher resolution such as transmission electron microscopy. It should be emphasized at the outset that x-ray topography should not be considered to be in competition with TEM, but rather complements it. X-ray topography is useful for examining large sample areas with poor resolution while TEM can examine only very small areas with high resolution. Thus the two techniques provide complementary information.

The earliest topographic methods dealt principally with imaging of

gross structural defect structures. The most popular were Lang's method, the Berg-Barrett method and the Double Crystal technique. The characteristic feature which distinguishes these methods is their relative sensitivity. It is generally conceded that the Double Crystal method has the greatest sensitivity and the Berg-Barrett method the least. Moreover, the types of samples which can be examined by each method varies considerably. The Lang and Double Crystal methods require nearly perfect crystals while the Berg-Barrett technique is often utilized in reflection to examine samples with high defect concentrations (e.g.- deformed metals).

Recently, many new topographic methods have been introduced for specific applications. These include the anomalous transmission geometry (1), the x-ray Moiré method (2), the x-ray interferometer (3) and the asymmetric crystal topographic method (4) among others. It is not the purpose of this paper to review these conventional x-ray topographic methods. There are several excellent reviews in the literature (5-7) and the interested reader should consult these. In addition, an excellent text by Tanner (8) discusses these and other methods in some depth along with several applications of topography, particularly in the area of electronic materials.

While the conventional x-ray topographic methods are useful for visualizing various types of defect structures and determining crystallographic orientations, they do not provide a complete picture. Much more information, particularly quantitative information, is available than is presently generated via topographic analyses. For example, it would be desirable to be able to determine completely the strain state and equally important, the uniformity of the strain.

In this paper, three unconventional x-ray techniques will be explored which apply topographic concepts to the quantitative determination of the strain state in single crystals. Of utmost interest are the description of the complete strain state including the determination of theelastic strain tensor and the magnitude and distribution of the plastic deformation. With these three techniques, very complex strain states can be examined, including three dimensional mapping. Thus, such problems as strain localization around internal defects can be analyzed.

The most versatile of these three methods is the Computer Aided Rocking Curve Analyzer (CARCA) which is based on the double crystal (+n,-n) arrangement. The rocking curve is a sensitive measure of the lattice misalignment induced by deformation. Thus by measuring the rocking curves on a point by point basis, a complete map of the deformation can be deduced. To facilitate this process, a Position Sensitive Detector (PSD) with interactive computer control has been incorporated. This method is extremely rapid and provides a deformation map with 50 μm resolution. By controlled etching (or alternatively using a more penetrating radiation), the deformation map can be extended into a full three dimensional map. This is a significant advantage over the conventional topographic methods which provide only a two dimensional projection of the plastic strain field.

The second method to be presented complements the CARCA method by providing a map of the elastic strain field. This method is based on enhanced anomalous transmission by a bent crystal. The experimental arrangement is

identical to the Lang arrangement, but the quantitative analysis utilizes x-ray microflourescence technique on the topograph in a scanning electron microscope. Such a method is useful for two dimensional mapping of elastic strain uniformity and is particularly well suited for examination of the effect of stress concentrators.

The final method to be discussed is an old technique which has only recently been applied to electronic materials. The Divergent Beam method has a history dating back to approximately 1915 and was used primarily for precision lattice parameter measurements (9). However, interest in these studies waned during the period 1950-1970 due to the stringent requirements that single crystals of nearly perfect materials be used. Around 1970, Ewing and Smith (10) and Glass and co-workers (11,12) revived the method for studies on semiconductor materials. Such materilas are ideally suited for analysis by the divergent beam method owing to their high perfection and small elastic strains. Schutz et al. (13-15) extended the method to study the role that surface layers damaged by ion implantation had on the depression of the superconducting transition temperature of V_3Si. In the present work, the divergent beam has been used to study the strain in thin epitaxial films of III-V semiconductors deposited by liquid phase epitaxy. Simultaneously, the strain in the underlying substrate is also determined, thus providing a complete description.

Details of all three methods will be presented and appropriate examples of their applications will be offered. Potential applications will also be included, particularly as they relate to studies of electronic materials.

COMPUTER AIDED ROCKING CURVE ANALYZER

The Computer Aided Rocking Curve Analyzer (CARCA) is a powerful tool for quantitatively analyzing plastic deformation in a crystal. Two arrangements have been constructed, one for polycrystalline materials (16,17), the other for single crystal studies (18). Only the single crystal method will be discussed here.

The method is based on the double crystal diffractometer in the (+n,-n) antiparallel arrangement. A monochromatic beam is produced by reflection from a (111) oriented Si crystal. After the K α_2 component is removed by the use of a long collimator and slit system, the highly monochromatic beam impinges on the test crystal. The test crystal is then rotated (or rocked) through its reflecting range and its intensity versus angular position is recorded. The rocking curve thus obtained is highly sensitive to the perfection of the lattice producing it as shown schematically in Figure I. A relatively perfect region produces a sharp reflection with a narrow reflecting range indicated by a small β value (total width at half maximum intensity). As plastic deformation proceeds, an excess number of dislocations of one sign are produced. If these are uniformly distributed, the rocking curve is broadened; but if the excess dislocations are non-uniformly distributed a multipeaked rocking curve is produced. If the rocking curves can be determined on a point-to-point basis, for example by use of a microbeam combined with movement of the sample, a complete deformation map can be obtained. A more practical solution to the problem however, is shown in Figure II. Instead of using a microbeam, a large area of the specimen is irradiated by a parallal line source and advantage is

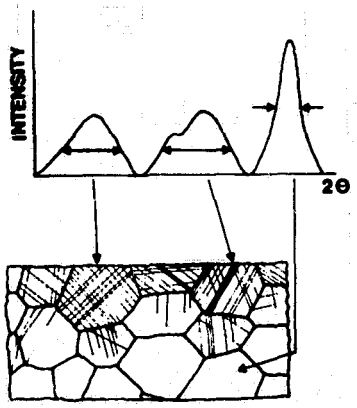

Figure I

Relationship between rocking curve halfwidth, β, and distribution of excess dislocations.

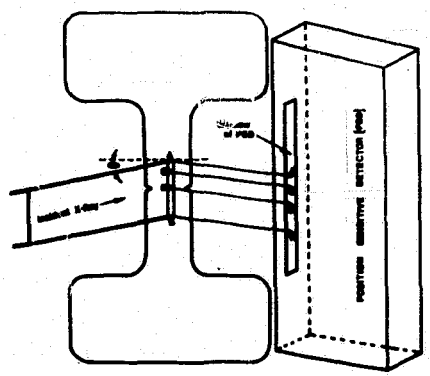

Figure II

Operating principle of the Computer Aided Rocking Curve Analyzer.

taken of the fact that the diffracted beam line is a true topographic image. Accrodingly, there is a one-to-one correspondence between the position in the diffracted beam and the spot on the sample giving rise to it. This reflected beam is then registered by a linear position sensitive detector (PSD) placed tangent to the Debye arc and parallel to the rotation axis of the sample. When combined with a multichannel analyzer (MCA), the diffracted beam can be broken into 60 μm increments. Thus, as shown in Figure II, the diffracted beam A' originates from point A on the sample, and similarly for pairs BB',CC',etc.. By step-rotations of the specimen, rocking curves are generated simultaneously and independently for each 60 μm segment of the sample. When the rocking curve analysis has been completed, the sample is step-wise translated so that adjacent regions can be similarly analyzed. In this way, a complete two dimensional map can be readily generated in a few hours. A schematic drawing of the system is shown in Figure III.

Extensive studies of deformation of Si have been undertaken with the overall objective of critically comparing the experimentally determined deformation map to that predicted by continuum mechanics. This is part of a larger program to study long-range elastic and plastic strains emanating from stress raisers and examining the interactions between multiple sources. One of the aims of this study is to determine the effect of elastic constraints on the formation of plastic zones.

In all of these studies (18,19), Si has been chosen as a model material since a.) Si can be readily obtained in large, essentailly dislocation free crystals; b.) can be plastically deformed above 650°C; and c.) the dislocation substructure formed during deformation is frozen when the specimen is cooled. Prior to testing the 0.03 ± 0.003 Ωcm samples were dislocation free as determined by Pendellösung and Lang projection topography. The tensile axis was chosen parallel to $(0\bar{1}\bar{1})$ and hyperbolic notches were introduced by electro-

ORIGINAL PAGE IS
OF POOR QUALITY

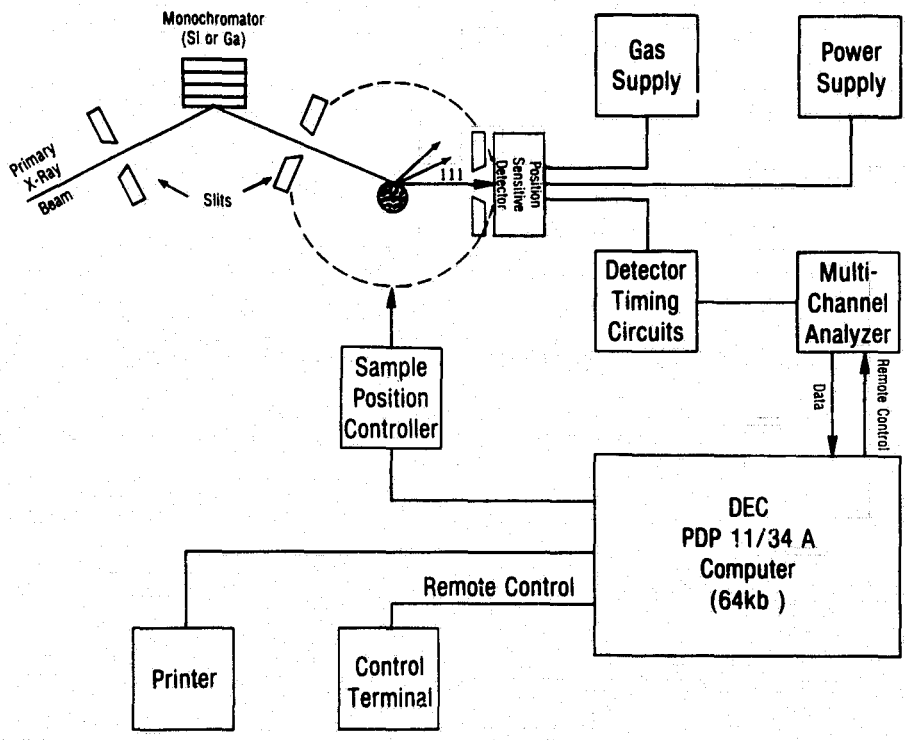

Figure III
Schematic diagram of the Computer Aided Rocking Curve Analyzer

spark cutting followed by chemical etching to remove any mechanical damage.

Regions more than 3-4 mm above or below the notch were essentially free of plastic deformation. However, large elastic strains were noted as evidenced by a shift in the Bragg angle on either side of the notch. As shown in Figure IV, the deformation in a single notched specimen is confined to a narrow band perpendicular to the tensile axis. The contour map shown in this Figure is constructed by determining regions of equivalent lattice misalignment. Note that the map generated by the CARCA method contains substantially greater detail than the conventional reflection topograph of the same region. Moreover, the computer generated map is capable of distinguishing easily between elastic and plastic deformation; information which is usually lost in topographs unless great care is taken.

Similar contour maps for a double notched specimen are shown in Figure V. Although the individual β contours could be determined to an accuracy of seconds of arc, this Figure is shown with a vary course increment for the sake of clarity. The shape of the plastic zone in the double notch specimen strained to 1.04% is similar to that for the single notch, but the interaction between the two notches is evident. This is apperent in samples strained at smaller

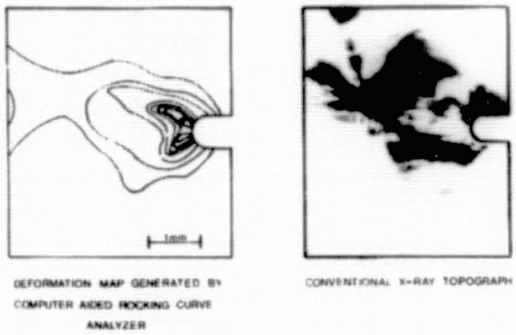

Figure IV

Contour map of plastic deformation concentration at a notch.

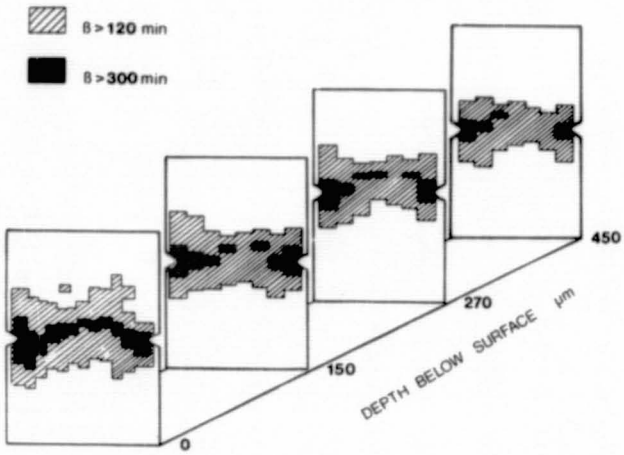

Figure V

Depth profile of deformation in a double notched specimen (ε= 1.04%)

value of 0.83% (not shown). An interesting result is seen when the deformed sample is examined through the thickness. By etching away successive layers of approximately 150 μm, the full 3 dimensional plastic deformation map is obtained. It will be seen that the severity as well as the extent of the plastic deformation decreased with distance below the surface. This is a surprising result since it is generally assumed that thin specimens (0.75-1.00 mm) undergoing tensile deformation will have a uniform strain distribution. But is it clear from the present results that such is not the case.

The Computer Aided Rocking Curve Analyzer was an invaluable tool in the studies of plastic deformation described above. The method has an excellent sensitivity ($\Delta\beta \simeq 10''$) and is extremely rapid. It can be used for the quantitative deformation gradient mapping just described and is also capable of isolating regions of intense deformation. This latter function would be useful for indicating those regions for additional analysis, perhaps by TEM.

DETERMINATION OF ELASTIC STRAIN CONCENTRATION BY ENHANCED X-RAY MICROFLOURESCENCE METHOD

It is well known (20,21) that the diffracted intensity from a perfect crystal is dependent on the degree of elastic bending. In a rigorous treatment of the dynamical theory, Kalman and Weissmann (22) have shown that the diffracted intensity is linearly related to the radius of curvature due to simple bending over a very wide range. In a very recent paper (23), they were able to extend their analysis to include the full range of possible curvatures which indicated a departure from linearity only for the most strongly bent crystals. In such cases, anomalous absorption of the propagating wave field within the Borrmann fan must be taken into account in order to fully explain the observed intensities. Thus, measurements of the observed intensities offer a quantitative method of measuring elastic bending in nearly perfect crystals.

In a series of papers (22-24), this method was applied to determine the strain concentration factors around holes and inclusions. This mapping capability was achieved by analyzing a conventional Lang projection topograph in a novel way. Since the image is a true topographic projection, the determination of the intensity at any point on the photographic plate will immediately give the local radius of curvatureat the corresponding point in the sample. However, the problem of intensity measurement on the nuclear track plate is formidible since the optical opacity is not linearly related to the incident photon density. Instead, Kalman and coworkers developed a method based on the principle that the amount of precipitated silver in the developed emulsion is proportional to the photon flux. Then by measuring the local silver density, the desired intensity measurements are obtained. For this purpose, a scanning electron microscope and its associated energy dispersive analyzer were utilized to carry out the x-ray denitometry measurements. The spatial resolution of the method is of the order of less than 10 μm, making it one of the most sensitive x-ray techniques. It was also found that the microflourescence could be greatly enhanced if the topograph were first coated with a metal deposit (Cu is favored). This increased the fluorescence of the Ag Lα and greatly increased the microfluorescence yield.

The method has been successfully applied to the study of elastically bent Si. As in the previous study, Si was chosen as a model material and a number of sample configurations were examined. These included an elliptical hole, a circular hole and a double notched specimen subjected to out-of-plane bending. Samples were elastically bent a prescribed amount, after which the x-ray topographs were prepared in situ.

An example of the results obtained with this method are shown in Figure VI

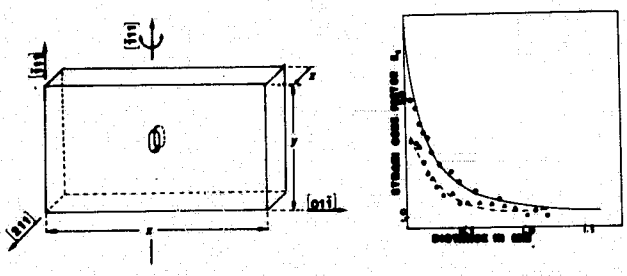

Figure VI

Comparison of experimentally measured strain concentrations with theory . (o= circular hole ; Δ= circular hole filled with amalgam).

for the case of a circular hole. Two sets of curves are shown; one plots the

strain concentration factor for the hole itself as a function of distance from the bending axis; the second curve plots the concentration factor for the hole filled with dental amalgam. The latter case was chosen to represent an inclusion problem. Also shown in the Figure are the results of numerical calculations based on a closed form solution of the problem (24). Note the excellent agreement between the theroy and the experimentally determined values. It is interesting to note also that the strain concentration is reduced in the presence of the inclusion, presumably due to the fact that the second phase carrys part of the load and thus reduces the strain concentration.(24).

It is clear that the x-ray microfluorescence technique is an important quantitative tool for mapping of nonuniform elastic strains and will be invaluable for the studies continuing in the area of stress concentrators.

DIVERGENT BEAM METHOD

The divergent beam x-ray technique has been used extensively for high precission measurement of lattice parameters in nearly perfect single crystals including semiconductor materials (9). Although this method may be utilized in either a transmission or back reflection mode, the former is used only when the sample is thin ($\mu t < 10$). Since most crystals do not satisfy this condition only the back reflection method is appropriate. The experimental arrangement for the back reflection divergent beam method is shown schematically in Figure VII:

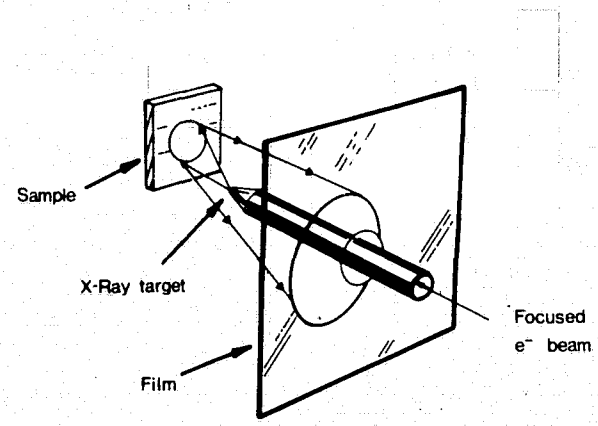

Figure VII

Schematic drawing of the Divergent Beam Method

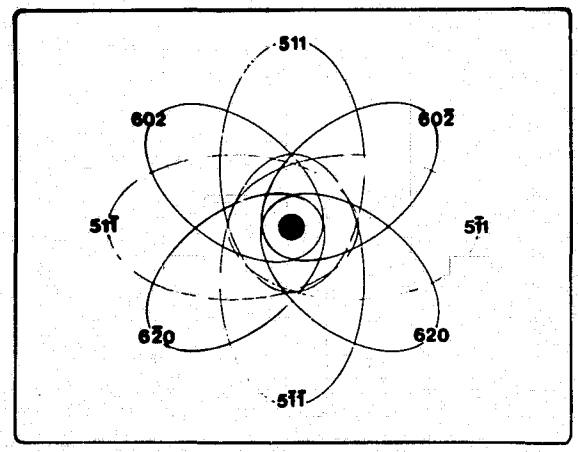

Figure VIII

Schematic drawing of diffracting conics in the DB method

A focused electron beam of approximately 20 microns diametr impinges upon the tip of a thin metal target acting as a vacuum seal for the electron gun. The resulting x-ray beam consists of both white and characteristic radiation, but with a suitable choice of accelerating voltage, the charcteristic radiation can be made to dominate. A unique feature of the method is that the x-ray beam generated in this way has a divergence of nearly 180 degrees as shown in the

Figure. Each diffracting plane in the crystal chooses an incident x-ray beam which uniquely satisfies Bragg's law for that plane resulting in a diffracting conic. Each set of reflecting planes thus results in a unique conic as shown in Figure VIII. Indexing of these conics is achieved by suitable matching of the observed pattern to a computed pattern based upon the known crystal orientation and the measured distance between the crystal surface and the x-ray source.

In order to determine the d spacing for each set of (hkl) planes, the multiple exposure method of Ellis et al (25) is employed and is shown schematically in Figure IX. In this method, the x-ray film is first placed at an arbitrary

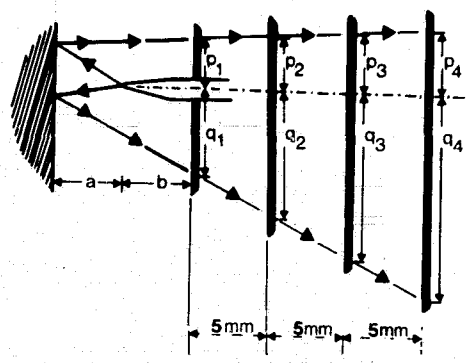

Figure IX

Schematic drawing of the multiple exposure method of Ellis et al. (25).

distance from the sample and then exposed, yielding a pattern similar to Figure VIII. A second exposure is then taken after the film has been shifted by a known amount (usually 5.000 mm) This process is then repeated several times before the film is developed for the strain analysis.

The divergent beam method provides a means of determining the strain for each reflecting plane in a deformed crystal. Thus a single experiment provides strain information for a large number of planes and makes possible a complete analysis of the overall strain state. Imura et al.(26) have consided the calculation of the full strain tensor from the individual strains of 6 or more planes. Their analysis requires a minimum of 6 planes whose normal vectors do not form two subsets of three mutually orthogonal vectors. This restriction is necessary since the resultant matrix equation contains no unique solution for such non-independent vectors. To avoid this problem, and to minimize errors, it is necessary to use more than six reflecting planes and their corresponding strain values from which a least squares fit to the strain tensor is obtained. Once the full strain tensor is obtained, it is then a simple matter to determine the principal strains and their directions by conventional means.

Under favorable conditions (sharp conics, multiple readings, etc.),accuracies of the order of 10-20 ppm are possible (26) for precision lattice parameter measurements and a sensitivity of 0.0002 for the elastic strain are obtainable.

A number of structures have been examined by the divergent beam method. All of these samples were based on III-V semiconductor devices formed either by vapor deposition or by liquid phase epitaxy. Among the samples investigated were:

a.) SiO_2 or SiN_x dielectric films on an InP substrate;
b.) SiO_2 or SiN_x dielectric films on an InGaAsP epitaxial layer deposited onto an InP substrate;
c.) InGaAs diodes with varying degrees of lattice mismatch with the substrate; and
d.) Be/Au diffused contacts on InP substrates.

Of particular interest was the dielectric films on the epi/substrate structure. This configuration has been investigated by other researchers utilizing a double crystal diffractometer, and it is instructive to compare the two set of experiments. The present results obtained with the divergent beam method indicates that the epi layer is in a state of nearly perfect plane strain in the plane of the film. This refers however, to the principal strains, and the actual strains in the conventional crystallographic set of axes is far more complex than that proposed by other investigators (27,28). Results of these previous studies concluded that in InGAAsP or InGaAs films that the strain state is a simple nearly balanced triaxial state oriented along the three (100) directions. This conclusion is based on their assumption that the shift in the Bragg angle for peaks of like form (for example (511) and ($\bar{5}$11)) is due to a simple tetragonal distortion. They assumw that there is no bending or other distortion which may lead to the generation of shear strains. This appears to be a particularly severe restriction, especially in light of the large body of work which clearly demonstrates the presence of bending strains (29-32). Indeed, the operating principle of the Automatic Bragg Angle Control (ABAC) relies on such a phenomenon (29,31). In addition, theoretical calculations of stresses produced by thin films support the view that shear stresses are present and in fact are quite large (33). Therefore, the simple model of Matsui et al. (28) and Kawamura et al. (27) appears to be an oversimplified view.

The results of the divergent beam investigation are summarized in Figure X where they are compared to the results obtained with a double crystal diffractometer. Note that in the present results the principal strains are nearly perfectly balanced plane strain in the plane of the film oriented along the {110} directions. The present results also found the substrate to be slightly deformed. This conflicts directly with the current model that the substrate is undeformed and that shear strains are negligible. (27,28). Clearly, the neglect of shear strains can have a profound influence on the description of the strain state.

Similar results were found in most of the other systems investigated. In general, the strain in the substrate and in the thin film could adequately be described by a state of plane strain in the plane of the film. Moreover, the direction of the maximum principal strain was always oriented in the {110} direction. Overall, the divergent beam method has been shown to be a powerful tool to monitor strains in thin films. Semiconductor materials such as the III-V family satisfy the stringent requirements of the DBM, namely, a single crystal

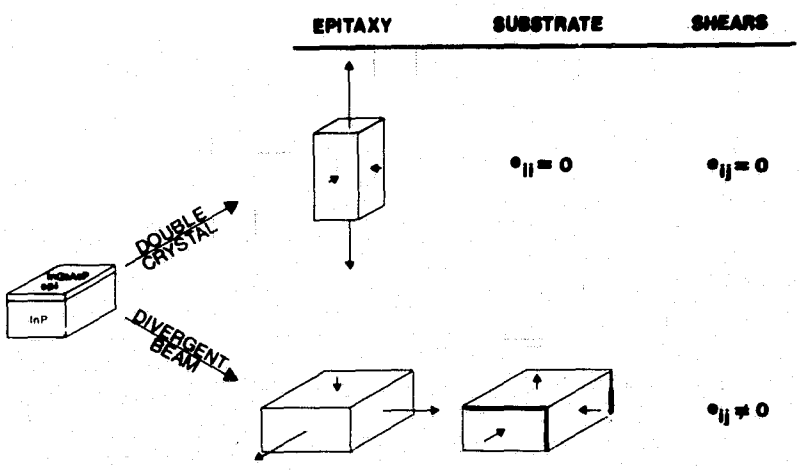

Figure X

Comparison of the strain measurements with the Divergent Beam Method and the Double Crystal Diffractometer.

which is nearly perfect with only elastic strains.

ACKNOWLEDGEMENTS

The deformation mapping and the development of CARCA were supported by the Division of Materials Research, Ceramics Program, Metallurgy, Polymer and Ceramics Section of the National Science Foundation under Grant No. DMR 81-04985. We are deeply grateful for their assistance. One of the authors (WEM) is also indebted to Bell Telephone Laboratories and Dr. Subash Mahajan for their support of the Divergent Beam work. Finally, the authors would like to acknowledge the careful guidance and attention of Prof. S. Weissmann during the course of these studies.

REFERENCES

1.) Roessler, B., Phys. Stat. Sol.,20(1967)713.
2.) Lang,A.R. and V.F.Muiscov,Appl.Phys.Lett.,7(1967)214.
3.) Bonse,U. and M.Hart,Appl.Phys.Lett.,7(1965)99.
4.) Rosemeier,R.G.,R.W.Armstrong,S.M.Johnson,G.M.storti and C.Cm.Wu, Trans. IEEE,(1981)1331.
5.) Bonse,U.,M.Hart and J.B.Newkirk,Adv.X-RayAnalysis,10(1967)1.

6.) Lang,A.R., in "Modern Diffractionand Imaging Techniques", ed. by Amelinckx et al.,North-Holland,(1970)407.
7.) Weissmann,S.,in "Nondestructive Evaluation of Materials", ed. by J.J. Burke and V.Weiss, Plenum,(1979)69.
8.) Tanner,B.K.,"X-Ray Diffraction Topography",Pergammon,(1976).
9.) Yakowitz,H., in "Advances in Electronics and Electron Physics",Academic, (1969)361.
10.) Ewing,R.E. and D.K.Smith,J.Appl.Phys.,39(1968)5943.
11.) Glass,H.L. and L.A.Moudy,J.Appl.Cryst.,7(1974)22.
12.) Glass,H.L.,P.J.Besser,T.C.Hamilton and R.L.Stermer,Mater.Res.Bull., 8(1973)309.
13.) Schutz,R.J.,L.R.Testardi and S.Weissmann,J.Appl.Phys.,52(1981)5501.
14.) Ibid,5496.
15.) Schutz,R.J.,PhD Thesis,Rutgers University,New Brunswick,N.J.,(1980).
16.) Mayo,W.E.,PhD Thesis,Rutger University,New Brunswick,N.J.,(1982).
17.) Yazici,R.,W.Mayo,T.Takemoto and S.Weissmann,J.Appl.Cryst.,16(1983)89.
18.) Liu,H.Y.,W.E.Mayo and S.Weissmann, Submitted to Mat.Sci.Eng.
19.) Liu,H.Y.,PhD Thesis,Rutgers University,New Brunswick,N.J.,(1982).
20.) White,E.G.,J.Appl.,Phys.,21(1950)855.
21.) Kato,N.,in "X-RAy Diffraction",ed. by L.V. Azaroff,McGraw Hill,(1974).
22.) Kalman,Z.H. and S.Weissmann,J.Appl.Cryst.,12(1979)209.
23.) Kalman,Z.H. and S.Weissmann,J.Appl.Cryst.,16(1983)295.
24.) Chaudhuri,J.,Z.H.Kalman,G.J.Weng and S.Weissmann,J.Appl.Cryst.,15(1982)423.
25.) Ellis,T.,L.F.Nanni,A.Shrier,S.Weissmann,G.E.Padawer and N.Hosokawa, J.Appl.Phys.,35(1965)3364.
26.) Imura,T.,S.Weissmann and J.J.Slade Jr.,Acta Cryst.,15(1962)786.
27.) Kawamura,Y. and H.Okamoto,J.Appl.Phys.,50(1979)4457.
28.) Matsui,J.,K.Onabe,T.Kamejima and I.Hayashi,J.Electrochem.Soc.,126(1979)664.
29.) Rozgonyi,G.A. and D.C. Miller,Thin Solid Films,31(1976)185.
30.) Wang,C.C. and S.H.McFarlane III,Thin Solid Films,31(1976)3.
31.) Rozgonyi,G.A. and T.J.Ciesielka,Rev.Sci.Inst.,44(1973)1053.
32.) vanMellaert,L. and G.H.Schwuttke,J.Appl.Phys.,43(1972)687.
33.) Serenbrinsky,J.H.,SolidStateElec.,13(1970)1435.

DISCUSSION

MILSTEIN: You described a very fascinating set of techniques. I don't know whether you or many other people in the room are familiar with both the superlattice concept that is being used by Gene Blakesley at SERI, which has the propensity to cause dislocations to roll over where the strain is between two rather thin layers, and more recently the strain layer superlattice, which is been proposed by the people at Sandia. In that case they are growing epitaxial layers, by MBE, of two materials that can have quite dissimilar lattice parameters. I wonder whether you would have any comments?

MAYO: In our own laboratory, Tom Tsakalakos is doing a lot of work on modulated structures where he is looking at 20 Å films of completely dissimilar materials, and actually, when they are 20 Å thick, they are basically dislocation-free. I don't know what happens in thicker structures. But, yes, we can measure elastic strains quite easily in these things, although when they come down to 20 Å thick you have a problem with intensity, from a practical point of view.

MILSTEIN: A quick comment on the strain layer superlattice is that you can grow these layers anywhere from about 16 Å to hundreds of Å and it might be interesting to look at the features that you see as a function of thickness, or something.

MAYO: Are you familiar with the term super-modulus effect? There is a tremendous enhancement in modulus when these films are of the order of 20 Å. In fact, a copper-palladium thin film has been made with an elastic modulus that is 50% higher than that of diamonds. You get up to 500% enhancement in the modulus and there are a number of extraordinary effects that occur when you have these ultra-thin layers and, yes, we are looking at them with some of these techniques. One of the reasons that these materials have these unusual anomalous properties is the fact that there is strain. The two materials have very different lattice parameters, but the energy of the dislocation is so high compared with the strain energy that the two lattices will exist in the strain state, and you get very unusual electronic behavior.

ROSEMEIER: Can you comment on the analysis times for your various quantitative measurements?

MAYO: The two-dimensional mapping can be done in the space of a day or two with a low-power X-ray machine. With the high-powered one, you could probably do this in a few hours.

FAN: Can you do a three-dimensional mapping of the elastic strains?

MAYO: No. Because, in order to get into the third dimension, we have two alternatives. One is, we can actuate the surface; the other one is, you can use a more penetrating radiation. However, when you etch down into the surface, you immediately remove any residual elastic strains. We have

no success there. The only alternative is to use a more penetrating radiation to look at the line shape that comes out and then, by a numerical number-crunching scheme, you can actually determine the elastic strain profile in the third dimension.

AST: In your double-notched silicon specimen, where you studied plastic strain around the notches, how was that thing actually deformed?

MAYO: It is raised to 800°C, and then it is simply tensiled to forms.

AST: Were they dislocation-free silicon?

MAYO: Yes. Initially it was a Cz-grown silicon and was lightly doped to improve electro-sparks.

AST: That probably explains, when you etched it down, why the strain was not homogeneous through the thickness: because you had to generate all the dislocations, probably at the surface, that had to slip in.

MAYO: I don't know. I think the fact is, the strain is generated at the notch, even well below the surface. You see the strain concentration around the notch, and I think that is the effect. We are talking about very high strain levels here.

AST: When you polish layer by layer, does it disappear in the midplanes to a certain degree?

MAYO: It didn't really disappear, but it is greatly reduced.

N84 28646

Maximization of Growth Rates During Czochralski Pulling

Michael J. Wargo

Massachusetts Institute of Technology
Cambridge, Massachusetts 02139

ABSTRACT

It has been suggested from theory[1-4] that silicon can be grown from the melt at rates far exceeding the current state of the art. Previous theoretical and experimental investigations which predict maximum rates of pulling during Czochralski growth are reviewed. Several experimental methods are proposed to modify the temperature distribution in a growing crystal to achieve higher rates of pulling. A physical model of a Czochralski crystal of germanium in contact with its melt has been used to quantitatively determine, by direct measurement of the axial temperature distribution in the solid, the increase in axial temperature gradients effected by an inverted conical heat reflector located above the melt and coaxially about the physical model. Preliminary results indicate that this is an effective method of increasing the thermal resistance between the hot melt and crucible wall and a growing crystal. Under these conditions the enhancement of the interfacial temperature gradients permit a commensurate increase in the rate of crystal pulling.

Introduction

It is well established that in order for photovoltaic energy conversion to compete successfully with other major sources of energy (eg. coal, hydroelectric, gas, oil etc.) a significant increase in the economy of solar electronic materials production must be achieved. One of many parallel approaches being pursued to achieve this goal is an ongoing effort to increase the throughput of bulk melt growth techniques, principally Czochralski crystal pulling. The primary focus is on growing larger diameter crystals at higher rates of pulling.

The conditions for maximized rate of crystal growth by the Czochralski technique have been given before.[5] Included are the assumptions of a flat crystal/melt interface and zero axial as well as radial temperature gradients in the melt at the solidification front. Under these circumstances the maximum rate of growth has been calculated to be[5]:

$$V_{max} = -\frac{k_S}{\rho_S \Delta H}\frac{dT}{dz} \qquad [1]$$

where k_S is the thermal conductivity of the solid at the melting point, ρ_S is the density of the solid, ΔH is the latent heat of solidification and the temperature gradient in the solid (dT/dz) is evaluated at the crystal/melt

interface. Eq. [1] shows that to increase the rate of pulling it is necessary to increase the axial temperature gradient in the solid.

Many investigators have formulated thermal models of Czochralski growth to determine theoretically the magnitude of the axial temperature gradient in a growing crystal. Their models commonly assume: 1) constant rate of pulling (but may be zero), 2) constant crystal diameter (cylindrical symmetry), 3) zero temperature gradients in the liquid, 4) a flat crystal/melt interface at temperature T_m, 5) temperature independent crystal properties (except, in some treatments, thermal conductivity), 6) one-dimensionality and 7) steady state heat transfer conditions. The various models differ in the assumptions made concerning the thermal boundary conditions to which the growing crystal is exposed.

A one-dimensional heat transfer model, in cylindrical coordinates, that describes the axial temperature distribution in a growing crystal has been developed by Rea[4,6]:

$$\frac{d}{dz}\left(k_s \frac{dT}{dz}\right) - V\rho_s c \left(\frac{dT}{dz}\right) - \frac{2h}{R}(T - T_a) - \frac{2}{R} q_R = 0 \qquad [2]$$

where T is the temperature of the solid at z, V is the rate of growth, c is the specific heat of the solid, h is the convective heat transfer coefficient, R is the crystal radius, T_a is the average furnace interior ambient temperature and q_R is the radiation heat flux from the solid at z. The first term in [2] is the heat transferred through the crystal by conduction. The second term accounts for the transfer of sensible heat due to the motion of the crystal. The third term describes the loss of heat from surface of the crystal by convection and the fourth term represents heat loss from the surface by radiation.

Rea[4,6] has solved [2] for the case of silicon growth using thermal boundary conditions that attempt to closely account for the thermal exchange between the surface of the growing crystal and the hot melt and crucible walls. His results suggest that the temperature gradient in the growing crystal, and thus the maximum rate of pulling, is strongly influenced by the temperatures, surface emittances and geometry of the crystal/melt/crucible system. For example, as the melt is depleted during the pulling of a long crystal, the crystal/melt interface drops well below the upper rim of the crucible exposing the growing crystal to heat exchange with the hot, high crucible walls. Such radiant heat transfer to the crystal leads to reduced estimates of pulling rates.

Billig[5] and Ciszek[3] (who corrected a minor error by Billig) neglected the second and third terms in [2] and assumed that radiation was lost to a black body ambient held at 0^oK. The emmisivity of the crystal was assumed to be temperature independent and the thermal conductivity was taken to have an inverse temperature dependence. Their closed form solution gave a square root dependence of the pulling rate on diameter which has been verified experimentally by Rea[6]. Their predicted maximum rates of pulling (for silicon) are a factor of two greater than those predicted by Rea.

Kuo and Wilcox[2] combined the radiative and convective components of the heat transfer (terms three and four in [2]) through use of an overall heat transfer coefficient as embodied in the Biot number, $H = hR/k_s$. Their results indicate that, as would be expected, the interfacial temperature gradient increases as the Biot number at the crystal circumference is increased. In addition, they found that the critical crystal length at which the axial temperature gradient ceases to be length dependent decreases with increasing Biot number. When their results are expressed in terms of maximum pulling rates (of silicon) using [1] they exceed the predictions of Rea by approximately 30%.

Heat Transfer Conditions Leading to Increased Interfacial Temperature Gradients

As indicated by Rea, the energy exchange between the growing crystal and its thermal environment plays a key role in determining the degree to which axial temperature gradients may be increased. When comparing the results of Billig[5], Ciszek[3] and Kuo and Wilcox[2] with those of Rea[4,6] it is seen that substantial improvements in the rate of pulling should be realized if the thermal boundary conditions during growth are modified to approach those of the more simplified models. To this end it is desirable to analyze the dominant thermal resistances between the growing crystal and its immediate environment (Fig. 1). An increase in the axial temperature gradient in the crystal requires that the heat flow from its surface be increased in order to balance the increased heat flow from the crystal/melt interface. This flow of heat from the surface of the crystal can be increased in two ways: first, improve the heat transfer away from the hot crystal to the cold environment; second, decrease the heat flow to the crystal from hot crucible and melt surface. The mechanisms of heat transfer from the crystal include convective transport in a surrounding gas as well as radiation and conduction to a cold ambient. This is shown schematically in figure one as a resistor between the crystal and the environment at temperature, T_R. This resistance to heat transfer should be minimized. Similarly, heat transfer to the crystal from the hot crucible and melt surface occurs via the thermal resistances shown originating at T_C and T_M respectively. An increase in these thermal resistances is desired without degrading the required low thermal resistance between the crystal and the environment at T_R.

The thermal resistance to radiant heat transfer is proportional to the radiation exchange factor, $\tilde{F}$:

$$q_{cr,x} = \tilde{F}_{cr,x} A_{cr} \sigma (T_{cr}^4 - T_x^4) \qquad [3]$$

$$\tilde{F}_{cr,x} = \frac{1}{\frac{1}{F_{cr,x}} + (\frac{1}{\varepsilon_{cr}} - 1) + \frac{A_{cr}}{A_x}(\frac{1}{\varepsilon_x} - 1)} \qquad [4]$$

where:

$\frac{q_{cr,x}}{A_{cr}}$	=	energy per unit area transferred by radiation from the crystal to grey surface, x
σ	=	Stefan-Boltzman constant
T_{cr}	=	temperature of the surface of the crystal
T_x	=	temperature of radiating surface, x
$F_{cr,x}$	=	radiative view factor between the crystal, cr, and a radiating surface, x
ε_{cr}	=	emissivity of the crystal
ε_x	=	emissivity of the radiating surface, x
A_{cr}	=	surface area of the crystal
A_x	=	surface area the radiating surface, x

where x denotes either the cold environment at T_R, the crucible wall at T_c or the melt surface at T_m. (These expressions assume that the surface, x, and the crystal may be approximated as grey bodies at uniform temperature.) Increasing the radiant thermal resistance demands a small view factor and surface emissivities and vice-versa.

Application of an Inverted Conical Heat Reflector for Thermal Resistance Modification

Modification of the thermal resistances in a conventional Czochralski puller for increased axial temperature gradients can be achieved by placing above the melt an inverted conical heat reflector mounted coaxially about the growing crystal (Fig. 2). In this way the thermal resistance from the hot zone to the crystal is increased while the heat transfer to the ambient remains largely unchanged.

The effectiveness of such a heat reflector has been indirectly observed during liquid encapsulated Czochralski (LEC) growth of PbSnTe[7]. A conical heat reflector was positioned above the melt but within the B_2O_3 encapsulant (Fig. 3). The temperature distribution within the liquid glass was modified by the heat reflector resulting in a higher viscosity (lower temperature) encapsulant. In this way a coherent encapsulating film was established on the growing crystal. Previous attempts at LEC growth of this material had been limited by the rupture of the low viscosity encapsulating film resulting in the loss of volatile constituents.

The choice of an optimized geometry (included angle, physical dimensions and position) for the conical reflector is influenced by two orthogonal and counter-productive sets of constraints. First are those related to producing a minimum value of the radiation exchange factor between the heat reflector and the growing crystal while the second set are those that permit an optimized use of the reflector for the duration of crystal growth.

An effective method of minimizing the radiation exchange factor between the heat reflector and the crystal is to reduce the radiation view factor given in [4]. This can be accomplished by increasing the included angle of

the conical section. However, as the included angle is increased the vertical position at which it would contact the crucible wall decreases. This permits two types of wide angle reflectors. 1) A relatively short heat reflector can be fabricated that will remain within the confines of the crucible and thus maintain its position relative to the crystal/melt interface as the melt height drops during growth (or equivilantly, as the crucible is raised). The drawback to this design of a short reflector is that at low melt levels the crystal is again affected by the hot crucible walls. 2) To preclude this last condition the heat reflector can be made taller and thus wider at the upper end. In this case it will not be able to track the melt height drop since its O.D. is greater than the crucible's I.D. During the latter stages of growth (at low melt heights) there will be a large separation between the end of the conical reflector and the crystal/melt interface which negates and even reverses the effect of the reflector.

A smaller included angle can be used to offset some of the above effects. In this way the reflector can be made taller and yet still remain within the crucible over appreciable melt height drops. The effectiveness of the heat reflector is deminished at the beginning of growth due to its height. Under these circumstances the heat reflector causes an increase in the thermal resistance between the crystal and the environment. The radiative view factor is increased with this design which further reduces its effectiveness.

Experimental System: Physical Modelling of the Axial Temperature Distribution in Czochralski Grown Germanium

Germanium was chosen as a model semiconductor/melt system. The insitu determination of the axial temperature distribution in a growing semiconductor crystal is problematical. Replacement of the crystal by a physical model permits this measurement to be made without incurring those problems inherent in using the crystal itself. These difficulties include: 1) accurately machining and drilling small diameter holes in germanium, a brittle material and 2) maintaining, during transient heat transfer conditions (i.e. when exchanging gases), a fixed geometry of the crystal and a constant relationship between the position of the crystal/melt interface and the measurement thermocouples.

Since there is less than a five percent difference in the thermal conductivity of the two materials near the melting point of germanium (937°C), stainless steel (type 303) was chosen as a physical model for solid germanium. The simulated Czochralski crystal was 10.0 cm in length (7.5 cm at constant diameter, 2.5 cm crown) with 9.5 mm radius. A graphite disk (3 mm thick) was attached to the end of the model in contact with the melt to serve as a buffer between the corrosive germanium melt and the stainless steel. An array of seven inconel sheathed, ungrounded chromel-alumel thermocouples (0.020" O.D., Omega Engineering) was positioned along the centerline of the model in holes (0.086 mm diameter) drilled perpindicular to the axis of symmetry. Figure four shows the positions of the thermocouples relative to the melt surface, crucible and conical heat reflector. While the holes were drilled offset at 90° intervals to

facilitate insertion of the thermocouples they are shown in the figure for clarity to be parallel. Temperature compensated (electronic ice point reference) rotary switches and digital displays were used for data acquisition.

The hot zone of an otherwise standard Czochralski crystal puller was modified by placing a isothermal furnace liner (heat pipe) coaxially between the graphite heating element and the crucible. The thermal boundary conditions associated with the heat pipe are reproducible and characterized by reduced axial and radial temperature gradients in the melt as well as improved thermal symmetry. Temperature control during the experiments was maintained using a standard P.I.D. (proportional, integral, derivative) system with the control thermocouple located on the active region of the heat pipe (Fig. 4).

A conical heat reflector was formed from molybdenum sheet (0.127 mm) with a 60° included angle. This angle was chosen as a compromise between the previously stated diametric effects of the included angle on mechanical implementation and performance. The reflector's axial and azimuthal position was determined by three graphite tipped support arms arranged radially that were attached to an auxiliary heat shield. The lower opening of the reflector (22 mm diameter) was positioned 3.5 mm above the melt surface. It was considered of primary importance to maintain a minimum separation between the reflector, the physical model of the crystal and the melt. In this way the heat reflector could influence to the maximum extent possible for the chosen geometry the axial temperature gradient at the crystal/melt interface. This corresponds to experimental conditions that permit the maximum rate of crystal pulling. The height of the truncated cone reflects the need to provide shielding of the 'crystal' from the hot zone while not significantly inhibiting the loss of heat to the ambient.

A multi-regulator gas flow system was used to exchange argon and helium gases during the experiment. A pressure of 2 psig was maintained in the growth chamber and the gas flow rate was adjusted to approximately 3 ℓ/hr (2 bubbles/sec).

Temperature distributions within the physical model were measured under four sets of experimental conditions: argon and helium gases were used both with and without the conical heat reflector. Each set of measurements was taken with the physical model in contact with liquid germanium (45 g) at its melting point. The upper rim of the graphite crucible was positioned at the opening to the heat pipe. The heat reflector (when employed) was positioned 3.5 mm above the surface of the melt.

After melting the germanium charge the temperature of the system was reduced until freezing was observed at the edge of the graphite buffer. It was then raised until remelting forced the crystal/melt interface to retreat beneath the buffer. It was subsequently confirmed by rapid separation of the model from the melt that solid germanium was still present beneath the buffer. A thermal soak of not less than 30 minutes followed any change in hot zone conditions. This permitted the temperature distribution within the hot zone and model to reach a new equilibrium condition. Temperature

distribution data were converted to non-dimensional form normalized to the first (lowest position) thermocouple reading and room temperature:

$$\theta_i = \frac{T_i - T_R}{T_1 - T_R} \qquad [5]$$

where: θ_i = non-dimensional temperature at position i
T_i = temperature at position i
T_R = room temperature
T_1 = temperature at position 1

The axial position, Z, of the measurement thermocouples was non-dimensionalized in terms of the radius, R, of the physical model:

$$\eta = Z/R \qquad [6]$$

Results and Discussion

Figures 5 and 6 show the measured temperature distributions within the physical model in helium and argon atmospheres respectively. It can be seen in both cases that the conical heat reflector does indeed enhance the axial temperature gradient. Also of note is that the reflector has a larger effect on the temperature distribution in the presence of argon than helium. This is to be expected since, in the case of helium, a larger fraction of the total heat transfer is by convection which is not expected to be affected by the conical heat reflector to the same extent as the the radiative heat transfer component. Also, as expected, the greater heat transfer capability of helium resulted in larger absolute temperature gradients.

The results are quantitatively summarized in tables 1 and 2 where the axial temperature gradients have been calculated from the temperature distribution data. Table 1 presents the information in non-dimensional terms while in table 2 the temperature gradients are given in units of $^{o}C/cm$. The influence of the conical heat reflector on the axial temperature gradient was found to be substantial in the case of an argon ambient. An increase in the axial temperature gradient of greater than 40%, from $55^{o}C/cm$ to $78^{o}C/cm$, was achieved. When helium was used as an inert ambient the increase in the temperature gradient due to the heat reflector was limited to approximately 25%, from $75^{o}C/cm$ to $95^{o}C/cm$. In both cases the absolute change in the axial temperature gradient was an increase of approximately $20^{o}C/cm$.

The maximum rate of crystal pulling is linearly related to the axial temperature gradient in the solid at the crystal/melt interface (see [1]). The changes in the temperature distribution within the model caused by the conical heat reflector could, in principle, be translated directly to a coresponding increase in the rate of crystal pulling. These results are a minimum improvement of approximately a factor of two over unpublished

Table 1 Change in Axial Temperature Gradients Due To Conical Heat Reflector: Non-Dimensional

ARGON

T/C Loc. (z/R)	$\frac{d\theta_s}{d\eta}$ (reflector)	$\frac{d\theta_s}{d\eta}$ (no reflector)	Percent Change
0.5-1.0	0.094	0.065	44
1.0-1.5	0.081	0.055	47
1.5-2.0	0.079	0.060	31
2.0-2.5	0.074	0.058	28
2.5-3.5	0.075	0.064	17
3.5-4.5	0.056	0.051	9

HELIUM

T/C Loc. (z/R)	$\frac{d\theta_s}{d\eta}$ (reflector)	$\frac{d\theta_s}{d\eta}$ (no reflector)	Percent Change
0.5-1.0	0.106	0.086	23
1.0-1.5	0.084	0.067	26
1.5-2.0	0.084	0.074	14
2.0-2.5	0.079	0.071	11
2.5-3.5	0.080	0.077	4
3.5-4.5	0.056	0.062	-3

Table 2 Change in Axial Temperature Gradients Due To Conical Heat Reflector: Dimensional

ARGON

T/C Loc.	$\frac{dT_s}{dz}$ (reflector) ($^oC/cm$)	$\frac{dT_s}{dz}$ (no reflector) ($^oC/cm$)	Percent Change
1-2	78	55	42
2-3	67	46	45
3-4	65	50	29
4-5	61	48	26
5-6	62	54	16
6-7	46	41	7

HELIUM

T/C Loc.	$\frac{dT_s}{dz}$ (reflector) ($^oC/cm$)	$\frac{dT_s}{dz}$ (no reflector) ($^oC/cm$)	Percent Change
1-2	95	75	25
2-3	75	59	29
3-4	73	65	13
4-5	69	63	10
5-6	71	68	5
6-7	52	55	-4

experimental results on increasing the pulling rate of silicon[8] using this technique. The differences in the implementation of the two different conical heat reflectors illustrate the importance of the design factors described previously. The reflector used in the previous investigation was tall thus preventing the hot growing crystal from exchanging heat with the cold environment of the growth chamber. In addition, it was positioned high above the melt which reduced (and ma) have eliminated) its effectiveness in establishing an increased axial temperature gradient in the solid in the critical region near the crystal/melt interface.

Proposals for Future Study

A) Experimental System: An Active Heat Transfer Control System for Axial Temperature Gradient Modification

The geometric limitations imposed upon the design and mechanical implementation of an optimized conical heat reflector can, in principle, be eliminated by substitution of an annular isothermal furnace liner (heat pipe) (Fig. 7). A heat pipe based active heat transfer control system would have significant advantages over the passive conical heat reflector.

The temperature distribution within the growing crystal can be adjusted and controlled by actively heating or cooling the heat pipe. In addition, by maintaining a small gap between the crystal and the heat transfer control system, the radiative view factor can be made to approach unity and the ratio of the radiating and absorbing surface diameters can be optimized. The small gap and potential low temperature environment about the growing crystal establish conditions of enhanced heat transfer from the crystal.

Kuo and Wilcox[2] have shown that this high Biot number condition (due to the large value of the heat transfer coefficient, h, leads to increased concavity of the crystal/melt interface. This interface curvature is characteristic of presently obtainable Czochralski grown silicon. While it has not as yet been shown to significantly influence the liquid/solid phase transformation at rates of pulling presently employed, it must be considered as a potential problem due to the adverse effect on defect generation and propogation inherent in this interface morphology. It must also be noted that these problems are a priori magnified in III-V and II-VI compounds due to the defect structure control of the electronic properties in these materials. To this end, the design of the heat transfer control system (Fig. 7) makes provision, through a separately controlled booster heater, for introduction of heat to the meniscus region to modify the shape of the crystal/melt interface[9].

The axial position of the heat pipe can be repositioned during growth to maintain a constant distance from the melt. In this way, unlike the passive conical heat reflector, the heat transfer control system may be positioned at all times close to the hot melt in order to increase the thermal resistance between the crystal and the melt while maintaining a uniformly cold environment into which the crystal may radiate thus developing the high axial temperature gradients required for high rates of crystal pulling. Furthermore, the geometry is such that it is never

necessary for the crystal to interact with the hot crucible walls near the end of the growth run.

B) Absorption of the Latent Heat of Solidification by the Peltier Effect

It has been indicated previously in this discussion that maximizing the rate of Czochralski crystal pulling requires efficient removal of the latent heat of solidification from the crystal/melt interface. Thus far the emphasis has been on obtaining heat transfer conditions which produce increased axial temperature gradients in the growing crystal for this purpose. However, the latent heat can be absorbed directly at its source by the Peltier effect thus permitting an increased rate of crystal pulling with no change in the axial temperature gradient in the solid.

The Peltier effect describes the absorption or release of heat at an interface between two dissimilar materials when an electric current flows across it. (Whether heat is absorbed or released depends on the direction of the electric current and the nature of materials.):

$$q = \pi_{l,s} J \qquad [7]$$

where:
- q = heat absorbed or released
- $\pi_{l,s}$ = relative Peltier coefficient between liquid and solid (negative for absorption, positive for release)
- J = current density

Introduction of the Peltier effect modifies the expression for conservation of energy at the crystal/melt interface:

$$k_s \frac{dT_s}{dz} - k_l \frac{dT_l}{dz} = \rho_s \Delta H R + \pi_{l,s} J \qquad [8]$$

Maintaining the assumption that the maximum rate of growth is obtained with zero temperature gradient in the liquid, [8] can be rearranged to express the maximum velocity in terms of the Peltier term, $\pi_{l,s}J$, the temperature gradient in the solid and physical constants:

$$R_{max} = \frac{k_s \frac{dT_s}{dz} - \pi_{l,s} J}{\rho_s \Delta H} \qquad [9]$$

The direction of J is chosen to make the Peltier term in [9] positive (i.e. absorption of heat), thus increasing the rate of growth. To be effective in increasing the rate of growth, the heat absorbed due to the Peltier effect must be significant when compared with the heat removed from the crystal/melt interface by conduction. Therefore, materials for which this technique is optomized should have 1) a low thermal conductivity

2) a large Peltier coefficient and 3) a low latent heat of solidification. Table 3 lists these quantities for several major electronic materials. It is seen that the properties of silicon make it unsuitable for this application. However, InSb and CdTe are materials which can be expected to benefit significantly from this approach.

It has been shown[10] that pulses of direct current passed across the crystal/melt interface during Czochralski pulling of doped InSb result in a modulation of the microscopic rate of growth. Figure 8 shows a photomicrograph of the polished and etched surface of InSb where interface demarcation (50 ms current pulses at 1 s intervals) was superimposed on a 9.5 A/cm^2 current pulse of 20 s duration. It clearly delineates the transient change in the microscopic rate of growth caused by the absorption of heat associated with the current pulse. While this result reflects the transient relocation of the crystal/melt interface it is recognized that under conditions of steady state heat flow the microscopic rate of growth is equal to the pulling rate (corrected for the drop in melt height) and the temperature gradient in the solid would be reduced accordingly. Thus an increase in the rate of pulling is permitted if the identical temperature gradient in the solid is reestablished.

Application of this technique is seen as problematical if high current densities are required to establish the desired degree of temperature gradient modification. Joule heating is proportional to the square of the current density whereas the Peltier effect depends only linearly on J. Thus the adverse effect of reducing the axial temperature gradient caused by Joule heating must, at some value of J, outweigh the benefit of increased rates of crystal pulling due to Peltier cooling.

Table 4 Selected Properties of Major Electronic Materials

Material	Latent Heat of Solidification ΔH (j/g)	Thermal Conductivity (w/°C cm)	Peltier Coeff. (V)
Si	1806	0.216	0.1
GaAs	567	0.08	0.1
Ge	466	0.173	0.09
CdTe	209	0.015	0.4
InSb	238	0.046	0.09

Summary and Conclusions

It has been shown that an inverted conical heat reflector can be used to influence the the thermal boundary conditions within a standard Czochralski crystal puller. The result is the establishment of heat transfer conditions that more closely conform to those that are predicted to permit high rates of crystal pulling. A physical model of solid germanium was used to measure the change in axial temperature gradients caused by the change in hot zone design. Experimental results indicate that the enhanced axial temperature gradients caused by the heat reflector should permit more than a 40% increase in the rate of crystal pulling when argon is used as the ambient gas. A similar 25% increase can be achieved for the case of helium.

These findings furthermore indicate the necessity to carefully consider the design and implementation of the reflector to achieve optimized performance. Primary considerations are the geometry and positioning of the reflector. Not indicated but considered of equivalent importance is the choice of heat reflector material and subsequent construction. Multi-layer heat shields should provide an even greater thermal resistance between the exposed areas of the hot zone and the growing crystal.

A proposed active heat transfer control system was described. Its design reduces or eliminates many of the problems inherent to the inverted conical heat reflector approach to heat transfer control for obtaining maximized rates of crystal pulling.

Peltier cooling assisted growth was described and shown to be applicable to systems which exhibit a large Peltier coefficient and low values of thermal conductivity and latent heat of solidification. Experimental results are shown for the case of InSb.

Acknowledgments

The author wishes to thank Dr. T. Jasinski for his help in the heat transfer analysis and preparation of this manuscript, Dr. Z.J. Xing for his assistance in the experimental portion of this work and Prof. A.F. Witt for his helpful suggestions on the proposed experimental approaches.

REFERENCES

1. W.R. Wilcox and R.L. Duty, J. Heat Transfer 88, 45 (1966).

2. V.H.S. Kuo and W.R. Wilcox, J. Crystal Growth 12, 191 (1972).

3. T.F. Ciszek, J. Appl. Phys. 47 (2) 440 (1976).

4. S.N. Rea and G.F. Wakefield, Conf. of Internat'l. Solar Energy Soc., Winnipeg (Aug., 1976).

5. E. Billig, Proc. Royal Soc. 229, 346 (1955).

6. S.N. Rea, J. Crystal Growth 54, 267 (1981).

7. E.D. Bourret and A.F. Witt, accepted for publication in the Journal of Crystal Growth.

8. R. Lane, Private Communication.

9. T. Jasinski and A.F. Witt, "Control of Temperature and/or Spatial Gradients in Temperature in Crystals Pulled From Melts of Solutions", MIT Patent Case No. 3753.

10. M.J. Wargo and A.F. Witt, accepted for publication in the Journal of Crystal Growth.

Conventional Czochralski Growth With Heat Pipe

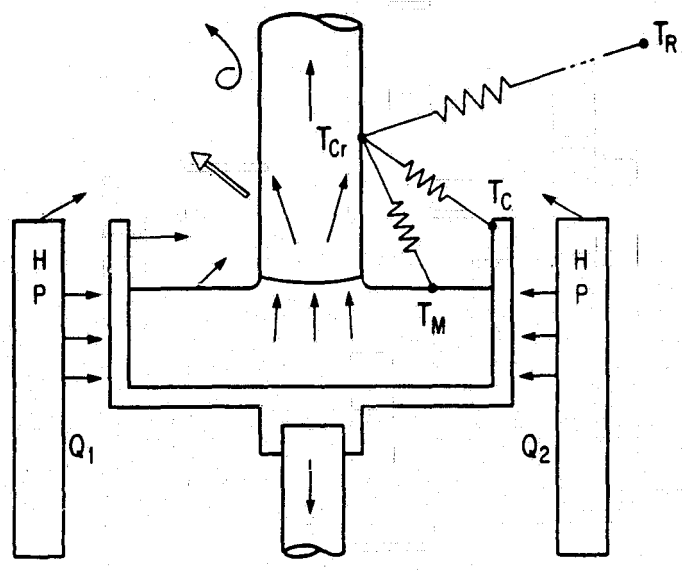

Figure 1. Heat transfer conditions in conventional Czochralski growth. Arrows schematically indicate the direction of heat flow by conduction, convection and radiation. Heat transfer to and from a point on the crystal (at T_{Cr}) occurs via the indicated thermal resistances.

Czochralski Growth With Heat Pipe and Conical Heat Reflector

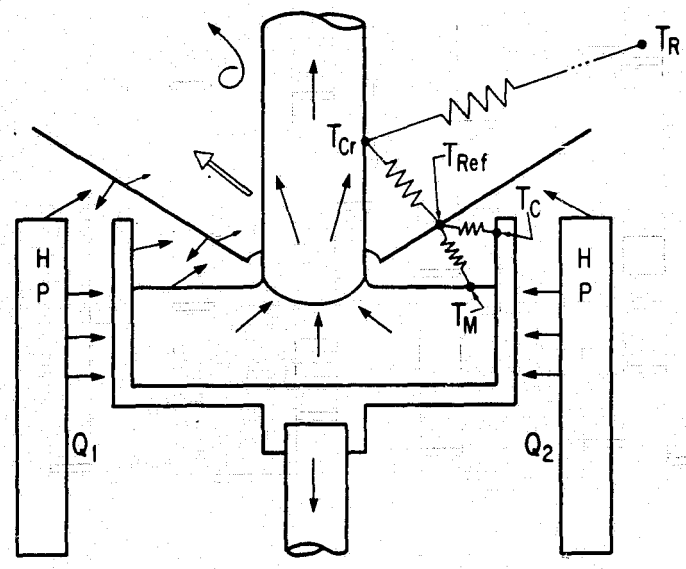

Figure 2. Thermal resistances modified by a conical heat reflector located coaxially about the growing crystal.

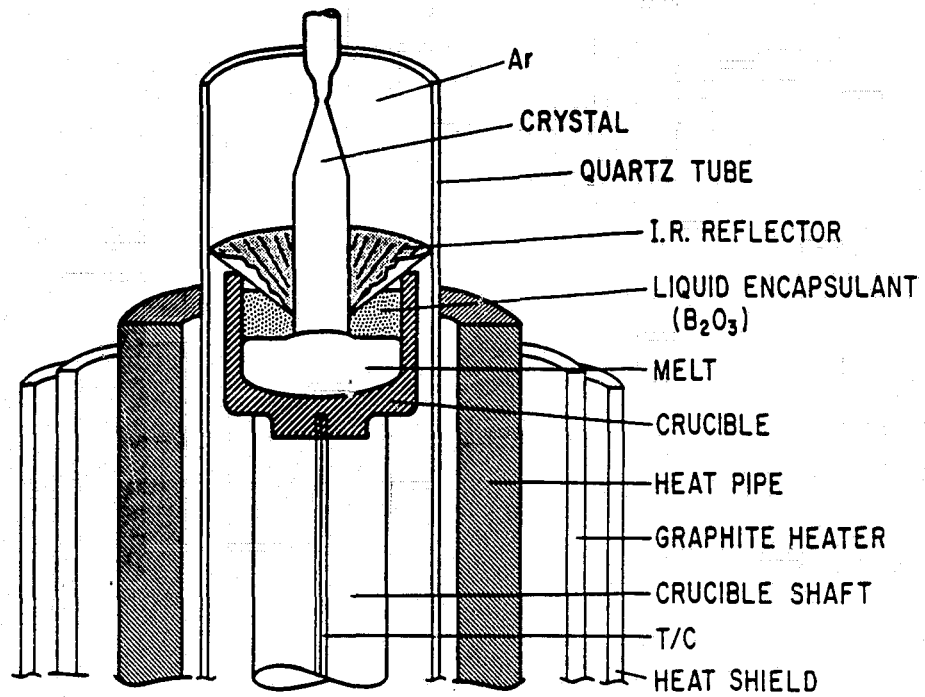

Figure 3. Application of a conical heat reflector to modify the temperature distribution in liquid B_2O_3 during LEC growth of PbSnTe.[7] The viscosity of the encapsulant is raised due to the increase in the temperature gradient effected by the conical heat reflector. As a result, a coherent encapsulating film is established on the growing crystal.

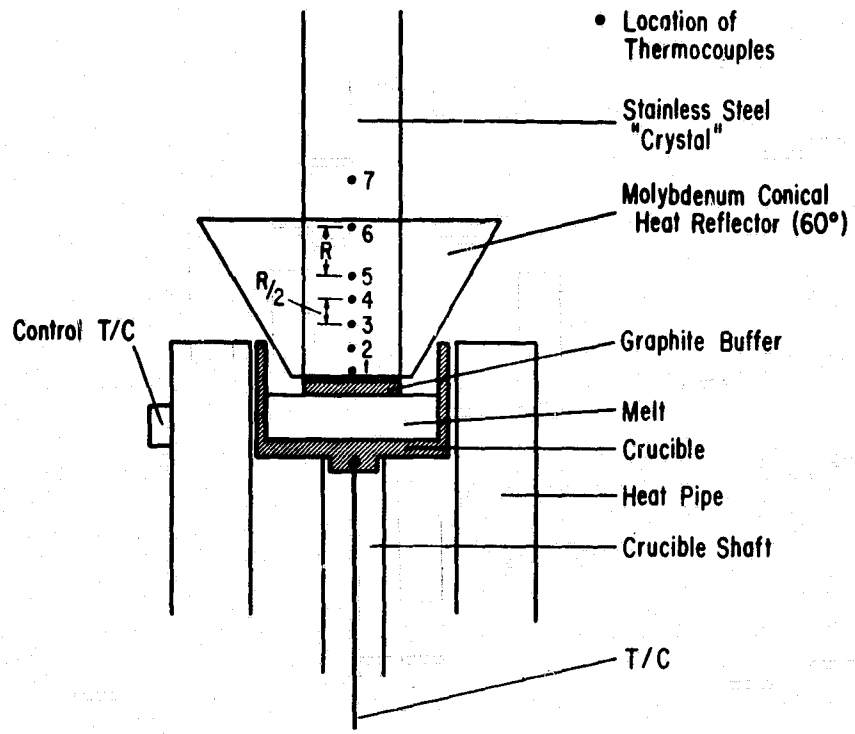

Figure 4. Schematic representation of the hot zone configuration and physical model used to measure the effect of a conical heat reflector on the axial temperature distribution in germanium.

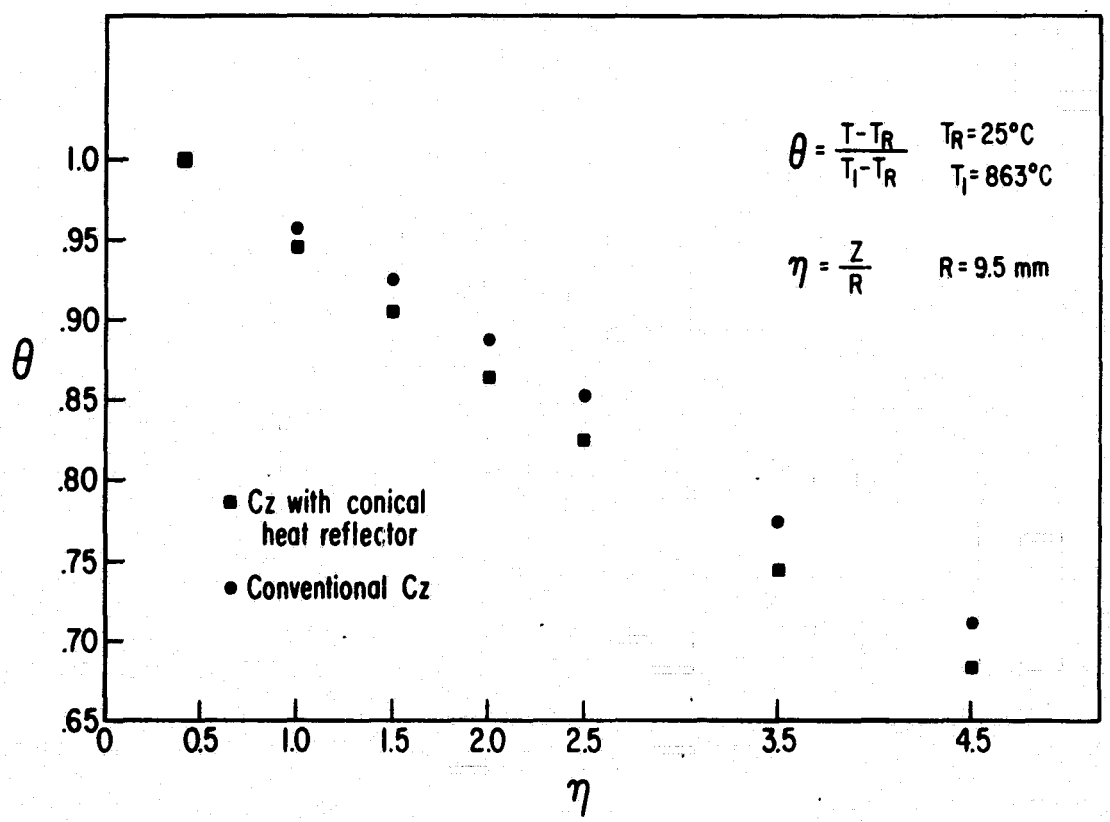

Figure 5. Measured temperature distributions (non-dimensional) within the physical model in a helium atmosphere.

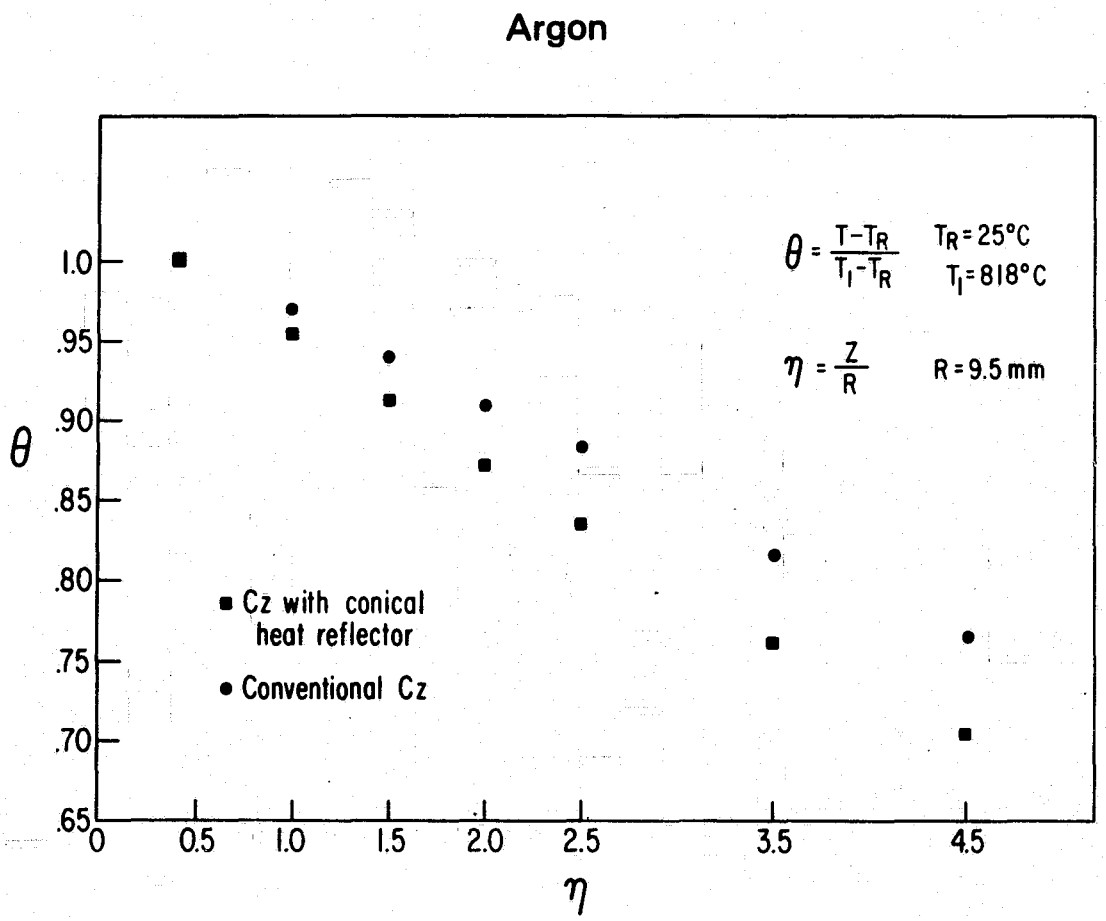

Figure 6. Measured temperature distributions (non-dimensional) within the physical model in an argon atmosphere.

Heat Exchange System for Optimized Control of the Following Interdependent Parameters:

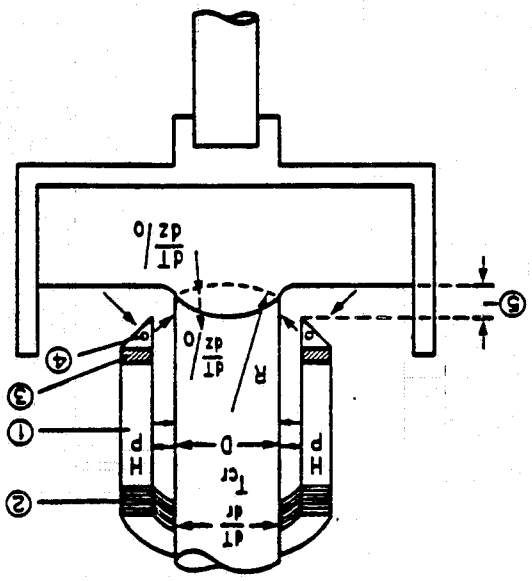

Figure 7. Active heat transfer control system system based on heat pipe technology.

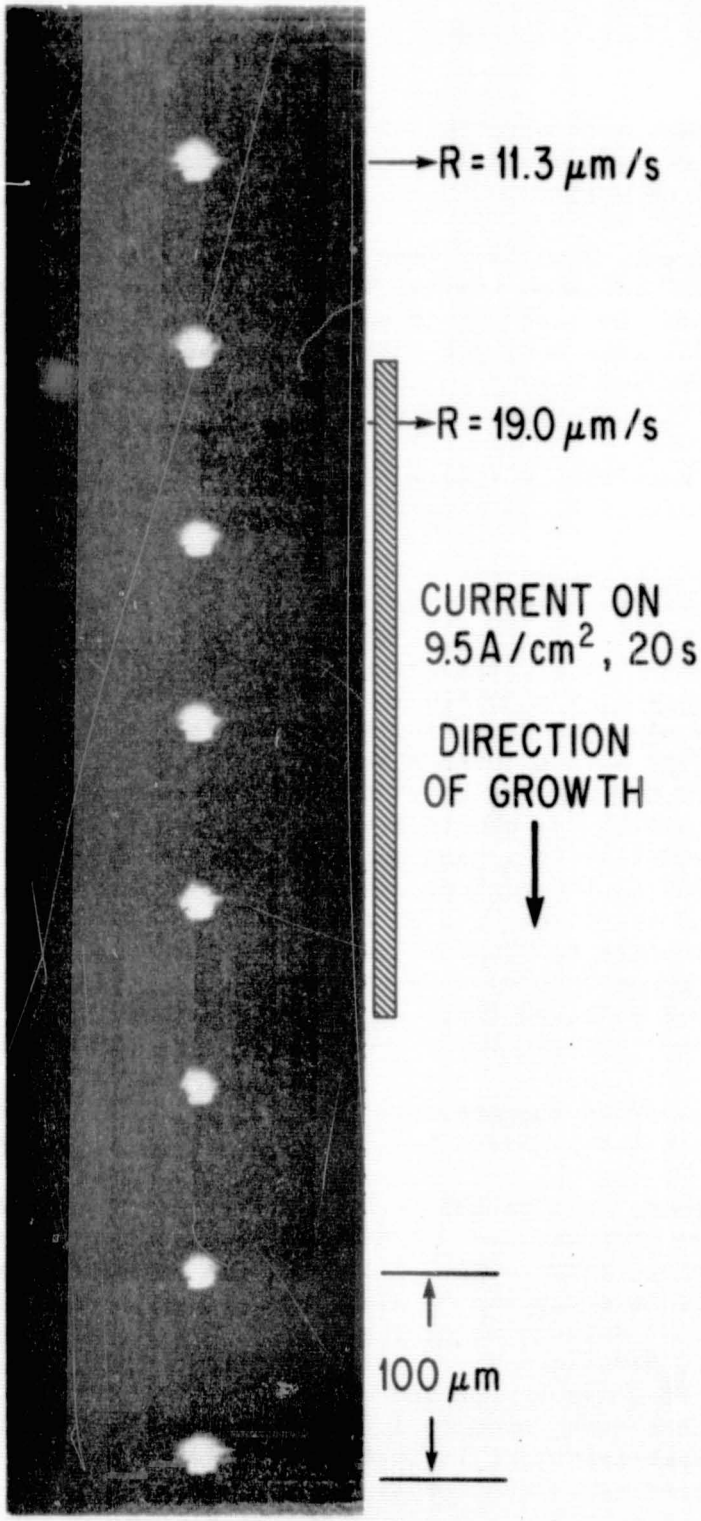

Figure 8. Effect of long duration (20 s) pulse of direct current on the microscopic rate of growth of InSb. Spreading resistance impact traces (bright spots) were used for sample alignment and as a spatial reference standard.

DISCUSSION

SACHS: In your experiments with the stainless-steel crystalline and the graphite puck, are you concerned with thermal contact between those two, and how you maintain it?

WARGO: I certainly am. When they were machining the graphite puck I said 'save some dust,' and when they saved the dust I packed dust between the graphite puck and the stainless steel. What I was really concerned about was, even in that case when you exchange the helium with the argon you get entrained helium, and I have to go by and look at how much influence there was on the heat transfer down there.

MOODY: Won't that heat pipe actually have to be in physical contact with the growing crystal to be truly effective?

WARGO: No. The original idea for the heat pipe about the growing crystal came from work we are doing for NASA on double-heat-pipe Bridgeman systems. What we find is that we want to work for absolutely reduced dimensions between the growing crystal, and the heat pipe, but in the case of Bridgeman there is a crucible in the way. We find that even with the crucible in the way, and maintaining that gap to on the order of a millimeter, we can have a substantial effect on the Biot in the system, and, in fact, if our calculations are appropriate for that condition compared to Cz growth, we should have the Biot go from about 0.005 to the order of 0.1, and that is a substantial improvement. I would like to make one comment about active control systems in Cz growth. You notice I am putting a lot of stuff down there, and I can't see very well, so what we have to do is provide for innovative active control of diameter and of temperature in those systems. We are looking at that very closely with computer assisted multi-variable control systems, and with focal-plane-array infrared imaging of the liquid melt surface.

LANE: Are you considering the pressure of the gas? Does it matter in your calculations what the pressure is? Is it a variable there?

WARGO: It does matter. All of this was done at a few lb/in^2 above atmospheric, and that was because we were changing things so much and there were so many thermocouples going in. We have to keep an overpressure, because you end up with junk all over your system. If we compared vacuum to vacuum, which I really didn't have the guts to do because it would have gotten very dirty in there very fast, I think what you would have found is a profound effect because that molybdenum heat reflector, in that case, becomes a radiation shield, and since the only mechanism for heat transport in that case is radiation, we should see significant increases in the actual temperature rate.

LANE: In our laboratory a couple of years ago we did exactly what you propose, the conical shield. We saw what we considered a marginal increase in pull speed. Our intuition told us that the bottom of that

cone should be as close to the interface as possible, about one inch away from the melt, and I think we were really too high.

WARGO: I agree. That is probably too high. I was concerned that in my case, in even a smaller system, that I was three millimeters away. The other thing to consider is, let's look at what happens up here due to the presence of the heat reflector, because in this case you are actually killing yourself. If I go back to my numbers, where I measured the gradient, did you notice that one of the gradients went negative, that you actually got worse gradients with the heat reflector in place? In the case of helium, what happened was, you actually got better temperature gradients without the shield than with it. In this case, you were actually increasing that thermal resistance between the growing crystal and the environment. The shield was getting in the way, and that is what is happening in this case as you go high up on the shield. In principle, what you would like to do is have this shield be down near the surface, be flat, come up and then be flat again. But then you don't have that active control that you need, and that is where the coaxial heat pipe really helps, because I can move that 'way down to the bottom and, with even a minor heat reflector in there, be able to take care of it. We need to pursue this vigorously, because I think it can have substantial effect on the actual temperature gradients and the interface morphology.

LOFGREN: You mentioned that the material out of which the conical heat shield was made is molybdenum. Do you believe that moly is the best material out of which to make the heat shield?

WARGO: I honestly don't know what is the best material. The reason I used moly is, first of all, we had it, the second thing was, in fact primary to having it, I looked at the design of the ASTP furnace that we used to grow directional solidification germanium aboard Apollo-Soyuz. It is a very small furnace, 150 watts got it to the melting point of germanium, and they had a very nice radiation shielding set up with molybdenum and it was done in a vacuum. The other thing here is, I am only affecting radiant energy. If I could do this, as I indicated before, under vacuum, we are in much better shape. I am not sure, and we certainly should find out. An enormous amount can be done in terms of hot-zone design with increased research into the influence of really well-designed radiation heat shields. We were discussing before what happens when you put all that graphite in the system: you end up with a virtual leak all the time, because it is all porous.

MORRISON: The first concepts for the heat shield picture that Dick [Lane] built and ran were that it be a double-walled heat shield. I wonder if you would consider a double-walled heat shield that is in fact a sodium heat pump, so that the heat that you carry away from the interface region gets physically carried far from the top of your growing crystal and also that structure acts as a conical heat shield and provides you with all the visibility you want?

WARGO: The compaction of that heat pipe, the fact that it is very narrow in diameter, still preserves that nice viewing angle. I agree.

LANE: You have a practical problem, though, the monoxide. The outside of that cone ought to be hot. The inside could be cold because you have clean gas coming down there. Anything that is cold above that melt is going to precipitate silicon monoxide, and that is bad.

LEIPOLD: Your suggestion of controlling the spherical shape at the bottom of the ingot by an auxiliary heater--unless I am mistaken, the maximum temperature gradient in the crystal needs to be at the liquid-solid interface, because that is before any heat is removed. It would seem that putting a heater down there would definitely counteract the advantage that you get by the heat pipe.

WARGO: It will certainly reduce the advantage but it shouldn't counteract it totally. One of the reasons that you have such a large curvature is because you have very high gradients near that edge, so what you can do is maintain the axial gradients because of all the heat transfer above that. I can now get rid of more heat and then give up some on the actual gradients near the edge of the crystal by the auxiliary heater. It would be one thing to grow the crystal fast; it is another thing to grow it fast with quality, and so to preserve the quality, we have to give up something.

N84 28647

Segregation of Impurities in Directionally Solidified Silicon

P. S. Ravishankar and L. B. Younghouse
Exxon Research and Engineering Co.
Solar Electric Conversion Unit
P. O. Box 45
Linden, New Jersey 07036

ABSTRACT

Hall measurements and four-point probe resistivity measurements are used to determine the concentration profile of boron and iron in doped semiconductor silicon ingots grown by the Bridgman technique. The concentration profiles are fitted to the normal segregation equation and the effective segregation coefficient, k_{eff}, is calculated. The average value of k_{eff} is 0.803 for boron. For iron, k_{eff} is concentration dependent and is in the range 8×10^{-5} to 1.2×10^{-4}.

1. INTRODUCTION

Polycrystalline silicon from solar grade material made by directional solidification [1, 2, 3] and other [4, 5] methods has gained increasing importance in recent years, particularly for solar photovoltaic applications [6, 7, 8]. Segregation of impurities during directional solidification allows the use of "solar grade" starting material which is less pure, but substantially less expensive than semiconductor-grade silicon. A knowledge of effective segregation coefficient (k_{eff}) of impurities for a given crystal growth process is necessary for optimizing the upgrading process. In this paper, the segregation of two specific impurities--boron and iron--is addresssed.

Effective segregation coefficient data are available in the literature only for the Czochralski and float zone crystal growth processes which yield single crystals. Even these data are at variance from each other. For example, in the case of boron, values from 0.7 to 0.85 are reported [9, 10, 11]. In the case of iron a value of 6.4×10^{-6} is reported by Hopkins et al. [10] and a value of $\sim 10^{-4}$ is given by James and Richards [12]. Hopkins et al. [10] measured the impurity concentrations C_s, in the crystal, by neutron activation analysis and the concentration in the solidified residual melt, C_l by atomic absorption method. The value of k_{eff} was then calculated as $\frac{C_s}{C_l}$. James and Richards [12] measured the value of C_s at the seed end of the crystal (first to freeze) by neutron activation analysis and from the known initial concentration C_o, calculated k_{eff} as $\frac{C_s}{C_o}$. Such measurements assume k_{eff} to be independent of concentration and are also subject to large errors since they are single point measurements.

In order to obtain k_{eff} more precisely, the distribution of impurities along the growth axis of the entire crystal should be measured. This distribution is then fitted to the normal segregation equation

$$\ln \left(\frac{C_s}{C_o}\right) = \ln k_{eff} + (k_{eff}-1) \ln (1-g) \qquad (1)$$

where, g is the fraction solidified. K_{eff} can be calculated both from the slope and from the intercept. If the two values do not agree, an anamoly, such as a concentration dependent k_{eff} may be suspected.

In this paper, the methods used to obtain the concentration distribution are described. Using the procedure outlined above, the value of k_{eff} for boron and iron in polycrystalline ingots grown by the Bridgman method is calculated.

2. Experimental

The Bridgman crystals for the determination of k_{eff} of boron were grown by directional solidification of semiconductor silicon doped to ~0.3 ohm-cm. A vertical section of the resulting polycrystalline ingot was etched in NaOH. Four-point-probe measurements were made at several positions along the vertical axis. An average resistivity of a number of readings at each location was converted to dopant concentration using the equation suggested by Thurber et. al. [13]. The interface shape for different growth conditions was estimated from experiments where this parameter was measured independently. From the interface shape, the value of the fraction solidified was calculated geometrically. The g vs. C_s data were treated as described in the previous section.

The Bridgman crystal for the determination of k_{eff} of iron was grown by directional solidification of a semiconductor silicon melt to which 0.1% by weight of iron had been added as granules. The ingot was grown very slowly to avoid constitutional supercooling and interface breakdown. 5 cm x 5 cm x 0.45 cm thick slices were cut at several positions along the growth axis, with the surface of the slices perpendicular to that axis. Slices from 12 locations along the axis were chosen for this evaluation. On each slice, Hall measurements were made at three random positions. The average of the carrier concentrations obtained by these three Hall measurements was taken as representing the C_s at that axial location. The value of g was calculated for each axial location as before. The C_s vs. g data were treated as described in the previous section.

In order to assure that the electrically active iron concentration calculated using Hall data are representative of total (chemical) iron, three slabs weighing about 20 g each and chosen from the bottom, middle and top of the ingot were analyzed by neutron activation analysis at General Activation Analysis, San Diego, CA.

3. RESULTS AND DISCUSSION

Boron:

Table 1 shows k_{eff} of boron calculated from the slope and intercept for Bridgman crystals grown under different conditions. The difference between the value of k_{eff} as estimated from the slope and the intercept is expressed as a percentage "error" in Table 1. Since the intercept value requires a knowledge of C_o and the slope value is independent of C_o, the value from the slope should be more reliable. However, the value from the intercept is within 30% of the slope value. This error probably represents the accuracy with which a few milligrams of boron can be weighted for use as the dopant.

It is important to note that the k_{eff} from the slope has much less scatter. The mean k_{eff} from the slope for all the ingots is 0.803 ± 0.036.

Iron:

The C_s vs. g data is plotted as ln $(\frac{C_s}{C_o})$ vs. ln (1-g) in Figure 1. The K_{eff} from the intercept is 1.18×10^{-4}. This suggests that the slope (= k_{eff}-1) should be equal to -1. However, as shown in Figure 1, a line with a slope of -1 does not fit the data. This behavior might be attributed to a non-ideal phenomenon such as interface breakdown. Since such a phenomenon was not observed, an alternative explanation may be that the value of k_{eff} is concentration dependent. Following the procedure suggested by Wilcox [14], the variation of k_{eff} along the length of the ingot can be determined. From the mass balance,

$$C_l = \frac{C_o - \int_o^g C_s dg}{1-g} \qquad (2)$$

For $k_{eff} \ll 1$ and $g \ll 1$, the average impurity concentration in the solid is negligible compared to C_o. Under these conditions equation 2 reduces to

$$C_l = \frac{C_o}{1-g} \qquad (3)$$

From the definition of k_{eff},

$$k_{eff} \equiv \frac{C_s}{C_l} = (\frac{C_s}{C_o})\ (1-g) \qquad (4)$$

Using equation 4 and the C_s vs. g data, k_{eff} was calculated at different values of g. The value of k_{eff} varied from 1.2×10^{-4} at g = 0 to 8.3×10^{-5} at g = 1. Linear regression of the k_{eff} vs. g data gives

$$k_{eff} = 1.218 \times 10^{-4} - 3.9 \times 10^{-5}\, g \qquad (5)$$

with a correlation coefficient of 91%. Accounting for the variation of k_{eff} with g according to equation 5, the normal segregation equation is replotted in Figure 2 along with the C_s vs. g data. The fit to the data is excellent.

In order to check if all the iron present in the crystal were measured using the Hall method, the crystal was analyzed at three locations using neutron activation analysis. In all three locations, the iron concentration was below the detection limit of about 100 ppba. The concentration range measured by Hall method was between 60 and 300 ppba. Thus, all the iron that is present seems to be electrically active and accounted for by the Hall method.

4. CONCLUSIONS

(i) The effective segregation coefficient, k_{eff} for boron in directionally solidified polycrystalline silicon is 0.803 ± 0.036.

(ii) k_{eff} for iron is concentration dependent. The value ranges from 1.2×10^{-4} to 8×10^{-5} for the concentration range 60 ppba to 320 ppba in the solid.

(iii) The electrically active iron concentration measured by the Hall method is in fair agreement with the chemical concentration measured by neutron activation analysis, suggesting that all the iron is electrically active.

ACKNOWLEDGMENTS

We wish to acknowledge L. Hunt for helpful discussions, E. Shipp and R. Francis for assistance in Hall measurements and R. Sylvain of Solar Power Corporation for growing the crystals.

REFERENCES

[1] F. Schmid and C. P. Khattak, DOE/JPL-954373-81/19, Crystal Systems Inc. (1982).

[2] S. Pizzini, C. Calligavich, C. Chemilli, M. Gasharini, P. Rava and L. Sardi, ECS Meeting, San Francisco (1983).

[3] J. Fally and C. Guenel, Comm. Eur. Communities (1982).

[4] F. Dietl, ECS Meeting, San Francisco (1983).

[5] J. H. Wohlgemuth, J. S. Culik and P. Alexander, ECS Meeting, San Francisco (1983).

[6] J. A. Amick, J. P. Dismukes, L. P. Hunt, R. W. Francis, P. S. Ravishankar, M. Schneider, R. Sylvain, K. Larsen and A. Schei, ECS Meeting, San Francisco (1983).

[7] J. A. Amick, J. P. Dismukes, P. S. Ravishankar, M. Schneider, J. Blake, K. Matthei, R. Sylvain, K. Larsen and A. Schei, to be presented at Photovoltaic Solar Energy Conf., Greece (1983).

[8] P. S. Ravishankar, L. P. Hunt and R. W. Francis, ECS Meeting, San Francisco (1983).

[9] H. R. Hubb, T. G. Diggs, Jr. and O. B. Cecil, J. Appl. Phys., 42, 1235 (1971).

[10] R. H. Hopkins, J. R. Davis, P. D. Blais, A. Rohatgi, R. B. Campbell, P. Rai-Choudhury and R. E. Stapleton, DOE/JPL-954331-78/3, Westinghouse R&D Center (1978).

[11] H. F. Wolf, Semiconductors. Wiley-Interscience, New York, (1971).

[12] J. A. James and D. H. Richards, Int. Journal of Electronics, 3, 500 (1957).

[13] W. R. Thurber, R. L. Mattis, Y. M. Liu and J. J. Filliber, J. Electrochem. Soc., 127, 2291 (1980).

[14] W. R. Wilcox, Mat. Res. Bul., 13, 287 (1978).

NOMENCLATURE

c - Concentration [Atom Fraction]

g - Fraction Solidified [Dimensionless]

k - Segregation Coefficient [Dimensionless]

R - Correlation Coefficient [Dimensionless]

Subscripts

eff - Effective

s - Solid

l - Liquid

o - Initial

Table 1: EFFECTIVE SEGREGATION COEFFICIENT OF BORON IN POLYCRYSTALLINE SILICON

Run #	R^2	k_{eff} from Slope	k_{eff} from Intercept	$\left\| 1 - \frac{k_{eff,\ Intercept}}{k_{eff,\ Slope}} \right\| \times 100$ (%)
EB-38	0.961	0.838	0.928	10.7
EB-43	0.968	0.767	0.806	5.1
EB-98	0.970	0.783	0.568	27.5
EB-99	0.981	0.805	0.698	13.3
EB-104	0.975	0.822	0.683	16.9

Mean k_{eff} from slope = 0.803 ± 0.036*

* 95% Confidence Limits

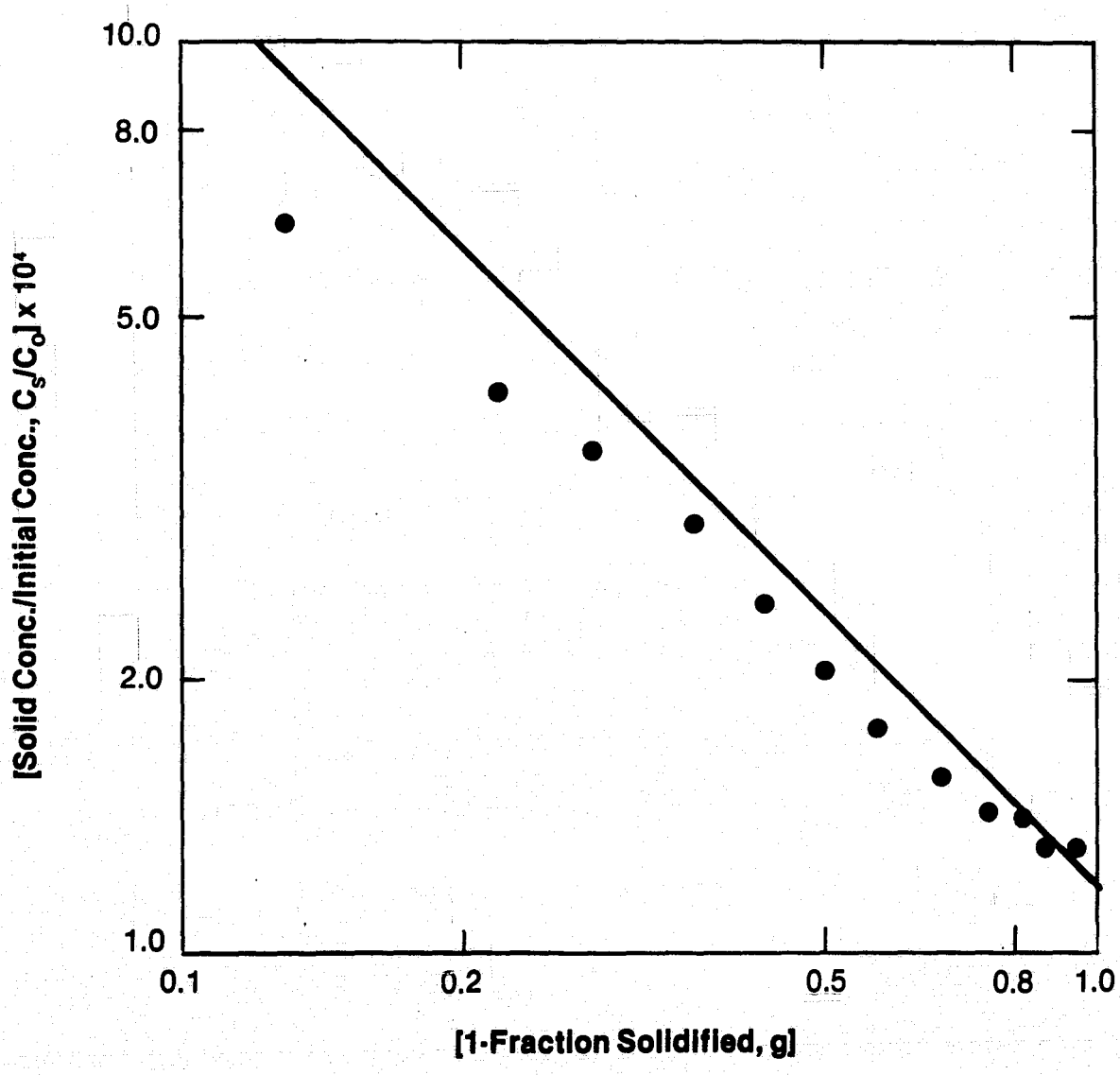

Figure 1: Normal segregation equation with constant k_{eff} fitted to experimental data with the slope forced to -1 (—) theory.
• Experimental Data

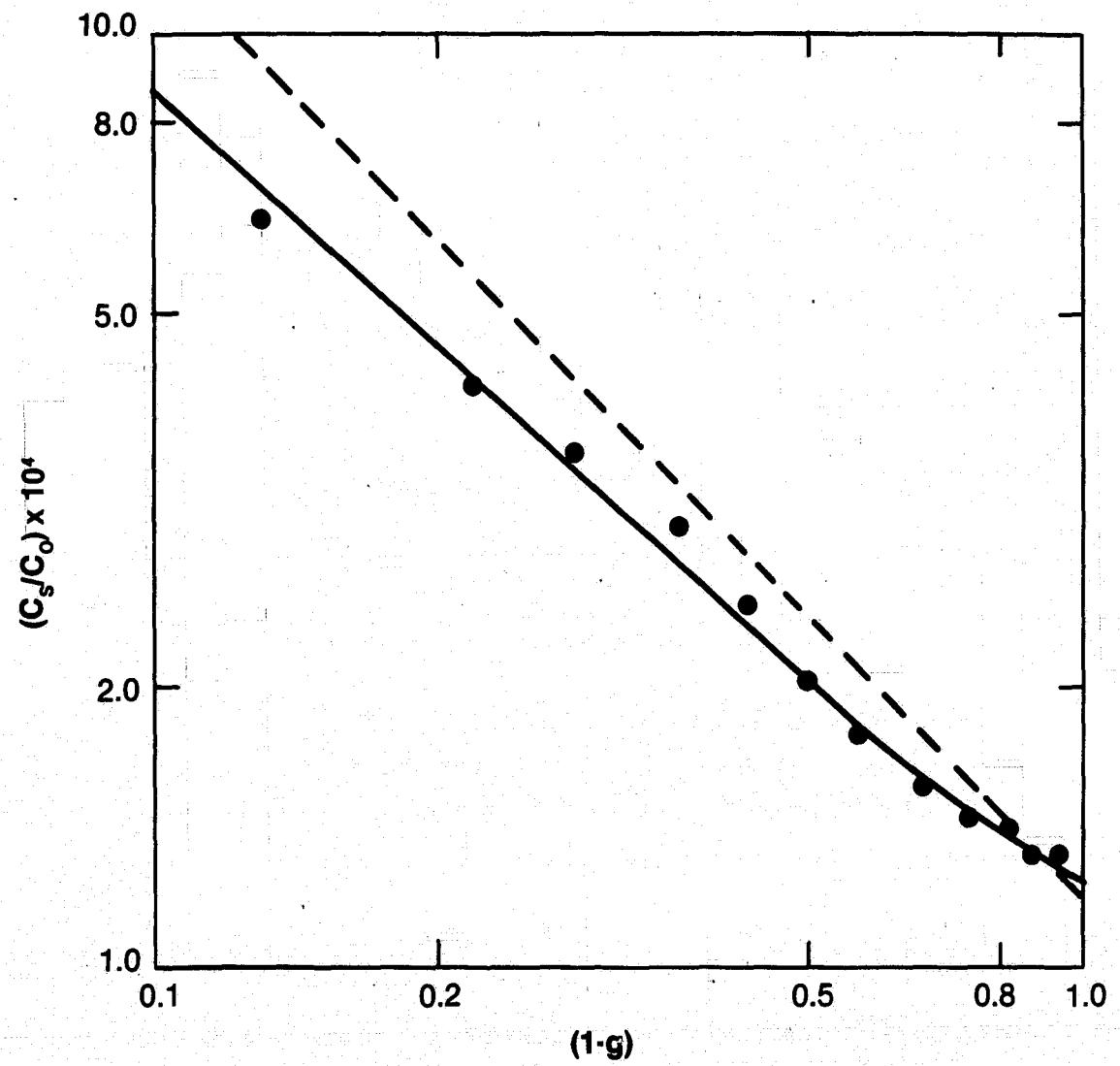

Figure 2: Normal segration equation with (—) conc. dependent k_{eff} and (---) Constant k_{eff} with slope forced to -1.

● Experimental Data.

DISCUSSION

KALEJS: I don't know if you aware of work that a colleague of mine, Mary Crettella, has done at Mobil Solar in doping EFG ribbon melts with iron and aluminum. She has co-doped normal EFG melts with and without boron, with both iron and aluminum between levels of about 10^{16} to 10^{18} atoms per cc. In our EFG systems, she has done this for growth from both graphite crucibles and quartz crucibles, the implication being that with a graphite crucible you have no oxygen, but with a quartz crucible you still have high carbon. It is a matter of just turning the oxygen on and off, rather than removing the carbon, when you go to the quartz crucible. What she has found, generally, is a lot of synergistic effects such that there are significant changes in the resistivity. For example, if you start with aluminum and dope from 10^{16} up to 10^{18} when you add iron, and if you start out with iron and add aluminum, then you also get change in resistivity. We are interpreting these results in terms of synergistic effects of impurity complexing between iron, aluminum, and perhaps carbon and oxygen. Of course, aluminum is always in the melt in Czochralski growth and the quartz crucible, so that bias level unfortunately probably is there in your experiments. I think it probably would have a first-order effect on the results that you are seeing. We speculate that the results mainly come from some kind of bulk-melt crucible interactions and perhaps, in the case of your experiments, it might be well to monitor the bulk melt to find out whether more iron stays behind there in some kind of complex or precipitate form already, before the fluid moves into the growth interface.

RAVISHANKAR: The problem with iron and aluminum is that iron is an n-type impurity and aluminum is p-type. So when you are looking at them together, you are really looking at a compensated crystal.

KALEJS: I should mention that we do find precipitates in the ribbon, large precipitates that contain iron and aluminum, with silicon and carbon, perhaps.

RAVISHANKAR: What level of impurities?

KALEJS: We go around 10^{16} to 10^{18} and above.

RAVISHANKAR: In a solid?

KALEJS: We put it in the melt and then by various types of analysis, including neutron activation analysis, we have monitored the crystal content. We find k_{eff} roughly on the order of a half, but again it fluctuates quite drastically as a function of the relative levels of the two impurities, implying some kind of bulk-melt interactions.

RAVISHANKAR: When we started working with metallurgical silicon in the Alcan-Exxon program, we found that every time we grew a crystal by Czochralski or Bridgeman, and sent the crystal for analysis for spark source, it always came back with one part moly and iron. So we didn't

know whether the published segregation coefficients are wrong, or we have a limitation of mechanical analysis. The reason I took the up study was to see what segregation coefficient we would measure, and it turns out that even though it is automatically different from Westinghouse data, it still is fairly low and is not enough to explain the 1:10 part moly and iron we always see by spark source and other chemical techniques. At least we can now conclude that the values we saw there were more of a limitation of the chemical analysis than a fundamental problem with segregation.

N84 28648

EFFECTS OF NON-EQUILIBRIUM SOLIDIFICATION ON THE MATERIAL PROPERTIES OF BRICK SILICON FOR PHOTOVOLTAICS

W. F. REGNAULT*, K. C. YOO*, **, P. K. SOLTANI*, S. M. JOHNSON***

*SEMIX INCORPORATED, Gaithersburg, MD, **UNIVERSITY OF MARYLAND, College Park, MD, ***SOLAREX CORPORATION, Rockville, MD

INTRODUCTION

Silicon ingot growth technologies like the Ubiquitous Crystallization Process (UCP) are solidified within a shaping crucible. The rate at which heat can be lost from this crucible minus the rate at which heat is input from an external source determines the rate at which crystallization will occur. Occasionally, when the process parameters for solidification have been exceeded, the normally large multi-centimeter grain size material associated with the UCP will break down into regions containing extremly small, millimeter or less, grain size material. Accompanying this breakdown in grain growth is the development of so called sinuous grain boundaries. Morrison first reported on these boundaries as appearing in an equiaxed region that occurs as a result of solute concentration in the solidifying melt (1). Also, because of the large surface area of a sinuous grain boundary, Armstrong et. al. speculated that the formation of such boundaries was to allow excess solute to be incorporated into the material during solidification (2).

The photovoltaic properties of solar cells fabricated on this material are, in general, quite poor. Storti et. al. presented a laser scan of a 2 cm x 2 cm cell which contained a small segment of a sinuous boundary (3). This cell showed an increase in photoresponse at the sinuous grain boundary at a wavelength of 1150 nm, but in general, the cell performance was quite poor. It was assumed that the observed increase in photoresponse was due to an increase in the collection volume caused by the diffusant pentrating down the grain boundary creating, in effect, a vertical junction. Putney and Regnault also presented solar cell data on fine grain material with open boundaries which they called Type 2 boundaries (4). Their results showed cells that had shunt resistances less than one ohm but that had an enhanced red to blue short circuit current response which they also attributed to the diffusant penetrating the grain boundary.

The breakdown in grain growth which results in this type of small grain structure with sinuous boundaries is usually associated with the rapid crystallization that would accompany a system failure. This suggests that there are limits to the growth velocity that one can obtain and still expect to produce material that would possess good photovoltaic properties. It is the purpose of this paper to determine the causes behind the breakdown of this material and what parameters will determine the best rates of solidification.

PRECEDING PAGE BLANK NOT FILMED

TECHNICAL DISCUSSION

The term mush and mushy zone, which refer to the fine equiaxed grain structure found in the casting of alloys (5) has been adopted here to describe the small grain structure observed in this investigation. In order to study the onset and the physical properties of this mush material two ingots were grown under laboratory conditions. One was produced so as to contain the material of interest, the other was a control. Thermocouples were equally spaced along the central axis of these ingots in order to obtain data on the rate of solidification and the thermal gradients inside the ingot. The ingots were cut in half and etched with sodium hydroxide to reveal the internal grain structure and then two 10 cm x 10 cm quadrants were cut from each half. One quadrant from each ingot was wafered normal to the principle axis, the other was wafered parallel to the central axis. The resultant wafers could then be analyzed by techniques such as optical and scanning electron microscopy and X-ray topography.

Figures 1a and 1b are macrophotographs of the longitudinal cross section of the mush and control ingot, respectively. It can be seen that from Figure 1a that the fine grain structure begins about 3 cm up from the bottom of the ingot and is roughly in the shape of a right circular cone. This structure encompasses about 10% of the total volume solidified. The white material in the center of the ingots is a quartz thermocouple protection tube. As the freezing front passes a thermocouple location, there is a marked change in the thermocouple response due to a change in the thermal conductivity in going from the liquid to the solid. By knowing the distance between the thermocouples an average growth rate can be obtained. In the ingots grown for this study, the ingot with the equiaxed grain structure solidifed at an average rate of 1.9 cm/hr while the control ingot solidified at 1.6 cm/hr. Average growth rates have been measured as high as 3.3 cm/hr in UCP material without breakdown into mush.

It has been reported that sinuous grain boundary regions will exhibit anomalous etch characteristics (1)(2). In the current study both longitudinal and transverse cut wafers were etched with a chemical polish etchant. The wafers exhibited three distinct zones with remarkably different etch chacteristics as shown in Figure 2. In zone 1, the etching properties were normal. Both grains and grain boundaries were etched equally, and a very smooth surface was obtained. In zone 2, the grain volumes continued to etch to a smooth polished surface but the sinuous boundaries are chemically resistant, leaving ridges on the surface of the wafers. In zone 3, the etching character of both the grain volumes and the sinuous boundaries has changed. In this region the chemical attack at the boundaries is greater leaving deep trenches over a highly textured surface. This marked change in the etching character across the surface of a wafer is suggestive that impurities are incorporated into the grains and grain boundaries and alter the chemistry of the etching process.

It is reasonable to assume that if this structure is caused by an impurity build-up in the material, that there should be changes in the internal grain structure preceeding the breakdown in grain growth. Figure 3 is a photograph of a longitudinally cut wafer showing the breakdown of the large grains into a much smaller grain structure. From the photograph it can be seen that grain 1 appears to breakdown into a dentritic looking structure that eventually gives way to grains of even smaller dimensions. These smaller grains appear to be entwined with one another as the solidification proceeds. Orientation studies were carried out using Laue back reflection techniques on grains 3, 4, and 5. As in previous studies (3) (6) (7) (8) (9) (10) the large semicrystalline grains are crystallograpically related. Grains 3 and 4 possess a common <111> direction and are in a first order twinning relationship. Likewise, grains 4 and 5 are first order twins with a common <111> direction. This double twinning relationship across grain 4 puts grain 3 and 5 in a second order twinning relation with a common <221> direction.

X-ray topography was used to determine the internal grain structure prior to the breakdown in grain growth. Due to its large size, grain 1 was chosen for study. Figure 4 is a (404) Berg-Barrett reflection topograph of the grain labeled 1 in Figure 3. Figure 4 is rotated approximately 45° counterclockwise relative to Figure 3 so that the growth direction is from the lower left hand corner to the upper right hand corner. It can be seen that as the growth of grain 1 proceeds the dislocation density increases from about 10^4 dislocations/cm^2 to over 10^6 dislocation/cm^2. The dislocations are seen to coalesce and finally, due to the high strain fields present, the lattice develops a subgrain structure as a way of dissipating the strain energy. From previous investigations of subgrain formation in semicrystalline material it is known that subgrains tend to be rotated 5°-7° about a common <110> type direction (6)(7). The possession of a common <110> rotation axis is also the case in the present material. The subgrain labeled A in Figure 4 is rotated out of the Bragg reflecting condition in a (313) Berg-Barrett reflection topograph.

In an effort to further characterize the structure of these mush grains two additional orientation studies were undertaken on a 2 cm x 2 cm sample cut from the upper left corner of the wafer shown in Figure 2. Since this wafer is near the middle of the ingot and the grain growth is nearly columnar at this point the surface normals of the grain in this region will be in the direction of grain growth.

Since these grains are generally less than a millimeter in size, the electron channeling pattern (ECP) mode of the SEM was used to determine surface normals and relative orientations. The ECP micrograph's were obtained by first setting the specimen perpendicular to the optic axis of the SEM using single crystal silicon of known orientation and tilting the stage until the correct ECP was obtained. All experimental patterns were then obtained without further adjustments to the specimen stage.

The channeling pattern is obtained by rocking a nearly collimated beam of electrons through several Bragg angles on the specimen surface. The result is the modulation of the backscattered electrons by the crystal lattice, yielding a characteristic pattern for a given orientation. Using this method, electron channeling patterns of 10-20 μm size grains are readily obtained. The surface normal of a grain can then be determined by matching its ECP with a complete channeling map of the same material (11).

Figure 5 is a plot of the surface normals of sixteen mush grains as determined from their ECP's. It can be seen that the normals lie along the [111]-[100] zone axis as far from [110] as possible. This was also found to be the case in a previous study of the orientation of grains surrounded by sinuous boundaries (12).

While determining the surface normals of the small grain material, it was occasionally found that numerous isolated grains, designated "a" in Figure 6, would be surrounded by a larger grain, designated "b", and that these small island grains would posses identical electron channeling patterns indicating that they are part of one grain. The relitive orientation of the surface normals of these grains are indicated on the unit triangle shown in Figure 5, as a and b, respectively. In order to determine if there is a crystallographic relationship between these two grains, their full orientations were determined from the electron channeling patterns by a method described by Joy et. al. (11). The relative orientations of grains a and b are indicated on the combined stereographic projection shown in Figure 7. It can be seen that these grains have a nearly coincident <110> type direction, with a misorientation of 4°, and that there is a 22° rotation of grain a relative to grain b about the <110> axis. The 4° misfit in the <110> poles is probably caused by the highly strained nature of this material as shown in Figure 4.

As mentioned above, solar cells fabricated on this material are, in general, quite poor. There is, however, evidence that seems to suggest that diffusant may be penetrating down the grain boundaries and enhancing the collection efficiency there (3)(4). This is likely due to the highly strained nature of this material. In order to study this hypothesis, bevel and staining experiments were carried out on a number of different types of semicrystalline samples. The samples that were selected consisted of a control sample, a sample containing previously investigated subgrain boundaries (7), and two samples containing mush. One of the mush wafers was diffused and another was not. The samples were type tested prior to diffusion using a hot probe technique and all indicated p-type substrates. The samples were then diffused at 1000°C for approximately 10 minutes to a sheet resistance of 10-15 ohms/□. After diffusion the samples were ground at an angle of 1°9' to the horizontal and stained using commercial preparations. The results are shown in Figures 8-10. Figure 8 is a photomicrograph of the control semicrystalline sample. This specimen contained an example of a non-crystallographic grain boundary and two twin boundaries. It can be seen

that the diffusion has penetrated about 35 microns down the grain boundary but that there is no evidence of any diffusion down the twin boundaries. Figure 9 is a photomicrograph of diffused sample containing a pure dislocation subgrain boundary. It can be seen that there is only a slight penetration of the diffusant down this type of boundary, as indicated by the arrows. Thus, from these two samples, it seems unlikely that dislocations alone can be responsible for the shunting observed in devices fabrication on mush wafers. Figures 10a and 10b are photomicrographs of the mush samples. The sample shown in Figure 10a has been diffused while the one shown in Figure 10b was not. Since both samples indicate a staining at the grain boundary it may be possible that the shunt paths found in this material are due to impurities segregated into the grain boundaries as well as by phosphorous diffusing down the grain boundaries.

It can be seen from the preceeding discussion why this material exhibits such a poor photovoltaic response when processed into solar cells. The high stress concentration and associated high dislocation density both in the bulk and at the grain boundaries is responsible for the low minority carrier lifetime observed in this material while impurities and/or diffusion down the grain boundaries are responsible for shunting these devices.

In addition to the studies just discussed, the grain morphology of this material was also studied. As noted above, while examining this mush region, one would observe isolated grains surrounded by a larger matrix grain. This is dramatically illustrated in the Namarski interference contrast photomicrograph, Figure 11, of one of these regions. As expected from the orientation studies these islands grains all exhibit the same etch texture, further indicating that they all posses the same orientation. If one looks in the longitudinal direction at one of these areas, the crystal growth pattern shown in Figure 12 can be observed. Here, it can be seen that there are two grains growing together in a lamellar type of structure. The degeneration into this type of structure is characteristic of grain growth in solute rich melts.

The final study that was carried out on this material was a detailed microscopic investigation of this mush region. A 2 cm x 2 cm sample from the upper left hand corner of the wafer adjacent to the one shown in Figure 2 was mechanically polished to a 1 micron finish with diamond grit. Figure 13 is a relatively low, 100x, magnification dark field illuminated photomicrograph of the mush area with the sinuous grain boundaries. The grain boundaries show up as the white serpentine lines. Under high magnification (1000x) these line revealed themselves as a series of dots, approximately 1μ m across. It is observed that these dots are not angular as would be expected if they were inclusions, but rather the corners are soft and rounded as would be expected from liquid entrapment as the primary field of silicon freezes. Figure 14 is the identical area from the CP etched wafer shown in Figure 2. It can be seen from this photomicrograph the highly textured nature of the grain volumes. In order to see the development of the island nature of these grains one can see the isthmus marked with an arrow in Figure 14 has completely disappeared in Figure 13. The two wafers are approximately 700 μ m apart.

In optical microscopy there is not enough depth of field to reveal any detail in the grain boundary of the etched wafer so a scanning electron microscope was used to further investigate this sample. The area marked with an "0" in Figure 14 was chosen for investigation. Since this is a region where several sinuous boundaries join, a greater evidence of solute should be expected in this region. Figure 15 is a scanning electron photomicrograph of this region. In this figure the deep trench like nature of the grain boundaries can be observed and in the center of these trenches a fiberous residue can be seen. This residue was chemically analyzed by electron microprobe techniques using wavelength dispersive spectroscopy, and it was found to be silicon carbide. Figure 16 is a high magnification image, approximately 2500x, of the large precipitate found at "0". As can be seen from this figure that the residue does not appear to have a well defined crystal morphology. Further investigation into the nature of this material are planned. A similar structure, which was identified as silicon carbide, was also found in Heat Exchanger Method (HEM) produced silicon (13).

From the preceeding discussion on the nature of this mush zone material, i.e. the highly strained nature of the grains, the morphology of the grains that make up this area, and the nature of the sinuous grain boundaries with the solute trapped at the boundaries, it is felt that the onset of this structure is driven by a constitutional supercooling of the melt (14).

In order to ascertain, in a general way, the effects of constitutional supercooling on the solidifying ingot it is possible to apply one of the models for solute redistribution to the current system. One of the earlier models was developed by Tiller et. al. (15). This model assumed that the solidification front is planar, that the segregation coefficient, which is the ratio of the equilibrium concentration of solute in the solid to the liquid at the interface and is denoted by "k", was constant over the entire freezing range, that diffusion in the solid was negligible, and that there was no mixing of the melt to aid in solute redistribution. This model was later extended by Burton, Prim, and Slichter to account for complete solute redistribution in the liquid beyond a dead layer of width β as would be expected in Czochralski growth (16).

In the present system, mixing of the melt would only be accomplished by convective means and since at present there is no good way of estimating the fluid dynamics of the system, the Tiller model was used in the following analysis.

If we assume that the initial impurity concentration is given by C_o, then from the definition of the segregation coefficent the amount of impurity incorporated into the initial volume solidified will be given by kC_o. As the solidification progresses the solute will increase ahead of the freezing front and more and more impurities will be incorporated into the solid until a steady state value of C_o is reached. By considering the dynamics of the system, the impurity concentration in the solid as a function of distance solidified, x, can be written as (15)

$$C_s = C_o \left\{ (1-k) \left[1 - \exp\left(-k \frac{R}{D_L} x\right) \right] + k \right\} \quad (1)$$

where, R is the solidification rate in cm/sec and D_L is the diffusion coefficient in the liquid in cm^2/sec. From the definition of the segregation coefficent given above the amount of solute at the liquid-solid interface is simply given by

$$C_T = C_s/k \quad (2)$$

Since there is no mixing of solute in the melt the value of C_T must decay back to the equilibrium concentration of C_o some distance away from the interface. The shape of this transient is given by

$$C_\alpha = C_o \left\{ \frac{1-k}{k} \left[1-\exp\left(-k \frac{R^2}{D_L} t\right) \right] \exp\left(-\frac{R}{D_L} (x'-Rt)\right) + 1 \right\} \quad (3)$$

where, x' is the distance ahead of the freezing front.

In order to compare this model to the experimental results obtained in this study, it is necessary to make some estimate of the initial impurity concentration. This can be accomplished by considering the mush region a right circular cone 10 cm in height with a radius of 7 cm. Included in this volume are cylindrical grains with a diameter of 0.05 cm and a length of 4.5 cm. These grains are covered with a skin of solute 0.5 microns thick. Calculating the total amount of solute trapped in this volume and dividing it back into the total volume of silicon present one obtains a value for C_o of 2×10^{18} atoms/cm^3.

The diffusion coefficient, D_L, for most impurities in liquid silicon is between 1.5×10^{-4} and 5×10^{-4}/sec so for convenience a value of 1×10^{-4} cm^2/sec was chosen for this analysis (17). The solidification rate for this mush ingot was 5.3×10^{-4} cm/sec. If we assume that the major impurity is carbon with a segregation coefficient of 0.05 then we can evaluate the above expressions (17). The results are shown in Figure 17. It can be seen that even with a modest segregation coefficent of 0.05 that equilibrium solidification has not occurred for most of the ingot height. The final transient rise is solute concentration which will occur in the last two centimeters to freeze was not included in this analysis as it does not pertain to the grain growth breakdown due to constitutional supercooling.

It can be seen from Figure 17 that the impurity concentration in the solid is in the range of $5\text{-}10 \times 10^{17}$ atoms/cm^3. FTIR measurements on UCP semicrystalline material have been about 5×10^{17} atoms/cm^3 for carbon. Thus, it is felt that the numbers used in this analysis are approximately correct.

Constitutional supercooling of the melt will occur when the thermal gradient in the melt is less than the liquidus temperature. From heat and mass flow at this interface the general constitutional supercooling criteria is given by (5)

$$\frac{G_L}{R} \geq \frac{m_L\ C_s\ (1-k)}{k\ D_L} \tag{4}$$

where G_L is the thermal gradient in the liquid and
m_L is the slope of the liquid curve

Thus, for a specific impurity concentration there is a ratio of the thermal gradient in the liquid to the solidification rate below which the grain growth will breakdown.

In the present example an estimate of where the breakdown will occur can be obtained by combining equation 1 and 4 and solving for x. Performing the algebra one obtains

$$x = \frac{D_L}{R} \ln \left\{ - \frac{\frac{G_L\ k\ D_L}{R m_L\ (1-k) C_o} - k}{1-k} \right\} \tag{5}$$

For dilute solutions the liquidus slope depends on the number rather than the kind of atoms present. A value of -464°C (at. fract.)$^{-1}$ can be obtained from the data of Thurmond and Kowalchick for this slope (17)(18). From the thermocouple measurements a value of 0.8°C/cm was obtained for the thermal gradient in the liquid. Substituting these value into Equation 5, one obtains a distance of 1.5 cm for the breakdown in grain growth to occur. In actuallity the breakdown occurs at a distance of about 3 cm from the onset of crystallization. From all of the estimations that were used in obtaining these numbers it is felt that the experiment is in fairly good agreement with the theory.

CONCLUSIONS

In the preceding discussion it was shown that under certain conditions the large grain UCP material will breakdown into a cellular type of structure. This breakdown, as predicted by the theory of constitutional supercooling, is the result of solute building up in the liquid as solidification progresses. The resultant grain structure is characterized by crystallites of small cross section growing together in a lamellar type of structure separated by sinuous grain boundaries. Orientation studies using the electron channeling mode of the scanning electron microscope have shown that these grains possess a nearly coincident <110> type of direction with a 4° misfit and a rotation of approximately 20° about the <110>.

Optical and scanning electron microscopy have indicated the presence of a liquid second phase trapped in the sinuous grain boundaries after the primary field of silicon has frozen. Etching and microscopic studies have revealed a fiberous nature to this traped solute. Electron microprobe analysis of this fiberous material has shown silicon carbide to be one of its constituants. As the impurity concentration is increasing in the solid, it can be seen from the X-ray topographic studies that the dislocation content is also increasing. As grain growth proceeds the dislocations coalesce to form the sinuous grain boundaries.

Historically, solar cells fabricated on this material have performed poorly. It is now felt that degraded performances is due to low minority carrier lifetimes caused by the highly dislocated nature of this material and due to shunt paths created, in part, by the solute trapped in the grain boundaries.

Ultimately the rate of solidification in ingot technologies such as UCP is dictated by the general constitutional supercooling criteria. In photovoltaics, the thrust has been to lower the cost of producing material by lowering the energy input into the solidification process, which will tend to lower the thermal gradient in the liquid silicon, and to use less pure starting material (so called solar grade silicon). The criteria for the breakdown of grain growth states that the rate of solidification is proportional to thermal gradient and inversely proportional to the impurity concentration. Thus, as the thermal gradient is lowered and the impurity content increased the rate of solidification must decrease so that the inequality is preseved. This means that in order to produce high quality material, there is a practical upper limit to the rate of solidification that can be achieved under these conditions.

REFERENCES

1) Morrison, A.D., "Microstructure of Semicrystalline Silicon," Proceedings of the 13th IEEE Photovoltaics Specialist Conference, Washington, D.C., 1978.

2) Armstrong, R.W., M.E. Taylor, G.M. Storti, and S.M. Johnson, "The Relative Orientations of Grains and the Nature of Grain Boundaries in Polycrystalline Solar Cells," Proceedings of the 14th IEEE Photovoltaics Specialist Conference, San Diego, 1980.

3) Storti, G.M., S.M. Johnson, H.C. Lin, and C.D. Wang, "The Influence of Grains and Grain Boundaries on the Device Characteristics of Polycrystalline Silicon Solar Cells," Proceedings of the 14th IEEE Photovoltaic Specialist Conference, San Diego, 1980.

4) Putney, Z.C., W.F. Regnault, "Grain Boundary Defects in Thin Semicrystalline Material," Solar Cells, 1, 285, 1980.

5) Flemings, M.C., Soldification Processing, McGraw-Hill, New York, 1974.

6) Regnault, W.F., K.-C. Yoo, S.M. Johnson, G. Breidenthal, R.G. Rosemeier, C.D. Wang, R.W. Armstrong, H.C. Lin, "Investigation of the Microstructure and Photovoltaic Properties of Semicrystalline Silicon," Proceedings of the Electrochemical Society Spring Meeting, Montreal, 1982.

7) Regnault, W.F., K.-C. Yoo, R.G. Rosemeier, S.M. Johnson, "Structural Characterization of Large Grain Semicrystalline Silicon," Presented at the annual meeting of the Materials Research Society, Boston, November 1982, to be published.

8) Johnson, S.M., K.-C. Yoo, H.C. Lin, R.G. Rosemeier, P. Soltani, "The Interface Structure of Grain Boundaries in Polysilicon," Defects In Semiconductors II, North-Holland, New York, 1983.

9) Johnson, S.M., R.W. Armstrong, R.G. Rosemeier, G.M. Storti, H.C. Lin, W.F. Regnault, "An Enchanced Photoresponse at Dislocation Subgrain Boundareis Revealed by X-ray Topography of Polysilicon Solar Cells," Grain Boundaries in Semiconductors, North-Holland, New York, 1982.

10) Ast, D.G., B. Cunningham, H. Strunk, "EBIC/TEM Investigation of Defects in Solar Cell Silicon," Grain Boundaries in Semicondcutors, North-Holland, New York, 1982.

11) Joy, D.C., D.E. Newbury, D.L. Davidson, "Electron Channelling Patterns in the Electro Microscope," J. App. Phys., 53, R81, 1982.

12) Storti, G.M., W.F. Regnault, S.M. Johnson, H.C. Lin, R.W. Armstrong, "Investigation of the Impurity Tolerance of Semicrystalline Silicon Solar Cells Silicon Impact Program," Final Report, Contract No. XS-9-8272-1, 1980.

13) Schmid, F., C.P. Khattak, T.G. Diggs, Jr., L. Kaufman, "Origin of SiC Impurities in Silicon Crystal Grown from the Melt in Vacuum," J. Elect. Chem. Soc., 126, 935, 1979.

14) Rutter, J.W., B. Chalmers, "A Prismatic Substructure Formed During Solidification of Metals," Cand. J. Phys. 31, 15, 1953.

15) Tiller, W.A., K.A. Jackson, J.W. Rutter, B. Chalmers, "The Redistribution of Solute Atoms During the Solidification of Metals," Acta. Met. 1, 428, 1953.

16) Burton, J.A., R.C. Prim, W.P. Slichter, "The Distribution of Solute in Crystals Grown from the Melt," J. Chem. Phys. 21, 1987, 1953.

17) Hopkins, R.H., J.R. Davis, A. Rohatgi, M.H. Hanes, P. Rai-Chaudbury, H.C. Mollenkopf, "Effects of Impurities and Processing on Silicon Solar Cells," Final Report Contract # 954331, 1982.

18) Thurmond, C.D., M. Kolalchick, "Germanium and Silicon Liquidus Curves," Bell Syst. Tech. J. 39, 169, 1960.

Figure 1a

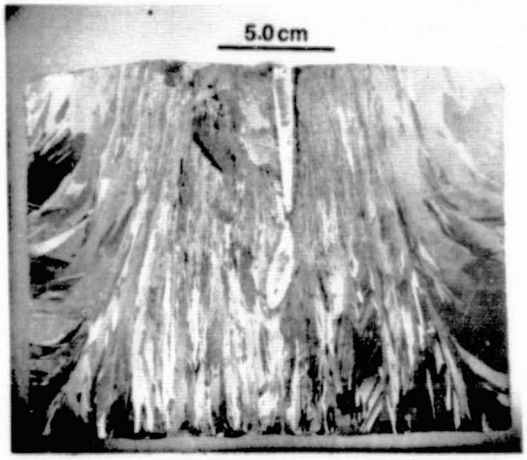

Figure 1b

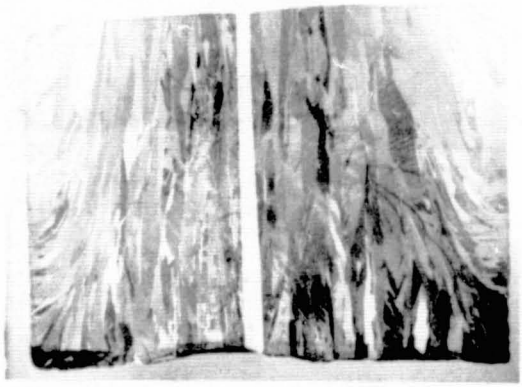

Longitudinal section through the middle of the mush and control ingots, respectively

Figure 2

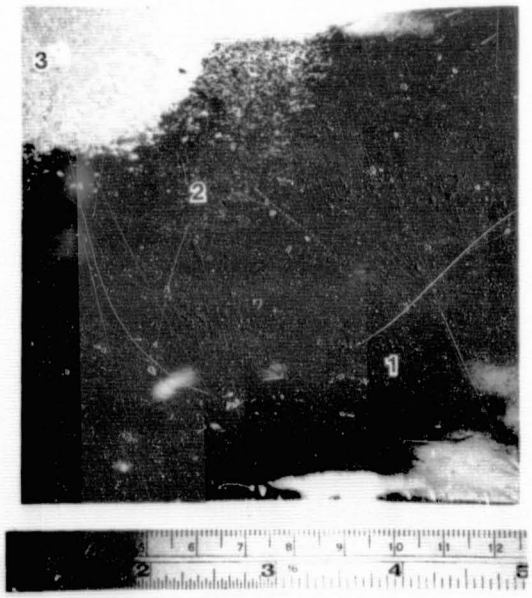

Chemical-polish-etched wafer from the middle of mush-containing ingot showing three distinct regions, each with different etch characteristics

Figure 3

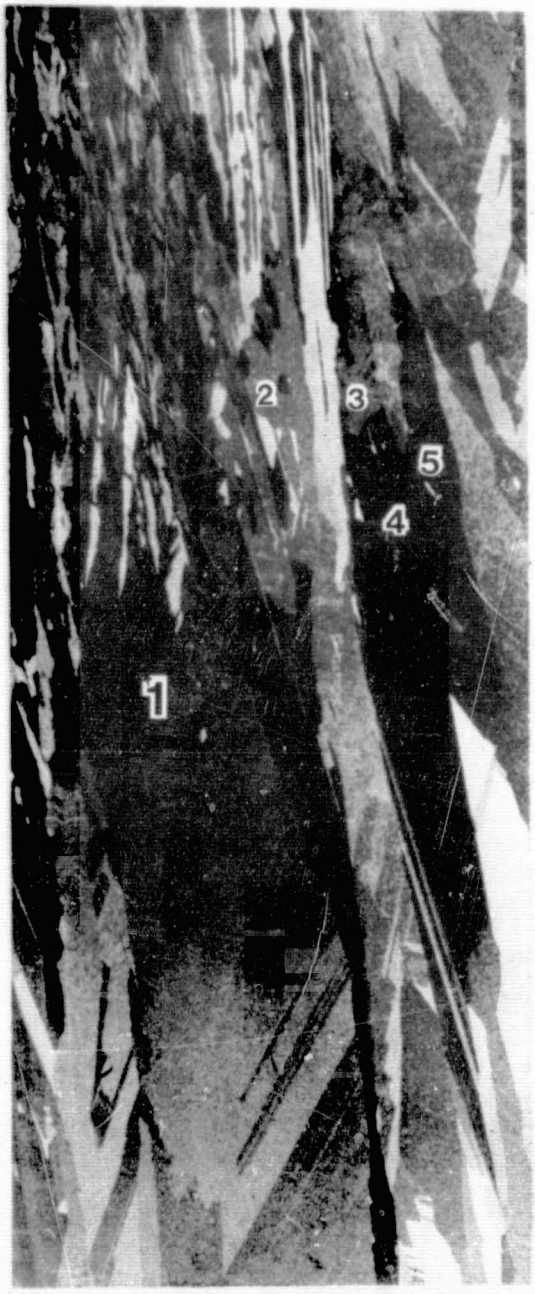

Longitudinal section showing breakdown of large grains into sinuous grain boundaries and mush

Figure 4

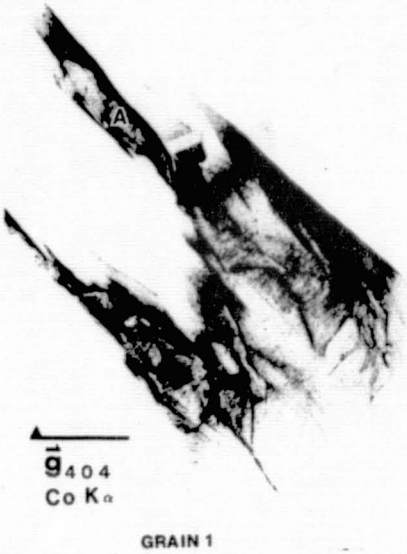

Berg-Barrett X-ray topograph of grain 1, shown in Figure 3, employing (404) as the reflecting plane

Figure 5

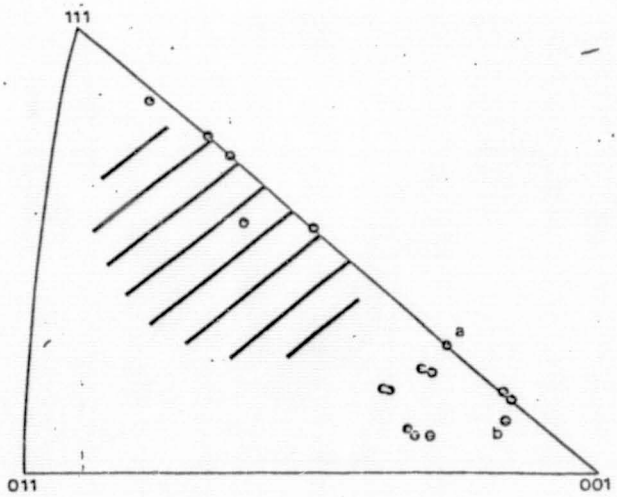

Plot of the surface normals of mush grains on the silicon unit triangle; shaded area indicates region of surface normals of non-mush grains

Figure 6

SEM photo of several grains used in the orientation analysis. Surface normals of grains a and b are shown in Figure 7

Figure 7

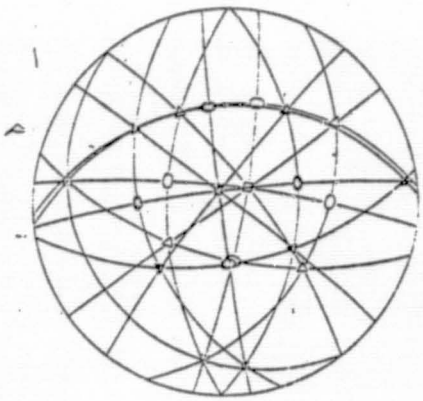

Complete stereographic projection of grains a and b showing severed degree misfit from perfect second-order twin relationship with coincident (110) directions

Figure 8

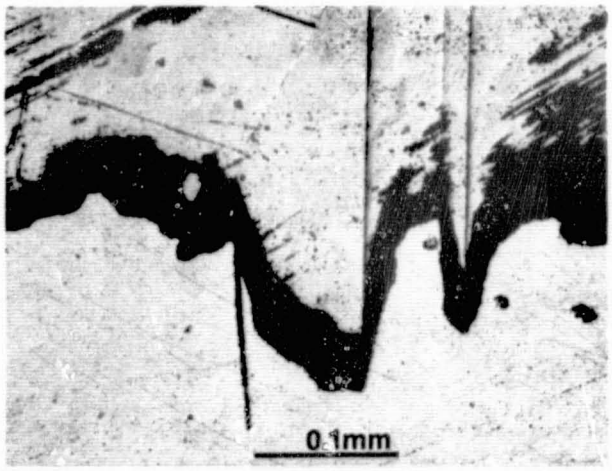

Beveled and stained diffused junction sample showing diffusion down grain boundary and no diffusion down twin boundaries. Bevel angle is $1^{o}9'$

Figure 9

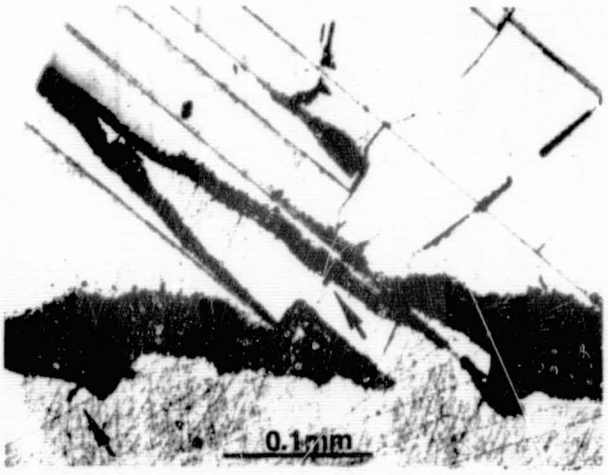

Beveled and stained diffused junction sample showing a slight diffusion down a dislocation subgrain boundary. Bevel angle is $1^{o}9'$

Figure 10a

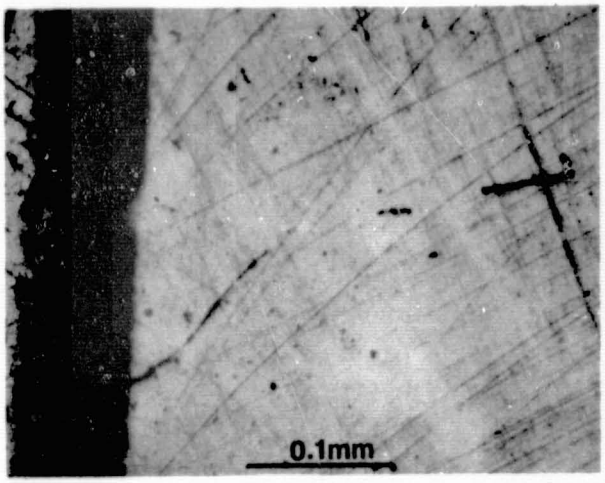

Beveled and stained diffused junction mush sample indicating junction formation deep into sample. Bevel angle is $1^{o}9'$

Figure 10b

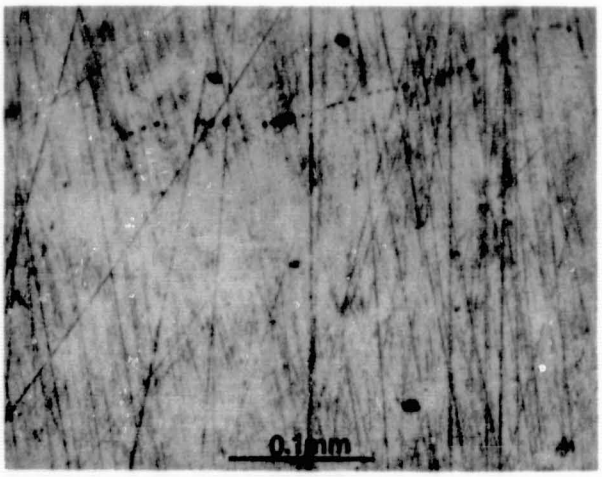

Beveled and stained mush sample that was not diffused also showing N-type regions at the grain boundries. Bevel angle is $1^{o}9'$

Figure 11

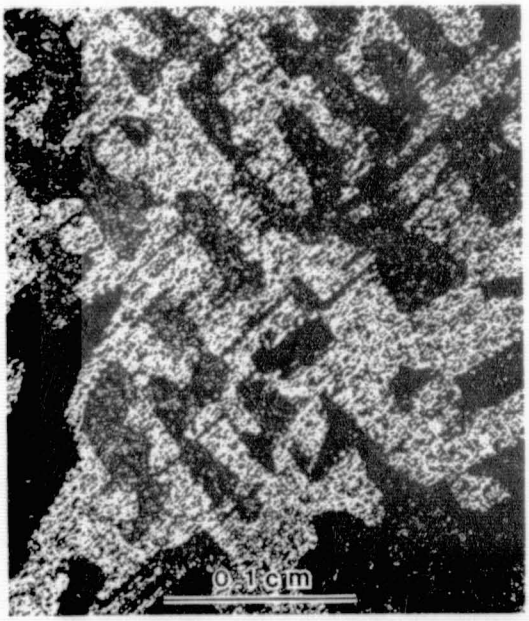

Namarski interference contrast photomicorgraph of mush area showing numerous isolated grains of the same orientation contained in a host matrix grain

Figure 12

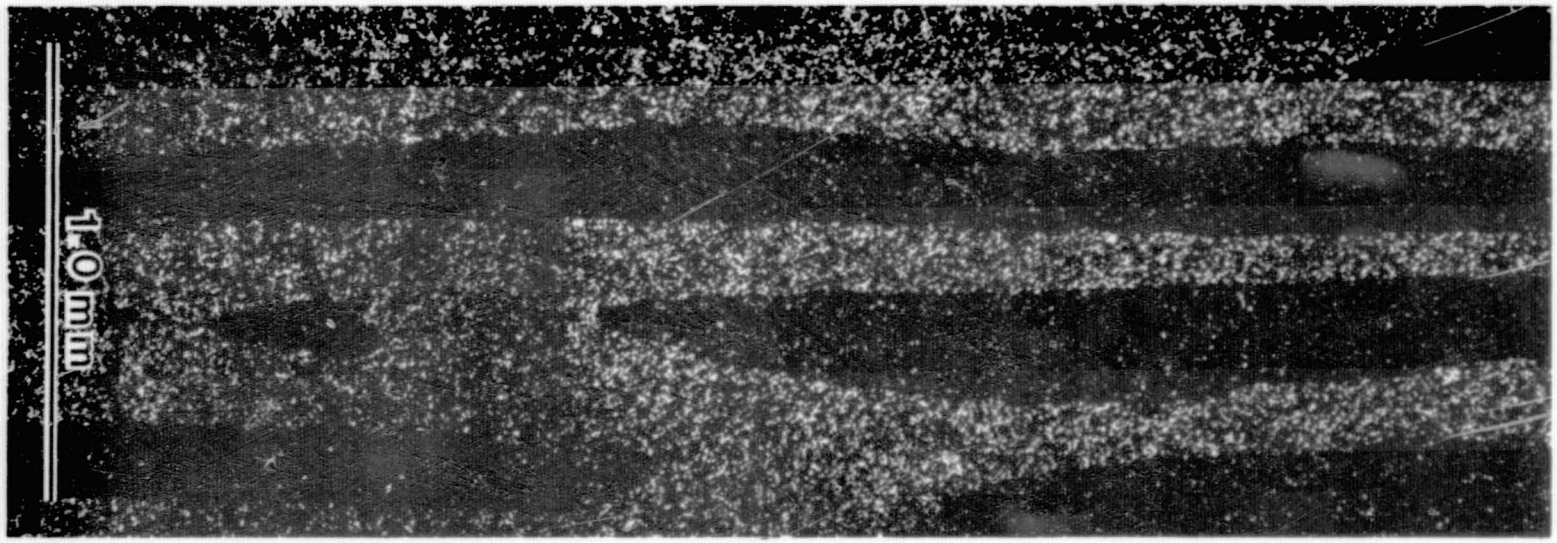

Namarski interference contrast photomicrograph of mush grains growing together in a lamallar structure

Figure 13

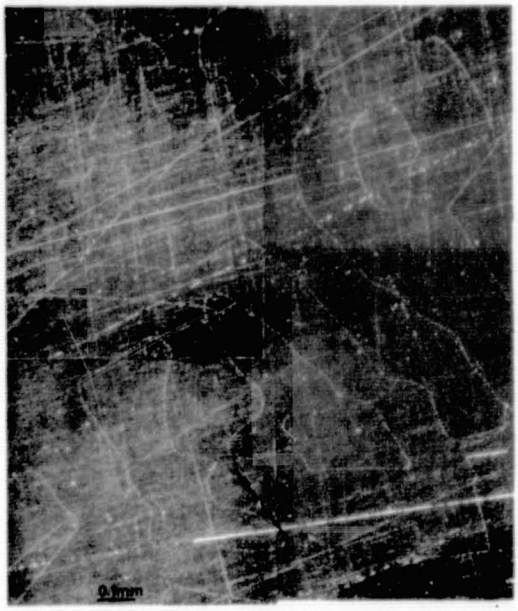

Dark-field-illuminated photomicrograph of mechanically polished mush region showing sinuous grain boundaries as white serpentine lines

Figure 14

Dark-field-illuminated photomicrograph of chemically polished mush region as shown in Figure 13

Figure 15

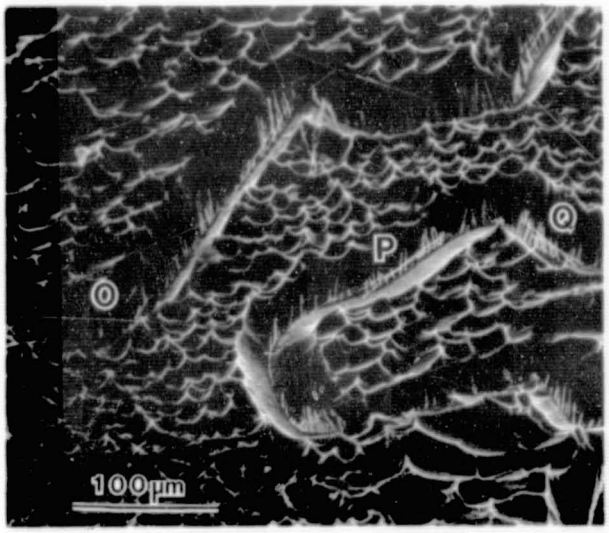

SEM photo of region "O" in Figure 14; note highly textured surface and trenghlike appearance of sinuous grain boundaries

Figure 16

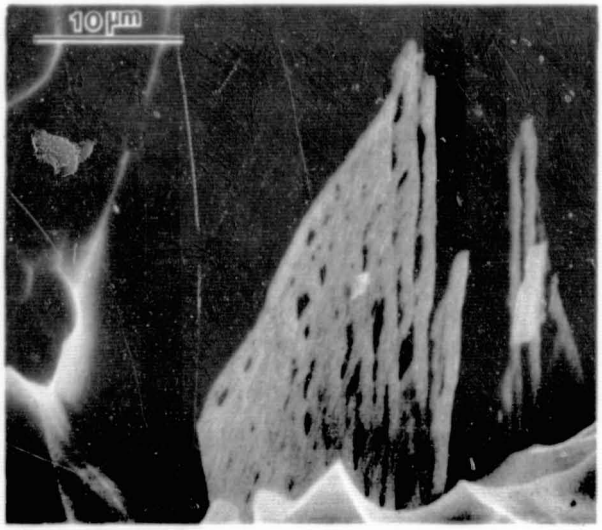

High-magnification SEM photo of perpetration found at "O" in Figures 14 and 15

Figure 17

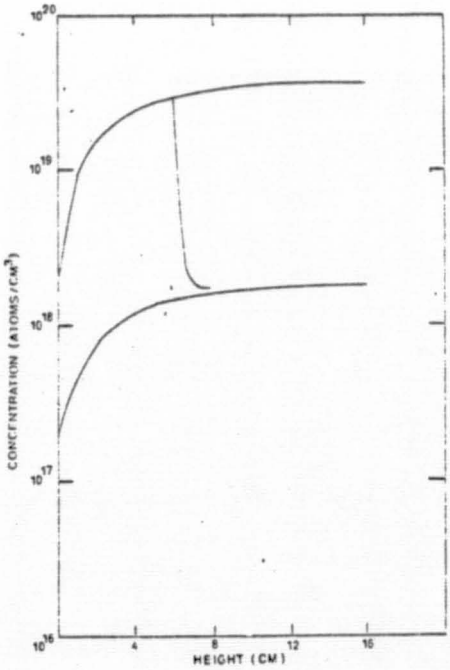

Solute redistribution curves based on model by Tiller et al

DISCUSSION

RAVISHANKAR: In the first couple of slides you indicated two different growth rates. One was 1.9, the other was 3.3 centimeters per hour. I wasn't sure if they were UCP or some other crystal-growth method.

REGNAULT: The ingots we produced for this study were produced at the first two growth rates of 1.9 and 1.6. The 3.3 is an ingot that we produced in the lab trying to get the growth speed up. They are all UCP crystals.

RAVISHANKAR: So why was it that you didn't see this happening at 3.3 centimeters per hour?

REGNAULT: Cleaner melt.

RAVISHANKAR: You can see the same sort of sinuous grain boundaries, mushy grain boundaries with superclean melts, by just growing it a bit too fast, and this is not the way constitutional supercooling shows up itself. In constitutional supercooling, you see more like what Dieter Helmreich showed, and also the way Westinghouse has demonstrated Czochralski growth, when that happens. This seems to be more related to heat transfer limitations than impurity limitations.

REGNAULT: Have you etched it to see what the etching characteristics of the material are?

RAVISHANKAR: Yes. It looks exactly like what you see. We were planning to do it ourselves, and you have saved us a lot of work. Have you ever answered the question of why a columnar grain stops growing and a second grain decides to nucleate, instead of the first grain continuing to grow all the way?

REGNAULT: No, not really. Just through some mechanism it has developed a twinning relationship, and a second grain nucleates off of it.

LEIPOLD: You implied, but didn't explicitly state, that there was nothing else in those precipitates but carbon, by wavelength analysis.

REGNAULT: We have only looked for the two components. I suspect that there probably are other things in it.

WARGO: I would like to make a couple of comments, and I hope a couple of suggestions for you. First of all, your use of the Tiller treatment in a segregation analysis isn't really all that appropriate. It assumes no convection. If you take a look at the shape of your interface, the radial temperature gradients must be absolutely fierce. We did some work growing semiconductor materials directionally in space in a microgravity environment, where you expect to at least approach diffusion control growth. When you compare that with ground-based studies, those characteristic distances can change by an order of magnitude as to when you approach some steady-state value. What I might suggest to you is to

work more with a generalized directional-freezing equation where you assume, not zero boundary layer or film thickness, but one that is controlled by the hydrodynamics. I think you will come into a much better agreement because if you look you see that your characteristic distance is larger than than what is predicted. The other thing that is not accounted for in that transient prediction in the Tiller treatment is there is no melt enrichment until you get to the end of the crystal. When you use a modified directional-freezing condition, you will have that melt enrichment, which will give rise to that increase in solute distribution, which will force the interface to break down.

REGNAULT: I don't have any feel for what the convective currents are in the material. The thermal properties are measured along the center line of the ingot, and I just picked the model because, again, the assumptions that I was making are very crude in nature. I don't have a good quantifiable number to say 'this is the impurity concentration in the beginning,' and I am surprised that with the assumptions I made that it came out as well as it did.

WARGO: What is nice about the directional solidification treatment is, all that it really assumes is conservation of mass. The only problem that you might have with that in terms of segregation is that you can load up grain boundaries and dislocations with a lot of junk. So conservation of mass appears not to hold, unless you try to count all that stuff.

REGNAULT: Once grain growth breaks down, the rest of that curve was useless, because you get into a local solute distribution.

RAVISHANKAR: When we observed this sort of sinuous-grain boundaries, and when we Secco etch them, we found out that the dislocation density of the intergrain material, inside what you call a fibrous material, or the number of those grains which were dislocation free, weren't any different from normal grains that we would observe otherwise.

REGNAULT: We are seeing a big pileup in the dislocation density.

RAVISHANKAR: The appearance of the grains is exactly like what you showed; they are raised up from the surface when you etch them, and they go round and round like worms, just like you saw.

REGNAULT: There must be some dislocations showing up in the grain boundaries that are being gettered out of the grain volumes, or something like that.

RAVISHANKAR: The amount of that material dislocated is not much different from a normal grain.

MORRISON: You have described growth in systems with more and less pure silicon at growth rates varying by a factor of 2. Can give us an idea of what the growth rate is in the material we see now, in the production cells that come out of Solarex?

REGNAULT: We are constantly evolving the UCP process. The material that we started with in the JPL program was grown about 1.5 to 2 cm/h growth rate. We are working on ways of trying to get the growth rate up.

APPENDIX A: SPEAKER AND (AUTHOR) INDEX

C-8

APPENDIX B: PARTICIPANT LIST

HIGH-SPEED GROWTH & CHARACTERIZATION OF CRYSTALS FOR SOLAR CELLS

RESEARCH FORUM

ABBASCHIAN, G. J., Professor
University of Florida
Materials Science and Engineering Dept.
Gainesville, FL 32611
(904) 392-6609

AST, Dieter
Cornell University
123 Day Hall, P. O. Box DH
Ithaca, NY 14853
(607) 256-4140

BATES, Herbert E.
Energy Materials Corp.
Sterling Rd., Box 1143
So. Lancaster, MA 01561
(617) 365-7383

BELOUET, Christian
Laboratoires de Marcoussis
Route de Nozay
Marcoussis, France 91460
(6) 449.12.37

BRIGLIO, Anthony
Jet Propulsion Laboratory
4800 Oak Grove Dr., M.S. 238-343
Pasadena, CA 91109
(818) 354-4883

BROWN, Robert A.
Massachusetts Institute of Technology
66-544 MIT
Cambridge, MA 02139
(617) 253-5726

CHALMERS, Bruce
Harvard University
Pierce Hall
Cambridge, MA 02138
(617) 548-7770

CHEN, Chern "Bing"
Jet Propulsion Laboratory
4800 Oak Grove Drive, M.S. 67/201
Pasadena, CA 91109
(818) 354-5353

CHEN, Chenson K.
Research Staff
Lincoln Laboratory, C-232
P.O. Box 73
Lexington, MA 02173
(617) 863-5500, X4502

CISZEK, Ted F.
Solar Energy Research Institute
1617 Cole Blvd.
Golden, CO 80401
(303) 231-1769

COULBERT, Cliff
Jet Propulsion Laboratory
4800 Oak Grove Dr., M.S. 67-201
Pasadena, CA 91109
(818) 354-2610

CULLIS, A. G.
Royal Signals & Radar Establishment
St. Andrews Rd.
Malvern, Worcs., WR14 3PS
England
(UK) 6845-2733 X2509

DANYLUK, Steven
University of Illinois
P.O. Box 4348
Dept. of Civil Eng. Mech. & Metall.
Chicago, IL 60680
(312) 996-2437

DILLON, Oscar W.
University of Kentucky
Department of Engineering Mechanics
Lexington, KY 40506
(606) 257-3775

DUMAS, Katherine A.
Jet Propulsion Laboratory
4800 Oak Grove Dr., M.S. 238-343
Pasadena, CA 91109
(818) 354-6546

DURANCEAU, J.
Massachusetts Institute of Technology
66-544 MIT
Cambridge, MA 02139
(617) 253-5726

ETTOUNEY, Hisham M.
Massachusetts Institute of Technology
66-544 MIT
Cambridge, MA 02139
(617) 253-5726

FAN, John C. C.
MIT Lincoln Laboratory
Electronic Materials Group
P.O. Box 73
Lexington, MA 02173-0073
(617) 863-5500, X 7836

FERBER, Robert R.
Jet Propulsion Laboratory
4800 Oak Grove Drive, M.S. 502-404
Pasadena, CA 91109
(818) 577-9396

GIESSEN, William
Northeastern University
Institute of Chemical Analysis
360 Huntington Ave., 341 Mugar
Boston, MA 02115
(617) 437-2827

GILMER, George H.
Bell Labs
600 Mountain Ave., Rm 1D447
Murray Hill, NJ 07974
(201) 582-5547

GLICKSMAN, Martin E.
Rensselaer Polytechnic Institute
Materials Research Center - 102
Materials Engineering Dept.
Troy, NY 12181
(518) 270-6372

GRABMAIER, Josef G.
Siemens AG Research Laboratories
Otto Hahn Ring 6
D8000, Munchen 83
West Germany
(089) 636-44680

HELMREICH, Dieter
Heliotronic GmbH
Burghausen
Postfach 1129
West Germany, D8263
08677/83-2736

HURD, Jeff L.
Solar Energy Research Institute
1617 Cole Blvd.
Golden, CO 80401
(303) 231-1779

JASKIE, Jim
Solavolt International
P. O. Box 2934
Phoenix, AZ 85062
(602) 231-6460

JEWETT, David N.
Energy Materials Corp.
Sterling Rd., Box 1143
So. Lancaster, MA 01561
(617) 365-7383

JOHNSON, Scott M.
Solarex Corporation
1335 Piccard Drive
Rockville, MD 20850
(301) 948-0202

KALEJS, Juris P.
Mobil Solar Energy Corp.
16 Hickory Dr.
Waltham, MA 02254
(617) 890-0909

KOCHKA, E. (Ed)
Westinghouse Electric Co.
P. O. Box 10864
Pittsburgh, PA 15236
(412) 892-5600

KOLIWAD, Kris
Jet Propulsion Laboratory
4800 Oak Grove Dr., M.S. 238-343
Pasadena, CA 91109
(818) 354-5197

LAMBROPOULOS, John C.
Division of Applied Sciences
323 Pierce Hall
Harvard University
Cambridge, MA 02138
(617) 495-3248

LANE, Richard L.
Director of Technology
Kayex Corporation
1000 Millstead Way
Rochester, NY 14624
(716) 235-2524

LEIPOLD, Martin
Jet Propulsion Laboratory
4800 Oak Grove Dr., M.S. 507-231
Pasadena, CA 91109
(818) 577-9267

LIEBERMANN, Howard H.
Senior Metallurgist
Metglas Products - An Allied Company
6 Eastmans Road
Parsippany, NJ 07054
(201) 455-6145

LIN, Wen
Bell Laboratories
555 Union Blvd.
Allentown, PA 18103
(215) 439-6663

LIU, James
Jet Propulsion Laboratory
4800 Oak Grove Dr., M.S. 238-343
Pasadena, CA 91109
(818) 354-6500

LOFGREN, Dwight K.
Atlantic Richfield
515 South Flower St., Rm 1730
Los Angeles, CA 90071
(213) 486-2230

MAEDA, Yasuhiro, Manager
Hoxan Research Laboratories
Hoxan Corporation
5-2 Kikusui, Shiroishi-ku
Sapporo, Japan 003
(011) 823-0252

MAYO, William E.
Rutgers University
Dept. Mechanics & Mat. Sci.
P. O. Box 909
Piscataway, NJ 08854
(201) 541-5507

McKEE, William R.
Manager, Solar Cell Development
Texas Instruments Inc.
P.O. Box 225303, M/S 158
Dallas, TX 75265
(214) 995-6577

MILSTEIN, Joseph
Solar Energy Research Institute
1617 Cole Blvd.
Golden, CO 80401
(303) 231-7299

MOKASHI, Anant
Jet Propulsion Laboratory
4800 Oak Grove Dr., M.S. 238-343
Pasadena, CA 91109
(818) 354-6017

MOODY, Jerry
Monsanto Company
P. O. Box 8, 501 Old Highway 79
St. Peters, MO 63376
(314) 272-6281

MORRISON, Andrew D.
Jet Propulsion Laboratory
4800 Oak Grove Drive, M.S. 238-343
Pasadena, CA 91109
(818) 354-7200

NARASIMHAN, M. C.
Stam, Inc.
885 Watermann Ave.
E. Providence, RI 02914
(401) 438-6784

PETRICK, S. Walter
Jet Propulsion Laboratory
4800 Oak Grove Drive, M.S. 157-102
Pasadena, CA 91109
(818) 354-2869

PHILLIPS, Mary J.
Jet Propulsion Laboratory
4800 Oak Grove Drive, M.S. 502-422
Pasadena, CA 91109
(818) 577-9096

RAO, C. V. Hari
Mobil Solar Energy Corp.
41 Suburban Para Dr.
Billerica, MA 01821
(617) 893-8826

RAVI, K. V.
Mobil Solar Energy Corp.
16 Hickory Drive
Waltham, MA 02254
(617) 890-0909

RAVISHANKAR, P. S.
Exxon Research & Engineering Company
P.O. Box 45, E-1-3004
Linden, NJ 07036
(201) 474-2405

REGNAULT, William F.
Semix Inc.
15801 Gaither Drive
Gaithersburg, MD 20877
(301) 948-4680, X 59

ROSEMEIER, Ronald G.
Brimrose Corp. of America
7527 Belair Rd.
Baltimore, MD 21236
(301) 668-5800

SACHS, Emanuel
Arthur D. Little
Acorn Park
Cambridge, MA 92140
(617) 864-5770 X2458

SCHWUTTKE, Guenter
GHS Research and Development
8162 E. Del Pico Dr.
Scottsdale, AZ 85258
(602) 951-0422

SCOLARO, Anthony F.
U. S. Department of Energy
Forrestal Building, CE-333
Washington, DC 20585
(202) 252-5548

SEIDENSTICKER, Raymond G.
Westinghouse Research Laboratories
1310 Beulah Rd.
Pittsburgh, PA 15235
(412) 256-3484

SEKERKA, Robert F.
Carnegie Mellon University
Dean of Mellon College of Science
Scaife Hall, 115
Pittsburgh, PA 15213
(412) 578-2484

SHAPIRO, Hymin
Ethyl Corp.
P. O. Box 341
Baton Rouge, LA 70821
(504) 359-2230

SHIH, Choon-Foo
Jet Propulsion Laboratory
4800 Oak Grove Drive, M.S. 157-316
Pasadena, CA 91109
(818) 354-7014

SMITH, Bruce
Solavolt International
P. O. Box 2934
Phoenix, AZ 85062
(602) 231-6434

SUREK, Thomas
Solar Energy Research Institute
PV Programs Office
1617 Cole Blvd.
Golden, CO 80401
(303) 231-1371

TRIVEDI, Rohit
Iowa State University-Ames Laboratory
100 Metallurgy Building
Ames, IA 50010
(515)294-5869

TUSTIN, David G.
Jet Propulsion Laboratory
4800 Oak Grove Drive, M.S. 502-422
Pasadena, CA 91109
(818) 577-9597

WARGO, Michael
Massachusetts Institute of Technology
Room 13-4154
Cambridge, MA 02139
(617) 253-6993

WHITE, C. W.
Oak Ridge National Laboratory
Solid State Division - Bldg. 3025
Oak Ridge, TN 37830
(614) 574-6295

WHITEHOUSE, Daniel
Semix, Inc.
15801 Gaither Drive
Gaithersburg, MD 20877
(301) 948-4680

WILCOX, William R.
Clarkson College of Technology
Chemical Engineering
Potsdam, NY 13676
(315) 768-6650